NBSIR 88-3082

TECHNICAL REPORTS

MATERIALS STUDIES FOR MAGNETIC FUSION ENERGY APPLICATIONS AT LOW TEMPERATURES -XI

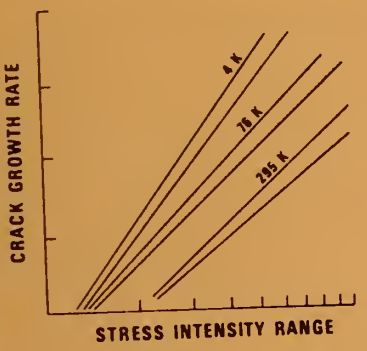

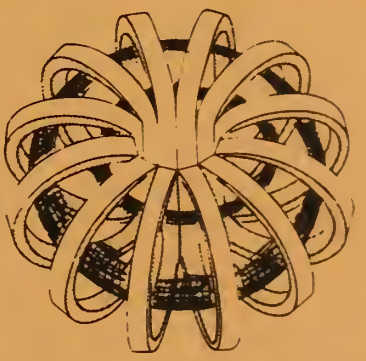

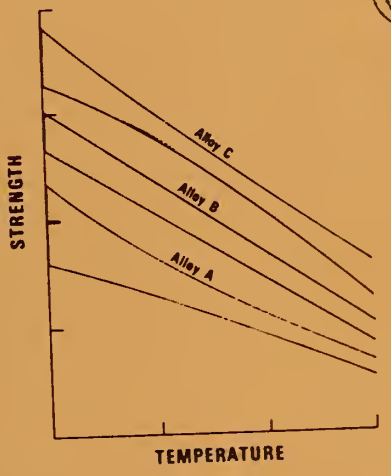

To
Department of Energy
Office of Fusion Energy
Washington, D.C. 20545

Prepared by
Fracture and Deformation Divisio
National Bureau of Standards
Boulder, Colorado 80303

UC 20b, c

NBSIR 88-3082

TECHNICAL REPORTS

MATERIALS STUDIES FOR MAGNETIC FUSION ENERGY APPLICATIONS AT LOW TEMPERATURES - XI

Edited by

R.P. Reed
Fracture and Deformation Division
National Bureau of Standards
Boulder, Colorado 80303

May 1988

Sponsored by

Department of Energy
Office of Fusion Energy
Washington, D.C. 20545

Stimulating America's Progress
1913-1988

U.S. DEPARTMENT OF COMMERCE, C. William Verity, Secretary
NATIONAL BUREAU OF STANDARDS, Ernest Ambler, Director

CONTENTS

WELDING

NONMETALLICS

TECHNOLOGY TRANSFER

UNITED STATES–JAPAN DEVELOPMENT OF TEST STANDARDS

SUMMARY

This report contains the results of a research program to determine the properties of materials that may be used in cryogenic structures for the superconducting magnets of magnetic fusion energy power plants and prototypes. Its purpose is to facilitate their design and development. The program was developed jointly by the staffs of the National Bureau of Standards and the Office of Fusion Energy of the Department of Energy; it is managed by NBS and sponsored by DOE. Research is conducted at NBS and at other laboratories through subcontracts with NBS.

Research results for 1987 are presented in technical papers under five headings that reflect the main program areas: Structural Alloys, Welding, Nonmetallics, Technology Transfer, and United States–Japan Development of Test Standards. Objectives and research highlights are summarized in the introduction to each program area.

NOTE: Certain commercial equipment, instruments, or materials are identified in this report to specify the experimental procedure adequately. In a few instances, company names are used to identify the source of specific research. In no case does such identification imply recommendation or endorsement by the National Bureau of Standards, nor does it imply that the material or equipment identified is necessarily the best available for the purpose.

ORGANIZATIONAL CONTACTS

Specific technical questions may be directed to the following people, who contributed to major aspects of the program during the fiscal year 1987.

Department of Energy, Office of Fusion Energy, Washington, D.C. 20545

Program Monitor	A. L. Opdenaker	(301) 353-4954

National Bureau of Standards, Boulder, Colorado 80303

Program Manager	R. P. Reed	(303) 497-3870 (FTS) 320-3870
Structural Alloys	M. W. Austin	(303) 497-3504
	H. Ledbetter	(303) 497-3443
	P. T. Purtscher	(303) 497-5789
	R. P. Reed	(303) 497-3870
	N. J. Simon	(303) 497-3687
	R. L. Tobler	(303) 497-3421
	R. P. Walsh	(303) 497-3818
Welding	C. N. McCowan	(303) 497-3699
	T. A. Siewert	(303) 497-3523
Nonmetallics	H. Ledbetter	(303) 497-3443
Technology Transfer	R. P. Reed	(303) 497-3870
	N. J. Simon	(303) 497-3687
United States–Japan Development of Test Standards	P. T. Purtscher	(303) 497-5789
	R. P. Reed	(303) 497-3870
	R. L. Tobler	(303) 497-3421
	R. P. Walsh	(303) 497-3818

PROGRAM DESCRIPTION

The overall objective of the program is to assist in the design, construction, and safe operation of magnetic fusion energy (MFE) systems that use cryogenic components, especially superconducting magnets. The specific steps taken to achieve this objective are: (1) evaluation of the materials research needs specific to MFE devices; (2) research programs to acquire the necessary data; and (3) effective materials technology transfer by rapid dissemination of the data to potential users through personal contacts, publications, and workshops.

Efforts directed at the first specific objective began with the publication of the "Survey of Low Temperature Materials for Magnetic Fusion Energy" in March 1977. A publication updating part of this survey, "Structural Alloys for Superconducting Magnets in Fusion Energy Systems," was included in volume IV (1981) of this series. In volume VI (1983), reviews of the properties of austenitic stainless steels and of their elastic constants also contributed to this objective. Through interactions with low-temperature design, construction, and measurement programs, such as the Large Coil Project, MFTF-B, and ITER (International Thermonuclear Experimental Reactor), we are aware of new problems as they arise. This year's report contains results of continued research on copper and copper alloys, in support of Compact Ignition Tokamak designs by the Princeton Plasma Physics Laboratory and the Massachusetts Institute of Technology. Research projects contributing to the second objective are described in the technical papers. Again, research toward the establishment of test standards was emphasized. The third objective is satisfied, in part, by these annual reports and by the series of workshops on Cryogenic Structural Materials. Since 1982, handbook pages presenting the available data for specific materials have been distributed to members of the magnetic fusion energy community who are involved with low-temperature materials.

STRUCTURAL ALLOYS

STRUCTURAL ALLOYS PROGRAM

LEADER: R. P. Reed
CONTRIBUTORS: M. W. Austin, L. A. Delgado, H. Ledbetter, P. T. Purtscher, D. T. Read, N. J. Simon, R. P. Walsh

OBJECTIVES

- Development of strong, tough structural alloys for use in superconducting magnets
- Development of strong, fatigue-resistant structural alloys for use in pulsed superconducting magnets
- Development of effective codes and standards for low-temperature property measurements and structural design

RESEARCH HIGHLIGHTS

- Two new reviews have been written:

  Austenitic Stainless Steels with Emphasis on Their Low-Temperature Behavior. Austenite, ferrite, body-centered cubic and hexagonal close-packed martensite, stacking-fault energy, carbides, and sigma phase were described. Recent international development of higher strength, tougher austenitic stainless steels was summarized. Discussions of the effect of martensite phase transformations on the stress–strain characteristics, nitrogen strengthening, and strengthening theory based on lattice-parameter and elastic-property data, all at low temperatures, were included.

  Low-Temperature Properties of High-Manganese Austenitic Steels. Emphasis was placed on strength, toughness, elastic properties, thermal expansion, and magnetic properties, those properties most critical for materials used in cryogenic structures. Strength and toughness parameters and mechanisms were discussed, including alloying, martensitic transformations, twinning, and grain size. Information was included from many recent studies, particularly Japanese studies, of alloy development for superconducting-magnet applications at 4 K.

- Regression analysis for significant design parameters has been carried out on a matrix of 99 recent NBS measurements at 4 K on a variety of 316, 316LN, and 316LHN alloys. This matrix includes alloying, refining, and processing data on alloys obtained from suppliers in Japan, Europe, and the United States. For structural use in 4-K superconducting magnet applications, alloy 316LN offers higher strength than 304LN with equivalent toughness. Nitrogen additions permit the attainment of high yield-strength levels with little added cost.

- The fracture process at low temperatures in tension and from fatigue precracking has been better characterized. Cleavage-like facets along slip planes in austenite have been identified. Ductile dimples in the fracture of tensile specimens have been related to inclusion parameters. A new model has been developed for better understanding of void nucleation, which sometimes controls the fracture of austenitic steels.

SUMMARY OF MECHANICAL PROPERTY MEASUREMENTS OF STRUCTURAL ALLOYS

Alloy [Designation]	Country of Supplier	Tensile 295-4 K	Elastic 295-4 K	Fracture Toughness 295, 76, 4 K	Fatigue Crack Growth Rate 295, 76, 4 K	Fatigue S-N 4 K	Report* Volume (page)
AUSTENITIC STEELS							
Fe-5Cr-25Mn-0.2C	Japan	VII					VII (65)
Fe-5Cr-26Mn	Japan		VI				VI (181)
Fe-13Cr-19Mn	USSR		III		VI		III (79) VI (41)
Fe-13Cr-22Mn-0.2N	Japan	VI					VII (65)
Fe-16Cr-8Ni-8Mn	U.S.	VIII		VIII			VIII (151,181)
Fe-17Cr-18Mn-0.5N	U.S.	VII, VIII		VIII			VII (65) VIII (181)
Fe-17Cr-9Ni-8Mn	U.S.		III				III (91)
Fe-17Cr-13Ni-2Mo [316]	U.S.	I,II, III,IV, VI,VIII, IX, X	VI	I,II, VIII, IX, X	II,VIII, IX	I	I (15,71) II (79) III (49,105,117) IV (147) V (185) VI (157) VIII (181,209,251) IX (15,27,43) X (77)
Fe-17Cr-13Ni-2Mo [316LN]	U.S.	II,IX		II,IX	II		II (79) IX (15,27,53)
Fe-18Cr-(11-14)Ni-(0-4)Mo [316LN]	U.S.	X	X	X			X (9,31,43,55)
Fe-18Cr-3Ni-13Mn	U.S.	I,VI, VIII	III	I,VIII	I,VI,VII		I (93) III (91) VI (53) VII (85) VIII (167,219)
Fe-18Cr-8Ni-(0-6)Mn	U.S.		X				X (67)
Fe-19Cr-(6-15)Ni-4Mn-(0.1-0.3)N	USSR	VIII		VIII,IX			VIII (123) IX (53)
Fe-19Cr-9Ni [304]	U.S.	I,II, III,IV, VI,VII, IX, X	I,II, III,IV, VI,VII	I,II, III,IV, IX X	II,III,IV		I (15,71,213) II (79,149,175) III (15,91,105,117) IV (37,101,203,215,227) V (71) VI (73) VII (13,47,75,157) IX (27) X (77)

**Materials Studies for Magnetic Fusion Energy Applications at Low Temperatures:*
NBSIR 78-884 (I); NBSIR 79-1609 (II); NBSIR 80-1627 (III); NBSIR 81-1645 (IV);
NBSIR 82-1667 (V); NBSIR 83-1690 (VI); NBSIR 84-3000 (VII); NBSIR 85-3025 (VIII);
NBSIR 86-3050 (IX); NBSIR 87-3067 (X).

SUMMARY OF MECHANICAL PROPERTY MEASUREMENTS OF STRUCTURAL ALLOYS, continued

Alloy [Designation]	Country of Supplier	Tensile 295-4 K	Elastic 295-4 K	Fracture Toughness 295, 76, 4 K	Fatigue Crack Growth Rate 295, 76, 4 K	Fatigue S-N 4 K	Report* Volume (page)
Fe-19Cr-9Ni [304L]	U.S.	II,III, IV,VIII, IX, X	I,II,IV	II,IV VIII,IX	III.IV, VIII		I (213) II (79,123,175) IV (37,101,131, 215,302) VIII (181,229,251) IX (27,141) X (9)
Fe-19Cr-9Ni-(1-10)Mn	U.S.	IV,V, VIII	V	IV,V,VIII, IX			IV (77) V (15,59,189) VIII (181) IX (53)
Fe-19Cr-9Ni-N [304N]	U.S.	I,III, IV,IX	IV	I,III,IV, IX	I,III,IV		I (93) III (15) IV (37,101,203, 215) IX (27)
Fe-19Cr-9Ni-N [304LN]	U.S.	II,III, IV,V,VI VIII,IX	IV,VIII	II,III,IV, VIII,IX	II,III,IV, VIII		II (35,79) III (15) IV (37,101,203) V (29) VI (113) VIII (181,207,229) IX (159)
Fe-19Cr-10Ni-(0.03-0.29)N-(0.03-0.09)C	U.S.	III,VIII	VIII,IX	III,VIII	III		III (15) VIII (145,181) IX (159)
Fe-20Cr-7Ni-8Mn [216]	U.S.	VIII		VIII			VIII (151,181)
Fe-20Cr-8Ni-2Mn [304HN]	U.S.	VIII		VIII			VIII (151,181)
Fe-20Cr-16Ni-6Mn	USSR	V,VI	V				V (29,213) VI (113)
Fe-21Cr-6Ni-9Mn	U.S.	I,VIII	III,VI	I,VIII		I	I (15,71) III (91) VI (157) VIII (151,181)
Fe-21Cr-12Ni-5Mn	U.S.	I,II	III	I,II	I,II		I (93) II (79) III (91)
Fe-25Cr-21Ni [310]	U.S.	V,VI, VII, VIII, IX, X	III,VI	V,VIII			III (105,117) V (71,145) VI (73) VII (65) VIII (181) IX (95) X (9)

**Materials Studies for Magnetic Fusion Energy Applications at Low Temperatures:*
NBSIR 78-884 (I); NBSIR 79-1609 (II); NBSIR 80-1627 (III); NBSIR 81-1645 (IV); NBSIR 82-1667 (V); NBSIR 83-1690 (VI); NBSIR 84-3000 (VII); NBSIR 85-3025 (VIII); NBSIR 86-3050 (IX); NBSIR 87-3067 (X).

SUMMARY OF MECHANICAL PROPERTY MEASUREMENTS OF STRUCTURAL ALLOYS, continued

Alloy [Designation]	Country of Supplier	Tensile 295-4 K	Elastic 295-4 K	Fracture Toughness 295, 76, 4 K	Fatigue Crack Growth Rate 295, 76, 4 K	Fatigue S-N 295, 4 K	Report* Volume (page)
Fe-19Ni-9Co [200-300 grades]	U.S.		IV				IV (237)
Reviews of austenitic steels		IV,V,VI	IV,V,VI	IV,V,VI	IV,V,VI,VII	IV, VI	IV (17,257), V (171) VI (11,127,157) VII (103)
ALUMINUM ALLOYS							
Al-2.7Cu-2.2Li-0.12Zr	U.S.		X				X (163)
Al-6Cu-0.2Mn-0.1Fe [5083-0]	U.S.		II	II	II	II	II (19)
Al-0.6Fe-0.2Cu-0.1Si [1100]	U.S.	IX					IX (107)
Al-4Mg [5083-0]	U.S.	IV				II	II (35) IV (185)
COPPER ALLOYS							
99.99Cu-Ag [C10100, C10200]	U.S.	IX					IX (95,107)
99.5Cu-Ag [C10400]	U.S.	X	X			X	X (83,127,139)
99.75 Cu-Ag [C15500]	U.S.	X	X			X	X (83,127,139, 151)
97.6 Cu-Ag-0.38Be [C17510]	U.S.	X					X (83)
SUPERCONDUCTORS							
Nb-45Ti	U.S.		III				III (133)

*Materials Studies for Magnetic Fusion Energy Applications at Low Temperatures:
NBSIR 78-884 (I); NBSIR 79-1609 (II); NBSIR 80-1627 (III); NBSIR 81-1645 (IV);
NBSIR 82-1667 (V); NBSIR 83-1690 (VI); NBSIR 84-3000 (VII); NBSIR 85-3025 (VIII);
NBSIR 86-3050 (IX); NBSIR 87-3067 (X).

AUSTENITIC STAINLESS STEELS
WITH EMPHASIS ON STRENGTH AT LOW TEMPERATURES*

R. P. Reed
Fracture and Deformation Division
National Bureau of Standards
Boulder, Colorado

The structure and properties of austenitic stainless steels are reviewed, with emphasis on their low-temperature behavior. Austenite, ferrite, body-centered cubic and hexagonal close-packed martensite, stacking-fault energy, carbides, and sigma phase are described. Recent international development of higher strength, tougher austenitic stainless steels is summarized. This chapter also includes discussions of the effect of martensite phase transformations on the stress–strain characteristics, nitrogen strengthening, and strengthening theory based on lattice-parameter and elastic-property data, all at low temperatures.

INTRODUCTION

Rustproof steels, with increased passivity, were discovered at the turn of the century. These new steels, called stainless steels, are characterized by high Cr (>10%†) and low C (<0.3%). Research beginning in 1904 by Guillet (1904–1914, France),[1] followed by Portevin (1909–1912, France),[2] Giesen (1909, England),[3] and Monnartz (1911, Germany)[4] led to an understanding of the corrosion behavior of Fe–Cr–C alloys. During the same period, Guillet (1906)[5] and Giesen (1909)[3] published studies of Fe–Cr–Ni austenitic stainless steels. Clearly, the objective of these early studies was to develop a rustproof or corrosion-resistant alloy.

Since then, an enormous amount of research has been directed toward understanding and improving the properties of Fe–Cr–Ni alloys. From their initial use as cutlery, the application of these steels has

---

*To be published in *Alloying*, ASM International, Metals Park, Ohio.
†Unless otherwise specified, wt.% is used.

broadened considerably, along with their composition. Only two criteria determine whether steels are classified as stainless (or rustproof or pitless): They must be Fe-base elements and they must contain about 11Cr or more. This broad classification is divided into six principal subclasses:

1. Ferritic steels contain 11 to 30Cr, have little or no Ni, and low C. Ferritic structure is body-centered cubic (bcc) and ferromagnetic; it is usually obtained by slow cooling from the hot forming temperature.
2. Martensitic steels typically have high Cr and low C and Ni contents. Martensitic structure is bcc; its greater hardness and strength are obtained by quenching.
3. Austenitic steels typically contain 18Cr and 8Ni. The face-centered cubic (fcc) austenitic structure is stabilized by the Ni content.
4. High-manganese, austenitic steels typically contain 24Mn, instead of 8Ni, to stabilize the austenitic structure. Their development was driven by the relative scarcity and high costs of Cr and Ni.
5. Duplex steels contain varying amounts of Ni (4–8%) to adjust the relative amounts of ferrite and austenite and, thus, to achieve high strength (from the ferrite) and adequate toughness (from the austenite).
6. Precipitation-hardened steels contain Aℓ, Nb, and Ti, which form carbides during aging at high temperatures. The carbides precipitate in either martensitic or austenitic structures, increasing the strength at the higher temperatures.

The ternary Fe–Cr–Ni and Fe–Cr–Mn diagrams in Fig. 1 show the chemical boundaries of these elements for the six types of stainless steels. Often these steels are strengthened by adding interstitial C or N or the solid-solution alloying element Mo.

The earliest book (1935) on stainless steels that has come to our attention is a series of technical papers on production and fabrication, properties, test techniques, and applications edited by Thum.[6] Then in 1949 Zapffe produced a simplified book[7] that emphasized the three structures (ferritic, martensitic, and austenitic) of stainless steels. This book also contains the fascinating history of the development and industrial manufacture of these steels. Two volumes devoted to stainless steel applications, production, corrosion resistance, properties, and alloying effects were written by Monypenny in 1951 and 1954.[8,9] In 1956, Keating wrote a user-oriented book[10] on Cr–Ni austenitic steels that focused on properties and fabrication techniques.

The American Society for Metals published Source Book on Stainless Steels (1976)[11] that includes property, fabrication, corrosion, forging and heat-treatment, phase-diagram, and other information central to the use of stainless steels. To date, the exhaustive handbook assembled in 1977 by Peckner and Bernstein[12] represents the most comprehensive review of these alloys; it documents stainless steel melting, fabrication, metallurgy, corrosion resistance, properties, and applications. Lula

recently (1986) revised a general introductory book by Parr and Hanson,[13] in which they discuss metallurgy, properties, corrosion, and fabrication of stainless steels. In the same year, he also wrote a careful review of the metallurgy, properties, and applications of high-manganese stainless steels.[14]

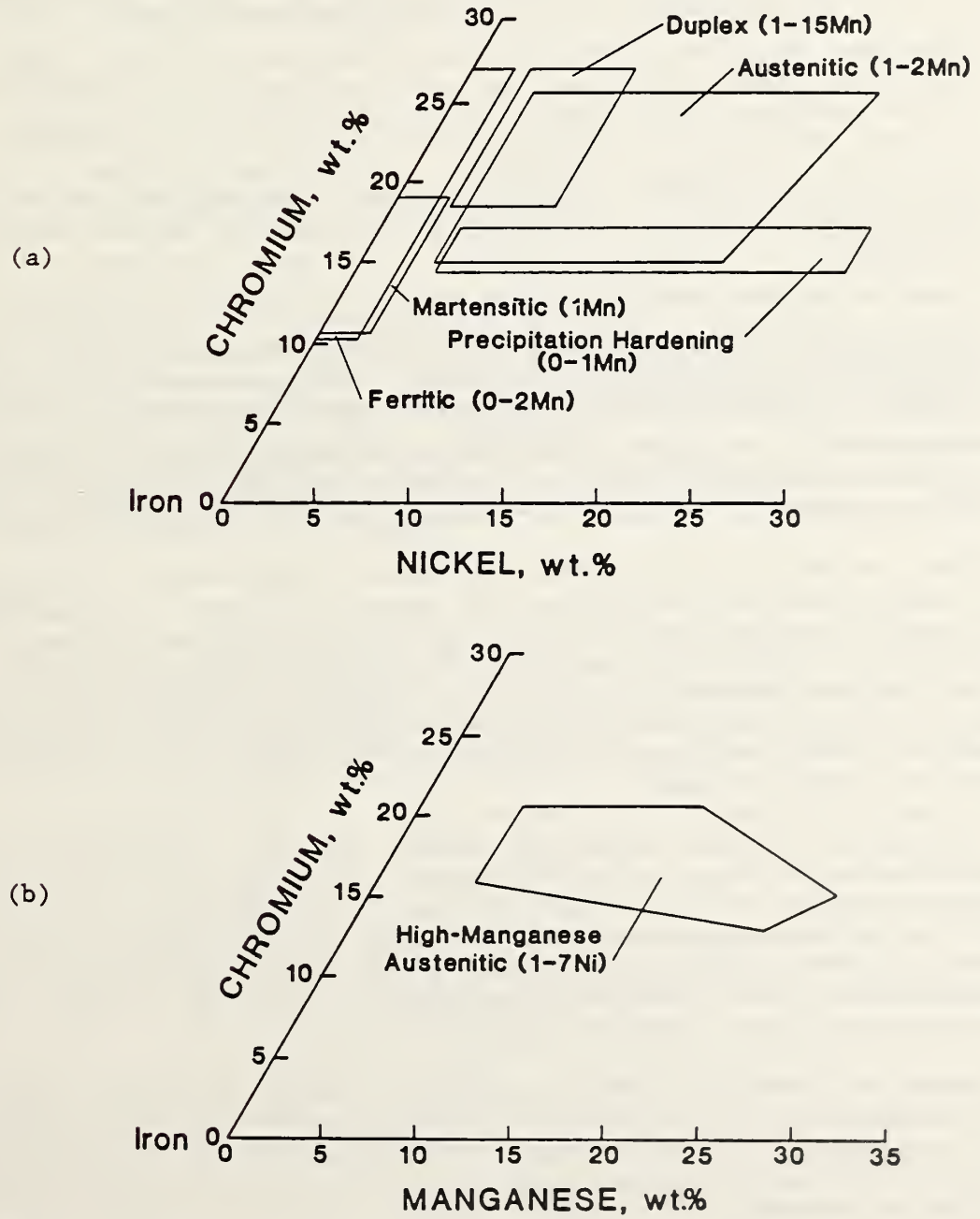

Fig. 1. Composition ranges of various types of stainless steels. (a) Fe–Cr–Ni ternary alloys; (b) Fe–Cr–Mn ternary alloys.

From the 1950s into the 1980s, several major international conferences have been held on stainless steels in general and specific aspects of these alloys. Those of which we are aware are:

1. Symposium on σ-phase formation and verification; 1950; sponsored by the American Society for Testing and Materials[15]
2. Symposium on the residual-element effects on properties; 1966; sponsored by the American Society for Testing and Materials[16]
3. Conference, Stainless Steels for the Fabrication and User; 1969; proceedings published by the Iron and Steel Institute, London.[17] At this conference, the some of the first reports of dual-phase stainless steels were presented.
4. Conference on stainless steels in general, with emphasis on new applications; 1977; sponsored by Climax Molybdenum Company and held in London[18]
5. Symposium on stainless steel castings; 1980; sponsored by ASTM[19]
6. Conference on stainless steels with emphasis on properties and alloy development for cryogenic applications; 1982; sponsored by the International Cryogenic Materials Conference and held in Kobe, Japan[20]
7. Conference on stainless steels with emphasis on fabrication techniques, selection criteria, new developments, and new applications; 1985; proceedings published by the American Society for Metals[21]

Thus, notable stainless steel development, applications, and associated research have been significant for about fifty years. During this time, stainless steels have been used in many applications with material requirements far exceeding the definitive rustproof property of the steels. They are versatile because they have high toughness, variable strength, high elastic moduli, excellent weldability, and other practical properties. Their stainless nature, of course, ensures low maintenance costs in most applications.

Austenitic stainless steels are usually chosen for cryogenic applications because of their low thermal conductivity, good weldability, and excellent toughness. They are well suited for applications that require unusual safety considerations, such as storage of some liquefied gases. Currently, stronger, tougher austenitic steels are needed for use at very low temperature, 4 K. Nitrogen-strengthened Fe–Cr–Ni and Fe–Cr–Mn steels are being studied and developed, especially in Japan.

Subsequent sections review how alloying affects the general structural characteristics and properties of stainless steels. The first section discussed their solidification, precipitation, and transformation structures; the second section presents the effects of alloying on their cryogenic properties.

STRUCTURES

Stainless steels are complex. They solidify as either an austenitic (fcc) or a ferritic (bcc) structure. At intermediate temperatures, carbide precipitates, an intermetallic compound (σ-phase), or both may form. During cooling or plastic deformation, two martensitic transformation products with bcc and hexagonal close-packed (hcp) structures may form. At least three magnetic phases are possible: austenite is typically paramagnetic at high temperatures and antiferromagnetic at very low temperatures; ferrite is ferromagnetic.

Austenite

Austenite is naturally the dominant phase of austenite stainless steels at ambient temperatures. Austenite is sometimes called γ-phase and is always designated γ in phase diagrams. Solid-solution alloying elements, such as Cr, Ni, and Mn, assume normal lattice sites in the Fe-base, fcc structure; there is no convincing evidence of ordering of these elements in the austenitic steels. Smaller atoms, such as C, N, P, and S, are thought to be located interstitially in fcc octahedral lattice sites. For these elements (especially N), electronic bonding or short-range ordering may be present, but so far the evidence is circumstantial. Austenite remains paramagnetic on cooling until about 50 K; then it usually becomes antiferromagnetic. The magnetic structure of alloys with high-Ni content may become mictomagnetic or spin-glass at low temperatures. The Néel temperatures or transition to mixed ferromagnetic states is strongly dependent on alloying.

Ferrite

Ferrite may form during solidification or high-temperature treatment, depending on alloy content. It is occasionally present in small amounts (usually less than 10%) in alloys that are rapidly cooled, such as weldments. This bcc phase is conventionally called δ-ferrite when it forms at temperatures above the γ loop or range and α-ferrite when it forms at lower temperatures. Most austenitic stainless steels have sufficient stabilizing elements, such as Ni, Mn, C, and N, to lower the temperature of the γ loop or range sufficiently to prevent the diffusion-controlled $\gamma \rightarrow \alpha$ transformation. In wrought alloys, the retained δ-ferrite is typically transformed to austenite during forging or hot rolling. However, since the solubilities of many elements differ between the two phases, the solidification structure affects the location of these elements. This is especially significant for elements, such as P and S, that are more soluble in ferrite; therefore, they are less prone to precipitate along grain boundaries during solidification when δ-ferrite is present. For this reason, δ-ferrite is thought to avert hot cracking in austenitic stainless steel weldments.

The relative amounts of austenite and ferrite that form during solidification are critically dependent on alloying. The liquidus and solidus surfaces of the Fe–Cu–Ni ternary have been presented by Speich[22] and Schurmann and Brauckman.[23] The eutectic trough extends from near the

Fe corner (76Fe–10Ni–14Cr) to a ternary eutectic (about 8Fe–43Ni–49Cr). Primary austenite solidifies if the composition is on the Ni side of the eutectic liquidus. Nearer the eutectic liquidus on the Ni side, limited ferrite forms, mainly in the dendritic cell boundaries. On the Cr-rich side of the liquidus line, primary ferrite solidifies.[24] Upon cooling, however, ferrite transforms to austenite in compositions typical of austenitic stainless steels. The ternary isothermal sections at 1350°C and 1100°C are shown in Fig. 2. At lower temperatures, the $\delta + \gamma$ region increases with attendant decreases in both δ and γ single regions.

The tendency to transform from δ-ferrite to γ is illustrated by the phase diagrams at constant Fe content but varying Ni and Cr contents (Fig. 3). Notice that the minimum Ni content for stable γ at 70Fe is about 8% (22Cr) and at 60Fe, about 14.5% (25.5Cr). In practice, these limits are adjusted by small additions of C, N, Mn, Si, and, sometimes, Mo.

The binary Fe–Cr and Fe–Ni phase diagrams are shown in Fig. 4. Whereas adding Cr encourages ferrite, adding Ni stabilizes the austenite. Indeed, in both binaries, there is an extensive solid-solution range (>85 wt.% alloy contents) at temperatures above 800°C (below 800°C, σ-phase forms in Fe–Cr alloys, and below 500°C Fe–high-Ni alloys tend to order). Binary Fe-alloy phase diagrams for Mo, Si, and Mn are reviewed by Novak.[25] Like Cr, Mo and Si have extensive ferrite ranges; the γ-loop extends to only about 2 Mo and 2 Si. Austenite is encouraged by alloying Fe with Mn; at 1000°C, the γ-loop extends to 70Mn.

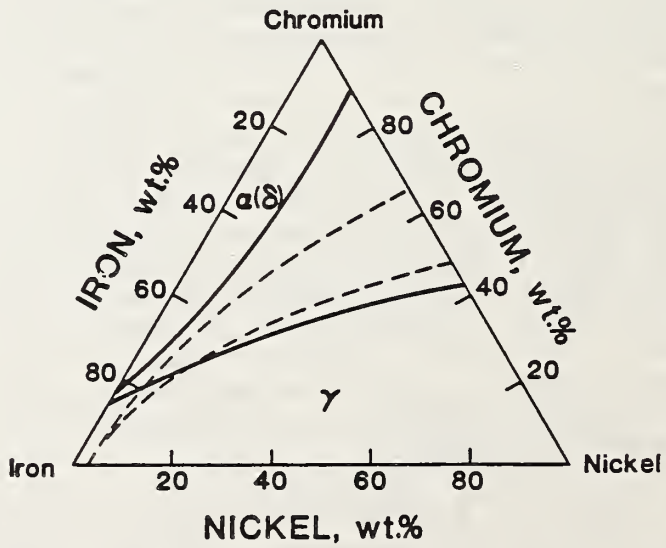

Fig. 2. Isothermal sections at 1350°C (dashed lines) and 1100°C (solid lines) for the Fe–Cr–Ni ternary system.

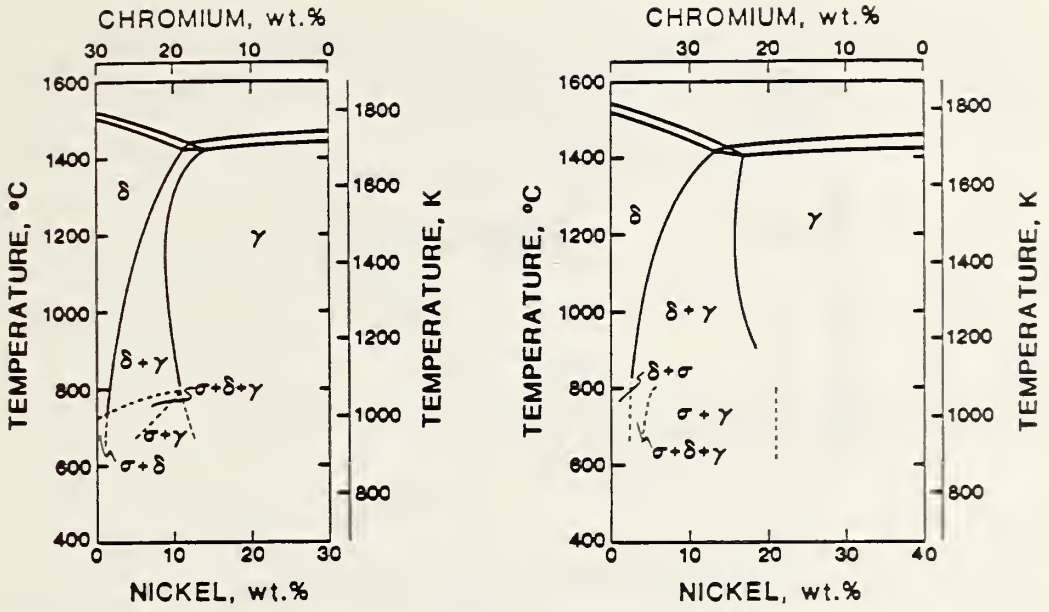

Fig. 3. Binary Fe–Cr_x–Ni_y phase diagrams depicting phase dependence on Cr and Ni at constant Fe content: (a) 30 wt.% Fe; (b) 40 wt.% Fe.

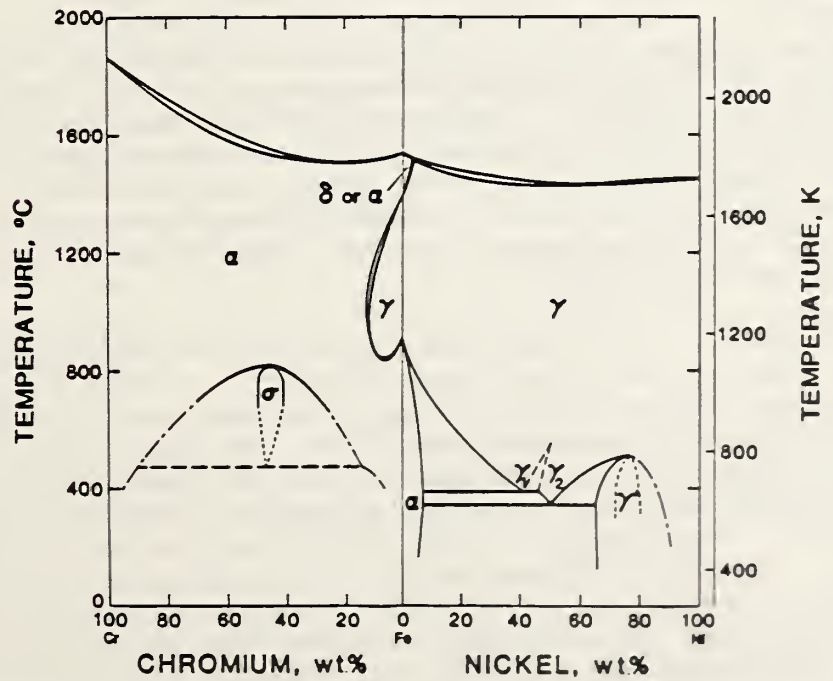

Fig. 4. Binary Fe–Cr and Fe–Ni phase diagrams.

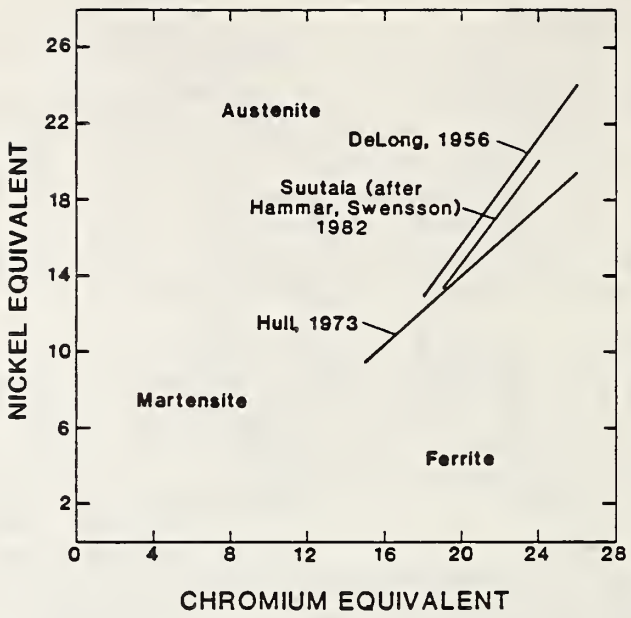

Fig. 5. Ferrite portion of Schaeffler diagram depicting lines that estimate the first solidification of ferrite during cooling to room temperature after welding.

For welding, the amount of δ-ferrite present is normally estimated from a Schaeffler[26] or DeLong[27] diagram. The ferrite portion of this type of diagram is shown in Fig. 5; the lines representing zero ferrite, or the demarcation between pure austenite (above) or small amounts of ferrite (below), are plotted. Tie lines depicting constant ferrite amounts have been developed empirically in terms of the Ni equivalent (austenite-forming tendency) and Cr equivalent (ferrite-forming tendency). These equivalents serve to identify the austenite–martensite and austenite–ferrite boundaries at ambient temperatures, where many alloying elements are present.

The proposed Ni- and Cr-equivalent equations are summarized in Table 1. Presumably, the Suutala formulations[28] are the most reliable equations because they are the most recent and were developed from the most data. Manganese additions up to 2 to 4% have been found to promote austenite formation; greater amounts tend to promote ferrite formation.[29] Nitrogen additions result in greater austenite stability. Notice in Table 1 that the more recent Hammar[30] equivalents emphasize C more than N. Suutala concludes that at low (normal) contents, Mn additions stabilize austenite, but at higher contents (>5%), Mn additions enhance ferrite formation. Thus Hull's formulation,[29] which includes a negative Mn^2 term, provides the best representation of Mn effects.

Ferrite is ferromagnetic at temperatures below about 600°C and paramagnetic at higher temperatures.

Table 1. Ferrite Solidification Equivalent Coefficients

Investigator (Year)	Cr-Equivalent Coefficient (per wt.%)					
	Cr	Mo	Si	Nb	Ti	Aℓ
DeLong et al. (1956)	1	1	1.5	0.5	–	–
Hull (1973)	1	1.21	0.48	0.14	2.2	2.48
Hammar, Svensson (1979)	1	1.37	1.5	2	3	–

	Ni-Equivalent Coefficient (per wt.%)						
	Ni	Mn	C	N	Cu	Co	Mn^2
DeLong (1956)	1	0.5	30	30	–	–	–
Hull (1973)	1	0.11	24.5	18.4	0.44	0.41	−0.0086
Hammar, Svensson (1979)	1	0.31	22.5	14.2	1	–	–

Martensite

The use of austenitic stainless steels is complicated by the metastability of the austenitic structure of most alloys. The metastability leads to martensitic transformation, which is a significant design consideration in applications requiring fracture-control planning, close dimensional tolerances, the absence of a ferromagnetic phase, and high toughness of weldment, heat-affected zone, and base metal. Either upon cooling, under applied elastic stresses, or during plastic deformation, the austenitic phase of Fe–Cr–Ni alloys may transform to bcc (α') and hcp (ϵ) martensite phases. The alloy composition affects the chemical free-energy difference between the two phases.

Kaufman[31] derived free-energy relationships between γ and α' for the Fe–Cr–Ni ternary system. Reed[32] reviewed the Fe–Cr–Ni ternary free-energy relations between fcc and bcc and suggested a relationship for the free-energy differences between fcc and hcp structures based on the earlier work of Kaufman on binary Fe–Cr and Fe–Ni alloys.[31]

Other alloying elements, such as C, N, Mn, Mo, and Si, contribute to austenitic stability in austenitic stainless steels. The complexity of the final structure has led to many studies to characterize the effects of alloying on the stability of the austenitic structure with respect to α'-martensite.

Expressions relating the stability of the austenite and the temperatures of transformation during cooling (T_{ms}) or during deformation (T_{md}) have been developed empirically and are summarized in Table 2. Eichelman and Hull,[33] working with austenitic alloys with compositions of 10 to 18Cr, 6 to 12Ni, 0.6 to 5Mn, 0.3 to 2.6Si, 0.004 to 0.129C, and 0.01 to 0.06N, established that all these alloying elements stabilize the austenite and thus lower T_{ms}. Monkman et al.,[34] using a larger of number of specimens with compositions of 5 to 13Ni, 11 to 19Cr, and 0.035 to 0.126(C + N), produced a similar analysis and concluded that T_{ms} was linearly dependent on composition only to a first approximation. The dependence of T_{ms} on the C and N concentrations seemed to be influenced by the Cr and Ni concentrations.

Table 2. Temperature-Equivalent Coefficients for Calculation of T_{ms}.

Investigator (Year)	Temperature-Equivalent Coefficient (degrees K per wt.%)							
	Base	Cr	Ni	Mn	Si	C	N	Mo
Eichelman, Hull (1953)	1578	−41.7	−61.1	−33.3	−27.8	−1670	−1670	
Monkman et al. (1957)	1455	−36.7	−56.7			−1460	−1460	
Andrews (1965)	273	−12.1	−17.7	−30.4			−423	−7.5
Hull (1973)	1755	−47	−59	−54	−37	−2390	−3720	−56*
Self (1986)	794	−14.3	−17.5	−28.9	−37.6	−350		−29.6†

* Other: −180(Ti)
† Other: −1.19(CrNi) + 23.1(Cr+Mo)C

Hull[29] studied the effects of Ni, Cr, Mn, C, N, Si, and Co (Aℓ, Th, V, W sometimes were added) on α′-martensite formation during low-temperature cooling-and-deformation experiments and on ferrite retention after cooling to room temperature from the melt. Hull's study confirmed that all the above elements suppress low-temperature α′ formation during either cooling or deformation. To predict the effects of elemental additions on T_{ms}, Hull assumed that the Ni contribution was the average of the Monkman et al. and Eichelman and Hull results and then compared all the effects of alloying additions with that of Ni. The formulation of Andrews[35] applies to lower Cr and Ni concentrations, and thus higher T_{ms}, and his results are included in Table 2 to indicate the disparity between the high- and low-temperature empirical results. In all studies,

specimens of various compositions were prepared and cooled, and their T_{ms} values were measured. Regression analyses were used to obtain the empirical dependence of T_{ms} on alloy concentration. Self[36] recently studied a wide range of compositions of weld deposits. For analyses, he assumed nonideal behavior, and with regression analysis, he derived a predictive equation containing interactive Cr–Ni and (Cr + Mo)–C terms (Table 2).

From Tables 1 and 2, it is apparent that the roles of Cr, Mo, and Si are reversed in the stabilization of the bcc structure (ferrite and α' martensite) between high and low temperatures. Binary Fe–Cr free-energy derivations[31,32] do not suggest this trend. Perhaps the explanation for the stabilizing effect at lower temperatures is the contribution of these elements to the increase in austenite flow strength. The affect of Mo on flow strength is discussed later in this paper.

The analytic expressions of Schaeffler, Eichelmann and Hull, and Self are plotted in terms of Ni and Cr equivalents in Fig. 6. The less conservative analysis of Self implies that at room temperature, considerably less than 18Cr is required to achieve the complete austenite stability of an 8Ni-equivalent alloy. Also, the nonlinear nature of the Self equivalent indicates the possibility of martensite control by means of alloy optimization rather than alloy "trade-offs," as offered by the linear trend lines.

Experiments have been conducted to assess the influence of cold work (either tensile or compressive) on T_{md}. Results are contained in Table 3. The experimental definition of T_{md} varied in each study: Angel[37] used 50% α' at 30% tensile elongation; Williams et al.[38] used 2.5% α' at 45% compressive elongation; and Hull[29] used the minimum detection level (probably about 1% α') at 50% compressive elongation. There are subtle distinctions among the coefficients for T_{ms} and T_{md} calculations. After cooling, the Cr and Ni coefficients are nearly equal, Mn is higher, C and N are higher by a factor of 50; after deformation, Cr and Mn are decidedly less than Ni, and C and N are higher by a factor of about 10. Careful research to delineate the dependence of composition on free energy, stacking-fault energy, and deformation parameters is needed to understand these distinctions.

Upon cooling or during deformation, fcc austenite may transform to two martensitic products. The hcp phase is associated with extended stacking faults and forms as thin sheets on (111) austenite planes. In most austenitic stainless steels, the α' product forms as laths. Breedis[39] reported a lath α' morphology for compositions ranging from Fe–19Cr–11Ni to Fe–10Cr–16Ni; at lower Cr and higher Ni concentrations the α' morphology changed to surface martensite and then to a plate-like structure (Fig. 7). From Reed,[40] the α' lath-like structure is parallel to $\langle 110 \rangle_\gamma$, with $(225)_\gamma$, $(112)_\gamma$, or both habit planes.[41] The laths are restricted within $\{111\}_\gamma$ bands, and usually three sets of habit planes form within the band.

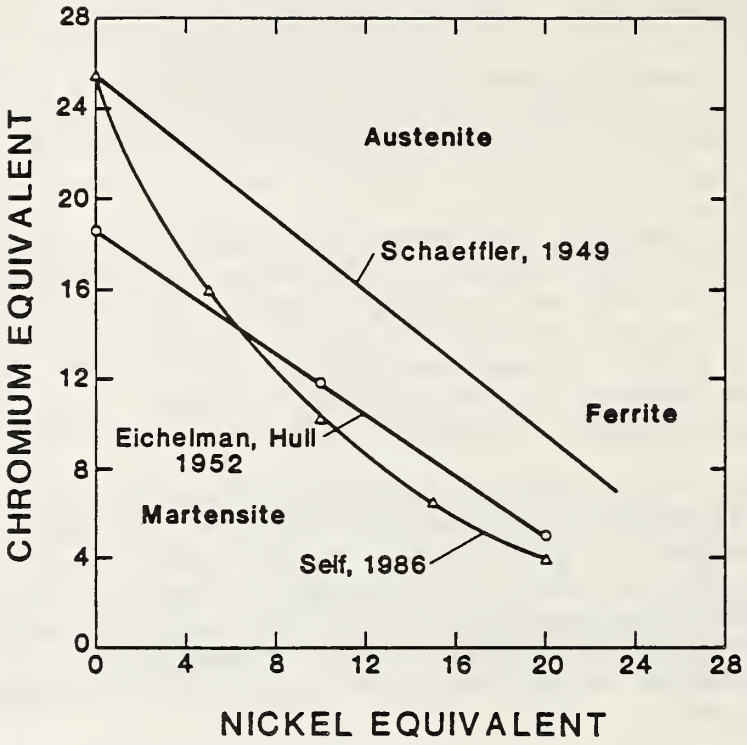

Fig. 6. Martensite portion of the Schaeffler diagram depicting lines that estimate the first formation of martensite during cooling to room temperature after welding. Constant amounts of 1Mn, 0.03C, and 0.5Si.

Table 3. Temperature-Equivalent Coefficients for Calculation of T_{md}

Investigator (Year)	Temperature-Equivalent Coefficients (degrees K per wt.%)								
	Base	Cr	Ni	Mn	Si	C	N	Mo	Other
Angel (1954)	686	−14	−9.5	−8.1	−9.2	−46.2	−46.2	−18.5	
Hull (1973)	1655	−23	−59	−41	−20	−777	−315	−24	12(Co)
Williams et al. (1976)	686	− 6	−25	−16	+21	−222	−222	−11	

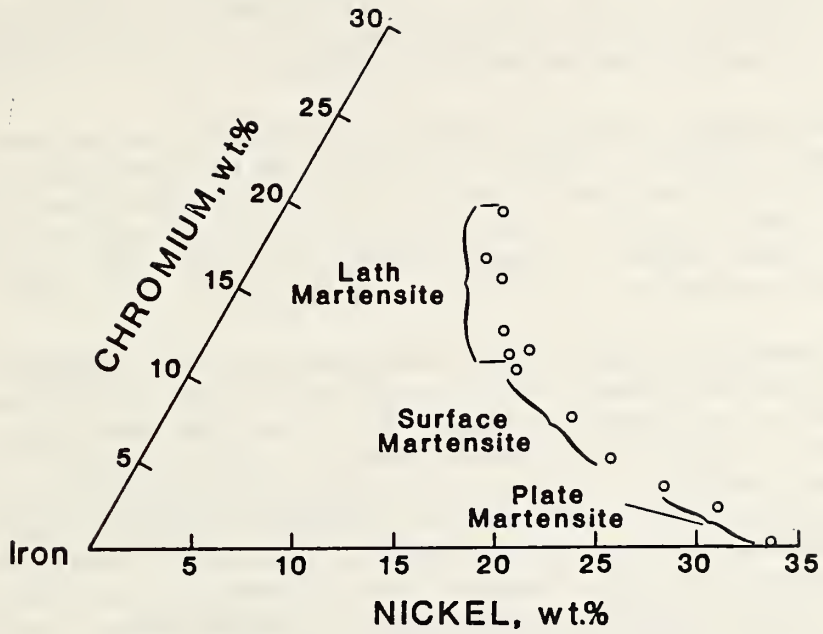

Fig. 7. Compositional dependence of α′-martensite morphology in Fe–Cr–Ni ternary alloys.

There is a considerable amount of accommodation deformation in the austenite after transformation during cooling, particularly within the {111} bands containing the α′ laths. Either ε martensite or large amounts of stacking faults are present.

The orientation relationships between the γ-, ε-, and α′-phases[41] are

$$(111)_\gamma \parallel (0001)_\epsilon \parallel (101)_{\alpha'}$$

$$[110]_\gamma \parallel [\bar{1}210]_\epsilon \parallel [111]_{\alpha'}$$

These relationships are apparently retained regardless of the manner of ε or α′ formation.

Transformation during plastic deformation initially results in α′ at intersections of active {111} deformation bands. The α′ assumes the shape of laths along <110> common to the two active {111} systems. Evidence of dislocation pileups at α′ laths has been observed.[32] Also, more than one lath forms at each transformation site, and in contrast to the α′ that forms on cooling, all laths have the same habit-plane variant.

The internal defect structure of the α′-phase in Fe–Cr–Ni steels consists predominantly of dislocations. As Cr is replaced by Ni,

Breedis[39] reports that the cellular, irregular distributions of dislocations that are typical of α' laths change to the planar, regular arrays that are typical of α' plates. Also, as Ni replaces Cr, the amount of ϵ transformation decreases, the sharpness of the hcp reflections decreases, and the fcc twin reflections become more diffuse.

Many metallurgists have been concerned with the role of the ϵ transformation: does ϵ act as a precursor transformation ($\gamma \rightarrow \epsilon \rightarrow \alpha'$), or is the ϵ an accommodation effect ($\gamma \rightarrow \alpha'$, $\gamma \rightarrow \epsilon$)? Both effects have been observed. The stainless steels with low stacking-fault energies tend to form ϵ, and the α' tends to form from ϵ. Higher stacking-fault-energy alloys require transformation stresses for observable ϵ formation.

Several characteristics of the transformation from austenite to bcc martensite in stainless steels cause problems in many applications. The martensitic bcc has a specific volume 1.7% larger than the parent austenite; therefore, these steels expand during transformation. The martensite forms as individual crystals, and the shear stress and volume expansion associated with transformation disrupt localized regions. For example, α' formation near or at the surface results in localized surface upheavals. For service that requires close tolerances, such as valves or bearings, these local surface fluctuations are disastrous.

Another concern, mostly in the presence of magnetic fields or pulsed currents, is that the bcc martensitic product is ferromagnetic, whereas the parent austenite is paramagnetic. A simple rule is that each 1% of bcc martensite results in a permeability increase of 0.01. Therefore, if time-dependent field changes corresponding to material changes on the order of 0.10 are significant, than alloy selection is important.

Stacking-Fault Energy

The stacking-fault energy is related to the free-energy difference between the fcc principal structure and the hcp structure. Lower stacking-fault energy leads to wider partial-dislocation separation (larger fault ribbons) and, hence, more planar dislocation slip structures and reduced cross slip.

Schramm and Reed[42] used x-ray peak-shift measurements, coupled with previous stacking-fault energy measurements, to estimate the dependence of the stacking-fault energy on chemical composition. This dependence should correspond to the dependence of the $\gamma \rightarrow \epsilon$ transformation on composition, because a stacking fault represents a local planar area of ϵ. Rhodes and Thompson[43] suggested that the stacking-fault energy values of the Schramm and Reed analysis were too large, considering additional weak-beam electron-microscopy data. Weak-beam electron-microscopy measurements by Bampton, Jones, and Loretto[44] confirmed that the least-square analysis of Schramm and Reed produced stacking-fault energies that were large. From measurements of individual nodes, they estimated a data spread of ±25%. Brofman and Ansell[45] added C content to the factors affecting stacking-fault energy. Dependencies of stacking-fault energy on composition are contained in Table 4.

Table 4. Stacking-Fault Energy at Room Temperature

Investigator (Year)	Energy Equivalent ($mJ/m^2 \cdot wt.\%$) Base	Cr	Ni	Mn	Si	C	Mo	Other
Dulieu, Nutting	0	—	0.5	1.4	—	3.4	0.1	3.6(Ti), 3.2 (Cu), −0.55 (Co)
Schramm, Reed (1975)	−53	0.7	6.2	3.2	—	—	9.3	—
Rhodes, Thompson (1977)	1.2	0.6	1.4	17.7	−4.7	—	—	—
Brofman, Ansell (1978)	16.7	0.9	2.1	—	—	26	—	—

Ledbetter and Austin[46] recently examined with x-rays the effects of additions of C and N (C + N ≤ 0.325 wt.%, N ≤ 0.21 wt.%) on the stacking-fault energy of an Fe–8Cr–10Ni alloy. They reported an increase of about 10% in the stacking-fault energy per at.% C + N. Earlier, Stoltz and VanderSande[47] determined with weak-beam microscopy, that N in excess of about 0.24 wt.% dramatically decreased the stacking-fault energy of an Fe–19Cr–7Ni–8Mn–0.03C alloy. Fujikuma et al.[48] measured stacking-fault probabilities on an Fe–18Cr–10Ni–8Mn alloy. They reported a minimum at about 0.15N; a slight increase at lower N contents, and a rapid increase at higher N contents. Thus, all three sets of measurements appear to be consistent: the stacking-fault energy increased slightly with N contents up to about 0.20 wt.%; it decreased substantially for higher N contents.

Carbides

The solid-solution solubility of the mobile interstitials C and N in austenitic alloys is very temperature dependent (Fig. 8).[49,50] At temperatures less than about 950°C, C begins to precipitate as a carbide in practically all austenitic steels, since the solubility limit is about 0.035. Using electron microscopy, the solubility of C in type 316 steel (Fe–19Cr–14Ni–2Mo) has been represented by the expression[51]

$$\log [C\ (ppm)] = 7.771 - 6272/T, \qquad (1)$$

where T is in K. The solubility limits determined from Eq. (1) are considerably less than those given in Fig. 8, which reflects the higher sensitivity of electron microscopy for detection of carbides. Carbides precipitate in the range 500 to 1000°C; below 500°C the atom mobility is too low, and above 1000°C the solubility of C and N is sufficient. The most common carbide is $M_{23}C_6$, where M represents a metal, normally Cr. However, Fe, Mo, Ti, and Nb also may assume the position of the metallic element, and N and B may assume the position of C in the $M_{23}C_6$ structure.

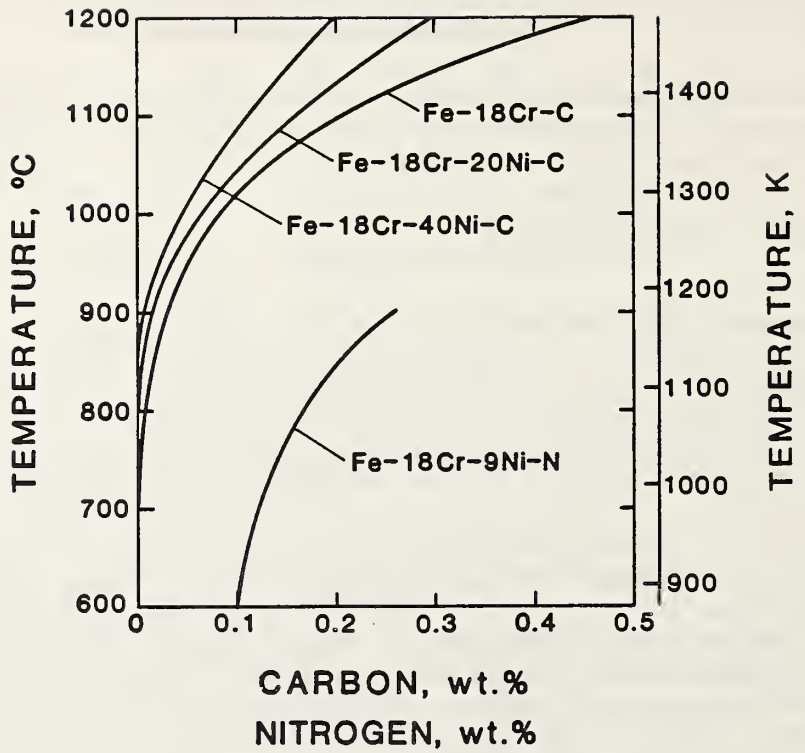

Fig. 8. Solubility limits for carbon[49] and nitrogen[50] as a function of temperature for various alloys.

The solubility limits of both C and N are reduced by the presence of Ni (see Fig. 8 for C). On the basis of binary Fe–Ni data,[52] Fig. 9 shows that this reduction is about 0.014N from the addition of 20Ni. The data of Sakamoto et al.,[53] obtained from observations of bubbling vacuum-induction melts, are quite consistent and represent the practical limits of maximum N contents (Fig. 9). These limits are particularly important to define the N-strengthening limitations that are discussed under Strength. Consistent with the binary alloy solubility limits, these data show that both Cr and Mn increase the ingot capacity for N.

Carbides prefer to precipitate at ferrite–austenite interfaces, followed by grain boundaries, noncoherent and coherent twin boundaries, and, finally, within grains. This is depicted schematically in Fig. 10.[54,55] The temperature decreases and the time for nucleation increases as the precipitation site changes from high- to low-energy boundaries. Increased C content increases precipitation temperature and decreases time; increased N content has the reverse effect, suppressing carbide formation.[12]

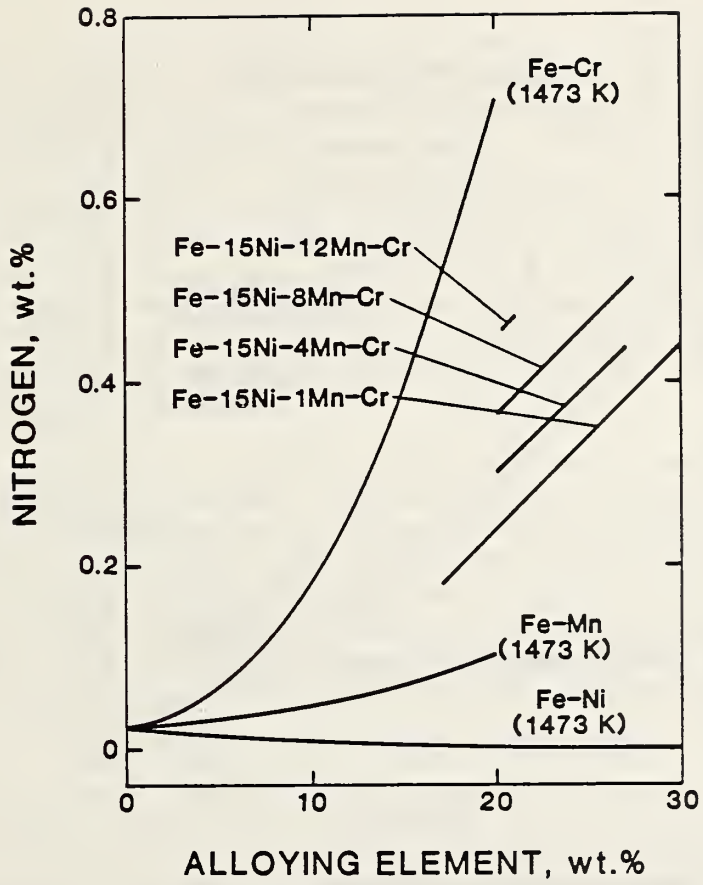

Fig. 9. Solubility limits of nitrogen in Fe–Cr, Fe–Ni, and Fe–Mn binary alloys at 1473 K[52] and in Fe–15Ni–Cr–Mn alloy liquids.[53]

The $M_{23}C_6$ carbide has a complex fcc structure with 92 metallic atoms and 24 smaller (C, N, or B) atoms and a lattice parameter of 10.61 to 10.64 Å.[12] But there is only minor mismatch between the {111} $M_{23}C_6$ and {111} austenite, estimated at 1.3% by Lewis and Hatterslay.[56] Thus, it is not surprising that the common plane of the interface between the two structures has been identified as {111}.[55,56] Alloy additions to the $M_{23}C_6$ structure, such as N, tend to decrease its lattice parameter and to increase the amount of interface mismatch. This should retard the growth kinetics.

Carbide precipitates normally have a sheet-like morphology at lower temperatures (480–730°C), dendritic shapes at intermediate temperatures (600–875°C), and are particles at the higher temperatures (>850°C).[55] Higher temperatures, as well as longer aging times, promote coarsened structures.

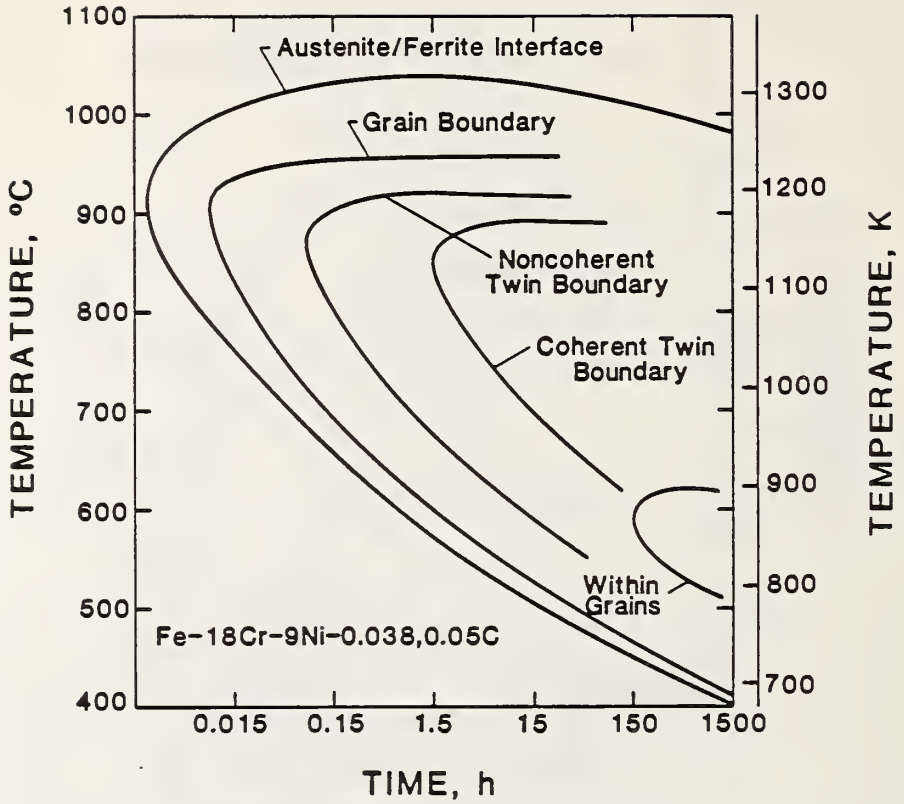

Fig. 10. Time-temperature carbide precipitation kinetics, with specific sites identified.[54,55]

Carbide precipitation in austenitic steels has long been associated with increased sensitivity to intergranular corrosion, termed sensitization. For many applications, suppression of sensitization is achieved by rapid cooling from solution-treatment temperature. During welding, however, the heat-affected zone unavoidably enters the temperature range of carbide formation. To prevent severe sensitization during welding, two courses have been followed: (1) low-carbon (≤0.03%) grades, designated by AISI with the "L" nomenclature, have been provided and (2) alloys with Ti, AISI(321), and Nb, AISI(347), have been developed to achieve more random TiC or NbC precipitation within grains, rather than $M_{23}C_6$ precipitation at grain boundaries. These alloys are often called stabilized grades of stainless steel, since the C, taken out of solution, is unavailable for carbide formation and precipitation at grain boundaries.

More thorough reviews of carbide formation in austenitic steels are provided by Novak[25] and Lai.[57]

Sigma Phase

Notice the Fe–Cr part of the phase diagram in Fig. 4: at Cr contents greater than about 15%, the σ-phase may form when the alloy is exposed to temperatures between 400 to 800°C. The σ-phase extends into the Fe–Cr–Ni ternary diagram, as indicated by Fig. 3. Alloys rich in Cr and lean in Ni tend toward σ-phase formation at lower temperatures. Maehara et al.[58] studied the effects of alloy additions on the amounts and aging times for σ-phase formation. They found that Ni decreases the amount of σ-phase formation, but increases the rate of formation in an Fe–25Cr–2.8Mo-base alloy. Additions of Cr and Mo increase both the aging kinetics and amount of σ-phase in Fe–6.5Ni–2.8Mo and Fe–25Cr–6.5Ni-base alloys, respectively.

In Fe–Cr, the highest temperature of σ-phase formation is 821°C (Fig. 4); Ni additions gradually increase this temperature (Fig. 3). The constant-Fe vertical sections of the Fe–Cr–Ni ternary of Fig. 3 are consistent with the liquidus, solidus, 1100°C, and 650°C isotherms of Speich[22] and the 802°C and 648°C isotherms of Talbot and Furman.[59] Like carbides, the σ-phase forms preferentially at high-energy surfaces. Also, when ferrite is present, there is a strong tendency for σ-phase to form initially within the ferrite or at the ferrite side of the γ–δ boundary.

The σ-phase has a tetragonal structure, 30 atoms per unit cell, an a_o lattice parameter range of −8.29 to 9.21 Å, and c_o lattice parameter range of −4.60 to 4.78 Å.[12] Sigma-phase alloy constituents do not have fixed stoichiometric ratios; they may range from B_4A to BA_4. Alloy additions, such as Cr, Mo, V, and Si, promote σ-phase formation.

For a more extensive review, see Novak[25] and Lai.[57]

PROPERTIES

Stress–Strain Characteristics

The AISI 300 series stainless steels used in cryogenic applications range from metastable to stable austenites. Alloys such as 304, containing 18Cr and 8Ni, are metastable, whereas 310, containing 26Cr and 20Ni is stable with respect to martensitic transformation. The stress–strain behavior and temperature dependence of the flow strength of these alloys differ and depend on the austenite stability. In the less stable alloys, both ϵ- and α'-martensite form; in the slightly metastable alloys, such as 316, only α'-martensite forms; and in the stable alloys, neither ϵ- nor α'-martensite forms during deformation to fracture at any temperature.

At low temperatures, the tensile stress–strain characteristics of austenitic stainless steels depend on the stability of the austenitic structure. Consider the engineering stress–strain curves of a stable austenitic steel, alloy 310 (Fig. 11a) and a metastable alloy 304 (Fig. 11b) at low temperatures. As the temperature decreases, the yield strength of alloy 310 increases significantly, and the work-hardening rates, reflecting only dislocation interactions, remain relatively constant.

In a metastable austenitic, polycrystalline alloy at low temperatures, three distinct stages are present in the stress–strain curves. The contours of their stress–strain curves (Fig. 12) are remarkably similar to single-crystal shear-stress–strain curves. Stage I represents the microstrain and early microstrain behavior. The formation of α'-martensite is not thought to occur in this range; stacking-fault clusters or ϵ-martensite, or both, are most likely to complement dislocation interactions to reduce the rate of work hardening.

Stage II, the "easy glide" range, is associated with increasing ϵ-martensite formation and the formation of α'-martensite laths at cross-slip intersections. Suzuki et al.[60] proposed that such α' laths, with the long <110> direction representing the intersection of two active slip systems, act as windows to assist cross slip. Another possible explanation is that strain-induced ϵ-martensite (whose formation is prevalent in this stage), contributes a larger strain component (or, alternatively, exhibits lower work-hardening rates). Stage II is most prevalent in the temperature range 76 to 200 K. In this temperature region, the range of strain at which the stress remains relatively constant is large, usually from 0.04 to 0.10.

In stage III, the rate of work hardening increases and then becomes constant, over a relatively large amount of plastic deformation (20 to 40%). The volume percentage of α'-martensite is linearly related to plastic deformation in stage III. The nature of the transition in the roles of α'-martensite formation—from possibly promoting easy glide in stage II to being associated with a linear, high rate of work hardening in stage III—is not clear. Perhaps in stage III essentially all active

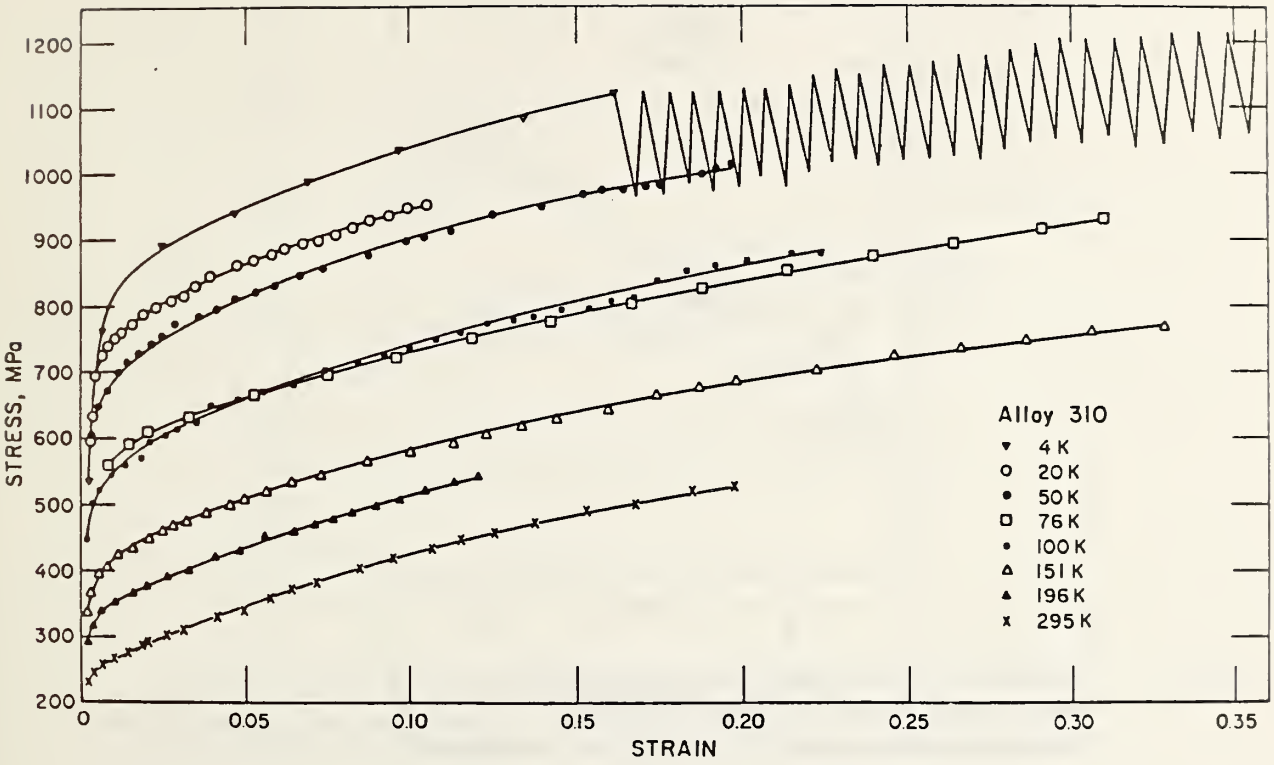

(a)

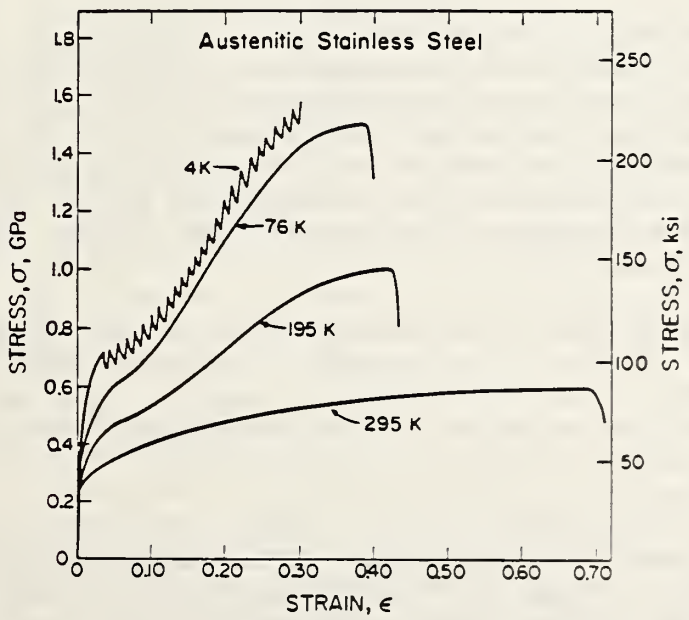

(b)

Fig. 11. Low-temperature stress–strain curves of (a) a stable austenitic alloy 310 (Fe–23Cr–20Ni) and (b) a metastable austenitic alloy 304 (Fe–19Cr–9Ni).

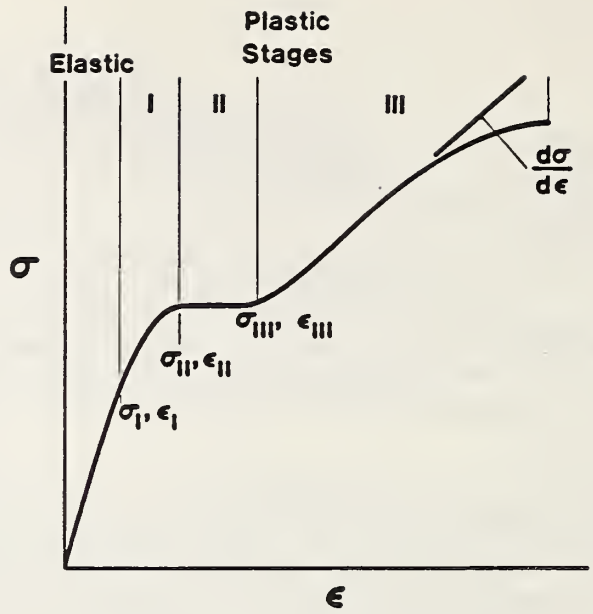

Fig. 12. Schematic depiction and characterization of three stages associated with the stress–strain curves for polycrystalline metastable austenitic stainless steels at low temperatures.

cross-slip sites have been transformed to α'-martensite, and subsequent α'-martensite formation occurs within active glide bands. Such α'-martensite formation would not be expected to promote stacking-fault glide. There is a hint from the x-ray data of Reed and Gunter[61] that the following sequence may occur: A maximum value of the volume concentration of ϵ-martensite occurs at about the transition from stage II to stage III. There is apparently no ϵ-martensite formation during stage III; the amount of ϵ-martensite decreases with strain, presumably transforming to α'-martensite.

Stages I and II decrease in significance in more stable austenites, but stage III is retained. For instance, AISI 316 exhibits neither stage I nor stage II, but does begin to transform to α'-martensite at strains of about 0.02 below 190 K. No ϵ-martensite was detected in 316LN alloys.

Alloying of austenitic stainless steels affects the stress and strain parameters of the three stages of low-temperature deformation. The effects of Mn alloying on these parameters at 4 K have been studied by Reed and Tobler.[62] The yield strength, σ_y (flow strength at 0.002 plastic strain) is within stage I. As shown in Fig. 13, σ_y is linearly dependent on Mn content, increasing with increasing Mn. The linear dependence matches that of σ_{II}, the stress at which stage II begins. The increase of σ_y with Mn is considerable, about 33 MPa per wt.% Mn. The addition of Mn to austenite solid solution does not alter the lattice

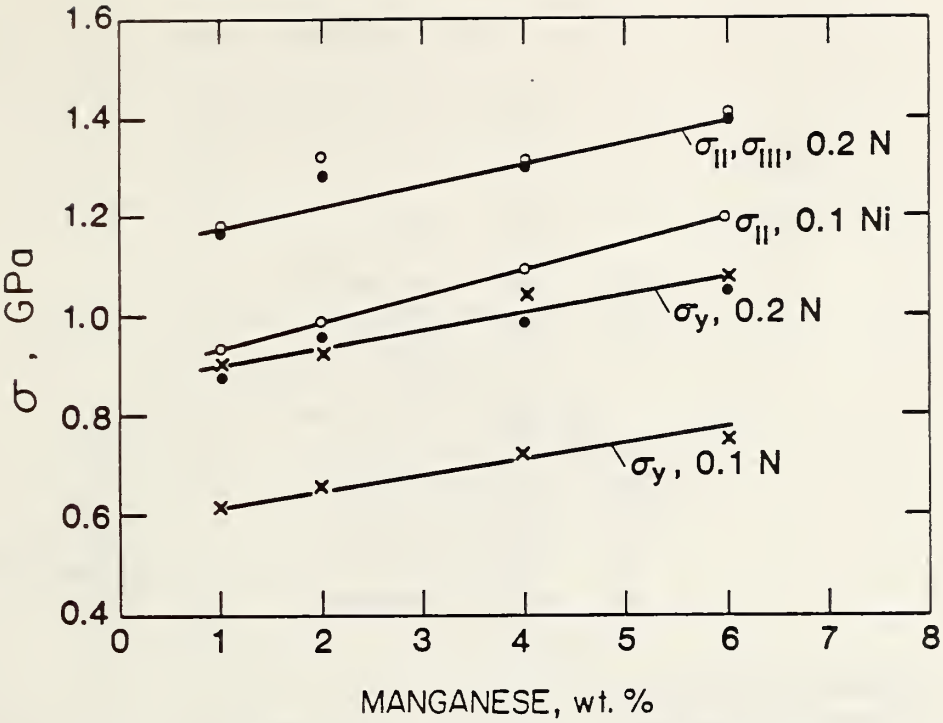

Fig. 13. Dependence of stages I and II strength parameters on Mn and N content at 4 K.

parameter nor the shear modulus significantly (see later discussion), therefore traditional solid-solution strengthening should not result from Mn addition. But Mn increases the stacking-fault energy and suppresses α'- and ϵ-martensite transformation; these phase transformations influence the stress and strain parameters. Therefore, the increases in strength that occur when Mn is added are due to the contribution of Mn to austenite stability. Figure 13 shows that an addition of 0.1N increases σ_y about 290 MPa. Nitrogen has the same strengthening effect in stable alloys, which implies that it has little effect on hcp or bcc stability within the composition range 0.1 to 0.2 wt.%.

The stress denoting transition to the region of high work-hardening rates, σ_{III}, tracks very closely with σ_{II}. The rate of work hardening (from engineering stress–strain curves) of stage III decreases with increasing Mn and N, as shown in Fig. 14. The addition of N slightly affects the dependence of Mn content; N contributes to the reduction of $d\sigma/d\epsilon$ about ten times more strongly (on the basis of wt.% addition) than Mn. The dependence of the work-hardening rate in stage III on the percent α'-martensite per unit elongation is shown in Fig. 15. Clearly, there is a strong linear correlation, and the rate of work hardening can be regarded as a function of austenite stability with respect to α'-martensite formation, as determined by composition.

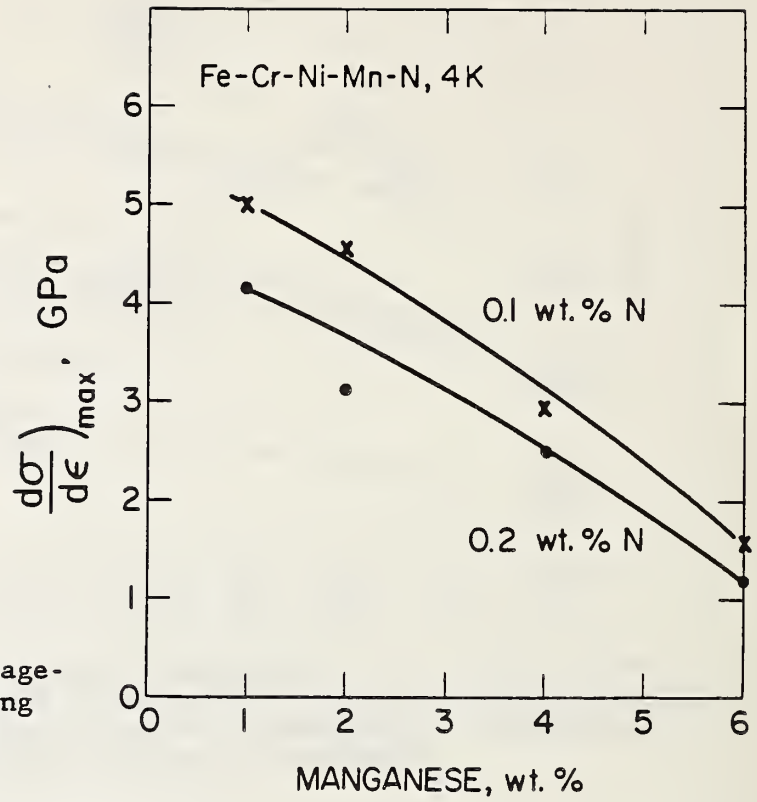

Fig. 14. Dependence of stage-III work-hardening rate on Mn and N contents at 4 K.

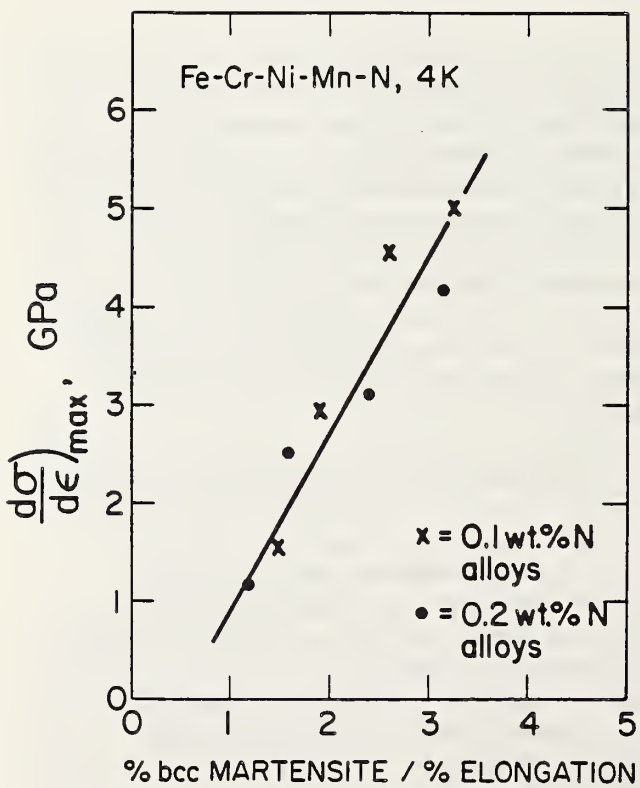

Fig. 15. Dependence of stage-III work-hardening rate on the normalized amount of α-martensite formed during uniform elongation at 4 K.

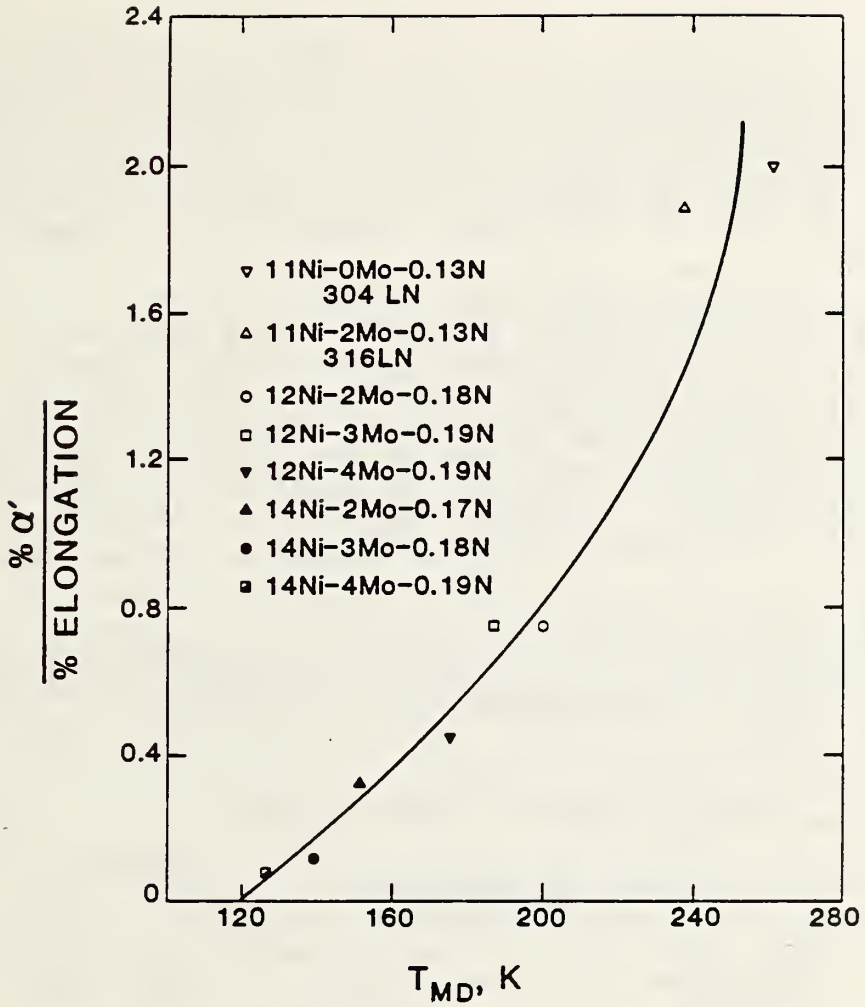

Fig. 16. Correlation between normalized α′-martensite formation in stage III with alloying, as characterized by the T_{md} calculations of Williams et al.[37]

We have performed numerous correlations between the normalized amount of strain-induced α′-martensite at final elongation at 4 K and the alloy composition. Our best correlation for this normalized strain-induced martensite was obtained by using the Williams et al.[38] regression analysis for T_{md}. In Fig. 16 their expression is plotted versus α′/% tensile elongation at 4 K for a series of modified 316LN alloys. Correlation is excellent for these alloys with a calculated T_{md} ranging from 120 to 240 K.

Therefore, the deformation characteristics of austenitic stainless steels can be significantly controlled by alloying. Sufficient alloy additions to stabilize the austenite result in typical solid-solution-strengthened, fcc stress–strain characteristics. The shape of the stress–strain curves of metastable austenites during and strain-induced α′- and ε-martensite transformations is affected by alloying.

Strength

In addition to austenite stability, the strength of austenitic stainless steels is influenced by temperature, grain size, cold and hot working, and interstitial and solid-solution alloying. Temperature and grain-size effects have been discussed previously.[63-66] We focus here on the effects of alloy strengthening on stable austenitic steels at low temperatures.

At very low temperatures, the variation of tensile yield strength (σ_y) with N, C, Mo, Mn, and Ni additions to Fe–Cr–Ni austenitic steels has been recently and extensively studied. In Japan a program to develop an alloy with a yield strength of 1200 MPa and a toughness of 200 MPa·m$^{\frac{1}{2}}$ has now been completed.[67–69] At NBS we have tested at low temperatures some of the new Japanese alloys, the European 316LN alloys, and selected laboratory heats from U.S. suppliers in which N, C, Mo, Mn, and Ni alloy additions were systematically varied. A summary of these test results follows.

The interstitial additions substantially strengthen the alloys at low temperatures.[64,65,70-83] In Fig. 17, the effect of C + N on yield strength at 4 K for an Fe–18Cr–10Ni steel is presented.[72] The break in

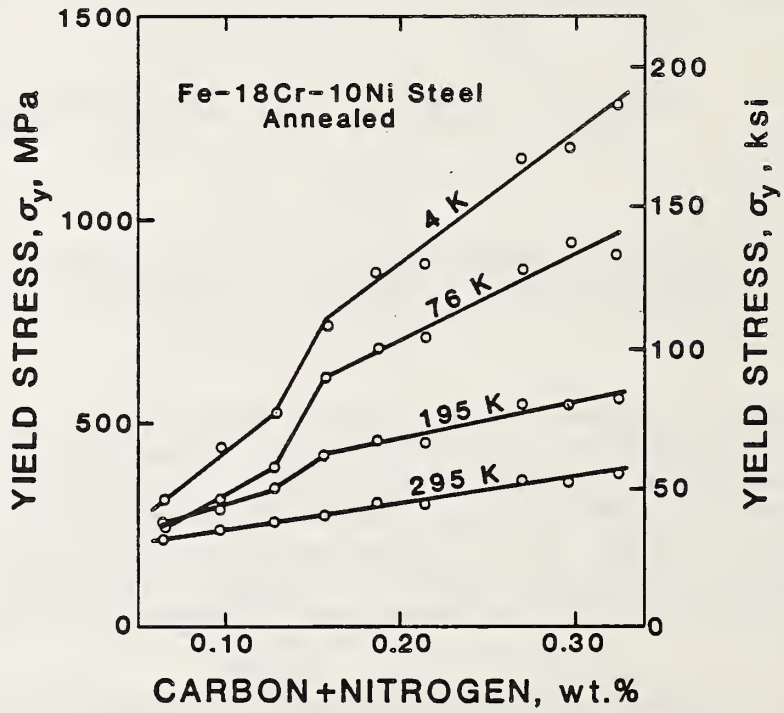

Fig. 17. Dependence of yield strength on C + N contents in Fe–18Cr–10Ni austenitic stainless steels at low temperatures.

the linear dependencies at about 0.15(C + N) is related to martensitic transformation; at lower C + N contents, the strain-induced martensite reduces the flow strength, as discussed in the Stress–Strain Characteristics section. Regression analysis of 99 data points for alloy 316LN (and alloys with similar compositions) at 4 K indicated that yield strength increased 237 MPa per 0.1N;[77] an earlier analysis of 30 data points for 304LN-type alloys at 4 K found that yield strength increased 319 MPa per 0.1N.[70] Strengthening from C is about half that from N at 4 K.[70] Thus, N addition strengthens considerably more than equivalent C addition at low temperatures. Alloying with N instead of C also reduces the tendency toward sensitization, as discussed under Carbides. Furthermore, N is less expensive than C. For these reasons, N is now usually selected to increase the low-temperature strength of austenitic stainless steels. Many recent studies have measured the strengthening contribution from N for both Fe–Cr–Ni and Fe–Cr–Mn base austenitic structures at 4 K.[64,65,70-75,77-83] Reed and Simon[70,77] found a smaller standard deviation from regression analyses by using the power of one to express the N-content dependence rather than a 1/2 or 2/3 power dependence. Fundamental theories for solid-solution strengthening[84-86] predict dependence of the flow strength on concentration to the power 1/2 or 2/3 from dislocations cutting through the stress field created by individual atoms of this concentration. The linear dependence of yield strength on C + N shown in Fig. 17 also supports this assessment. This dependence of yield strength on N alloying is strongly dependent on temperature (Fig. 17). Reed and Simon[70] found that the N coefficient increased by a factor of 6 from 295 to 4 K, while the coefficient for C increased by only a factor of 2. This strong temperature dependence implies increased N bonding strength, or clustering, below room temperature, since the temperature dependence of C (the larger atom), should reflect the modulus and size effects (see later discussion).

The dependence of yield strength on solid-solution alloying additions, such as Mo, Mn, and Ni, is not as great. Molybdenum increases strength most effectively, about 50 MPa per wt.% at 4 K.[74,87-89] There is evidence that at higher Ni contents the strengthening effects of Mo are reduced.[89] Manganese, when not affecting austenite stability, increases yield strength by about 10 MPa per wt.% at 4 K.[53,73,75,89,90] Nickel does not contribute directly to solid-solution strengthening, but it does affect strength through its strong contribution to austenite stability. The temperature dependence of the solid-solution strengthening additions has not been assessed.

In Table 5, the strengthening contributions from substitutional and interstitial alloying additions in fcc elements[92-97] and in austenitic stainless steels[62-91] are listed in terms of a fraction of the shear modulus. This refers to the increase of yield strength from adding 100% (by atoms) of the solute, found by extrapolating from available data that usually range from 1 for interstitials to 5 to 20 at.%.

Table 5. Strengthening Contributions in fcc Alloys

Solvent	Solute	Temperature	Amount ($\Delta\sigma$/100%)
Ag	Aℓ	4	G/30
	Sb	294	G/100
		76	G/30
Ni	Mo	295	G/45
	C	4	G/7
		295	G/30
Cu	Ni	76	G/120
	Au	76	G/100
Pb	Ag*	4	2G
	Sn	4	0
Fe–Cr–Ni (austenite)	N	4	G/2.5
		295	G/15
	C	4	G/5.5
		295	G/10
	Mo	4	G/60
		295	0
	Mn	4	G/200
		295	0
	Ni	4	0
		295	0

*Quenched from 300°C

Adding C to Ni[95] or C to austenite produces roughly the same increases in strength at low temperatures. The addition of Mo to Ni or to Fe–Cr–Ni is also approximately equivalent. Galligan and Goldman[92] have achieved much stronger strengthening effects from alloying by quenching-in Ag into probable split-interstitial sites in Pb. In their work, strength increases are linearly proportional to Ag content, not to a fractional power of it.

From the theory of solid-solution strengthening,[84-86] the shear strength, τ, resulting from a random array of single atoms interacting with mobile dislocations is

$$\tau = A[C_F^{2/3}]\ [f_o^{4/3}], \qquad (2)$$

where C_F is the concentration of a solute species, and A is considered to be a constant for this discussion. The maximum interaction force is given by

$$f_o^2 = \eta^2 + \alpha^2\delta^2, \quad (3)$$

where the modulus misfit is

$$\delta = \frac{1}{G}\frac{dG}{dc}. \quad (4)$$

In Eq. (4), G is the shear modulus, c is the concentration, and the size misfit,

$$\delta = \frac{1}{a}\frac{da}{dc},$$

where a is the lattice parameter. The constant α is typically about 20.[84] Thus, the relative magnitudes of the strengthening contributions of various solutes may be estimated by comparing the modulus and size misfit parameters, assuming that other possible strengthening effects (e.g., electrostatic, stacking-fault interactions) are small.

Ledbetter and Austin[98] studied the elastic properties of austenitic stainless steel alloy series and measured their lattice parameters. Their measurements are summarized in Table 6, where E is Young's modulus, G is shear modulus, B is bulk modulus, ν is Poisson's ratio, and V is atomic volume. Lattice parameter measurements at 4 K are planned in the near future.

Table 6. Effect of Alloying on Volume and Elastic Constants

	$\frac{1}{a}\frac{da}{dc}$	$\frac{1}{E}\frac{dE}{dc}$		$\frac{1}{G}\frac{dG}{dc}$		$\frac{1}{B}\frac{dB}{dc}$		$\frac{1}{\nu}\frac{d\nu}{dc}$		$\frac{V(X)}{V(Fe)}$
	295 K	295 K	4 K	295 K	4 K	295 K	4 K	295 K	4 K	
C	0.218	−0.78	0.61	−0.76	0.81	−0.93	−0.52	−0.11	−0.90	0.34
N	0.240									0.30
Ni	−0.003	0.07	—	0.09	—	−0.01	—	−0.06	—	0.93
Mn	0.022	−0.30	−0.38	−0.27	−0.37	−0.45	−0.48	−0.12	−0.08	1.04
Mo	0.150	−0.91	−0.14	−1.18	−0.38	0.79	1.30	1.22	1.13	1.32
Cr	0.075	—	—	—	—	—	—	—	—	1.02

At room temperature both C and N show a large size misfit despite their small atom size [signified by the V(X)/V(Fe) ratio]; obviously they must occupy interstitial lattice sites to achieve this increase. This size misfit is larger for N than for C, although the atom size of N is less than that of C. The divergence of E and G trends from B and ν trends implies electronic bonding effects that alter shear modes differently than dilatational modes; this divergence is found for N and C at 4 K and for Mo at both temperatures. Furthermore, the changes in sign of the Young's and shear moduli parameters of N and C on cooling from 295 to 4 K imply a low-temperature transition toward increased covalent bonding.

The maximum interaction forces, assuming $\alpha = 20$, for each solute are summarized in Table 7. The order of ratios of the interaction forces is nearly correct when compared with the strengthening contribution listed in Table 5; only C and N are reversed. However, the relative magnitudes of the interaction forces of C and N show greater disparity than the relative magnitudes of the solute contributions. The interstitial-element interaction forces are smaller than would be expected if one considered their strengthening contributions. This disparity undoubtedly will be increased at 4 K when the lattice-parameter measurements at 4 K are obtained: the ratio of strengthening contributions from interstitials increases relative to substitutional solid-solution elements at 4 K.

This leads to the suggestion that, particularly at low temperatures, the dislocation–interstitial interaction is distinct from that of the dislocation–solid-solution interaction. The interaction-force ratios could be brought more in line with the strengthening contributions by increasing α, the parameter related to the curvature of the interaction potential of the solvent with the moving dislocations,[83] since the size-misfit parameters relate directly to the relative strengthening contributions for each type of atom. These disparities, combined with the linear dependence of strength on solute interstitial content, leads to the consideration of interstitial clustering.

Galligan and Goldman[92] measured strengthening factors of 2G at room temperature for presumably split interstitials of Ag in Pb, where Ag has only slightly lower specific volume than Pb. It is not difficult to envision that the much smaller C and N interstitials, in similar lattice positions, strengthen by factors of G/10 to G/15 at room temperature and that this strong, short-range interaction force is very temperature dependent.

Table 7. Maximum Interaction Forces* for Solutes in Austenitic Stainless Steel

T(K)	C	N	Ni	Mn	Mo
295	4.43	4.86	0.26	0.52	3.22

*$f_o^2 = \eta^2 + \alpha^2\delta^2$, where α is assumed to equal 20

SUMMARY

Austenitic stainless steel structures and strengths have been reviewed, with emphasis placed on low-temperature characteristics to include recent studies that have led to stronger alloys for cryogenic applications. The stress–strain characteristics of austenitic stainless steels depend on austenite stability. A region of low work hardening, following initial plastic deformation, is associated with hcp-martensite formation and bcc-martensite formation at cross-slip sites. The final work hardening stage is associated with bcc martensite formation. All stages are related to alloying effects on austenite stability.

The interstitials C and N have been shown to contribute to more strength than that predicted by solution-hardening dislocation theories. It is argued that C and N must act in clusters to increase solution hardening. Nitrogen has proven to be the best alloying element for increasing strength at low temperatures.

ACKNOWLEDGMENT

This work was partially funded by the Office of Fusion Energy, U.S. Department of Energy.

REFERENCES

1. L. Guillet, "Chromium Steels," Rev. Metall. 1, 155 (1904).
2. A. M. Portevin, "Contribution to the Study of the Special Ternary Steels," Iron and Steel Institute, Carnegie Sch. Mem. 1, 230 (1909).
3. W. Giesen, "The Special Steels in Theory and Practice," Iron and Steel Institute, Carnegie Sch. Mem. 1 (1909).
4. P. Monnartz, "The Study of Iron–Chromium Alloys with Special Consideration of their Resistance to Acids," Metallurgie 8, 161 (1911).
5. L. Guillet, "Nickel–Chrome Steels," Rev. Metall. 3, 332 (1906).
6. The Book of Stainless Steels, Ed. E. E. Thum, American Society for Metals, Metals Park, Ohio (1935), 787 pp.
7. C. A. Zapffe, Stainless Steels, American Society for Metals, Metals Park, Ohio (1949), 368 pp.
8. J. H. G. Monypenny, Stainless Iron and Steel, vol. 1, Chapman and Hall, London (1951), 524 pp.
9. J. H. G. Monypenny, Stainless Iron and Steel, vol. 2, Chapman and Hall, London (1954), 330 pp.
10. F. H. Keating, Chromium Nickel Austenitic Steels, Butterworth Scientific, London (1956), 138 pp.
11. Source Book on Stainless Steels, American Society for Metals, Metals Park, Ohio (1976) 408 pp.
12. Handbook of Stainless Steels, Eds. D. Peckner and I. M. Bernstein, McGraw–Hill, New York (1977).
13. J. G. Parr and A. Hanson (revised by R. A. Lula) Stainless Steel, American Society for Metals, Metals Park, Ohio (1986), 173 pp.

14. R. A. Lula, Manganese Stainless Steels, The Manganese Centre, Paris (1986), 83 pp.
15. Symposium on the Nature, Occurrence, and Effects of Sigma Phase, STP 110, American Society for Testing and Materials, Philadelphia (1951), 181 pp.
16. Effects of Residual Elements on Properties of Austenitic Stainless Steels, STP 418, American Society for Testing and Materials, Philadelphia (1967), 136 pp.
17. Stainless Steels, The Iron and Steel Institute, London (1969), 214 pp.
18. Stainless Steel '77, Climax Molybdenum Company, Climax, Colorado (1977), 256 pp.
19. Stainless Steel Castings, Eds. V. G. Behal and A. S. Melilli, STP 756, American Society for Testing and Materials, Philadelphia (1982) 444 pp.
20. Austenitic Steels at Low Temperatures, Eds. R. P. Reed and T. Horiuchi, Plenum Press, New York (1983), 388 pp.
21. New Developments in Stainless Steel Technology Conference Proceedings, Ed. R. A. Lula, American Society for Metals, Metals Park, Ohio (1985), 391 pp.
22. G. R. Speich in: Source Book on Stainless Steels, American Society for Metals, Metals Park, Ohio (1976), pp. 424–426.
23. E. Schurmann and S. Brauckman, "Untersuchungen über die Schmelzgleichgewichte in der Eisenecke des Dreistoffsystems Eisen–Chrom–Nickel," Arch. Eisenhüttenw. 48, 3–8 (1977).
24. J. A. Brooks, J. C. Williams, and A. W. Thompson, "STEM Analysis of Primary Austenite Solidified Stainless Steel Welds," Metall. Trans. 14A, 23–31 (1983).
25. C. J. Novak in: Handbook of Stainless Steels, Eds. D. Peckner and I. M. Bernstein, McGraw–Hill, New York (1977), pp. 401–478.
26. A. L. Schaeffler, "Constitution Diagram for Stainless Steel Weld Metal," Met. Prog., 56, 680 (1949).
27. W. T. DeLong, G. A. Ostrom, and E. R. Szumachowski, "Measure and Calculation of Ferrite in Stainless Steel Weld Metal," Weld. J. 35, 521s–528s (1956).
28. N. Suutala, "Effects of Manganese and Nitrogen on the Solidification Mode in Austenitic Stainless Steel Welds," Metall. Trans. 13A, 2121–2130 (1982).
29. F. C. Hull, "Delta Ferrite and Martensite Formation in Stainless Steels," Weld. J. 52, 193s–203s (1973).
30. O. Hammar and U. Svensson in: Solidification and Casting of Metals, The Metals Society, London (1979), pp. 401–410.
31. L. Kaufman, "The Lattice Stability of the Transition Metals," in: Phase Stability in Metals and Alloys, Eds. P. S. Rudman, J. Stringer, and R. I. Jaffee, McGraw–Hill, New York (1967), pp. 125–150.
32. R. P. Reed, "Martensitic Phase Transformations," in: Materials at Low Temperatures, Eds. R. P. Reed and A. F. Clark, American Society for Metals, Metals Park, Ohio (1983), pp. 295–341.

33. G. H. Eichelman and F. C. Hull, "The Effect of Composition on the Temperature of Spontaneous Transformation of Austenite to Martensite in 18–8 Type Stainless Steel," Trans. Amer. Soc. Met. 45, 77–104 (1953).
34. F. C. Monkman, F. B. Cuff, and N. J. Grant, "Computation of M_s for Stainless Steels," Met. Prog. 71, 94–96 (1957).
35. K. W. Andrews, "Empirical Formulae for the Calculation of Some Transformation Temperatures, J. Iron Steel Inst. 203, 721–727 (1965).
36. J. A. Self, "Effects of Compositions upon the Martensite Transformation Temperature of Austenitic Steel Welds," Center for Welding Research, MT-CWR-086-037, Colorado School of Mines, Golden, Colorado (1986).
37. T. Angel, "Formation of Martensite in Austenitic Stainless Steels," J. Iron Steel Inst. 177, 165–174 (1954).
38. I. Williams, R. G. Williams, and R. C. Capellano, "Stability of Austenitic Stainless Steels between 4 K and 373 K," in: Proceedings of the Sixth International Cryogenic Engineering Conference, IPC Science and Technology Press, Guildford, Surrey, England (1976), pp. 337–341.
39. J. G. Breedis, "Martensitic Transformation Iron–Chromium–Nickel Alloys," Trans. AIME 230, 1583–1596 (1964).
40. R. P. Reed, "The Spontaneous Martensitic Transformations in 18% Cr, 8% Ni Steels," Acta Metall. 10, 865–887 (1962).
41. R. M. Kelly, "The Martensite Transformation in Steels with Low Stacking Fault Energy," Acta Metall. 13, 635–646 (1965).
42. R. E. Schramm and R. P. Reed, "Stacking Fault Energies of Seven Commercial Austenitic Stainless Steels," Metall. Trans. 6A, 1345–1351 (1975).
43. C. G. Rhodes and A. W. Thompson, "The Composition Dependence of Stacking Fault Energy in Austenitic Stainless Steels," Metall. Trans. 8A, 1901–1906 (1977).
44. C. C. Bampton, L. P. Jones, and M. H. Loretto, "Stacking Fault Energy Measurements in Some Austenitic Stainless Steels," Acta Metall. 26, 39–51 (1978).
45. P. J. Brofman and G. S. Ansell, "On the Effect of Carbon on the Stacking Fault Energy of Austenitic Stainless Steels," Metall. Trans. 9A, 879–880 (1978).
46. H. M. Ledbetter and M. W. Austin, "Stacking-Fault Energies in 304-Type Stainless Steels: Effects of Interstitial Carbon and Nitrogen" in: Materials Studies for Magnetic Fusion Energy Applications at Low Temperatures—VIII, Ed. R. P. Reed, National Bureau of Standards, NBSIR 85-3025, Boulder, Colorado (1985), pp. 271–294.
47. R. E. Stoltz and J. B. VanderSande, "The Effect of Nitrogen on Stacking Fault Energy of Fe–Ni–Cr–Mn Steels," SAND 79-8735, Sandia Laboratories, Albuquerque, New Mexico (1979).
48. M. Fujikuma, K. Takada, and K. Ishida, "Effect of Manganese and Nitrogen on the Mechanical Properties of Fe18%Cr10%Ni Stainless Steels," Trans. Iron Steel Inst. Jap. 15, 464–469 (1975).
49. H. Tuma, M. Vyklicky, and K. Lobl, "Activity and Solubility of C in Austenitic 18 Percent Cr–Ni Steels," Arch. Eisenhüttenw. 41, 983–988 (1970).

50. T. Masumoto and Y. Imai, "Structural Diagrams and Tensile Properties of the 18 Percent Cr–Fe–Ni–N Quarternary System Alloys," J. Jpn. Inst. Met. 33, 1364–1371 (1969).
51. M. Deighton, "Solubility of $M_{23}C_6$ in Type 316 Stainless Steel," J. Iron Steel Inst. 208, 1012–1014 (1970).
52. D. Kumar, A. D. King, and T. Bell, "Mass Transfer of Nitrogen from N_2–H_2 Atmospheres into Fe–18Cr–Ni–Mn Alloys," Met. Sci. 17, 32–40 (1983).
53. T. Sakamoto, Y. Nakagawa, and I. Yamauchi, "Effect of Mn on the Cryogenic Properties of High Nitrogen Austenitic Stainless Steels" in: Advances in Cryogenic Engineering – Materials, Vol. 32, Eds. R. P. Reed and A. F. Clark, Plenum Press, New York (1986), pp. 65–71.
54. S. J. Rosenberg and C. R. Irish, "Solubility of Carbon in 18 Percent Chromium – 10 percent Nickel Austenite," J. Res. Nat. Bur. Stand. 48, 40–48 (1952).
55. R. Stickler and A. Vinckier, "Morphology of Grain-Boundary Carbides and Its Influence on Intergranular Corrosion of 304 Stainless Steel," Trans. Amer. Soc. Met. 54, 362–380 (1961).
56. M. H. Lewis and B. Hattersley, "Precipitation of $M_{23}C_6$ in Austenitic Steels," Acta Metall. 13, 1159–1168 (1965).
57. J. K. L. Lai, "A Review of Precipitation Behavior in AISI Type 316 Stainless Steel," Mater. Sci. Eng. 61, 101–109 (1983).
58. Y. Maehara, Y. Ohmori, J. Murayama, N. Fujino, and T. Kunitake, "Effects of Alloying Elements on σ Phase Precipitation in $\delta\gamma$ Duplex Phase Stainless Steels," Met. Sci. 17, 541–547 (1983).
59. A. M. Talbot and D. E. Furman, "Sigma Formation and Its Effect on the Impact Properties of Iron–Nickel–Chromium Alloys," Trans. Amer. Soc. Met. 45, 429–442 (1953).
60. T. Suzuki, H. Kojama, K. Suzuki, T. Hashimoto, and M. Ichihara, "An Experimental Study on the Martensite Nucleation and Growth in 18/8 Stainless Steel," Acta Metall. 25, 1151–1162 (1977).
61. R. P. Reed and C. J. Guntner, "Stress-Induced Martensitic Transformations in 18Cr–8Ni Steel," Trans. AIME 230, 1713–1720 (1964).
62. R. P. Reed and R. L. Tobler, "Deformation of Metastable Austenitic Steels at Low Temperatures," in: Advances in Cryogenic Engineering – Materials, vol. 28, Eds. R. P. Reed and A. F. Clark, Plenum Press, New York (1982), pp. 49–56.
63. R. P. Reed, and J. M. Arvidson, "The Temperature Dependence of the Tensile Yield Strength of Selected Austenitic Steels," in: Advances in Cryogenic Engineering – Materials, vol. 30, Eds. A. F. Clark and R. P. Reed, Plenum Press, New York (1984), pp. 263–270.
64. N. J. Simon and R. P. Reed, "Strength and Toughness of AISI 304 and 316 at 4 K," J. Nucl. Mater. 141–143, 44–48 (1986).
65. R. P. Reed, N. J. Simon, P. T. Purtscher, and R. L. Tobler, "Alloy 316LN for Low Temperature Structures: A Summary of Tensile and Fracture Data, in: Proceedings, Eleventh International Cryogenic Engineering Conference, Eds. G. Klipping and I. Klipping, Butterworths, Guildford, Surrey, England (1986), pp. 786–790.

66. R. L. Tobler, R. P. Reed, and D. S. Burkhalter, "Temperature Dependence of Yielding in Austenitic Stainless Steels," in: Advances in Cryogenic Engineering – Materials, vol. 26, Eds. A. F. Clark and R. P. Reed, Plenum Press, New York (1980), pp. 107–110.
67. H. Nakajima, K. Yoshida, Y. Takahashi, E. Tada, M. Oshikiri, K. Koizumi, S. Shimamoto, R. Mira, M. Shimara, and S. Tone, "Development of the New Cryogenic Structural Material for Fusion Experimental Reactors," in: Advances in Cryogenic Engineering – Materials, vol. 32, Eds. R. P. Reed and A. F. Clark, Plenum Press, New York (1984), pp. 219–226.
68. K. Yoshida, N. Nakajima, K. Koizumi, M. Shimada, Y. Sanda, Y. Takahashi, E. Tada, H. Tsuji, and S. Shimamoto, "Development of Cryogenic Structural Materials for Tokamak Reactor," in: Austenitic Steels at Low Temperatures, Eds. R. P. Reed and T. Horiuchi, Plenum Press, New York (1983) pp. 29–39.
69. S. Shimamoto, H. Nakajima, K. Yoshida, and E. Tada, "Requirements for Structural Alloys for Superconducting Magnet Cases," in: Advances in Cryogenic Engineering – Materials, vol. 32, Eds. R. P. Reed and A. F. Clark, Plenum Press, New York (1986), pp. 23–32.
70. R. P. Reed and N. J. Simon, "Low Temperature Strengthening of Austenitic Stainless Steels with Nitrogen and Carbon," in: Advances in Cryogenic Engineering – Materials, vol. 30, Eds. A. F. Clark and R. P. Reed, Plenum Press, New York (1984), pp. 127–136.
71. K. Nohara, T. Kato, T. Sasaki, S. Suzuki, and A. Ejima, "Strengthening and Serrated Flow of High-Manganese Nonmagnetic Steel at Cryogenic Temperatures," in: Advances in Cryogenic Engineering – Materials, vol. 30, Eds. R. P. Reed and A. F. Clark, Plenum Press, New York (1984), pp. 193–201.
72. R. L. Tobler and R. P. Reed, "Tensile and Fracture Properties of Manganese-Modified AISI 304 Type Stainless Steel," in: Advances in Cryogenic in Engineering – Materials, vol. 28, Eds. R. P. Reed and A. F. Clark, Plenum Press, New York (1982), pp. 83–92.
73. T. Horiuchi, R. Ogawa, M. Shimada, S. Tone, M. Yamaga, and Y. Kasamatsu, "Mechanical Properties of High Manganese Steels at Cryogenic Temperatures," in: Advances in Cryogenic Engineering – Materials, vol. 28, Eds. R. P. Reed and A. F. Clark, Plenum Press, New York (1982), pp. 93–103.
74. S. Yamamoto, N. Yamagami, and C. Ouchi, "Effect of Metallurgical Variables on Strength and Toughness of Mn–Cr and Ni–Cr Stainless Steels at 4.2K," in: Advances in Cryogenic Engineering – Materials, vol. 32, Eds. R. P. Reed and A. F. Clark, Plenum Press, New York (1986), pp. 57–64.
75. T. Horiuchi, R. Ogawa, and M. Shimada, "Cryogenic Fe–Mn Austenitic Steels," in: Advances in Cryogenic Engineering – Materials, vol. 32, Eds. R. P. Reed and A. F. Clark, Plenum Press, New York (1986), pp. 33–42.
76. R. L. Tobler, D. H. Beckman, and R. P. Reed, "Factors Influencing the Low Temperature Dependence of Yielding in AISI 316 Stainless Steels," in: Austenitic Steels at Low Temperatures, Eds. R. P. Reed and T. Horiuchi, Plenum Press, New York (1983), pp. 135–157.

77. N. J. Simon and R. P. Reed, "Design of 316LN-Type Alloys," in: Advances in Cryogenic Engineering – Materials, vol. 34, Eds. A. F. Clark and R. P. Reed, Plenum Press, New York (1988), pp.165–172.
78. R. P. Reed, P. T. Purtscher, and K. A. Yushchenko, "Nickel and Nitrogen Alloying Effects on the Strength and Toughness of Austenitic Stainless at 4 K, in: Advances in Cryogenic Engineering – Materials, vol. 32, Eds. R. P. Reed and A. F. Clark, Plenum Press, New York (1986), pp. 33–42.
79. T. Sakamoto, Y. Nakagawa, and I. Yamauchi." Effect of Mn on the Cryogenic Properties of High Nitrogen Austenitic Stainless Steels," in: Advances in Cryogenic Engineering – Materials, vol. 32, Eds. R. P. Reed and A. F. Clark, Plenum Press, New York (1986), pp. 65–71.
80. Y. Takahashi, K. Yoshida, M. Shimada, E. Tada, R. Miura, and S. Shimamoto, "Mechanical Evaluation of Nitrogen-Strengthened Stainless Steels at 4 K," in: Advances in Cryogenic Engineering – Materials, vol. 28, Eds. R. P. Reed and A. F. Clark, Plenum Press, New York (1986), pp. 73–81.
81. H. Masumoto, K. Suemune, H. Nakajima, and S. Shimimoto, "Development of High-Strength, High-Manganese Steels for Cryogenic Use," in: Advances in Cryogenic Engineering – Materials, vol. 30, Eds. A. F. Clark and R. P. Reed, Plenum Press, New York (1984), pp. 169–176.
82. K. Shibata, Y. Kobiti, Y. Kishimoto, and T. Fujita, "Mechanical Properties of High Yield Strength High Manganese Steels at Cryogenic Temperatures," in: Advances in Cryogenic Engineering – Materials, Vol. 30, Eds. R. P. Reed and A. F. Clark, Plenum Press, New York (1984), pp. 169–176.
83. T. Sakamoto, Y. Nakagawa, I. Yamauchi, T. Zaizen, H. Nakajima, and S. Shimamoto, "Nitrogen-Containing 25Cr–13Ni Stainless Steel as a Cryogenic Structural Material," in: Advances in Cryogenic Engineering – Materials, vol. 30, Eds. A. F. Clark and R. P. Reed, Plenum Press, New York (1984), pp. 145–152.
84. P. Haasen, "Solution Hardening in f.c.c. Metals," Chapter 15 in: Dislocations in Solids, Ed. F. R. N. Nabarro, North-Holland, New York (1976), pp. 155–189.
85. F. R. N. Nabarro, "The Theory of Solution Hardening," Philos. Mag. 35, 613–622 (1977).
86. R. Labusch, "Statistische Theorien der Mischkristallhartung," Acta Metall. 20, 917–927 (1972).
87. K. Suemune, K. Sugino, H. Masumoto, H. Nakajima, and S. Shimamoto, "Improvement of Toughness of a High-Strength, High-Manganese Stainless Steel for Cryogenic Use," in: Advances in Cryogenic Engineering – Materials, vol. 32, Eds. R. P. Reed and A. F. Clark, Plenum Press, New York (1986), pp. 51–56.
88. K. Ishikawa, K. Hiraga, T. Ogata,and K. Nagai, "Low Temperature Properties of High-Manganese–Molybdenum Austenitic Iron Alloys," in: Austenitic Steels at Low Temperatures, Eds. R. P. Reed and T. Horiuchi, Plenum Press, New York (1983), pp. 295–309.

89. P. T. Purtscher, R. P. Walsh, and R. P. Reed, "Effect of Chemical Composition on the 4 K Mechanical Properties of 316LN-Type Alloys," in: Advances in Cryogenic Engineering – Materials, vol. 34, Eds. A. F. Clark and R. P. Reed, Plenum Press, New York (1988), pp. 191–198.
90. R. Muira, H. Nakajima, Y. Takahashi, and K. Yoshida, "32Mn–7Cr Austenitic Steel for Cryogenic Applications," in: Advances in Cryogenic Engineering – Materials, vol. 30, Eds. A. F. Clark and R. P. Reed, Plenum Press, New York (1984), pp. 245–252.
91. K. Hiraga, K. Ishikawa, K. Nagai, and T. Ogata, "Mechanical Properties of Cold-Rolled and Aged Fe–Ni–Cr–Ti-Austenitic Alloys for Low Temperature Use," in: Advances in Cryogenic Engineering – Materials, vol. 30, Eds. R. P. Reed and A. F. Clark, Plenum Press, New York (1984), pp. 203–210.
92. J. M. Galligan and P. D. Goldman, "Metal Interstitial Solid-Solution Strengthening," in: Strength of Metals and Alloys, Proceedings of the Fifth International Conference, Pt. II, Peramon, New York (1980), pp. 983–988.
93. A. A. Hendrickson and M. E. Fine, "Solid Solution Strengthening of Ag by Aℓ," Trans. AIME 221, 967–974 (1961).
94. T. A. Bloom, U. F. Kocks, and P. Nash, "Deformation Behavior of Ni–Mo Alloys," Acta Metall. 33, 265–277 (1985).
95. Y. Nakada and A. S. Keh, "Solid-Solution Strengthening in Ni–C Alloys," Metall. Trans. 2 441–447 (1971).
96. G. J. den Otter and A. Van den Beukel, "Flow Stress and Activation Volume of Some Cold-Worked Copper-Based Solid Solutions," Phys. Status Solidi(a) 55, (1979), pp. 785–792.
97. J. H. Tregilgas and J. M. Galligan, "Hardening from Metal Interstitials in a Face-Centered Cubic Lattice—Pb–Ag," Scr. Metall. 9, 1225–1227 (1975).
98. H. M. Ledbetter and M. W. Austin, unpublished measurements, National Bureau of Standards, Boulder, Colorado (1987).

LOW-TEMPERATURE PROPERTIES OF HIGH-MANGANESE AUSTENITIC STEELS*

R. P. Reed, P. T. Purtscher, and L. A. Delgado
Fracture and Deformation Division
National Bureau of Standards
Boulder, Colorado

The low-temperature properties of high-Mn austenitic steels are reviewed. Emphasis is placed on strength, toughness, elastic properties, thermal expansion, and magnetic properties, those properties most critical for materials used in cryogenic structures. Strength and toughness parameters and mechanisms are discussed, including alloying, martensitic transformations, twinning, and grain size. Information is included from many recent studies, particularly Japanese studies, of alloy development for superconducting magnet applications at 4 K.

INTRODUCTION

Strong structural alloys are required to withstand the large magnetic forces of superconducting magnets. Since structural failure in these applications would result in unacceptable loss, these structural alloys must also have excellent fracture toughness. Many of the low-temperature applications, such as those in magnetic-fusion-energy reactors and high-energy-physics magnets, require materials with high elastic properties and low thermal and electrical conductivities. Austenitic steels have been almost exclusively selected for these uses. Recently, the Japan Atomic Energy Research Institute[1] has stimulated the Japanese steel companies to develop even stronger (1200-MPa yield strength at 4 K) and tougher (200-MPa$\sqrt{m}$ fracture toughness at 4 K) austenitic steels for future use for structural constraint of the large magnetic fields. The impetus to achieve these goals in Japan, coupled with research at the National Bureau of Standards and other laboratories in the United States, has led to development of even better Fe—Cr—Ni and

*To be published in *High-Manganese Austenitic Steels*, ASM International, Metals Park, Ohio.

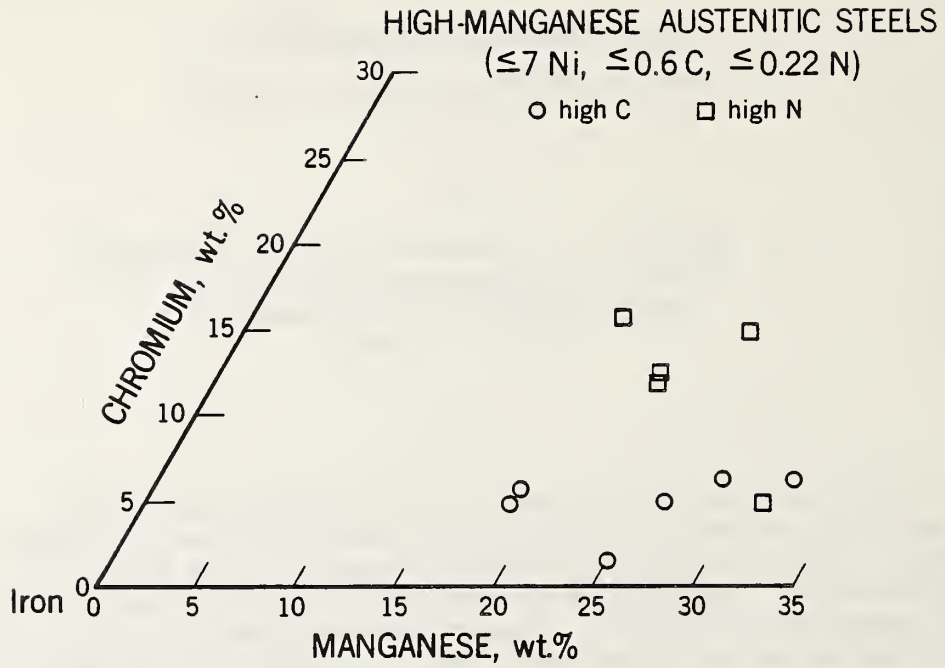

Fig. 1. Portion of the Fe–Mn–Cr ternary diagram with compositions of recently developed high-Mn austenitic steels.

Fe–Mn–Cr austenitic steels. The compositions of the high-Mn steels that have been recently developed are summarized in Fig. 1. Those with high Cr contents meet the Japanese corrosion-resistance requirements; those with low Cr contents were developed prior to the corrosion-resistance requirement or were developed for other applications. All contain sufficient Mn to stabilize the austenitic structure against martensitic transformation on cooling.

This paper summarizes our understanding of the behavior of these high-Mn austenitic steels at cryogenic temperatures. The most significant design parameters—strength, toughness, and physical properties—are emphasized.

STRUCTURE

Additions of Cr to Fe–Mn alloys serve two purposes: (1) improvement of corrosion resistance and (2) retardation of the intergranular failure mechanism of the Fe–Mn binary alloys (discussed later). Additions of Cr have little affect on the austenite stability of the Fe–Mn alloys, as illustrated in Fig. 2.[2] Neither the thermally induced α (bcc) and ϵ (hcp) transformations nor the strain-induced α' and ϵ' transformations are significantly affected. Additions of Cr greater than approximately

15% result in high-temperature δ ferrite or σ phase (at high Mn contents). Alloying with relatively small amounts of Ni, C, or N is needed to suppress these high-temperature phases that are deleterious to fracture. Figure 2 also shows that at Mn contents greater than about 22%, no strain-induced α' is detected, even at 4 K. The strain-induced ϵ'-martensitic structure is suppressed above about 32% Mn, and the thermal ϵ-martensitic phase is suppressed above about 28% Mn.[4]

Although Fig. 2 is taken primarily from Horiuchi et al.,[2] similar studies were conducted earlier by Namekata and Higashi[3] at temperatures ranging from 4 to 273 K. They also studied the effect of 6%* Ni addition to Fe–Mn–Cr alloys and found that neither ϵ nor ϵ' was detected at Mn contents higher than 25%.

Additions of Ni and C to Fe–Mn alloys enhance austenite (γ) stability. The Fe-rich portion of the Fe–Mn–Ni ternary diagram[5] containing both thermally and strain-induced phases at 76 K is shown in Fig. 3.

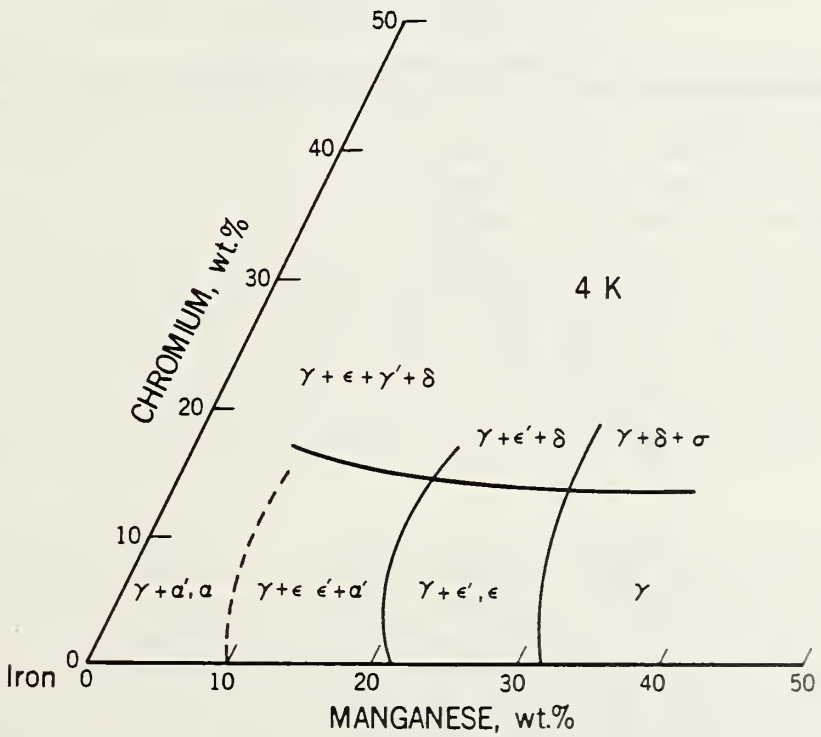

Fig. 2. Portion of the Fe–Mn–Cr ternary diagram illustrating alloy dependence of phases formed during deformation or cooling to 4 K.[2]

*All compositions in this paper are in wt.% unless otherwise specified.

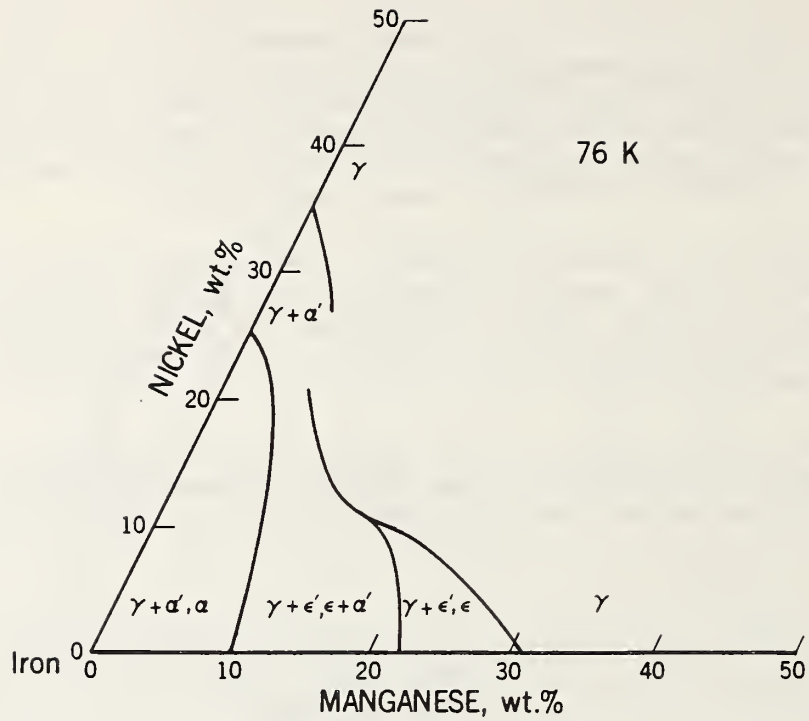

Fig. 3. Portion of the Fe–Mn–Ni ternary diagram illustrating alloy dependence of phases formed during deformation or cooling to 76 K.[5]

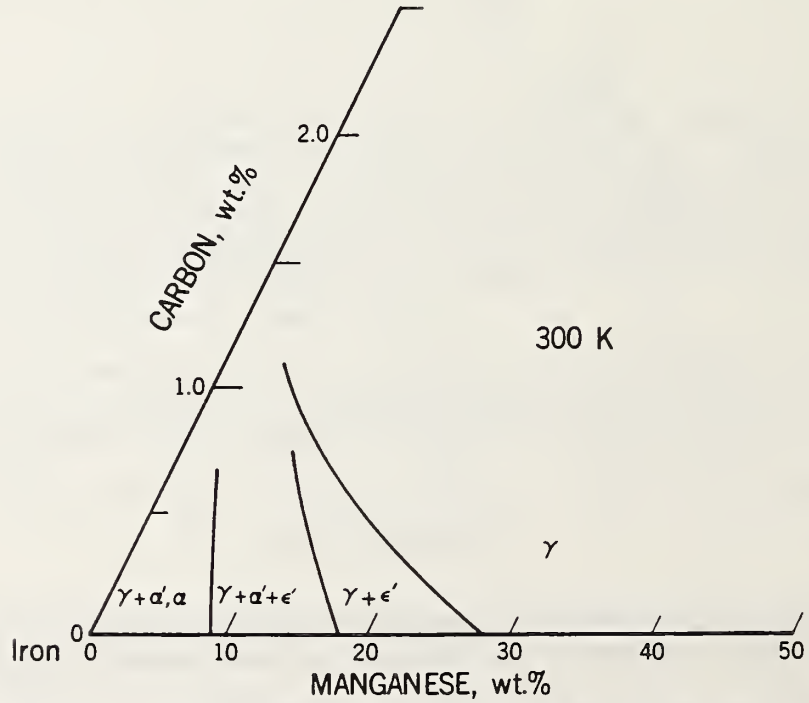

Fig. 4. Portion of the Fe–Mn–C ternary diagram illustrating alloy dependence of phases formed during deformation or cooling to 300 K.[6]

From this figure, it is apparent that the addition of about 10% Ni to alloys having greater than about 15% Mn is sufficient to prevent the formation of both α' and ϵ' formation at low temperatures. Even less Ni is required for austenitic thermal stability if C, N, or even Cr is present. Similarly, C additions increase γ stability,[6] as illustrated in Fig. 4. Although a ternary Fe–Mn–N phase diagram was not discovered in review for this paper, N additions are also expected to increase austenite stability.

Thus, to achieve austenite that is stable with respect to martensite, Mn, Ni, C, or N is added. To prevent high-temperature phases, Ni, C, or N is added and Cr is kept to about 15% or lower. If corrosion resistance is desirable, 10 to 15% Cr must be added.

STRENGTH

Mechanisms

There are four distinct deformation mechanisms in high-Mn austenitic steels at low temperatures: slip, deformation twinning, transformation to ϵ martensite, and transformation to α' martensite.

Slip. In very stable austenite or at higher temperatures, the only deformation mechanism is slip. Figure 5, which is based on data from Remy and Pineau,[7] shows that slip is found at high temperatures and high Mn contents. Additions of Cr, Ni, C, and N reduce the temperature and the Mn content at which slip is the dominant deformation mechanism. These alloying elements increase austenite stability with respect to α'-martensite formation and are expected to increase (or, at least, not to decrease) the stacking-fault energy. Since slip occurs by dislocation nucleation and motion, the factors that affect dislocation dynamics control the flow strength in this regime. These factors include long-range interactions with dislocation cells or grain boundaries; shorter range, temperature-dependent interactions with interstitials such as C and N; and dynamic recovery.

Deformation Twinning. At lower temperatures or Mn contents, deformation twinning is observed. Twins have been associated with bundles of stacking faults aligned on $(111)_\gamma$ planes. Figure 6 shows the etched surface of an Fe–22Mn–13Cr–5Ni–0.22N alloy with 10% elongation at 76 K. The broad bands are thought to represent deformation twinning, since no ϵ' was detected using x-ray diffraction, no α' was detected using magnetic measurements, and simple slip bands would not be expected to etch. As shown in Fig. 5, the addition of C to Fe–Mn alloys tends to increase the temperature range of deformation twinning, but the addition of Cr decreases the range of twinning while increasing the occurrence of ϵ' martensite. Little is known of the quantitative effect of deformation twinning on stress–strain characteristics, although the results of a study by Tomota et al.[8] of Fe–31Mn and Fe–36Mn-alloy flow strengths imply that twinning does not substantially alter the tensile behavior, as slip does.

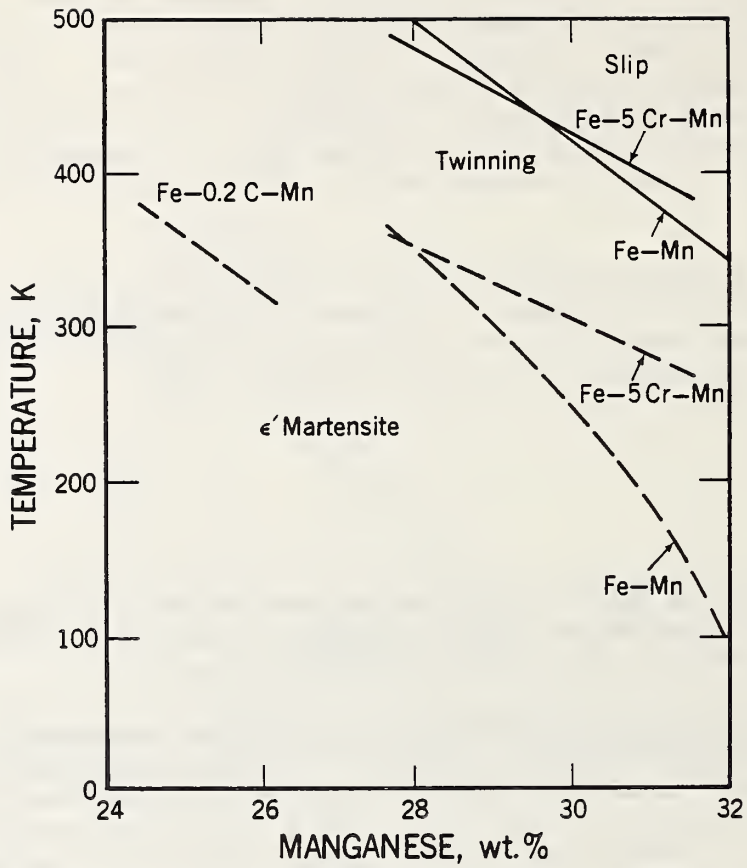

Fig. 5. Deformation mechanisms in Fe–Mn–(Cr or C) alloys as a function of temperature and Mn content.[7]

Transformation to ϵ' Martensite. Transformation to ϵ' martensite, rather than slip or twinning, occurs at lower temperatures and Mn contents (Fig. 5). Formation of ϵ' martensite during deformation increases the rate of work hardening.[8] The platelets of ϵ' on $\{111\}_\gamma$ are thought to segment the austenite grains, considerably obstructing the dislocation motion through effective reduction in grain size. This effect of ϵ' formation on stress–strain behavior is illustrated in Fig. 7. In the absence of α' formation, strain-induced ϵ' continuously increases with a linear dependence on strain (Fig. 7).[2]

Transformation to α' Martensite. At even lower temperatures or Mn contents (see Figs. 2 through 4), α' martensitic transformation is strain induced. In a manner similar to Fe–Cr–Ni alloy deformation behavior,[9] α' formation has two effects,[8] which are illustrated in Fig. 7. At strains usually less than 0.10, α' forms at slip-band intersections as laths with a $\langle 110 \rangle_\gamma$ axial direction corresponding to the common direction of $\{111\}_\gamma$ intersection. These laths effectively reduce the flow stress

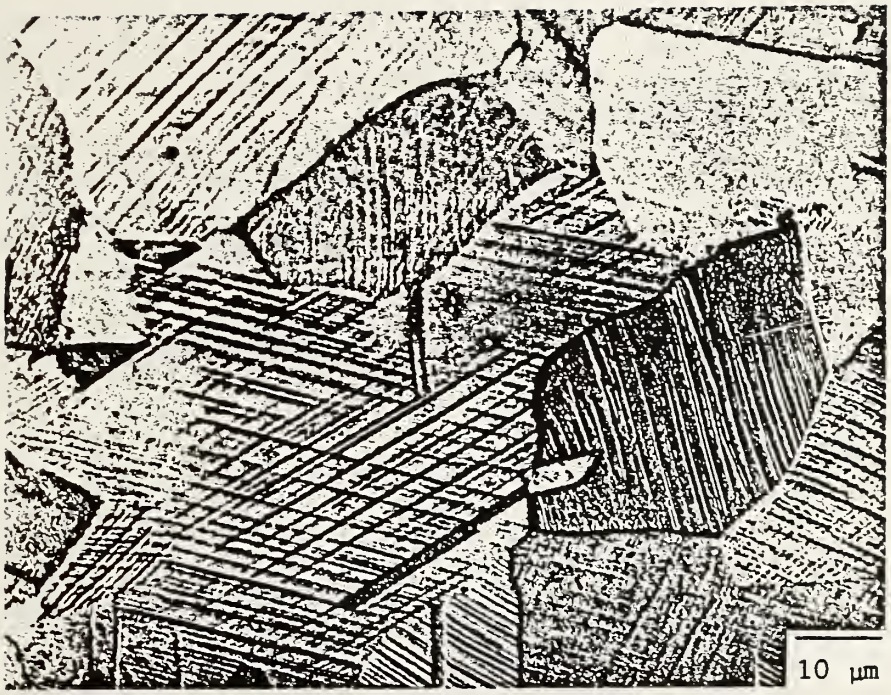

Fig. 6. Photomicrograph of Fe–22Mn–13Cr–5Ni–0.22N austenitic steel deformed in tension to 10% elongation at 76 K.

by relieving stress, transmitting dislocation pile-ups, or both. Subsequent α' formation acts in the opposite direction, increasing the rate of work hardening. At larger strains, presumably the slip-band intersection sites for α' formation have been exhausted, and α' forms from ϵ'. This produces a maximum in the dependence curve of ϵ' on strain. Thus at low temperatures, metastable polycrystalline austenitic steels can have characteristic stress–strain curves, very similar in shape to single-crystal curves, with three stages.[10]

Alloying Effects

Although solid-solution alloying elements, such as Cr and Ni, may affect the flow or fracture properties by influencing the relative stability of the austenite (thus affecting α', ϵ', or twinning deformation mechanisms), they contribute virtually nothing to the flow strength of stable high-Mn austenitic steels (whose deformation mechanism is slip). This lack of influence is understandable, because these elements have effective volumes close to Fe ($V_{Ni}/V_{Fe} = 0.93$, $V_{Cr}/V_{Fe} = 1.02$).[11] This similarity results in similar lattice parameter changes with alloying additions. However, additions of the much smaller elements C and N, which presumably occupy interstitial lattice sites, increase strength considerably at low temperatures. The effective volume of C relative to Fe is 0.34; that of N, 0.30.[11] In Fe–Cr–Ni alloys, the smaller N

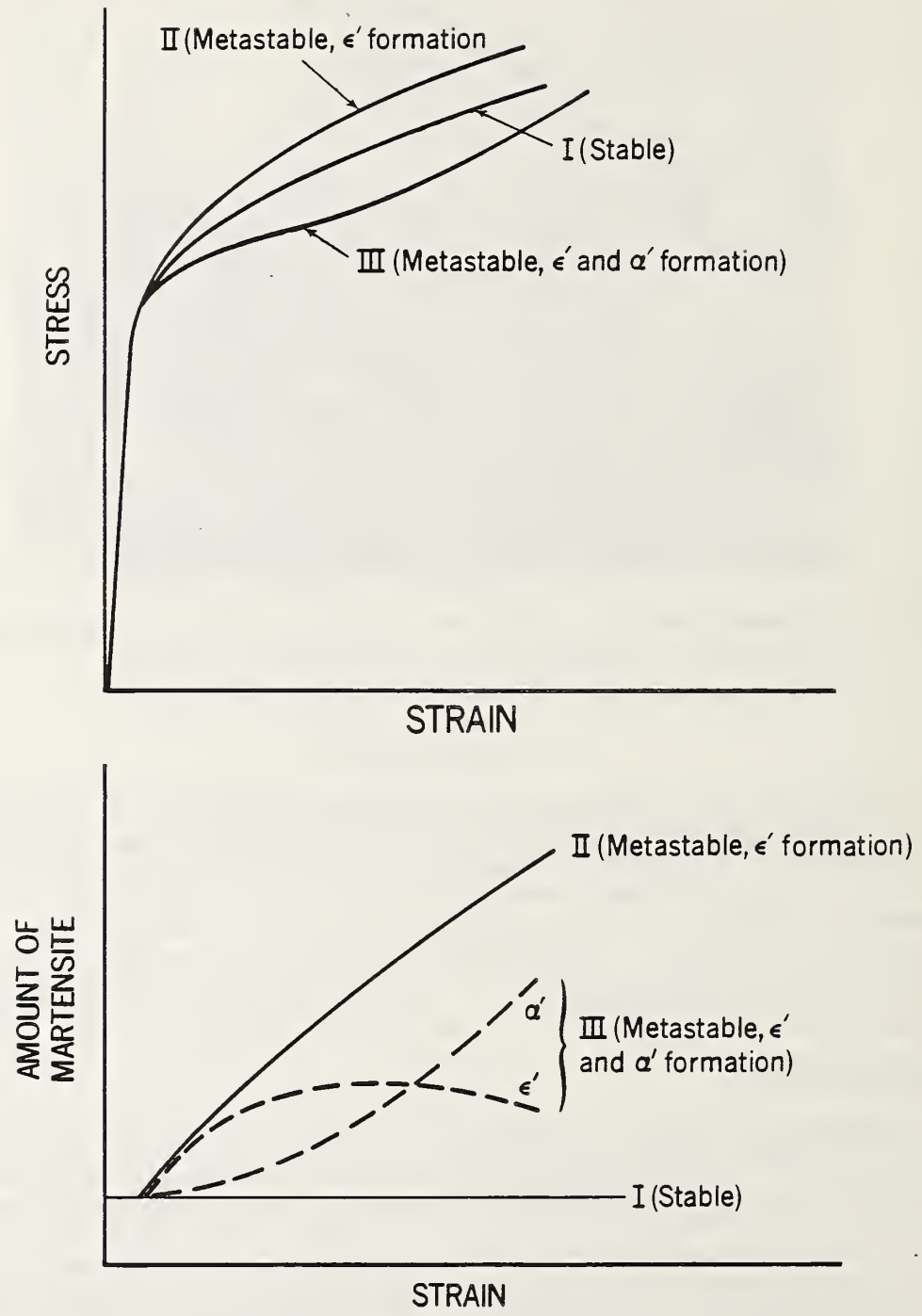

Fig. 7. Stress–strain and associated martensite-transformation characteristics for austenitic steels at low temperatures.

atom produces larger changes in the lattice parameter (a): at 295 K, $(1/a)(da/dc) = 0.218$ for C and 0.240 for N!,[11] where c is composition in at.%. We expect a similar lattice-parameter dependence in high-Mn austenites.

We conducted regression analyses on all high-Mn austenitic steel data at 295, 76, and 4 K that we could gather.[12-26] We defined high-Mn steel as any steel having an austenitic structure on cooling to low temperature and Mn as the principal alloying element.

The dependences of yield strength (σ_y, in MPa) on C and N content ([C] and [N], in wt.%) and grain size (d, in μm) were analyzed using the expression

$$\sigma_y = \sigma_0 + a[C] + b[N] + kd^{-\frac{1}{2}}, \quad (1)$$

where σ_0 is the strength before C and N additions.

The results are listed in Table 1 and plotted in Fig. 8. Brackets drawn about the N and C coefficients in Fig. 8 represent one standard deviation; the brackets about the data points for the ratios of N/C coefficients represent the estimated fractional error (F.E.), using

$$\text{F.E.} = \pm(b^2P_c^2 + a^2P_n^2)^{\frac{1}{2}}/ab, \quad (2)$$

where P_c and P_n, the probable errors in a and b, were taken as one standard deviation (Table 1).

Notable results are: (1) The temperature dependences of the C and N strengthening contributions are larger than that of σ_0, implying shorter range stress fields from the interstitials. (2) The ratio of these contributions are plotted versus temperature in Fig. 8 along with the ratios for identically determined Fe–Cr–Ni alloy data.[27,28] It is apparent that the relative contribution from N is higher in the Fe–Mn–Cr alloys than in the Fe–Cr–Ni austenites. Furthermore, in the Fe–Cr–Ni alloys,

Table 1. Regression Analysis of C, N, and Grain-Size Contributions to Tensile Yield Strength in Eq. 1

Temperature (K)	Number of Data Point	Coefficients (MPa/wt.%)				Standard Deviation (MPa/wt.%)				
		σ_0	a	b	k	σ_y	σ_c	a	b	k
4	58	551	773	2140	1140	77	52	142	178	161
77	25	264	315	1580	1060	76	64	44	145	454
295	66	118	132	683	462	53	23	24	46	89

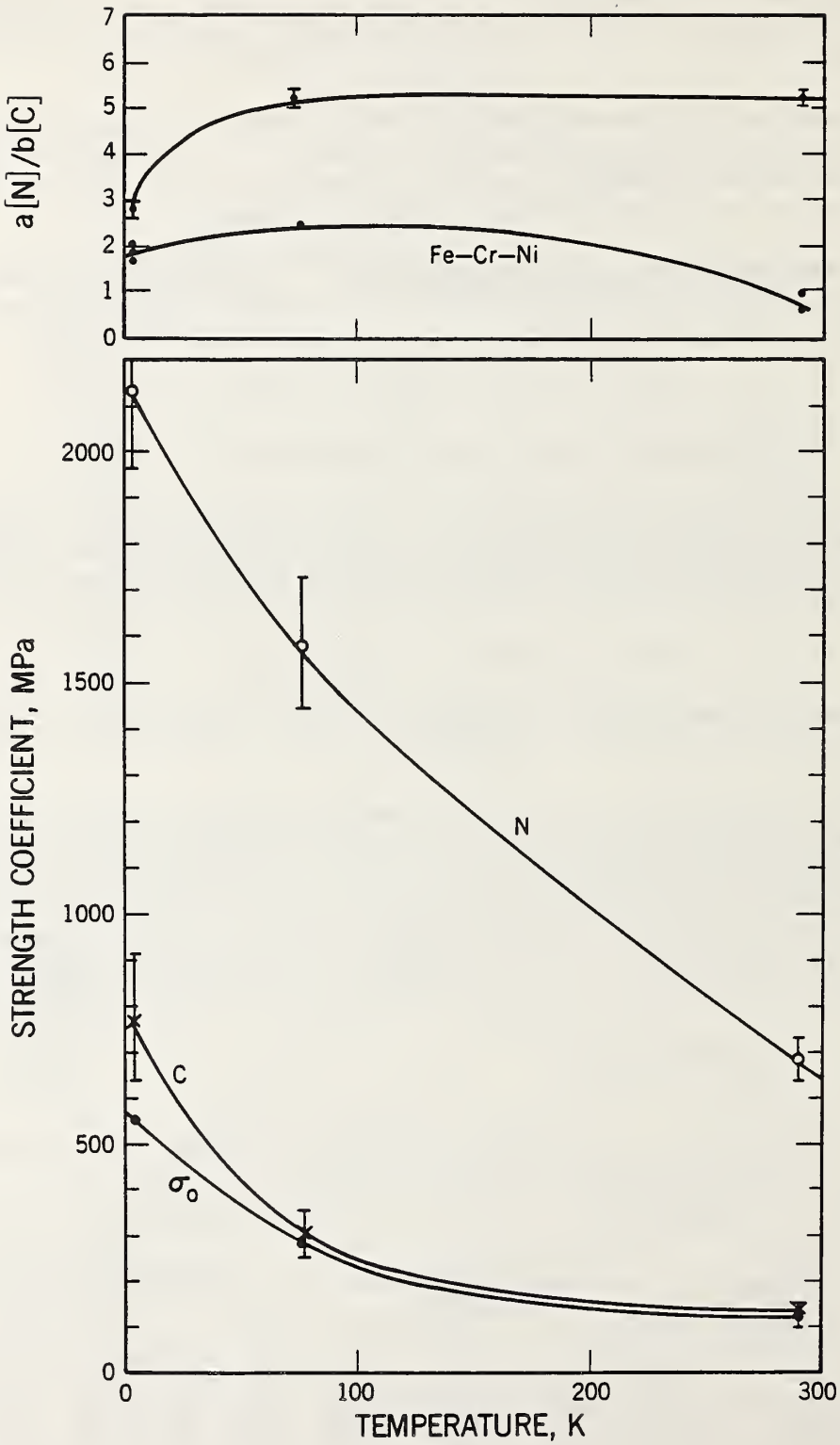

Fig. 8. Regression analyses results for the dependence of yield strength on C and N content and grain size at low temperatures.

N strengthens more than C at low temperatures; in the Fe–Mn–Cr alloys, the reverse is true. (3) Comparison of the coefficients with results of previous Fe–Cr–Ni regression analyses[27,28] indicates that the magnitude of the strengthening contribution from C and N is less in Fe–Mn–Cr alloys than in Fe–Cr–Ni and Fe–Cr–Ni–Mo (316-type) alloys. However, the smaller contribution to interstitial strengthening in the Fe–Mn–Cr alloys is offset by two factors: The strength, σ_0, is almost twice that of Fe–Cr–Ni alloys (see Table 2) at 4 K, and the solubility of C and N in Fe–Mn–Cr alloys is about twice that in Fe–Cr–Ni alloys. Lula[29] lists the predicted and measured N solubilities at 1873 K for Fe–15Mn–15Cr and Fe–15Ni–15Cr alloys as 0.29 and 0.13 wt.%, respectively. Both Mn and Cr additions increase the solubility of N in austenite; Ni addition results in slightly lower N solubility.

The addition of N to Fe–Mn–Cr austenites increases their strength by about a factor of three more than the addition of C (Fig. 8). This very significant distinction between C and N strengthening is not predictable on the basis of size or modulus misfit,[9] which leads to the suspicion that N is positioned differently in the lattice than C, possibly in pairs[9] or ordered within short range.[30]

Grain Size Dependence

The published data[15-17,20,25,31-33] on the effects of grain size on tensile yield strength, using the Hall–Petch relationship, are included in Fig. 9. Here,

$$\sigma_y = \sigma_0' + kd^{-\frac{1}{2}}, \qquad (3)$$

where σ_0' includes all grain-size-independent contributions.

Table 2. Nitrogen and Carbon Contributions to Tensile Yield Strength

Source	Alloy	Nitrogen 4 K	Nitrogen 76 K	Nitrogen 295 K	Carbon 4 K	Carbon 76 K	Carbon 295 K
		(MPa/wt.%)			(MPa/wt.%)		
This paper	Fe–Mn–Cr	2140	1580	680	770	320	130
Simon, Reed, 1986([28])	Fe–Ni–Cr	3190			1660		
Reed, Simon, 1984([27])*	Fe–Ni–Cr	3400	2080	420	1700	840	830
Simon, Reed, 1986([28])	Fe–Ni–Cr–Mo	2780			1690		

*Did not include a grain-size term in the analysis

The results of our regression analyses (using Eq. 1) in calculating the grain-size dependence, k, are also included in Fig. 9. A typical 4-K value of k for Fe–Cr–Ni alloys[28] is 1090 MPa/$\mu m^{-\frac{1}{2}}$; for Fe–Cr–Ni–Mo alloys, 810 MPa/$\mu m^{-\frac{1}{2}}$.[34] The lower average values for these alloys are outside the data spread of individual Fe–Mn–Cr-alloy studies. The increased grain-boundary contribution of the Fe–Mn–Cr alloys implies increased alloy segregation at their grain boundaries, presumably by C and N.

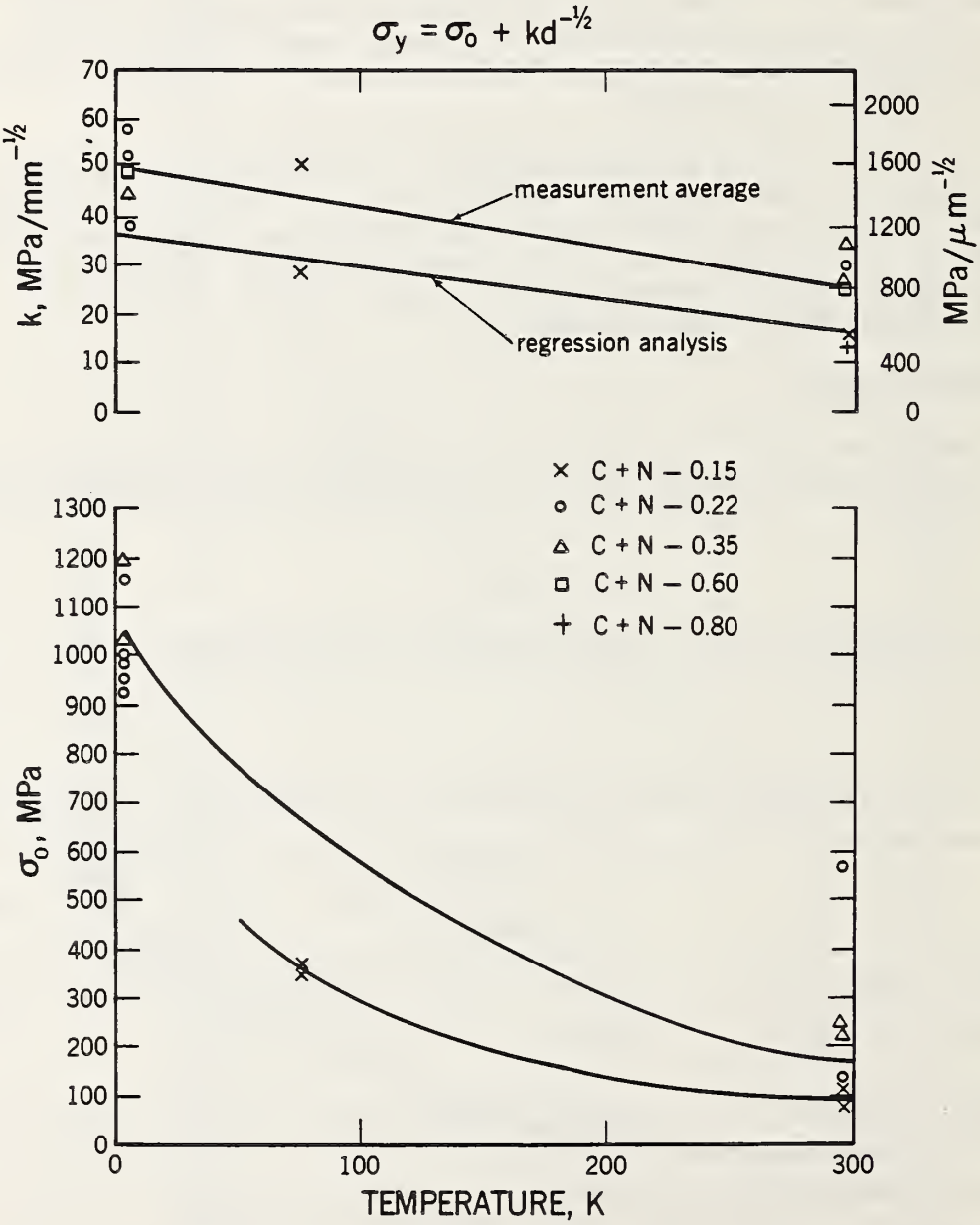

Fig. 9. Summary of literature data on the Hall–Petch constants of high-Mn austenitic steels at low temperatures. Also included are the k results of the regression analyses of this study.

The dependence of flow strength on grain size is quite strongly dependent on temperature, increasing by a factor of 2 from 295 to 4 K. Purer face-centered cubic metals, such as 99.95% Cu, exhibit about a 30% increase in k from 295 to 4 K.[35] Thus, the stronger temperature dependence of the grain-size influence on flow strength also probably reflects more impurity segregation at grain boundaries of the austenite structure. However, as illustrated in Fig. 9, there is no clear trend of k as a function of C and N content.

Temperature Dependence

From analyses of the temperature dependence of many austenitic steels, we found that for most alloys at low temperatures, the log of the yield strength is linearly and inversely related to the temperature. This is illustrated in Fig. 10 for several high-Mn alloys,[22] and can be expressed as

$$\sigma_y = \sigma_0" \exp(-AT), \qquad (4)$$

where $\sigma_0"$ is the yield strength at absolute zero and A is a constant, the slope of log σ_y versus temperature, T. This slope is proportional to the estimated stacking-fault energy of the austenitic alloys.[22]

Near room temperature, most alloys deviate from logarithmic dependence (Fig. 10), but there is no other evidence that this deviation

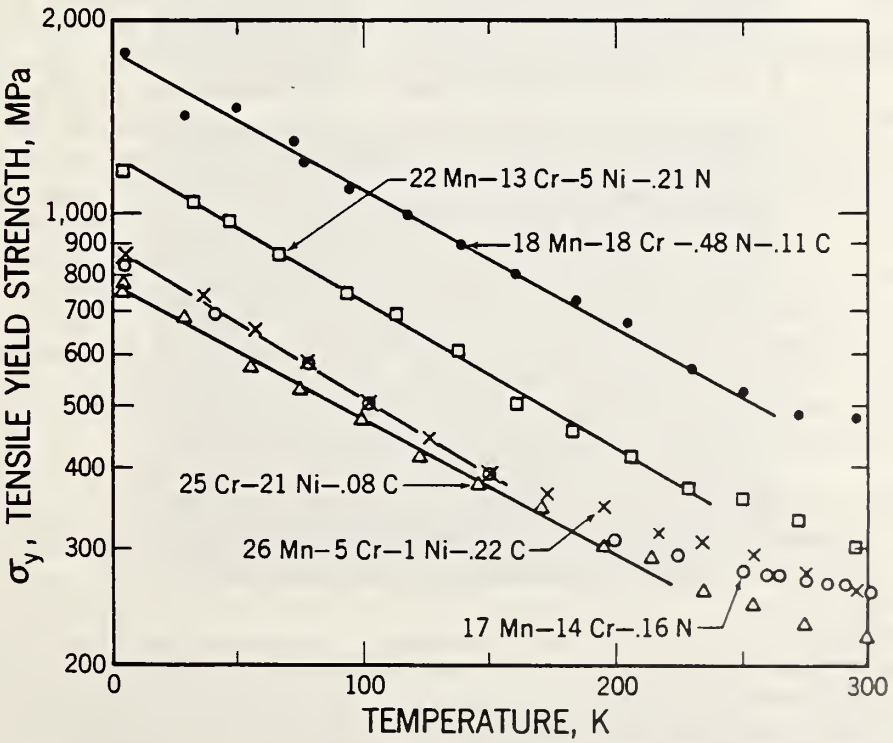

Fig. 10. Temperature dependence of austenitic alloy yield strengths at low temperatures.

signifies a change of the deformation mechanism. Many of these alloys are completely stable: there is no strain-induced martensite. The macroscopic contours of the stress–strain curves remain the same. Obviously, fundamental studies are needed to assess the significance of the temperature-dependence trends.

TOUGHNESS

Mechanisms

The toughness of binary Fe–Mn alloys is degraded by intergranular fracture, even in stable austenite.[4,15] Recent studies[4,15] have not succeeded in detecting segregation at the grain boundaries; thus, at present, there is no remedy for this fracture mechanism in the binary alloys. However, additions of the order of 5% Cr or Ni or small amounts of C do inhibit intergranular fracture.

At low temperatures, Fe–Mn–Cr and Fe–Mn–Cr–Ni alloys with high N contents or low austenite stabilities exhibit faceting of the stacking-fault clusters on $\{111\}_\gamma$ in impact or fracture toughness tests.[4,36-38] This brittle-looking faceting is similar to that reported by Tobler and Meyn[39] as slip-band cracking on compact-tension specimen fracture surfaces in high-N alloys. These facets usually have other $\{111\}_\gamma$ traces on their surfaces (Fig. 11a). The fracture surfaces following fracture-toughness tests at low temperatures are seldom dominated by these $\{111\}_\gamma$ facets; elongated, shallow dimples are the prevalent morphological structure (Fig. 11a). At higher temperatures or in more stable structures, the faceting is reduced and the elongated dimples are dominant on the fracture surfaces (Fig. 11b). This change is usually associated with increased toughness. Perhaps the reduction of fracture-surface faceting is assisted by Ni addition. This is the case for Fe–Cr–Ni alloys.[40] Yamamoto et al.[20] and Suemune et al.[41] have also found that Ni increases the toughness of the Fe–Mn–Cr alloys, but the fracture mechanisms in their studies were not identified. It is still uncertain whether the role of Ni in Fe–Mn–Cr austenite fracture is to increase toughness by increasing the stacking-fault energy (suppressing ϵ' formation, deformation twinning, and stacking-fault clusters) or to affect the toughness of alloys that fail by void growth and coalescence.

At higher temperatures, decreased strengths, higher Ni contents, or lower stress concentrations, typical ductile dimple fracture is prevalent (Fig. 11c). Nonmetallic inclusions are associated with most ductile dimples. Yamamoto et al.[20] and Suemune et al.[41] have both obtained excellent correlations between reduced S content (to reduce MnS inclusions) and toughness at low temperatures for Fe–22Mn–(13–15)Cr–(1–7)Ni austenitic steels. Apparently, the conditions, such as those illustrated in Fig. 11b, reflect the fracture morphology transition between faceting and dimpling. In this transition, many of the shallow, elongated dimples do not appear to be nucleated at inclusions.

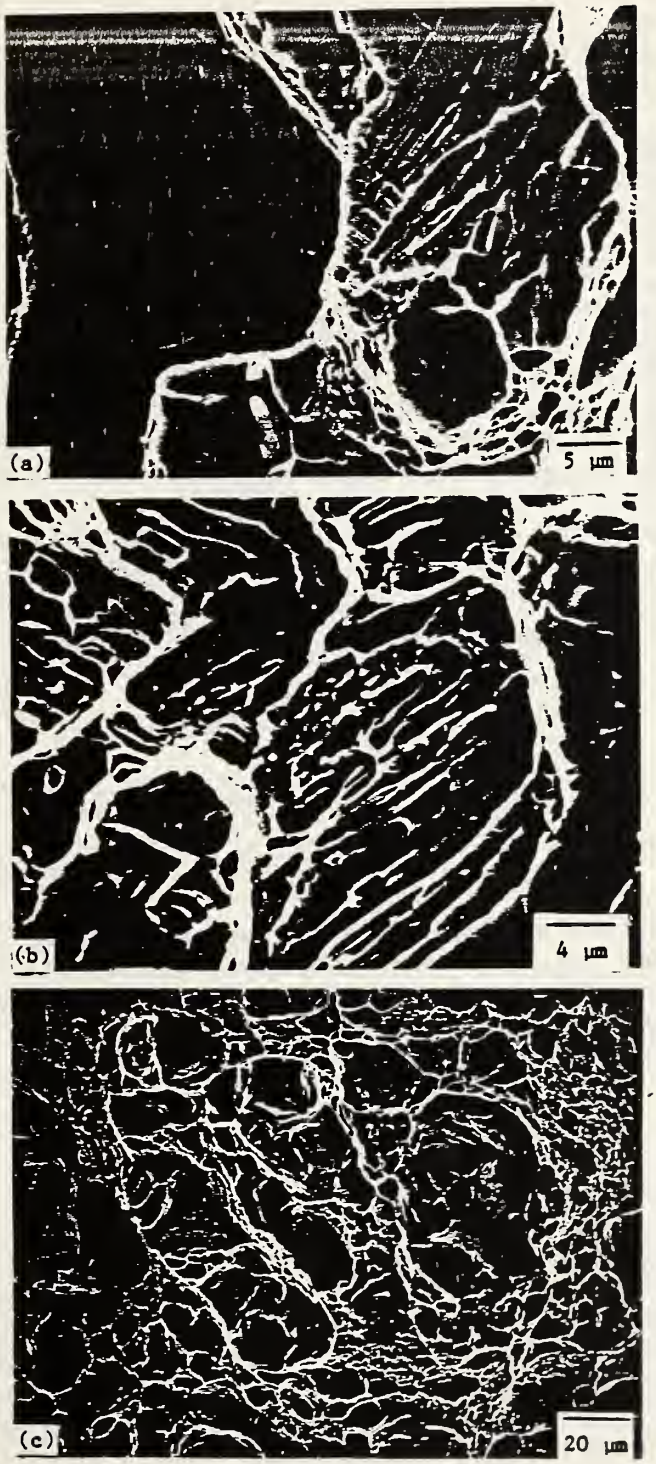

Fig. 11. (a) Fracture surface of a compact-tension specimen of Fe–8Mn–20Cr–7Ni–0.37N alloy, tested at 4 K, displaying $(111)_\gamma$ brittle facet and elongated, shallow microvoid dimples. (b) Fracture surface of a compact-tension specimen of Fe–22Mn–13Cr–5Ni alloy tested at 4 K. (c) Fracture surface of tensile specimen of Fe–22Mn–13Cr–5Ni alloy tested at 4 K.

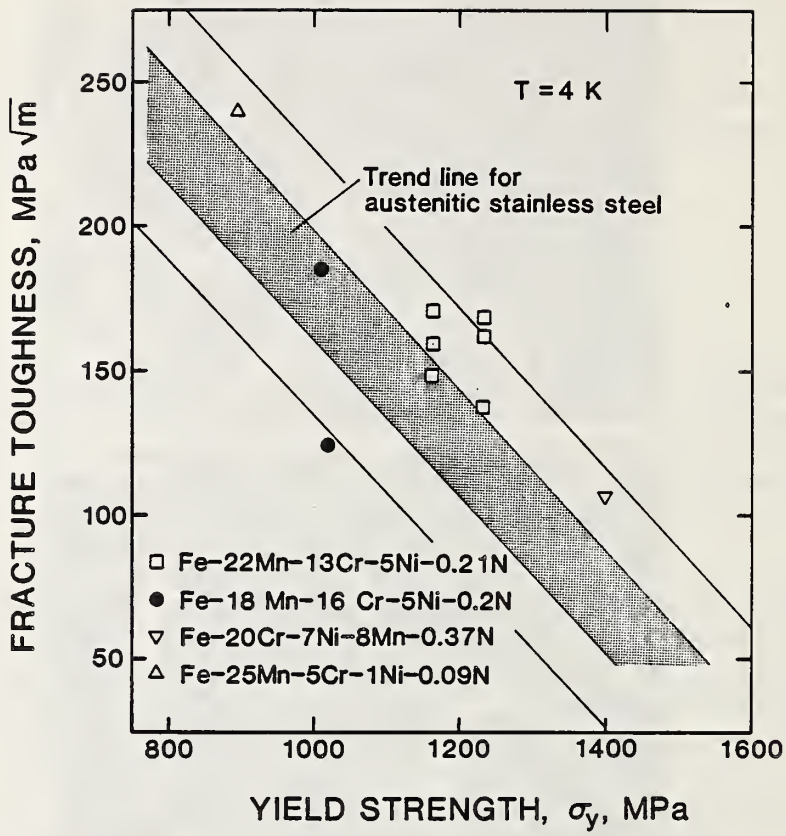

Fig. 12. Dependence of fracture toughness on tensile yield strength at 4 K for (1) a series of Fe–Cr–Ni alloys with controlled amounts of C and N (shaded band), (2) all Fe–Cr–Ni austenitic steels measured at NBS (wide band), and (3) high-Mn austenitic steels measured at NBS.

Strength Dependence

The dependence of toughness on strength in high-Mn austenitic alloys is similar to that in Fe–Cr–Ni alloys. The inverse dependence of yield strength of a series of Fe–20Cr–10Ni–C+N alloys (the shaded band) is shown in Fig. 12; the lines on each side of the band indicate the data spread of all Fe–Cr–Ni base metals that we have measured at 4 K. The $K_{Ic}(J)$ fracture toughness values plotted in this figure were converted from J-integral measurements using

$$[K_{Ic}(J)]^2 = EJ_{Ic}, \qquad (5)$$

where E is Young's modulus. The compact tensile specimens measured were oriented in the TL direction (J_{Ic} measurements are about 10 to 20% lower in this orientation than in the LT orientation). The tensile yield-strength data in Fig. 12 were measured in the transverse direction. The individual data points portray our measurements of high-Mn austenites.

The several data points of the solution-treated alloys 18Mn–16Cr–5Ni–0.2N and 22Mn–13Cr–5Ni–0.2N reflect test and material variability. The location of these high-Mn-alloy data points on the high side of the trend lines probably reflects increased steel cleanliness. The fracture appearance of these high-Mn alloys varies: high-yield-strength alloys have more $\{111\}_\gamma$ facets; low-yield-strength alloys have larger dimples.

PHYSICAL PROPERTIES

At low temperatures, high-Mn austenites are antiferromagnetic; at high temperatures, they are usually paramagnetic. The magnetic transformation at their Néel temperature significantly influences their elastic properties, thermal expansion, and magnetic susceptibility.

Magnetic susceptibility is probably the best indicator of the Néel temperature. At the transition temperature, magnetic susceptibility peaks sharply (Fig. 13). The data of Collings[42] show dependence of the Néel temperature on composition: The Néel temperature of 13Mn–18Cr–3Ni is 160 K higher than that of 5Mn–22Cr–13Ni.

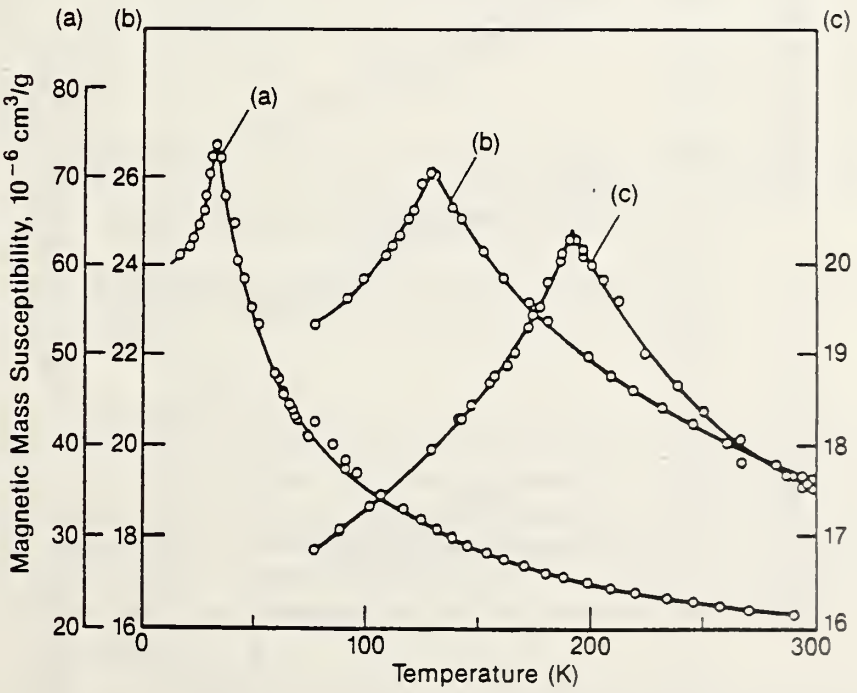

Fig. 13. Magnetic susceptibility dependence on temperature and alloy content for three Fe–Mn–Cr–Ni alloys [Collings[38]]. The three susceptibility scales refer to alloy designations (a) Fe–22Cr–13Ni–5Mn, (b) Fe–21Cr–6Ni–9Mn, and (c) Fe–18Cr–3Ni–13Mn.

The transition to an antiferromagnetic state produces a softening of the elastic properties. This softening is relatively large, as illustrated by Ledbetter's data[43] in Fig. 14 for a Fe–26Mn–5Cr alloy. Both Young's modulus (E) and the shear modulus (G) decrease about 8% through the Néel temperature. The bulk modulus (B) is less affected; Poisson's ratio (ν) increases about 8%.

The magnetic transition also strongly affects thermal expansion. Below the Néel temperature (T_N), there is positive magnetostriction in the antiferromagnetic state, which reduces the thermal-expansion coefficient. Even at temperatures up to 100 K above the transition temperature, there is limited magnetic ordering that lowers the coefficient.

Richter and Pepperhoff[44] have measured the thermal-expansion characteristics of a number of Fe–Mn base alloys at low temperatures. They observed that C and Cr additions tend to lower T_N and reduce the volume magnetostriction (Fig. 15).

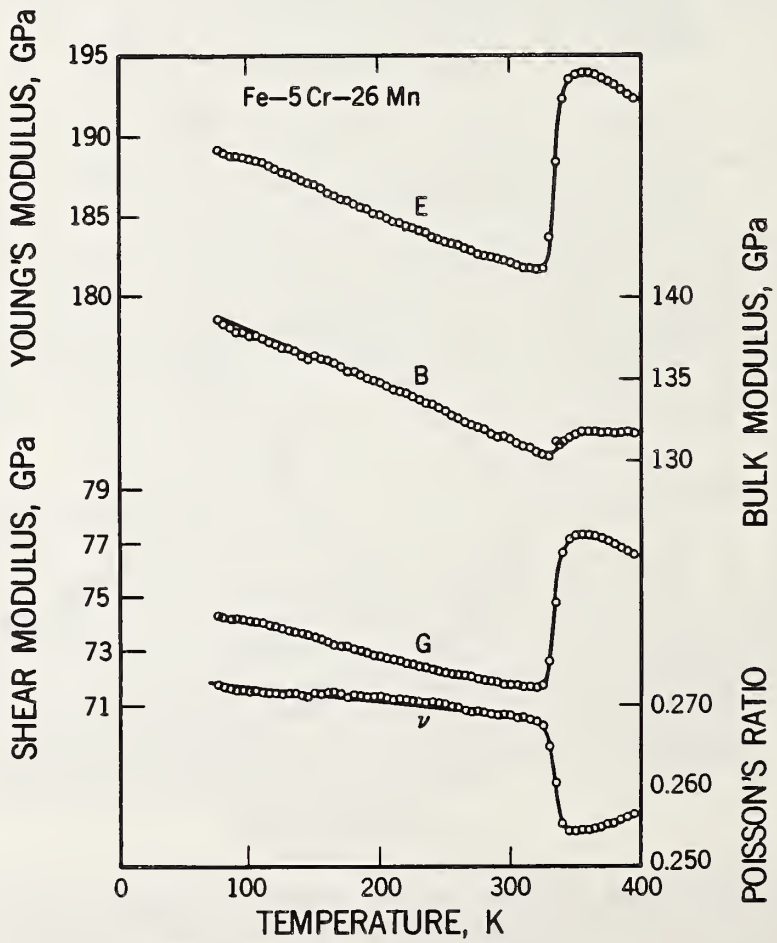

Fig. 14. Elastic properties for an Fe–26Mn–5Cr alloy at low temperatures [Ledbetter[39]].

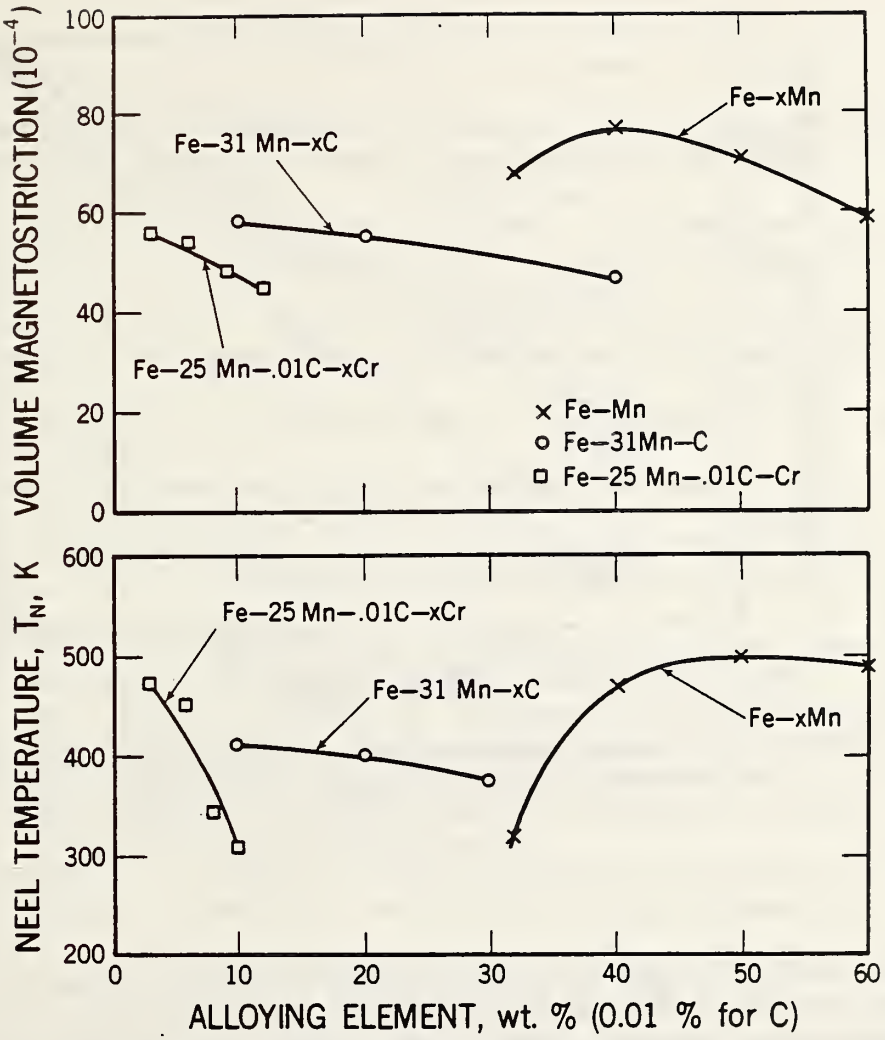

Fig. 15. Effects of alloying on Néel temperature and volume magnetostriction of Fe–Mn-base alloys.[40]

In the Fe–Mn binary system, Mn additions of 32 to 50% increase T_N, and Mn additions of 32 to 40% increase the volume magnetostriction; further additions of Mn decrease both terms. Thus, the amount of thermal expansion depends critically on the location of the Néel temperature. In general, the lower the Néel temperature, the higher the expansion coefficient. Sasaki et al.[45] have developed an empirical relation suggesting a nearly linear, inverse dependence of the thermal-expansion coefficient on T_N.

In principle, high-Mn austenitic alloys may be designed to produce varying contraction characteristics at low temperatures. If an alloy is desired with a lower thermal contraction matching that of a low-alloy ferritic steel, the Mn content should be high enough to ensure that T_N is above room temperature (Fig. 16). If a high-Mn steel is to approximate the contraction characteristics of Cu, Al, or Fe–Cr–Ni alloys, the Mn content should be lower.

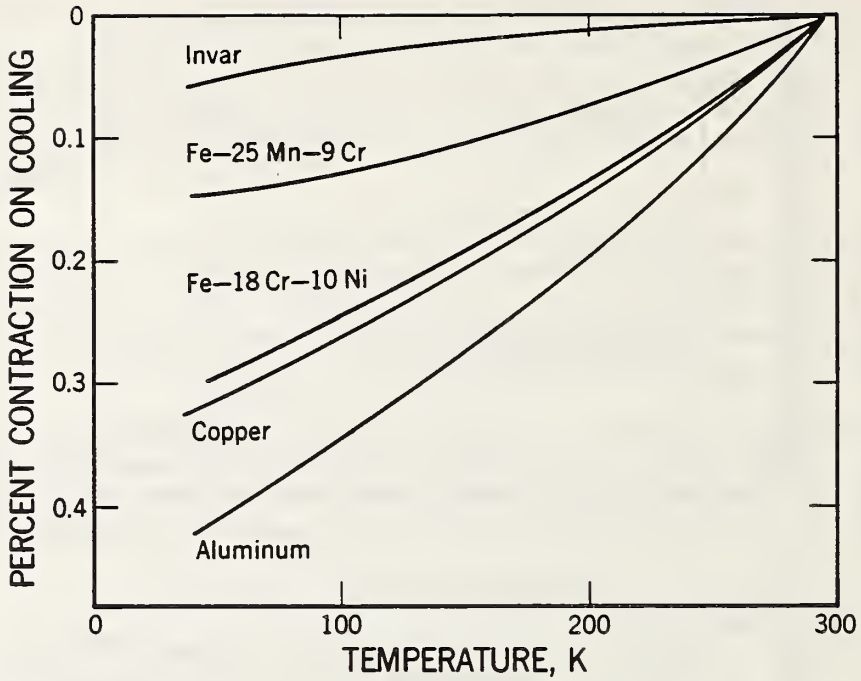

Fig. 16. Percent contraction of various face-centered cubic structural alloys on cooling.

SUMMARY

The strength, toughness, and selected physical properties of high-Mn austenitic steels at low temperatures have been reviewed. Compared with Fe–Cr–Ni austenitic steels, the high-Mn steels have several distinct characteristics:

The solubility of N and C is higher, which enables the attainment of higher strengths. More hcp martensite is induced by deformation. The hcp phase increases the rate of work hardening during deformation. In toughness tests, increased fracture faceting on $\{111\}_\gamma$ is observed in lower stacking-fault-energy alloys. Binary Fe-Mn alloys are more susceptible to intergranular fracture. Therefore, high-Mn austenites are easier to strengthen than Fe–Cr–Ni austenites, but more troublesome to toughen.

The elastic properties and thermal expansion are strongly influenced by the magnetic transition from the high-temperature paramagnetic state to antiferromagnetism at low temperatures.

ACKNOWLEDGMENT

This work was supported, in part, by the Office of Fusion Energy, U.S. Department of Energy.

REFERENCES

1. Shimamoto, S., H. Nakajima, K. Yoshida, and E. Tada, in "Advances in Cryogenic Engineering – Materials," vol. 32, pp. 23–32, Plenum Press, New York (1986).
2. Horiuchi, T., R. Ogawa, and M. Shimada, in "Advances in Cryogenic Engineering – Materials," vol. 32, pp. 33–42, Plenum Press, New York (1986).
3. Namekata, J. and K. Higashi, J. Iron Steel Inst. Jap. 66, 355 (1980)
4. Tomota, Y., M. Strum, and J.W. Morris, Metall. Trans. A 18A, 1073–81 (1987).
5. Schaller, A., M.A. Shtremel, and A.A. Petrunenkov, Neue Hütte 7, 253–57 (1979).
6. "Recent Developments of High Manganese Structural Steels," Daido Steel Co., Ltd., Nagoya, Japan (1984).
7. Remy, L. and A. Pineau, Mater. Sci. Eng. 28, 99–107 (1977).
8. Tomota, Y., M. Strum, and J.W. Morris, Metall. Trans. A 17A, 537–47 (1986).
9. Reed, R.P., in "Materials at Low Temperatures," pp. 295–341, American Society for Metals, Metals Park, Ohio (1983).
10. Reed, R.P. and R.L. Tobler, in "Advances in Cryogenic Engineering – Materials," vol. 28, pp. 49–56, Plenum Press, New York (1982).
11. Reed, R.P., Austenitic stainless steels with emphasis on strength at low temperatures, in Alloying, American Society for Metals, Metals Park, Ohio (1988); to be published.
12. Sakamoto, T., Y. Nakagawa and I. Yamauchi, in "Advances in Cryogenic Engineering – Materials," vol. 32, pp. 65–71, Plenum Press, New York (1986).
13. Guntner, C.J. and R.P. Reed, ASM Trans. Quart. 55, 399–419 (1962).
14. Tone, S., M. Shimada, T. Horiuchi, Y. Kasamatsu, H. Nakajima, and S. Shimamoto, in "Advances in Cryogenic Engineering – Materials," vol. 32, pp. 89–96, Plenum Press, New York (1986).
15. Strum, M.J., "Control of Cryogenic Intergranular Fracture in High-Manganese Austenitic Steels" Ph.D. Thesis, University of California, Berkeley, LBL-22650, Lawrence Berkeley Laboratories, Berkeley, California (Dec. 1986).
16. Rao, V.K., D.M.R. Taplin, and P.R. Rao, Metall. Trans. 6A, 77–86 (1975).
17. Ishikawa, K., K. Hiraga, T. Ogata, and K. Nagai, in "Austenitic Steels at Low Temperatures," pp. 295–309, Plenum Press, New York, (1983).
18. Yoshimura, H., H. Sumitomo, H. Masumoto, and K. Suemune, in "Cryogenic Properties of Metals and Welds," pp. 247–255, International Cryogenic Materials Conference, Boulder, Colorado (1987).
19. Yamagami, N., Y. Kohsaka, and C. Ouchi, presentation at United States–Japan Workshop on Low Temperature Structural Materials and Measurements for Magnetic Fusion Applications, Technical Research Center, Nippon-Kokan K.K., Kawasaki, Japan (1985).
20. Yamamoto, S., N. Yamagami, and C. Ouchi, in "Advances in Cryogenic Engineering – Materials," vol. 32, pp. 57–64, Plenum Press, New York (1986).

21. Tone, S., M. Hiromatsu, J. Numata, T. Horiuchi, H. Nakajima, and S. Shimamoto, in "Advances in Cryogenic Engineering – Materials," vol. 32, pp. 89–96, Plenum Press, New York (1986).
22. Reed, R.P. and J.M. Arvidson, in "Advances in Cryogenic Engineering – Materials," vol. 30, pp. 263–70, Plenum Press, New York (1984).
23. Kaji, H., M. Hiromatsu, S. Tone, M. Shimada, and S. Shimamoto, "The Development of a 22Mn–13Cr–5Ni Nonmagnetic Steel Plate for Cryogenic Applications," Kobelco Technical Bulletin 1093, Kobe Steel Co., Kobe, Japan (Nov. 1985).
24. Suemune, K., T. Sakamoto, T. Ogawa, T. Okazaki, S. Maehara, H. Nakajima, and S. Shimamoto, in "Advances in Cryogenic Engineering – Materials," vol. 34, pp. 123–29, Plenum Press, New York (1988).
25. Ouchi, I., Nippon Kokan K.K., Kawasaki, Japan; unpublished data (1988).
26. Muira, R., K. Ohnishi, H. Nakajima, Y. Takahashi, and K. Yoshida, in "Austenitic Steels at Low Temperatures," pp. 287–93, Plenum Press, New York (1983).
27. Reed, R.P. and N.J. Simon, in "Advances in Cryogenic Engineering – Materials," vol. 30, pp. 127–36, Plenum Press, New York (1984).
28. Simon, N.J., and R.P. Reed, J. Nucl. Mater. 141–143, 44–8 (1986)
29. Lula, R.A., in "Manganese Stainless Steels," pp. 30–1, The Manganese Centre, Paris, France (1986).
30. Bynes, M.L.G., M. Grujicic, and W.S. Owen, Acta Metall. 35, 1853–62 (1987).
31. Kato, T., M. Fujikura, S. Yahagi, and K. Ishida, Tetsu-to-Hagane 67, 587–95 (1981).
32. Yoshimura, H., H. Masumoto, and T. Inoue, in "Advances in Cryogenic Engineering – Materials," vol. 28, pp. 115–25, Plenum Press, New York (1982).
33. Ogawa, R. and J.W. Morris, in "Advances in Cryogenic Engineering – Materials," vol. 30, pp. 177–84, Plenum Press, New York (1984).
34. Reed, R.P., N.J. Simon, P.T. Purtscher, and R.L. Tobler, in "Proceedings, International Cryogenic Engineering Conference," pp. 786–90, Berlin, Butterworths, London, England (1986).
35. Reed, R.P., R.P. Walsh, and F.R. Fickett, in "Advances in Cryogenic Engineering – Materials," vol. 34, pp. 299–308, Plenum Press, New York (1988).
36. Thompson, L.D., in "Mechanical Properties and Phase Transformations in Engineering Materials," pp. 391–408, AIME Metallurgical Society, Warrendale, Pennsylvania (1986).
37. Kato, T., S. Fukai, M. Fujikura, and K. Ishida, Trans. ISIJ 16, 673–79 (1976).
38. Defilippi, D.P., K.G. Brickner, and E.M. Gilbert, Trans. AIME 245, 2141–48 (1969).
39. Tobler, R.L. and D. Meyn, Cleavage-like fracture along slip planes in Fe–18Cr–3Ni–13Mn austenitic stainless steel at liquid helium temperature, Metall. Trans.; accepted for publication.
40. Purtscher, P.T., R.P. Walsh, and R.P. Reed, in "Advances in Cryogenic Engineering – Materials," vol. 34, pp. 379–386, Plenum Press, New York (1988).

41. Suemune, K., K. Sugino, H. Masumoto, H. Nakajima, and S. Shimamoto, in "Advances in Cryogenic Engineering – Materials," vol. 32, pp. 51–6, Plenum Press, New York (1986).
42. Collings, E.W., in "Advances in Cryogenic Engineering – Materials," vol. 26, pp. 37–47, Plenum Press, New York (1979),
43. Ledbetter, H.M., Physica 119B, 115–8 (1983).
44. Richter, F. and W. Pepperhoff, Arch. Eisenhüttenw. 47, 45–50 (1976).
45. Sasaki, T., K. Watanabe, K. Nohara, Y. Ono, N. Kondo, and S. Sato, Trans. Iron Steel Inst. Jap. 22, 1010–20 (1982).

DESIGN OF 316LN-TYPE ALLOYS*

N. J. Simon and R. P. Reed
Fracture and Deformation Division
Institute for Materials Science and Engineering
National Bureau of Standards
Boulder, Colorado

For structural use in 4-K superconducting-magnet applications, alloy 316LN offers higher strength than 304LN with equivalent toughness. Nitrogen additions permit the attainment of high yield-strength levels with little added cost. To meet the goal of combined high yield strength and high fracture toughness at 4 K, careful consideration of alloy design parameters is necessary. Regression analysis for significant design parameters has been carried out on a matrix of 99 recent NBS measurements at 4 K on a variety of 316, 316LN, and 316LHN alloys. This data matrix includes more extensive numerical data on alloying, refining, and processing parameters than have previously been available. The alloys were obtained from suppliers in Japan, Europe, and the United States. Predictive equations are presented for the yield strength at 4 K as a function of N and Mo content and grain size. Predictive equations for the 4-K fracture toughness, $K_{Ic}(J)$, of these alloys are derived from a matrix of 45 measurements. The inverse relationship of $K_{Ic}(J)$ to yield strength established from earlier NBS data at 4 K had allowed an approximate prediction of $K_{Ic}(J)$ if the yield strength was known. By including the effects of Ni content and inclusion spacing in the regression equations, $K_{Ic}(J)$ at 4 K can be predicted with higher certainty.

---

*A condensed version of this paper was published in *Advances in Cryogenic Engineering – Materials*, vol. 34, Plenum, New York (1988), pp. 165–172.

INTRODUCTION

Fusion energy reactors with 4-K superconducting magnets will require cryogenic structural alloys with improved combinations of yield strength and fracture toughness at 4 K. These structural alloys are required to withstand large magnetic forces in a superconducting magnet system of restricted dimensions, and thus, high strength is needed. In addition, because most structures are complex and have regions of high stress concentration, good fracture toughness is required. However, fracture toughness correlates inversely with yield strength at 4 K,[1,2] and the quantitative dependence of 4-K strength and toughness upon other parameters has been undetermined. Recently, we deduced predictive equations for strength and toughness at 4 K in which parameters of alloying, refining, and processing were expressed quantitatively.[3,4] Since then, testing of a series of 316LN and 316LHN alloys at NBS has greatly expanded the data base of 4-K measurements of strength and toughness. In this paper, using the enlarged data base, we re-examined and expanded the predictive equations to include additional parameters.

The strength of austenitic steels at 4 K depends quite strongly on N content: each 0.1 wt.% N raises the tensile yield strength (σ_y, 0.2% offset) by approximately 300 MPa.[5] Other elements, such as C, Ni, Mn, and Cr, contribute much less to the low-temperature strength. The effect of Mo, however, is sizeable; σ_y measurements on 316-type alloys with Mo content above the AISI specifications (2 to 3 wt.%) are included in the present regression analyses to permit a quantitative determination. The yield strength is also strongly dependent upon grain size; an increase of grain size from 20 to 100 μm results in a decrease of σ_y of about 90 MPa.[6] Thus, yield strength can be significantly increased through alloying and thermomechanical processing.

Toughness is adversely affected by increased strength: the elastic stress-intensity factor, $K_{Ic}(J)$,* has a negative linear dependence upon σ_y at 4 K.[1,2] Toughness also is adversely affected by the presence of inclusions,[6,7] which act as initiation sites for microvoid formation. The addition of some alloying elements, such as Ni, has previously been shown to increase the low-temperature toughness of austenitic steels when strength and inclusion content are held constant.[8]

NBS measurements of $K_{Ic}(J)$ at 4 K on 32 specimens that meet the 316LN or 316LHN specifications range from 147 to 390 MPa·m$^{1/2}$. The arithmetic mean is 227 MPa·m$^{1/2}$, the standard deviation (SD) is 74 MPa·m$^{1/2}$, and the coefficient of variation, defined as the ratio of the SD to the mean, is 32%. Such large scatter in mechanical-property data is typical at 4 K: a much smaller variation is normal at room temperature.[9] To

---

*K_{Ic} is obtained from measurement of the elastic–plastic critical J-integral (J_{Ic}) and calculated from $K_{Ic}(J) = (J_{Ic} \cdot E)^{1/2}$, where E is Young's modulus.

analyze this variability, an expanded set of 4-K strength and fracture toughness data on 316-type alloys was assembled, combining recent 316LN and 316LHN test data with earlier NBS 316-type-alloy measurements. This expanded data set, which includes measurements of grain size and inclusion spacing for each specimen, permitted the derivation of predictive equations that expressed the effects of grain size and composition on strength and the effects of strength, alloying, and inclusions on toughness. The predictive equation obtained for $K_{Ic}(J)$ has a standard deviation equivalent to a coefficient of variation of 14%, which is a considerable improvement over the coefficient of 32% quoted above. (The predictive equation was obtained from the expanded data set of 45 measurements, which has a coefficient of variation of 36%.) Alloy design (in terms of strength and toughness) is now feasible, within statistical limits of uncertainty. Of course, at this time, only research data are generally available. Before large-scale use of one of these alloys in a low-temperature structural application, additional heat-by-heat qualification testing is imperative.

PROCEDURE

A series of specimens from both laboratory and commercial heats of AISI 316-type alloys were tested. The alloys were prepared in the United States, Japan, and Europe.[10-14] Measurements were made of fracture toughness [$K_{Ic}(J)$] (predominantly TL orientation), tensile yield strength, and other tensile properties at 4 K. Grain size, hardness, and chemical composition were also determined, and the inclusion counts were obtained, as described by Reed et al.[6] Only measurements made at NBS were used in the data matrices, because previous experience has indicated that lab-to-lab variations in test results are large enough to obscure the dependence of cryogenic properties upon some parameters.

There are 45 complete rows in the $\sigma_y \times K_{Ic}(J)$ matrix for AISI 316-type alloys. When several σ_y measurements on a particular material were available, they were averaged and the mean σ_y was paired with the $K_{Ic}(J)$ values. The additional tensile data without corresponding $K_{Ic}(J)$ measurements were used in the regression analyses of σ_y; a total of 99 values were available. Table I shows the data used in the regression analyses and the reference symbols. (A listing of σ_y in table I without grain size, d, denotes a value that was using in the K_{Ic} analysis only.) Table II presents the chemical analyses of the alloys studied. Nitrogen content ranges from 0.03 to 0.20 wt.%; nickel content, from 10.5 to 14.2 wt.%; and Mo content, from 2.0 to 4.0 wt.%. Variation of Mo content outside the AISI 316 specifications permitted a more accurate determination of its effect on σ_y. Grain size varies from 11 to 242 μm in the matrix. Inclusion spacing, λ, ranges from 0.044 to 0.11 mm ($\lambda = n^{-\frac{1}{2}}$, where n = the number of inclusions per mm^2). The $K_{Ic}(J)$ values obtained from the relationship $K_{Ic}(J) = [J_{Ic} \cdot E/(1 - \nu^2)]^{\frac{1}{2}}$, where ν is Poisson's ratio, were adjusted in accord with the formulation $K_{Ic}(J) = (J_{Ic} \cdot E)^{\frac{1}{2}}$. All data points of the matrices were weighted equally in the linear least-squares regression analyses used to fit the series of equations described below.

Table I. Combined σ_y and K_{Ic} Matrices, AISI 316-Type Alloys

Alloy	σ_y, MPa	N, wt.%	d, μm	K_{Ic}, MPa·m$^{1/2}$	Ni, wt.%	Mo, wt.%	λ, mm
A[10]	937	0.16	63	—	13.7	2.70	—
	933	0.16	63	—	13.7	2.70	—
B[10]	942	0.16	70	—	11.4	2.50	—
	924	0.16	91	318	11.4	2.50	0.109
	918	0.16	129	335	11.4	2.50	0.109
	1076	0.16	13	214	11.4	2.50	0.129
	1096	0.16	13	218	11.4	2.50	0.100
C*[10]	832	0.10	—	390	13.9	2.20	0.096
	834	0.10	31	360	13.9	2.20	0.096
	831	0.10	31	380	13.9	2.20	0.096
	788	0.10	104	—	13.9	2.20	—
	786	0.10	103	—	13.9	2.20	—
	783	0.10	100	—	13.9	2.20	—
	783	0.10	100	—	13.9	2.20	—
	777	0.10	100	—	13.9	2.20	—
	779	0.10	100	—	13.9	2.20	—
	790	0.10	100	—	13.9	2.20	—
	780	0.10	100	—	13.9	2.20	—
	790	0.10	93	—	13.9	2.20	—
	772	0.10	100	—	13.9	2.20	—
	779	0.10	100	—	13.9	2.20	—
	779	0.10	100	—	13.9	2.20	—
	771	0.10	100	—	13.9	2.20	—
	753	0.10	100	—	13.9	2.20	—
D[10]	1056	0.13	—	147	10.9	2.20	0.080
	885	0.13	20	187	10.9	2.20	0.083
	869	0.13	30	—	10.9	2.20	—
	842	0.13	50	—	10.9	2.20	—
	935	0.13	11	177	10.9	2.20	0.081
E*[11]	1020	0.17	105	200	13.9	2.50	0.057
	992	0.17	105	214	13.9	2.50	0.057
F*[11,12]	718	0.03	65	266	13.5	2.30	0.054
	704	0.03	65	254	13.5	2.30	0.054
	711	0.03	—	243	13.5	2.30	0.054
	663	0.03	67	—	13.5	2.30	—
	656	0.03	67	—	13.5	2.30	—

* commercial heat

Table I. Combined σ_y and K_{Ic} Matrices, AISI 316-Type Alloys (continued)

Alloy	σ_y, MPa	N, wt.%	d, μm	K_{Ic}, MPa·m$^{\frac{1}{2}}$	Ni, wt.%	Mo, wt.%	λ, mm
G*[13,14]	550	0.03	64	406	12.2	2.16	0.092
	690	0.03	22	—	12.2	2.16	—
	661	0.03	28	—	12.2	2.16	—
	640	0.03	32	—	12.2	2.16	—
	553	0.03	49	—	12.2	2.16	—
	540	0.03	55	—	12.2	2.16	—
	562	0.03	58	—	12.2	2.16	—
	535	0.03	61	—	12.2	2.16	—
	535	0.03	81	—	12.2	2.16	—
	530	0.03	118	—	12.2	2.16	—
	505	0.03	138	—	12.2	2.16	—
H*[10]	882	0.16	85	203	10.5	2.12	0.044
	854	0.14	64	195	10.5	2.12	0.044
	862	0.16	67	—	10.5	2.12	—
	860	0.14	70	181	10.5	2.12	0.052
	848	0.15	70	159	10.5	2.12	0.052
	845	0.15	63	—	10.5	2.12	—
	856	0.15	66	—	10.5	2.12	—
	851	0.15	67	—	10.5	2.12	—
	852	0.15	66	—	10.5	2.12	—
	847	0.15	73	—	10.5	2.12	—
	874	0.15	62	—	10.5	2.12	—
	922	0.15	73	—	10.5	2.12	—
	857	0.15	64	—	10.5	2.12	—
	886	0.15	63	—	10.5	2.12	—
	836	0.15	58	—	10.5	2.12	—
	856	0.15	60	—	10.5	2.12	—
	877	0.15	64	—	10.5	2.12	—
	927	0.17	75	—	10.5	2.12	—
	859	0.15	51	—	10.5	2.12	—
	922	0.17	75	—	10.5	2.12	—
	919	0.17	75	—	10.5	2.12	—
	821	0.15	48	—	10.5	2.12	—
	934	0.17	57	—	10.5	2.12	—
	927	0.17	87	—	10.5	2.12	—
	868	0.15	56	—	10.5	2.12	—
	919	0.17	78	—	10.5	2.12	—
	835	0.15	48	—	10.5	2.12	—
	945	0.17	75	—	10.5	2.12	—
	927	0.17	78	—	10.5	2.12	—
	859	0.15	51	—	10.5	2.12	—
	905	0.17	75	—	10.5	2.12	—

* commercial heat

Table I. Combined σ_y and K_{Ic} Matrices, AISI 316-Type Alloys (continued)

Alloy	σ_y, MPa	N, wt.%	d, μm	K_{Ic}, MPa·m^{½}	Ni, wt.%	Mo, wt.%	λ, mm
I[10]	1049	0.18	34	163	12.0	2.06	0.055
	1014	0.18	28	172	12.0	2.06	0.055
	945	0.18	100	—	12.0	2.06	—
	1109	0.19	34	157	11.8	3.00	0.053
	1119	0.19	35	148	11.8	3.00	0.053
	1096	0.19	70	—	11.8	3.00	—
	1222	0.19	—	98	12.1	4.08	0.057
	1181	0.19	—	103	12.1	4.08	0.057
	1068	0.19	75	—	12.1	4.08	—
	1063	0.17	—	188	13.8	2.05	0.058
	1060	0.17	—	202	13.8	2.05	0.058
	1129	0.18	—	167	14.0	2.98	0.057
	1109	0.18	—	181	14.0	2.98	0.057
	994	0.18	100	—	14.0	2.98	—
	1162	0.19	—	98	14.2	4.02	0.051
	931	0.17	47	211	13.8	2.05	0.063
	934	0.17	57	226	13.8	2.05	0.063
	863	0.17	127	241	13.8	2.05	0.063
	894	0.17	68	201	13.8	2.05	0.063
	903	0.17	94	213	13.8	2.05	0.063
	905	0.17	118	210	13.8	2.05	0.063
	942	0.19	—	149	14.2	4.02	0.040
	968	0.19	—	165	14.2	4.02	0.040
	915	0.19	—	145	14.2	4.02	0.040
	1013	0.19	78	193	14.2	4.02	0.040
	1007	0.19	118	170	14.2	4.02	0.040
	981	0.19	187	195	14.2	4.02	0.040
J*[10]	937	0.15	66	—	10.5	2.12	—
	916	0.15	58	—	10.5	2.12	—
	891	0.16	51	—	10.5	2.12	—
	873	0.15	58	—	10.5	2.12	—
	908	0.15	58	—	10.5	2.12	—
	883	0.15	58	—	10.5	2.12	—
K†[10]	923	0.18	242	350	13.9	2.70	0.107
	923	0.18	—	360	13.9	2.70	0.107

* commercial heat
† electroslag remelted

Table II. Chemical Composition of AISI 316-Type Alloys

Alloy	Cr	Ni	Mn	Mo	C	N	P	S	Si
A[10]	16.7	13.7	1.26	2.7	0.014	0.16	0.016	0.010	0.41
B[10]	18.5	11.4	1.40	2.5	0.006–0.010	0.16	0.002	0.0002–0.001	0.40
C*[10]	16.8	13.9	1.84	2.2	0.028	0.10	0.022	0.009	0.33
D*[10]	18.6	10.9	1.01	2.2	0.020	0.13	0.002	0.003	0.29
E*[11]	17.4	13.9	1.58	2.5	0.016	0.17	0.021	0.021	0.48
F*[11,12]	17.2	13.5	1.86	2.3	0.070	0.03	0.024	0.016	0.58
G*[13,14]	17.3	12.2	1.55	2.2	0.051	0.03	0.026	0.014	0.68
H*[10]	18.0	10.5	1.10	2.1	0.016	0.14–0.17	0.020	0.015	0.54
I[10]	18.0	12.0	1.00	2.1	0.024	0.18	0.003	0.004	0.30
	18.0	11.8	1.01	3.0	0.023	0.19	0.002	0.005	0.29
	18.2	12.1	1.03	4.1	0.020	0.19	0.002	0.005	0.28
	18.5	13.8	1.05	2.0	0.021	0.17	0.002	0.004	0.30
	18.2	14.0	1.02	3.0	0.022	0.18	0.002	0.005	0.30
	17.9	14.2	1.00	4.0	0.022	0.19	0.002	0.004	0.30
J*[10]	18.0	10.5	1.10	2.1	0.016	0.15–0.16	0.020	0.015	0.54
K†[10]	17.6	13.9	0.97	2.7	0.021	0.18	0.019	0.006	0.54

* commercial heat
† electroslag remelted

In an earlier study, only the effects of grain size and N content upon σ_y were assessed.[3] In accord with the well-known Hall–Petch grain-size effect on yield strength and the higher temperature results of Norström,[15] the form of the equation fitted to the data was

$$\sigma_y = \sigma_o + \sigma_N \cdot [N] + k \cdot d^{-\frac{1}{2}}, \tag{1}$$

where [N] is N content (wt.%), d is the grain size (μm), and σ_o is the yield strength in the absence of N with infinite grain size. The contribution from C is expected to be about one-half that of N,[5] but since it is best to hold C content low (~0.03 wt.%) to minimize sensitization during welding, the alloys used in this study did not have a sufficient range of C content to determine this coefficient accurately. In equation (1), the [C] dependence is included in the constant term, σ_o.

To determine whether the addition of a term expressing the dependence upon Mo would lower the SD, the following equation was also fitted to the data:

$$\sigma_y = \sigma_o + \sigma_N \cdot [N] + k \cdot d^{-\frac{1}{2}} + \sigma_{Mo} \cdot [Mo], \tag{2}$$

where [Mo] represents Mo content in wt.%. Graphical analysis, especially of the I alloys (see tables I and II), had indicated an additional interactive effect of Ni and Mo upon σ_y;[16] this was expressed in a trial form:

$$\sigma_y = \sigma_o + \sigma_N \cdot [N] + k \cdot d^{-\frac{1}{2}} + \sigma_{Mo} \cdot [Mo] + \sigma_{Ni} \cdot [Ni] + \sigma_i \cdot [Mo][Ni], \tag{3}$$

where [Ni] represents Ni content in wt.%. The Ni term was included for completeness. The units of the coefficients in equations (1) through (3) are as follows: σ_o, MPa; σ_N, MPa/wt.%; k, MPa$\cdot\mu$m$^{\frac{1}{2}}$; σ_{Mo}, σ_{Ni}, MPa/wt.%; σ_i, MPa/(wt.%)^2.

The dependence of $K_{Ic}(J)$ upon yield strength at 4 K has been observed previously in our laboratory,[1,17] and a recent study of the effect of Ni on toughness of AISI 304-type alloys showed a strong dependence.[8] To assess the relative importance of inclusion spacing with respect to these two variables, the following equation was previously fitted to a smaller set of data from 316-type alloys:[3,4]

$$K_{Ic}(J) = k_o + k_\sigma \cdot \sigma_y + k_{Ni} \cdot [Ni] + k_\lambda \cdot \lambda, \tag{4}$$

where k_o is a constant.

Another expression for the dependence of these parameters that better expresses the form of current theories[18] is

$$K_{Ic}(J) \cdot \sigma_y / [Ni] = k'_o \cdot \lambda^\beta, \tag{5}$$

where β is an exponent to be determined in a least-squares fit. The units of the coefficients in equations (4) and (5) are: k_o, MPa$\cdot$m$^{\frac{1}{2}}$; k_σ, m$^{\frac{1}{2}}$; k_{Ni}, MPa$\cdot$m$^{\frac{1}{2}}$/wt.%; k_λ, MPa/mm; k'_o, (MPa)$^2\cdot 10^{3\beta}$/(wt.%)m$^{\beta-\frac{1}{2}}$.

Both equations (4) and (5) were fitted to the expanded data set. Figure 1 presents a plot of $K_{Ic}(J)\sigma_y/[Ni]$ versus λ for this data set. The letter keys to the symbols in this and succeeding figures are given in table I. For clarity, overlapping data points are omitted from all figures.

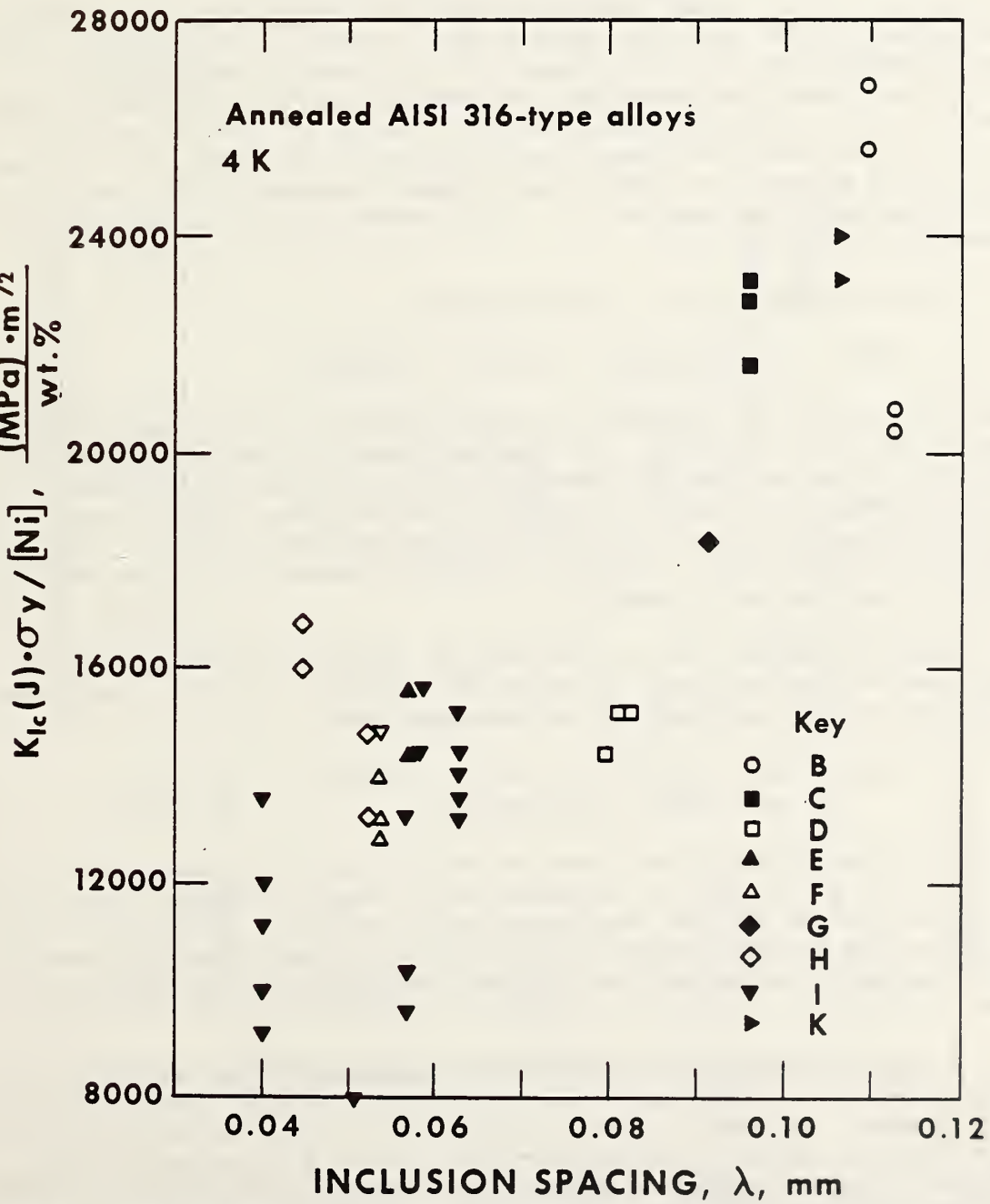

Figure 1. The quantity $K_{Ic}(J)\cdot\sigma_y/[Ni]$ versus λ for 316-type alloys at 4 K. The letter keys to the symbols are given in tables I and II.

RESULTS AND DISCUSSION

The result of fitting equation (1) to the set of 99 measurements is:

$$\sigma_y \text{ (MPa)} = 429 + 2500[N] + 740d^{-1/2}. \quad (6)$$

The SD of the fit to the data is 45 MPa; the SDs of the three coefficients are 20, 90, and 116, respectively. When we consider their SDs, these coefficients are in agreement with the coefficients found in the earlier study for which only 26 measurements were available. Equation (1) with the substitution of $[N]^{1/2}$ or $[N]^{2/3}$ for [N] was also fitted to the data; the result was a substantially higher SD. Following the work of Norström at ambient and higher temperatures,[15] the term $[N] \cdot d^{-1/2}$ was added to equation (1). This expression also resulted in a substantially higher SD.

Fitting equation (2) to the data gave

$$\sigma_y \text{ (MPa)} = 316 + 2370[N] + 790d^{-1/2} + 53.8[Mo]. \quad (7)$$

The SD of the fit to the data is 40 MPa; the SDs of the four coefficients are 28, 84, 102, and 10.2. The constant term, σ_o, has decreased because of the addition of the [Mo] term. The best-determined coefficient (lowest fractional uncertainty) is that of the [N] term; this term also contributes the most to σ_y for 316N-alloy composition. Figure 2, which presents a plot of $(\sigma_y - 790d^{-1/2} - 53.8[Mo])$ versus [N], illustrates the strong dependence of σ_y upon [N].

Fitting equation (3) to the data set results in a change in the magnitude of the [Mo] term, as would be expected, but also changes both the sign and the magnitude of the constant term:

$$\sigma_y \text{ (MPa)} = -689 + 2510[N] + 823d^{-1/2} + 436[Mo] + 78.1[Ni] - 30.0[Mo][Ni]. \quad (8)$$

The SD of the fit is 34 MPa, and the SDs of the six coefficients are 225, 80, 96, 103, 17.1, and 7.7, respectively. Figure 3 presents the measured σ_y values plotted against the values calculated from equation (8). The straight line in this figure corresponds to agreement between measured and calculated values, and the scatter band represents two SDs about the line.

Equations without the last term of equation (3) or with the first three terms and an [Ni] term only have larger SDs when fitted to the data set. However, fitting a subset of the data (I) plus 304-alloy data from heats supplied by the same manufacturer (alloys H in reference 4) to equation (3) gave different signs, magnitudes, or both for the constant term and the last three terms. Most of the Mo variation occurs in subset I of the data, so at present, the correct form of the interaction terms is considered uncertain. Further analysis[16] of this subset of the

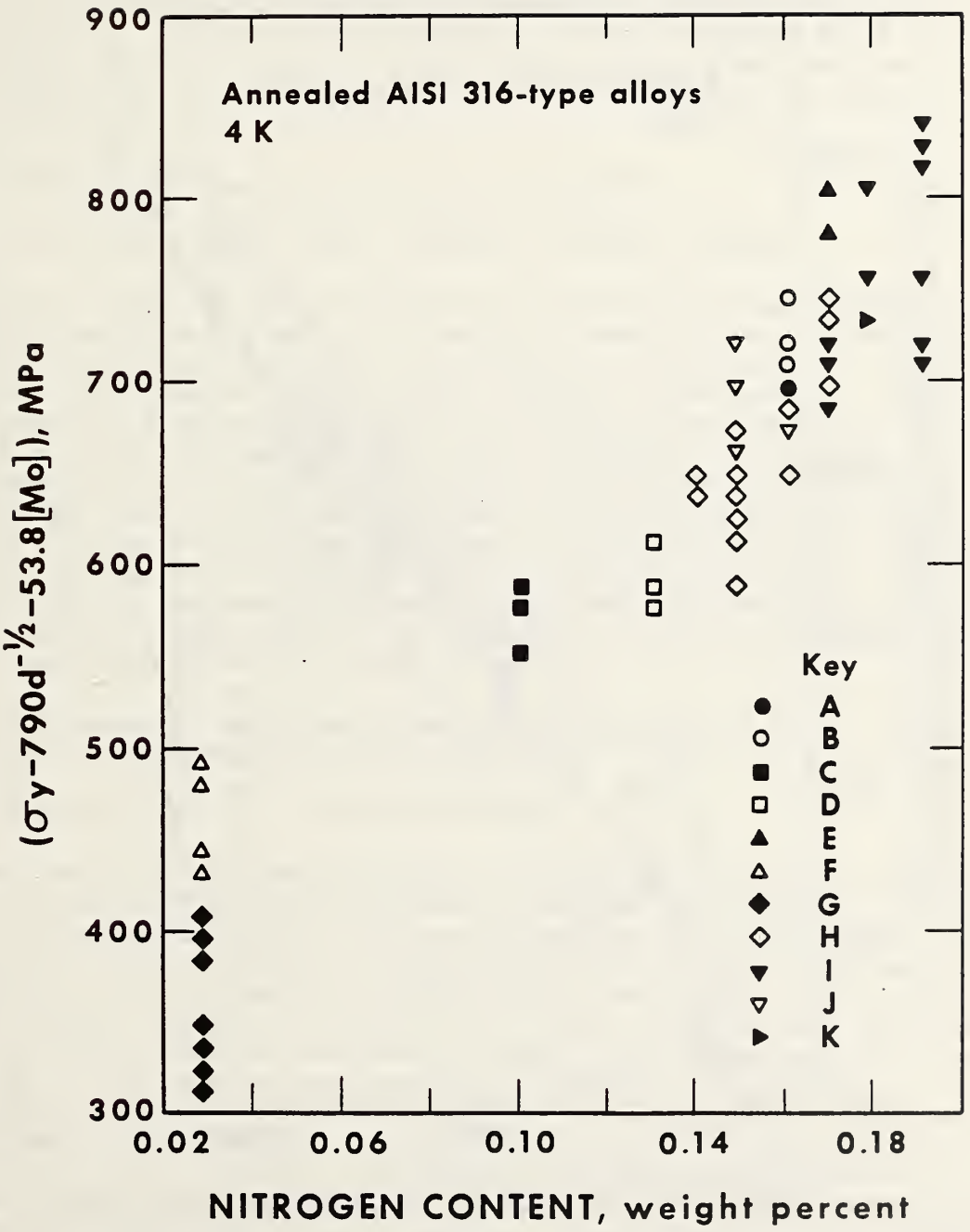

Figure 2. Tensile yield strength at 4 K for 316-type alloys less the expected contributions from grain size and Mo content [calculated from equation (7)] versus N content. The letter keys to the symbols are given in tables I and II.

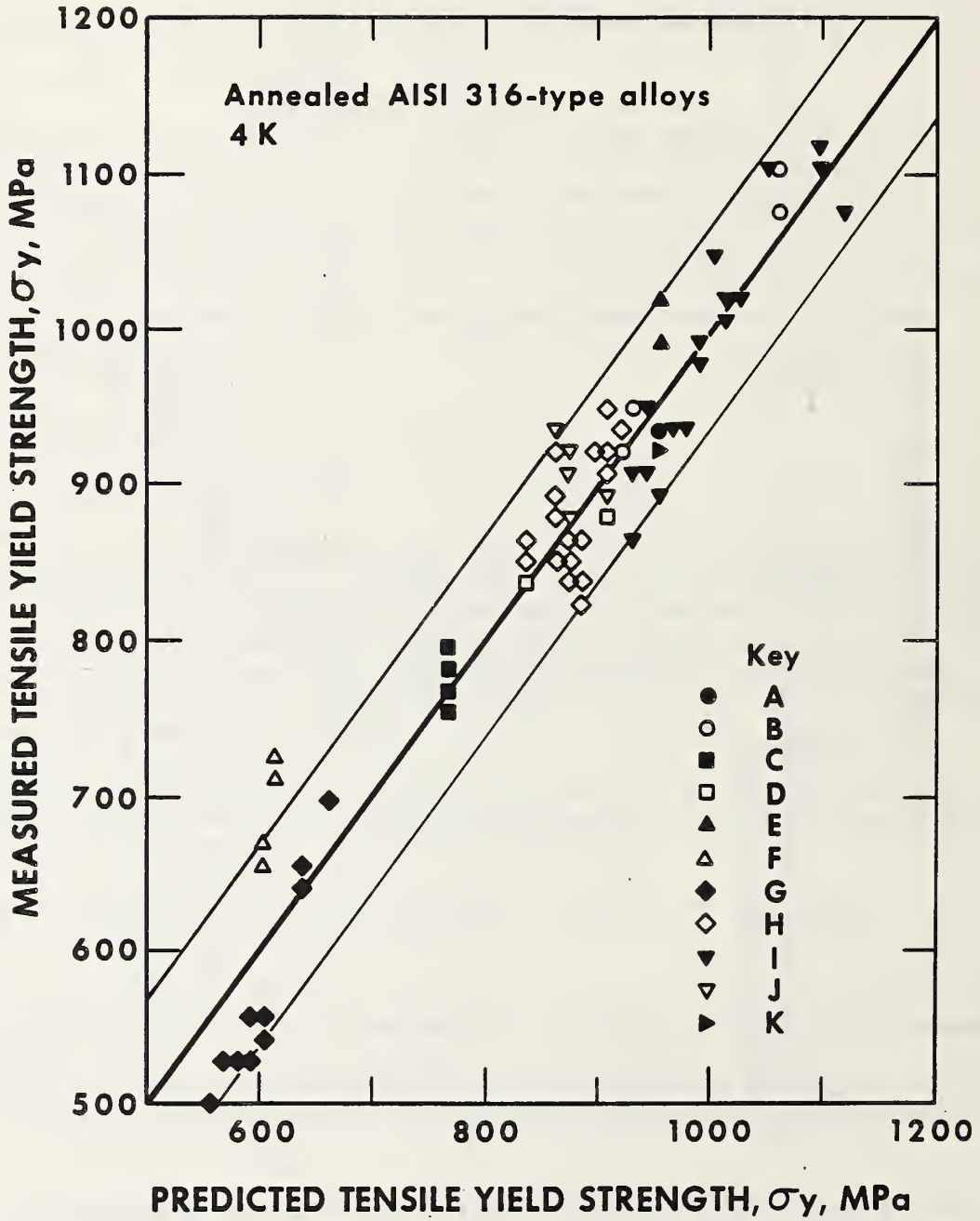

Figure 3. Measured tensile yield strength at 4 K of 316-type alloys versus tensile yield strength calculated from equation (8). The scatter band represents ± 2 SDs. The letter keys to the symbols are given in tables I and II.

data has shown a saturation of the effect of Mo on σ_y at 3 wt.%; this nonlinear effect is not considered in the present linear analysis. The negative coefficient, σ_i, does qualitatively reproduce other results of reference 16, which show a decrease in σ_y with increased Ni if Mo is present. For Mo $\geq$ 2.6 wt.%, equation (8) gives a small decrease in σ_y with increased Ni. In general, the effect of Ni on σ_y is expected to be small.

The fit of equation (4) to the data gives:

$$K_{Ic}(J)\ (MPa \cdot m^{1/2}) = 150 - 0.314\sigma_y + 16.6[Ni] + 2300\lambda, \qquad (9)$$

where the SD of the fit of the data is 30 MPa·$m^{1/2}$ and the SDs of the coefficients are 62, 0.034, 3.5 and 207. When the SDs are considered, these coefficients again are in good agreement with the results from the earlier work that was based on only 19 $K_{Ic}(J)$ measurements. Figure 4 presents the measured $K_{Ic}(J)$ values plotted against the values calculated from equation (9); the straight line corresponds to agreement between measured and calculated values, and the scatter band represents two SDs about the line. It is surprising that λ correlates so well with $K_{Ic}(J)$ since it does not represent accurately the volume fraction or shape factor of inclusions (long MnS stringers are equated with small, spherical inclusions in the simplified counting method). Furthermore, inaccuracies in λ, due to inhomogeneities and counting statistics, may be as large as 30%, particularly in the cleaner alloys.

Equation (5) was also fitted to the data using a linear least-squares program; the resulting equation is

$$K_{Ic}(J)\sigma_y/[Ni] = (9.56 \cdot 10^4)\lambda^{0.668}, \qquad (10)$$

where the SD of the predicted $K_{Ic}(J)$ is 30 MPa·$m^{1/2}$, comparable to the SD of equation (9). The SD of the coefficient of λ is 0.077. The form of this expression may be more easily compared with theory than equation (9), which is simply a linear combination of terms. An equation similar to (5), $K_{Ic}(J) = k_o'' \cdot [Ni]^{\alpha} \cdot \lambda^{\beta}/(\sigma_y)^{\gamma}$, was also fitted to the data. The exponents α and γ were found to be close to unity, and the exponent β was 0.64, similar to the power of about 2/3 in equation (10). The difference in repeated measurements of specimens from the same alloy sample is often 20 to 30 MPa·$m^{1/2}$, so SDs below this range may not be attainable. (See table I for examples.) Also, the effect of side-grooving during J-integral testing has recently been documented.[19] This research raises the possibility that earlier NBS measurements not using side grooves may overestimate the true, plane-strain fracture toughness for lower strength alloys.

Equations (7) and (9) can be used for 316-type-alloy design. For example, to achieve a σ_y of 1000 MPa with [N] = 0.16 wt., and [Mo] = 3.0 wt.% (316LN alloy), a grain size of 38 (+29,−14) μm is required.

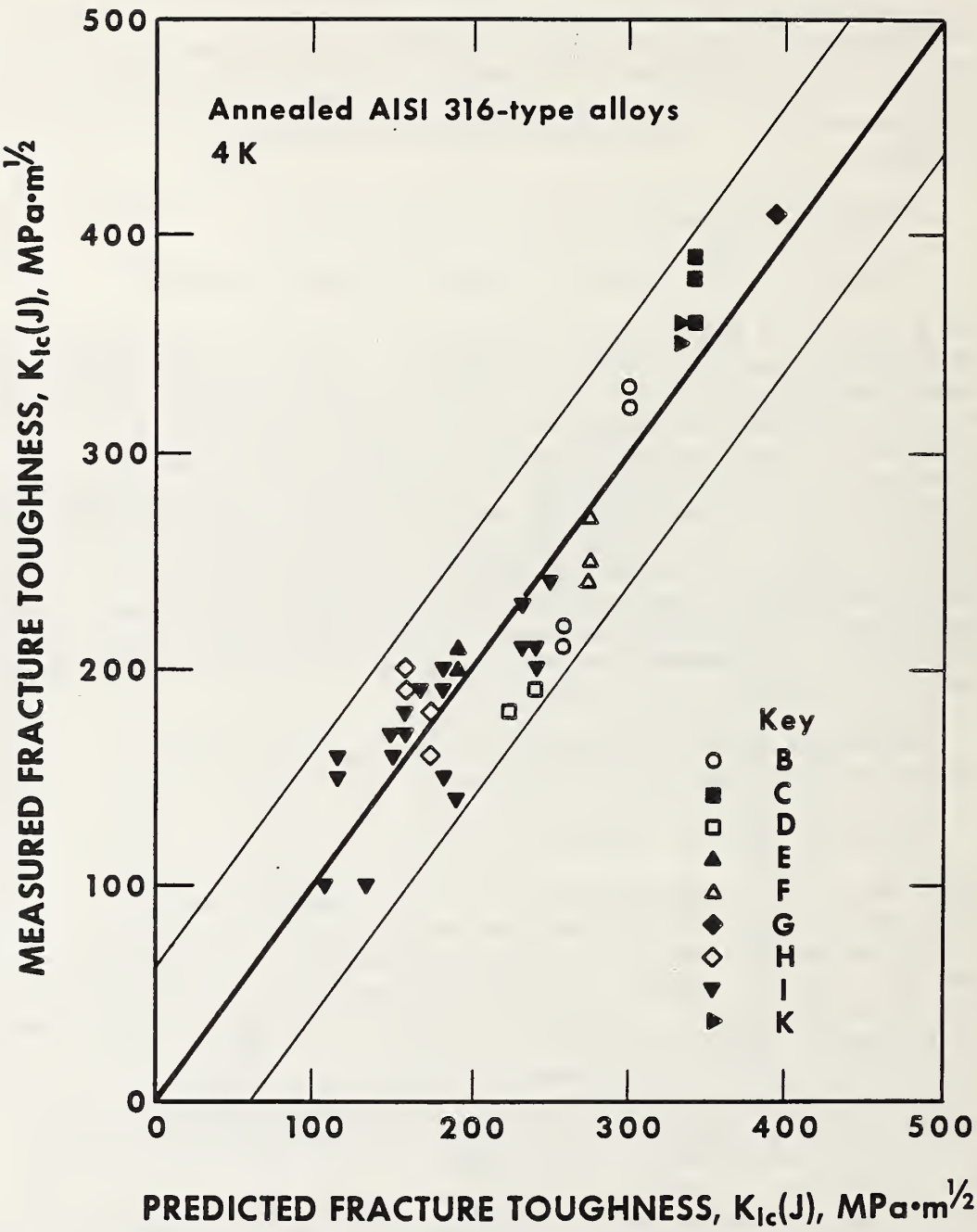

Figure 4. Measured fracture toughness at 4 K of 316-type alloys versus fracture toughness calculated from equation (9). The scatter band represents ± 2 SDs. The letter keys to the symbols are given in tables I and II.

If [N] = 0.20 wt.% (316LHN alloy), the predicted grain size is 742 (+561, −263) μm; thus, the large contribution of the [N] term to σ_y outweighs the grain-size effect.*

To achieve a $K_{Ic}(J)$ of 200 MPa·$m^{\frac{1}{2}}$ with σ_y = 1000 MPa would require, for the 316LN alloy, that λ = 0.09 (± 0.05) mm if [Ni] = 10 wt.%, and λ = 0.06 (± 0.03) mm if [Ni] = 14 wt.%, the maximum allowed under the AISI 316 specifications. The uncertainties are determined in the same manner as above. These inclusion spacings are similar to those found for the commercial heats in this study (see table I). However, at present, inclusion spacing is not a conventional specification parameter in commercial alloy production. Further correlation with other parameters is required.

SUMMARY

Matrices of NBS measurements of σ_y and $K_{Ic}(J)$ at 4 K that include numerical data on alloying, refining, and processing variables were analyzed using linear regression methods. The results of the analysis corroborated and extended the results of an earlier study carried out when fewer data were available.[3,4] The AISI 316-type alloys tested were obtained from a variety of sources and included both commercial and laboratory heats.

Tensile yield strength: Provisional equations were developed for estimating σ_y at 4 K from [N], $d^{-\frac{1}{2}}$, and [Mo]. These equations were derived for a range of [N] from 0.03 to 0.20 wt.%, a range of d from 11 to 242 μm, and a range of [Mo] from 2.0 to 4.0 wt.%. Results from fitting an equation for σ_y with an interactive term for [Ni] and [Mo] were inconclusive.

Fracture toughness: Provisional equations for estimating $K_{Ic}(J)$ at 4 K from σ_y, [Ni], and λ were determined. In addition, the quantity $K_{Ic}(J)\cdot\sigma_y/[Ni]$ (fracture toughness normalized for the effects of yield strength and Ni content) was found to vary approximately as the 2/3 power of λ. These equations were developed for a range of λ from 0.04 to 0.11 mm and a range of [Ni] from 10.5 to 14.2 wt.%.

---

*The uncertainties noted in parentheses for these grain sizes are determined by assuming the fractional error in $d^{-\frac{1}{2}}$ is given by the square root of the sum of the squares of the fractional errors in the terms of the equation. The fractional error of each term is obtained by dividing the SD of the coefficient by the value of the coefficient.

ACKNOWLEDGMENTS

The research was partially supported by the Office of Fusion Energy, U.S. Department of Energy, V. Der, Project Monitor. We are indebted to L. A. Delgado, R. P. Walsh, P. T. Purtscher, and L. L. Scull for assistance in obtaining the data and carrying out the analysis.

REFERENCES

1. R. L. Tobler and R. P. Reed, in: Materials Studies for Magnetic Fusion Energy Applications at Low Temperatures – III, Internal Report 80–1627, Ed. R. P. Reed (U.S. National Bureau of Standards, Boulder, Colorado, 1980) p. 15.

2. R. L. Tobler, D. T. Read, and R. P. Reed, in: ASTM STP 743 (American Society for Testing and Materials, Philadelphia, Pennsylvania, 1982), p. 250.

3. N. J. Simon and R. P. Reed, J. Nucl. Mater. 141–143 (1986) 44.

4. N. J. Simon and R. P. Reed, in: Materials Studies for Magnetic Fusion Energy Applications at Low Temperatures – IX, Internal Report 86–3050, Ed. R. P. Reed (U.S. National Bureau of Standards, Boulder, Colorado, 1986) p. 27.

5. R. P. Reed and N. J. Simon, in: Advances in Cryogenic Engineering – Materials, vol. 30, Eds. A. F. Clark and R. P. Reed (Plenum Press, New York, 1984) p. 127.

6. R. P. Reed, N. J. Simon, P. T. Purtscher, and R. L. Tobler, in: Materials Studies for Magnetic Fusion Energy Applications at Low Temperatures – IX, Internal Report 86–3050, Ed. R. P. Reed (U.S. National Bureau of Standards, Boulder, Colorado, 1986) p. 15.

7. T. Sakamoto, Y. Nakagama, I. Yamauchi, and T. Zaizen, in: Advances in Cryogenic Engineering – Materials, vol. 30, Eds. A. F. Clark and R. P. Reed (Plenum Press, New York, 1984) p. 137.

8. R. P. Reed, P. T. Purtscher, and K. A. Yushchenko, in: Advances in Cryogenic Engineering – Materials, vol. 32, Eds. R. P. Reed and A. F. Clark (Plenum Press, New York, 1986) p. 43.

9. N. J. Simon and R. P. Reed, Preliminary Draft, Structural Materials for Superconducting Magnets, III. AISI 304 Stainless Steel, (U.S. National Bureau of Standards, Boulder, Colorado, 1985); unpublished.

10. R. P. Reed, P. T. Purtscher, R. P. Walsh, and L. A. Delgado, Test results on AISI 316-type alloys, U.S. National Bureau of Standards, Boulder, Colorado, unpublished data (1987).

11. D. T. Read and R. P. Reed, in: Materials Studies for Magnetic Fusion Energy Applications at Low Temperatures – II, Internal Report 79–1609, Eds. F. R. Fickett and R. P. Reed (U.S. National Bureau of Standards, Boulder, Colorado, 1979) p. 79.

12. R. L. Tobler, R. P. Reed, and D. S. Burkhalter, in: Advances in Cryogenic Engineering – Materials, vol. 26, Eds. A. F. Clark and R. P. Reed (Plenum Press, New York, 1980) p. 107.

13. R. L. Tobler, R. P. Mikesell, R. L. Durcholz, C. W. Fowlkes, and R. P. Reed, in: Semi-Annual Report on Materials Research in Support of Superconducting Machinery, Internal Report 74–359, (U.S. National Bureau of Standards, Boulder, Colorado, 1974) p. 182.

14. R. L. Tobler and R. P. Reed, in: Materials Studies for Magnetic Fusion Energy Applications at Low Temperatures – IV, Internal Report 81–1645, Eds. R. P. Reed and N. J. Simon (U.S. National Bureau of Standards, Boulder, Colorado, 1981) p. 147.

15. L.-Å. Norström, Met. Sci. 11 (1977) 208.

16. P. T. Purtscher, R. P. Walsh, and R. P. Reed, in: Advances in Cryogenic Engineering – Materials, vol. 34, Eds. A. F. Clark and R. P. Reed (Plenum Press, New York, 1988) p. 191.

17. R. L. Tobler, T. A. Siewert, and H. I. McHenry, in: Materials Studies for Magnetic Fusion Energy – IX, Internal Report 86–3050, Ed. R. P. Reed (U.S. National Bureau of Standards, Boulder, Colorado, 1986) p. 239

18. J. P. Hirth and F. H. Froes, Metall. Trans. 8A (1977) 1165.

19. T. Ogata, K. Ishikawa, T. Yuri, R. L. Tobler, P. T. Purtscher, R. P. Reed, T. Shoji, N. Nakano, and H. Takahashi, in: Advances in Cryogenic Engineering – Materials, vol. 34, Eds. A. F. Clark and R. P. Reed (Plenum Press, New York, 1988) p. 259.

CLEAVAGE-LIKE FRACTURE ALONG SLIP PLANES IN Fe–18Cr–3Ni–13Mn–0.37N AUSTENITIC STAINLESS STEEL AT LIQUID-HELIUM TEMPERATURE*

R. L. Tobler
Fracture and Deformation Division
National Bureau of Standards
Boulder, Colorado

and

D. Meyn
Materials Science and Technology Division
Naval Research Laboratory
Washington, D.C.

Contrary to usual expectations for the face-centered cubic crystal structure, some nitrogen-alloyed austenitic stainless steels are brittle at temperatures approaching absolute zero. In this communication, results of plane-strain fracture toughness and fractographic tests are presented for an Fe–18Cr–3Ni–13Mn–0.37N steel tested at liquid-helium temperature (4 K). The strength of this steel increases significantly at cryogenic temperatures owing to high-nitrogen content. At 4 K, the yield strength reaches 1540 MPa. Low toughness (K_{Ic} = 70 MPa·m$^{\frac{1}{2}}$) and linear-elastic behavior is observed in compact specimens at this temperature, in association with a brittle failure mechanism consisting of transgranular facets. Valid fracture-toughness (K_{Ic}) measurements at 4 K are reported, the cleavage-like failure mechanism is described, and the crystal plane indices of the transgranular facets produced during fatigue and fracture are identified by x-ray diffraction and slip-line traces.

---

*Submitted to *Metallurgical Transactions*.

The test material was a 25.4-mm-thick plate of Fe–18Cr–3Ni–13Mn–0.37N austenitic stainless steel in the commercially annealed condition: 1080°C for 1 h and water quenched. The mill chemical analysis in weight percent is: Fe–18.09Cr–3.26Ni–13.22Mn–0.37N–0.038C–0.12Mo–0.52Si–0.005S–0.028P. The material in the as-received condition had an average austenite grain diameter of 48 μm and a microstructure free of carbide precipitation. The mechanical properties are listed in Table 1.

Table 1. Mechanical properties of as-received Fe–18Cr–3Ni–13Mn–0.37N austenitic steel [1].

Temperature (K)	Yield Stress (MPa)	Ultimate Strength (MPa)	Elongation (%)	Reduction of Area (%)	Rockwell Hardness (R_B)
295	400	796	56	53	93
4	1540	1811	4	26	–

Toughness tests according to Methods E 399-83 [2] were performed using compact specimens 25.4-mm thick (B) and 50.8-mm wide (W). Two specimens were machined from the as-received material, and one from laboratory-annealed material. The laboratory anneal (1093°C, 37 h, water quenched) was applied to a sample of this steel to enlarge its grains. All specimens were fatigue-cracked at stress-intensity factor ranges from 20 to 50 MPa·$m^{½}$ and then fractured at 4 K. The average grain diameter after the laboratory anneal was large enough (about 1 mm) to enable Laue x-ray analysis of individual crystal facets situated on the fracture surface of the polycrystalline aggregate.

The load-versus-deflection curve for the Fe–18Cr–3Ni–13Mn–0.37N specimen in the as-received condition at 4 K is shown in Fig. 1. A type-I [2] linear-elastic behavior was observed, with only slight nonlinearity prior to fast fracture. The typical fracture-specimen surface (Fig. 2) displayed no shear lips. Both the fatigue and overload failure zones were both covered by smooth, highly reflective facets producing a macroscopic appearance; such facets are commonly seen in body-centered cubic (bcc) metals fractured at low temperatures. There was a relatively large degree of fatigue crack curvature: the edge crack lengths were about 14 percent shorter than the three-point average crack lengths calculated according to Methods E 399-83. Thus, the crack front curvature was sizable, but it did not exceed the 15 percent limitation set by section 8.2.2 of Methods E 399-83 [2]. Magnetometer and x-ray examination of the 4-K fracture surface revealed no detectable bcc martensitic phase; the sensitivities were 0.2 and 3 percent, respectively.

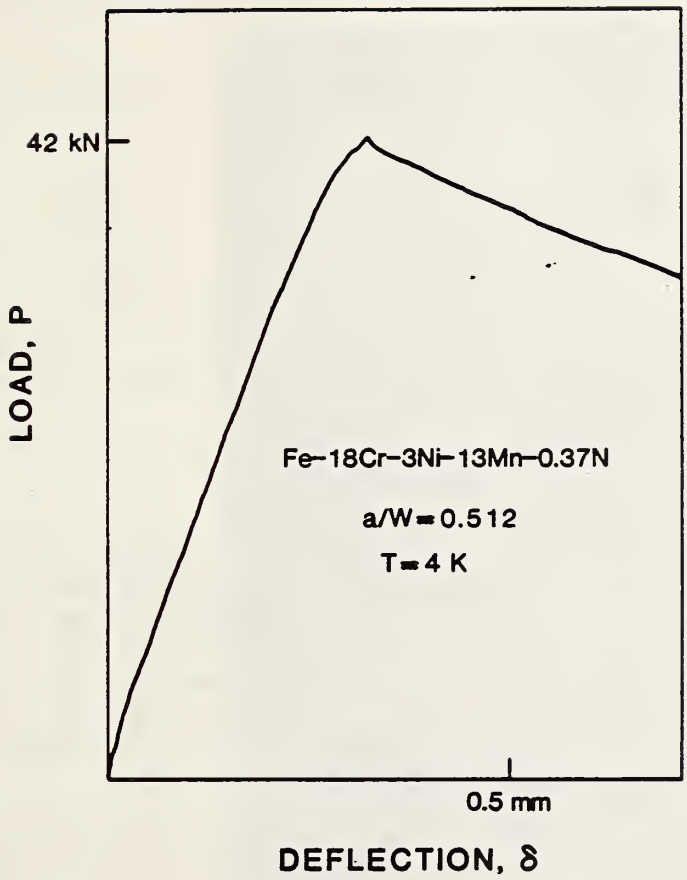

Figure 1. Load-versus-deflection test record at 4 K for a chevron-notched specimen of Fe–18Cr–3Ni–13Mn–0.37N steel in the as-received condition.

The fracture-toughness (K_{Ic}) measurements for the as-received material are listed in Table 2. Also listed are specimen dimensions and test-validity criteria, as defined in Methods E 399-83. Although the fracture toughness of the Fe–18Cr–3Ni–13Mn–0.37N steel seems low for an austenitic alloy, in fact it meets expectations for steels of this strength level, based on the known inverse trend of K_{Ic} versus σ_y [1]. The results for a chevron-notched and a straight-through-notched specimen proved indistinguishable: Their K_{Ic} values were nearly equal, and their crack-front curvatures were identical. Thus, the crack-starter notch type had no influence on the final crack-front shape.

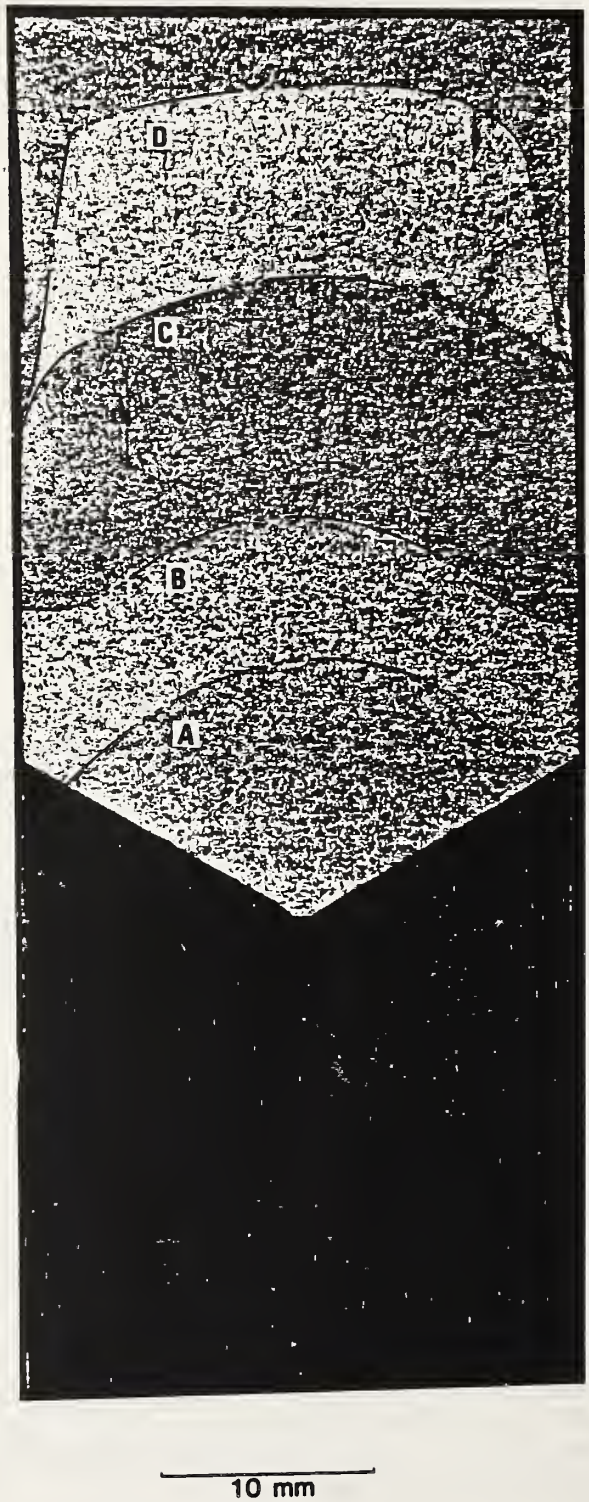

Figure 2.

Macroscopic fracture surface of chevron-notched Fe–18Cr–3Ni–13Mn–0.37N steel after testing:
A) 76-K fatigue zone,
B) 4-K fatigue zone,
C) 4-K overload failure zone,
D) final fracture zone at $T > 4$ K.

Table 2. Fracture-toughness data for as-received Fe–18Cr–3Ni–13Mn–0.37N austenitic steel at 4 K.

Specimen Number	Specimen Thickness, B (mm)	Specimen Width, W (mm)	Average Crack Length, a (mm)	Relative Crack Length, a/W	Load Ratio P_{max}/P_Q	Required Thickness $2.5(K_{Ic}/\sigma_y)^2$ (mm)	Fracture Toughness, K_{Ic} (MPa·m$^{1/2}$)
1*	25.400	50.725	25.975	0.512	1.05	5.2	70
2†	25.425	50.600	26.650	0.527	1.01	5.3	71

* chevron-notch design
† straight-through-notch design

Our K_{Ic} values agree well with the average K_Q value (71 MPa·m$^{1/2}$) reported by Read and Reed [1] for the same plate of steel. Their K_Q values are reported as invalid because they did not satisfy the crack-front-curvature requirements of Methods E 399-74, the current standard at the time. Although similar curvatures occurred in the present study, our measurements are valid because the curvature tolerances were relaxed in the updated Methods E 399-83 standard.

Figures 3 and 4 show facets produced in the coarse-grained specimen of Fe–18Cr–3Ni–13Mn–0.37N steel that was fatigued and fractured at 4 K. The facet planes in both zones were oriented at angles from 90° to 53° with respect to the loading axis, or 0° to 37° from the macroscopic plane of fracture. As shown at higher magnification in Figs. 5 and 6, the facets displayed steps and slip-line markings, but no river patterns, such as those observed on classical cleavage facets for ferritic steels.

Three facets in the fatigue-failure zone of the coarse-grained specimen were examined by Laue x-ray diffraction, and all three were identified as {111} planes in an fcc structure. The crystallographic directions in these {111} planes were apparently randomly oriented with respect to the crack propagation direction. The fcc structure underlying the facets was verified by careful structure factor analysis of the Laue back-reflection patterns and comparison with known fcc and bcc patterns.

Overload-zone facets for the coarse-grained specimen were also identified as {111} planes on the basis of the 60° angle between the slip-line traces and between facet edges. Again, three facets in this zone were x-rayed. The planar indices could not be confirmed by x-ray diffraction because the diffraction technique produced no spot pattern, only general blackening due to microplastic deformation induced at fracture. Consequently, the crystallographic directions for overload facets could not be determined.

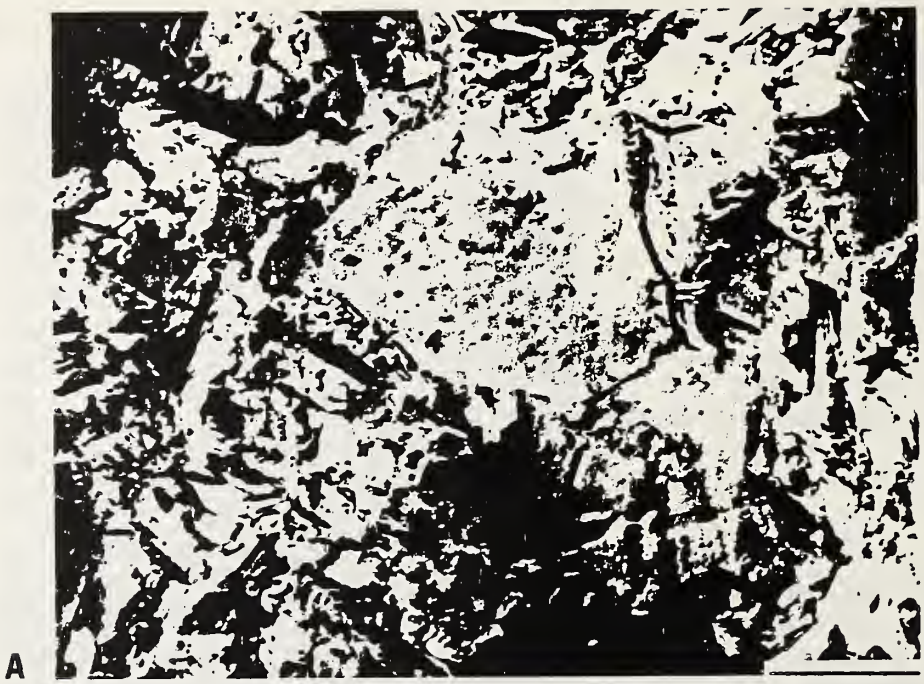

Figure 3. Scanning-electron microscope photographs of crystallographic facets on the fatigue failure zone of coarse-grained Fe–18Cr–3Ni–13Mn–0.37N steel fractured at 4 K: A) facet no. 2, B) facet no. 1.

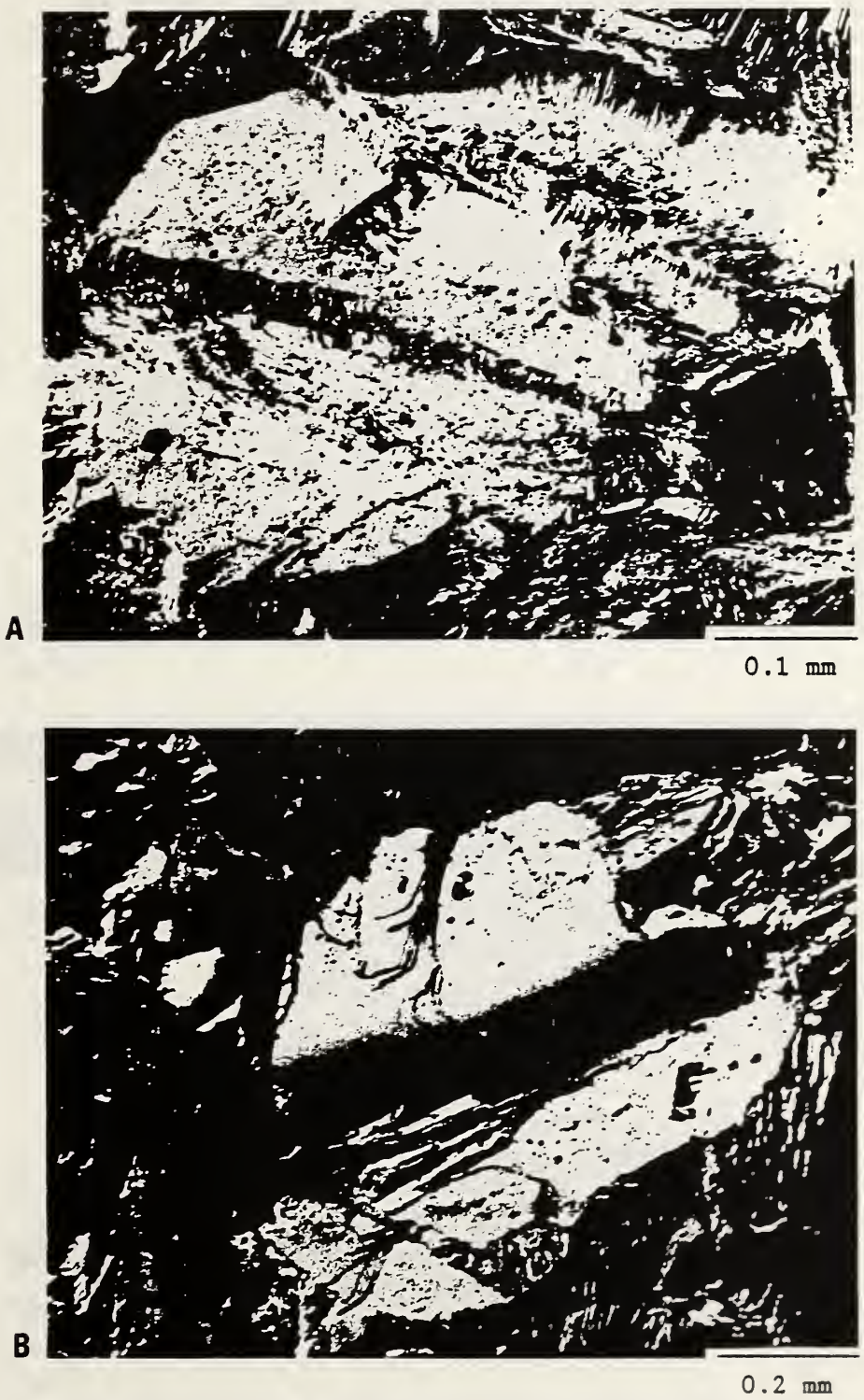

Figure 4. Scanning-electron microscope photographs of crystallographic facets on the overload fracture zone of coarse-grained Fe–18Cr–3Ni–13Mn–0.37N steel fractured at 4 K: A) facet no. 4, B) facet no. 5.

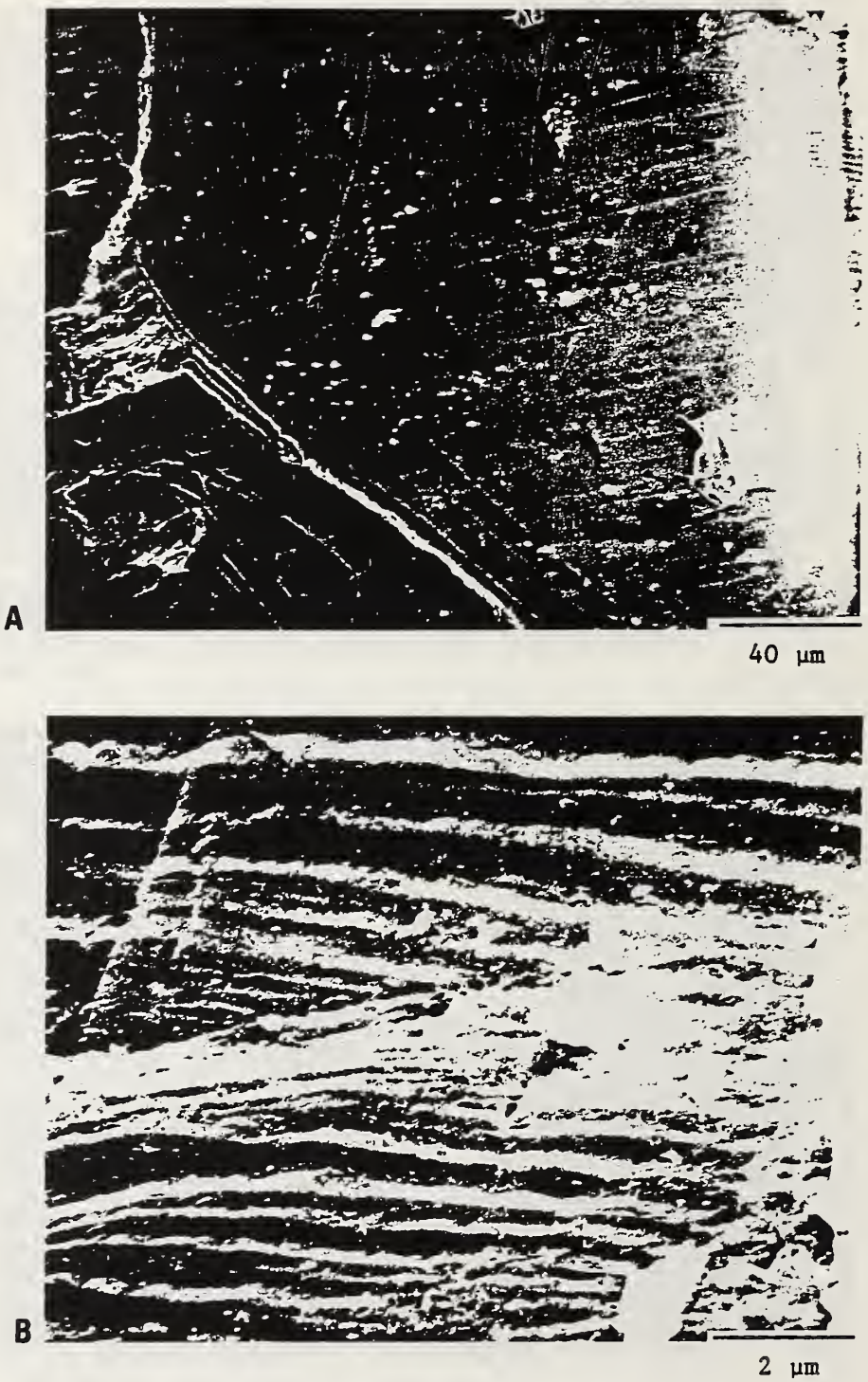

Figure 5. Scanning-electron microscope photographs of microscopic steps and fine slip-line traces on a fatigue-zone facet (facet no. 2 of Fig. 3): A) smooth area, B) same facet, but showing slip markings in detail.

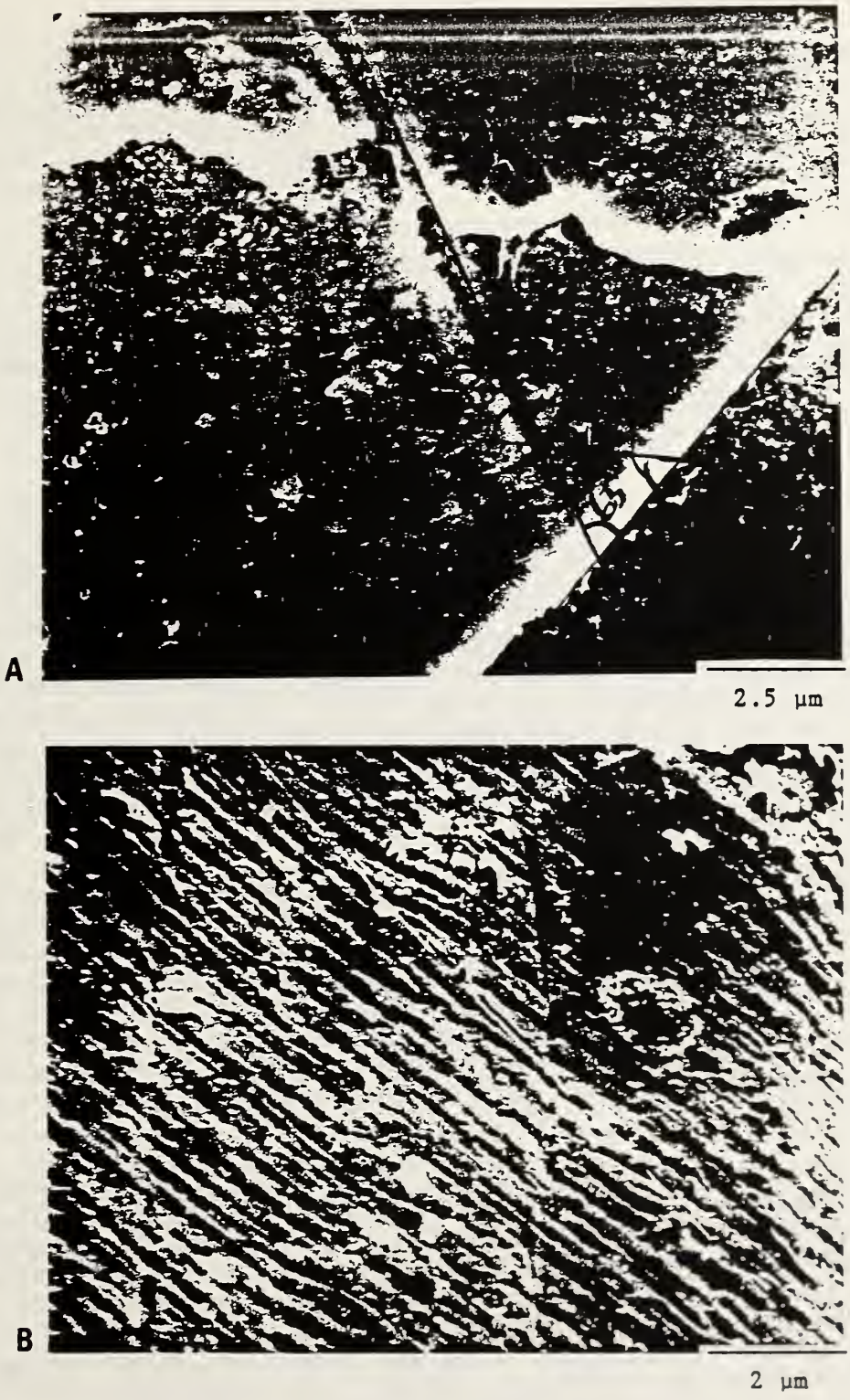

Figure 6. Scanning-electron microscope photographs of slip-line traces on an overload-zone facet (facet no. 4 of Fig. 4): A) plane area with intersecting slip lines, B) area with "striations" caused by regularly spaced slip bands.

According to a simple model, the occurrence of ductile or brittle fracture at a given test temperature depends on whether the yield strength (σ_y) or the cleavage strength (σ_c) is reached first [3,4]. For metals, σ_c is relatively high and temperature insensitive. Critical factors, then, are the magnitude of σ_y and its rate of increase at low temperatures.

For most bcc metals and alloys, including ferritic steels, σ_y is strongly temperature dependent. As the test temperature is lowered, the lattice resistance to slip increases until, at some temperature, σ_c is reached before slip can occur. As a result, cleavage is common in bcc materials at low temperatures. There are exceptions to the rule, however. For example, zone-refined, high-purity bcc iron remains ductile in tensile tests at temperatures as low as 4 K [5].

In the case of most fcc metals and alloys, including austenitic stainless steels, σ_y is low and not strongly temperature dependent. Early observations led to the traditional view that "fcc metals do not fracture by cleavage" [3], and we overgeneralized that "slip occurs readily in fcc metals at all temperatures, their shear strengths are always lower than their cleavage strengths, and they always fail in a ductile manner" [4]. In reproof, a number of exceptions have not appeared as our experience has grown [6–19]. For example, rhodium and iridium cleave in inert environments at room temperature [6,7]; nickel and Al–6Zn–3Mg cleave in liquid metals at various temperatures [8]; and strong nitrogen-alloyed austenitic stainless steels cleave at liquid-nitrogen temperature [9].

Regarding failure mechanisms, tensile loading of iridium in inert environments at room temperature, or of aluminum in liquid mercury, produces cleavage on {001} planes [6,8]. Corrosion-fatigue cracking in aluminum alloys also produces cleavage on {001} planes [11]. Cleavage on {111} planes has been observed in fcc metals under conditions of fatigue in alloys with coarse-grained structures and limited cross-slip [12]. Also, cleavage-like slip-plane cracking on {111} proves to be the usual crack-growth mechanism for nickel-base superalloys fatigued at room temperature [13–15].

For austenitic steels, Caskey [9] reports cleavage for an Fe–17.44Cr–15.31Mn–(0.4–0.6)N alloy in tensile tests at 78 K. The fracture surface displayed cleavage facets lying along coherent twin boundaries, transverse to the tensile axis. The fracture progressed by brittle microcracking across individual grains, followed by ductile fracture of the intervening material. The faceted failure mechanism was attributed to deformation faulting and to ϵ-phase formation. Others reported similar brittleness in Fe–Cr–Mn–Ni steels at low temperatures [16–19]; this was attributed to several possible mechanisms, including the formation of brittle martensites and the high localization of strain arising from deformation faulting.

The Fe–18Cr–3Ni–13Mn–0.37N steel of this study is related to the Fe–Cr–Mn–Ni steels discussed above. They were all developed for the

economical replacement of nickel by manganese and nitrogen. Manganese increases the solubility for nitrogen, the most potent austenite-strengthening element at low temperatures. Thus, the steel of this study contains 0.37% nitrogen, and its yield strength more than triples between 295 and 4 K, promoting brittle fracture, as mentioned above.

Various definitions of cleavage have been offered, but ASTM Standard E 616-82 on terminology defines cleavage (strictly, crystallographic cleavage) as "separation of a crystal along a plane of fixed orientation relative to the three-dimensional crystal structure within which the separation process occurs, with the separation process causing the newly formed surfaces to move away from one another in directions containing major components of motion perpendicular to the fixed plane" [20]. The facets on our Fe–18Cr–3Ni–13Mn–0.37N steel surfaces satisfy this definition of cleavage, even though the failure mechanism is evidently slip-band cracking.

Fractographically, slip band-cracking is similar to tensile cleavage, but the distinction is noteworthy. If the brittle fracture mechanism for our steel were pure tensile cleavage, then the cleavage plane would be {001}, not {111}. The usual tensile-cleavage plane in fcc alloys is {001}, as discussed above, whereas {111} cleavage has been observed only under conditions giving rise to slip-band cracking, such as that which occurs during Stage-I fatigue-crack propagation [13–15]. Such observations, which are common for high-temperature nickel alloys, indicate features strongly resembling those of the present study, including cleavage planes at high angles to the stress axis. Slip-band or shear-band cracking has been identified as the mechanism for {111} cleavage in the nickel-alloy studies, and it is distinct from simple slipping off, or "slip-plane decohesion," which causes chisel-edge fractures in single crystals.

In general, slip-band cracking is facilitated by planar slip (low stacking-fault energies, short-range order, and shearable precipitates) and by coarse grain size. The sequence of events for slip-band cracking in our steel might be: a narrow, well-defined shear (slip) band forms in a suitably oriented grain, and because of the difficulty of activating out-of-plane secondary slip and the restriction of shear to the original plane by metallurgical factors, shear strain continues to accumulate in the narrow band. The accumulation of dislocation-induced defects in this band weakens it to the extent that the component of tensile force on the band causes final separation in the tensile mode, and this gives rise to the observed cleavage-like appearance.

Given the complex character of the stress and strain states and the various grain orientations in the crack-tip region, it is not surprising that significant amounts of shear strain might accumulate in a few grains on slip bands oriented nearly perpendicular to the gross-stress axis. The amount of shear-strain accumulation needed to facilitate tensile cracking on such a band would be a function of its orientation, which determines the magnitude of the resolved tensile component. The overall slip-band cracking mechanism, seen in this light, becomes an interplay

tensile component: the more nearly perpendicular the slip band is to the gross-tensile-load axis, the higher the local tensile stress across the slip band and the less shear-strain accumulation needed to trigger separation. One would expect that some range of angles between 90° and 45° (with respect to the gross-stress axis) would be most favorable for slip band cracking, as defined here.

Finally, Koss and Chan [21] have analyzed the conditions for crack advance along planar slip bands in non-work-hardening materials. They assume a condition in which slip is allowed to occur in the plane of the crack, with plastic displacements restricted to shear that is parallel to the crack plane. Then, once a crack forms in a coplanar slip band, it follows that it is difficult to activate secondary slip with shear displacements inclined to the crack plane. The result: a large local shear strain, combined with large normal or hydrostatic stresses near the crack tip, a condition conducive to easy crack propagation and low toughness. This analysis also shows that even if cross-slip could occur, it would not be able to relax the large normal stress on slip bands coplanar with the crack [22]. Thus, the stress state that exists under the assumed conditions is the paramount factor, and the role of specific dislocation arrangements or the weakening of slip bands by accumulated shear is deemphasized. This model helps to rationalize some features of slip-band cracking in nickel-, aluminum-, and titanium-based alloys [21]. Similarly, it gains relevance to the austenitic steel of our study in view of its decreased work-hardening capability, increased strength, and increased planarity of slip at 4 K.

ACKNOWLEDGMENT

This study was supported by the U.S. Department of Energy, Office of Fusion Energy.

REFERENCES

1. D. T. Read and R. P. Reed: The Metal Science of Stainless Steels, E. W. Collings and H. W. King, eds., Metallurgical Society of the AIME, New York, 1979, pp. 92–121.
2. Standard Test Method for Plane-Strain Fracture Toughness of Metallic Materials, ASTM Designation E 399-83, 1987 Annual Book of ASTM Standards, Section 3, American Society for Testing and Materials, Philadelphia, 1987, pp. 680–715.
3. A. S. Tetelman and A. J. McEvily, Jr.: Fracture of Structural Materials, Wiley, New York, 1967, p. 212.
4. D. A. Wigley: Mechanical Properties of Materials at Low Temperatures, Plenum, New York, 1971, pp. 94–95.
5. Z. S. Basinski and A. Sleeswyk: Acta Metall., 1957, vol. 5, pp. 176–179.
6. S. S. Hecker, D. L. Rohr, and D. F. Stein: Metall. Trans. A, vol. 9A, 1978, 481–487.

7. C. Gandhi and M. F. Ashby: Scr. Metall., 1979, vol. 13, pp. 371–379.
8. C. F. Old, Met. Sci., 1980, vol. 14, pp. 433–440.
9. G. R. Caskey, Jr.: Fracture of Fe–Cr–Mn austenitic steel, Report DP-MS-78-68, E. I. du Pont de Nemours, Aiken, South Carolina, 1978, pp. 1–21.
10. S. P. Lynch: Met. Sci., 1981, vol. 15, pp. 463–467.
11. G. G. Garrett and J. F. Knott: Acta Metall., 1975, vol. 23, pp. 841–848.
12. K. R. L. Thompson and J. V. Craig: Metall. Trans. A, 1970, vol. 1A, pp. 1047–1049.
13. D. J. Duquette, M. Gell, and J. W. Piteo: Met. Trans. A, 1970, vol. 1A, pp. 3107–3115.
14. D. J. Duquette and M. Gell: Met. Trans. A, 1971, vol. 2A, pp. 1325–1331.
15. M. Gell and G. R. Leverant: Acta Metall., 1968, vol. 16, pp. 553–561.
16. F. W. Schaller and V. F. Zackay: Trans. ASM, 1951, vol. 51, pp. 609–628.
17. C. M. Hsiao and E. J. Dulis: Trans ASM, 1960, vol. 52, pp. 855–877.
18. J. C. Shyne, F. W. Schaller, and V. F. Zackay: Trans. ASM, 1960, vol. 52, pp. 848–854.
19. J. D. Defilippi, K. G. Brickner, and E. M. Gilbert: Trans. Metall. Soc. AIME, 1969, vol. 245, pp. 2141–2148.
20. Standard Terminology Relating to Fracture Testing, ASTM Designation E 616-82, 1987 Annual Book of ASTM Standards, Section 3, Vol. 03.01, American Society for Testing and Materials, Philadelphia, 1987, p. 864.
21. D. A. Koss and K. S. Chan: Acta Metall., 1980, vol. 28, pp. 1245–1252.
22. K. S. Chan: Acta Metall., 1987, vol. 35, pp. 981–987.

FRACTURE BEHAVIOR OF 316LN ALLOY IN UNIAXIAL TENSION AT CRYOGENIC TEMPERATURES*

P. T. Purtscher, R. P. Walsh, and R. P. Reed
Fracture and Deformation Division
National Bureau of Standards
Boulder, Colorado

The fracture behavior of an austenitic stainless steel, commercial-grade 316LN alloy, at cryogenic temperatures was studied by careful examination of the fracture surfaces and polished cross sections through the fracture surfaces of round tensile specimens. The fracture was ductile (a dimpled rupture process) and was controlled by inclusions (MnS stringers and smaller spherical particles) in the structure. The main effect of the MnS stringers was to decrease the percent reduction in area in the tensile test at 4 K. The true stress and strain at fracture varied as a function of test temperature; they were related to the nucleation of microvoids around the spherical particles.

INTRODUCTION

Many studies[1-4] have characterized the mechanical properties of austenitic stainless steels at 4 K. Typically, the previous studies looked at the toughness, tensile yield strength, and serrated yielding behavior, but paid little attention to the tensile fracture behavior. The tensile fracture behavior can provide additional information on the deformation and fracture processes and increase our understanding of fracture in more complex stress states.

In this study, we examined the fracture behavior of a commercial-grade 316LN austenitic stainless steel at cryogenic temperatures. Specifically, we considered the role of inclusions and the effect of

---

*In *Advances in Cryogenic Engineering — Materials*, vol. 34, Plenum, New York, 1988, pp. 379–386.

temperature. Round tensile specimens with a uniform gage length fractured in uniaxial tension were chosen for this initial study to simplify the interpretation of the results. The fracture surfaces were examined carefully and related to the features found in longitudinal cross sections through the fracture surfaces. The mechanical properties of the commercial alloy at 4 K are compared with the same properties from a laboratory heat of 316LN with a different inclusion content.

MATERIALS AND PROCEDURE

A commercial-grade 316LN alloy was supplied as 50-mm-thick plate, mill annealed at a minimum temperature of 1038°C. The 4-K mechanical properties of this alloy are reported elsewhere.[5] The tensile properties at 4 and 76 K from NBS tests are listed along with the steel mill's 295-K results in Table I. The 4-K mechanical properties of a laboratory heat of 316LN are also listed for comparison.

The composition, grain size, and inclusion spacing for the two 316LN alloys are shown in Table II. The inclusion spacing was determined by counting all inclusions greater than 0.5 μm in diameter in a given area, normalizing that number to a 1 mm^2 area, and taking the inverse square root.

Table I. Tensile Properties of 316LN Alloys

Source	Temperature (K)	Strength (MPa) Yield	Ultimate	Ductility (%) El.	R.A.
Commercial*	295	275	581	60	68
Commercial†	76	757 to 761	1430	53	65
Commercial‡	4	845 to 860	1630 to 1640	38 to 46	37 to 48
Laboratory‡	4	840 to 1060	1620 to 1730	36 to 43	49–58

* results from steel mill
† one specimen pulled to failure; four more interrupted tests
‡ five specimens pulled to failure

Table II. Composition (wt.%) of 316LN Alloys

	C	Mn	P	S	Si	Cr	Ni	Mo	N
Commercial heat	0.016	1.1	0.020	0.015	0.54	18.0	10.5	2.12	0.15
Laboratory heat	0.020	1.0	0.002	0.003	0.29	18.6	10.9	2.2	0.12

The commercial alloy contained two distinct types of particles in the austenitic matrix. Figure 1 shows both types in the etched microstructure. The first type is a large, elongated MnS inclusion that runs parallel to the rolling direction. The second type of particle is spherical and much smaller in size (1 to 2 μm in diameter). X-ray analysis with an energy-dispersive analyzer showed that these smaller particles contain Al, Ti, and Ca, but we could not definitely identify the particles as carbide, nitride, oxide, or silicate types. The laboratory heat did not contain large elongated MnS stringers. All the inclusions were spherical, approximately 1 to 2 μm in diameter; all contained Mn, S, Si, Ca, and Al.

Standard round tensile specimens, 6.2 mm in diameter and 38 mm in gage length, were machined so that the tensile axis was transverse to the rolling direction. The tests were conducted in displacement control with a strain rate of 2×10^{-4} per second. At 76 K, the strain rate was reduced one order of magnitude after the maximum load. A total of five tests were performed in liquid nitrogen (76 K). Only one specimen was actually broken; the others were stopped at different points past the

Figure 1. Etched microstructure showing the two types of particles: A – MnS stringers; B – smaller, spherical particles.

maximum load. At 4 K, the results of five tests, in which all specimens were pulled to failure, are reported. The initial strain was determined from clip-on extensometers. At the end of the test, the strain was determined from the diameter of the specimen and

$$\epsilon = 2 \ln D_o/D_f, \tag{1}$$

where D_o and D_f are the original and final diameters, respectively.

RESULTS

Figure 2 shows a schematic of the load-vs.-time output from the tests. The most obvious difference between the test results is the serrated flow of the curve at 4 K. Extensive studies of serrated yielding have shown that the load drops are associated with local temperature rises and avalanches of dislocation motion in the region of the temperature rise.[4,6,7] The plastic deformation occurs in discrete steps along the gage length similar to Lüders bands.

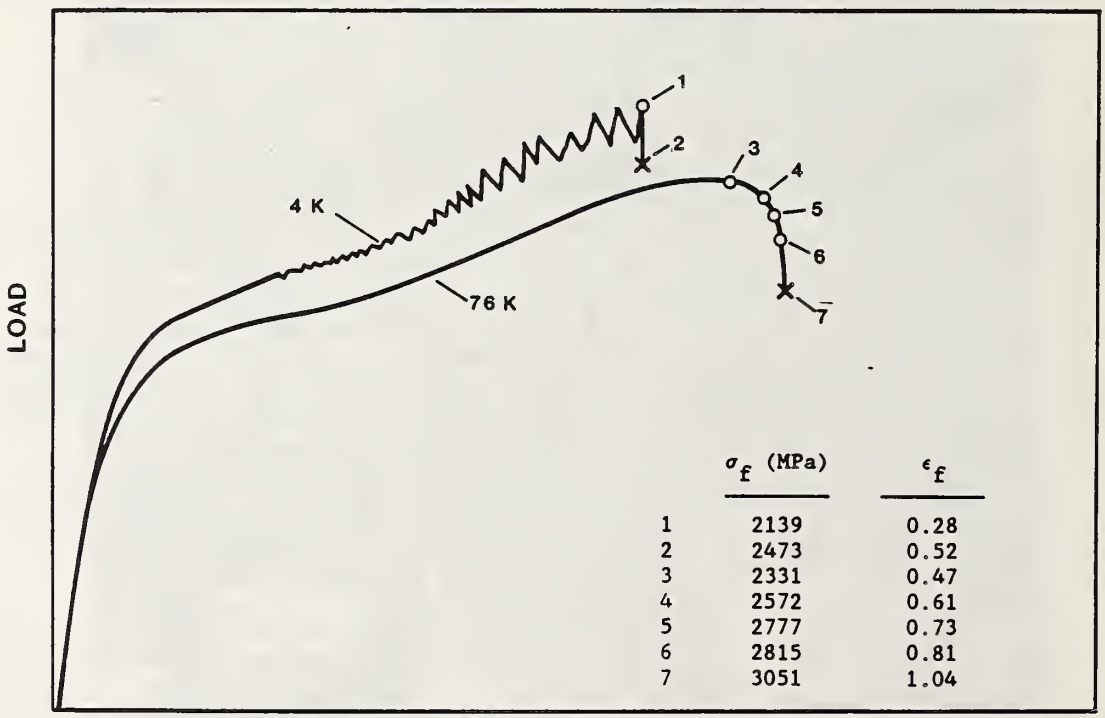

	σ_f (MPa)	ϵ_f
1	2139	0.28
2	2473	0.52
3	2331	0.47
4	2572	0.61
5	2777	0.73
6	2815	0.81
7	3051	1.04

Figure 2. Schematic curves representing the load-vs.-time behavior of tensile specimens at 4 and 76 K, where σ_f and ϵ_f are the true stress and strain to fracture.

In general, the yield and flow strengths at 76 K are proportionately lower than at 4 K. Excepting the serrated yielding, the load-vs.-time curves at the two temperatures have similar shapes until maximum load. Both curves initially show low work hardening owing to the strain-induced martensitic transformation. At the maximum load, the specimens at 4 K fractured with a total elongation of about 43%. At 76 K, the total elongation was slightly higher, and the load decreased about 20% with further straining before the specimen fractured. Approximately the same amount of strain-induced martensite formed at each test temperature.

At 76 K, four tests were stopped before fracture so that the progression of events that led to the final fracture could be studied. The maximum true stress and true strain for each of these specimens is shown in Figure 2 at approximately the point at which the tests were stopped. At 4 K, the maximum load could not be detected prior to fracture. The true stress and true strain for the two points marked on the 4-K curve in Figure 2 were taken from a representative specimen. The true stress and strain at fracture were calculated from the final load and final cross-sectional area. The lower values of true stress and strain at 4 K were calculated from the load at the point on the curve just prior to the final serration and the cross-sectional area outside the localized neck in a region of relatively uniform strain.

The fracture surfaces of the broken tensile specimens were examined in a scanning electron microscope to determine the fracture morphology. The tensile fracture surfaces of the 76- and 4-K specimens were very similar. The surface had an outer ring of smooth shear lip and an inner region with a rougher, "woody" texture. In the higher magnification of the rough-textured area in Figure 3, large, deep delaminations can be seen; they varied in size from less than 1 μm to 2 or 3 μm in diameter. The larger dimples had spherical particles in their center that served as the nucleation site. Particles were not observed in the smaller dimples. However, it is possible that particles less than 0.5 μm in diameter could exist in the austenitic matrix and serve as a nucleation site for dimple formation. Some of the small dimples lie on a plane at a 45-degree angle to the tensile axis; they are either closed or open-ended elongated dimples. The other small dimples appear equiaxed and are approximately perpendicular to the tensile axis.

Selected specimens were sectioned longitudinally and mechanically polished to observe the profile of the fracture surface and the area below the surface. At 4 K in the region outside of the neck, MnS stringers were cracked, but no apparent void growth was observed. In the necked region (Figure 4), the MnS stringers produced voids that formed delaminations. These delaminations are linked by microvoids on the fracture surface. There is no apparent nucleation of the smaller dimples below the fracture surface. The linking of the delaminations by the nucleation and the growth of the smaller dimples appears to be a sudden, catastrophic event.

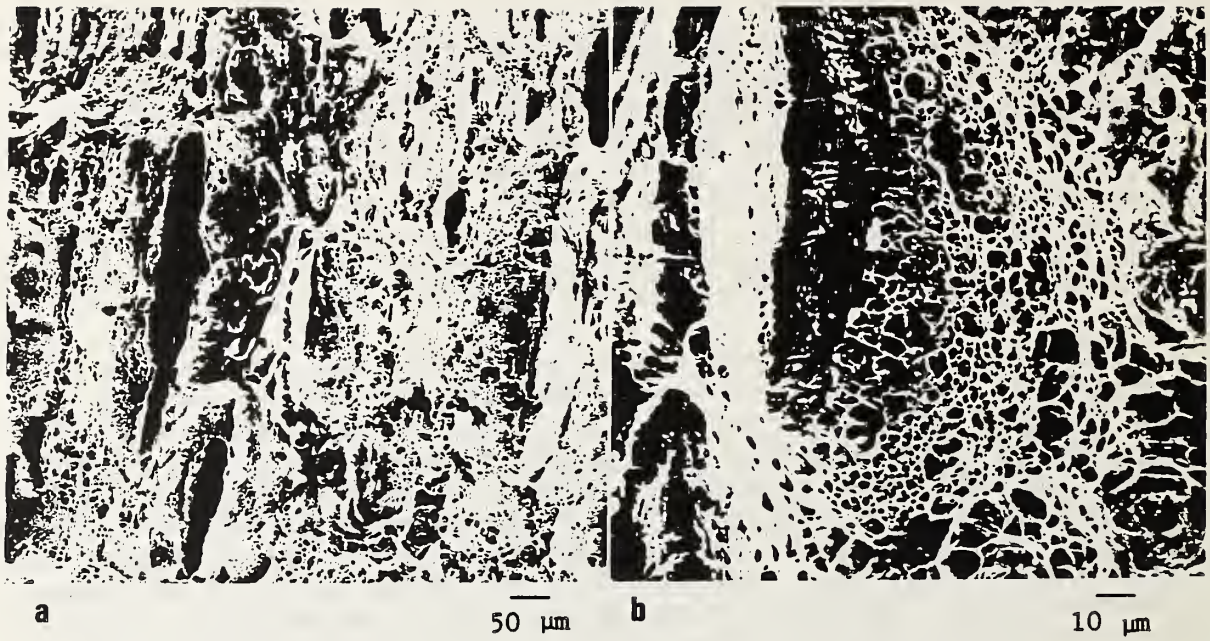

Figure 3. High-magnification views of tensile fracture surface specimen tested at 4 K.

Specimens tested at 76 K had a very similar appearance. The large MnS stringers had fractured by the time the load reached a maximum, but there was no apparent void growth. As the load dropped from the maximum point, delaminations formed around the stringers. The smaller voids that linked the delaminations on the fracture surface did not appear on the polished cross sections of the interrupted tests. Presumably, the nucleation and growth of the microvoids by tensile loading created a transverse crack in the center of the necked region. The outer ligament then failed in shear. These presumed events must have occurred between points 1 and 2 at 4 K and points 6 and 7 at 76 K in Figure 2.

DISCUSSION

The results show that there was very little change in the fracture behavior of the 316LN specimens tested in tension at 76 and 4 K. The same physical processes occurred at both temperatures. The serrated yielding did not change the process; it only made the process discontinuous and localized.

We interpreted our observations of the tensile fracture behavior in terms of two distinct steps: (1) the nucleation and limited growth of delaminations around the large MnS stringers and (2) the nucleation of a second set of smaller dimples in the ligaments between the large delamination, which occurred suddenly and led directly to the fracture without any additional applied strain.

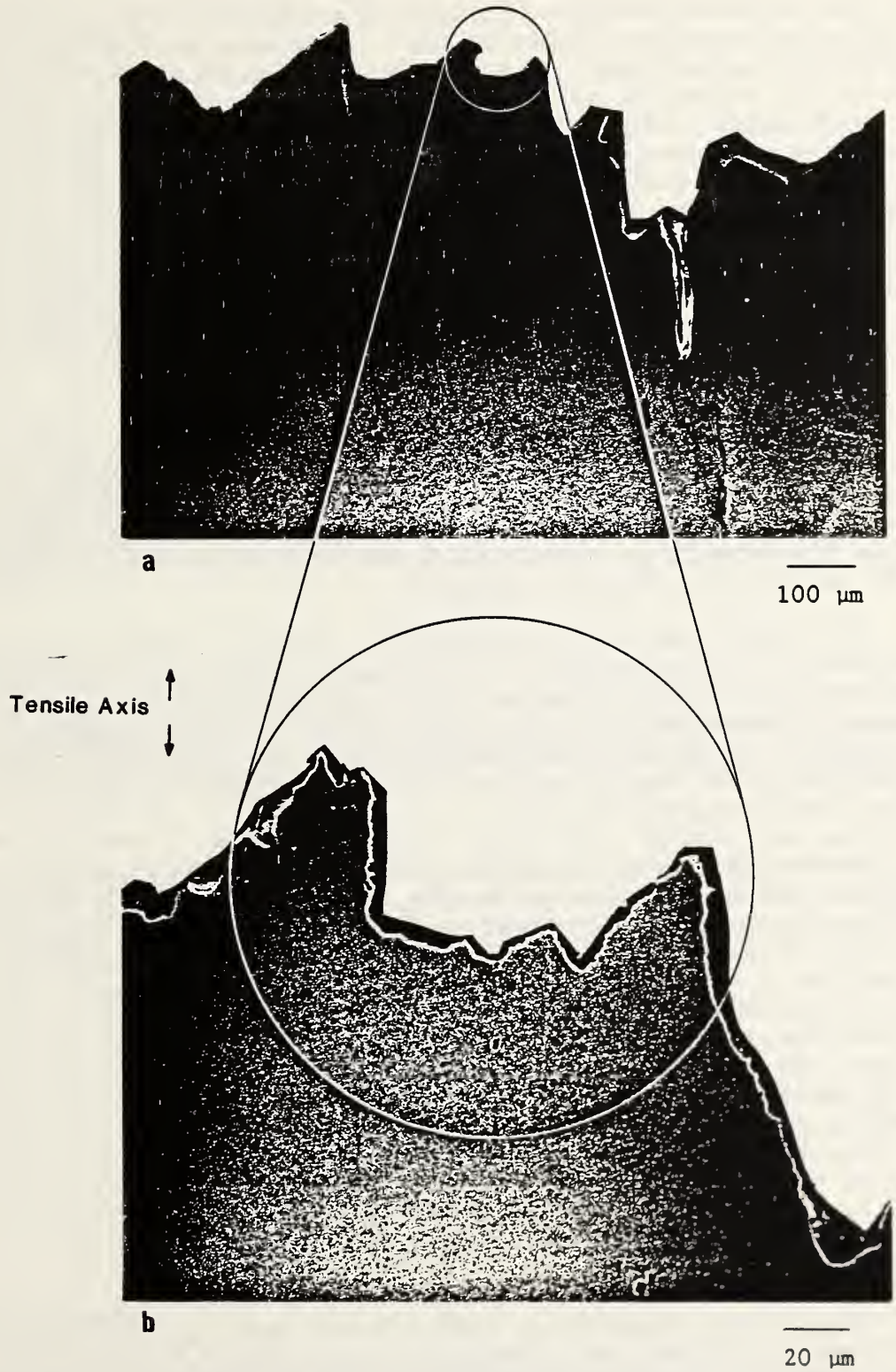

Figure 4. Magnified view of the longitudinal cross section from a fracture surface of a 4-K tensile specimen.

The large MnS stringers produced the delaminations that effectively transformed the necked region of the tensile specimen into many smaller tensile specimens (step 1). If the MnS stringers could be eliminated, the tensile properties would improve. The magnitude of the improvement we would expect in the 4-K properties can be obtained by comparing the properties of this commercial-grade steel with those of the laboratory-produced heat of 316LN (Table I). The compositions of the two heats were similar, except the S and P content of the laboratory heat was approximately one order of magnitude lower. The lower impurity content reflected its larger inclusion spacing. In addition, no MnS stringers were observed in the laboratory-produced heat. The only mechanical property that appears to have been affected by the presence of the large stringers is the reduction in area. The commercial heat with the large stringers had 20% less reduction in area than the laboratory heat.

Modern steel-making methods have made it possible to produce austenitic stainless steels with smaller and fewer MnS stringers. Our results indicate that these methods will not significantly improve the tensile ductilities of the alloy. The additional cost of producing steels free from large MnS stringers may be justified on the basis of other test results, such as toughness.

The second step had two components. The small dimples on a plane that was at a 45-degree angle to the tensile axis can be described as void-sheet coalescence or shear lip. High shear stresses near the free surface of the delamination were responsible for their formation. The rest of the smaller dimples formed in step 2 lay on a plane roughly perpendicular to the tensile axis and were produced by the normal stresses acting along the tensile axis.

The second step was controlled by the formation of the smaller dimples. The macroscopic true stress and strain present at the point of fracture varied with the test temperature, as shown in Figure 2: 2473 MPa and 0.52 at 4 K; 3051 MPa and 1.04 at 76 K. To understand the nucleation of the small dimples (step 2), we present a simple model to describe nucleation, similar to one proposed by LeRoy et al.[8] The model assumes that nucleation occurs when the interfacial stress (σ_c) between the particle and matrix reaches a critical value. The critical stress in the model is composed of a local stress (σ_ℓ), a function of the nucleation strain (ϵ_n), and the macroscopic stress (σ_m):

$$\sigma_c = \sigma_\ell + \sigma_m \tag{2}$$

and

$$\sigma_\ell = \sigma_H(\epsilon_n)^{1/2}. \tag{3}$$

The critical stress for a tightly bound particle (in two ferritic steels and a Cu alloy) was determined by Argon and Im[9] to be equal to the Young's modulus (E) of the matrix divided by 120 when the macroscopic stress is assumed to be equal to the hydrostatic component of the applied stress. The σ_H parameter is related to the stress associated with the dislocations piled up at obstacles, namely the particles in the matrix.

Since cross-slip is the mechanism likely to relieve the stress concentration at the front of a pileup, the parameters that affect cross-slip, such as temperature and stacking-fault energy, are likely to affect σ_H.

The stresses and strains at fracture (the applied stresses and strains required for nucleation of the smaller dimples) can be substituted into Equations 2 and 3 in place of the macroscopic stress and the nucleation strain. Because we are using the total applied stress for the macroscopic component in Equation 2, then the critical stress we use should be approximately 3 times greater than Argon and Im[9] reported, E/40 rather than E/120. If σ_c does not change with temperature, then the σ_H value can be calculated as a function of temperature, 3500 MPa at 4 K and 1875 MPa at 76 K.

The model predicts that σ_H will decrease as the test temperature is raised from 4 to 76 K, indicating, as expected, that the stress associated with dislocation pileups is less at 76 K than at 4 K. The nucleation model provides a simple method of relating the macroscopic stresses and strains to the microscopic process. The parameters σ_c and σ_H must be better defined and correlated with other results before they can be used reliably.

CONCLUSIONS

1. The fracture behavior of the commercial-grade 316LN alloy at cryogenic temperatures was influenced by both the large MnS stringers and the small spherical particles.

2. The presence of large stringers in this alloy affects the measured mechanical properties mainly by reducing the percent reduction in area during the tensile test. The other mechanical properties, percent elongation, yield strength, ultimate strength, and fracture toughness, appear to be unaffected by the large stringers.

3. The serrated yielding that occurs in this alloy at 4 K and not at 76 K has no discernable effect on the fracture behavior.

4. The fracture conditions, true stress and strain, increase as the test temperature increases and appear to be controlled by the nucleation of microvoids at the small, spherical particles. A simple model describes the fracture conditions to be a function of (a) the strength of the particle–matrix interface and (b) the stress associated with the dislocations that are piled up against the interface.

ACKNOWLEDGMENTS

This work was partially supported by the Department of Energy, Office of Fusion Energy. The authors thank Luz Delgado for her assistance in the mechanical testing and Lawrence Livermore Laboratory for supplying the commercial-grade alloy.

REFERENCES

1. R. P. Reed, P. T. Purtscher, and K. A. Yushchenko, in: Advances in Cryogenic Engineering – Materials, vol. 32, R. P. Reed and A. F. Clark, eds., Plenum Press, New York, 1986, p. 43.

2. K. Suemune, K. Sugino, H. Masumoto, H. Nakajima, and S. Shimamoto, in: Advances in Cryogenic Engineering – Materials, vol. 32, R. P. Reed and A. F. Clark, eds., Plenum Press, New York, 1986, p. 51.

3. S. Yamamoto, N. Yamagami, and C. Ouchi, in: Advances in Cryogenic Engineering – Materials, vol. 32, R. P. Reed and A. F. Clark, eds., Plenum Press, New York, 1986, p. 57.

4. D. T. Read and R. P. Reed, in: Advances in Cryogenic Engineering – Materials, vol. 26, A. F. Clark and R. P. Reed, eds., Plenum Press, New York, 1980, p. 91.

5. R. P. Reed, N. J. Simon, P. T. Purtscher, and R. L. Tobler, in: Materials Studies for Magnetic Fusion Energy Applications at Low Temperatures – IX, R. P. Reed, ed., National Bureau of Standards, Boulder, Colorado, 1986, p. 15.

6. K. Shibata and T. Fujita, Trans. ISIJ, vol. 26, 1986, p. 1065.

7. Z. S. Basinski, Proc. Roy. Soc., vol. A240, 1957, p. 229.

8. G. LeRoy, J. D. Embry, G. Edwards, and M. F. Ashby, Acta Metall., vol. 29, 1981, p. 1509.

9. A. S. Argon and J. Im, Metall. Trans., vol. 6A, 1975, p. 839.

EFFECT OF VOID NUCLEATION ON FRACTURE TOUGHNESS OF HIGH-STRENGTH AUSTENITIC STEELS*

P. T. Purtscher, R. P. Reed, and D. T. Read
Fracture and Deformation Division
National Bureau of Standards
Boulder, Colorado

The fracture of seven austenitic stainless steels with varying Ni and N contents were studied at 4 K. Smooth, 6-mm-diameter tensile specimens and 22-mm-thick compact specimens were used. Nitrogen content controlled the yield strength and influenced fracture toughness by its effect on yield strength. At a constant N content, increasing the Ni content increased the fracture toughness. Observations of the fracture surfaces and polished cross sections through the fracture surfaces of test specimens showed that nucleation controlled the dimpled rupture fracture process. A critical stress criterion for nucleation that depends on both the applied stress and strain was developed and applied to the fracture toughness test. This fracture criterion explained the increase in fracture toughness with increasing Ni and the decrease in fracture toughness with increasing yield strength for strengths over 600 MPa.

INTRODUCTION

The fracture toughness characterizes the initiation of the ductile fracture process ahead of a fatigue precrack. Two measures of fracture toughness, J_{Ic} and K_{Ic}, have been used for applications where high strength and high reliability are required, such as aircraft parts and pressure vessels. Nevertheless, the basic mechanisms that relate the microstructure of a material to its fracture mechanics properties are not understood. It is extremely difficult to predict J_{Ic} from the microstructure and strength of an alloy.[1]

Austenitic stainless steels are used in low-temperature structural applications where J_{Ic} is an important design consideration: liquefied gas storage tanks and supports for superconducting magnets.[2] At cryogenic temperatures, these alloys can have high yield strengths and retain a relatively high J_{Ic}.

---

*Submitted to American Society for Testing and Materials.

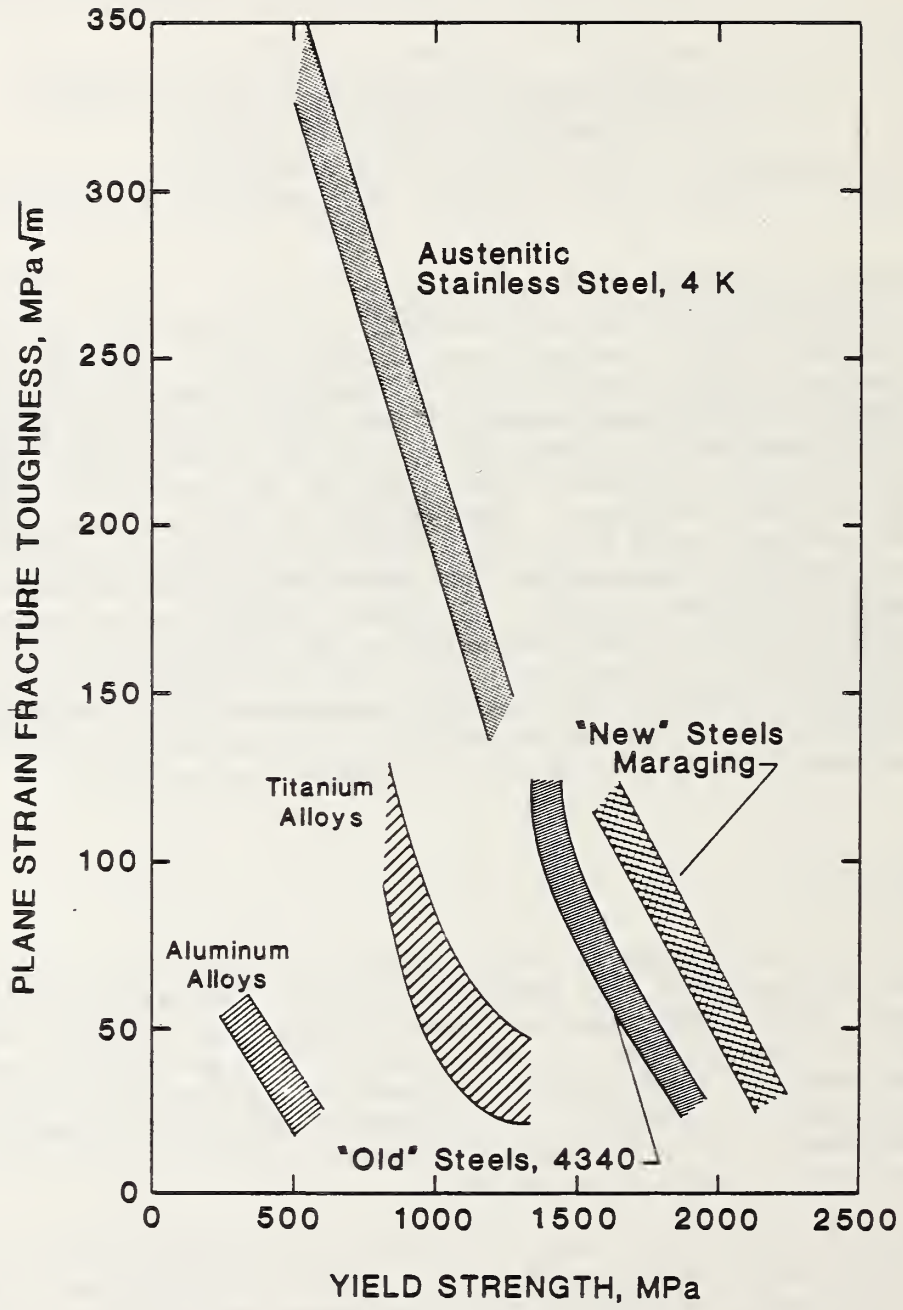

Figure 1. Fracture toughness vs. yield strength for structural alloys. Data for Al, Ti, new steels, and old steels are from Reference 7. Austenitic stainless steel data are from Reference 8.

The relationship between strength and fracture toughness of structural alloys has been studied extensively.[3-5] Wanhill[6] has summarized the results of numerous studies on the most common high-strength alloys. To Wanhill's data, we added the strength-vs.-toughness data for a controlled series of austenitic stainless steels whose strength was raised systematically by increasing the concentration of interstitial alloying elements[7] (see Figure 1). For these austenitic steels, the two properties are related empirically by the following equation:

$$K_{Ic}(J) = 500 - 0.3\ \sigma_y \qquad (1)$$

where $K_{Ic}(J)$ is in MPa·m$^{\frac{1}{2}}$; σ_y, the yield stress, is in MPa. This equation predicts the fracture toughness within 20 MPa·m$^{\frac{1}{2}}$. All the curves in Figure 1 have similar negative slopes, reflecting the significant influence of strength on the fracture toughness of high-strength, structural alloys.

Steels fracture in a ductile manner by a dimpled rupture process in which voids nucleate at discontinuities in the microstructure, typically nonmetallic inclusions, and grow under the influence of the local stress state. In the uniaxial tensile test, the main direction of void growth is along the tensile axis until a local neck is formed. The neck introduces triaxial stresses that cause any existing voids to expand uniformly in all directions. In the fracture toughness test, the region ahead of a sharp crack resembles the locally necked area of a tensile specimen.

Van Stone et al.[1] recently reviewed various models that have been proposed to describe fracture toughness in terms of the dimpled rupture fracture process. It is generally assumed that voids nucleate in the plastic zone ahead of the crack tip at relatively low plastic strains and that most of the energy measured in the J-integral test procedure is related to void growth.[8-10] Van Stone et al. argued that any successful modeling of ductile fracture ahead of a sharp crack must explicitly treat all three stages of the process: void initiation, growth, and coalescence.

In this paper, we examine the fracture process in a series of seven austenitic stainless steels broken at 4 K. A careful fractographic and metallographic study was conducted of the broken specimens to observe the dimpled rupture process. From these observations, a model for fracture toughness was developed that relates the void nucleation process to the mechanical properties that were presented in another report.[11]

MATERIALS

The seven laboratory heats of steel were supplied in the form of 25-mm-thick plates in the hot-rolled condition. The plates were annealed at 1170°C for 2 h and then water quenched. The treatment produced coarse-grained, fully annealed, austenitic structures. The composition, grain size, λ, and inclusion spacing of the seven alloys are presented in Table I. They differ mainly in their Ni and N contents.

Table I. Composition, Grain Size, and Inclusion Spacing of the Alloys

Alloy Number	Content (wt.%)								Grain size	λ
	Cr	Ni	Mn	C	N	S	P	Si	(μm)	(μm)
1	18.8	5.6	4.1	0.020	0.256	0.005	0.014	0.25	122	47
2	18.4	8.9	4.2	0.018	0.281	0.005	0.014	0.28	165	63
3	20.5	12.8	5.5	0.024	2.265	0.004	0.015	0.34	200	66
4	20.8	14.9	5.2	0.028	0.277	0.004	0.015	0.41	160	63
5	18.7	8.7	3.7	0.014	0.093	0.005	0.013	0.23	220	57
6	19.7	11.5	3.9	0.012	0.141	0.005	0.013	0.27	250	57
7	20.8	14.7	4.4	0.016	0.197	0.004	0.014	0.33	207	70

The inclusion contents of these alloys were nearly identical. Inclusion spacing was calculated by counting all of the inclusions larger than 0.5 μm in diameter in a given area, normalizing that number to 1 mm^2, and taking the inverse square root to obtain an approximate value of spacing. Energy-dispersive x-ray analysis determined that the inclusions found in the polished cross sections of these alloys were predominantly MnSi and MnS types.

TEST PROCEDURES

Smooth, 6-mm-diameter, 38-mm-gage tensile specimens and 22-mm-thick compact specimens were machined from the annealed plates. Standard ASTM E 8 and E 813 procedures were followed for obtaining the tensile and fracture toughness properties of these alloys. Specific descriptions of the techniques are available elsewhere.[7]

Table II. Summary of Mechanical Properties at 4 K

Alloy	Ni content (wt.%)	N content (wt.%)	σ_y* (MPa)	σ_u* (MPa)	σ_f* (MPa)	ϵ_f* $\ln \frac{A_o}{A_f}$	J_{Ic}† (kJ/m^2)	$K_{Ic}(J)$ (MPa·m$^{1/2}$)
1	5.6	0.26	1050	1418	1710	0.21	27	75
2	8.9	0.28	950	1650	3160	0.55	99	143
3	12.8	0.27	1000	1580	3130	0.78	201	204
4	14.9	0.28	1165	1630	2990	0.66	276	239
5	8.7	0.09	460	1417	2550	0.55	360	273
6	11.5	0.14	720	1370	2770	0.70	288	244
7	14.7	0.20	870	1425	2790	0.67	312	254

* Average value from 2 or 3 tests; σ_y + σ_u are engineering stress values, σ_f is the true stress at fracture, and ϵ_f is the true strain at fracture.

† Measured value from one test.

RESULTS

The results of tensile and fracture toughness tests at 4 K are listed in Table II. The variation of the Ni and N contents produced a wide range of mechanical properties. Nitrogen, dissolved into the fcc lattice at the interstitial sites, controls the yield strength of these austenitic alloys at cryogenic temperatures. Yield strength affects the fracture toughness, similar to the trend shown in Figure 1, but at a constant yield strength, Ni content determines the fracture toughness of these alloys (see Figure 2). Increasing Ni and N concentrations suppress the strain-induced martensitic transformation, but the transformation does not directly affect the σ_y and J_{Ic} mechanical properties.[11]

Scanning electron microscopy was performed on all the test specimens to determine the fracture morphology and the microstructural features that participate in the fracture process. The observations, summarized in Table III and illustrated in the next three figures, were always made in the fracture-surface region with the highest triaxial stress. Most specimens fractured in a ductile manner, which is characterized on a macroscopic scale by large shear lips on the tensile specimen and elastic-plastic behavior in the fracture toughness test. On a microscopic scale, the predominant features were large dimples that originated at the MnSi and MnS inclusions (see Figure 3). These inclusions were spherical in shape, between 1 and 2 μm in diameter, and identical to those found on the polished cross section (see Table I).

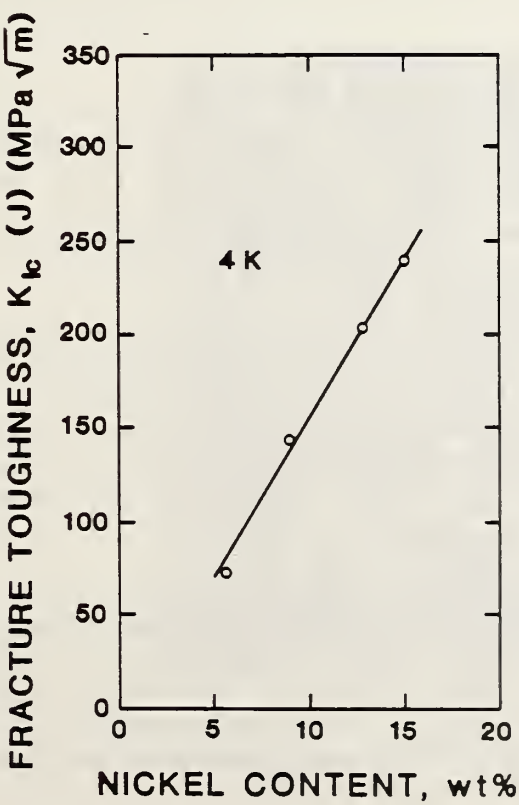

Figure 2. Fracture toughness vs. Ni content for alloys 1 through 4 with constant N content and similar yield strengths.

Table III. Summary of Fracture Behavior

Alloy	Tensile	Fracture Toughness
1: 5.6Ni–0.26N	2-μm dimples; small shear lips	facets; linear elastic
2: 8.9Ni–0.28N	20–30 μm dimples; large shear lips	facets; elastic–plastic
3: 12.8Ni–0.27N	20–30 μm dimples; large shear lips	30-μm dimples; elastic–plastic
4: 14.9Ni–0.28N	20–30 μm dimples; large shear lips	20–40 μm dimples; elastic–plastic
5: 8.7Ni–0.09N	duplex dimples, 2- and 10-μm; large shear lips	duplex dimples, 2- and 10-μm; elastic–plastic
6: 11.5Ni–0.14N	20-μm dimples; large shear lips	20–30 μm dimples; elastic–plastic
7: 14.7Ni–0.20N	20 μm dimples; large shear lips	20–30 μm dimples; elastic–plastic

Specimens from alloys 1 and 5 exhibited a much smaller dimple size (1 to 2 μm in diameter) on the fracture surface (see Figure 4). No inclusions are visible in the smaller dimples; however, the existence of inclusions smaller that 0.5 μm in diameter, the smallest counted on the polished cross sections, cannot be discounted.[12]

Fracture toughness specimens of alloys 1 and 2 had a distinctly different fracture morphology than the other specimens in this test series. Their fracture surfaces were faceted; the facet size varied from 2-μm steps on the surface to a relatively smooth surface extending across a complete austenite grain. This type of faceted fracture, shown in Figure 5, has been described by Tobler and Meyn[13] as a process of slip-band cracking along {111} planes.

Selected tensile specimens were sectioned along the tensile axis after testing to observe the microstructural processes that led to the formation of the large dimples (Figure 3) on the fracture surface. Figure 6 shows a typical example. The rounded features of the dimples on the fracture surface are visible at the edge of the cross section. The area directly below the fracture surface appears undamaged despite the

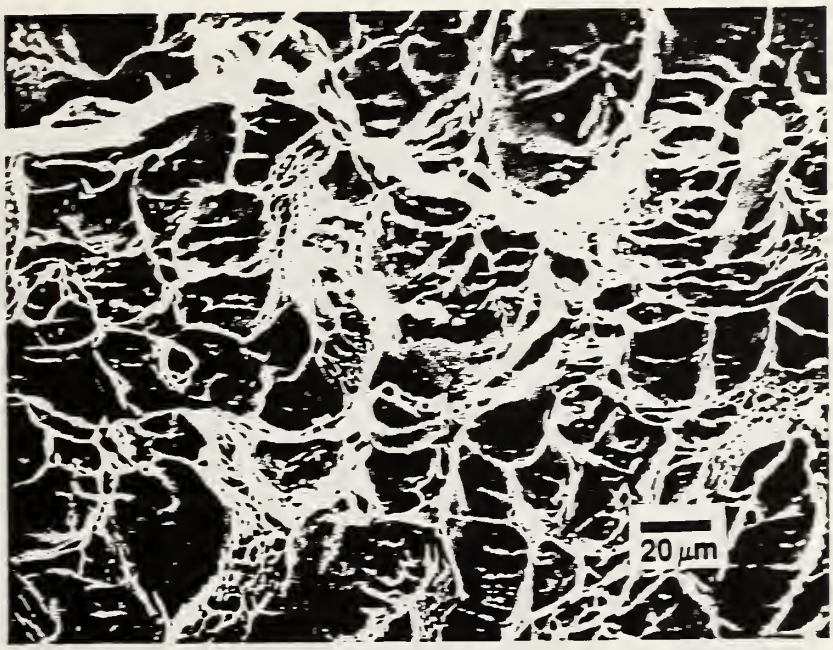

Figure 3. Fractograph (SEM) of the tensile specimen for alloy 2 showing 20- to 30-μm dimples in the center region of the fracture surface.

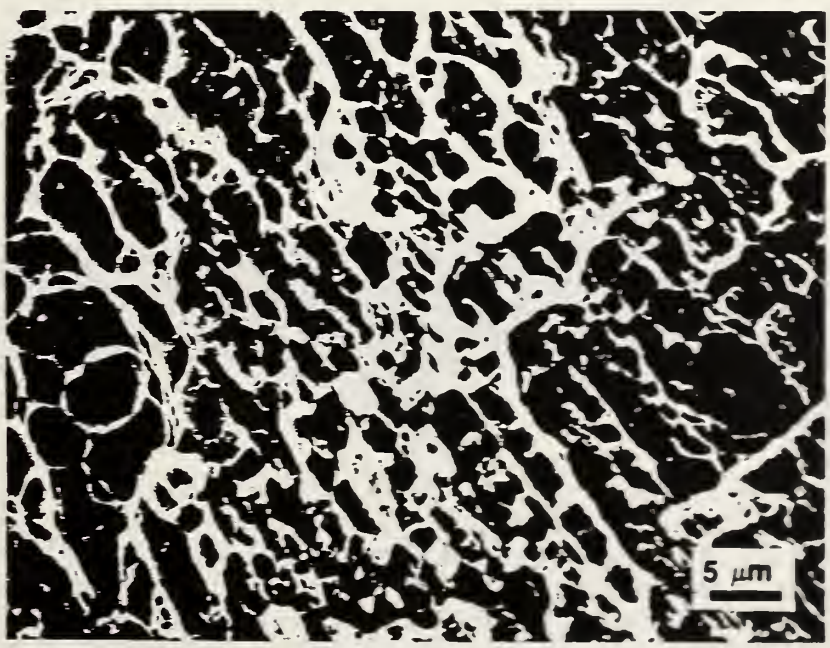

Figure 4. Fractograph (SEM) of the tensile specimen for alloy 1 showing 2-μm dimples on the fracture surface.

Figure 5. Fractograph (SEM) of the fracture toughness specimen for alloy 1 showing facets on the fracture surface.

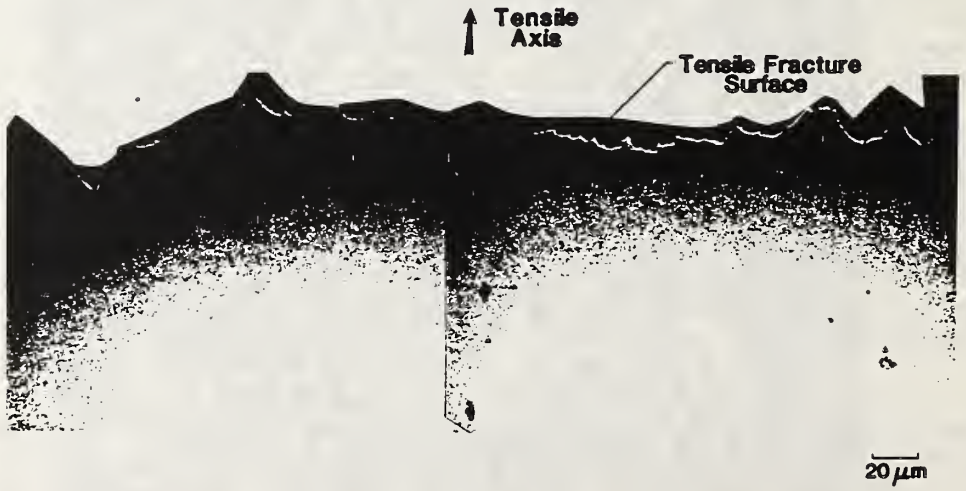

Figure 6. Micrograph (SEM) of the polished cross section of a tensile specimen of alloy 3 showing void initiation at inclusions with limited void growth.

high local stresses and strains present in the area. There is no gradient of voids below the fracture surface. Void area fraction vs. true strain for one representative tensile specimen is shown in Figure 7. An arbitrary function has been drawn through the data points to emphasize the limited amount of void growth present below the tensile fracture surface. A value of nucleation strain can be defined as the strain at zero area fraction of voids. In this example, the nucleation strain is about 0.75 of the true strain to fracture of the specimen, but approximately equal to the average true strain to fracture reported in Table II for the alloy.

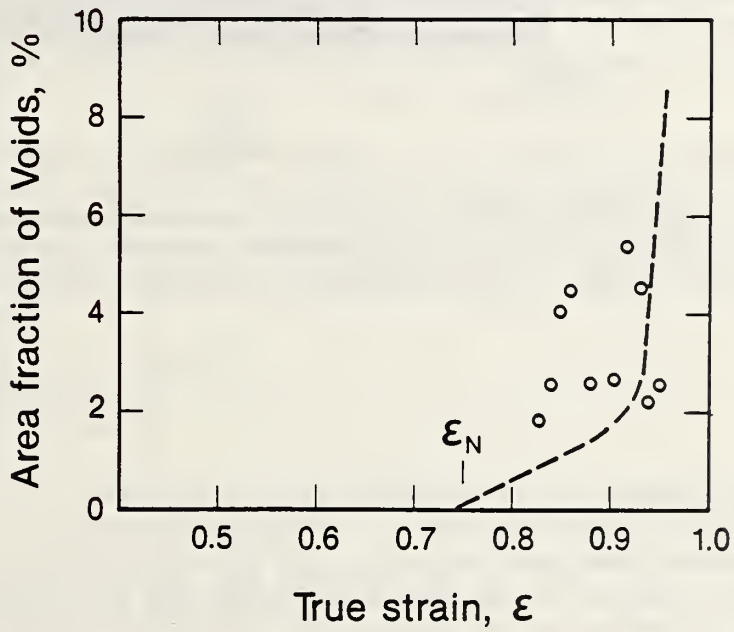

Figure 7. The area fraction of voids in the polished cross section of a tensile specimen from alloy 3 vs. the applied true strain.

A cross section through the crack tip of a tested, but unbroken compact tensile specimen from the highest yield strength alloy is shown in Figure 8. The applied J at the crack tip was approximately equal to J_{Ic} (zero physical crack growth). The crack tip was not blunted significantly, and damage was accumulating in the plastic zone before actual crack growth was detected. The damage was focused straight ahead, along the path of subsequent macroscopic crack growth. This suggests that a stress-controlled process is important.[14]

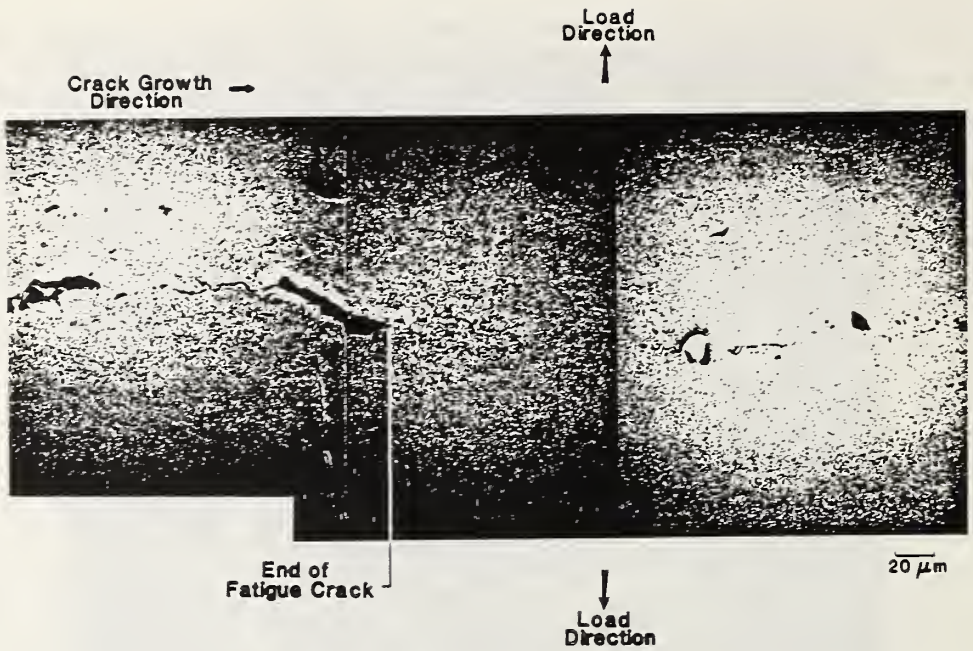

Figure 8. Micrograph (SEM) shows a cross section through the crack tip of a tested, but unbroken, compact tensile specimen of alloy 4. The applied J is approximately equal to J_{Ic}.

DISCUSSION

Development of Model

The fracture process in these steels can be interpreted in terms of two separate stages: 1) a nucleation stage and 2) a growth and coalescence stage. In the uniaxial tensile test, the void nucleation stage occurs at strains very close to the fracture strain (Figures 6 and 7). Growth and coalescence occur very rapidly and require nearly zero additional strain. The micrograph of the crack tip (Figure 8) shows a similar trend for limited void initiation at applied energy levels less than J_{Ic}.

These observations indicate that the conditions for nucleation are difficult to reach and require a large plastic strain, but once nucleation occurs, the conditions for growth and coalescence have already been met so fracture can occur with little or no additional applied strain. Broek[15] describes a very similar type of behavior in high-strength aluminum alloys, in which the nucleation stage dominates the fracture process.

From the observations, we assume that the nucleation of microvoids at the nonmetallic inclusions is the critical event that controls the fracture of austenitic stainless steels at 4 K. LeRoy et al.[16] modeled

the nucleation condition in a tensile test specimen by assuming that nucleation of a void at an inclusion occurs when the stress across the interface exceeds a critical value (σ_c) that is related to both the local stress (σ_L, a function of the strain), and the macroscopic stress (σ_m):

$$\sigma_c = \sigma_L + \sigma_m \tag{2}$$

and

$$\sigma_L = \sigma_H(E_N)^{\frac{1}{2}} , \tag{3}$$

where ϵ_N is the nucleation strain and σ_H is a parameter that relates the stress produced by dislocations piled up at an inclusion to the average strain. We modified the equation of LeRoy et al. to use the full value of the applied stress rather than the hydrostatic component of the applied stress for the macroscopic stress. Work of Cox and Low[17] on high-strength steels showed that void nucleation was dependent on the applied stress rather than the triaxial stress.

In the fracture toughness test, the stresses and strains ahead of a stationary crack subjected to tensile (Mode I) opening can be predicted by continuum mechanics. For elastic-plastic conditions, a solution for the local strain (ϵ) at a distance ahead of a blunt crack has been calculated by Hutchinson,[18] and Rice and Rosengren[19] (HRR) in terms of the J-integral (J):

$$\epsilon = \alpha\epsilon_o\left(\frac{J}{\alpha\epsilon_o\sigma_o I_n r}\right)^{n/n+1} \tilde{\epsilon} , \tag{4}$$

where α and n are constants of the Ramberg-Osgood fit to the material's true-stress vs. true-strain curve, ϵ_o and σ_o are the yield strain and stress in the Ramberg-Osgood fit, and r is the distance from the crack tip. The term I_n, a function of n, is about 4.5, and $\tilde{\epsilon}$ contains the angular dependence of the strain.

The constant n is of the order of 10, so for simplicity, we assume $n/(n+1) = 1$. For crack advance all along the crack front, we assume that the relevant distance, r, is the spacing of large inclusions, L. With $J = K^2/E$, where K is the stress-intensity factor and E is Young's modulus, then the HRR solution for strain ahead of a crack at the important inclusions is:

$$\epsilon = \frac{K^2}{4.5\sigma_o EL} . \tag{5}$$

Nucleation was observed only very near the crack tip of the fracture toughness test specimens. Thus, nucleation strain is a major part of the plastic strain needed to initiate tearing. Therefore, we equate the nucleation strain to the strain that is one inclusion spacing ahead of a blunt notch in the fracture toughness test and obtain an equation for the stress-intensity factor associated with the nucleation process (K_{nuc}):

$$K_{nuc} = \frac{(\sigma_c - 3.5\sigma_y)}{\sigma_H} (4.5\sigma_y EL)^{\frac{1}{2}} \quad (6)$$

We have also assumed that the $\sigma_m = 3.5\sigma_y$, because of crack-tip constraint.

The value of σ_c in this model is the cohesive energy of the interface between the defect and the matrix. We expect the value of σ_c to be relatively independent of the chemical composition of the matrix, but it can depend on the size, shape, and type of inclusions. Exact values of σ_c for these alloys are not known. LeRoy et al.[16] and Argon and Im[20] obtained σ_c values from 1200 to 1800 MPa for cementite particles in a ferritic steel matrix. In general, it appears that the σ_c value for a tightly bond particle in a ductile matrix is about E/120.[20] In the terms of our model for fracture toughness, this value must be multiplied by 3 because we used the applied stress rather than the hydrostatic component of the stress in Equation 2. The elastic properties of austenitic stainless steels at cryogenic temperatures vary slightly, depending on the exact chemical composition, but are essentially the same as ferritic steels at room temperatures.[21] Therefore, we will assume that σ_c is E/40 or 5000 MPa for all the alloys.

The parameter σ_H in Equation 6 is also an unknown parameter that is a measure of the local stress exerted by the dislocation structures. An idealized model would be of a slip band in the austenitic matrix where dislocations have piled up against a barrier (a nonmetallic inclusion). In this case, the σ_H constant represents the stress concentration ahead of the pile-up and is a function of the stacking-fault energy. The dislocation structures in the vicinity of the inclusions in these steels are difficult to characterize completely, so σ_H cannot be calculated from first principles. We assume that σ_H is a relatively strong function of the Ni content and not the N content. We do expect dislocation mobility and the ability to cross slip to vary with stress state,[22] so the value of σ_H determined from the tensile test results cannot be used to predict the fracture toughness.

Evaluation of Model

To test this model for nucleation-controlled fracture toughness, we need to determine how σ_H varies with the Ni content. Therefore, considering only the highest strength alloys (1 through 4 in which Ni content varies and N content is constant), we set $K_{nuc} = K_{Ic}(J)$ and calculate the change in σ_H from Equation 6 for the range of Ni values at a constant yield strength using L (average value of 0.060 mm), σ_y (average value of 1040 MPa), σ_c (estimated value of 5000 MPa), and E (estimated value of 205 GPa). The calculated values are plotted vs. Ni content in Figure 9.

Now we can evaluate the model and our assumptions. First, we consider alloys 5, 6, and 7 that have a range of both N and Ni contents. We can estimate σ_H from the Ni content in Figure 9 and calculate a K_{nuc} using the measured yield strengths and the constant values of L, σ_c, and E.

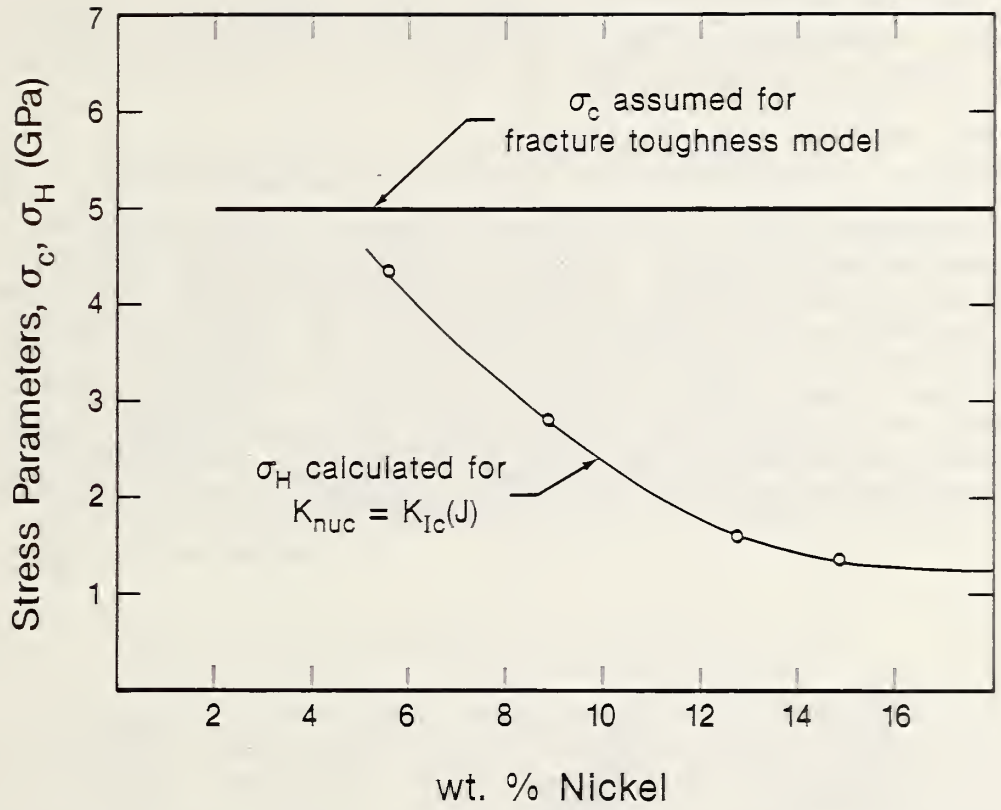

Figure 9. The stress parameters σ_c and σ_H in the nucleation-controlled model vs. Ni content.

Table IV. Summary of Data Used in Nucleation Model for Fracture Toughness

Alloy	σ_H (MPa)	σ_c (MPa)	σ_y (MPa)	K_{nuc} (MPa·m$^{\frac{1}{2}}$)	$K_{Ic}(J)$ (MPa·m$^{\frac{1}{2}}$)	$K_{nuc}/K_{Ic}(J)$
1	4350	5000	1050	73	75	0.98
2	2280	5000	950	169	143	1.18
3	1600	5000	1000	221	204	1.08
4	1365	5000	1165	173	239	0.72
5	2900	5000	460	186	273	0.6
6	1900	5000	722	260	244	1.07
7	1375	5000	865	318	254	1.25

We can take the same approach to examine the prediction of K_{nuc} for alloys 1 through 4, using the measured yield strengths rather than the average. The variables used in the calculations and the results for all seven alloys are found in Table IV.

The ratio of $K_{nuc}/K_{Ic}(J)$ for alloys 1, 3, and 6 is very close to 1, as expected, if nucleation does control the measured fracture toughness. For alloy 5 with the lowest yield strength, the model underpredicts the measured value by 30%. We interpret this to be a yield strength effect. For lower strength alloys, we expect nucleation strains to be less than the fracture strains so that additional plastic strain is required to grow the voids to the point of coalescence. For alloys 2, 4, and 7, the ratio is not very close to 1, indicating that the model is sensitive to the values of the unknown parameters, σ_H and σ_c. If there is a variation in the σ_c value with Ni or N or Ni-plus-N content or if the true variation of σ_H is different from that shown in Figure 9, then the model cannot accurately predict the fracture toughness.

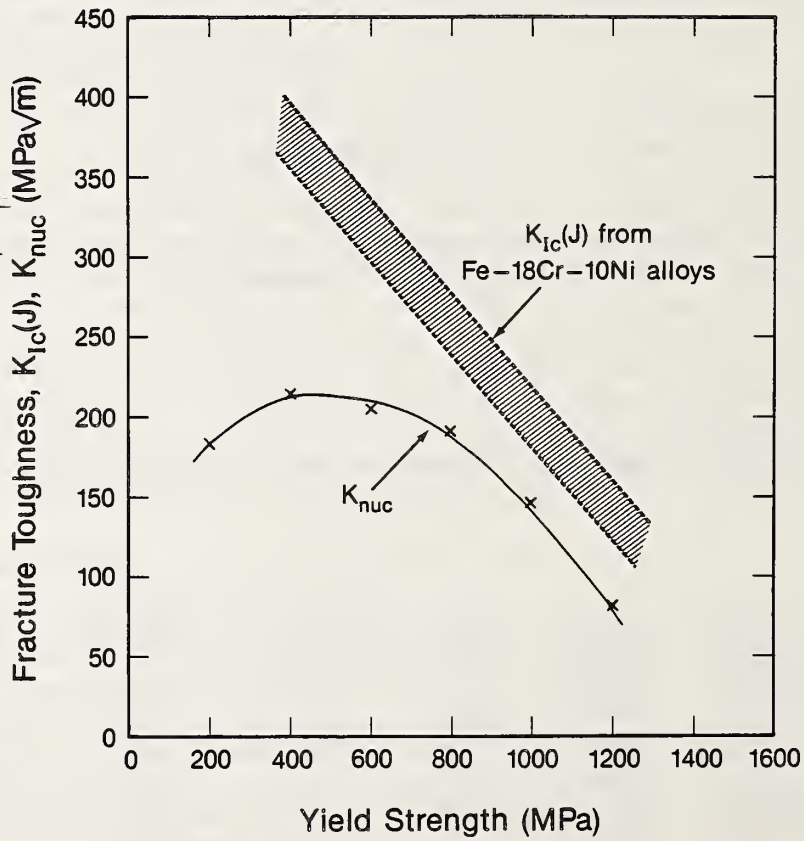

Figure 10. Fracture toughness, model prediction and measured, for Fe–18Cr–10Ni alloys vs. yield strength.[8]

A second, independent test of the model is found in Equation 1 for the Fe-18Cr-10Ni alloys with various N contents. From Figure 9, we estimate σ_H to be 2400 MPa and assume the same values for σ_c and E. The average inclusion spacing for this alloy series was 0.055 mm. The predicted values of K_{nuc} and the calculated $K_{Ic}(J)$ from Equation 1 are plotted as a function of the yield strength in Figure 10.

The model predicts a maximum toughness at a yield strength of 400 MPa and a decrease in toughness for higher yield strengths. The slope of the predicted curve for yield strengths greater than 600 MPa matches that for the experimental data. The different intercept for the predicted values from that of the model and measured values from Equation 1 could be due to a systematic error. In general, the model works reasonably well for the higher strength alloys in which we expected nucleation to dominate the fracture process. For yield strengths below 600 MPa, the model underpredicts the fracture toughness, reflecting the lesser role of nucleation and a significant contribution of void growth and coalescence to the measured fracture toughness.

SUMMARY

In high-strength austenitic stainless steels fractured at 4 K, large plastic strains, nearly equal to the true fracture strain, are needed to nucleate voids in the tensile test. In the fracture toughness test, the void nucleation is limited to the region directly ahead of the advancing crack tip. On the basis on these observations, we assumed that tearing in the fracture toughness test is a stress-controlled process and begins when the stress at an inclusion-matrix interface ahead of the crack reaches the critical value required for nucleation. From this criterion for ductile fracture, we have developed a model that relates the stress-intensity factor for nucleation to the inclusion spacing, the critical stress for void nucleation, the material's strength, and the local stress at inclusions produced by dislocation pile-ups. The model can predict reasonably well the relative effect of changes in the dislocation structure and yield strength on the fracture toughness.

The model represents an attempt to understand fracture toughness on the basis of the micromechanisms that control void nucleation. We have assumed that the fracture toughness represents an average nucleation strain. The model can be used to explain the results for high-strength austenitic steels at low temperatures where the inclusions are widely spaced in, and tightly bound to, the matrix. The model has shortcomings: it considers only the nucleation contribution to the fracture process; it is sensitive to the stress terms, so they must be known; and it ignores the effect of inclusion size, shape, and local spacing. The model has many advantages: it relates the effect of dislocations and interfacial stresses directly to the fracture toughness, and it does not require a detailed analysis of the fracture surface features, which we think are more representative of the tearing modulus than the fracture toughness of

high-strength materials. The development of a more comprehensive model is certainly possible through more extensive testing and thorough material evaluation.

ACKNOWLEDGMENT

This work was partially supported by the U.S. Department of Energy, Office of Fusion Energy. The seven laboratory heats of steel were supplied by the E. O. Paton Institute of Electrowelding, Kiev, USSR.

REFERENCES

1. R.H. Van Stone, T.B. Cox, J.R. Low, Jr., and J.A. Psioda: International Metals Review, vol. 30, 1985, p. 157.

2. H.I. McHenry and R.P. Reed: Nuclear Engineering Design, vol. 58, 1980, p. 219.

3. J.M. Krafft: Applied Materials Research, vol. 3, 1964, p. 88.

4. G.T. Hahn and A.R. Rosenfield: Metallurgical Transactions, vol. 6A, 1975, p. 653.

5. J.P. Hirth and F.H. Froes: Metallurgical Transactions, vol. 8A, 1977, p. 1165.

6. R.J.H. Wanhill: Engineering Fracture Mechanics, vol. 10, 1978, p. 337.

7. R.L. Tobler, D.T. Read, and R.P. Reed: in Fracture Mechanics, Thirteenth Conference, ASTM STP 743, R. Roberts, ed., American Society for Testing and Materials, Philadelphia, 1981, p. 350.

8. J.R. Rice and M.A. Johnson: in Inelastic Behavior of Solids, M.F. Kanninen, W.G. Adler, A.R. Rosenfield, and R.I. Jaffee, eds., McGraw-Hill, New York, 1970, p. 641.

9. R.O. Ritchie and A.W. Thompson: Metallurgical Transactions, vol 16A, 1985, p. 223.

10. W.M. Garrison, Jr.: Metallurgical Transactions, vol, 17A, 1986, p. 669.

11. R.P. Reed, P.T. Purtscher, and K.A. Yushchenko: in Advances in Cryogenic Engineering—Materials, vol. 30, R.P. Reed and A.F. Clark, eds., Plenum Press, New York, 1986, p. 43.

12. A.W. Thompson and P.F. Weihrauch: Scripta Metallurgica, vol. 10, 1976, p. 205.

13. R.L. Tobler and D. Meyn: in Materials Studies for Magnetic Fusion Energy Applications at Low Temperatures—XI, R.P. Reed, ed., National Bureau of Standards, Boulder, Colorado, 1988, p. 89.

14. R.M. McMeeking: Journal of Mechanics and Physics of Solids, vol. 25, 1977, p. 357.

15. D. Broek: Engineering Fracture Mechanics, vol. 5, 1973, p. 55.

16. G. LeRoy, J.D. Embry, G. Edwards, and M.F. Ashby: Acta Metallurgica, vol. 29, 1981, p. 1509.

17. T.B. Cox and J.R. Low, Jr.: Metallurgical Transactions, vol. 5A, 1974, p. 145.

18. J.W. Hutchinson: Journal of Mechanics and Physics of Solids, vol. 16, 1968, p. 13.

19. J.R. Rice and G.K. Rosengren: Journal of Mechanics and Physics of Solids, vol. 16, 1968, p. 1.

20. A.S. Argon and J. Im: Metallurgical Transactions, vol. 6A, 1975, p. 839.

21. H.M. Ledbetter: in Austenitic Steels at Low Temperature, R.P. Reed and T. Horiuchi, eds., Plenum Press, New York, 1983, p. 83.

22. S. Floreen, H.W. Hayden, and T.M. Devine: Metallurgical Transactions, vol. 2A, 1971, p. 1403.

LOW-TEMPERATURE PHASE AND MAGNETIC INTERACTIONS IN FACE-CENTERED-CUBIC Fe–Cr–Ni ALLOYS*

C. Almasan, T. Datta, R. D. Edge, and E. R. Jones
University of South Carolina
Columbia, South Carolina

J. W. Cable
Oak Ridge National Laboratory
Oak Ridge, Tennessee

H. Ledbetter
Institute for Materials Science and Engineering
National Bureau of Standards
Boulder, Colorado

The magnetic properties of a set of nine isostructural face-centered-cubic Fe–Cr–Ni alloys were studied by SQUID magnetometry, neutron diffraction, and ultrasonic techniques from 5 to 300 K. Type-1 antiferromagnetic ordering was observed below the Néel temperature (T_N). The dc susceptibility [$\chi(T)$] did not exhibit a simple Curie–Weiss dependence. Above T_N, $\chi(T)$ contained a temperature-independent component (χ_0): $\chi(T) = \chi_0 + C/(T + \Theta)$. The lattice parameter (a) systematically influenced T_N, which decreased from 47.9 ± 0.05 to 35.0 ± 0.5 K as a increased only 0.25%. The average magnetic moment, $\simeq 0.5\ \mu_B$, obtained from neutron scattering was lower than the $\simeq 1.0\ \mu_B$ value obtained from the SQUID measurements. Mean-field estimates of the antiferromagnetic first-neighbor exchange interaction (J_1) and the ferromagnetic second-neighbor interaction (J_2) indicated that $|J_2/J_1| \simeq 1.5$. We take this as evidence for RKKY interaction and argue self-consistently that only the external d electrons are responsible for the localized average moment. This may mean that s–d hybridization of the external electrons is weak in these alloys.

---

*Draft; intended for *Physical Review*.

INTRODUCTION

The nature of the ground state of γ-Fe, Fe in the face-centered-cubic (f.c.c.) structure, has been controversial ever since Weiss and Foex argued that γ-Fe has an antiferromagnetic ground state,[1,2] unlike the familiar body-centered-cubic α-Fe. Two other issues[3,4] related to itinerant-electron magnetism are also important in γ-Fe: (i) the nature of the magnetic interaction and (ii) the localization of the magnetic moments.

Although the f.c.c. allotrope is unstable at room temperature, it may be obtained by alloying with Ni and then stabilizing the resulting structure by adding Cr, Mn, V, or Cu. The behavior of Fe–Cr–Ni alloys is typical of iron in the f.c.c. structure.[1] These alloys are the basis for commercial "nonmagnetic" austenitic stainless steels. Many of their useful properties relate intimately to their magnetic behavior[5,6] because the magnetic properties reflect the electronic structure of the alloys. This system is also a solid-state experimental material with a rich array of physical properties (including composition and lattice spacing) that can be systematically varied. Clustering and the amount of short-range order may also be influenced by careful thermal–mechanical treatment.

This study concerns the low-temperature (from 5 to 300 K) properties of a set of austenitic Fe–Cr–Ni alloys with Ni concentration less than 10 at.%. Emphasis is given to ultrasonic measurements, the effects of lattice dilation on the phase transition, the exchange interaction, and the average magnetic moment as determined by SQUID magnetometry, and neutron scattering.

EXPERIMENTAL DETAILS

Materials

All nine sets of specimens studied were type-304 polycrystalline austenitic stainless steel. As mentioned above, these isostructural alloys represent a close realization of γ-Fe. The lattice spacing (a) was systematically dilated by introducing of interstitial C and N atoms. In alloys 1 through 9, the C+N concentration ranged from 0.5 to 1.5 at.%. The crystal structures and values of a were determined at room temperature for all nine compositions by using a modified commercial x-ray spectrometer. For four samples, the values of a at different temperatures were determined from the nuclear Bragg peaks observed in the elastic-neutron-diffraction powder pattern. Both microprobe (EDAX) and chemical analysis were performed to determine the chemical composition of the specimens.

Ultrasonic Measurements

Acoustic velocities were measured as functions of polarization and temperature by a technique detailed elsewhere.[7,8] Briefly, a pulse-echo method was used to obtain the velocity, $v = 2\ell/\tau$, where τ denotes the

round-trip time for an ultrasonic pulse between two flat, parallel faces of the specimen separated by a distance ℓ. Both longitudinal and transverse waves were studied.

Magnetic Measurements

Specimens were cut into rectangular prisms with a typical size of 1.5 mm × 3 mm × 7 mm. They were cleaned in a solution containing equal parts of HCl and HNO_3 and a small amount of H_2SO_4. Ultrasonic agitation accelerated the cleaning. Finally, they were washed in distilled water, rinsed in alcohol, and dried in air. The specimens were initially cooled to 5 K in zero applied magnetic field (B).

With a computer-controlled SQUID variable-temperature susceptometer,[9] the longitudinal dc susceptibility [$\chi(T)$] was measured from 5 to 200 K in magnetic fields of 1, 5, 20, and 50 mT. Thermohysteresis was not observed, although it has been reported in related alloys.[10-12]

Neutron-Diffraction Measurements

Specimens for the elastic-neutron-scattering experiments were flat, 2-cm × 2-cm × 0.5-cm polycrystalline plates. A closed-cycle system controlled the specimen temperature; measurements were made from 10 to about 300 K. A thermal neutron beam from the High Flux Isotope Reactor with a wavelength of 0.2350 nm (14.816 meV) was used.

Experiments were performed on the HB1A triple-axis neutron spectrometer adjusted for elastic scattering. A pyrolytic graphite filter removed the $\lambda/2$ components. We obtained low-resolution measurements of angular powder patterns ($5° \leq 2\theta \leq 80°$) and high-resolution angular scans over the anticipated regions of the magnetic and nuclear Bragg peaks as a function of temperature.

At all temperatures studied, large nuclear peaks arose from the (111) and (200) lattice reflections. The widths of these nuclear lines were limited by the spectrometer resolution, which indicated a well-defined long-range crystalline order. A (110) peak was also observed. The neutron counts for the (110) peak were composed of a temperature-independent nuclear component and a temperature-dependent component caused by magnetic scattering. The small critical-scattering component was observed only above the T_N appropriate for each specimen. Below T_N, the magnetic scattering increased with decreasing temperature. Because $\lambda/2$ components were eliminated from the measurements, we think that only a small fraction of the (110) line arises from $\lambda/2$ contamination. The small (001) peak reported by Ishikawa et al.[1] for a monocrystal specimen of similar composition was not observed with the polycrystalline sample, even after carefully scanning the anticipated angular region.

A large, approximately uniform background arose from incoherent or diffuse scattering in the specimen. The ratio of the magnetic peak height to this background was typically 0.2, although large differences occurred among the specimens.

Table I. Chemical Composition (at.%)

Alloy	Fe	Cr	Ni	Mn	P	S	Si	Mo	Cu	C	N	C+N
1	68.19	19.4	9.49	1.58	0.037	0.033	0.98	0.115	0.182	0.174	0.165	0.340
2	68.19	19.4	9.49	1.58	0.037	0.033	0.98	0.115	0.182	0.285	0.169	0.454
3	68.19	19.4	9.49	1.58	0.037	0.033	0.98	0.115	0.182	0.514	0.173	0.687
4	68.65	19.1	9.30	1.50	0.039	0.029	1.12	0.118	0.171	0.252	0.539	0.791
5	68.65	19.1	9.30	1.50	0.039	0.029	1.12	0.118	0.171	0.349	0.531	0.88
6	68.65	19.1	9.30	1.50	0.039	0.029	1.12	0.118	0.171	0.440	0.507	0.94
7	66.32	21.5	9.34	1.42	0.043	0.027	1.08	0.112	0.173	0.165	1.13	1.29
8	66.32	21.5	9.34	1.42	0.043	0.027	1.08	0.112	0.173	0.284	1.09	1.38
9	66.32	21.5	9.34	1.42	0.043	0.027	1.08	0.112	0.173	0.435	1.04	1.4

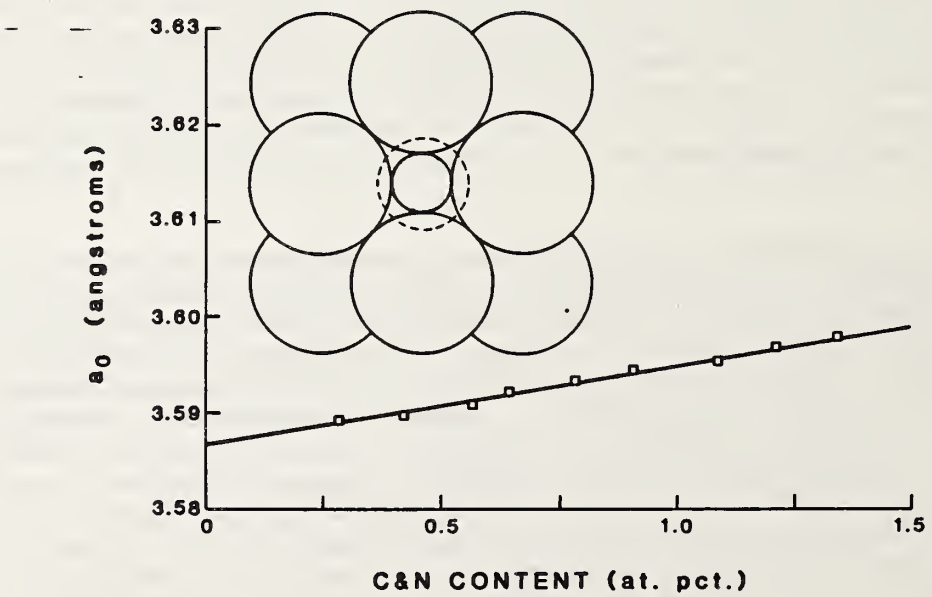

Fig. 1. Lattice parameters determined by x-ray and neutron diffraction at room temperature.

RESULTS

Structure and Composition

The chemical compositions determined for the specimens appear in Table I. The interstitial concentration (C_i) clearly correlates with the lattice spacing (a) at room temperature (Fig. 1). We determined the rate of increase in lattice spacing per atomic percent of interstitial C+N to be $da/dC_i = 8.62 \times 10^{-3}$ Å C_i^{-1}.

Elastic Constants

The ultrasonic experiments[7,8] indicated that the elastic constants were strongly affected by cooling the specimens through the paramagnetic–antiferromagnetic transition temperature. The bulk modulus softened above and around T_N, but the shear modulus softened only at and below T_N. Also, in the low-temperature region, an anomalous temperature dependence was observed in Poisson's ratio. These observations are consistent with a paramagnetic–antiferromagnetic phase transition at T_N.

Magnetic Susceptibility

The magnetic susceptibility [$\chi(T)$] of each of the nine alloys showed a distinct peak as a function of temperature. This behavior is characteristic of a paramagnetic–antiferromagnetic phase transition. However, $\chi(T)$ was independent of the Curie–Weiss temperature. Instead, over a limited range of temperatures above the transition, the susceptibility was well described by

$$\chi(T) = \chi_0 + C/(T - \Theta). \qquad (1)$$

Here, χ_0, C, and Θ are independent of temperature. The constants C and Θ represent the Curie constant and the paramagnetic Curie temperature, respectively. The temperature independence of χ_0 may result from the underlying diamagnetism, Pauli spin paramagnetism,[13] and a saturated ferromagnetic component caused by small ferromagnetic clusters within the alloy.[14] Table II gives the values of χ_0, C, T_N, and μ_{eff} (the effective magnetic moment per atom) obtained from the analysis of Eq. (1). The small and negative values of Θ for all specimens (Table III) indicate a weak net antiferromagnetic interaction. The value of χ_0 generally decreases as the lattice parameter increases. This behavior is consistent with expected changes in the Landau–Peierls and Pauli susceptibilities[13,14] caused by the lattice dilation and the reduction of the Fermi energy.

Table II. Summary of magnetic measurements

Alloy	χ_0* ($10^{-7}m^3/kg$)	C* ($10^{-5}K \cdot m^3/kg$)	T_N† (K)	effective (d+s) electrons/atom	μ_{eff}‡ (μ_B)	μ_{eff}‖ (μ_B)
1	3.68 ± 0.15	3.49 ± 0.19	47.9	7.6	1.11	0.63
2	2.89 ± 0.05	3.64 ± 0.09	48.1	7.6	1.13	
3	2.70 ± 0.06	3.5 ± 0.09	47.1	7.6	1.11	0.75
4	2.38 ± 0.10	3.19 ± 0.15	44.3	7.67	1.06	
5	2.72 ± 0.06	3.66 ± 0.10	43.8	7.67	1.13	
6	2.13 ± 0.21	4.47 ± 0.31	42.25	7.67	1.25	
7	2.92 ± 0.03	4.17 ± 0.07	36.5	7.85	1.21	0.48
8	2.17 ± 0.01	3.05 ± 0.05	36.4	7.85	1.04	
9	1.45 ± 0.61	4.13 ± 0.68	35.0	7.85	1.21	0.66

*Constants obtained from a fit of $\chi = \chi_0 + C/(T + \theta)$ to the data

†Ordering temperature obtained from susceptibility maxima

‡Average magnetic moment per atom, μ_{eff}, as determined by static magnetic results

‖μ_{eff} determined from neutron-diffaction data

Table III. Calculated parameters

Alloy	θ (K)	γ_1/γ_2	$-\theta/T_N$	J_2/J_1	γ_1 (kg/m^3)	J_1/k (K)
1	−13.96	−0.699	0.291	−1.398	−13.289	−0.824
2	−13.15	−0.714	0.273	−1.428	−12.632	−0.783
3	−14.86	−0.680	0.315	−1.360	−13.268	−0.822
4	−14.77	−0.667	0.333	−1.334	−15.223	−0.944
5	−13.61	−0.684	0.311	−1.368	−11.768	−0.729
6	−6.10	−0.832	0.144	−1.664	−8.123	−0.504
7	−4.20	−0.862	0.115	−1.724	−3.186	−0.454
8	−7.01	−0.785	0.193	−1.570	−10.69	−0.663
9	−5.75	−0.812	0.164	−1.624	−7.406	−0.459

The maximum value of the susceptibility decreased with increased dc magnetic field. This behavior is similar to that reported[15] for a 20-Cr, 16-Ni (wt.%) alloy. In the present study, however, the peak was noticeably sharper and, at the fields used, did not disappear as in the cases reported by Warnes and King[15] and by Ishikawa et al.[1] Over the fields studied (1 to 50 mT), the position of the susceptibility maximum, which we take as T_N, was unaffected by the field magnitude. In contrast, Warnes and King reported a gradual reduction in T_N with increasing magnetic field for fields from 58 to 460 mT.

Pinski et al.[4] predicted that increasing the lattice spacing decreases the transition temperature. We observed that T_N decreased from 47.9 ± 0.5 K for the first alloy to 35.0 ± 0.5 K for the ninth alloy. Since the monotonically varying quantity in these alloys is the lattice parameter (which increases from alloy 1 to alloy 9), we think that the observed change in T_N is caused by interdependence of the lattice parameter and the transition temperature. This shift in T_N for three alloys is shown in Fig. 2.

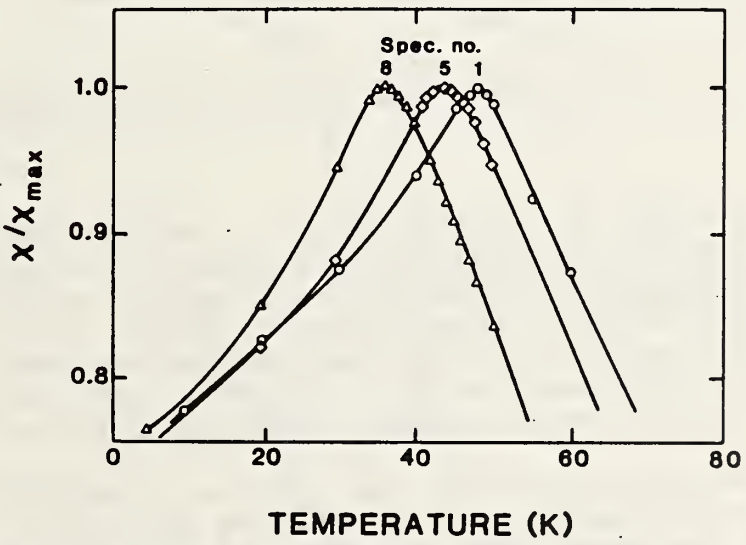

Fig. 2. Magnetic evidence for the systematic shift in the transition temperature. The specimens were first cooled to 5 K under zero applied magnetic field. These measurements were made during warming in a 1.0-mT field.

Neutron Diffraction

A typical neutron-diffraction powder pattern at 10 K is shown in Fig. 3. For quantitative analysis of the neutron-diffraction peaks, the observed background was eliminated by numerical methods. For the broad peaks, an average of several high-temperature (≃ 300 K) spectra, taken over the same angular region, was subtracted from the low-temperature spectrum being analyzed. This procedure provided a sharp, single peak

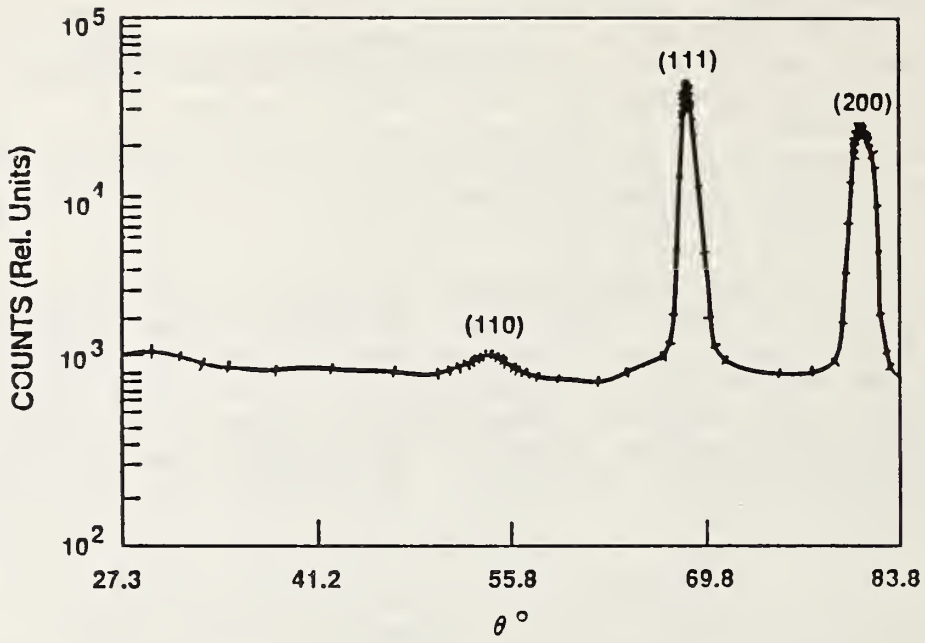

Fig. 3 Neutron-diffraction powder pattern for specimen 3.

that was then fitted to a Gaussian profile. For measurements showing an initial sharp peak, the background was assumed to be a second-order polynomial, and the spectra were fitted with a Gaussian profile and the background. Results of these methods generally agreed. The results of the analysis of the magnetic lines for two specimens are shown in Fig. 4. The temperature dependences of the full width at half maximum of the lines and of the estimated coherence lengths are given in the inset.

The transition temperatures (T_N) were also obtained from the neutron-diffraction measurements by analyzing the magnetic-scattering intensity (N) for temperatures less than T_N. When N was scaled as $N \propto (T_N - T)^{2\beta}$,[16] we obtained $0.29 \leq \beta \leq 0.43$. In all cases, the correlation coefficient exceeded 0.97, which indicated a good fit to the scaling law. Absolute structure factors for the (110) magnetic reflections were obtained by means of an internal calibration against the nucleus reflections. From these, the effective ordered magnetic moments were determined.

Ishikawa et al.[1] showed that the presence of the (110) reflection and the absence of (001) reflection in these alloys are evidence for colinear magnetic structure, or type-1 antiferromagnetism. In this structure, successive planes of atoms perpendicular to the (001) direction have atoms parallel and antiparallel to this axis. Such an arrangement would not produce a (001) reflection because only those moment components perpendicular to the scattering vector are effective in the scattering.

We observed the (110) peaks but found no measurable (001) reflection for any specimen studied; we conclude that the moments are either parallel or antiparallel to the c axis. Hence, in all specimens studied, the neutron-diffraction powder patterns are consistent with a low-temperature type-1 antiferromagnetism.

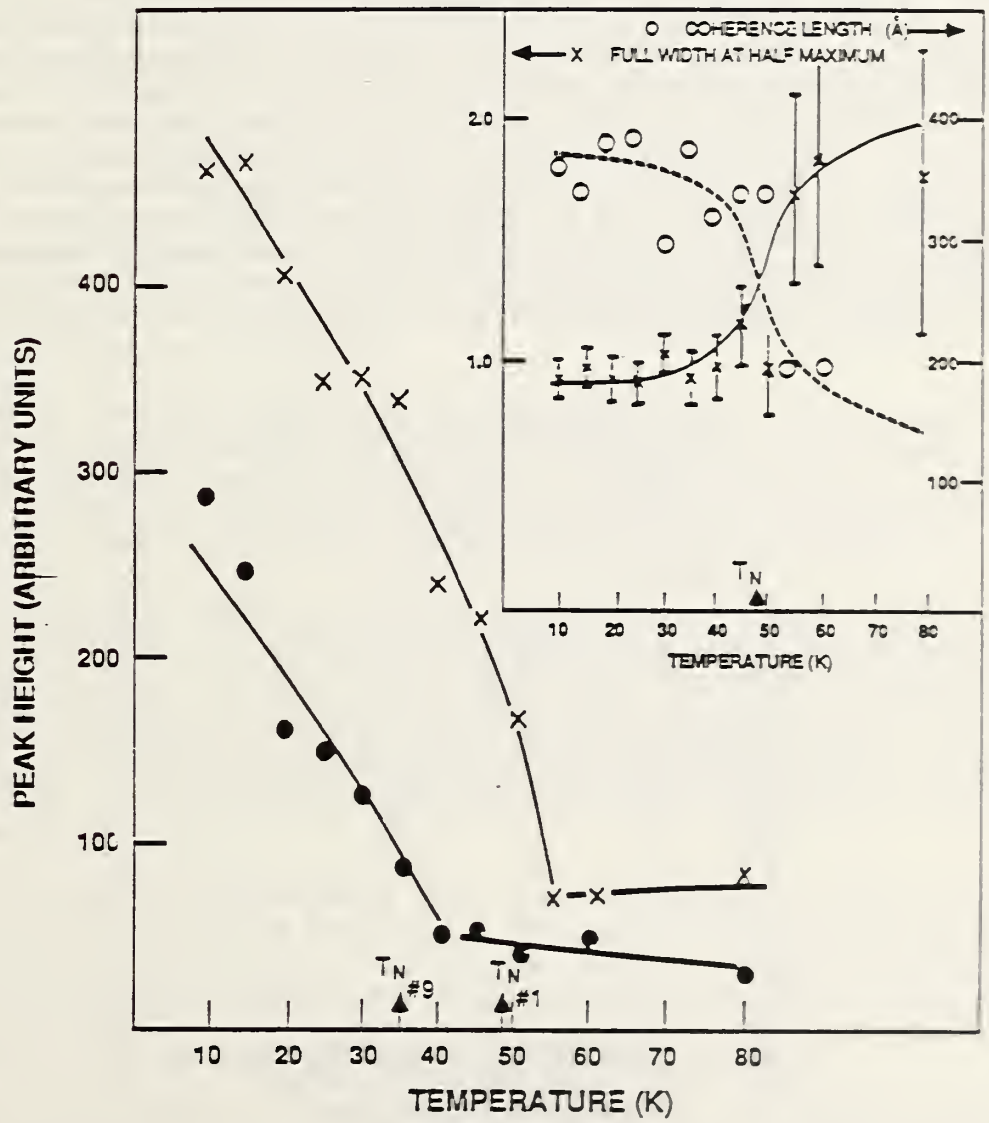

Fig. 4. Temperature dependence of a magnetic peak for two alloys. The x's denote specimen 1; filled circles denote specimen 9. Inset shows the coherence length and the full-width at half-maximum as functions of temperature for specimen 1. The Néel temperatures, determined by magetometry, are also indicated.

ANALYSIS

The values of T_N obtained from the longitudinal ultrasonic wave velocities and from the neutron-diffraction results were higher than the values obtained from the susceptibility maxima; the values of T_N obtained from the transverse wave velocities were slightly lower than the values from the susceptibility maxima. The general trend of T_N versus lattice parameter from both the elastic and the neutron results parallels that of the magnetic-susceptibility measurements. A fit of the ultrasonic results to a linear regression gives slightly different slopes for the transverse and longitudinal wave velocities, but within their statistical uncertainties, they agree with the slope obtained from the susceptibilities. A coherent picture of the low-temperature phase transitions in these nine alloys is shown in Fig. 5. It is a composite of the effect of the lattice expansion on T_N as determined by SQUID magnetometry, longitudinal and transverse elastic anomalies, and the neutron measurements. Overall, the results concur. The decrease in the transition temperature as the lattice expands is clear.

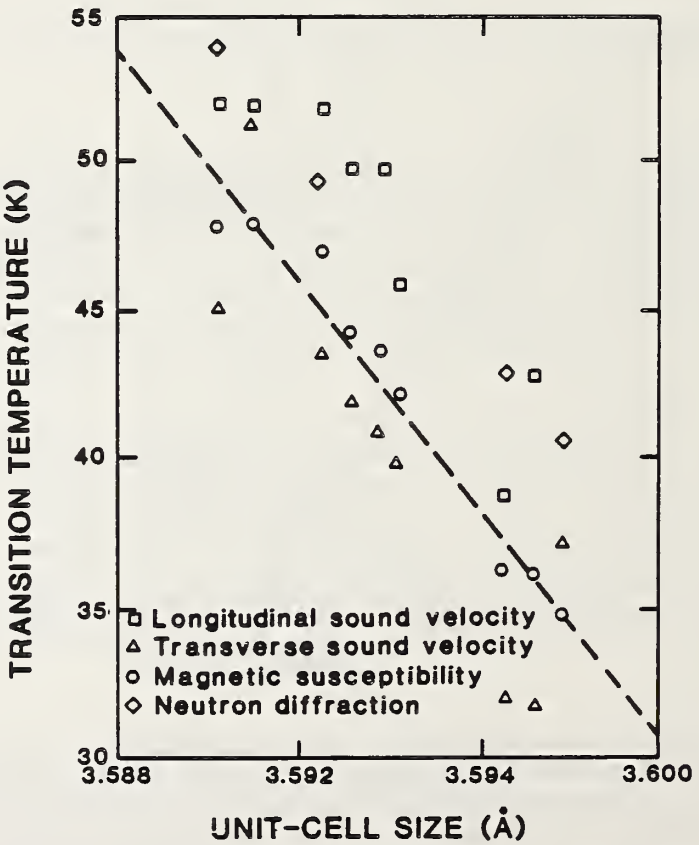

Fig. 5. Composite picture of T_N versus lattice parameter. Measurements of T_N from static magnetometry, longitudinal and transverse sound velocities, and neutron diffraction are shown.

This phenomenon is reminiscent of the behavior of the ferromagnetic (Ni > 19 at.%) γ-Fe alloys described by Ishikawa et al.[1] For both the ferromagnetic and the antiferromagnetic specimens, the magnetic phase-transition temperature was strongly influenced by the effective number (n) of the external electrons per atom. In the ferromagnetic case, both the spontaneous magnetization (M) and the Curie temperature (T_C) rapidly increased as n increased beyond 8. In the antiferromagnetic system, T_N decreased with increasing n as n approached 8 from lower values. However, μ_{eff} appeared unchanged. From empirical results on itinerant antiferromagnetic alloys, we speculate that, for the f.c.c. structure, itinerant antiferromagnetic order occurs if $n \lesssim 7$, ferromagnetic order occurs if $n > 8$, and a spin-glass phase occurs in the intermediate region. In the ferromagnetic case, the Curie temperature is a monotonic function of the electrons contributed by only the Fe and Ni atoms.[1] In contrast, for the antiferromagnetic alloys of this study, a monotonic variation of T_N was observed when all electrons (Table II), including those of Cr and Mn, were counted. This indicates that the role of the "stabilizing" atoms cannot be ignored in determining the properties of the antiferromagnetic materials.

The net magnetic moment per atom averaged over all the atomic components) was determined from the neutron structure factors as well as from the values of the Curie constants.[17] These values of μ_{eff} (presented in Table II) agree satisfactorily with those reported by Ishikawa et al.[1] for similar Fe alloys with the f.c.c. crystal structure.

The antiferromagnetic order was determined to be type 1[3] for all materials studied. The magnetic moment per atom determined from neutron measurements was = 0.6 μ_B. This is about half the value determined from the static magnetic measurements.[18] The lower value obtained from the neutron measurements may reflect the itinerant-electron nature of the spin system. Similar differences between moments determined from static-magnetic and neutron measurements of other austenitic stainless steels have been reported.[1]

The transition temperature (T_N) is more sensitive to the variation in the lattice separation than μ_{eff}. This behavior has been predicted theoretically.[4] However, we have not yet observed an abrupt increase in μ_{eff} with increasing a caused by localized effects at large lattice separations.[4] Probably, the maximum lattice dilation observed in the present specimens is too small to produce sufficient localization.

The drop of about 35% in T_N for a mere (≈ 0.3%) increase in the lattice parameter is surprising. Such a variation in T_N is also disproportionately large compared with the change in the atomic composition.

We analyzed the experimentally determined parameters T_N, C, and Θ to determine J_1, J_2, γ_1, and γ_2. Here J_i is the effective-field exchange interaction between the ith neighbors. Likewise, γ_1 and γ_2 are the first-neighbor and second-neighbor molecular-field coefficients.[17]

Calculations appropriate for the f.c.c. structure with type-1 antiferromagnetic ordering were made (Table III).[17] For all specimens, the value of Θ/T_N lies between -0.33 and -0.12. The small values of θ/T_N for these antiferromagnetic alloys are in stark contrast with the large values (>1) observed in the spin-glass alloys with similar compositions.[10,12] The ratios of $\Theta/T_c > 1$ indicate strong "frustration" so that, even for a large net interaction Θ, the spin-glass ordering temperature is suppressed by the frustrations. Conversely, in the alloys of this study, the frustration effects were minimal.

Smart[17] showed that type-1 antiferromagnetic phase is possible over this region of the $(\gamma_1/\gamma_2, \Theta/T_N)$ parameter space. This is a theoretical consistency check of the presumed magnetic ground state and the experimental measurements.

The negative values of J_1 and J_2/J_1 in all cases indicate that the first-neighbor interaction is antiferromagnetic, and the second-neighbor interactions are ferromagnetic. Furthermore, $|J_2/J_1| > 1$ implies that the second-neighbor interaction is stronger than the first-neighbor interaction. The larger value of J_2 compared with that of J_1 does not affect the effective-field approximation used here because there are twelve first neighbors, each contributing $-|J_1|$ towards Θ, whereas there are only six second neighbors, each contributing about $1.5J_1$. Hence, Θ is still small and negative, or antiferromagnetic, consistent with experimental observations.

Because of the deviations from the Curie–Weiss susceptibility and because $|J_2/J_1| > 1$, we conclude that the alloys of this study must have strong itinerant-electron antiferromagnetic contributions. Perhaps some of the external electrons are localized and the rest are in extended states. The delocalized electrons contribute to the temperature-independent susceptibility (χ_0) and mediate the interaction of J and the localized moments. Friedel oscillation would cause J to oscillate as a function of the distance (r). For large x, where $x = 2r \cdot k_F$ and k_F is the Fermi wave vector, J is represented by the well-known RKKY function:[19,20]

$$J(x) = J_0\left(\frac{x\cos x - \sin x}{x^4}\right). \qquad (2)$$

In this equation, J_0 is assumed to be independent of k_F and r. Equation (2) may be used to determine the interactions J_1 and J_2 at $r_1 = 0.707a$ and $r_2 = a$, respectively, for given values of k_F. Instead, we used Eq. (2) to determine the free-electron band-filling factor $[\phi = k_F(\pi/a)]$ for the nine alloys from the values of a and the previously determined J_1 and J_2. At least in the mean-field limit, all the experimental facts (type-1 antiferromagnetism, Θ, T_N, C, and a) were self-consistently incorporated into the determination of the Fermi wave vector. Equation (2) was solved numerically to determine the value of

k_F, and hence, ϕ, needed to satisfy $J = -J_1$ at $r = r_1$ and $J = J_2$ at $r = r_2$. The values of ϕ for different alloys were: $\phi(1) = 1.905$, $\phi(2) = 1.905$, $\phi(3) = 1.90$, $\phi(4) = 1.90$, $\phi(5) = 1.0904$, $\phi(6) = 1.925$, $\phi(7) = 1.926$, $\phi(8) = 1.917$, and $\phi(9) = 1.92$. On the other hand,

$$k_F = (3\pi^2 n)^{1/3}, \tag{3}$$

where n is the density of free electrons. Considering that there are four atoms per unit cell and that n_{eff} is the effective free-electron contribution per atom, Eq. (3) takes the form

$$k_{eff} = (3\pi)^{1/3} \left[\frac{4n_{eff}}{a^3}\right]^{1/3} \tag{4}$$

When the expression for the wave vector as a function of the free-electron band-filling factor, $k_F = \phi(\pi/a)$, is combined with Eq. (4), we obtain the following expression for n_{eff}:

$$n_{eff} = (\pi/12)\phi^3. \tag{5}$$

The value of n_{eff} for each of the nine alloys was calculated from Eq. (5) and the band-filling-factor results. For all alloys, we obtained $n_{eff} \simeq 2$ electrons per atom. The total number of external d and s electrons calculated directly from the chemical composition gives $n_{eff} \simeq 8$. When only the d electrons on the Fe and Ni atoms are counted, we obtain $n_{eff} \simeq 5$. On the other hand, when only the s electrons are included, we obtain $n_{eff} \simeq 2$. This suggests that the observed exchange interaction, the transition temperature, and the type-1 antiferromagnetic ordering can be accounted for by considering the extended free-electron cloud caused by only s electrons.

The observed sensitivity of T_N to the lattice parameter (a) may be qualitatively explained by the variation of the RKKY interaction with x. If x, the Fermi wave vector times the interneighbor separation, is such that there is a node between $x_1 = (k_F \cdot a/\sqrt{2})$ and $x_2 = (k_F \cdot a)$, then the first-neighbor and second-neighbor interactions (J_1 and J_2) will be oppo-&2site. Furthermore, as shown in Fig. 6, if the values of x are close to

a node, then a change in a will greatly affect J_1 and J_2 in opposite directions. So, a small increase in x_1 and x_2 will decrease $|J_1 - J_2|$ by a large amount and lower the transition temperature.

We cannot justify using Eq. (2) for the concentrated alloys studied here because Eq. (2) is thought to be appropriate for interactions in a dilute system, but it has been reported[21] that the behaviors of concentrated and dilute alloys are often similar. So, empirically, it may be appropriate to express the interaction by Eq. (2).

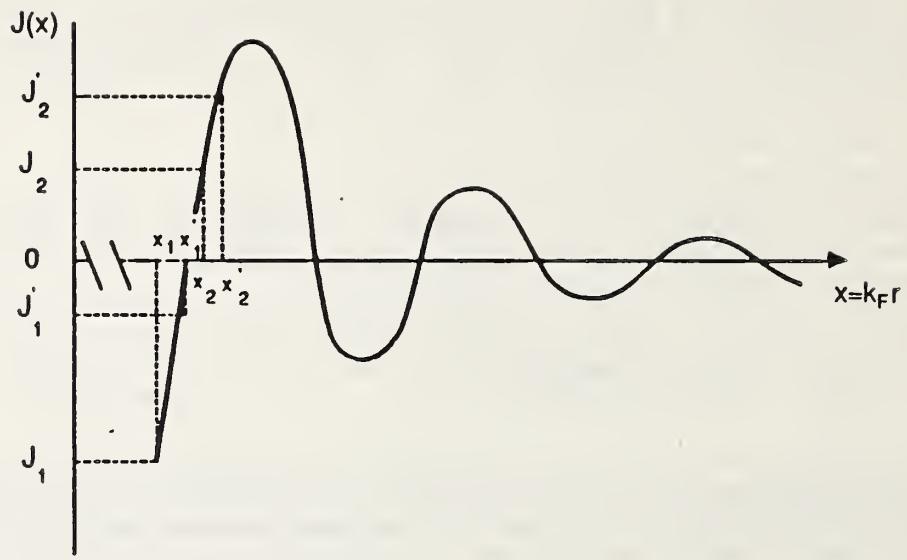

Fig. 6. A pictorial explanation of the extreme sensitivity of the net interaction (J_1–J_2) to the variation of $x = k_F r$.

CONCLUSIONS

We studied a family of isostructural Fe–Cr–Ni alloys with the γ-Fe structure. Elastic, magnetic, and neutron-scattering measurements were analyzed using self-consistent methods to determine the nature of the magnetic ground state and the mechanism of the magnetic interaction. We think that both localized and delocalized electronic contributions are present.

- Our estimates of k_F suggest that only the s states are strongly delocalized. At this stage, we have no explanation for the weak s–d hybridization, and we do not know how many of the d states are delocalized.

- It appears that the type-1 antiferromagnetic ground state is attained by the ordering of the moments of the partially localized d orbitals. These moments were modeled to interact via the extended s states. This oscillatory RKKY interaction gives rise to a weak net antiferromagnetic behavior.

- The sharp decrease in T_N with increasing electronic density or lattice separation can be explained by the rapid change in the exchange interaction near the zeros of the RKKY function.

- For γ-Fe alloys with fewer than 7 electrons per atom, we argue that an antiferromagnetic ground state is to be expected, and for more than 8 electrons per atom, a ferromagnetic ground state is favored.[1] For intermediate electron densities, unusual ordering, such as spin-glass behavior, may be favored. Studies on monocrystals of these alloys with this intermediate composition are in progress and will be reported later.

ACKNOWLEDGMENTS

The work at South Carolina was partially supported by USC grant 13070-K101 and by O.R.A.U.S. contracts to travel to Oak Ridge National Laboratory for the neutron measurements. Work at Oak Ridge was supported under contract DE-AC05-840R21400 with the U.S. DOE. At the National Bureau of Standards, studies were supported partly by the DOE Office of Fusion Energy. C. A. acknowledges a fellowship from Zonta International.

REFERENCES

1. Y. Ishikawa, *Sci. Rep. Tohoku Univ.* 58, 151 (1975); Y. Ishikawa, Y. Endoh, and T. Takimoto, *J. Phys. Chem. Solids* 31, 1225 (1970); Y. Ishikawa, M. Kohgi, and Y. Noda, *J. Phys. Soc. Jap.* 39, 675 (1975); Y. Ishikawa, in *Physics and Application of Invar Alloys*, ed. H. Saito, Honda Memorial Series on MH. Sc. #3, Tokyo (1978).

2. A. Z. Menshikov, P. Burlet, A. Clamberod, and J. L. Tholence, *Solid State Commun.* 39, 1093 (1981).

3. F. Gautier, in *Magnetism of Metals and Alloys*, ed. M. Cyrot (North-Holland, New York, 1982), p. 1.

4. F. J. Pinski, J. Stanton, B. L. Gyroffy, D. D. Johnson, and G. M. Stocks, *Phys. Rev. Lett.* 56, 2096 (1986).

5. A. K. Majumdar and P. V. Blanckenhagen, *Phys. Rev. B* 29, 4079 (1984).

6. R. M. Bozorth, *Ferromagnetism* (Van Nostrand, Princeton, New Jersey, 1951), p. 148.

7. H. M. Ledbetter. *Metall. Trans. A* 11, 543 (1980).

8. E. W. Collings and H. M. Ledbetter, in *Metal Science of Stainless Steel*, eds. E. W. Collings and H. W. King (Metallurgical Society, New York, 1979), p. 22.

9. #VTS-805, BTI(SHE) Corp. San Diego, California.

10. T. Datta, S. D. Levine, D. Thornberry, and E. R. Jones, *Phys. Status Solidi (b)* 121, K125 (1984).

11. T. Datta, D. Thornberry, E. R. Jones, and H. M. Ledbetter, *Solid State Commun.* 52, 515 (1984).

12. T. Datta, D. Thornberry, C. Almasan, and E. R. Jones, *Solid State Commun.* 56, 523 (1985).

13. R. M. White, *Quantum Theory of Magnetism* (Springer, Berlin, 1983).

14. C. Kittel, *Introduction to Solid State Physics* (Wiley, New York, 1976).

15. L. A. A. Warnes and H. W. King, *Cryogenics* 16, 473 (1976); ibid 16, 569 (1976); ibid 21, 729 (1981).

16. A. Tucciarone, H. Y. Lau, L. M. Corliss, A. Delapalme, and J. M. Hastings, *Phys. Rev. B* 4, 3206 (1971).

17. J. S. Smart, *Effective Field Theories of Magnetism* (W. B. Saunders, Philadelphia, 1966).

18. E. R. Jones, T. Datta, C. Almasan, D. Edwards, and H. M. Ledbetter, *Mater. Sci. Eng.* 91, 181 (1987).

19. M. A. Ruderman and C. Kittel, *Phys. Rev.* 96, 99 (1954).

20. T. Kasuya, *Prog. Theor. Phys.* 16, 45 (1956); K. Yosida, *Phys. Rev.* 106, 893 (1957).

21. G. Aeppli, J. J. Hauser, G. Shirane, and Y. J. Uemuria, *Phys. Rev.* 54, 843 (1985).

EFFECTS OF GRAIN SIZE AND COLD ROLLING ON CRYOGENIC PROPERTIES OF COPPER*

R. P. Reed, R. P. Walsh, and F. R. Fickett
Fracture and Deformation Division
National Bureau of Standards
Boulder, Colorado

The effects of grain size and cold rolling on the tensile properties and electrical resistivity at 295, 76, and 4 K were studied for oxygen-free, high-conductivity copper. Tensile yield and ultimate strengths increase linearly with increasing $d^{-\frac{1}{2}}$ (d = grain diameter), following the Hall–Petch relationship. At low temperatures, the dependence on grain size increases. Increasing grain size lowers resistivity slightly at all temperatures. Cold rolling to 10 percent reduction of area significantly increases the yield strength at all temperatures; subsequent rolling produces smaller strength increases. Resistivity increases with cold rolling.

INTRODUCTION

In the annealed condition, copper is usually not strong enough for use as the stabilizing element for low-temperature superconductors or as a high-field magnet conductor. It must be strengthened or reinforced. Two conventional ways to strengthen copper are cold working and reduction of grain size. Yet quantitative low-temperature property data on the effects of these metallurgical variables are not available. This paper presents the effects of grain-size variation and cold rolling on the tensile properties and electrical resistivity of copper at 295, 76, and 4 K. The material studied was the oxygen-free, high-conductivity, silver-bearing copper (99.95 Cu + Ag) designated by the Copper Development Association (CDA) as CDA 104.

*In *Advances in Cryogenic Engineering – Materials*, vol. 34, Plenum, New York, 1988, pp. 299–308.

EXPERIMENTAL PROCEDURES

Tensile Measurements

Tensile specimens taken from the plate material were rods; their reduced sections were 6.3 mm in diameter and 38 mm in gage length, with 12.7-mm-diameter threaded ends. For rolled plate materials, the specimens were oriented so that the tensile force was applied transverse to the rolling direction.

For all tests, specimen strain was monitored with three clip-on strain-gage extensometers, 25 mm in gage length. They were mounted on the specimen within the 38-mm gage length. From specimen to specimen, the outputs of these extensometers reproduced within 14 μm with a sensitivity of 0.03 strain per volt (corresponding to a readout of ± 0.04 μm).

The tensile testing machine had a cryostat fixture mounted to the bottom of its screw-driven crosshead. The specimen strain rate was 8.8×10^{-5} s^{-1}. Cryostat equipment and procedures using liquid helium and nitrogen have been described.[1]

Resistivity Measurements

Resistance measurements at room temperature (295 K), in liquid nitrogen (76 K), and in liquid helium (4 K) were made on tensile specimens. A conventional four-probe resistivity technique[2] with a commercial nanovoltmeter and an automated data acquisition system was used. Voltage taps were placed along the uniform section of the specimen with a spacing of 30 to 35 mm, depending on the specific specimen. Current was provided through threaded end caps from a bipolar power supply with a 25-A capability. A precision shunt was monitored with a conventional DVM to supply current readings. Voltage measurements were made with the current flow in the sequence forward–reverse–forward. The program monitored drift of the readings and remeasured if the variation between the two forward readings exceeded 0.1 percent. In initial tests, a series of current values was used at each temperature to determine when heating of the specimen first occurred. These tests led to use of a specimen current of 2.0 A at room temperature and 10.0 A at lower temperatures; this gave voltages in the microvolt range. Owing to nonuniformities in the specimen cross section, uncertainty of the data is ± 1 percent.

Cold Rolling

Tensile specimens, in increments of cold rolling from 10 to 60 percent, were obtained for CDA 104. The alloy was received as rolled plate (32 mm thick, 76 mm wide, 280 mm long) in the half-hard condition; then it was annealed at 500°C for 90 min and air-cooled. The annealed plate was uniaxially cold-rolled to a 10 percent reduction in thickness; this was achieved in approximately five passes through 5000-kg, 150-mm-diameter rolls. Material for four tensile specimens was then removed

from the plate. The plate was again incrementally and uniaxially cold-rolled another 10 percent, and material for four more tensile specimens was removed. This procedure was repeated to obtain 30-, 40-, 50-, and 60-percent cold-rolled conditions.

Grain Size Control

The as-received, half-hard condition, plate material was uniaxially cold-rolled to 50-percent reduction in thickness. Tensile specimens were machined from the cold-rolled plate and recrystallized to selected grain sizes in a salt bath (sodium nitrite and potassium nitrate). Recrystallization of the cold-rolled plate occurred at temperatures as low as 410°C, but at the lower temperatures there was very little grain growth. The recrystallization and grain-growth time–temperature schedules are summarized in Table 1.

Table 1. Recrystallization Schedule and Grain Sizes

Number of Specimens	Temperature (°C)	Time (min)	Cooling	Resulting Grain Size (μm)
4	625	1	Air	23
4	625	5	Air	33
4	625	30	Air	44
4	720	90	Air	102

RESULTS AND DISCUSSION

Cold Rolling

The effects of cold rolling on tensile yield strengths at 295, 76, and 4 K are shown in Fig. 1. In the annealed condition, 10-percent cold rolling increased the yield strength substantially—by almost one order of magnitude. Only moderate temperature dependence was exhibited. The primary contributor appears to be the long-range stress fields (cell structure) that impede dislocation motion. These long-range stress fields are firmly established at 10 percent strain; subsequent deformation does not contribute as significantly to yield-strength increases. The initial rapid increase of yield strength with cold rolling, followed by a leveling off at higher deformations, has also been reported by Truckner and Mikkola[3] and Zehetbauer and Trattner[4] for oxygen-free, high-conductivity copper at room temperature. These studies included even larger deformations and reported eventual softening at strains greater than about 1.5.

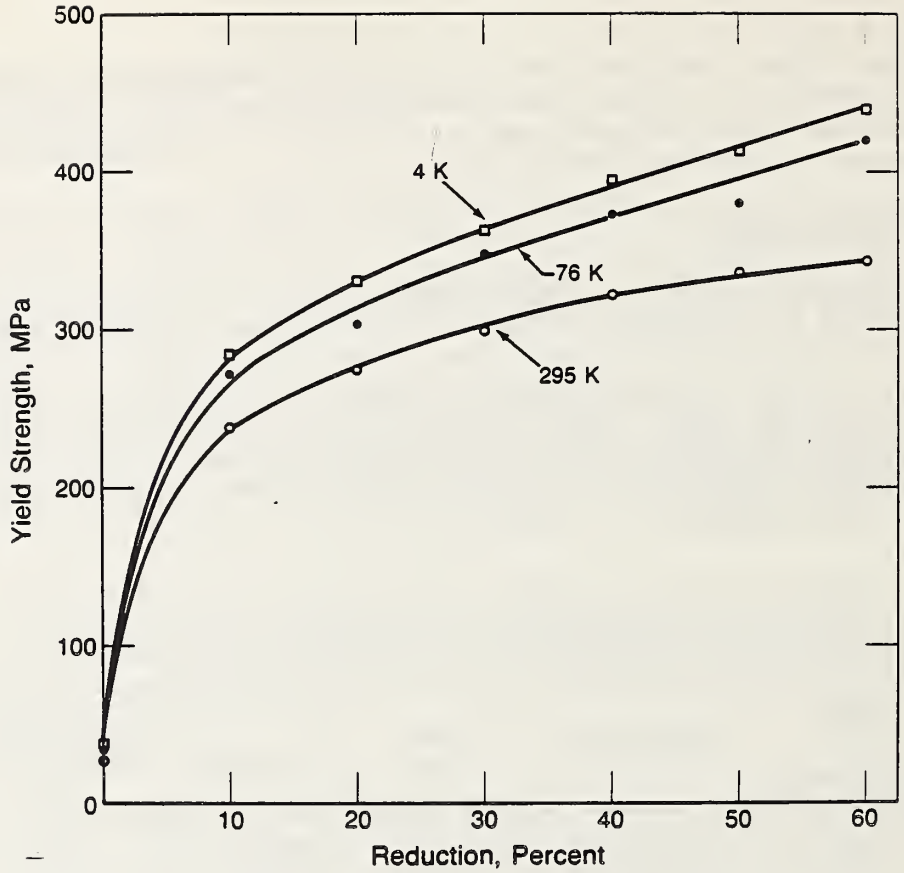

Fig. 1. Effects of cold-rolling CDA 104 copper on tensile yield strength.

The effect of cold rolling on tensile ultimate strength is illustrated in Fig. 2. In contrast with the effect on yield strength, (1) ultimate strength does not increase abruptly at small strains and (2) its dependence on cold work is lowest at low temperatures. Presumbly, the difference in dependence at small strains reflects the parabolic nature of copper stress–strain behavior. The stronger dependence of ultimate strength on deformation at higher temperatures probably reflects larger recovery effects at higher temperatures—during tensile deformation as opposed to during cold rolling.

Cold rolling of copper does not significantly affect tensile reduction of area at low temperatures (Fig. 3). There is virtually no dependence on temperature of reduction of area, especially at larger amounts of cold work. Since reduction of area normally correlates with fracture toughness for ductile, face-centered cubic alloys, the implications of these data are that toughness of copper is not affected by cold work. However, we must caution that there is strong correlation between yield strength and fracture toughness; therefore expect a decrease of fracture toughness with cold work on those grounds.

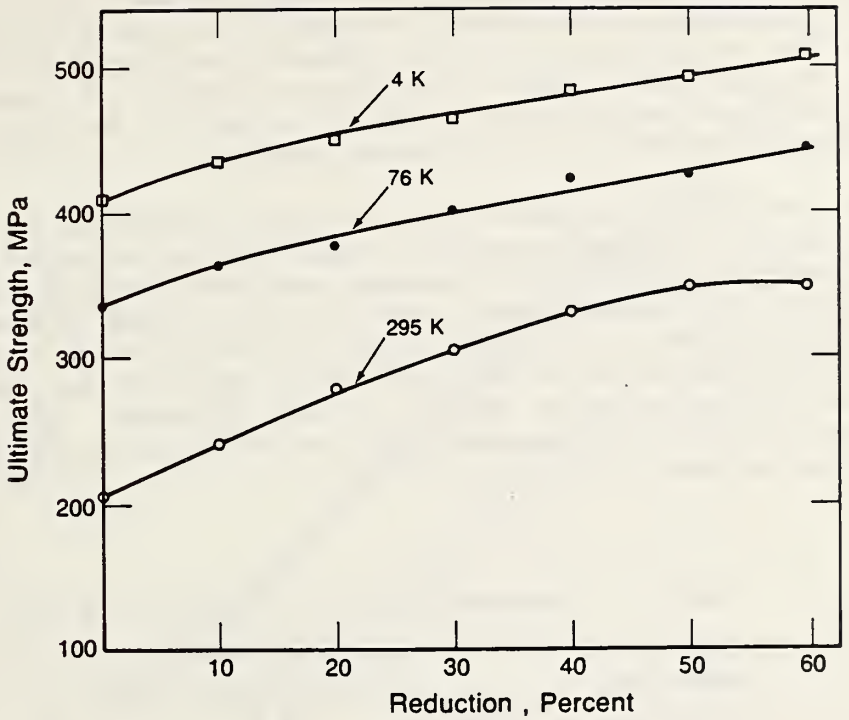

Fig. 2. Effects of cold-rolling CDA 104 copper on tensile ultimate strength.

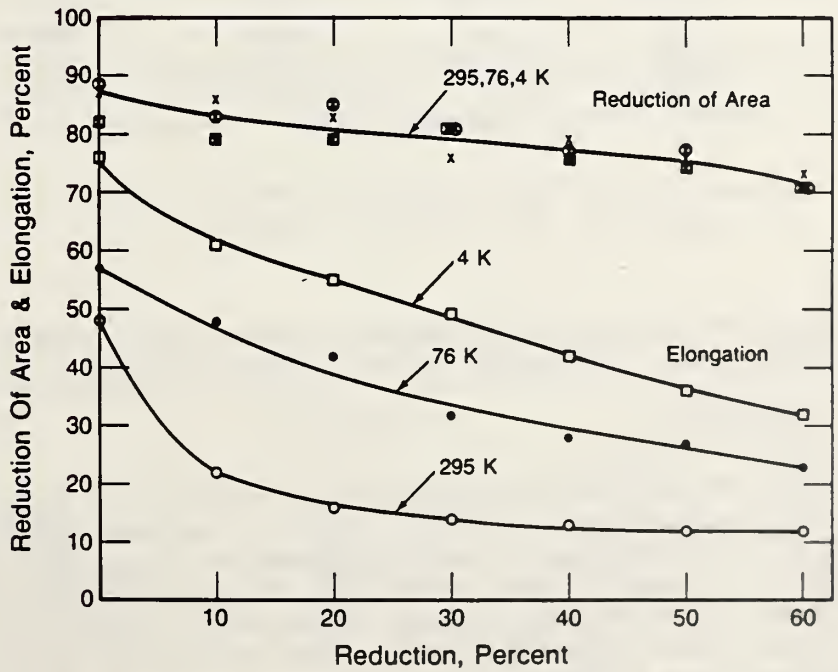

Fig. 3. Effects of cold-rolling CDA 104 copper on tensile elongation and reduction of area.

Tensile elongation of copper is inversely related to temperature (Fig. 3). Not only is the elongation highest (per unit cold work) at 4 K, but this increased ductility is generally maintained at larger increments of cold work. There is stronger dependence of elongation on cold work at lower temperatures, similar to that of the yield strength but in contrast to that of the ultimate strength.

The electrical resistivity data in Table 2 appear to be consistent with the behavior of the oxygen-free copper that we measured earlier.[5] This was expected, since the two coppers are quite similar in composition. In the earlier experiment, the shape of the RRR–deformation curves differed significantly for copper material from different sources. The 4-K data represent the contribution from the dislocations introduced during cold rolling. The $\Delta\rho$ for the 10- and 20-percent cold-rolled conditions are greatest, corresponding to the more rapid increase of yield strength during these increments.

Table 2. Resistivity of Cold-Rolled CDA 104

Reduction (%)	Resistivity ($\mu\Omega\cdot$cm) 295 K	76 K	4 K
0	1.75	0.206	0.0100
10	1.74	0.208	0.0168
20	1.76	0.219	0.0253
30	1.74	0.221	0.0279
40	1.75	0.223	0.0295
50	1.74	0.226	0.0320
60	1.76	0.231	0.0355

Grain Size

The yield and flow strengths of most metals and alloys increase with decreasing grain size, following the well-known Hall–Petch relation:

$$\sigma_y = \sigma_o + kd^{-\frac{1}{2}} \qquad (1)$$

where σ_o is the polycrystalline strength extrapolated to infinite grain size, d is the average grain diameter, and k is the dependence of strength on $d^{-\frac{1}{2}}$. Both σ_y and k usually depend on strain and temperature. This dependence is shown in Fig. 4 for CDA 104 copper at 295, 76, and 4 K. The slope, k, increases at lower temperatures; Hansen and Ralph[6] reported a lower slope at small strains (less than 0.05) at 76 K than at room temperature, but a higher slope at larger strains. Our Hall–Petch terms are summarized in Table 3; also included this in table are the results of a data review of CDA alloys 101–104 by Simon and Reed[7] and the

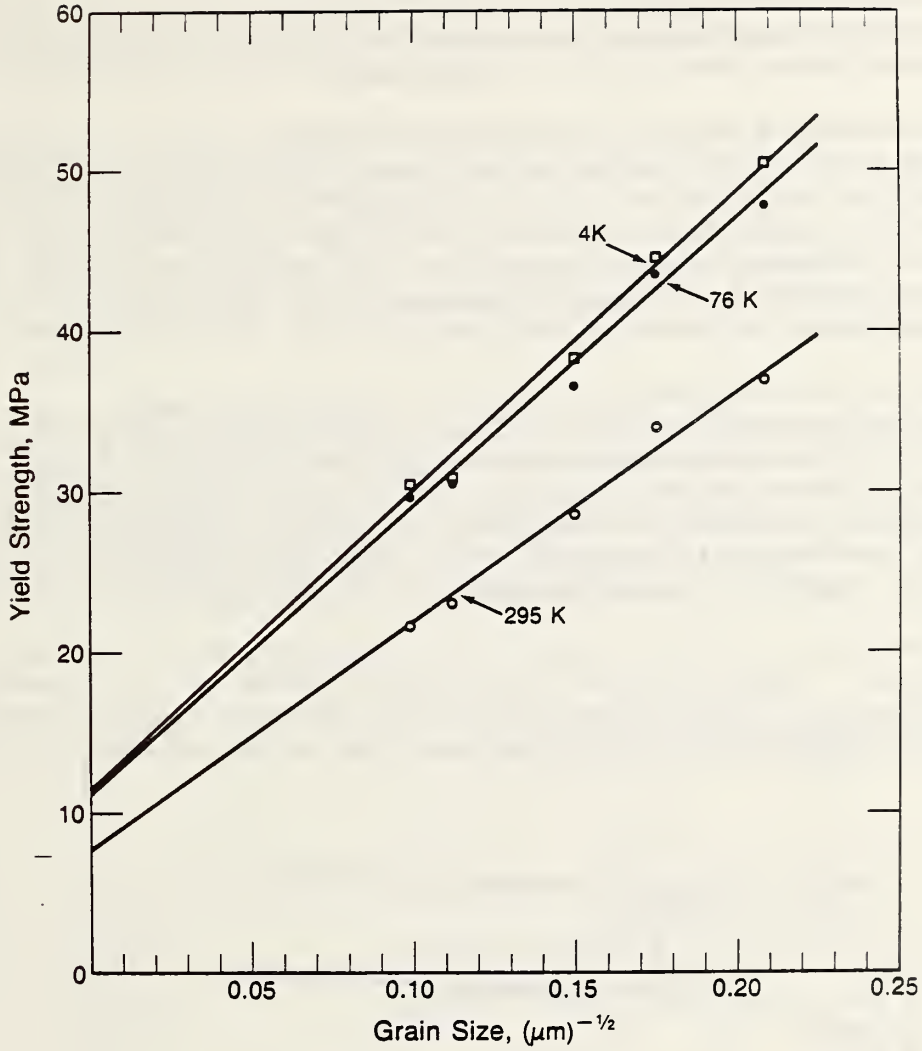

Fig. 4. Effects of grain size on the tensile yield strength of CDA 104 copper.

Table 3. Hall–Petch Parameters from Various Studies

Source	Temperature (K)	Parameters σ_o (MPa)	k (MPa/$\mu m^{-1/2}$)
This paper	295	7.5	142
Simon, Reed[7]	295	18.6	112
Hansen, Ralph[6]*	295	20	152
Merz, Dahlgren[8]	295	6.4	149
This paper	76	11	180
Hansen, Ralph[7]*	76	~45	–
This paper	4	11	188

*Extrapolated from strains >0.03

data of Merz and Dahlgren[8] who studied extremely fine grain sizes. Simon and Reed conducted regression analysis of all available data at room temperature using the Hall–Petch equation.

From Table 3 we can conclude that the slope of the Hall–Petch relationship between yield strength and grain size is fairly well-established at 295 K; it ranges from 142 to 152 MPa/$\mu m^{\frac{1}{2}}$ in the three studies. At low temperatures k increases, reaching about 188 MPa/$\mu m^{-\frac{1}{2}}$ at 4 K. The constant, σ_o, depends on specimen purity. Our data from specimens of constant purity indicate a modest increase of σ_o from 295 to 76 K, but little change of σ_o between 76 and 4 K.

Grain size only modestly affects ultimate strength; as shown in Fig. 5, this dependence follows a Hall–Petch relationship. The increase of σ_o with decreasing temperature reflects the stronger temperature dependence of the ultimate strength. The slope of the dependence is approximately independent of temperature. This is unexpected, since k at much lower strains is dependent on temperature (Table 3), and Hansen and Ralph reported a strong dependence of k on strain at 76 K. The

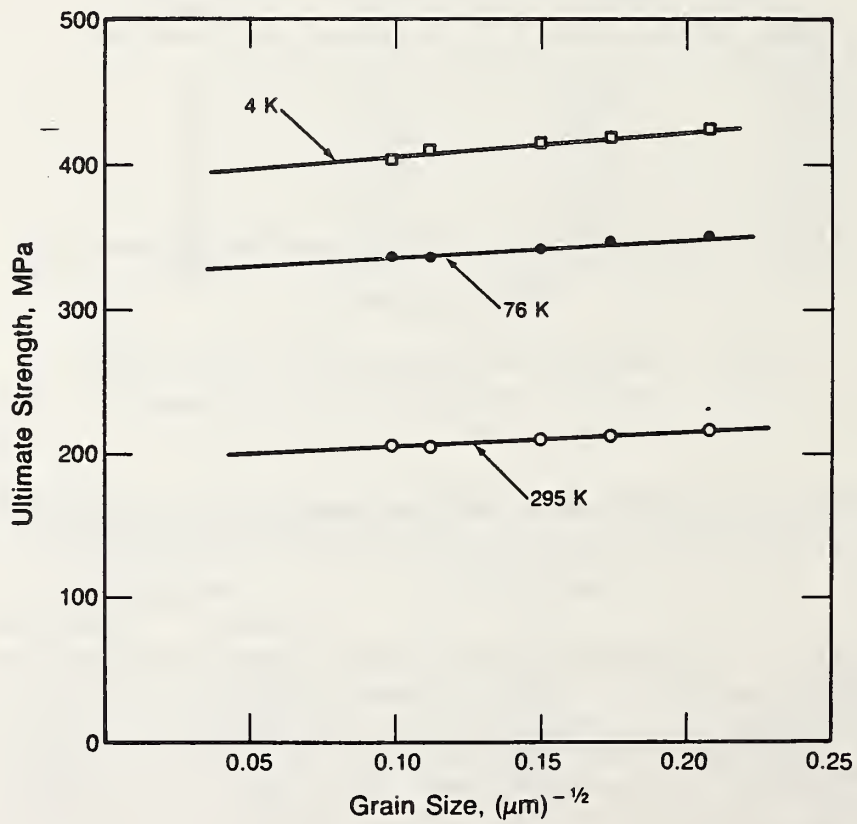

Fig. 5. Effects of grain size on the tensile ultimate strength of CDA 104 copper.[5]

implications are that grain boundaries and strength level play a strong role in the ductile fracture of copper tensile specimens and that this role is independent of low temperatures.

Tensile ductility, as measured by elongation and reduction of area, is independent of grain size in most cases, and reduction of area is practically independent of temperature (Fig. 6). The only apparent dependence is the effect of grain size on tensile ductility at 4 K: decreasing grain size reduces elongation (while increasing the tensile strength), and reduction of area remains constant. Deformation twinning, probably responsible for the serrated yielding at 4 K, may be responsible for this trend.

The electrical resistivities of copper with various grain sizes are plotted in Fig. 7. The 102-μm grain-size specimen, represented by the solid circle, was annealed at 720°C and then annealed at 25°C to give the circled point for that grain size. Error bars on the nitrogen and helium graphs represent measurement precision. On the 295-K graph, it represents the error possibly due to a ±0.5-K temperature change.

The resistivity measurements show a clear, if small, dependence of that parameter on the measured grain size for this copper. Two interesting features of Fig. 7 are the larger dependence of the resistivity on grain size at 295 K than at the lower temperatures and the relatively

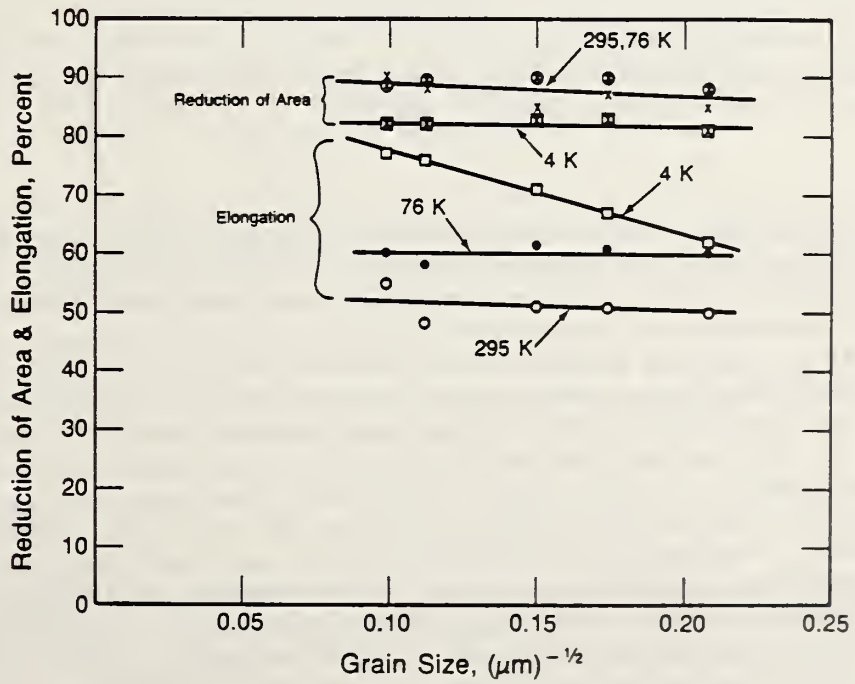

Fig. 6. Effects of grain size on the tensile reduction of area and elongation of CDA 104 copper strength.

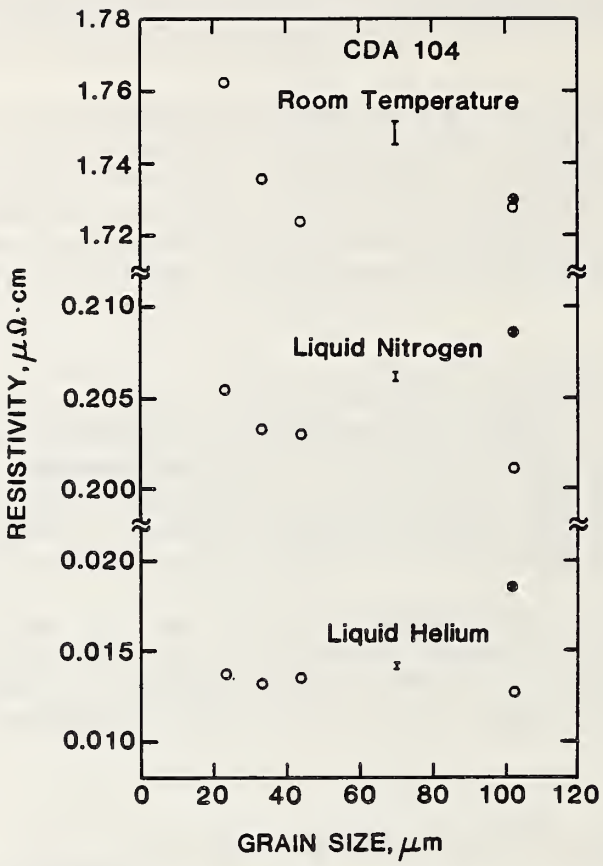

Fig. 7. Resistivity of CDA 104 copper as a function of grain size.

large change in the resistivity caused by annealing the specimen with the largest grain size at a higher temperature (720°C) than that used for the other specimens (625°C). In the case of the 295-K resistivity, one is tempted to postulate a temperature-dependent grain-boundary resistivity or an annealing effect on the lattice resistivity. Neither of these concepts is supported by previous work, to the best of our knowledge, and our data are too few to enable a detailed evaluation. The rather large increase in the residual resistivity observed to result from the higher temperature anneal of the largest grain-size specimen indicates that some sort of precipitation or strong clustering of resistive impurities is taking place. Reannealing this specimen at the lower temperature apparently removes the impurity, perhaps by reformation of an agglomerate. The resistivity of the smaller grain-size specimen is above the expected value for the fully annealed state (1.72–1.74 $\mu\Omega\cdot$cm). One explanation for this higher resistivity is that the initial cold-worked specimen was not completely recrystallized; however, the decrease of the lower temperature resistivities for the smallest grain size specimen do not support this interpretation.

High-Conductivity Alloy Strengthening

Usually, the objective in strengthening of high-conductivity metals is to maximize strength while maintaining minimum resistivity. Consider the ratio of yield-strength increase ($\Delta\sigma_y$) to resistivity increase ($\Delta\rho$) at low temperatures. Attendant with grain size decreases from 102 to 23 μm, the ratio $\Delta\sigma_y/\Delta\rho$ is about 5,400 (MPa/$\mu\Omega\cdot$cm) at 76 K and 19,600 at 4 K. After cold rolling, this same ratio ranges from about 37,000 at 4 K for 10-percent reduction in thickness to 15,600 at 76 K for 60-percent reduction in thickness. For low-temperature use, 10-percent cold rolling appears to optimal. Since both strengthening contributors produce nearly equivalent strength–resistivity ratios, it is likely that both grain-size and cold-rolling effects are desirable in terms of dislocation contributions. For 295-K applications, cold rolling appears to be superior, since neither reduction of grain size nor cold rolling contribute substantially to increases in resistivity.

CONCLUSIONS

From tensile and electrical resistivity measurements at 295, 76, and 4 K of 99.95 copper with varying amounts of cold rolling and differing grain sizes, the following conclusions emerge:

1. Cold rolling dramatically increases yield strength, ultimate strength and electrical resistivity, reduces elongation, but does not affect reduction of area. Cold rolling to 10-percent reduction in thickness increases the yield strength by a factor of about 8 at all low temperatures; subsequent rolling to 60 percent increases the yield strength by a factor of only about 1.5.

2. Yield and ultimate strengths are related to $d^{-\frac{1}{2}}$, where d is the grain size. This dependence increases at low temperatures. Ductility is unaffected by grain size, except for elongation at 4 K. Grain size has little effect on resistivity.

3. On the basis of optimal strength and minimal resistivity, a modest amount of cold rolling (about 10 percent) produces the best ratio of strength-to-resistivity at low temperature.

ACKNOWLEDGMENTS

Many thanks are due to L. Scull who assisted in cold-rolling the copper plate and K. Yu for electrical resistivity measurements. This study was partially supported by U.S. Department of Energy and the International Copper Research Association.

REFERENCES

1. R. P. Reed and R. P. Walsh, Low temperature tensile characteristics of copper and aluminum in "Magnetic Studies for Magnetic Fusion Energy Applications at Low Temperatures – IX," NBSIR 86-3050, National Bureau of Standards, Boulder, Colorado (1986) pp. 107–140.
2. F. R. Fickett, Electrical properties, chapter 5 in "Materials at Low Temperatures," R. P. Reed and A. F. Clark, eds. American Society for Metals, Metals Park, Ohio (1983), pp. 161–201.
3. W. G. Truckner and D. E. Mikkola, Strengthening of copper by dislocation substructures, Metall. Trans. 8A, 45–49 (1977).
4. M. Zehetbauer and D. Trattner, Strengthening characteristics of heavily cold-rolled copper, in "Strength of Metals and Alloys," Pergamon Press, New York (1985), pp. 105–110.
5. F. R. Fickett, The effect of mill temper on the mechanical and magnetoresistive properties of oxygen-free copper in liquid helium, Adv. Cryog. Eng. – Mater. 30, 453–460 (1984).
6. N. Hansen and B. Ralph, The strain and grain size dependence of the flow stress of copper, Acta. Metall. 30, 411–417 (1982).
7. N. J. Simon and R. P. Reed, Properties of copper and copper alloys, to be published, National Bureau of Standards, Boulder, Colorado.
8. M. D. Merz and S. D. Dahlgren, Tensile strength and work hardening of ultrafine-grained high-purity copper, J. Appl. Phys. 46, 3235–3237 (1975).

TENSILE AND CREEP–FATIGUE PROPERTIES OF A COPPER–STAINLESS-STEEL LAMINATE

L. L. Scull and R. P. Reed
National Bureau of Standards
Boulder, Colorado

The design of compact-ignition magnets uses a high-conductivity copper alloy. Since the large magnetic fields cause large stresses in the coil, this application may require a conductor with higher strength than that of the copper alloys and equally high electrical and thermal conductivity.

A candidate material was produced by reinforcing the copper alloy with a stainless-steel alloy. The steel is roll-bonded into the midplane between two copper sheets. This material has the high thermal and electrical conductivity of the copper alloy and, possibly, sufficient strength to be used in compact-ignition magnets.

Tests were conducted at 295 and 76 K to characterize the tensile and creep–fatigue behavior of this laminated composite material in three roll-bonded conditions. These conditions correspond to a bulk reduction of 40, 50, and 60% cold work in the laminate as a whole. A mixing rule was used to predict the tensile behavior of the composite on the basis of the individual tensile properties of copper and stainless steel.

INTRODUCTION

Compact-ignition magnets are produced by winding a helical conductor into a torus. When pulsed, the magnet is subjected to large thermal and mechanical stresses. The large current density causes a substantial amount of Joule heating within the conductor, and the magnetic field produces a large hoop stress within the torus. Copper alloys possess the required electrical and thermal conductivity, but they may not have sufficient strength for this application.

---

*In *Advances in Cryogenic Engineering – Materials*, vol. 34, Plenum New York, 1988, pp. 397–403.

A candidate material with both high strength and conductivity has been produced by roll-bonding a stainless steel alloy between copper sheets. The magnet conductors are cooled with liquid nitrogen (76 K) to reduce the electrical resistance and Joule heating after the magnet is pulsed.

Tensile tests were conducted to determine the strength of this composite at 295 and 76 K. The creep–fatigue behavior was also investigated to determine the effects of cyclic loading caused by the magnetic pulses.

SPECIMEN CHARACTERIZATION

A stainless steel alloy (Fe–18Cr–13Mn–3Ni–0.37N) was roll-bonded into the midplane between two copper sheets (99.95% Cu + Ag minimum). Three types of specimens were tested in conditions corresponding to bulk thickness reductions of 40, 50, and 60% in the roll-bonding process. Tensile tests were conducted on specimens with a uniform width in the gauge length and creep–fatigue tests were conducted on specimens with a uniform radius in the gauge length (see Fig. 1).

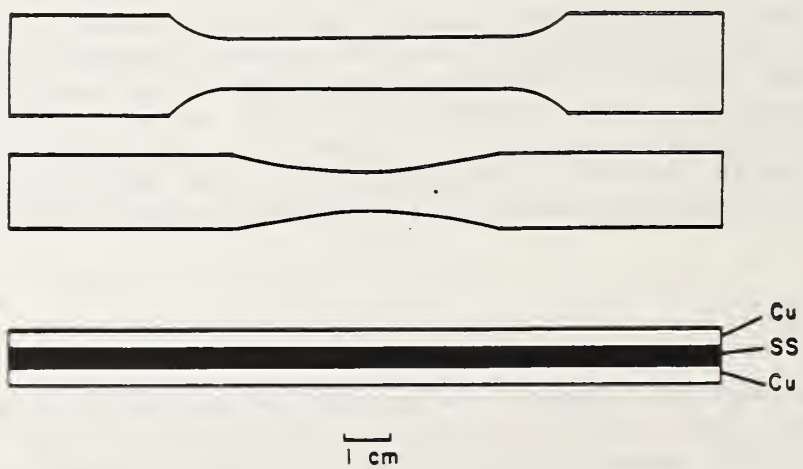

Figure 1. Specimen geometry of laminates tested in this study.

TEST APPARATUS AND PROCEDURE

Uniaxial tensile tests[1] were conducted at a constant displacement rate of 0.3 cm·min^{-1}, which corresponds to a strain rate of 5×10^{-2} min^{-1} at 295 and 76 K. The specimens were installed in conventional wedge grips on a servohydraulic load frame for the 295-K tests. An extensometer with a 38-mm (1.5-in) gauge length was used on all tensile tests.

The 76-K tests were conducted using a screw-driven load frame, which was fitted with a cryostat to enable the test specimen to be completely immersed in liquid nitrogen. The 76-K specimens were pinned and clamped in specially constructed grips designed for low-temperature applications.

The creep–fatigue tests were conducted on a servohydraulic load frame using the same grips as for the 295-K tests. All creep–fatigue tests were conducted at room temperature owing to expected specimen-to-specimen variations and a limited specimen supply. This gave two replicates for each cold-worked condition tested.

A waveform generator was used to program the hydraulic system in a load-controlled servo loop. The specimen stress was ramped up from 9 to 90% of the yield stress of the composite being tested (40, 50, or 60% reduction) in a period of 5 s. The 90% stress was held constant for 10 s, and then ramped down from 90 to 9% of the yield stress in 5 s. The stress was then held constant at 9% for an additional 10 s. This loading process was repeated several thousand times.

A strain gauge mounted at the center of the specimen across the thinnest portion of the gauge length measured the strain in the specimen as a function of the number of loading cycles. The same extensometer used in the tensile tests was also used as a less accurate, but independent, measure of the specimen strain.

RESULTS

The measured and predicted values of Young's modulus (E) and the 0.2% offset yield strength (σ_y) at 295 K are given in Table 1. The predictions were made by using a simple mixing rule that states: the strength (modulus) of the laminate equals the sum of the strengths (moduli) of each layer multiplied by the fraction that each layer forms in the laminate. Table 2 contains similar data obtained at 76 K. The parameter α is the fraction of the thickness of the laminate occupied by the copper.

Stress–strain curves for the laminate at 295 and 76 K are shown in Figs. 2 and 3, respectively. These curves indicate that the strength of the laminate increases with increasing cold work and with decreasing temperature. Figure 2 shows small spikes near failures at stresses of approximately 0.2 GPa. These spikes occurred when the copper arrested

Table 1. Predicted and Measured Mechanical Properties at 295 K.

Cold Work, %	E (meas.), GPa	E (pred.), GPa	σ_y (meas.) MPa	σ_y (pred.), MPa	α
40.1	106	144	526	582	0.7214
49.0	144	142	470	650	0.7418
60.3	137	142	593	663	0.7417

Table 2. Predicted and Measured Mechanical Properties at 76 K.

Cold Work, %	E (meas.), GPa	E (pred.), GPa	σ_y (meas.) MPa	σ_y (pred.), MPa	α
40.1	113	151	620	801	0.7214
49.0	101	149	618	863	0.7418
60.3	114	149	604	879	0.7417

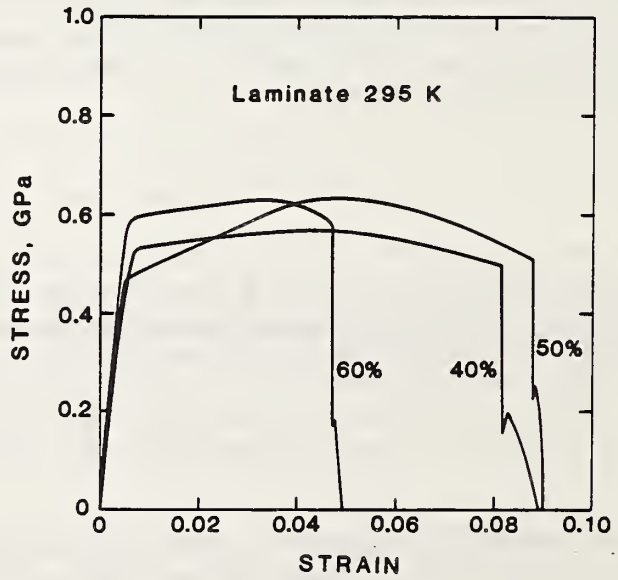

Figure 2. Stress–strain curves at 295 K.

the fracture in the tensile bar immediately after the stainless steel failed. The copper then was pulled to a knife edge with some strain hardening prior to final failure.

Figures 4 through 7 show Young's modulus, 0.2%-offset yield strength, ultimate tensile strength, and elongation to fracture, respectively, as a function of bulk cold work in the specimens tested. Figure 8 shows the curves of strain versus number of cycles that were obtained in the creep-fatigue tests.

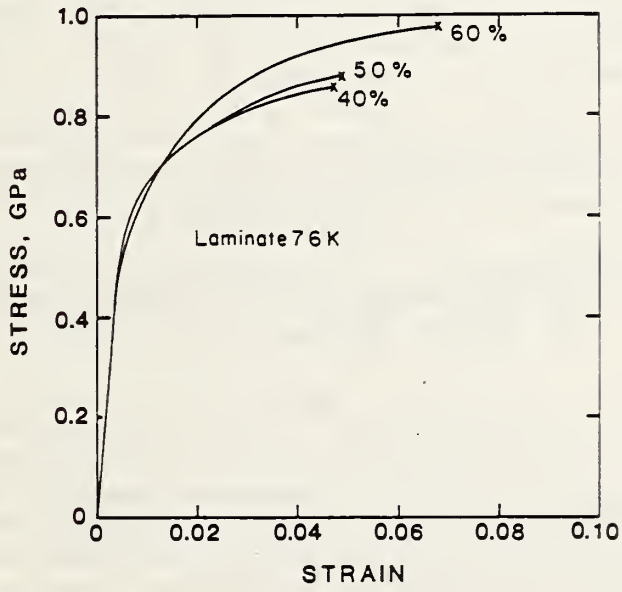

Figure 3. Stress-strain curves at 76 K.

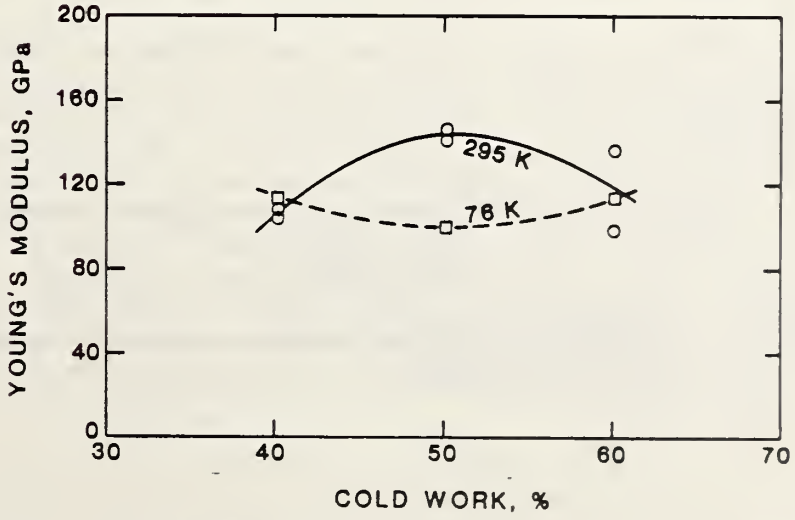

Figure 4. Young's modulus versus cold work at 295 and 76 K.

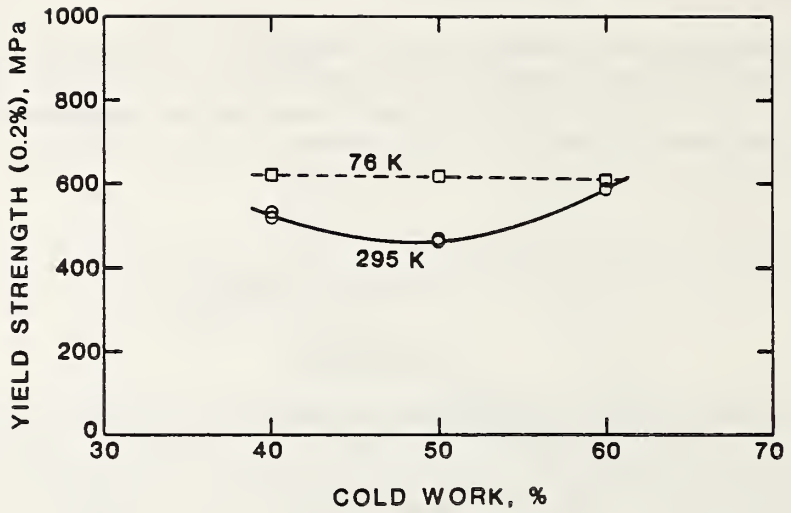

Figure 5. Yield strength (at 0.2% offset) versus cold work at 295 and 76 K.

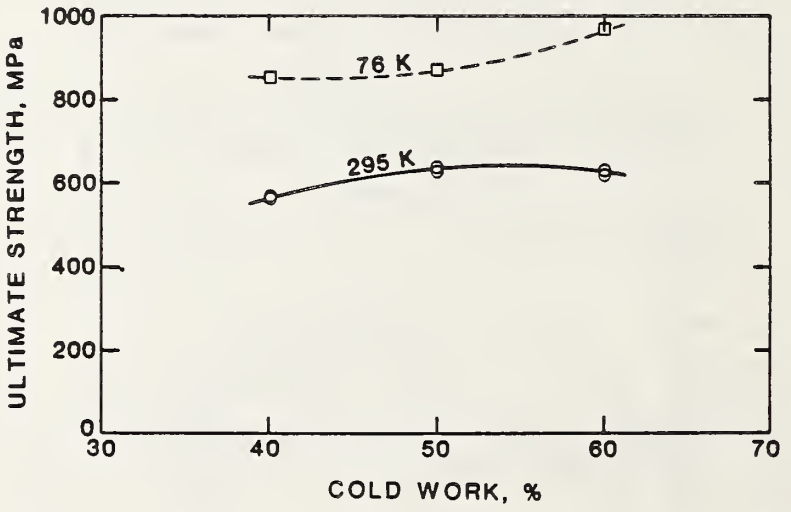

Figure 6. Ultimate tensile strength versus cold work at 295 and 76 K.

DISCUSSION

A mixing rule was proposed to enable predictions of laminate strength as a function of the strengths of the layers and their respective fractions of the thickness of the laminate.[2] This rule can also be applied to the modulus of elasticity. The mixing rule appears to overestimate the strengths measured in the tensile tests, as seen in Tables 1 and 2. The modulus data[3-4] and yield strength data[5-6] were obtained by extrapolating existing data.

The modulus was insensitive to cold work, as shown in Fig. 4, but it increased slightly as the temperature was decreased, as would be expected. The yield strength increased slightly with increased cold work at 295 K only (Fig. 5). This increase was not seen at 76 K, probably owing to thermally induced stresses caused by the difference in thermal expansion coefficients between the copper and stainless steel. Ultimate strength increased significantly with increasing cold work and decreasing temperature (Fig. 6). Elongation to fracture decreased slightly at 295 K with increasing cold work, as expected (Fig. 7). However, the elongation increased with increasing strength at 76 K. This may have been caused by the difference in the thermal expansivities, which affect the residual stress state in the laminate upon cooling.

Creep–fatigue data for the average of two tests for each cold-worked condition are shown in Fig. 8. More creep was observed as the cold work was increased, which was not expected. However, the fraction of stainless-steel thickness decreased as the cold work was increased (see Tables 1 and 2). Thus, with increased cold work, there was less stainless steel to support the loads, and more creep occurred. All specimens seemed to reach a degree of creep saturation after a large number of fatigue cycles.

CONCLUSIONS

In a copper–stainless-steel laminate, minor variations were observed in Young's modulus; these variations were probably due to specimen bending caused during the roll-bonding process. The yield strength increased slightly from 295 to 76 K at the lower cold-worked conditions. The ultimate tensile strength increased substantially from 295 to 76 K. At 76 K, fracture occurred at the ultimate strength. At 295 K, the fracture was arrested by the copper. The fatigue values were somewhat scattered, probably as a result of local bonding variations in the laminate. Creep seemed to saturate after a large number of fatigue cycles. The mixing rule provided a method to estimate composite behavior. However, the predictions were not conservative, so adjustments are required to improve the method.

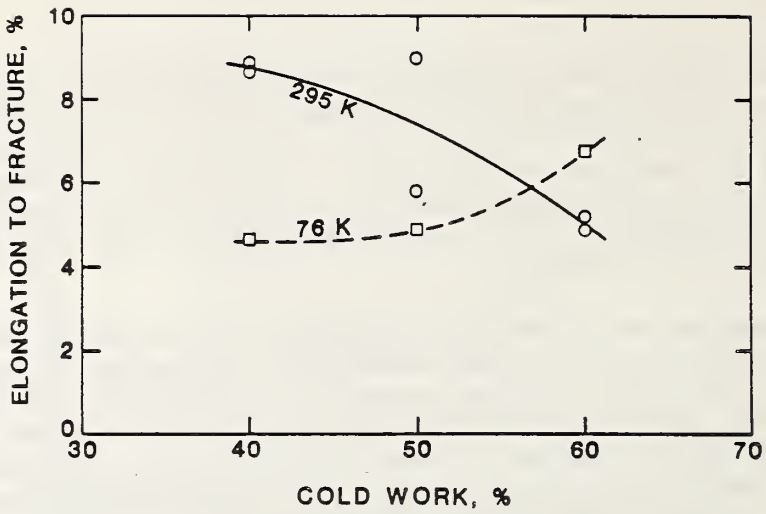

Figure 7. Total elongation to fracture versus cold work at 295 and 76 K.

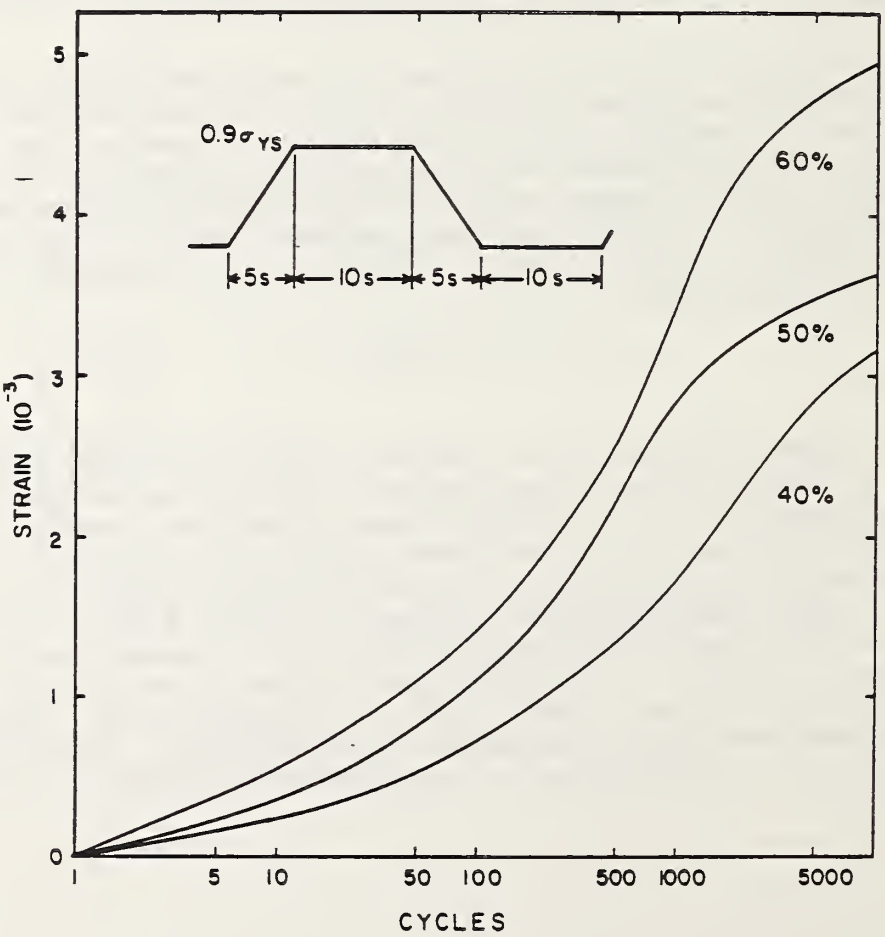

Figure 8. Creep–fatigue behavior at 40, 50, and 50% cold work at 295 K.

ACKNOWLEDGMENTS

This research was sponsored by the Office of Fusion Energy, U.S. Department of Energy. The authors are indebted to Dr. H. Becker, Massachusetts Institute of Technology, for the helpful discussions and for supplying the test specimens.

REFERENCES

1. Standard Methods of Tension Testing of Metallic Materials, ASTM E8-82, American Society of Testing and Materials, Philadelphia, 119 (1984).

2. H. Becker, M. Besen, E. Bobrov, J. Chen, and D. B. Montgomery, Structural Properties of Reinforced Copper, PFC/RR-86-12, Massachusetts Institute of Technology, Cambridge, Massachusetts (1986).

3. H. M. Ledbetter, Elastic constants of polycrystalline copper at low temperatures, Phys. Status Solidi 66:477–484 (1981).

4. H. M. Ledbetter and E. W. Collings, Elastic constant anomalies at the Néel transition in Fe–18Cr–3Ni–12Mn, Mater. Sci. Eng. 68:233–237 (1984–1985).

5. R. P. Reed, R. P. Walsh, and F. R. Fickett, Effects of Grain Size and Cold Rolling on the Cryogenic Properties of Copper, in "Advances in Cryogenic Engineering – Materials," vol. 34, Plenum, New York, 299–308 (1988).

6. D. T. Read and R. P. Reed, "Toughness, Fatigue Crack Growth, and Tensile Properties of Three Nitrogen-strengthened Stainless Steels at Cryogenic Temperatures," NBSIR 78-884, National Bureau of Standards, Boulder, Colorado, 91–154 (1978).

WELDING

WELDING PROGRAM

LEADER: T. A. Siewert
CONTRIBUTORS: C. N. McCowan, D. P. Vigliotti

OBJECTIVES

- Investigation of the metallurgical factors that affect the mechanical properties of stainless-steel weldments at cryogenic temperatures
- Contribution to the development of improved filler metals for welding stainless steels for use at 4 K
- Evaluation of the mechanical properties of weldments at 4 K
- Development of methods for detecting defects and evaluation of their significance in stainless steel weldments

RESEARCH HIGHLIGHTS

- In a study relating inclusions and fracture toughness, a yield strength of 991 MPa and a fracture toughness of 287 MPa·$m^{\frac{1}{2}}$ were measured for a gas metal arc weld, substantially higher than the 203 MPa·$m^{\frac{1}{2}}$ reported last year. The exceptionally high toughness in the Fe–18Cr–20Ni–5Mn–0.16N weld metal was achieved with a new welding procedure that decreases the oxygen content of the weld, in this case, to one-eighth that of a weld by other procedures. The lower oxygen content is related to smaller and fewer inclusions.

- A diagram was developed to predict the ferrite number (FN) in stainless steel welds. When it was evaluated with a database containing almost a thousand compositions, the diagram was substantially more accurate than the DeLong or Schaeffler diagrams. It is applicable from 0 to 100 FN and up to 10 wt.% manganese, 3 wt.% molybdenum, and 0.2 wt.% nitrogen. The new diagram is particularly useful for stainless steel welds in which fissuring resistance and fracture toughness must be controlled by the FN.

- Electron beam and laser welds were evaluated in two 25-mm-thick copper alloys, C10700 (Cu–0.08Ag) and C17510 (Cu–0.4Be–1.8Ni), candidate materials for use in the Compact Ignition Tokamak. A substantial drop in the yield strength of transverse tensile specimens occurred at both test temperatures, 76 and 295 K. By monitoring a series of 1-mm-wide regions in the gage length, we determined that the lower strength after welding was due to initial yielding in the very soft weld and HAZ regions.

- Yield and notched-fatigue strength were measured for stainless steel tube-to-flange welds at 4 and 295 K. Three flange materials, AISI 304L, AISI 316L, and 21Cr–6Ni–9Mn, were joined to 21Cr–6Ni–9Mn tube by gas tungsten arc welding. Welds with the 316L flange material had the best yield and fatigue strengths, close to that of the tube material, at both temperatures.

- An aluminum-deoxidized weld was compared with conventional silicon-deoxidized welds to clarify the role of inclusions in fracture. The inclusions in the aluminum-deoxidized weld were more resistant to void formation, but the poor strength–toughness combination (900 MPa–85 MPa·$m^{\frac{1}{2}}$) of this weld at 4 K is attributed to the large amount of residual aluminum in the matrix.

SUMMARY OF MECHANICAL PROPERTY MEASUREMENTS OF WELDS

Weld Alloy [designation]	Welding Process	Tensile	Charpy Impact	Fracture Toughness	Fatigue Crack Growth Rate	Report Volume* (page)
AUSTENITIC STAINLESS STEELS						
Fe-13Cr-20Ni-9Mn-2Nb	SMAW	I,II	I,II, VIII			I (159,169) II (299) VIII (29)
Fe-15Cr-12Ni-10Mn	SMAW	IV	IV,VIII			IV (453) VIII (29)
Fe-16Cr-15Ni-4Mo	SMAW	IV		IV		IV (275)
Fe-16Cr-16Ni-2Mo	FCAW	II		III	III,VI	III (155) VI (199)
Fe-16Cr-16Ni-4Mo	FCAW	IV	IV,VIII	IV		IV (275) VIII (29)
Fe-16Cr-35Ni-4Mn [330 modified]	SMAW	I	I,VIII	II		I (159) II (299) VIII (29)
Fe-17Cr-9Ni-Mn-N	SMAW	IX	IX			IX (217)
Fe-17Cr-16Ni-4Mo	SMAW	IV		IV		IV (275)
Fe-18Cr-11Ni-2Mo-N	EBW LBW	X X	X X	X X		X (299)
Fe-18Cr-16Ni-6.5Mn-2Mo	SMAW	IX	IX			IX (257)
Fe-18Cr-16Ni-9Mn-N	GMAW	III,IV	IV	III,IV	III,VI	III (155) IV (275,453) V (199)
Fe-18Cr-18Ni-2Mo-5Mn-N	SMAW	IV	IV			IV (453)
Fe-18Cr-20Ni-5Mn-N	GMAW	IX	IX			IX (247)
Fe-18Cr-20Ni-6Mn-0.3Nb	GMAW	IV	IV	IV		IV (275)
Fe-18Cr-20Ni-6Mn-0.2Ti	GMAW	IV	IV	IV		IV (275)
Fe-19Cr-12Ni-2Mo [316]	SMAW	II	II,VIII	II		II (315) VIII (29)
Fe-19Cr-12Ni-2Mo [316L]	EBW	IV		IV	IV,VI	IV (275,415) VI (199)
	GMAW	III,IV	III,IV, VIII	IV		III (155,195) IV (275) VIII (29)
	GTAW	III,IV	III,IV, VIII	IV		III (155,195) IV (275) VIII (29)
	SAW	III,IV, V	III,IV, V	III,IV	III,VI	III (155,195) IV (275,415) V (233) VI (199)

**Materials Studies for Magnetic Fusion Energy Applications at Low Temperatures:* NBSIR 78-884 (I); NBSIR 79-1609 (II); NBSIR 80-1627 (III); NBSIR 81-1645 (IV); NBSIR 82-1667 (V); NBSIR 83-1690 (VI); NBSIR 84-3000 (VII); NBSIR 85-3025 (VIII); NBSIR 86-3050 (IX); NBSIR 87-3067 (X).

SUMMARY OF MECHANICAL PROPERTY MEASUREMENTS OF WELDS, continued

Weld Alloy [designation]	Welding Process	Tensile	Charpy Impact	Fracture Toughness	Fatigue Crack Growth Rate	Report Volume* (page)
Fe-19Cr-12Ni-2Mo [316L], continued	SMAW	II,III, IV	II,VIII	II,III, IV	III,IV,VI	II (299,315) III (155,167) VI (199) VIII (29)
Fe-19Cr-12Ni-2Mo-N [316LN]	SMAW	II	II,VIII	II		II (299) VIII (29)
Fe-19Cr-16Ni-7Mn	GMAW	IV	IV			IV (453)
Fe-20Cr-10Ni [308]	SMAW	I	I,VIII			I (169) VIII (29)
Fe-20Cr-10Ni [308L]	FCAW	III		III	III,VI	III (155) VI (199)
	GMAW	III		III	III,VI	III (155) VI (199)
	SMAW	II,III	II,VIII	II,III	III,VI	II (299) III (155) VI (199) VIII (29)
Fe-20Cr-10Ni-N [308LN]	FCAW	IV		IV	IV,VI	IV (275,415) V (199)
Fe-20Cr-10Ni-9Mn-N	SMAW	I	I			I (159,169)
Fe-20Cr-16Ni-7Mo-2W	SAW	IV		IV		IV (275)
Fe-20Cr-34Ni-2Mo-Nb	SMAW	VII		VII		VII (253)
Fe-21Cr-6Ni-9Mn-N	SMAW	I,II	I,II			I (159,169) II (299)
AUSTENITIC STEELS						
Fe-15Mn-8Ni-1Mo-0.7C	SAW	VIII		VIII		VIII (15)
Fe-5Cr-25Mn-1Ni		V		V,VII	V,VI	V (233) VI (199) VII (245)
Fe-6.5Cr-25Mn-3Ni-1Mo	SMAW	V		V	V,VI	V (233,245) VI (199)
ALUMINUM ALLOYS						
Al-5Mg [5183]	GMAW	III		IV	IV	III (155,217) IV (323)
Al-5Mg-0.12Ti [5556]	GMAW	III		IV	IV	III (155, 217) IV (323)

**Materials Studies for Magnetic Fusion Energy Applications at Low Temperatures:*
NBSIR 78-884 (I); NBSIR 79-1609 (II); NBSIR 80-1627 (III); NBSIR 81-1645 (IV); NBSIR 82-1667 (V); NBSIR 83-1690 (VI); NBSIR 84-3000 (VII); NBSIR 85-3025 (VIII); NBSIR 86-3050 (IX); NBSIR 87-3067 (X).

FERRITE NUMBER PREDICTION TO 100 FN IN STAINLESS STEEL WELDS*

T. A. Siewert and C. N. McCowan
National Bureau of Standards
Boulder, Colorado

D. L. Olson
Colorado School of Mines
Golden, Colorado

To improve the accuracy of ferrite number (FN) prediction in stainless steel welds, a new diagram has been developed from a database containing more than 950 alloy compositions from worldwide sources. In accuracy, this diagram surpasses the DeLong diagram for the low-FN austenitic-stainless-steel compositions of the AISI 300 series, and it corrects a 2-FN bias detected for AISI type 309 stainless steel. The diagram is more accurate than the Schaeffler diagram for duplex stainless-steel alloys and ferrite contents to 100 FN. It is suitable for Mn contents to 10 wt.%, Mo contents to 3 wt.%, N contents to 0.2 wt.%, and Si contents to 1 wt.%. Changes in the primary solidification mode are indicated on the diagram; they appear to affect the FN response. Transitions in iso-FN line spacings may be caused by these mode changes.

I. INTRODUCTION

In many applications, the ability to control the delta-ferrite content of stainless steel welds is important. For example, the ferrite number (FN) is often used as an indicator of the resistance to fissuring (hot tearing) that occurs in many of the AISI 300-series stainless steels.[1] Fissuring decreases rapidly over a small range of ferrite contents in these primarily austenitic phase weld compositions, so an accurate predictor of the FN is necessary to ensure the minimum ferrite levels that will prevent cracking. Fissuring should not be avoided by

---

*Submitted to *Welding Journal*.

simply using materials with high FN values, since higher FN levels contribute to other undesirable behavior, such as an increased corrosion rate in certain environments.[2] Thus, there is incentive for keeping the FN in this limited range and for controlling the ferrite accurately.

At cryogenic temperatures, ferrite reduces the Charpy V-notch absorbed energy and the fracture toughness of stainless steels.[3-6] The response is as dependent on ferrite content as is fissuring, but it reacts in the opposite direction. To provide the appropriate balance of cracking resistance and fracture toughness, the ferrite content must be controlled in a narrow range. Cryogenic applications require the most stringent FN controls and justify a search for more accurate FN prediction.

These examples have all been in the 0 to 25 FN range. In the past ten years, we have seen the development of new duplex stainless steel compositions for service conditions under which the austenitic grades are unsuitable. As the name suggests, these alloys contain substantial amounts of both the austenite and ferrite phases, with the ferrite content being as high as 100 FN. For these alloys, Kotecki has recently shown relationships between the ferrite content and various mechanical properties, such as tensile strength and elongation.[7] So, in the high FN range also, it is important to control the ferrite content to achieve optimal weld properties. Unfortunately, fewer predictive diagrams have been developed for these compositions, and the data with which they were developed may not be accurate for today's compositions.

In the United States, the DeLong[8] and Schaeffler[9] diagrams are probably the most common methods for predicting the ferrite content of stainless steel welds. For both diagrams, a position on the diagram is determined from the composition and then related to a series of iso-ferrite or iso-FN lines. Both diagrams list the elements promoting the austenite phase along the vertical axis (as a term called Ni_{eq}) and the elements promoting the ferrite phase along the horizontal axis (as a term called Cr_{eq}). This nomenclature is based on naming the term after its primary component (Ni or Cr) and adding the other components, with appropriate coefficients to represent their relative power in promoting austenite or ferrite, to form an equivalent (Ni_{eq} or Cr_{eq}). The Schaeffler diagram (Figure 1) uses straight lines that pivot around a common focus to represent the amount of ferrite as volume percent over the range 0 to 100%.[9] The most recent version of the DeLong diagram (Figure 2) uses parallel lines to represent the amount of ferrite as FN over the range 0 to 18 FN.[8]

Earlier versions of the DeLong diagram represented ferrite in units of volume percent only. This recent version (Figure 2) was produced after the Welding Research Council (WRC) Subcommittee on the Welding of Stainless Steels promulgated a standard using the term ferrite number (FN) to define the ferrite content by its magnetic response. As a result, the DeLong diagram (now) contains both the FN and volume percent ferrite designations, and it indicates that the two measurement systems begin to diverge at ferrite contents near 8 FN.

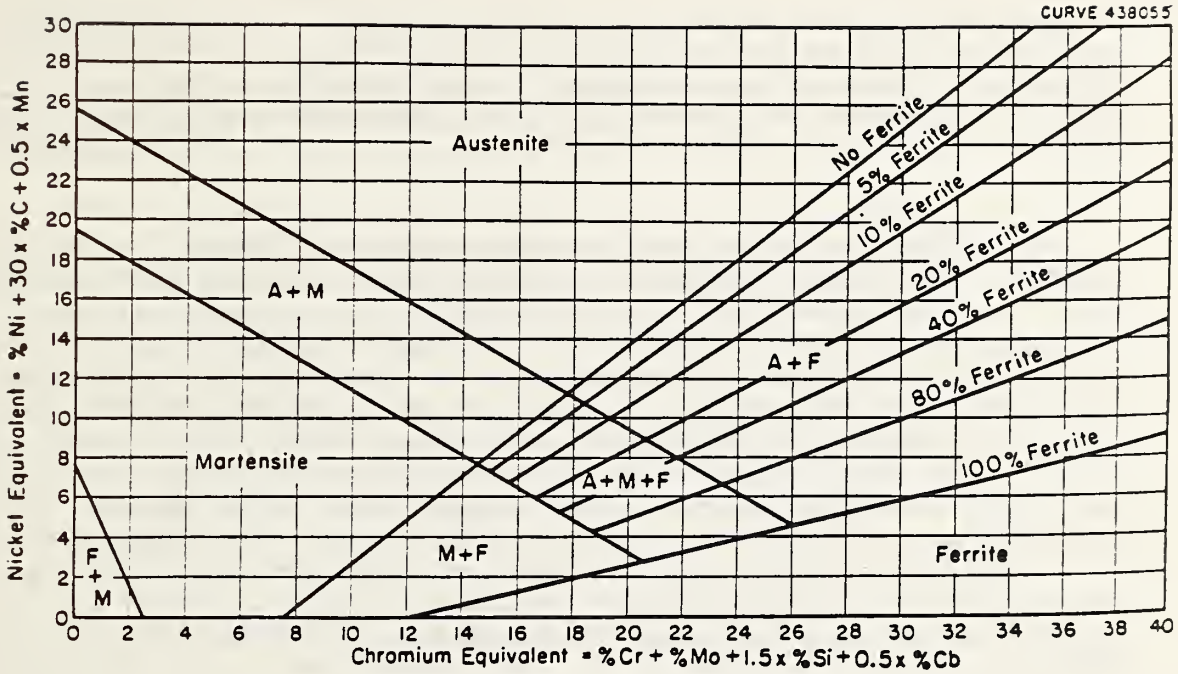

Fig. 1. The Schaeffler constitution diagram for stainless-steel weld metal.[9]

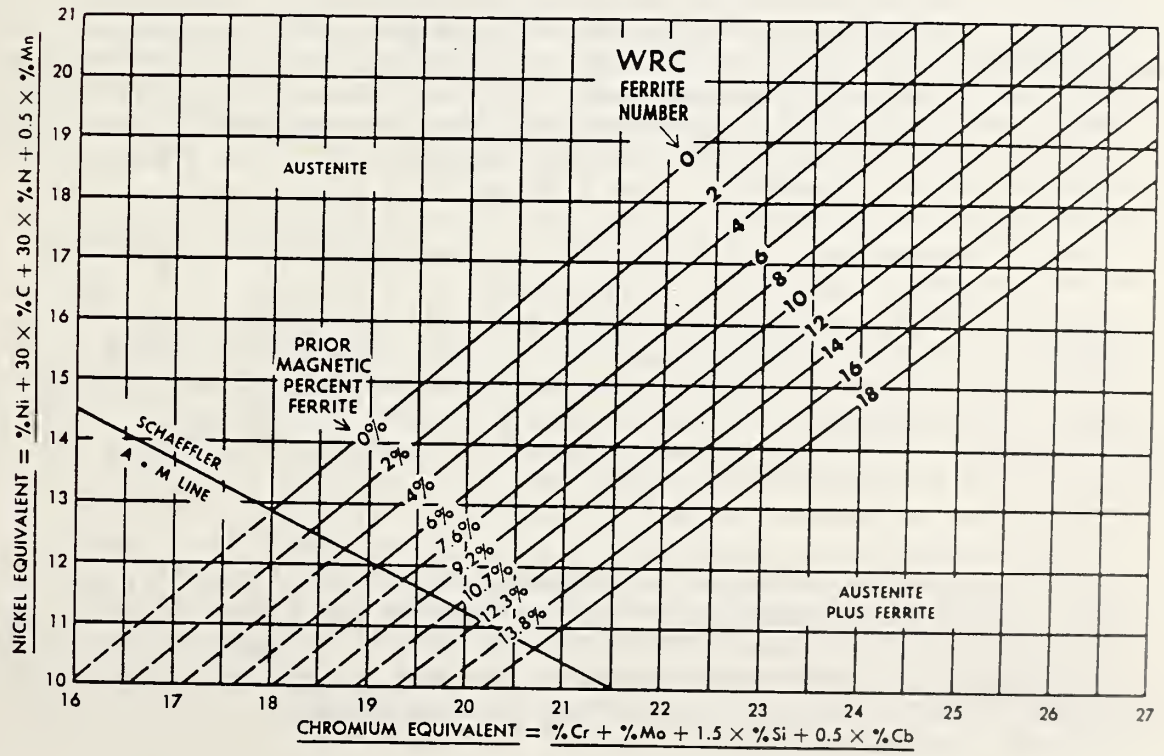

Fig. 2. The DeLong constitution diagram, revised January 1973 to convert it to the Welding Research Council's ferrite-number system for weld metals.[8]

The two diagrams differ only slightly in their representation of compositional effects on ferrite content. The Cr_{eq} expressions are identical in the two diagrams—even the coefficients are the same. The DeLong Ni_{eq} expression contains all the elements and coefficients of the Schaeffler diagram but adds a term to include the effect of nitrogen on FN.

The difference in the applicability of the two diagrams is substantial. The DeLong diagram is a finely tuned subset of the Schaeffler range, designed specifically for the AISI 300-series stainless steels containing small amounts of ferrite. Its widely accepted use with these alloys is documented by its inclusion in the American Welding Society filler metal specifications A5.4 and A5.9 and in the American Society of Mechanical Engineers (ASME) Boiler and Pressure Vessel Code. Prediction of FN for the compositions, such as the duplex stainless steels, that fall outside the range of the DeLong diagram seems to be the most common quantitative use of the Schaeffler diagram; however, its extension to fully ferritic compositions and the inclusion of martensitic regions provides much qualitative information about the general effect of alloying elements and the characteristic mechanical properties of alloy families.

Inaccuracies in both the DeLong and Schaeffler diagrams have become evident with the generation of new alloys and data. As a result, revisions of these diagrams have been proposed and several alternate diagrams have been developed.[10] The 0.5 coefficient for Mn is questioned by a number of researchers. Hull proposed a quadratic form indicating that Mn promoted austenite less as its content was increased, and actually promoted ferrite at very high levels.[11] Espy, in a study of stainless steels with up to 12.5 wt.% Mn and 0.31 wt.% N, concluded that Mn should not have a coefficient: its austenitizing potential could be better represented as a constant.[12] In a study of 41 specially formulated shielded-metal-arc electrodes with Mn levels gradually increasing to 13 wt.%, Szumachowski and Kotecki[13] also determined that the Mn austenitizing potential could be represented as a constant, but suggested a value slightly smaller than Espy's. From a matrix of 26 electrodes containing up to 10 wt.% Mn and 0.26 wt.% N, McCowan and coworkers concluded that Mn and N interacted in a complex manner that could be expressed best by $Ni_{eq} = Ni + 29(C + N) + 0.53(Mn) - 0.05(Mn)^2 - 2.37(MnN) + 0.94(MnN)^2 - 0.71$.[14] However, they also indicated that the effect of Mn could be adequately represented by a constant if a slightly poorer accuracy was accepted.

Other studies attempted to understand the effect of N. Espy reported a variable N coefficient, decreasing in value from 30 to 20 as the N content increases from 0.2 to 0.35 wt.%.[12] Others reported single-valued coefficients, ranging from 14.2 to 20.[11,15-18] Ogawa and Koseki reported a coefficient of 30 for FN but a coefficient of 18 for the effect of N on solidification mode.[17]

Recently Kotecki investigated the Si coefficient.[19] He found that the coefficient of 1.5, indicated by both the DeLong and Schaeffler

diagrams, overstates the effect. In a study of six welds spanning 0.34 to 1.38 wt.% Si, he determined a coefficient of 0.1, which was significant for a 68% confidence interval. Another recent study found the Si effect to be nonlinear; very small below 2 wt.% Si, but large at higher Si contents.[20]

Taken as a whole, these studies indicate that revisions of the DeLong and Schaeffler diagrams can substantially improve the accuracy of ferrite prediction for current stainless steel weld compositions.

Recent studies have emphasized that the solidification mode is more accurate than the FN for predicting the resistance to hot cracking.[21-23] These studies emphasize that the initial solidification structure (primary austenite or ferrite) directly determines the sensitivity to cracking by controlling the solubility of elements that promote cracking at these temperatures. These three studies contain data on both FN and the primary solidification mode. Incorporation of these data into the database for this study enabled comparison of the two types of data.

The goals of this study were 1) to develop a database containing recent FN data and new compositions, 2) to evaluate the DeLong and Schaeffler diagrams with these data, 3) to determine which elements were not being fit properly, and 4) to develop an improved predictive diagram that was continuous over the range 0 to 100 FN (roughly equivalent to 65 vol.% ferrite). Ideally, this diagram would predict the ferrite content of the conventional 300-series stainless steels with at least the same accuracy as the DeLong diagram and duplex steels with at least the same accuracy as the Schaeffler diagram, and it would be suitable for new alloys containing extended compositional ranges. It would also include primary solidification-mode data on the predictive diagram to reveal relationships to the FN response.

II. DATABASE DEVELOPMENT

The approach to the development of the database was (1) to gather a large sample of data for each of the common alloys that are now predictable by the DeLong diagram to ensure that these alloys would be predicted accurately by the new diagram, and (2) to include data of many special alloys to determine the limits of applicability and interactions.

Most of the data were obtained from members of the WRC Subcommittee on Welding of Stainless Steel. The nine sources of data included electrode manufacturers and research institutes, as well as archival journals. The data well represented the common 300-series stainless steel compositions: types 308, 308L, 309, 309L, 316, and 316L. These data provided a good basis for evaluating the accuracy of the diagram and comparing scatter within and among the various sources. Other data represented duplex stainless steel compositions, experimental compositions designed to evaluate extended ranges for certain elements, and other new alloys. These data were used to determine element interactions

and whether the behavior in the duplex range was a smooth extension of the behavior in the low FN range.

From the data sources, we requested an FN measurement by the procedure specified in AWS A4.2[24] or by the procedure developed by Kotecki[25] for extending the FN range to duplex alloys. The small fraction (approximately 1%) of the data for high-ferrite content alloys that was in volume percent was converted to FN using Kotecki's procedure.[25] Matching each FN determination, we requested a complete chemical analysis specifically including C, Mn, Si, Cr, Ni, Mo, Ti, Nb, and N. These data have been listed in the appendix to another report.[26] The compositional ranges in this database are summarized by element in Table 1.

Table 1. Compositional Range for Various Elements in the Database.

Element	Range (wt. %)
C	0.01 – 0.15
Mn	0.4 – 12
Si	0.1 – 1.3
Cr	15 – 32
Ni	5 – 25
Mo	0 – 7
N	0.03 – 0.9
Nb	0 – 0.9
Ti	0 – 0.1

Most of the data were received from manufacturers of welding electrodes, who had developed these data to certify that their products met the customers' requirements. Since specifications controlled the analysis and measurement techniques and these specifications contained limits for the critical parameters, the resulting data were quite consistent. This precluded the variation in the FN of a given composition that David et al. observed as the cooling rate was varied over several orders of magnitude.[27] In fact, the great majority of data were produced with shielded metal arc electrodes conforming to AWS specification A5.4. Such uniformity in the electrodes, welding process, welding procedure, and

measurement reduces variations in FN due to these variables and permits a better fit of the data. Conversely, the predictive equation does not consider these variables, and their effect must be determined before the equation can be used to estimate the FN of welds produced under other conditions.

Although the procedure developed by Kotecki for measurement of FN[24] can be applied to fully ferritic alloys, they are outside the scope of this study. This study was limited to about 100 FN since few data were available above this level (almost none were supplied for the database), and there does not seem to be a need to predict above 100 FN at present.

Some of the data included primary solidification mode information following the nomenclature of Suutala[21] (austenitic, austenitic–ferritic, ferritic–austenitic, and ferritic). These were projected on the FN predictive diagram for comparison of mode changes with iso-FN lines.

To evaluate the existing diagrams in the most careful manner and to facilitate the location of errors, the database was divided into groups, ten of which are listed below:

Group	Description	Cases
1.	types 308 and 308L	220
2.	types 309 and 309L	129
3.	types 316 and 316L	139
4.	FN < 18	796
5.	FN < 18, and Mo < 3 wt.%	724
6.	FN < 18, N < 0.1 wt.%, and Mo < 3 wt.%	652
7.	FN < 18, N < 0.1 wt.%, and Mn < 3 wt.%	662
8.	FN < 18, N < 0.1 wt.%, Mn < 3 wt.%, and Mo < 3 wt.%	605
9.	FN < 30, Nb > 0	443
10.	FN > 18	126

By comparing the quality of the fit of these groups with the fit of the entire database, we were able to determine the compositional range over which the elements could vary without degrading the accuracy of the predictive diagram. Similarly, these groups could be used to compare the effect of the various elements in the new and old diagrams.

III. PROCEDURE

A variety of statistical representations were used to evaluate the existing diagrams and the new expressions. To evaluate the existing diagrams, relative-frequency histograms were used. The measured FN was subtracted from the FN predicted by the diagram, and the difference (ΔFN) was plotted versus the error class intervals (different levels of error). A perfect fit would have resulted in a delta function centered at zero. The width of the distributions of the actual data around zero provided a measure of the variability, whereas an off-center peak revealed a bias.

The development of a new diagram began with a multiple linear regression, with FN as the dependent variable and the various elements that affect the FN as independent variables. The process has been described previously.[6] Briefly, it consists of the selection of the variable (element) that most strongly determines the FN and production of a predictive equation. The program then chooses the next most influential variable and develops a new equation. The process is repeated in a stepwise manner until the addition of further terms will not statistically improve the prediction of FN. The coefficients for the various elements in these equations were compared with the coefficients in the existing diagrams. After evaluating the various groups of data individually, differences in their coefficients could be used to determine which elements and compositions were the dominant sources of scatter in the overall predictive diagram.

Next, the coefficient of each element was checked for accuracy. Our approach was similar to a technique reported by Szumachowski and Kotecki.[13] To evaluate the various coefficients that have been suggested for Mn, they developed a term, ΔNi_{eq}, by subtracting from the measured FN value the contributions of all other elements and plotting this term versus the concentration of Mn. This ΔNi_{eq} term was effectively the combination of the response of the FN to one particular element (Mn) confounded with the random error in the data. When they were unable to resolve a slope for the data, they concluded that Mn had no effect.

Our stepwise linear regression program produced a file of the residuals (error left after the fitting program was finished) for the data. We plotted this versus the various elements that had not met the selection criteria of the regression program. For the elements that had been selected by the regression program, we added the residuals to the product of the element concentration and the selected coefficient. We called this term ΔNi_{eq} (or ΔCr_{eq} if the element functioned as a ferritizer) since it contains the same information as the term used by Szumachowski and Kotecki,[13] even though it was generated in a slightly different manner. The slope of the best-fit line through the ΔNi_{eq} or ΔCr_{eq} versus element concentration data was the coefficient for the element. This technique allowed us to evaluate the quality of the fit and to search for nonlinear behavior. By allowing various ranges of other elements, we also searched for element-interaction effects.

When we had incorporated the changes indicated by this technique into our predictive equation, we used the equation to produce an FN map. The map consisted of a blank FN diagram; its axes consisted of the Ni_{eq} and Cr_{eq} from our best linear equation. The computer calculated a position for each datum from the Ni_{eq} and Cr_{eq} expressions, and identified that point by the measured FN. The program created a map by linear interpolation between measured FN values and then generated iso-FN contour lines to represent the data. This technique enabled us to separate the nonlinear response of the individual elements over the entire range of the diagram from the nonlinear response in a specific region of the

diagram (i.e., to improve the fit by using either nonlinear coefficients or curved and unevenly spaced iso-FN lines). The difference, ΔFN, between measured and predicted FN, was plotted as an error bar.

As a final check on the accuracy of the diagram, the ΔFN values from the mapping program were plotted versus the element concentrations, as was done after the linear fit by using the procedure for the ΔNi_{eq} and ΔCr_{eq} terms. By comparing these plots to the ΔNi_{eq} and ΔCr_{eq} plots, we could assure ourselves that the mapping procedure produced a diagram that was at least of the same quality as the linear equation and determine whether any nonlinear behavior could now be resolved.

The solidification-mode data were also plotted on the map to relate the solidification mode to the FN behavior.

IV. RESULTS AND DISCUSSION

A. *Construction of a New Diagram*

To determine more accurate representations of the FN potential for the type 308, type 309, and type 316 alloys, the multiple linear regression technique was applied to each data group. Three predictive equations were generated:

for 308 type alloys,

$$FN = -25 + 2.8(Cr + 0.9Mo) - 1.8(Ni + 48C + 30N); \quad (1)$$

for 316 type alloys,

$$FN = -15 + 2.2(Cr + 3Mo) - 2(Ni + 40C + 30N); \quad (2)$$

for 309 type alloys,

$$FN = -40 + 3.6(Cr + 0.3Mo) - 2(Ni + 55C + 23N). \quad (3)$$

The R^2 values (a statistical measure of the fit that approaches 1 with better fits) for these three equations were 0.65, 0.84, and 0.68; the standard deviations of the residuals were 1.5, 1.2, and 1.6 FN respectively. The Cr_{eq} and Ni_{eq} terms are the quantities in parentheses with the various elements in units of weight percent. The differences in the coefficients for the elements and the Cr_{eq} and Ni_{eq} terms are due to differences in the behavior within the alloy range, as well as to difficulties in fitting a line to data that are in a small cluster. Because of inaccuracies due to data clusters, these equations are not recommended for general use, but the equations do point out that each alloy range generates a characteristic set of coefficients.

The differences in the equations also emphasize that an empirically developed predictive diagram developed for many alloys can only approximate the behavior of a specific alloy group. Until we can develop a

model that truly represents the physical phenomena of the ferrite transformations, we must use a variety of fitting constants and statistical techniques to develop a diagram that provides predictions of acceptable accuracy. Although the optimum coefficients for each alloy group are different, the general equation forms are quite similar. This suggests that a single equation with compromise values for the coefficients might be able to predict the FN with an acceptable degree of accuracy.

Next, we processed the data of group 8 (FN < 18, N < 0.1 wt.%, Mn < 3 wt.%, and Mo < 3 wt.%) through the multiple linear regression program. The group 8 data cover a broad range of compositions and produced equivalents with a range of applicability equal to that of the DeLong diagram. From group 8, we excluded the data for FN < 1 and the austenite–ferrite (AF) solidification mode, since we anticipated nonlinearities due to ferrite formed mechanically during surface preparation and in differing solidification modes. The predictive equation, for group 8 alloys and alloys with FN > 1, and solidifying in the ferrite–austenite (FA) mode,

$$FN = -18 + 2.9(Cr + Mo + 0.3Si) - 2.6(Ni + 35C + 20N + 0.3Mn), \quad (4)$$

is analogous to the DeLong diagram. For this equation, R^2 is 0.78, and the standard deviation of the residual is 1.6 FN. These parameters are similar to those for the alloy groups considered above and suggest that one equation can provide a fairly accurate prediction over a range of compositions. This equation has coefficients similar to those in equations 1 through 3; in fact, it is almost the average of the behavior for the three alloy groups. In equation 4, the coefficients of C and N within the parentheses are smaller, but when multiplied by the coefficient outside the Ni_{eq} parentheses, the values are close to those of equations 1 through 3. The main difference is the larger effective coefficient for Ni, 2.6 as compared to 1.8 or 2. Equations 1 through 4 all indicate that the effect of C is greater than that of N, unlike the equal effects predicted by DeLong. The C/N coefficient ratios are 1.6, 1.3, 2.4, and 1.8 for these equations, respectively. Similar C/N coefficient ratios have been found in other FN studies; a ratio of 1.5 is used in the Hammar solidification equivalents.[10,12,14,15]

Equation 4 is the best fit for a linear regression model, that is, an arithmetic combination of linear terms producing a diagram with equispaced and parallel lines. The following subsections investigate the possibility of improving the prediction when these requirements are relaxed.

1. *Changes in Nickel and Chromium Equivalents*

Compositional terms defined by the best-fit linear equation (equation 4) were evaluated by using ΔNi_{eq} and ΔCr_{eq} plots described in the procedure. Although the technique was intended primarily to find second-order or other nonlinear behavior, it also confirmed that the coefficient determined during the linear regression program was the best line through the data. We did note the existence of some interactions. Comparison of

ΔCr_{eq} for Cr and Mo plots revealed that Cr could be given a coefficient of 1 and possess little scatter when the Mo content was less than 3 wt.%. For higher Mo contents, the behavior was substantially different, with a level of scatter that precluded determination of a mathematical representation.

We were unable to confirm the nonlinear trends reported for Mn (Hull[11]) or Mn–N (McCowan et al.[14]), but unless these trends were of substantial magnitude, their effects would have been hidden by the scatter in the data collected from many sources. The ΔNi_{eq}–Mn plots did indicate that scatter about the 0.3 slope expressed for Mn in equation 4 depended on Mn and N contents. The effect is relatively small (about 3 FN at 10 wt.% Mn), however, and not statistically significant at an F level of 4 (roughly corresponding to a 95% confidence level). In addition, manganese was often chosen as a ferrite stabilizer when the duplex stainless steel data (group 10) was evaluated. For these reasons, a Mn term is not included in the Ni_{eq}.

Since the DeLong and Schaeffler diagrams include coefficients for Si and Nb, the ΔCr_{eq} plots for these elements were of particular interest. When welds having reported Nb contents were used (Group 9), the plot revealed a slope corresponding to a coefficient near 0.7. The absence of the 0.7-Nb term causes a 2-FN bias, so the term should be added to the Cr_{eq} to adjust for the Nb effect.

When the ΔCr_{eq} is examined for a Si effect, a slight trend is also evident. For equation 4, a coefficient of 0.3 was determined for Si, but as was the case for Mn, the statistical significance of the Si term was low. When this coefficient is multiplied by the expected range in Si content and converted to ΔFN, the value is near 1 FN. The small statistical significance of this value combined with the limited range in Si contents caused us to exclude it from the predictive diagram.

The ΔCr_{eq} plot for Ti was also examined for a coefficient or interaction with N or C. No clear relationships could be resolved.

Although no nonlinear terms could be resolved and used to refine the Ni and Cr equivalents in the FN equation, the levels at which the scatter increased (3 wt.% for Mo, 3 wt.% for Mn, and 0.1 wt.% for N) were used to evaluate the FN diagram.

2. *Mapping*

After confirming that they could not be improved by the use of nonlinear or interactive terms, the Ni and Cr equivalents were used with a mapping program, which relaxed the restriction of parallel and equispaced lines. The resulting diagram using the entire database is shown in Figure 3. Straight lines fit well in the Ni_{eq} range of 9 to 17 and in the Cr_{eq} range of 17 to 30. Above a Ni_{eq} of 17, there was some evidence of curvature (dotted lines), but a scarcity of data prevented deduction of the true behavior. The appearance is very similar to that of the Schaeffler diagram in Figure 1.

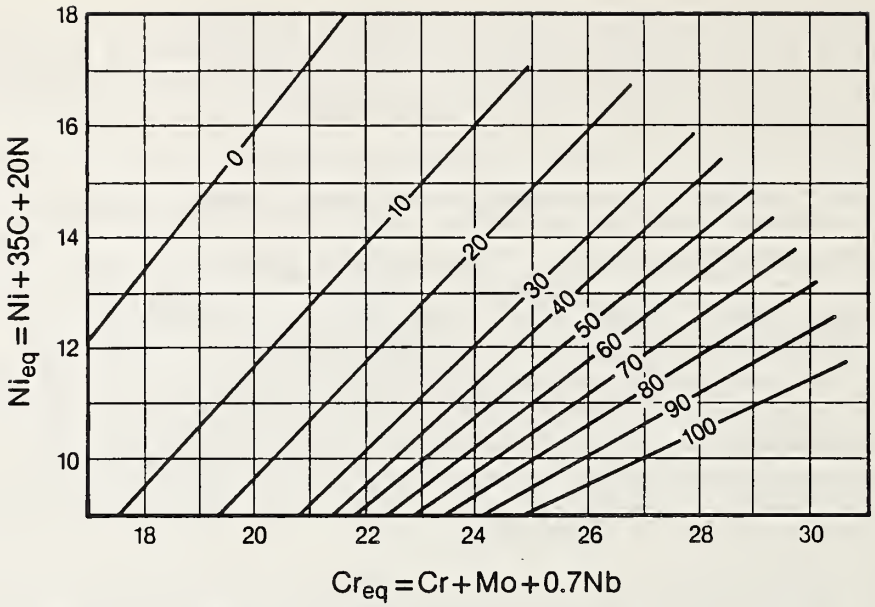

Fig. 3. New diagram, produced by mapping program.

The diagram contains equispaced parallel lines between FN values of 4 and 12, explaining the success of the DeLong diagram in the 0 to 18 FN range with parallel lines. The rapid compression of line spacing above an FN of 12 and the rotation of the lines above an FN of 35 explains why the DeLong diagram could not be extended to duplex compositions. The compression of line spacings and rotation at these higher FN lines explains why the Schaeffler diagram has provided the best estimate of FN in this region. To determine whether the new diagram represents the FN more accurately than the Schaeffler or DeLong diagrams, quantitative comparisons were made.

B. *Evaluation of the New Diagram*

The new diagram should have been evaluated using an independent database. However, all available data were used in the development of the new diagram. Since the data were gathered from many sources and are assumed to represent current alloy production, they were used to compare the accuracy of the new diagram to the DeLong and Schaeffler diagrams. Because these older diagrams have distinctly different ranges, they will be considered separately.

1. *Comparison to the DeLong Diagram (0 to 18 FN)*

Since the DeLong diagram was developed for use with the conventional 300-series stainless steel compositions, the measured FN values of the type 308, 309, and 316 data groups were compared with those predicted by the DeLong diagram. Relative-frequency histograms of the error distributions are included as Figures 4 through 6. Since each of the groups

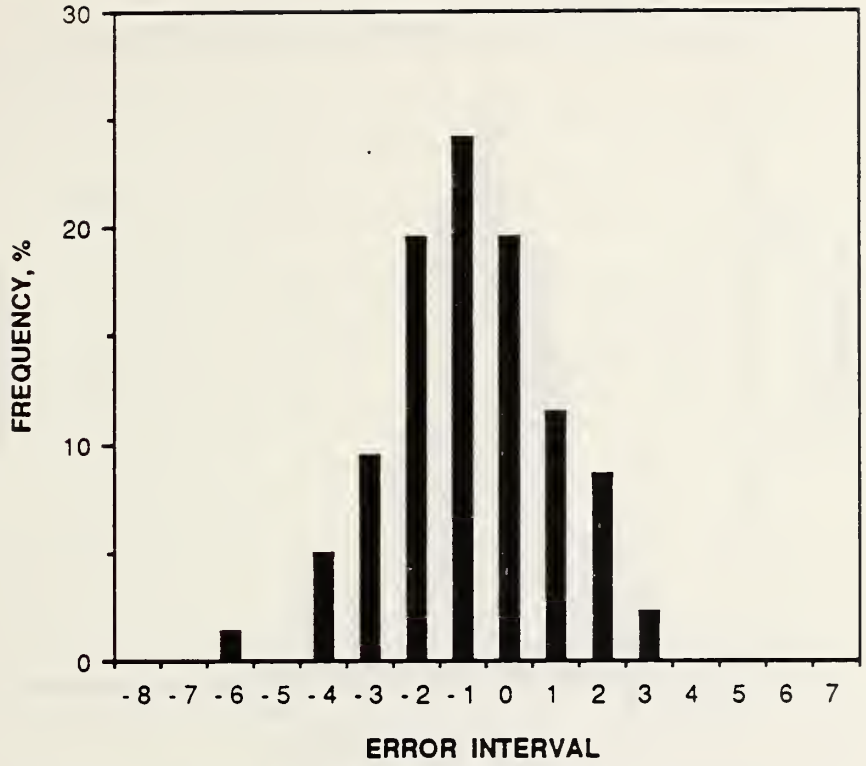

Fig. 4. Relative frequency histogram of the error distribution for the type 308 data as evaluated by the DeLong diagram.

contains the data for over 100 welds collected from many sources, each is considered to be representative of current alloy production. The type 308 and 316 data (Figures 4 and 6) exhibit the expected Gaussian error distribution centered on zero with a standard deviation near 2 FN. The type 309 data (Figure 5) exhibit a similar distribution shape and standard deviation, but they are centered near −2 FN. Such a bias in the mean indicates that predictions based on the diagram are inaccurate for these type 309 compositions and do not meet the ± 3 FN accuracy reported for 90% of the data during the development of the DeLong diagram.[8] Separation of the data by source confirmed the same bias for each. Only 43% of the type 309 data was predicted within a ± 2.5 FN error. For the type 308 and 316 data groups, 82 and 91% of the welds were predicted within a ± 2.5 FN error, respectively. In comparison, the new diagram predicted 88% of the type 308, 91 percent of the type 316, and 92% of the type 309 data within a ± 2.5 FN error. So, the new diagram is more accurate, especially for the type 309 compositions.

For a broader, more comprehensive evaluation, all the data that had an FN less than 18 (data group 4) were evaluated. Both the DeLong diagram and the new diagram were used to compute the FN for these compositions. Again, relative-frequency histograms were used to search for bias or a non-Gaussian shape in the error distribution: The histogram shapes

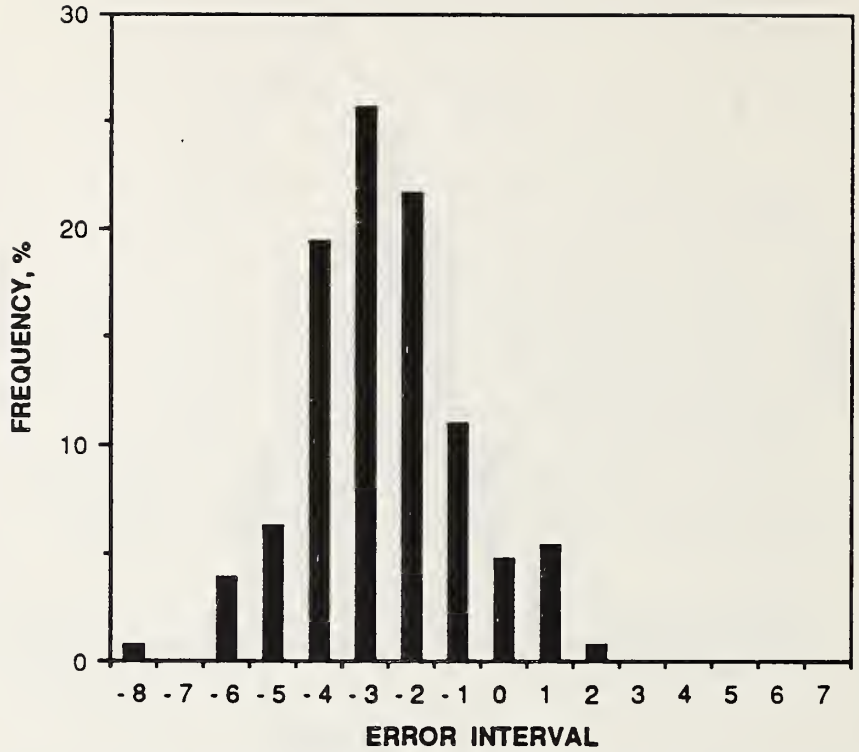

Fig. 5. Relative frequency histogram of the error distribution for the type 309 data as evaluated by the DeLong diagram.

were normal; no bias was found. For all the data with an FN less than 18, the DeLong diagram predicted 66% with an error less than 2.5 FN, whereas the new diagram predicted 84%.

Although the comparisons made between the relative errors found for DeLong and the new diagram are useful, error magnitudes determined for the DeLong diagram here should not be compared to the accuracy statement (90% of data within ± 3 FN) in that report.[8] The DeLong diagram was developed and evaluated on data from a single laboratory using procedures more stringent than those in AWS A4.2. This database contains additional error due to interlaboratory dissimilarities in welding procedures and specimen preparation techniques. Another complication in the evaluation is that some of the data were outside the Cr_{eq} boundaries of the published DeLong diagram. Since we chose to evaluate the DeLong diagram only over its reported range, we excluded these data. Similarly, for the proposed diagram, computer mapping restrictions limited the Cr_{eq} range and excluded a small portion of the data. Manual evaluation of these data revealed that they fit the extension of the reported lines, but the scarcity of the data and difficulty of manual calculations caused us to limit the scope of the diagram to that reported. The number of cases considered for the two diagrams is included in Table 2.

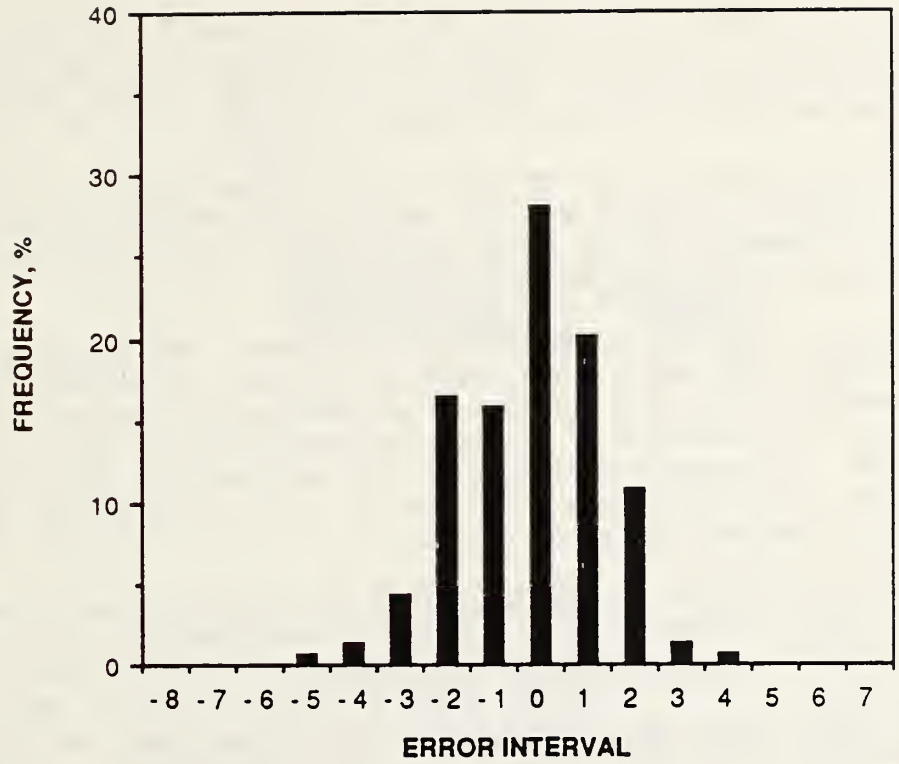

Fig. 6. Relative frequency histogram of the error distribution for the type 316 data as evaluated by the DeLong diagram.

Because this study and others have shown the behavior of some elements to be interactive and therefore the cause of some scatter, the diagrams were evaluated using data groups 5–8, which had several different combinations of compositional restrictions. Their evaluation is also summarized in Table 2.

The restriction of the Mo content to less than 3 wt.% resulted in a 2% improvement in the accuracy of the DeLong diagram and a 4% improvement in the accuracy of the proposed diagram. This significant improvement in the proposed diagram is the result of either a Cr–Mo interaction, which is excluded when Mo levels were limited to 3 wt.% during the ΔCr_{eq} analysis, or incomplete dissolution of the high-melting-point Mo contained in the electrode coating.

Smaller improvements are noted as the N content is restricted to less than 0.1 wt.% in group 6 or the Mn content is restricted to less than 3 wt.% in groups 6 and 7. The best fit for both diagrams occurs for group 8, when all four restrictions (similar to the reported range of applicability of the DeLong diagram) are invoked. However, the improvement over group 5 is so slight for the proposed diagram that the group 5 restrictions provide the best combination of accuracy and coefficient simplicity. Scarcity of data at very high element concentration levels does

suggest some further restrictions: Mn < 10 wt.% and N < 0.2 wt.%. With these restrictions, the proposed diagram has better than an 88% chance of predicting the FN with an accuracy of ± 2.5 FN, a value substantially better than the 68% chance for the DeLong Diagram.

To confirm the validity of these restrictions and to search for nonlinear behavior, the ΔFN for the proposed diagram was plotted versus the various elements. These plots more clearly show the trends seen during the ΔNi_{eq} and ΔCr_{eq} analyses.

The plot of ΔFN versus Cr content in Figure 7 has a larger FN range to include more data and a restricted carbon range to reduce the scatter. The increased scatter with increasing Mo content is clearly visible. Either a Cr–Mo interaction or incomplete dissolution of Mo would explain this scatter. No reduction in scatter was apparent for Mo limits lower than 3 wt.%. This reinforces the value of restricting the Mo content to 3 wt.% for increased prediction accuracy.

In the plot of ΔFN versus Mn content in Figure 8, the Mo content is below 3 wt.%, the FN is below 30, and the Ni content is above 8 wt.%. The divergence in the Mn response is evident for the two levels of N at Mn levels above 6 wt.%. At high Mn and N contents, little error in predicted FN values from the new diagram would be expected. For high Mn and low N contents, however, Mn appears to have a slight ferrite stabilizing effect. The error is much smaller than that for the Cr–Mo interaction. Limiting the Mn to 10 wt.% was dictated by the scarcity of data above this value.

Table 2. Comparison of the Accuracy of the DeLong Diagram and the Proposed Diagram for Various Data Groups.

Data Group	Description*	Error Less than ± 2.5 FN (%)		Cases Used	
		DeLong	Proposed	DeLong	Proposed
4	FN < 18	66	84	747	723
5	FN < 18 and Mo < 3	68	88	706	660
6	FN < 18, Mo < 3, and N < 0.1	68	87	643	606
7	FN < 18, Mn < 3, and N < 0.1	69	85	635	622
8	FN < 18, Mn < 3, Mo < 3, and N < 0.1	71	89	601	573

*element concentrations in wt.%

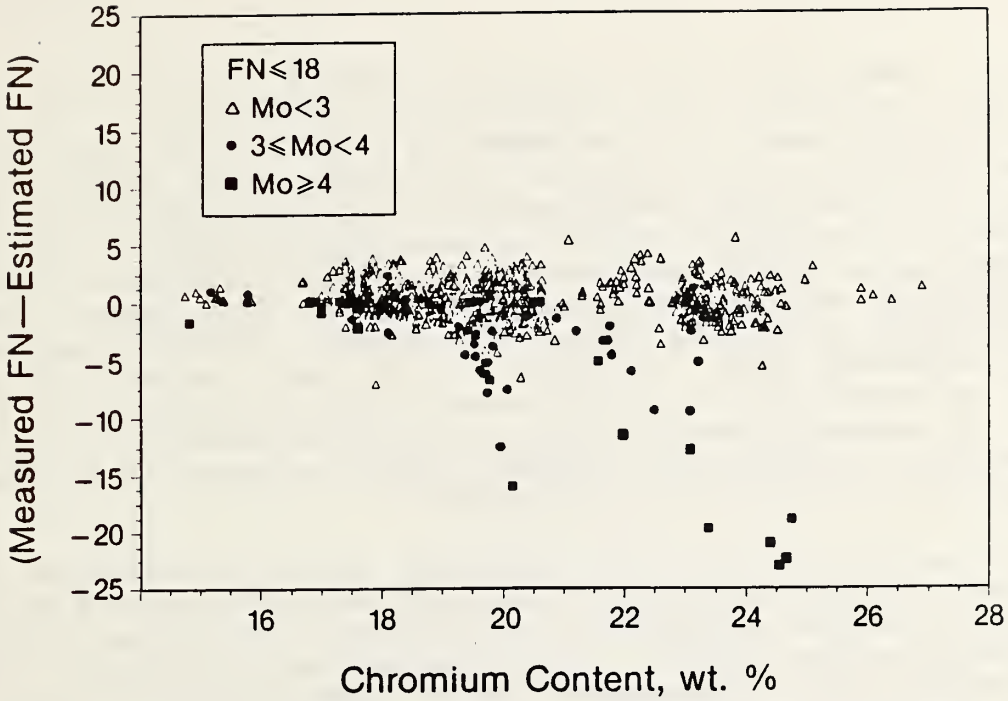

Fig. 7. Plot of ΔFN versus Cr content for the new diagram indicating a Cr–Mo interaction.

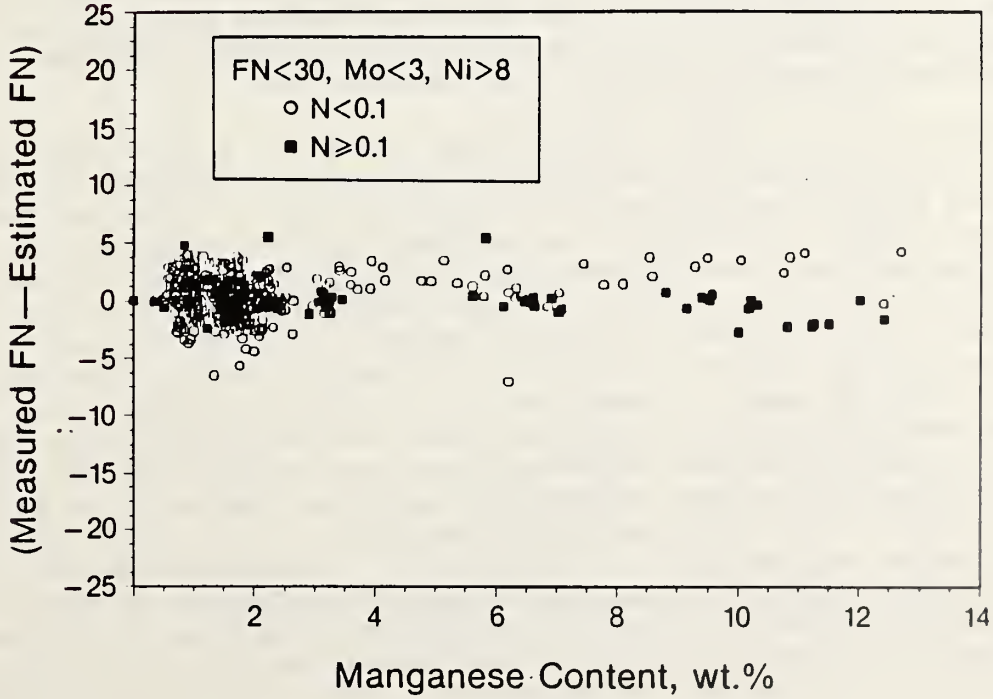

Fig. 8. Plot of ΔFN versus manganese content for the new diagram indicating a Mn–N interaction.

2. *Comparison to the Schaeffler Diagram (0 to 100 FN)*

The full range of ferrite content is covered by the Schaeffler diagram (Figure 2), but this diagram is in volume percent ferrite rather than FN. So the FN data were converted to volume percent ferrite by the procedure of Kotecki.[25] Thus we compared the error for the Schaeffler diagram (using this database converted to percent ferrite) with the error for the proposed diagram (using this database in FN). However, comparison of these two relative-frequency histograms is difficult because they are in different units. To bring the error class intervals into agreement, we assumed that 1% ferrite error is approximately equal to 1.5 FN error, a reasonable average for the range of the database. In this way, we produced comparable class interval widths to enable a more direct comparison of error in the two diagrams.

Since the addition of a N coefficient was one of the factors in the wide acceptance of the DeLong diagram, we also prepared a modified Schaeffler diagram containing N. Using DeLong's coefficient of 30, we fit the Schaeffler diagram to the entire database and obtained a 0.05 wt.% offset term. This meant that the N content should be reduced by 0.05 before being multiplied by 30 and added to the Ni_{eq}.

The proposed diagram and the Schaeffler diagram are compared in Table 2 for two FN ranges. For FN values greater than 18, the Schaeffler diagram is substantially less accurate than the proposed diagram. Examination of the error histograms revealed that the error for the new diagram had a Gaussian shape centered on zero, whereas that for the Schaeffler diagram was skewed but centered on zero.

For FN values smaller than 18, the Schaeffler diagram is substantially less accurate than the proposed diagram and somewhat less accurate than the DeLong diagram (Table 3). Again, the error histogram for the proposed diagram was Gaussian and centered on zero, while the error histogram for the Schaeffler diagram was centered on zero but skewed. For FN values smaller than 18, the addition of the N term improved the accuracy of the (revised) Schaeffler prediction to 70% (greater accuracy than the DeLong Diagram, but still less accurate than the proposed diagram in this FN range). Comparison of the three error histograms (proposed, revised Schaeffler with the N term, and DeLong diagrams) indicated the proposed diagram was characterized by a Gaussian shape centered on zero, whereas the revised Schaeffler diagram was characterized by a smaller skew to one side, and the DeLong diagram was characterized by a distribution not centered on zero (biased). It appears that the DeLong diagram improved on the Schaeffler diagram by adding the N term and reducing the skewed distribution for FN < 18. The proposed diagram improves on the DeLong diagram by eliminating the bias and choosing new coefficients that narrow the standard deviation of the error histogram.

Table 3. Comparison of the Accuracy of the Schaeffler Diagram and the Proposed Diagram.

Data Group Description	Error Less Than ± 9 FN (%)		Error Less Than ± 2.5 FN (%)		Cases Used	
	Schaeffler	Proposed	Schaeffler	Proposed	Schaeffler	Proposed
FN > 18	35	70	—	—	124	125
FN < 18	—	—	52	84	771	740

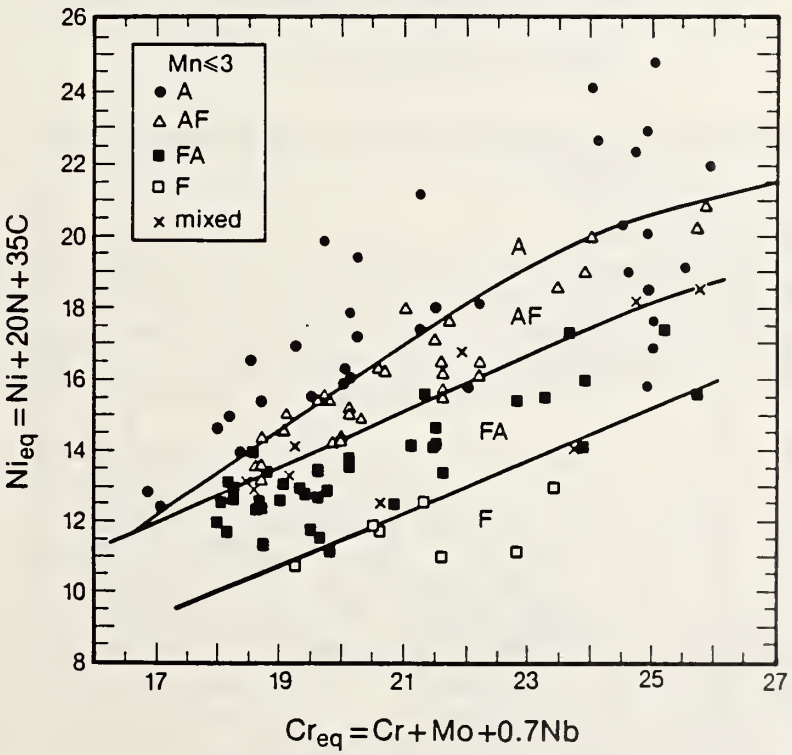

Fig. 9. Solidification-mode data on the coordinate axes of the new diagram.

D. *Solidification Mode*

Hammar[15] and Suutala[21] evaluated and discussed the use of a predictive equation for the boundaries between the various solidification modes. Suutala's solidification data, along with data from Kujanpaa[23] and Ogawa[17] were used in this study to evaluate solidification-mode boundaries for the proposed FN diagram. When the solidification mode was plotted on our Ni_{eq} and Cr_{eq} coordinate axes, the separation between the modes was very distinct (Figure 9), perhaps as good a separation as with the Hammar-Suutala coordinate axes (Figure 10), which were designed specifically for solidification-mode separation. This result indicates that the dependence of high-temperature solidification behavior on composition is similar to the dependence of the amount of ferrite retained to room temperature (FN). Because of the good separation of the solidification modes with our Ni_{eq} and Cr_{eq} expressions, we believe it is premature to conclude that separate Ni_{eq} and Cr_{eq} expressions are necessary to predict FN and solidification mode in stainless steel welds. Therefore, the boundaries determined for the various solidification zones in Figure 9 are included on the proposed predictive diagram in Figure 11.

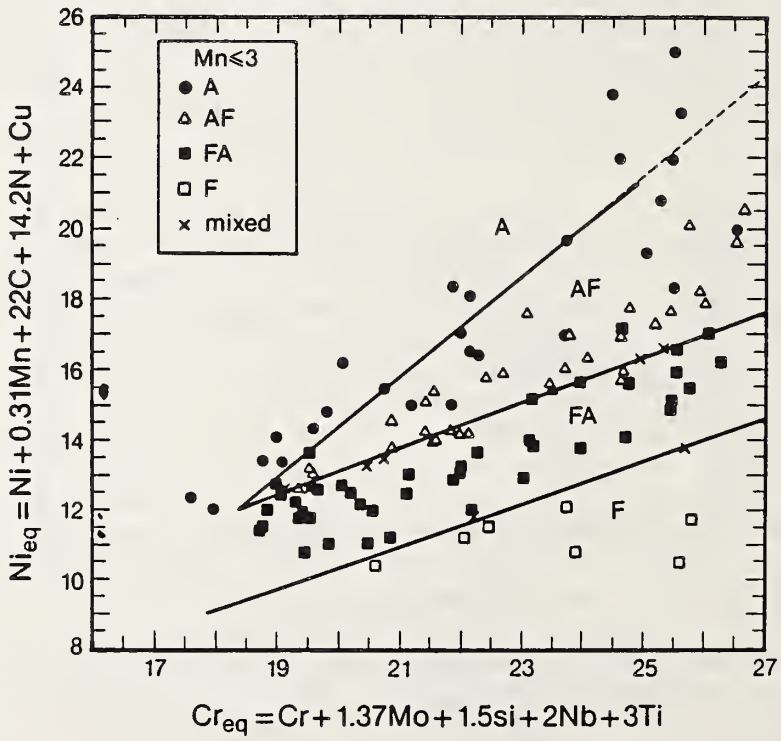

Fig. 10. Solidification-mode data on the coordinate axes of Hammar and Svenson.[15]

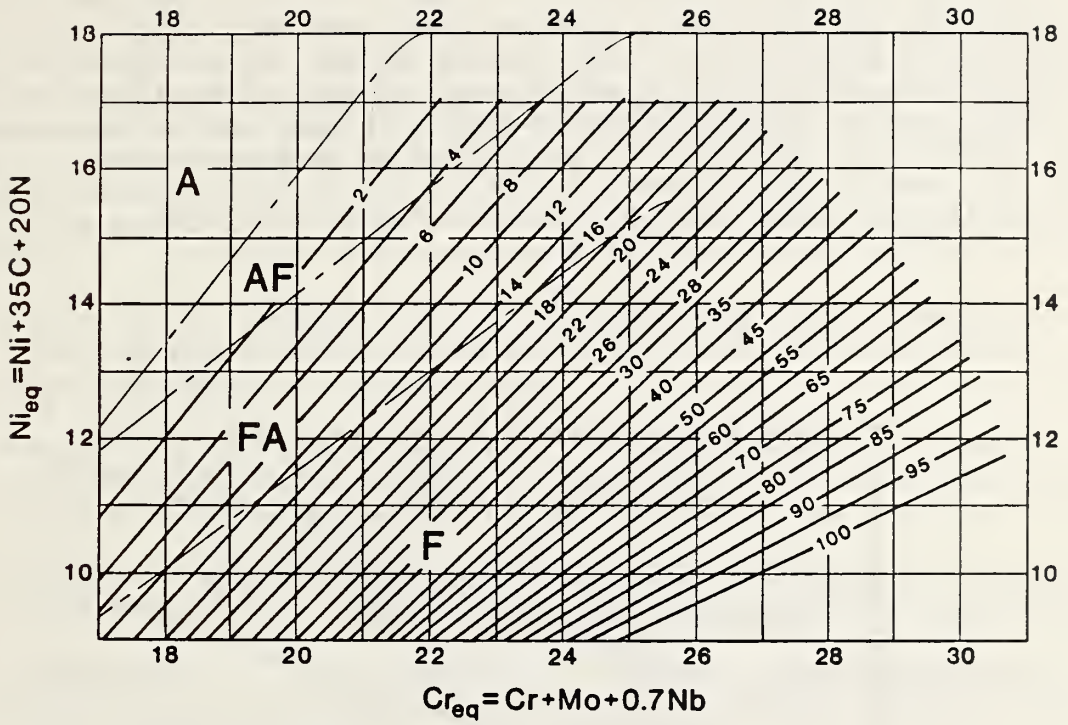

Fig. 11. New diagram, including solidification-mode boundaries.

The location of the solidification-mode boundaries corresponds well to changes in the FN response. When solidification boundaries from the top of the diagram are considered, the solidification boundary of A to AF (the transition from a fully austenitic structure to a partially ferritic structure) falls directly on the zero FN line.

The austenite–ferritic to ferritic–austenitic (AF to FA) boundary denotes the change to a primary ferritic structure, which has been related to a substantial reduction in hot-cracking sensitivity. Using the fissuring data given by Lundin et al.,[1] we noticed that the reported FN needed to eliminate fissures corresponds very closely to the AF to FA boundary on the diagram. They reported minimum FN values to prevent fissures 1.5 for type 316L (Cr_{eq} near 20), 2 for type 308 (Cr_{eq} near 18.5), 2.5 for type 316 (Cr_{eq} near 20.5), 3 for type 308L (Cr_{eq} near 18.8), and 4 for type 309 (Cr_{eq} near 23). This suggests that the AF to FA boundary could be used as an accurate guide for controlling the hot-cracking tendency, as Kujanpaa also noted in his study.[22]

The ferrite–austenite to ferrite (FA to F) transition corresponds to the beginning of a compression in FN spacing and the start of rotation of the lines. Microstructurally, this corresponds to a change from a vermicular to a lath structure as the austenitic phase is forced to nucleate within a ferritic phase.

The relationship between FN and solidification mode is shown from a slightly different perspective in Figure 12. Here, the modified solidification equivalents of Suutala[21] were used as coordinate axes when mapping the iso-FN lines. The FN lines are not as straight with these equivalents, and they do not model compositional effects over as broad a range as the proposed FN equivalents, but these equivalents indicate an interaction between FN and solidification mode. We noted a tendency for the iso-FN lines to move parallel to the boundary between AF and FA solidification zones and saw indications that iso-FN slopes may differ in these respective solidification zones.

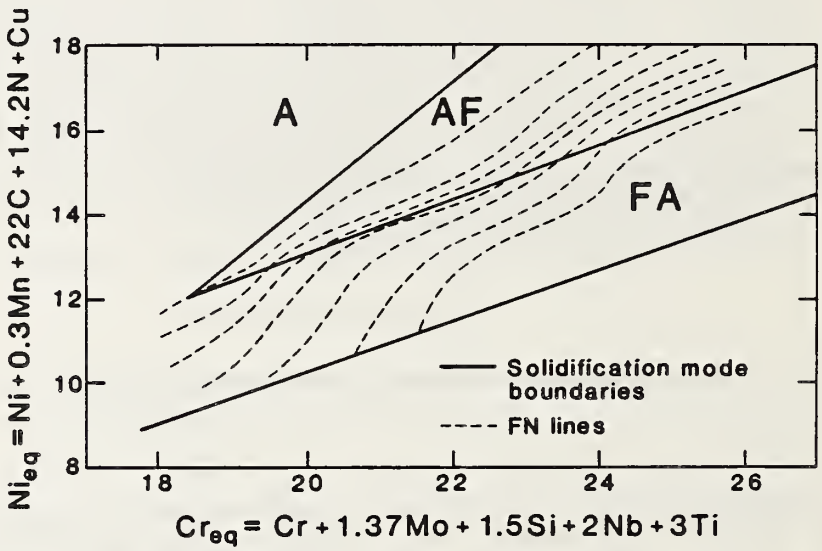

Fig. 12. Schematic representation of iso-FN line shape near solidification-mode boundaries, indicating a coupling between the two.

CONCLUSIONS

1. A new predictive diagram for ferrite in stainless steels has been developed for the range 0 to 100 FN.

2. The diagram is applicable for Mn contents to 10 wt.%, Mo contents to 3 wt.%, N contents to 0.2 wt.%, and Si contents to 1 wt.%.

3. The accuracy of the diagram surpasses that of the DeLong and Schaeffler diagrams in this range for a 950-point database.

4. The diagram includes solidification boundaries that correspond to changes in the FN response. The AF to FA boundary seems to be a good predictor of cracking sensitivity.

ACKNOWLEDGMENTS

Several of the authors received financial support from the Department of Energy and the Welding Research Council. The authors are also indebted to Alloy Rods Company, Teledyne McKay, Sandvik Steel Company, Welding and Wire Division, Smitweld, Soudometal, and the Welding Institute, who supplied data.

REFERENCES

1. Lundin, C. D., DeLong, W. T., and Spond, D. F. 1975. Ferrite–Fissuring Relationship in Austenitic Stainless Steel Weld Metals. Welding Journal 54. pp. 241s–246s.

2. Baeslack, W. A., III, Duquette, D. J., and Savage, W. F. 1978. Technical Note: Stress Corrosion Cracking in Duplex Stainless Steel Weldments. Welding Journal 57. pp. 175s–177s.

3. Siewert, T. A. 1978. How to Predict Impact Energy from Stainless Steel Composition. Welding Design and Fabrication 51. pp. 88–90.

4. Szumachowski, E. R. and Reid, H. F. 1978. Cryogenic Toughness of SMA Austenitic Stainless Steel Weld Metals: Part 1 – Role of Ferrite. Welding Journal 57. pp. 325s–333s.

5. Read, D. T., McHenry, H. I., Steinmeyer, P. A., and Thomas, R. D., Jr. 1980. Metallurgical Factors Affecting the Toughness of 316L SMA Weldments at Cryogenic Temperatures. Welding Journal 59. pp. 104s–113s.

6. Siewert, T. A. 1986. Predicting the Toughness of SMA Austenitic Stainless Steel Welds at 77 K, Welding Journal 65. pp. 23–28.

7. Kotecki, D. J. 1987. Ferrite Control in Duplex Stainless Steel Weld Metal. Welding Journal 66. pp. 273s–278s.

8. DeLong, W. T. 1974. Ferrite in Austenitic Stainless Steel Weld Metal. Welding Journal 53. pp. 273s–286s.

9. Schaeffler, A. 1949. Constitution Diagram for Stainless Steel Weld Metal. Metal Progress 56. pp. 680–680B.

10. Olson, D. L. 1985. Prediction of Austenitic Weld Metal Microstructure and Properties. Welding Journal 64. pp. 281s–295s.

11. Hull, F. C. 1973. Delta Ferrite and Martensite Formation in Stainless Steels. Welding Journal 52. pp. 193s–203s.

12. Espy, R. H. 1982. Weldability of Nitrogen-Strengthened Stainless Steels. Welding Journal 61. pp. 149s–156s.

13. Szumachowski, E. R. and Kotecki, D. J. 1984. Effect of Manganese on Stainless Steel Weld Metal Ferrite. Welding Journal 63. pp. 156s–161s.

14. McCowan, C. N., Siewert, T. A., Reed, R. P., and Lake, F. B. 1987. Manganese and Nitrogen in Stainless Steel SMA Welds for Cryogenic Service. Welding Journal 66. pp. 84s–92s.

15. Hammar, O. and Svenson, U. 1979. Solidification and Casting of Metals. The Metals Society. London. pp. 401–410.

16. Mel'Kumor, N. and Topilin, V. V. 1969. Alloying Austenitic Stainless Steel with Nitrogen. Obrabotka Metallor Aug. pp. 47–51.

17. Ogawa, T. and Koseki, T. 1988. Weldability of Newly Developed Austenitic Alloys for Cryogenic Service: Part II – High-Nitrogen Stainless Steel Weld Metal. Welding Journal 67. pp. 8s–17s.

18. Okagawa, R. K., Dixon, R. D., and Olson, D. L. 1983. The Influence of Nitrogen from Welding on Stainless Steel Weld Metal Microstructure. Welding Journal 62. pp. 204s–209s.

19. Kotecki, D. J. 1986. Silicon Effect on Stainless Weld Metal Ferrite. IIW. Doc. II-C-779-86. The American Council of the International Institute of Welding. Miami.

20. Takemoto, T., Murata, Y., and Tanaka, T. 1987. Effect of Manganese on Phase Stability of Cr–Ni Nonmagnetic Stainless Steel. In High Manganese Austenitic Steels, Ed R.A. Lula, ASM Conference Proceedings, Oct. 10–15, 1987, ASM International, Cincinnati, Ohio. pp. 23–31.

21. Suutala, N. 1982. Effect of Manganese and Nitrogen on the Solidification Mode in Austenitic Stainless Steel Welds. Metallurgical Transactions A 13(12). pp. 2121–2130.

22. Lippold, J. C. and Savage, W. F. 1982. Solidification of Austenitic Stainless Steel Weldments: Part III – The Effect of Solidification Behavior on Hot Cracking Susceptibility. Welding Journal 61. pp. 388s–396s.

23. Kujanpaa, V. 1985. Role of Steel Type and Impurities in Solidification Cracking in Austenitic Stainless Steel Welds. Metal Construction 17(1) pp. 40R–46R.

24. Standard Procedures for Calibrating Magnetic Instruments to Measure the Delta Ferrite Content of Austenitic Stainless Steel Weld Metal. 1986. ANSI/AWS A 4.2-86, American Welding Society. Miami.

25. Kotecki, D. J. 1982. Extension of the WRC Ferrite Number System. Welding Journal 61. pp. 352s–361s.

26. McCowan, C. N., Siewert, T. A., and Olson, D. L. 1988. Stainless Steel Welds: Prediction of Ferrite Content, Interagency report, National Bureau of Standards, Boulder, Colorado; in preparation.

27. David, S. A., Vitek, J. M., and Hebble, T. L. 1987. Effect of Rapid Solidification on Stainless Steel Weld Metal Microstructures and Its Implications on the Schaeffler Diagram. Welding Journal 66. pp. 289s–300s.

MECHANICAL PROPERTIES OF ELECTRON BEAM WELDS IN THICK COPPER

T. A. Siewert and D. P. Vigliotti
Fracture and Deformation Division
National Bureau of Standards
Boulder, Colorado

Electron beam welding was used to make similar and dissimilar butt joints in 25-mm-thick plates of copper alloys C10700 and C17510. The mechanical properties of these joints were measured at 76 and 298 K using reduced-section transverse tensile specimens. Elongation measurements of a 25-mm-long gage length consisting of weld, heat-affected zone (HAZ), and base metal were misleading. Therefore, for some specimens, elongation was measured on 1-mm lengths, a distance more characteristic of the weld and HAZ widths. These measurements revealed that the first strain occurred in the soft weld and HAZ. The effect of flow-localization constraint on the soft regions was small for the specimens tested, which ranged from 15 to 128 mm^2 in cross-sectional area.

INTRODUCTION

The design for the Compact Ignition Tokamak (CIT) could require welds in 25-mm-thick sheets of copper alloys. Copper alloy C10700 (Cu–0.08 mass % Ag), one candidate material, has a good combination of strength and conductivity, especially when work hardened. In regions of the structure where stresses could exceed the yield strength of alloy C10700, precipitation-hardenable copper alloy C17510 (Cu–0.4 mass % Be–1.8 mass % Ni) is being considered. To join the copper conductor segments into a continuous conductor, welds might be necessary for the following alloy pairs: C10700 to C10700, C10700 to C17510, and C17510 to C17510.

Copper alloys have been joined successfully for many years by the common welding processes, including shielded metal arc, gas metal arc, and gas tungsten arc welding.[1] Such welds are produced with high heat inputs and high preheat temperatures to overcome the effects of the high

Table 1. Material Characteristics and Properties*

	Alloy C10700	Alloy C17510
Heat	9049	50187
Yield strength (MPa)	304†	794
Tensile strength (MPa)	321	845
Elongation (%)	22	12
Hardness	96 Brinnell	102 R_B
Composition (mass %)		
Be	—	0.38
Ni	—	1.79
Ag	approx. 0.09	—
Thermomechanical history	cold work: 40%	cold work: 37%, followed by age hardening at 482°C for 2 h

* reported by the supplier

† determined by the 0.5%-strain (elastic and plastic) offset technique; estimated to be similar to data measured by the 0.2%-strain (plastic only) offset technique

Table 2. Welding Conditions for EB Welds

Voltage (kV)	55
Current (mA)	350
Power (kW at workpiece)	19.3
Travel speed (mm/min)	380
Focal plane (mm from top of plate)	20
Orientation	beam horizontal, normal to plate
Oscillation (mm)	1
Pass Sequence	single pass, one side

thermal conductivity of the copper alloys. This high heat input contributes to a loss in strength in the heat-affected zone (HAZ) through recrystallization of the cold-worked structure in alloy C10700 or solution heat treatment of the precipitation-hardened structure in alloy C17510.[2]

This study evaluated a high-energy beam welding process, electron beam (EB) welding, because the energy density enables it to produce a weld with a significantly narrower bead and HAZ width without preheating. These attributes are important: the elimination of preheating avoids the cost and safety considerations involved in bringing a joint to 500°C, and the narrower bead and HAZ contribute to a higher effective weld strength through flow localization.[3]

Another high-energy beam welding process, laser welding, was to be compared to the EB process. Unfortunately, acceptable welds could not be produced within the time constraints of this project. Although the CO_2 laser has a power of 12 kW, its wavelength was reflected strongly by the copper, so the beam could not penetrate the joint. Various attempts were made to reduce the section by beveling and later filling the bevel with molten copper, but these welds had an unacceptable level of porosity.

In addition to electrical conductivity and strength requirements, the welds must withstand thermal cycles. The structure is cooled initially by liquid nitrogen, but electrical resistance warms the structure to room temperature. To provide data for the design of the structure, the mechanical properties of these material combinations were evaluated at the extremes of this temperature range.

MATERIALS AND METHODS

Alloys C10700 and C17510 were from heats that met the compositional requirements of the Copper Development Association and the mechanical property requirements for CIT applications. Detailed information on the material is listed in table 1. Both materials were received in the form of 25-mm-thick plate.

Since the amount of plate was limited, reduced-section specimens were chosen for the tensile tests. The plates were sawn into 50-mm × 150-mm blocks, then welded along the 150-mm edge to form 100-mm × 150-mm × 25-mm weldments. The welding parameters are listed in table 2.

Tensile specimens were removed from the EB weldments and pulled to failure in uniaxial tension to evaluate the effect of welding on the mechanical properties. The tests were performed in a modified load frame that had a reaction cylinder which enabled placing a Dewar of liquid nitrogen around the specimen. The test procedure and the design of this load frame have been reported elsewhere.[4] The test matrix included two temperatures, three material combinations at the weld, and a variety of cross-sectional areas.

Normally, properties of welds are measured on tensile specimens oriented along the length of the weld and consisting only of weld metal. The narrowness of the EB welds precluded this specimen orientation and required transverse specimens. However, the transverse orientation is more desirable, since it will be the primary loading direction in the coil. In this orientation, the gage lengths of the standard round- and flat-section specimens were not homogeneous but included a variety of materials: starting from one gage mark, the gage length consisted of base metal, HAZ, weld metal, HAZ, and the second base metal. Because each of these regions has different properties, the mechanical properties must be interpreted on the basis of the specimen's composite nature. Two of the most important effects of the composite nature are flow-localization constraint and localized yielding.

Constraint

The HAZ regions, weakened by recovery and recrystallization of the grains during welding, affect the joint strength. These regions, each containing approximately 5 mm of the tensile specimen's 50-mm gage length, should strongly affect the tensile properties of a very thin (1-mm-diameter) tensile specimen. Conversely, because of the constraint of the adjacent base metal (Poisson's ratio effect), this HAZ should have less effect on a thicker, say 25-mm-diameter, tensile specimen. To measure this effect, a series of specimen cross sections was tested. With the limited material available, we were able to produce cross-sectional areas ranging from 15 to 128 mm^2. The 128-mm^2 cross section was that of a round specimen with a diameter of 12.8 mm. This diameter was expected to cause only marginal constraint in the 11-mm-thick weldment (5-mm HAZ, 1-mm weld, 5-mm HAZ-softened region), but it was the largest diameter obtainable from the small weldments.

Localized Yielding

Because the weld and HAZ have less strength than the base metal, the initial strains occur in these weaker regions until they reach the yield strength of the base material. Strain measurements at a series of marks 1 mm apart were used to determine the strain history for the various regions of the gage lengths in several specimens.

A bench-top lathe was used to scribe the marks on the tensile surface after it was coated with machinist's layout ink. When the specimen was placed in the tensile fixture, the marks were visible in the eyepiece of a traveling microscope, which had been mounted on the frame of the tensile machine.

By monitoring the stress–strain curve, we could stop the test at selected strain levels for measurement of the relative movement of these 1-mm-spaced marks, which enabled determination of the local strain in the base metal, HAZ, and weld metal.

RESULTS AND DISCUSSION

Microstructure

The welds were initially evaluated by removing transverse sections for microstructural evaluation. Figure 1 shows the etched cross section of the EB weld of the C10700–C10700 material combination. The weld fusion zone was approximately 1 mm wide and uniform over the 25-mm thickness of the joint. It was abutted on each side by a coarse-grained HAZ about 1 mm thick, then a fine-grained HAZ about 4 mm thick. Beyond the fine-grained HAZ was the base metal. Figure 2 shows the etched cross section of the EB weld joining alloy C17510 to C17510. The weld fusion zone was approximately 1-mm wide and uniform over the 25-mm thickness of the joint. The weld was abutted on each side by a visible HAZ, 6 mm in

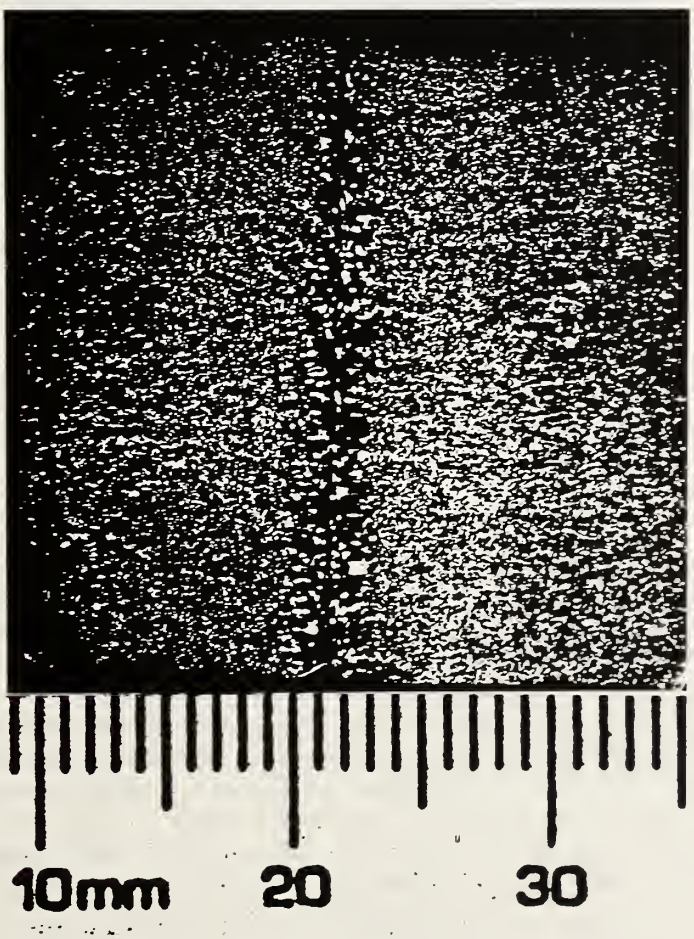

Figure 1. Cross section of alloy C10700–alloy C10700 weld; nitric and lactic acid etch.

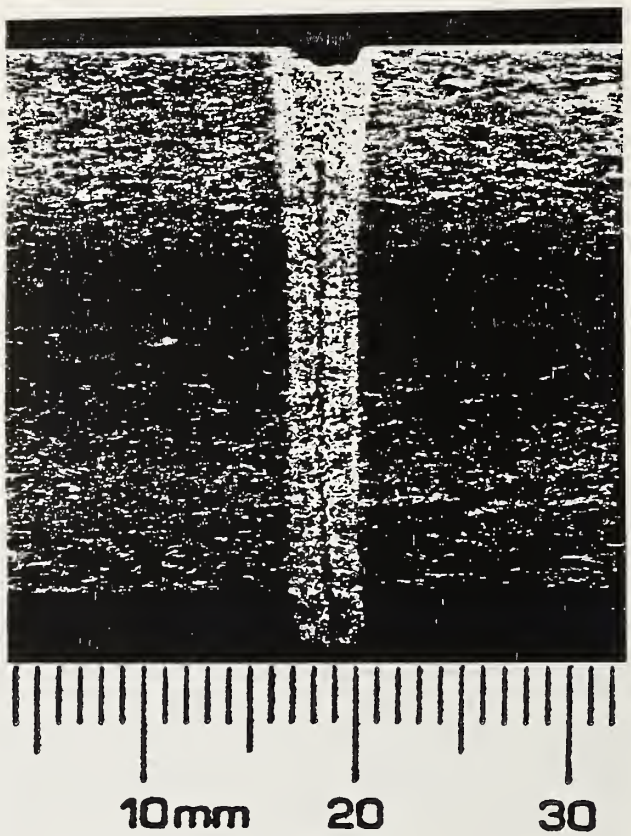

Figure 2. Cross section of the alloy C17510–alloy C17510 weld; nitric and lactic acid etch.

width. Figure 3 shows the etched cross section of the EB weld joining alloy C10700 to C17510. The different interaction of the two materials with the electron beam caused a deflection of the beam within the joint. The early, procedural development welds showed the beam centered in the joint at the surface, but deflected about 1 or 2 mm into alloy C10700 at the bottom. This was corrected by angling the beam toward alloy C17510. For this reason, the weld interface in figure 3 shows some curvature. Its width is similar to those of previous welds. The HAZ width is different on each side of the joint. The HAZ on the right matches the microstructure of the HAZ in figure 1; the haz on the left, that in figure 2.

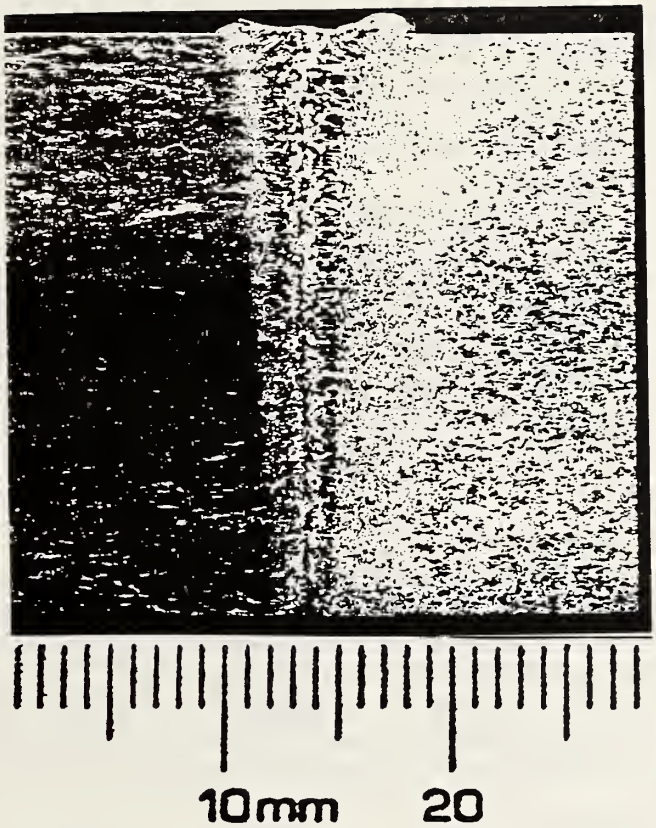

Figure 3. Cross section of the alloy C10700—alloy C17510 weld; nitric and lactic acid etch.

Hardness Tests

The polished cross section shown in figure 1 was evaluated for hardness by producing three hardness traverses across the weld at the top, midthickness, and bottom of the weld. The hardness was measured with the Rockwell F technique at 3-mm intervals; results are included in table 3. The hardness data on the base metal agree well with the data provided by the suppliers (table 1). On the basis of the general relationship between hardness and strength, the substantial reduction in hardness in the HAZ and weld should indicate a similar reduction of strength in these regions.

Tensile Tests

The tensile test results are summarized in table 4. The yield strength was determined by the 0.2%-strain-offset method, a method that assumes uniform elongation in the 25-mm gage length. The 0.5%-strain value measured under load (combined plastic and elastic strain) has traditionally been used for copper alloys. We chose the 0.2%-strain value

Table 3. Hardness Traverses across EB C10700–C10700 Weld

Location (mm)	Description	Hardness (R_F)		
		Top	Middle	Bottom
−9	Base metal	83	84	83
−6	HAZ–BM interface	56	49	48
−3	Fine HAZ	38	39	37
0	Weld	16	32	26
+3	Fine HAZ	36	37	37
+6	HAZ–BM interface	57	49	48
+9	Base metal	84	82	83
+12	Base metal	82	84	84

Table 4. Mechanical Property Data

Specimen	Material Couple	T (K)	Cross-sectional Area (mm^2)	Yield Strength* (MPa)	Tensile Strength (MPa)	Elongation† (%)	Reduction of Area (%)
EB-1	Cu–Cu	298	32	89	222	22	68
EB-2	Cu–Cu	76	32	187	376	23	68
EB-3	Cu–Cu	298	15.5	74	181	27	50
EB-4	Cu–Cu	76	15	132	319	36	75
EB-5	Cu–CuBe	298	15.5	87‡	158‡	17‡	46‡
EB-6	Cu–CuBe	76	15.5	144‡	261‡	14‡	42‡
EB-7	Cu–Cu	298	128	59	206	49	75
EB-8	Cu–Cu	76	128	70	328	41	69
EB-9	CuBe–CuBe	298	126	253	457	16	58
EB-10	CuBe–CuBe	298	125	251	454	15	60
EB-11	CuBe–CuBe	76	126	320	593	13	53
EB-12	CuBe–CuBe	76	126	318	591	14	47
EB-13	Cu–CuBe	298	126	74	225	45	90
EB-14	Cu–CuBe	298	126	87	232	34	74
EB-15	Cu–CuBe	76	126	98	359	36	77
EB-16	Cu–CuBe	76	126	105	356	46	89
107-1	Cu	298	126	280	308	40	86
107-2	Cu	76	126	356	427	56	82
175-1	CuBe	298	126	720	805	17	19
175-2	CuBe	76	126	795	–	–	–

* based on 0.2%-strain-offset method
† based on 25-mm gage length
‡ lower than expected, from preliminary weld with flaws (see EB-13 through EB-16 for second weld)

(plastic strain only), which is traditionally used for steel, since it is now favored. The transition from elastic to plastic strain is quite gradual for these specimens (see figure 4), and the two techniques (0.2% plastic and 0.5% total strain) provide similar estimates of the load-carrying capacity for this material.

Since this strain was not uniformly distributed in the weld specimens, the actual strain in the weld was greater. Figure 5 shows the development of strain at 1-mm intervals down the length of specimen EB-3. The first measurement was at an average strain of 10%. Figure 5 also indicates the locations of strain values in the weld and HAZ regions. The localization of the initial strain at the weld and two HAZs is apparent. As this material strains, it work-hardens and increases in strength. When it reaches the strength of the base metal, it also begins to strain plastically.

The amount of strain that occurs in the weld and HAZs is expected to be a function of the specimen's cross-sectional area. Increasing cross-sectional area results in greater constraint: the stronger base metal prevents plastic flow and work hardening in the softer weld and HAZs. Such behavior can be examined in a more quantitative manner by plotting the 0.2% yield strength as a function of cross-sectional area. However, figures 6 and 7 do not show any effect of constraint on yield strength for the cross-sectional areas included in this study.

Limited data linking hardness to strength for copper alloys are available.[5] The identities of these alloys are not available, but the data are probably a collection of various alloys, grain sizes, and amounts of cold work. These data, shown in figure 8, can be used to relate the microstructure and hardness to the mechanical properties of the alloy C10700 welds. The 298-K yield-strength data for the transverse specimens can be correlated to the 80-MPa yield strength predicted by the R_B-38 hardness of the fine-grained HAZ. The very soft (R_B-16) weld region should have caused the initial yielding to occur near 11 MPa. Therefore, the constraint of the specimen geometry was sufficient to prevent the 1-mm-wide weld from deforming, and the deformation occurred in the fine-grained HAZ. If the specimen cross section is increased further, the fine-grained HAZ will be constrained, and the yield strength should approach the base-metal value of 280 MPa.

The fact that the deformation was localized near the weld causes us to reconsider the applicability of a 0.2%-strain design limit. The 0.2%-strain limit prevents massive deformation in a large volume. However, for these welds, the plastic strain was limited to a region on the scale of millimeters, until the base metal yield strength was reached. Perhaps a 0.5 or 1% plastic strain in this region can be tolerated, especially for materials, such as these copper alloys, that have good work-hardening characteristics (figure 4). Table 5 lists the specimen strengths for differing plastic strains over the 25-mm gage length. The yield strength of the specimens increased by an average of 30% as the plastic strain was increased from 0.2 to 2%.

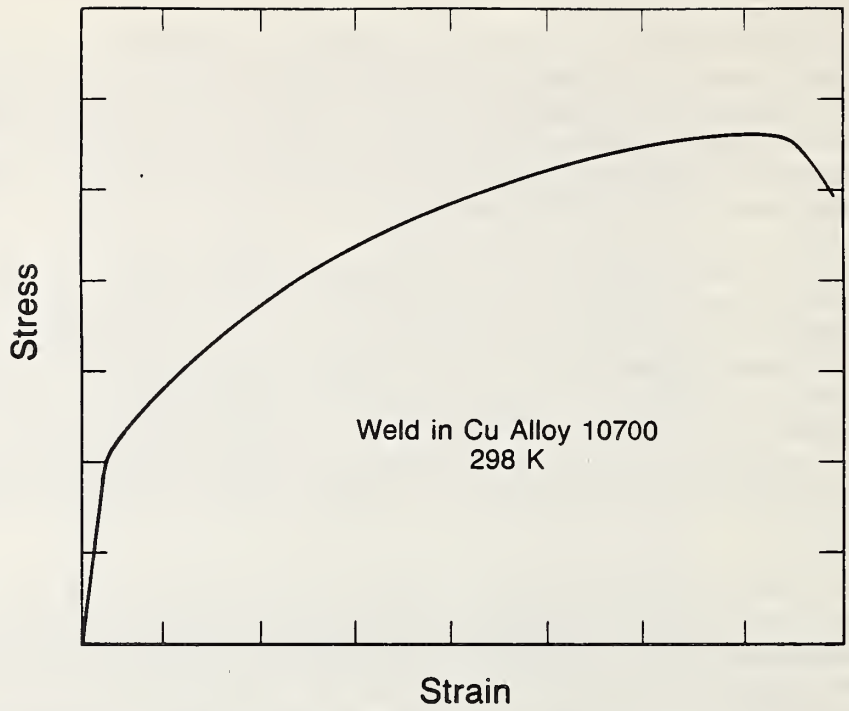

Figure 4. Representative stress-strain curve for alloy C10700–alloy C10700 weld showing substantial ductility and strain hardening.

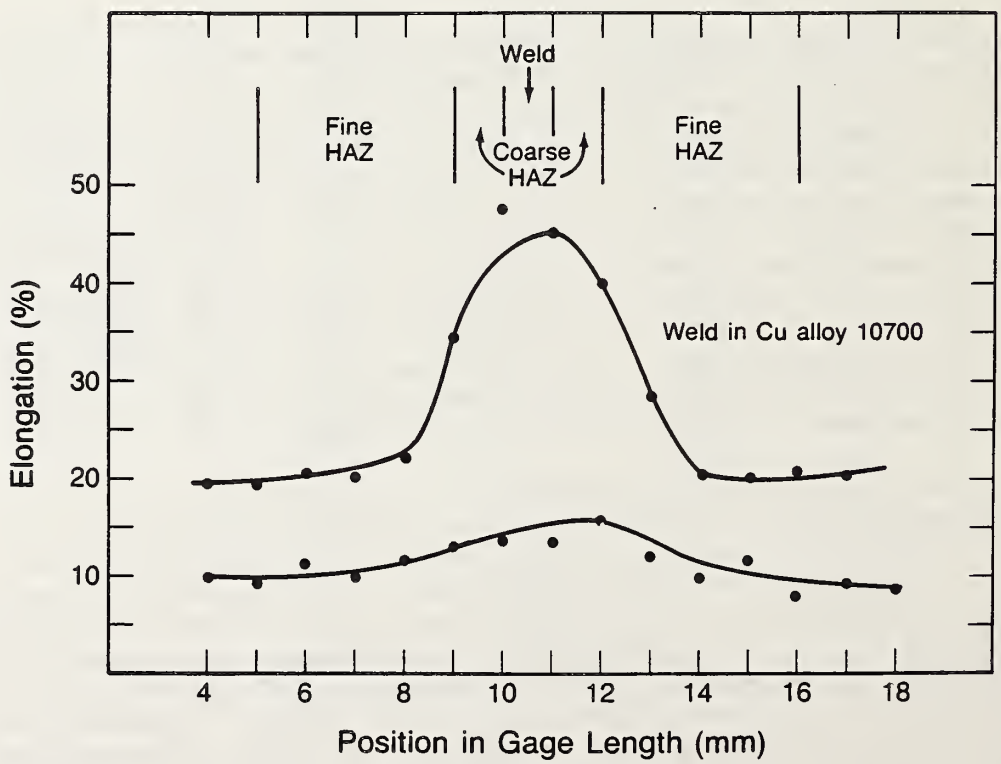

Figure 5. Elongation at 1-mm intervals during the straining of specimen EB-3 (measured at two levels of strain).

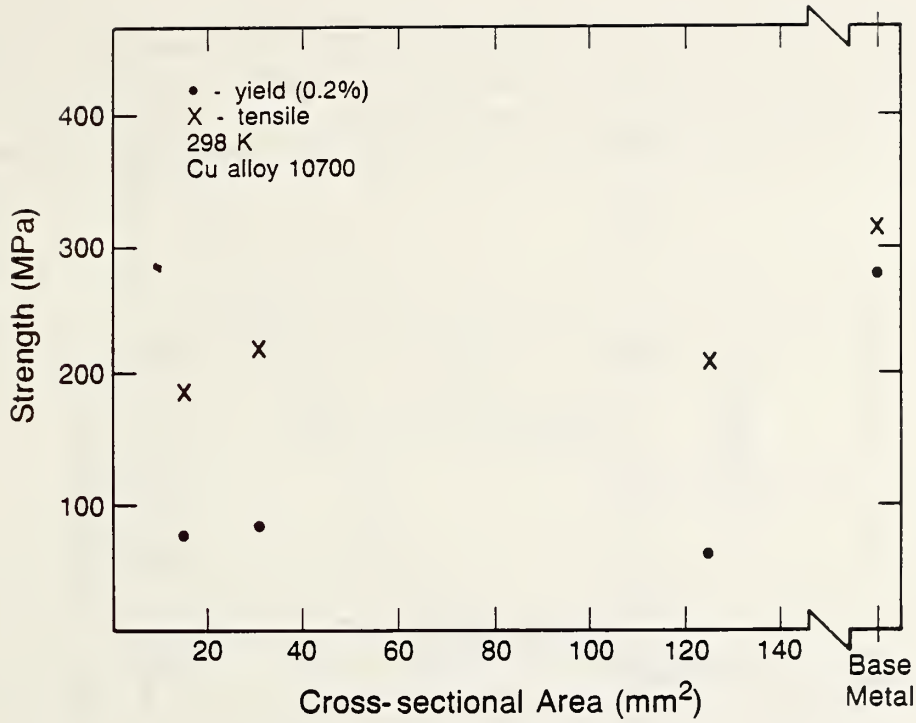

Figure 6. Strength versus cross-sectional area for alloy C10700–alloy C10700 weld at 298 K.

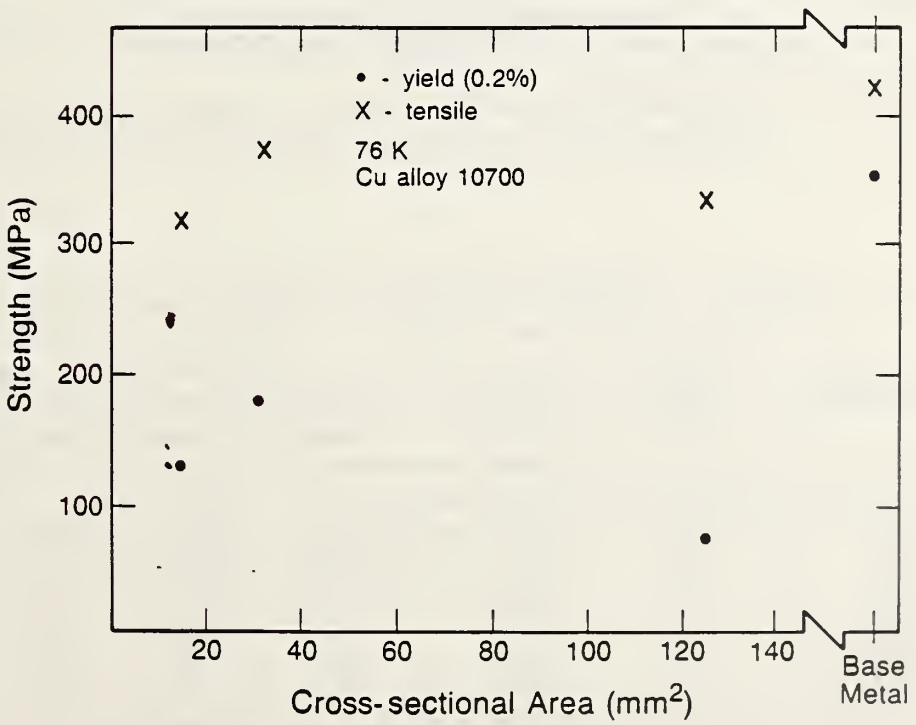

Figure 7. Strength versus cross-sectional area for alloy C10700–alloy C10700 weld at 76 K.

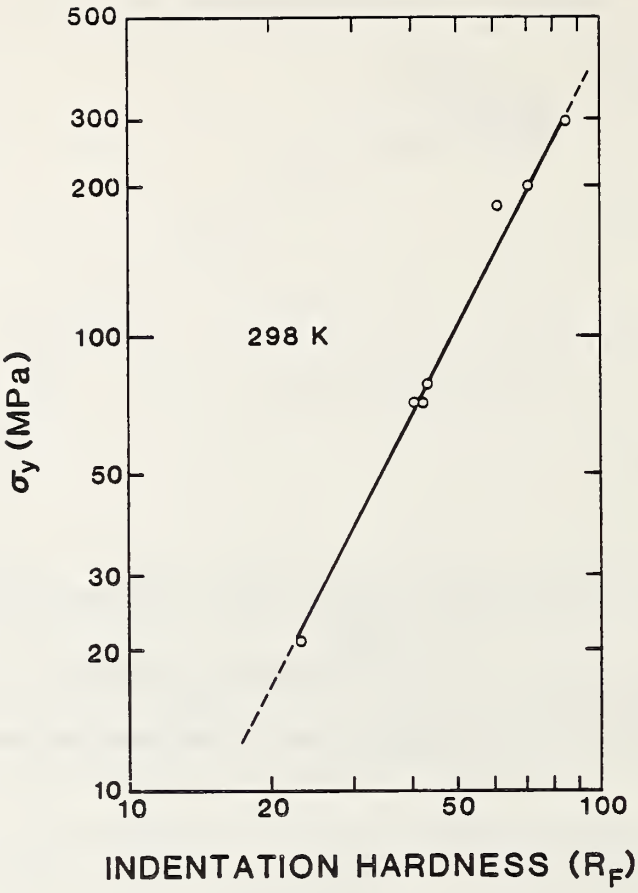

Figure 8. Yield strength (0.5% extension under load) versus hardness for a variety of copper alloys at 298 K.[5]

Table 5. Yield Strength as a Function of Strain

Specimen	Temperature (K)	Area (mm^2)	Yield Strength (MPa)			
			0.2%*	0.5%*	1%*	2%*
EB-1	298	32	89	100	109	125
EB-2	76	32	187	198	205	231
EB-3	298	15.5	74	80	88	103
EB-4	76	15	132	150	166	196
EB-7	298	128	59	70	83	101
EB-8	76	128	70	85	99	122

* plastic strain only

Both the weld and the base metals became stronger at reduced temperatures. Figure 9 portrays the data for the alloy C10700–alloy C10700 welds and base metal. The weld data are the average of the three tests at each temperature. Upon cooling from 298 to 76 K, the weld strength increased approximately 50%, and the base-metal strength increased approximately 25%.

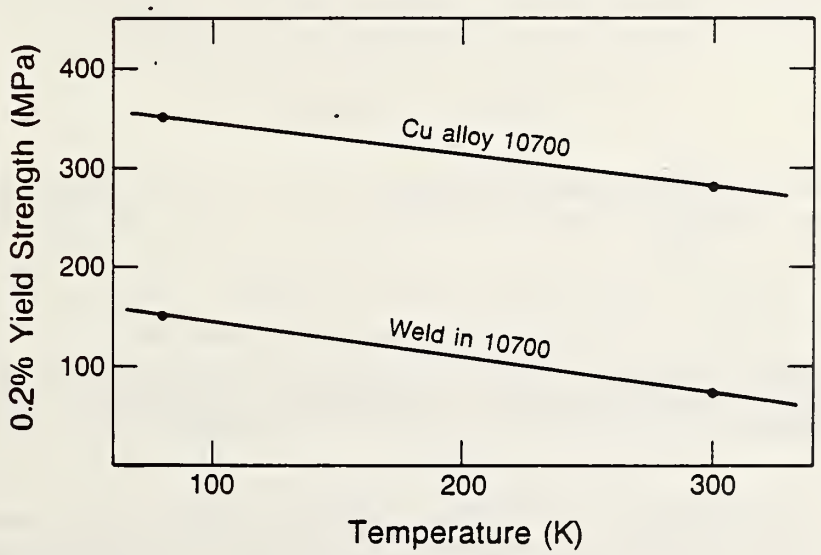

Figure 9. Yield strength versus temperature for alloy C10700–alloy C10700 welds and 40% cold-worked base metal.

CONCLUSIONS

1. The weld yield strengths were less than half those of the base metals.

2. Much of the early plastic strain during tensile testing is restricted to the weld and HAZ because the heat of welding softens the cold-worked structure.

3. Owing to the wide, fine-grained HAZs in the welds between alloys C10700 and C10700, few constraint effects were seen for the specimen sizes included in this study.

ACKNOWLEDGMENTS

This program was funded primarily by the Office of Fusion Energy, Department of Energy. The production of the welds was funded by Princeton Plasma Physics Laboratory. The authors acknowledge the assistance of C. N. McCowan in the tensile testing of the specimens and of D. Shepherd in the metallography and hardness testing. The EB weld was produced by Sciaky Brothers.* Lawrence Livermore National Laboratory supplied the C17510 copper alloy; Princeton Plasma Physics Laboratory, the C10700 copper alloy.

REFERENCES

1. Welding, Brazing, and Soldering, vol. 6 of the Ninth Edition of the Metals Handbook, American Society for Metals, Metals Park, Ohio (1983), p. 400.

2. Ibid, p. 418.

3. Mechanical Testing, vol. 8 of the Ninth Edition of the Metals Handbook, American Society for Metals, Metals Park, Ohio (1985), p. 573.

4. D. T. Read and R. L. Tobler, "Mechanical Property Measurements at Low Temperatures," in Advances in Cryogenic Engineering – Materials, vol. 28, Plenum Press, New York (1982), pp. 250-268.

5. C. Bushnell, Princeton Plasma Physics Laboratory, Princeton, New Jersey, private communication (1987).

*This company is listed for information only. No endorsement by NBS is implied.

CRYOGENIC MATERIAL PROPERTIES OF STAINLESS STEEL TUBE-TO-FLANGE WELDS*

T. A. Siewert, C. N. McCowan, and D. P. Vigliotti
Fracture and Deformation Division
National Bureau of Standards
Boulder, Colorado

The mechanical properties of stainless steel beam tube-to-flange welds for a cryogenic piping application were measured. A planar specimen was developed to duplicate the constraint, loading, and heat-sink properties of the circular joint while reducing preparation time and cost. We evaluated specimens containing welds between the tube material (21Cr–6Ni–9Mn) and the three stainless steels being considered for the flange materials: AISI types 304L and 316L and 21Cr–6Ni–9Mn. The mechanical property tests consisted of three phases: simple tensile testing to failure, tensile testing of notched specimens (where the notch simulated fabrication flaws), and fatigue testing of notched specimens for the 4×10^4 cycle design life of the structure. Flanges of type 316L stainless steel produced welds with the best combination of strength and ductility in all three phases of testing and at 295 and 4 K.

INTRODUCTION

Their very high current-carrying capacity has made 4-K superconductors the preferred choice for applications requiring powerful magnetic fields. Thin-walled stainless steel tubes at the center of the superconducting magnets will contain the proton and antiproton beams. These "beam tubes" are connected to the system by welds of their flanges. A failure in the flange welds would disable the system. This study provides the information needed for design of reliable beam tube-to-flange welds.

Various stainless steel alloys have been characterized for cryogenic service.[1] When these results were reviewed, austenitic stainless steel alloys had some of the best combinations of strength and toughness at 4 K.[2]

---

*Submitted to *Journal of Engineering Materials and Technology*.

An understanding of the role of nitrogen in determining the strength and toughness is necessary before appropriate combinations can be chosen for tube-to-flange welds. Nitrogen additions substantially increase the cryogenic strength of stainless steels, but at the same time, they reduce the fracture toughness. This reciprocal relationship is shown in Figure 1 for types 316L and 316LN stainless steels containing different amounts of nitrogen (N indicates intentionally added nitrogen).[2]

Figure 1 also includes data for welds of matching composition.[3] Their lower strength–toughness combinations indicate that, for equal weld-and base-metal strengths, welds are the fracture-critical portion of the structure.

These strength–toughness data for type 316 stainless steel welds were developed for thick, multipass welds because they will be used in joining the segments of large magnet structures, and they have dimensions suitable for the standard 25-mm-thick compact-tension fracture-toughness specimen. A literature search revealed no cryogenic data for the single-pass welds used to join stainless steel tubes to flanges. Since the properties for single-pass welds could differ substantially from those for multipass welds, we determined the 4-K strength and ductility of single-pass welds of the three flange materials under consideration.

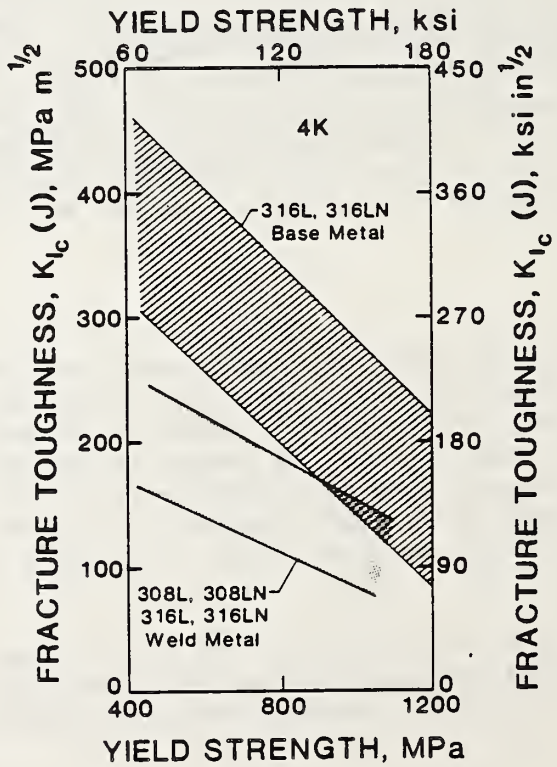

Figure 1. Yield strength versus fracture toughness for 316 type alloys at 4 K. Scatter bands represent one standard deviation.

MATERIALS

Three types of stainless steels were evaluated for use as the flange material. All were purchased from commercial sources with certificates of their room-temperature mechanical properties and composition, which are included in Table 1.

The alloy identified as 21Cr–6Ni–9Mn meets the cryogenic strength requirements for the application. It is included in the list of potential flange materials to provide a reference for the matching-composition joint. Although Figure 1 reports data for only types 316L and 316LN base-metal compositions, the inverse relationship between strength and toughness seems to apply to other austenitic alloys as well. Therefore, since this 21Cr–6Ni–9Mn alloy has a much higher nitrogen content than the other alloys in Table 1, its toughness is expected to be lower. Since measurements of fracture toughness are difficult for this joint configuration and thickness, we have attempted to compare the materials in terms of relative ductility, as measured by plastic strain to failure.

Type 304L stainless steel is included because it is probably the most common austenitic stainless steel. Its low cost, ready availability, and ample cryogenic mechanical property data (for multipass

Table 1. Mechanical Properties and Compositions of the Three Types of Stainless Steel at Room Temperature

Material Specification Designation	21Cr–6Ni–9Mn ASME SA-412 Type XM-11	304L ASME SA-240 Type 304L	316L ASME SA-240 Type 316L	316LN ASME SA-276 Type 316LN*
Thickness (mm)	9.5	9.5	9.5	—
Heat number	65724	Z1136	C2713	—
Yield strength (MPa)	427	322	357	—
Tensile strength (MPa)	749	588	609	—
Elongation (%)	50	56	52	—
Reduction of area (%)	62	63	69	—
Hardness (Brinell)	205	150	176	—
Composition (wt.%)				
C	0.023	0.018	0.014	0.02
Mn	9.16	1.69	1.50	1.50
Si	0.35	0.53	0.54	0.50
P	0.030	0.029	0.015	0.03
S	0.001	0.007	0.005	0.02
Cr	19.76	18.30	16.60	17.0
Ni	7.14	9.27	10.88	11.0
Mo	—	—	2.10	2.5
N	0.32	0.079	0.084	0.13

*Nominal values

welds)[4] make it a reference material to which the other steels can be compared. It has lower strength and higher toughness than 21Cr–6Ni–9Mn.

Type 316L stainless steel is included because it has one of the best strength–toughness combinations.[2,4] A type 316LN alloy was used in the first phase of testing because it was available from a previous program. Difficulty in obtaining more of this alloy for the second phase of testing forced the switch to type 316L. The primary difference in these alloys is nitrogen content—0.08 wt.% in type 316L and 0.13 wt.% in type 316LN.

The effect of substituting 316L for 316LN is expected to be small for this application. The nitrogen content in an autogenous (without filler metal) gas tungsten arc (GTA) weld is approximately the average of the nitrogen contents of the two joint materials, since each contributes about half the metal that fuses to form the weld bead. Thus, the expected nitrogen content of the joint between the 316L flange material and the 21Cr–6Ni–9Mn tube is 0.20 wt.%, whereas that for the joint between the 316LN flange material and the 21Cr–6Ni–9Mn tube is 0.22 wt.%. The 0.02-wt.% difference is considered to be insignificant because the expected nitrogen content of the joint of 21Cr–6Ni–9Mn flange material and tube of like composition is 0.32 wt.%.

These three flange materials were joined to the 21Cr–6Ni–9Mn tube with a 0.9-mm thick wall. Although the mechanical properties of 21Cr–6Ni–9Mn have been extensively characterized at room temperature, little information was available on its mechanical properties at 4 K, especially for tubing formed by either extrusion or rolling and seam-welding processes. During this test program, lack of this information plus the introduction of a new tube with different wall thickness prompted a cursory investigation of these properties of the 21Cr–6Ni–9Mn tube, which is reported in Appendix A. Although the difference in wall thickness and type of weld should not significantly alter our test results, the test program was completed without the introduction of these variables.

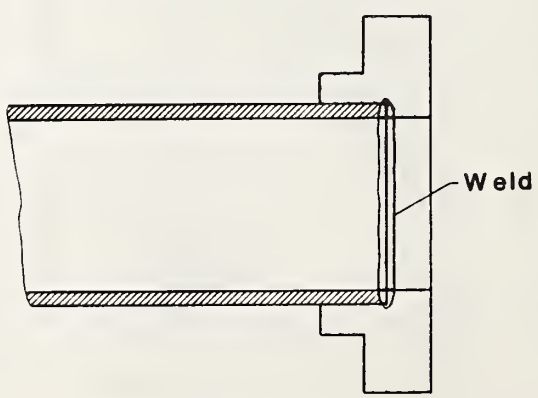

Figure 2. Cross section of a typical tube-to-flange joint.

PROCEDURE

Specimen Design

Tube-to-flange welds for cryogenic piping tend to be single-pass welds that are performed autogenously with gas tungsten arc welding. The tube is typically seated inside the flange where a circumferential weld forms a joint that provides mechanical strength and an air-tight seal. The schematic for the joint between a tube with a 0.9-mm-thick wall and a much heavier flange section is included in Figure 2. However, this type of joint is expensive to produce in the quantities needed for this test program, and reducing the specimen cost by slicing the joint into strips results in a bending stress when the joint is loaded.

To retain the differences in section mass while avoiding the bending moment, the test specimen configuration shown in Figure 3 was developed. Specimens of this design were produced rapidly and inexpensively while duplicating the critical characteristics of the tube-to-flange weld; they were suitable for standard methods of mechanical testing.[5] To simulate the fact that most of a circular tube-to-flange weld is free from starts or stops, wider specimens were produced, and the weld start and stop regions were removed. The welding was performed at 100 A with a travel speed of 12 cm/min. Figure 4 shows the welding fixture with clamps to maintain the alignment and with the gun held in a motorized carriage. When several lack-of-fusion flaws were found in the phase 1 specimens, the electrode tip angle was decreased from 60° to 30°; the problem did not occur in subsequent specimens.

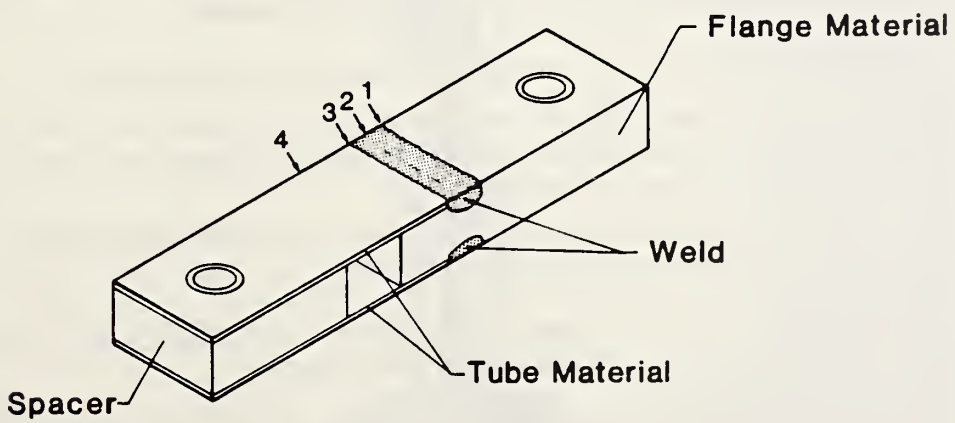

Figure 3. Schematic diagram of the specimen showing the four notch locations: 1 – flange HAZ; 2 – weld; 3 – tube HAZ; 4 – tube.

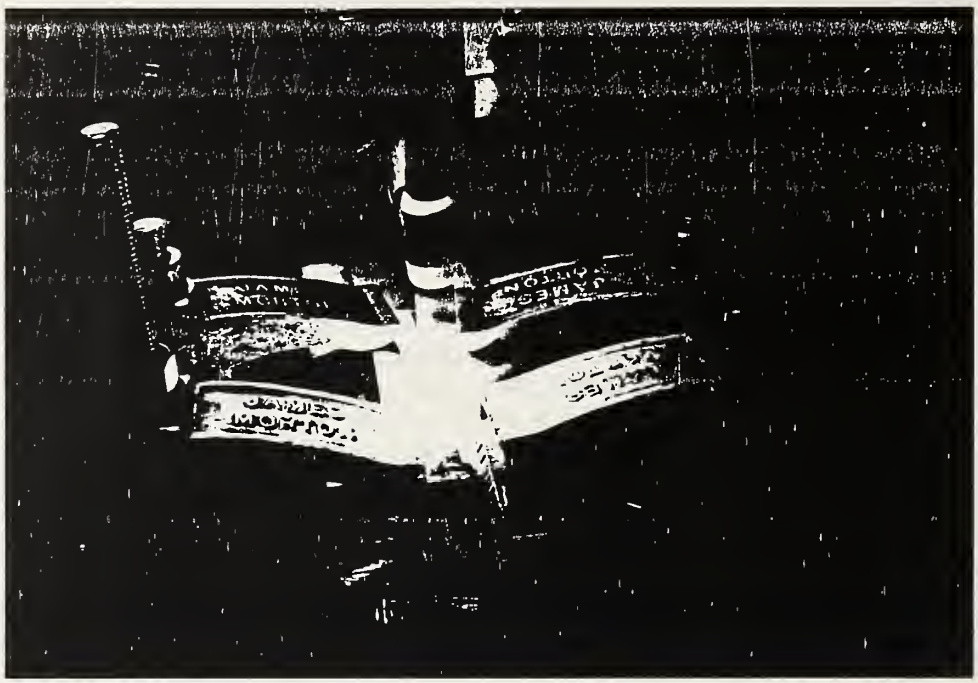

Figure 4. Welding of the specimens in an automated fixture.

Test Plan

To evaluate the sensitivity of the joints to the expected failure conditions, they were subjected to three test phases:

1. Uniaxial tensile testing to measure the joint strength
2. Uniaxial tensile testing of specimens with notches to simulate the effect of fabrication flaws and the inherent notch in the joint design on strength and ductility
3. Fatigue loading of notched specimens to evaluate the fatigue resistance to growth of fabrication flaws

Since each subsequent test phase increased in complexity and cost, correspondingly fewer material combinations were used.

The tensile-loading evaluation, phase 1, included all three flange materials joined to the 21Cr–6Ni–9Mn tube. Figure 5 shows a specimen in a room-temperature load frame. The two materials with the best strength and elongation results advanced to phase 2, where each was notched in four locations: the flange heat-affected zone (HAZ), the weld, the tube

HAZ, and the tube, as illustrated in Figure 3. The phase 2 specimen configuration was the same as phase 1, except a 60° included-angle notch was formed on each edge of the specimen at the desired locations. Each side was notched to a depth of 10% of the specimen width and a root radius of 0.064 mm. Figure 6 shows a typical notch, as photographed on our optical comparator. For this particular notch, the comparator calculated a root radius of 0.066 mm.

On the basis of the notch-tensile test results, the four most promising material-notch combinations advanced to the fatigue testing of phase 3. In phase 3, we determined the fatigue life of the tube, tube HAZs, welds to type 304L flanges, and welds to type 316L flanges. The specimen configuration was identical to that in phase 2. Specimens were tested in sets of five to enable a meaningful S–N curve to be drawn.

Because both the strength and ductility of the stainless steels are affected substantially by temperature, the joints were evaluated at two temperature extremes, 4 and 295 K. The 4-K tests were performed with the specimens immersed in liquid helium. Details of the 4-K load frame have been reported elsewhere.[6]

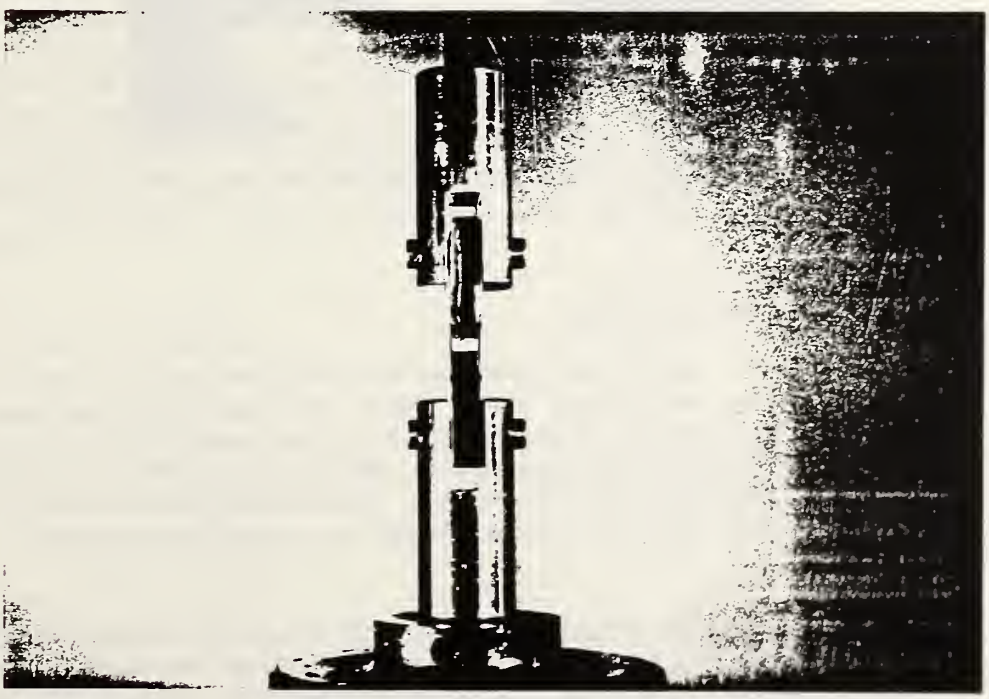

Figure 5. Specimen in a room-temperature load frame.

Figure 6. Examination of the notch radius on an optical comparator.

Material Property Measurements

For this study, the yield strength was defined as the load divided by the original cross-sectional area, where the value of the load is that when the testing machine crosshead had been displaced 0.05 mm beyond simple elastic loading of the specimen. The displacement of 0.05 mm is equivalent to an average of 0.2% plastic strain over the nominal 25-mm specimen gage length (distance from flange to reinforcing welds on the spacers).

The term fracture strength is used when failure occurs as the stress–strain curve is increasing; the term tensile strength, when failure occurs as the stress–strain curve is decreasing or when it has asymptotically reached a constant value. The term 0.2% yield strength is not accurate in this case because the composite nature of the gage length (weld + HAZ + base metal) encourages nonuniform, localized yielding.[7]

Therefore, in this study, fracture strength was used because the strength was influenced more by the geometry of the specimen than the inherent material response; it was defined as the maximum load divided by the original cross-sectional area after notching.

A substantial range in ductility was observed among the specimens. The composite nature of the gage length, however, precluded reporting this ductility in units of uniform strain. If the elongation had been uniform, this displacement could have been converted to strain by dividing by the gage length. Instead, the crosshead displacement of the testing machine was used. The displacement measurements were corrected to purely plastic extension. The elastic component was removed by measuring the displacement from a line parallel to the initial elastic loading slope. Plastic extension measurements provide an excellent measure of the relative ability of the joints to tolerate strain.

For fatigue testing, the pin-loaded specimen design required a minimum tensile load to eliminate vibration in the load train. Even for the lowest load levels, this minimum was never greater than 10% of the maximum load for any of the tests. The minimum load, rather than ΔP (the difference between the maximum and minimum loads), was kept constant throughout the tests to obtain the largest ΔP value for each test. This choice produces a more conservative value of the fatigue life. We did not evaluate the effect of multiple cracks in the specimens (four notches per specimen, as shown in Figure 3).

Since the structure is designed for 4×10^4 load cycles, stress at this life must be estimated to evaluate the various materials. We determined the life for several specimens near the desired range. Then we tested several more at a higher load, which resulted in shorter life). By drawing a smooth line through the average life at these load levels, we were able to determine the stress at which this line intersected 4×10^4 cycles and, thus, to evaluate the various materials and notch locations.

RESULTS AND DISCUSSION

Tensile Tests (Phase 1)

Uniaxial tensile tests were conducted on welds of the three flange materials at both 295 and 4 K.

A. Tensile Tests at 295 K

The yield strengths of the three types of specimens are very similar, as shown in Table 2, indicating that differences in nitrogen contents of the flange materials had little influence on the yield strengths of the joints at this temperature. Strengthening due to constraint effects in the welds exceeded the small differences in nitrogen strengthening at room temperature, so the 304L and 316LN results were similar.

Although the final fractures were typically in the weld, all specimens yielded noticeably in the tube material. This indicates that the weld and tube strengths were well matched at 295 K.

Fracture strengths were substantially (20% or more) above the yield strengths, which is characteristic of ductile fracture. The variation in fracture strengths can be correlated to lack-of-fusion defects at the root of the weld joint. These defects occurred over approximately 10% of the cross-sectional area and reduced the fracture strengths by as much as 25%. With the exception of specimen 304L-2, significant amounts of plastic extension were observed in both the weld and tube material. For example, specimen 316LN-4 necked and failed in the tube material at the center of the gage section. For this reason, the fracture strength of the tube material was near 700 MPa at room temperature. Overall, the 295-K test results show that all material combinations deformed and failed in a ductile manner.

Table 2. Results of the 295–K Tensile Tests

Specimen	Yield Strength (MPa)	Fracture Strength (MPa)	Plastic Extension (mm)	Lack of Fusion (%)
316LN-1	490	714	5.4	0
316LN-2	420	651	3.6	0
316LN-3	441	721	7.2	0
316LN-4	448	714	7.1	0
304L-1	434	567	1.4	10
304L-2	420	504	0.6	10
21Cr–6Ni–9Mo-1	434	672	4.4	2
21Cr–6Ni–9Mo-2	441	581	1.9	2

B. Tensile Tests at 4 K

Unlike the 295-K specimens, most 4-K specimens failed before reaching the yield-strength criterion. In other words, the plastic extension at fracture (Table 3) was less than that used to define the yield strength. Factors to be considered with regard to these premature failures are (1) fusion flaws, (2) ferrite content of the welds, (3) inherent low toughness and notch sensitivity of the 21Cr–6Ni–9Mn alloy at 4 K,[8] and (4) the relative stability of the welds in relation to stress-induced martensite formation at 4 K.

Table 3. Results of the 4-K Tensile Tests

Specimen	Yield Strength (MPa)	Fracture Strength (MP)	Plastic Extension (mm)	Lack of Fusion (%)
316LN-5	1484	1820	0.8	0
304L-4	—	1190	0.4	10
304L-5	—	1274	0.0	10
21Cr-6Ni-9Mn-3	—	1050	0.0	2
21Cr-6Ni-9Mn-4	—	1260	0.0	2

The ferrite of the as-received tube material was measured as 0 FN. Ferrite measurements, taken on autogenous GTA welds made on the various stainless steels (including the tube material), ranged between 2 and 3 FN. When dilution effects are taken into consideration, the FN for the welds between the various material combinations is not expected to exceed 3 FN. Therefore, magnetic responses exceeding 3 FN in deformed regions of the specimen would imply that some martensite had formed.

Magnetic-response measurements clearly indicated that small amounts of martensite formed upon deformation of the tube material at 4 K. Results from the deformed weld areas are more uncertain because varying amounts of plastic deformation occurred in the sample areas of different welds. The 316LN welds, however were stable: no martensite was detected after deformation.

Since the initial ferrite contents of the welds were similar, lack-of-fusion flaws and low ductility in the welds should have been the major contributors to premature failure. The effect of any stress-induced martensitic transformations on the failures for these specimens was assumed to be small.

Upon review of the 4-K test results (Table 3), the 316LN specimen had the highest strength and best ductility. Its strength was closest to that of the tube material (see Appendix A). Final failure occurred in the tube material after deformation occurred in both the weld and tube material. The good behavior of this joint was expected on the basis of the high ranking given to 316LN in material studies for DOE fusion-energy applications.[2] However, type 316LN is difficult to obtain, and type 316L is acceptable for this application.

The 21Cr-6Ni-9Mn specimens failed before reaching the displacement criterion for the yield strength. The fractures occurred in the welds and showed some signs of brittleness when examined macroscopically. The fractures apparently initiated at small lack-of-fusion flaws near the

root of the welds. These flaws constituted only about 2% of the weld area, however, so the result may be more indicative of a low tolerance for cracks in these welds than a loss of weld cross-sectional area.

The 304L specimens had an average fracture strength 20% higher than that of the 21Cr–6Ni–9Mn specimens, but they also failed before reaching a displacement for yield strength. These welds had been produced at a higher heat input, which eliminated the lack-of-fusion flaws, but created a wider (and weaker) HAZ, the location of their failures.

Notched-Specimen Tensile Tests (Phase 2)

Types 304L and 316L flange specimens were selected for phase 2 testing because they performed better than the 21Cr–6Ni–9Mn specimens in phase 1 testing. These specimens were notched to simulate a fabrication defect that might occur in any of four material regions (flange HAZ, weld, tube HAZ, and tube material). Then they were loaded in tension to failure.

A. Notched-Specimen Tensile Tests at 295 K

Tensile test results for notched specimens at 295 K (Table 4) indicated that the 316L specimens had higher strengths and greater ductilities than the 304L specimens.

Specimens notched in the flange HAZ. If the welding process did not degrade the flange materials, specimens notched in the flange HAZ would be expected to have mechanical properties similar to those of unnotched specimens (Table 2) because the fracture path is longer on the flange side. A comparison of the yield strength values of the notched and unnotched 304L and 316L specimens confirms that no severe degradation occurred in either of the flange materials. Visual examination indicated that general yielding initiated in the tube or weld portion of the specimen; no deformation was visible at the flange HAZ notch. Since the flange HAZ notch was resistant to fracture, the results for the notched flange HAZ specimens were interpreted as representative of the variation in the strength and ductility of the weld joint configuration in other regions. All specimens deformed significantly in the tube material prior to failure at 295 K, but the 316L specimens were slightly superior to the 304L specimens in both strength and ductility.

Specimens notched in the weld. The largest differences between strength and plastic extension of the notched specimens occurred in the weld-notched specimens. The 316L welds had slightly higher yield and fracture strengths and 38% more plastic extension than the 304L welds.

Specimens notched in the tube HAZ region. The yield strengths, fracture strengths, and ductilities of the specimens of two flange materials with notches in the tube HAZ were similar and slightly better than those of specimens with notches in the unwelded area of the tube. The similarity in the values for the two HAZ regions was expected since the welds were produced under the same conditions.

Table 4. Results of 295-K Notched-Specimen Tensile Tests

Specimen	Notch Location	Yield Strength (MPa)	Fracture Strength (MPa)	Plastic Extension (mm)
304L-9	Flange HAZ	405	599	2.30
304L-8	Flange HAZ	405	634	3.40
304L-16	Weld	495	714	1.96
304L-15	Weld	515	695	1.80
304L-19	Tube HAZ	493	629	1.36
304L-18	Tube HAZ	500	665	1.64
304L-13	Tube	522	631	1.08
304L-6	Tube	501	625	1.06
316L-3	Flange HAZ	435	656	4.00
316L-10	Flange HAZ	449	673	3.75
316L-7	Weld	558	766	2.38
316L-9	Weld	522	769	2.84
316L-1	Tube HAZ	505	655	1.40
316L-3	Tube HAZ	511	663	1.44
316L-14	Tube	493	626	1.14
316L-17	Tube	497	619	1.08

Specimens notched in the unwelded area of the tube. The presence of a notch increased the yield strength of the tube material by approximately 16% and reduced the fracture strength by approximately 13% (cf. the unnotched-specimen values recorded in Table 2). The plastic-extension results for these notched-tube specimens indicated that the tube material had lower ductility than other locations of the specimen configuration. Comparison of the plastic extension value of the notched-tube specimen (1.1 mm) with that of the unnotched 316LN-4 specimen (7.9 mm) shows that the reduction in 295-K ductility due to the notch is appreciable and should be an important fabrication consideration.

B. Notched-Specimen Tensile Tests at 4 K

Table 5 summarizes the results of notched-specimen tensile testing at 4 K.

Specimens notched in the flange HAZ. Results for specimens notched in the flange HAZ are representative of unnotched-specimen behavior, as mentioned previously, since failure did not occur at the notch. These specimens tended to fail at approximately 85% of the tensile strength determined for the tube (Appendix A). Failure occurred in the tube cross section at the end of the reinforcement weld (Figure 3). At 4 K, the

stress-intensity factors for this region of the unnotched-specimen configuration resulted in failures at stresses only slightly higher than those associated with the notched-tube material. Plastic-extension values for the flange HAZ specimens, however, indicated that more ductility was associated with the flange HAZ failures of unnotched specimens.

Specimens notched in the weld. The notched-weld specimens of the 316L flange material were superior in strength and ductility to notched-weld specimens of 304L flange material, as was the case at 295 K. The 316L notched-weld specimens had slightly higher yield strengths (closer to the tube yield strengths reported in Appendix A) than the 304 notched-weld specimens. They also had higher fracture strengths than of any of the specimens with different notch locations and greater ductilities than the 304L notched-weld specimens.

Specimens notched in the tube HAZ region and specimens notched in the unwelded area of the tube. Specimens of the two flange materials, whether notched in the tube HAZ or in the tube, had similar properties at 4 K as well as at 295 K. Three of the yield strength values for the 316L flange material specimens were undetermined, either because the specimens broke before our 0.05-mm-extension criterion for yield, or because of a serration in the curve. Nevertheless, the results indicate that welding did not significantly degrade the tube material at 4 K.

Table 5. Results of 4–K Notched-Specimen Tensile Tests

Specimen	Notch Location	Yield Strength (MPa)	Fracture Strength (MPa)	Plastic Extension (mm)
304L-10	Flange HAZ	1154	1369	0.16
304L-7	Flange HAZ	1125	1408	0.36
304L-17	Weld	—	1461	0.20
304L —	Weld	1380	1434	0.07
304L-20	Tube HAZ	1307	1414	0.12
304L-21	Tube HAZ	1319	1405	0.08
304L-11	Tube	1281	1387	0.10
304L-12	Tube	1342	1387	0.08
316L-11	Flange HAZ	1254	1519	0.64
316L-12	Flange HAZ	1213	1513	0.72
316L-5	Weld	1446	1682	0.31
316L-8	Weld	1510	1698	0.28
316L-2	Tube HAZ	—	1453	0.04
316L-4	Tube HAZ	—	1455	0.10
316L-15	Tube	—	1383	0.07
316L-16	Tube	1349	1391	0.08

Notched-Specimen Fatigue Tests (Phase 3)

Since phase 2 tests showed that the flange HAZ of notched specimens was an unlikely fracture path, and the results for specimens with notches in the tube and tube-HAZ areas were the same for both flange materials, type 304L and type 316L candidate flange materials could be completely evaluated in the fatigue test program with only four specimen configurations: one of each of the two flange materials with notches in their welds, one with a notch in the tube HAZ, and one with a notch in the tube.

A set of five specimens was used to determine the fatigue load for a life near 4×10^4 cycles at 295 and 4 K for each specimen configuration. Test results are listed in Tables 6 and 7 and summarized in Table 8 and Figures 7 through 10. Although the tabular data are more precise, the figures show the average S–N slope and the data scatter more clearly. In the figures, the solid and dashed lines were drawn through the data points to estimate the mean S–N response at 295 and 4 K, respectively.

Table 6. Results of 295–K Fatigue Tests

Specimen	Fatigue Strength (MPa)	Fatigue Life (cycles)
304L Weld-27	412	3.37×10^4
304L Weld-28	413	2.56×10^4
304L Weld-29	487	0.94×10^4
304L Weld-30	503	1.2×10^4
304L Weld-31	412	2.6×10^4
316L Weld-22	412	4.8×10^4
316L Weld-23	487	1.45×10^4
316L Weld-24	487	1.83×10^4
316L Weld-25	412	6.21×10^4
316L Weld-26	412	4.03×10^4
Tube HAZ-27	412	3.92×10^4
Tube HAZ-28	412	4.5×10^4
Tube HAZ-29	412	5.06×10^4
Tube HAZ-30	487	1.02×10^4
Tube HAZ -31	487	1.4×10^4
Tube-6	412	2.71×10^4
Tube-18	487	1.01×10^4
Tube-19	487	1.17×10^4
Tube-20	412	2.98×10^4
Tube-21	412	2.1×10^4

Table 7. Results of 4-K Fatigue Tests

Specimen	Fatigue Strength (MPa)	Fatigue Life (cycles)
304L Weld-22	449	1.95×10^4
304L Weld-23	487	1.7×10^4
304L Weld-24	487	2.11×10^4
304L Weld-25	449	1.7×10^4
304L Weld-26	487	1.87×10^4
304L Weld-C	389	2.80×10^4
304L Weld-D	389	3.75×10^4
316L Weld-42	493	1.15×10^4
316L Weld-43	493	0.71×10^4
316L Weld-44	410	3.15×10^4
316L Weld-45	449	1.49×10^4
316L Weld-46	389	4.16×10^4
Tube HAZ-32	450	2.54×10^4
Tube HAZ-33	410	3.10×10^4
Tube HAZ-34	410	2.45×10^4
Tube HAZ-35	375	3.41×10^4
Tube HAZ-36	450	1.40×10^4
Tube-37	412	1.16×10^4
Tube-38	375	1.27×10^4
Tube-39	487	0.63×10^4
Tube-40	450	0.98×10^4
Tube-41	487	0.18×10^4
Tube-A	340	1.37×10^4
Tube-B	290	4.66×10^4

Table 8. Estimated Fatigue Strength for a Fatigue Life of 4×10^4 Cycles

Specimen	Estimated Fatigue Strength (MPa)	
	at 295 K	at 4 K
304L Weld	378	357
316L Weld	420	392
Tube HAZ	420	392
Tube	371	287

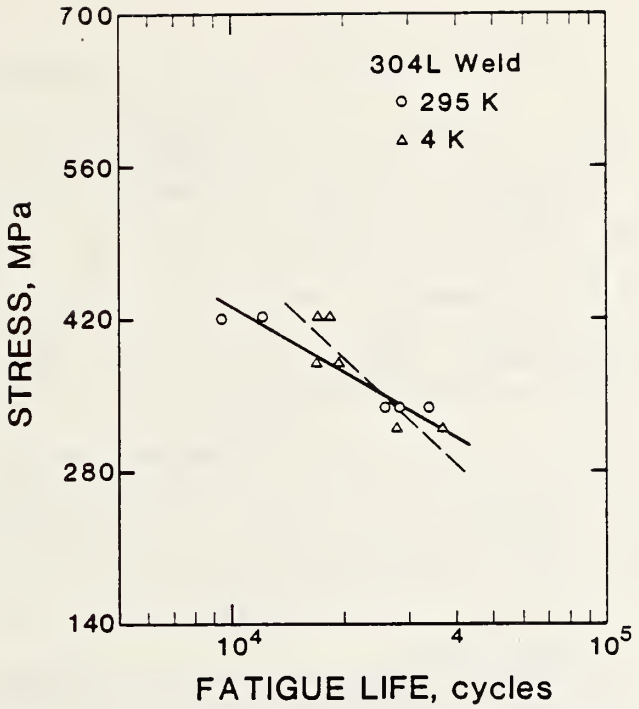

Figure 7. S–N curves for notched-weld specimens with 304L flange material.

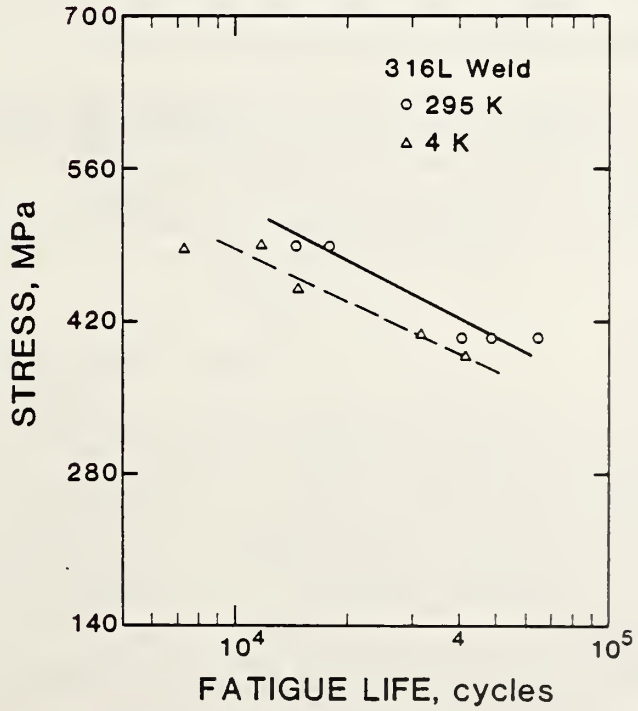

Figure 8. S–N curves for notched-weld specimens with 316L flange material.

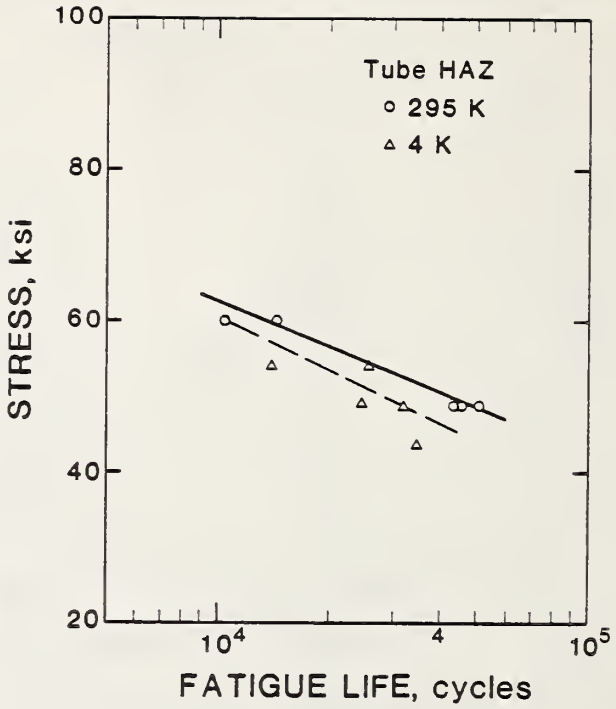

Figure 9. S–N curves for notched-tube-HAZ specimens.

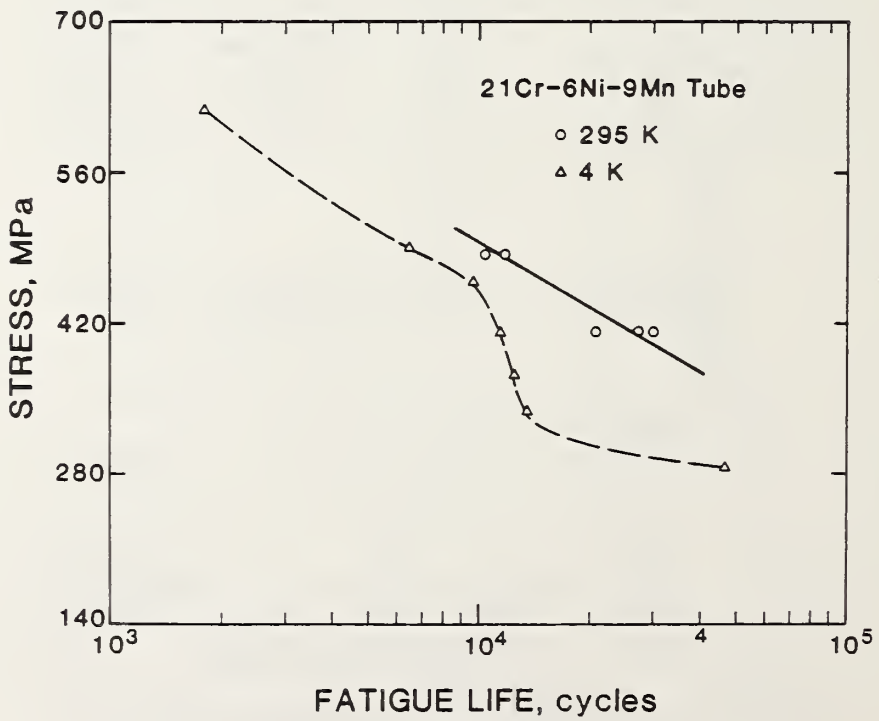

Figure 10. S–N curves for notched-tube specimens.

A. Notched-specimen fatigue tests at 295 K

Specimens notched in the weld. Examination of the strength at which the mean S–N lines intersect the design life of 4×10^4 cycles (Figures 7 and 8) shows that the type 316L flange specimen with a notch in the weld had a higher fatigue strength (420 MPa) than that of the 304L flange specimen (378 MPa). The scatter in life data is quite small (one standard deviation is nearly 14 MPa) when the complexity of the specimen design and gage region is considered; therefore, the higher fatigue strength for the weld to the 316L flange is statistically significant. The slopes of the S–N curves for the two welds are similar.

Specimens notched in the tube HAZ. The S–N slope for the specimen notched in the tube HAZ (Figure 9) is similar to that of specimens notched in the weld (Figures 7 and 8). Its fatigue strength (420 MPa) is the same as type 316L notched in the weld. This high fatigue strength might be attributed to metallurgical changes in the cold-worked tube structure due to the heat of welding.

Specimens notched in the unwelded area of the tube. The S–N slope for specimens notched in the unwelded area of the tube is similar to those for other specimens. The fatigue strength of these specimens (371 MPa) is nearly the same as that of the type 304L specimen with a notched weld (378 MPa). That the fatigue strength is lower than that of specimens with notches in the tube HAZ might be attributed to cold working during the formation of the strip or the effects of processing into tube form.

The 295-K test results in Table 8 can be summarized by stating that the notched-tube-HAZ specimens and notched-weld specimens with the type 316L flange had the highest fatigue strength for a life of 4×10^4 cycles. This is very beneficial because the virtual crack of the tube-to-flange joint ends near both of these materials. The low fatigue strength of welds to the type 304L flange suggest that this material should not be used.

B. Notched-specimen fatigue tests at 4 K

The mean S–N responses for specimens tested at 4 K were decidedly nonlinear, as shown in Figures 7 through 10. This nonlinearity challenges the accuracy of the S–N response determined from a limited test program. Therefore, more specimens were produced and tested, which eliminated the necessity to extrapolate the line to 4×10^4. The scatter in the life data was more at 4 K (perhaps a standard deviation as high as 28 MPa) than at 295 K.

The relative ranking of the estimated strengths of the four specimen designs was the same at 4 K as at 295 K (see Table 8).

C. Summary

The results at both 295 and 4 K indicate that welds with the 316L flange have a superior fatigue strength for a life of 4×10^4 cycles (Table 8). The tube had the lowest estimated strength at this life and would limit the design. However, this ranking was specific to a notch radius of 0.064 mm, which simulates a fabrication flaw. The response of unnotched tubes could be substantially better.

CONCLUSIONS

1. The type 316L flange material produced welds with greater tensile ductilities at 4 K than the type 304L or 21Cr–6Ni–9Mn flange materials. The type 316L flange material was less sensitive to martensite formation and had a lower magnetic response after deformation.

2. The type 316L flange material produced welds with higher notch strengths than the type 304L flange material.

3. The welds to type 316L flange material had a greater estimated fatigue strength than welds to type 304L flange material at both 295 and 4 K.

4. The 21Cr–6Ni–9Mn tube material had the lowest estimated failure strength at 4 K for fatigue testing with a 0.064-mm radius notch.

ACKNOWLEDGMENTS

This work was supported by the Superconducting Super Collider Central Design Group and the U.S. Department of Energy, Office of Fusion Energy.

REFERENCES

1. R. P. Reed, ed., Summary of mechanical property measurements of structural alloys, in: Materials Studies for Magnetic Fusion Energy Applications at Low Temperatures – X, NBSIR 87-3067, R. P. Reed, ed., National Bureau of Standards, Boulder, Colorado, 1987, pp. 5–7.

2. R. P. Reed, N. J. Simon, P. I. Purtscher, and R. L. Tobler, Alloy 316LN for low temperature structures: A summary of tensile and fracture data, in: Materials Studies for Magnetic Fusion Energy Applications at Low Temperatures – IX, R. P. Reed, ed., NBSIR 86-3050, National Bureau of Standards, Boulder, Colorado, 1986, pp. 13–26.

3. R. L. Tobler, T. A. Siewert, and H. I. McHenry, Strength–toughness relationship for austenitic stainless steel welds at 4 K, Cryogenics, vol. 26, 1986, pp. 392–396.

4. N. J. Simon and R. P. Reed, Strength and toughness of AISI 304 and 316 at 4 K, in Materials Studies for Magnetic Fusion Energy Applications at Low Temperatures – IX, R. P. Reed, ed., NBSIR 86-3050, National Bureau of Standards, Boulder, Colorado, 1986, pp. 27–42.

5. Standard test methods and definitions for mechanical testing of steel products – A370, 1987 Book of ASTM Standards, vol. 03.01, American Society for Testing and Materials, Philadelphia, Pennsylvania, 1987, p. 4.

6. D. T. Read and R. L. Tobler, Mechanical property measurements at low temperatures, in: Advances in Cryogenic Engineering – Materials, vol. 28, Plenum, New York, 1982, pp. 17–28.

7. Mechanical Testing, vol. 8 of the Ninth Edition of Metals Handbook, American Society for Metals, Metals Park, Ohio, 1983, p. 573.

8. R. L. Tobler and D. Meyn, Cleavage-like fracture along slip planes in Fe–18Cr–3Ni–13Mn–0.37N austenitic stainless steel at liquid helium temperature, in: Materials Studies for Magnetic Fusion Energy Applications at Low Temperatures – XI, NBSIR 88-3082, R. P. Reed, ed., National Bureau of Standards, Boulder, Colorado, 1988, pp. 89–101.

APPENDIX A. MECHANICAL PROPERTIES OF THE 21Cr–6Ni–9Mn TUBE AT 4 K

This adjunct study was prompted by (1) lack of information on the mechanical properties of 21Cr–6Ni–9Mn tube at 4 K and (2) information received during the testing program that seamless tube with a 1.2-mm wall thickness would replace the welded tube with a 0.9-mm wall thickness from which our test specimens had been constructed.

To evaluate the differences in tube material, both tubes were tested in uniaxial tension at 4 K. A simple reduced-section specimen design with a 6-mm width and a 40-mm gage length by tube thickness was used. To be conservative, the loading direction selected was normal to the tube length because the tube is weaker in this direction than along its length. This loading direction also enabled the seam weld to be centered in the gage length and transverse to the loading direction of the specimen.

The values for yield and tensile strength listed in Table A1 show no weakening of the specimen due to the weld. The higher yield strength for the welded specimen is attributed to the data scatter caused by our inability to completely remove the existing bend from the tube during specimen preparation without affecting the mechanical test results. Therefore, the yield strength values are nominal and should not be used in design calculations.

Although the elongation values (based on a nominal 25-mm gage length) indicate that the two tube thicknesses could be used interchangeably in the study of flange materials, we chose to use only the tube with 0.9-mm-thick walls to minimize the variables in the study. For the same reason, we excluded seam welds from the gage lengths of these specimens.

Table A1. Mechanical Properties for the 21Cr–6Ni–9Mn Tube at 4 K

Specimen	Yield Strength* (MPa)	Tensile Strength (MPa)	Elongation (%)
seamless – 1.2-mm wall	1420	1841	2.6†
welded – 0.9-mm wall only base metal in gage length	1246	1806	2.1†
welded – 0.9-mm wall transverse seam weld in gage length	1425	1806	17.5∓

* For information only. Since the tubes could not be totally straightened without introducing permanent deformation, the yield strength data contain substantial scatter.

† Broke outside the nominal 25-mm gage length.

∓ Broke within the gage length.

STRENGTH AND TOUGHNESS OF AN ALUMINUM-DEOXIDIZED WELD FOR CRYOGENIC SERVICE*

C. N. McCowan and T. A. Siewert
National Bureau of Standards
Boulder, Colorado

D. J. Kotecki
Teledyne McKay Research Laboratory
York, Pennsylvania

The strength and toughness of an aluminum deoxidized stainless steel weld (Fe–13Cr–13Ni–20Mn–0.17C) were evaluated for cryogenic service. At 4 K, the yield and tensile strengths of the weld were approximately 850 and 950 MPa, respectively; its fracture toughness [$K_{Ic}(J)$] was 85 MPa·m$^{\frac{1}{2}}$. At 76 K, its Charpy V-notch absorbed energy was 42 J. The strength–toughness relationship of this weld at cryogenic temperatures was no better than that of more conventional, silicon-deoxidized welds. Large (2- to 5-μm), aluminum-rich inclusions were observed in the weld, and data related to the role of inclusions in the ductile fracture process are reported.

I. INTRODUCTION

The fracture toughness of AISI type 316LN stainless steel at cryogenic temperatures is affected by inclusion content, size, and distribution.[1] Two parameters controlling the inclusion morphology are the welding process and the deoxidation system of the welding electrode. Silicon is the principal deoxidant in stainless steel electrodes, but manganese and chromium often combine with the SiO_2 because together a more stable compound is formed. The result is a closely spaced dispersion of spherical $MnSiO_3$ inclusions with 0.1- to 1-μm diameters.

The 4-K fracture toughness of welds is lower than that of matching composition base materials.[2] Preliminary studies indicate that the primary cause for this lower toughness is the higher inclusion content in the welds.[3] Since weld toughness limits the design of cryogenic structures, other inclusion-control processes and deoxidation systems are being sought.

---

*This paper was prepared specifically for this report; it will not be published elsewhere.

This study investigates the use of an aluminum-based deoxidation system for stainless steel welds as a means to improve the toughness at 4 K. To avoid precipitation of AlN particles, the weld was strengthened by carbon and manganese additions rather than nitrogen. To increase the toughness, levels of chromium and nickel were chosen to produce a weld with low ferrite and high nickel content.[4,5]

II. MATERIALS AND PROCEDURE

A. *Weld Material*

The weld composition and ferrite content are given in Table 1. To obtain the desired weld composition, a thin strip of type 304L stainless steel was used as the sheath for the flux core electrode. The flux components and the remainder of the alloy were added to the center. The electrode produced was 2.4 mm (3/32 in) in diameter.

Table 1. Weld Composition (wt.%) and Ferrite Number (FN)

C	Mn	Si	Cr	Ni	N	Al	O	P	S	FN
0.172	20.0	0.33	12.6	13.4	0.05	2.0	0.001	0.023	0.003	0.3

B. *Welding*

Welds were made using a flux core arc (FCA) electrode. A 25-mm-thick mild-steel plate material was beveled to produce a 45° included angle for the single-vee weld joint configuration. The base material was double buttered (surfaced with the welding electrode to prevent dilution effects) in accordance with AWS A5.22-80 prior to making the weld. After buttering, a root gap of 12.5 mm was used to ensure that an ample volume of undiluted weld metal was available for test-specimen preparation. The welds were made at 275 A and 28 V with a travel speed of about 380 to 400 mm/min (15 to 16 in/min).

C. *Mechanical Testing*

Uniaxial tensile specimens with a 12.5-mm diameter (conforming to ASTM A 370) were used for 293-K testing. Specimens with a 6.25-mm diameter were used in tests at 4 K. These all-weld-metal tensile specimens were removed from the welds so that the tensile axis was parallel to the welding direction. One 293-K tensile test and two 4-K tests were performed. Specifics of the liquid-helium tensile-testing apparatus are described elsewhere.[6]

The 25.4-mm-thick compact tension specimen was side-grooved to enhance plane strain conditions at the crack front; the notch was parallel to the welding direction and oriented to result in crack growth along the welding direction. Fracture toughness was measured at 4 K by using the J-integral test method designated by ASTM E 813-81 and the single-specimen unloading-compliance method.[7] The $K_{Ic}(J)$ value was calculated from

$$K_{Ic}(J) = (J_{Ic} \cdot E)^{\frac{1}{2}} \qquad (1)$$

For this calculation, the value used for Young's modulus (E) at 4 K was 200 GPa.

III. RESULTS AND DISCUSSION

A. *Metallography*

The weld had a cellular solidification structure and appeared to be fully austenitic (Figure 1). Inclusion diameters in the weld ranged from greater than 5 μm to less than 0.5 μm. The large, angular inclusions were rich in aluminum, according to energy-dispersive x-ray analysis of the polished surface with a scanning electron microscope. Manganese-rich inclusions were also identified in the matrix with x-ray analysis, but they occurred much less frequently than the aluminum-rich inclusions, and they were generally smaller (less than 1 μm) with a more spherical, glassy appearance.

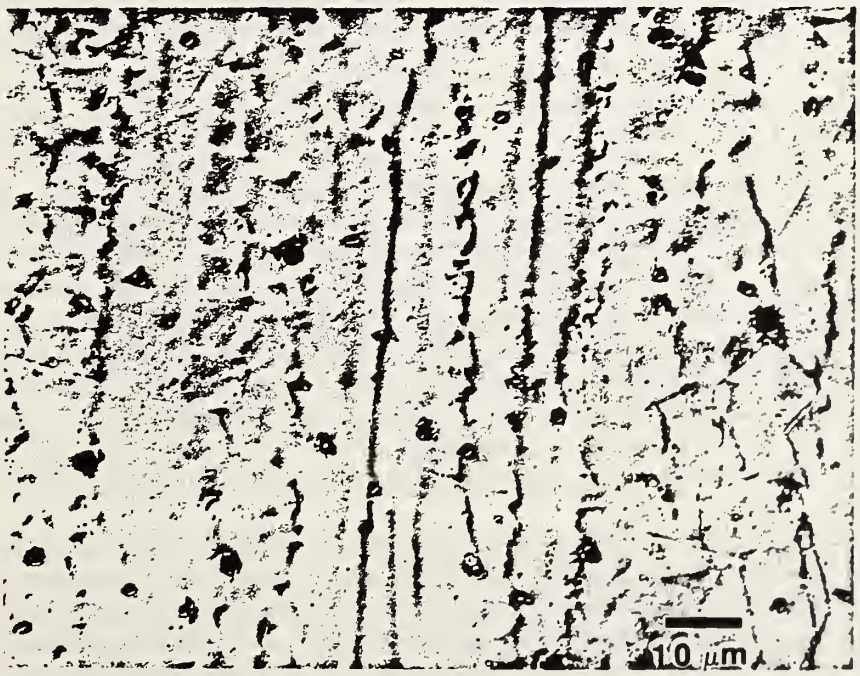

Fig. 1. Fully austenitic weld with large, faceted, aluminum-rich inclusions.

B. *Tensile Testing*

The tensile test results (Table 2) show that the yield strength of the weld increased from 383 to 850 MPa when the test temperature was decreased from 293 to 4 K. The tensile strength increased from 565 MPa at 293 K to 950 MPa at 4 K.

Table 2. Tensile Test Results

Temperature (K)	Yield Strength (MPa)	Ultimate Strength (MPa)	Elongation (%)
293	383	565	41
4	849	1000	20
4	849	924	12

On the basis of results of two previous studies, the relative strengthening contributions of alloying elements in the weld were estimated. The strengthening terms taken from these studies were

a. 14 MPa/wt.% for manganese, from a study of type 18Cr–8Ni stainless steel welds that contained up to 10 wt.% manganese;[8]

b. 1700 MPa/wt.% for carbon, from a study of the strengthening contributions of carbon and nitrogen in type 300 series stainless steels.[9]

Using these terms, we calculated that carbon would contribute 292 MPa, and manganese would contribute 280 MPa to the yield strength of the weld at 4 K. Subtracting these contributions from the total yield strength of 850 MPa leaves a base strength of 278 MPa, which includes the strengthening due to other solid-solution alloying elements in the weld. This result agrees well with the 275- to 300-MPa constants used in the equations from which the carbon and manganese coefficients were obtained. Although this excellent agreement may be somewhat fortuitous, the comparison indicates that the substitutional strengthening of manganese in the weld may be comparable to the interstitial strengthening of carbon.

The substitutional strengthening of aluminum was not considered in the estimates of strength. Bulk x-ray analysis, however, indicated that the weld matrix probably had more than 1 wt.% aluminum in solution. Since the volume occupied by aluminum atoms at substitutional lattice positions is greater than that of manganese atoms, the misfit and lattice distortion is greater, and some degree of strengthening by aluminum would be expected.[10-12] Rough estimates of atomic size indicate that aluminum

additions would result in a lattice expansion more similar to that of molybdenum than that of manganese.[13] Strengthening coefficients reported for molybdenum at 4 K range from 30 to 80 MPa/wt.%.[14-17]

C. *Fracture Testing*

Charpy V-notch test results for five weld specimens were an average absorbed-energy value of 41.6 J (30.5 ft·lbf) and a lateral expansion of 0.41 mm (0.016 in) at 76 K (Table 3). These values are similar to the 40-J and 0.45-mm values of 18Cr–8Ni stainless steel SMA welds strengthened to 850 MPa at 4 K by nitrogen and manganese additions, but they are somewhat lower than the 55-J and 0.75-mm values of the SMA welds with 14 wt.% nickel.[15]

Table 3. Charpy V-Notch Test Results at 76 K

Sample	Absorbed Energy (J)	Lateral Expansion (mm)
1	45.2	0.46
2	41.2	0.41
3	38.2	0.41
4	44.1	0.48
5	38.2	0.33

The fracture toughness of the weld was 85 MPa·$m^{\frac{1}{2}}$ at 4 K. The K_{Ic}(J) calculated for the weld is comparable to the lower limit of the strength–toughness trend observed for type 308L and 316L stainless steel weld metal at 4 K.[2] The upper band limit, at a 850-MPa strength level, however, is near 150 MPa·$m^{\frac{1}{2}}$, and base metal values are even higher. Therefore, the strength–toughness relationship of the carbon-strengthened, aluminum-deoxidized weld composition evaluated in this study was no better than that of the more conventional nitrogen-strengthened stainless steel welds.

D. *Fractography and Inclusion Characterization*

In a continuing effort toward improved modeling of the effect of inclusions on crack initiation and growth for ductile fracture processes, several kinds of measurements are a routine part of our microstructural characterization procedure. Data gathered for the weld composition investigated in this study include inclusion counts on a mechanically polished surface, ductile-dimple counts on fractured surfaces, and diameters for inclusion–dimple pairs found on the fracture surfaces.

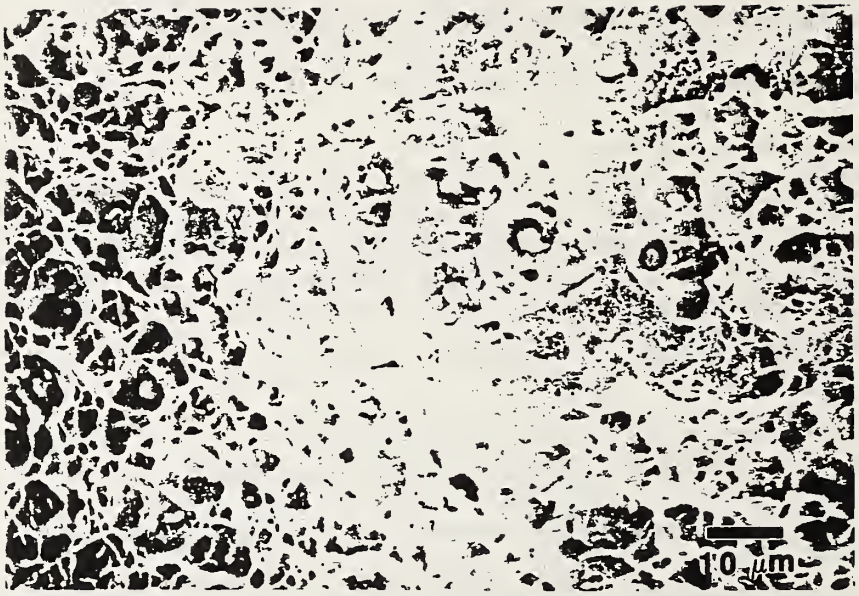

Fig. 2. Ductile-dimple morphology observed near the notch of a 4-K compact-tension specimen.

The fracture surfaces of the test specimens showed no signs of brittle behavior during failure (Figure 2). Ductile-dimple morphologies in areas near the notch on the compact tension specimens and in areas near the center of the tensile specimens were similar in appearance. The faceted appearance of the larger aluminum-rich inclusions is shown in Figure 3.

When cross sections taken normal to the fracture surface of 4-K tensile specimens were examined, void growth at inclusion sites was limited to a thin layer adjacent to the fracture surface or cracks that had branched away from the fracture surface. As shown in Figure 4, little or no void growth was observed at inclusions even when they were located very near the crack surfaces. At distances greater than 50 μm from the fracture surface, the inclusion–matrix interface generally appeared to be coherent, but several areas contained microcracks. We speculate that these areas may be due to microvoid coalescence at inclusion clusters or to weld flaws that later combine and cause fracture. Similar microcrack formation and linking processes have been postulated as a failure mechanism for more conventionally deoxidized, nitrogen-strengthened welds with $MnSiO_3$ inclusions.[1] The weld examined in this study, however, had fewer voids at inclusion sites than welds with $MnSiO_3$ inclusions. So, there may be significant differences in the critical stress and strain for void nucleation of the two inclusion types.

Fig. 3. Fractograph of a 4-K tensile specimen showing the large, faceted, aluminum-rich inclusions present in the weld.

Fig. 4. Voids located only at inclusions near cracks (crack branch) in cross sections normal to the fracture surface.

Inclusion counts from polished weld samples indicate an inclusion density of approximately 7,500/mm^2, which is low compared to the 30,000 to 40,000/mm^2 for flux core arc (FCA), shielded metal arc (SMA), and gas metal arc (GMA) welds evaluated in previous studies.[1] The low inclusion density reflects the low oxygen content of the weld metal. The planar inclusion spacing (proportional to the inverse square root of the inclusion density[18]), therefore, is larger than those of previously evaluated welds. Since the frequency of large inclusions observed on the fracture surfaces was high, any beneficial effect of the large inclusion spacing (11.5 μm) on the toughness of this weld composition appears to have been offset by the increased average size of the inclusions. Adverse effects on the toughness due to aluminum can not be ruled out, however; reductions in Charpy V-notch absorbed energies have been correlated to aluminum contents in ferritic steels.[19]

The ductile-dimple densities estimated from the fractured tensile and compact tension specimens had similar values—44,500 dimples/mm^2. The ratio of planar inclusion densities to dimple densities is approximately 6, lower than the values of 8 to 11 previously found for welds.[3] In general, these ratios may serve as a macroscopic roughness parameter: as dimple densities approach planar inclusion densities, toughness decreases. A ratio of 2 would indicate equal densities for these quantities, since a correction factor of 2 is generally used for the 2-D to 3-D surface conversion.[20] For now, too few data are available to evaluate the use of this variable in fracture models.

The inclusion-to-dimple diameter ratio is used to compare the ductile flow of the matrix during the fracture process of welds. The 0.55 ratio for the weld of this study is higher than the 0.25 to 0.35 ratios for previously evaluated welds, implying that there was less local plastic flow before fracture.[3]

IV. CONCLUSIONS

1. The aluminum-based deoxidation system used for the FCA weld evaluated in this study did not improve the fracture toughness of stainless steel welds at 4 K.

2. Inclusions found in the aluminum-deoxidized welds were large and appeared to be faceted crystals rather than glassy spheres, which are observed in silicon-based slag systems.

3. The use of aluminum deoxidation systems in stainless steel welds may result in increased toughness if the inclusion size can be substantially reduced.

ACKNOWLEDGMENTS

This work was supported by the U.S. Department of Energy, the Office of Fusion Energy.

REFERENCES

1. C. N. McCowan and T. A. Siewert, Inclusions and fracture toughness in stainless steel welds at 4 K, Advances in Cryogenic Engineering – Materials, vol. 34, Plenum Press, New York, 1988, pp. 355–342.

2. R. L. Tobler, T. A. Siewert, and H. I. McHenry, Strength–toughness relationship for austenitic stainless steel welds at 4 K, Cryogenics, vol. 26, 1986, pp. 392–296.

3. T. A. Siewert and C. N. McCowan, The role of inclusions in the fracture of austenitic stainless steel welds at 4 K, Welding Metallurgy of Structural Steels, ed. J.Y. Koo, The Metallurgical Society, New York, 1987, pp. 415–428.

4. E. R. Szumachowski and H. F. Reid, Cryogenic toughness of SMA austenitic stainless steel weld metals: Part 1 – Role of ferrite, Welding Journal, vol. 57, no. 11, pp. 325s–333s.

5. R. P. Reed, P. T. Purtscher, and K. A. Yushchenko, Nickel and nitrogen alloying effects on the strength and toughness of austenitic stainless steels at 4 K, Advances in Cryogenic Engineering – Materials, vol. 32, Plenum Press, New York, 1986, pp. 43–50.

6. D. T. Read and R. L. Tobler, Mechanical property measurements at low temperatures, Advances in Cryogenic Engineering – Materials, vol. 28, Plenum Press, New York, 1982, pp. 17-28.

7. R. L. Tobler, D. T. Read, and R. P. Reed, Strength/toughness relationship for interstitially strengthened AISI 304 stainless steel at 4 K temperature, Fracture Mechanics, ASTM STP 743, American Society for Testing and Materials, Philadelphia, Pennsylvania, 1981, pp. 250–268.

8. C. N. McCowan, T. A. Siewert, R. P. Reed, and F. B. Lake, Manganese and nitrogen in stainless steel SMA welds for cryogenic service, Welding Journal, vol. 66, no. 3, 1987, pp. 84s–92s.

9. R. P. Reed and N. J. Simon, Low temperature strengthening of austenitic stainless steels with nitrogen and carbon, Advances in Cryogenic Engineering – Materials, vol. 30, Plenum Press, New York, 1984, pp. 127-136.

10. P. Haasen, Solution hardening in f.c.c. metals, Dislocations in Solids, ed. F. R. N. Nabarro, North-Holland, New York, 1976, pp. 155–189.

11. F. R. N. Nabarro, The theory of solution hardening, Philosophical Magazine, vol. 35, 1977, pp. 613–622.

12. R. Labusch, Statistische Theorien der Mischkristallhartung, Acta Metallurgica, vol. 20, 1972, pp. 917–927.

13. B. D. Cullity, Elements of X-Ray Diffraction, 2nd Ed., Addison Wesley, Reading, Massachusetts, 1978.

14. R. P. Reed, Austenitic stainless steels with emphasis on strength at low temperatures, Materials Studies for Magnetic Fusion Energy Applications at Low Temperatures – XI, NBSIR 88-3082, National Bureau of Standards, Boulder, Colorado, 1988, pp. 1–37.

15. C. N. Mccowan and T. A. Siewert, Influence of molybdenum on the strength and toughness of stainless steel welds for cryogenic service, Welding Metallurgy of Structural Steels, ed J.Y. Koo, The Metallurgical Society of the AIME, New York, 1987, pp. 427-438.

16. S. Yamamoto, N. Yamagami, and C. Ouchi, Effect of metallurgical variables on strength and toughness of Mn–Cr and Ni–Cr stainless steels at 4.2 K, Advances in Cryogenic Engineering – Materials, vol. 30, Plenum Press, New York, 1986, pp. 57–64.

17. R. Miura, Development of high strength structural alloys for superconducting reactor, Japan Steel Works, Hokkaido, Japan; unpublished.

18. E. E. Underwood, Quantitative Stereology, Addison-Wesley, Reading, Massachusetts, 1970.

19. G. E. Linnert, Welding metallurgy: carbon and alloy steels, vol. 2, American Welding Society, Miami, Florida, 1967.

20. E. E. Underwood, Estimating feature characteristics by quantitative fractography, Journal of Metals, April 1986, pp. 30–32.

INCLUSIONS AND FRACTURE TOUGHNESS IN STAINLESS STEEL WELDS AT 4 K*

C. N. McCowan and T. A. Siewert
Fracture and Deformation Division
National Bureau of Standards
Boulder, Colorado

Eight stainless steel welds were studied to evaluate the effect of inclusion content on the fracture toughness at 4 K. The loss in toughness associated with the inclusion spacing agreed with the trend previously determined between inclusion spacing and toughness in stainless steel base materials. This finding indicates that the smaller inclusion spacings observed in welds are the principal reason why welds have lower fracture toughness than base materials of similar compositions at 4 K and why some welds are tougher than others. Inclusion-size distributions were found to be similar for the welds. The oxygen content of the welds was evaluated as an alternate means of representing the effect of inclusions on the weld toughness at 4 K.

INTRODUCTION

Type 316LN stainless steel is emerging as the preferred structural material for superconducting magnet casings designed to operate at 4 K. It has a higher strength than the older 316L grade and comparable toughness at cryogenic temperatures.[1-3] Unfortunately, welding electrodes matching this composition and strength have substantially poorer toughness at 4 K than the stainless steel plate.[4]

This study investigates the effect of inclusions on toughness as a step toward explaining the lower strength–toughness relationship that is observed for welds.

---

*Expansion of a previous study of three welds to eight welds. The earlier study was reported in *Materials Studies for Magnetic Fusion Energy Applications at Low Temperatures – X*. This paper was published in *Advances in Cryogenic Engineering – Materials*, vol. 36, Plenum, New York, 1988, pp. 335–342.

Although the role of inclusions in the dimple rupture fracture process has long been recognized, attempts to model effects of inclusions on the fracture toughness have only recently been undertaken.[5-7] Traditionally, the process of dimple rupture is separated into three stages: (1) void nucleation, (2) void growth, and (3) void coalescence. Nonmetallic inclusions are a common site for void nucleation. However, the relative amounts of the energy measured in the fracture toughness test due to void nucleation as opposed to void growth and coalescence may vary, depending on the inclusion morphology and composition, the testing conditions, and the strength of the matrix material.[6]

EXPERIMENTAL PROCEDURES

Eight stainless steel welds were selected for evaluation in this study. Only welds having FN values of less than 3 were selected to avoid any appreciable effect on toughness due to this variable. The compositions and ferrite numbers (FN) of the welds are given in Table 1.

The test matrix includes welds with varying nonmetallic inclusion content (a result of different welding processes), strength, and toughness. The welds are characterized and referenced in Table 2.

Table 1. Compositions (wt.%) and Ferrite Content (FN) of the Welds

Weld	C	Mn	Si	P	S	Cr	Ni	Mo	N	O	FN
497-5	0.01	2.2	0.46	0.010	0.013	18	15	2.3	0.03	0.059	0.9
508-2	0.02	1.4	0.47	0.020	0.003	18	12	2.1	0.07	0.025	3.0
1616						16	16	2		0.040	0
1	0.03	1.7	0.58	0.033	0.011	19	14	2.3	0.04	0.070	0.1
5	0.06	1.7	0.56	0.033	0.009	19	13	2.3	0.04	0.063	1.2
10	0.03	5.4	0.26	0.006	0.007	18	20	0.10	0.16	0.037	0
11	0.03	5.4	0.26	0.006	0.007	18	20	0.10	0.16	0.005	0
12	0.03	5.4	0.26	0.006	0.007	18	20	0.10	0.16	0.005	0

Table 2. The 4-K Mechanical Properties, Inclusion Data, and Welding Information for the Welds

Weld	Ref.	4-K Yield Strength (MPa)	K_{Ic}(J) (MPa$\sqrt{m}$)	Inclusion Density (no./mm^2)	Mean Inclusion Diameter (μm)	Welding Information
497-5	8	608	159	33,173	0.41	GMAW, tubular electrode, 99Ar–10$_2$
508-2	8	779	163	24,983	0.29	GMAW, 99Ar–10$_2$
1616	9	607	235	19,050	0.47	FCAW
1	10	694	179	31,796	0.39	SMAW
5	10	924	143	37,587	0.38	SMAW
10	11	1015	203	11,317	0.45	GMAW, 98Ar–20$_2$
11		991	287	9,801	—	GMAW, Ar
12		1027	263	8,300	—	GMAW, Ar

Welds 11 and 12 were made using the same GMA electrode and welding configuration as weld 10.[11] The shielding gas used for these welds, however, was commercial-grade argon instead of the 2%-oxygen, 98%-argon mixture used for weld 10. In addition, a second shielding enclosure was fabricated to reduce the oxygen contents around the arc. For weld 11, a droplet transfer was established (20 V; 175 A; 12-mm tip-to-work distance), and for weld 12, spray transfer was established (25 V; 280 A; 18-mm tip-to-work distance).

The oxygen contents of the welds were determined with an interstitial element analyzer. Sections (0.5 to 1 g) were cut from test specimens using an abrasive cut-off saw and then cleaned in hydrochloric acid prior to analysis. The average oxygen content of five samples was reported. Standard deviations did not exceed 0.01 wt.%.

Inclusion measurements were made on mechanically polished weld samples taken from the fractured tensile specimens. The data for welds 10, 1616, 297-5, 508-2, 1, and 5 were gathered using an image analysis program on a scanning-electron microscope (SEM) at a magnification of 3000X. Back-scattered electrons were used for imaging. Three hundred inclusions were counted per sample. Inclusion-density data for welds 11 and 12 were obtained visually at 3000X. These welds were recently tested, and size distribution data has not yet been accumulated. The average inclusion spacing (λ) was calculated as the inverse square root of the inclusion density.

RESULTS AND DISCUSSION

Distribution and Density of Inclusions

Three general types of inclusion-size distributions were observed for the welds. The distribution curves for the welds having inclusion densities larger than 30,000/mm^2 are similar and can be characterized by one line in Fig. 1. As might be expected, the two SMA welds are included in this group. The number of small-diameter inclusions in these welds increased rapidly up to a peak at approximately 0.25 μm. A similar inclusion-size distribution was found for weld 497-5. This weld was made using a tubular GMA electrode and a 99%-argon, 1%-oxygen shielding gas mixture. The inclusion density of the FCA weld (1616) was only 19,000/mm^2; the distribution curve was similar in shape to that of the GMA weld made with a 2%-oxygen, 98%-argon shielding gas.[10] These two welds are characterized by a second line; they show a broader distribution of inclusion sizes through the peak region. The two types of curves discussed thus far do not differ greatly: the majority of inclusions in these welds have diameters within the range 0.15 to 0.45 μm, the mean diameter values differ by less than 0.07 μm, and the curves have "tails" as larger inclusion diameters are approached. The only significant difference was the distribution for weld 508-2 (a GMA weld made using a 1%-oxygen, 99%-argon shielding gas). More than 50% of the inclusions in this weld had diameters of less than 0.3 μm.

Results here indicate that, with the exception of weld 508-2, the principal difference among the inclusions in these welds is the inclusion density and not the distribution. Weld 508-2, however, clearly indicates that different types of size-distribution curves are possible.

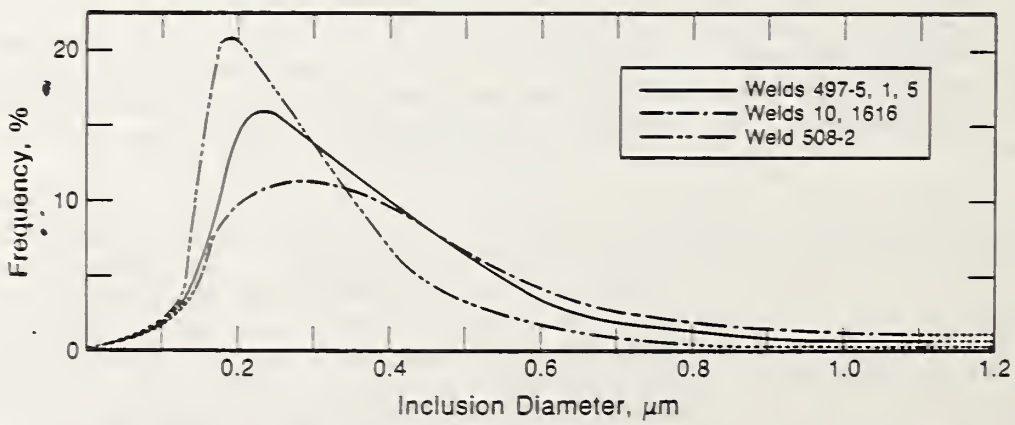

Figure 1. Inclusion-size distribution curves for the welds.

Inclusion Spacing as a Measure of Toughness

In type 316 and 316LN stainless steel base materials the effect of inclusion spacing on the fracture toughness at 4 K has been predicted by the equation:

$$K_{Ic}(J)\ (MPa\sqrt{m}) = 150 - 0.31\sigma_y + 16.6Ni + 2.3\lambda \qquad (1)$$

where Ni is defined as nickel content in weight percent, σ_y as the yield strength at 4 K, and λ as inclusion spacing ($1/\sqrt{\text{inclusion density}}$) in micrometers.[12]

Attempts to develop an equation from the weld data using stepwise linear regression were unsuccessful. The effects of strength, nickel, and inclusion spacing on the fracture toughness were confounded, partly because the welds with the larger inclusion spacings also had higher nickel contents.

Three welds from the test matrix can be used to evaluate the effect of inclusion spacing on the fracture toughness. These welds (10, 11, 12) have identical compositions and approximately equal yield strengths so that nickel content and strength variables need not be considered. Using the 2.3 coefficient for inclusion spacing in Eq. 1, an increase in inclusion spacing of 31 μm would be required to account for the 72 $MPa\sqrt{m}$ increase in toughness between weld 10 and the average toughness of welds 11 and 12. The measured difference in inclusion spacing, approximately 1 μm, indicates that the coefficient of 2.3 is an order of magnitude too low to express the effect of inclusion spacing on toughness in these three welds. Possibly other factors not considered here are responsible for the greater effect of inclusion spacing on the toughness. Errors in inclusion-spacing measurements on this fine scale could also be responsible for the disagreement between inclusion-spacing coefficients of the weld and base materials.

The effect of inclusion spacing for the welds can be compared with the effect observed in base materials in a more simple manner by using the concept of a Quality Index [$K_{Ic}(J)\cdot\sigma_y$].[13] For type 316 and 316LN stainless steel base materials, the inclusion spacing versus the Quality Index is shown in Fig. 2. The data are normalized to a 12 wt.% nickel content by using the 18.3×10^3 coefficient for the effect of nickel on the Quality Index determined in the base metal study.[13] A similar coefficient for nickel (18.7×10^3) was determined for the weld data. Although the regression coefficient (R^2) is low (0.75), the standard error for the coefficient (4.4×10^3) is similar to that for the base-metal coefficient. After normalizing the weld data to 12 wt.% nickel, the weld-metal inclusion spacing was plotted versus the normalized Quality Index, $K_{Ic}\cdot\sigma_y$ (Fig. 3). For comparison, the line expressing the effect of inclusions on types 316 and 316LN base materials and the scatter bands associated with it were extrapolated into the weld-inclusion-spacing region. Clearly, the trend observed for the welds

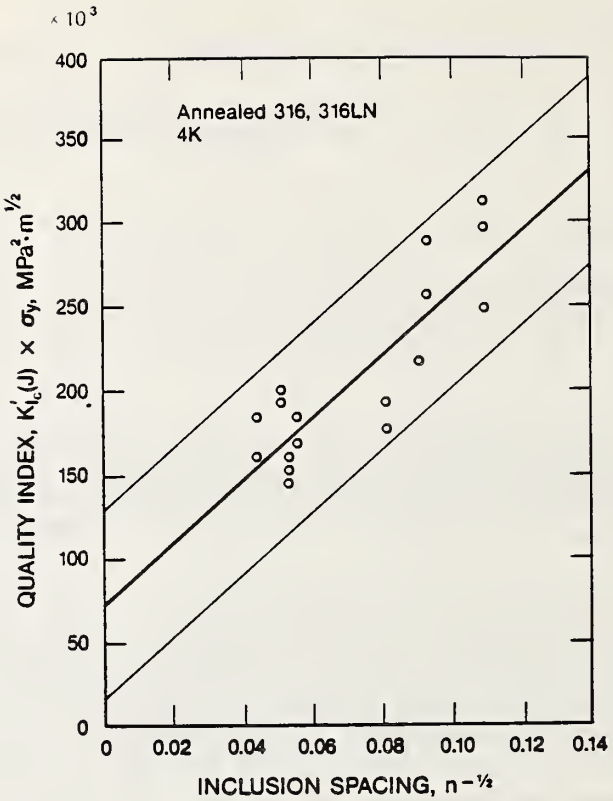

Figure 2. The Quality Index (normalized to 12 wt.% nickel) at 4 K, versus the inclusion spacing for type 316 stainless steel base materials. Scatter bands represent 2 SDs.[13]

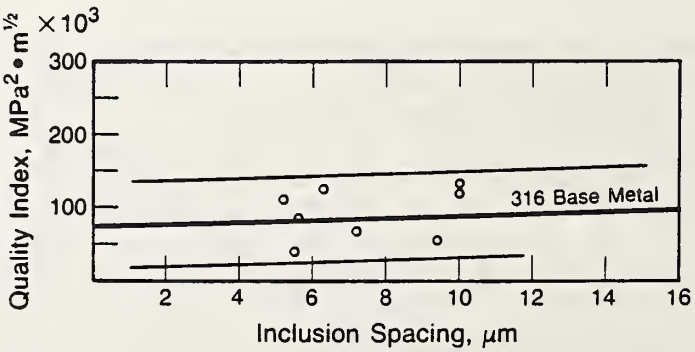

Figure 3. The Quality Index (normalized to 12 wt.% nickel) at 4 K versus the inclusion spacing for the welds.

between inclusion spacing and the Quality Index at 4 K agrees with that found for the base materials. In fact, the magnitude of the effect that inclusions have on the fracture toughness would indicate that this parameter alone may explain the lower strength–toughness relationship observed for the welds.

Oxygen Content as a Measure of Toughness

The oxygen content of a weld deposit is another means by which the inclusion content can be measured. When the bulk of the weld-metal inclusions are assumed to be oxides, the inclusion volume fraction is proportional to the oxygen content of the weld deposit.[14] On this basis, oxygen content was compared to weld toughness in Fig. 4. The Quality Index, normalized to 12 wt.% nickel, was used to indicate more clearly any relationship between the oxygen content and the toughness. The $K'_{Ic}(J)\cdot\sigma_y$ values decreased as the oxygen content increased.

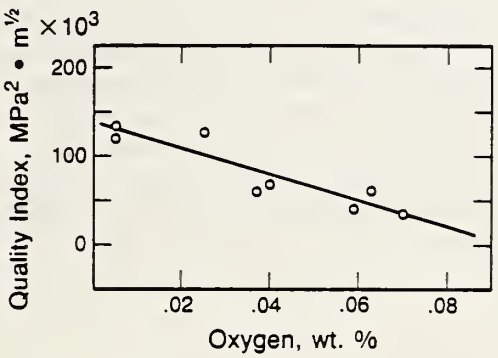

Figure 4. The Quality Index (normalized to 12 wt.% nickel) versus the oxygen content of the welds.

The usefulness of oxygen content as a measure of the inclusion content is a promising, but rather simplistic approach. It requires a similar distribution of the inclusion volume fraction for the welds, and it does not include the influence on toughness of the more fundamental quantity, inclusion spacing. Oxygen content, when used in conjunction with inclusion distribution data, may provide more meaningful parameters to be used in the prediction of fracture toughness. The inclusion spacing can be defined in terms of the inclusion volume fraction:[15]

$$\lambda = cf^{-1/3}\bar{r}, \qquad (2)$$

where c is a constant, f is the volume fraction, and $\bar{r}$ is the average inclusion radius. In this study, the use of $[O_2]^{-1/3}\cdot\bar{r}$ and other complex variables did not improve the correlations between the fracture toughness

and oxygen content. However, measurement of oxygen content is easy and reproducible, and with further study of its interaction with inclusion size distributions, an alternative means to express the effect of inclusions on toughness may be developed.

Fracture Mechanisms

To obtain a more accurate model of the influence of inclusions on the fracture toughness of stainless steel welds at 4 K, the relative importance of void nucleation versus void growth in the formation of an internal crack must be understood. As a first step, metallographic sections near the centers of two tensile specimens tested at 4 K were examined.

Voids formed at both the small and large inclusions in weld 10 (Fig. 5a). Only a small amount of void growth occurred, however, during the 26% uniform elongation in this specimen. There are some indications of void growth just before impingement and coalescence in Fig. 5a (upper right). Void coalescence, however, was rarely observed in the specimen. When it was observed, commonly it had occurred very near the fracture surface. The more traditional void impingement occurring in these areas may be the result of accelerated void growth due to the triaxial stresses imposed during the passage of the crack front.[6] In this case, coalescence would be the result of a crack rather than a source for crack formation. A comparison of void sizes on the polished surface with those on the fracture surface illustrates the sudden increase in void size that occurs during fracture.

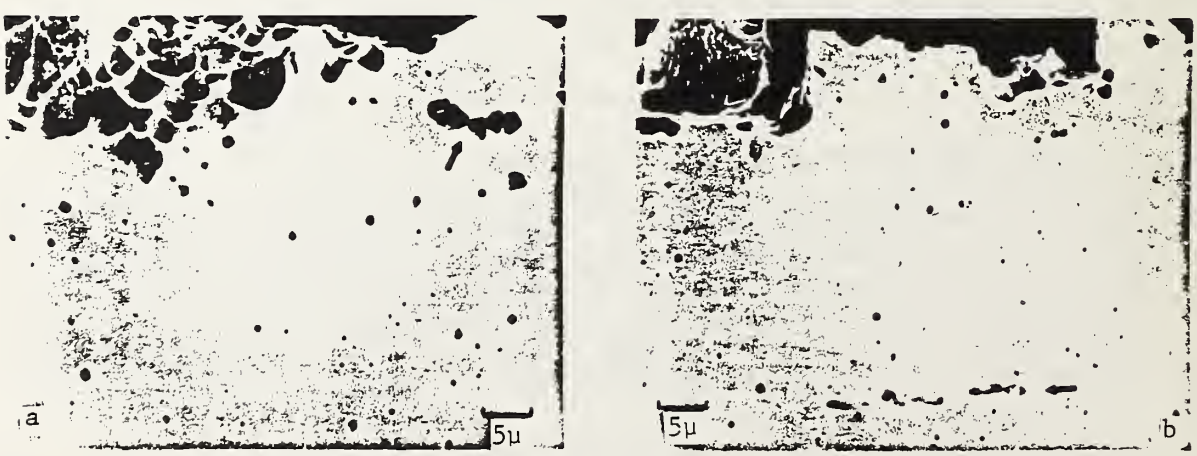

Figure 5. Cross-sectional views along the axis of tensile specimens fractured at 4 K: void impingement in weld 10 (a); void linkage in weld 497-5 (b).

Evidence that crack formation at 4 K was occurring by the linking of small voids rather than by void impingement was observed in weld 497-5. The crack perpendicular to the applied stress in Fig. 5b appears to be forming by "microcrack-linking" (lower, center region of the figure). Small cracks can be seen joining several of the voids in this area.

In summary, the observations of fractured tensile specimens indicate that void growth plays a lesser role in the fracture of stainless steel welds at 4 K than expected. Similar findings have been reported in stainless steel base materials at 4 K.[16] Since the extent of void growth is small compared with the inclusion spacing, it appears that the stress or strain required for the onset of void growth and a factor to increase the energy required for fracture as the inclusion spacing increased would be two meaningful parameters for modeling the fracture event.

CONCLUSIONS

1. The inclusion spacing was the principal reason for the lowering of the fracture toughness for stainless steel welds below the values observed in the base materials at 4 K.
2. The inclusion density was highest for the SMA welds and decreased for the GMA as a function of the shielding gas and type of electrode used.
3. The distribution of inclusion sizes in the welds did not differ substantially on the basis of the welding process used.
4. The oxygen content of the welds is another way to express the effect of inclusions on toughness.

ACKNOWLEDGMENT

This study was sponsored, in part, by the Office of Fusion Energy, U.S. Department of Energy.

REFERENCES

1. G. M. Goodwin, Weld. J. 64:19–25 (1985).
2. S. Yamamoto, N. Yamagami, and C. Ouichi, in: "Advances in Cryogenic Engineering—Materials," vol. 32, Plenum Press, New York (1985), pp. 57–64.
3. N. J. Simon and R. P. Reed, J. Nucl. Mater.; 141–143: 44–48 (1986).
4. R. L. Tobler, T. A. Siewert, and H. I. McHenry, Cryogenics 26:392–396 (1986).
5. G. Leroy, J. D. Embry, G. Edwards, and M. F. Ashby, Acta Metall., 29:1509–1522 (1981).
6. R. H. Van Stone, T. B. Cox, J. R. Low, Jr., and J. A. Psioda, Int. Met. Rev. 30:157–179 (1985).

7. J. P. Hirth and F. H. Froes, Metall. Trans. 8A:1165–1176 (1977).
8. T. A. Whipple and D. J. Kotecki, in: "Material Studies for Magnetic Fusion Energy Applications at Low Temperatures – IV" (NBSIR 81-1645), National Bureau of Standards, Boulder, Colorado 1981, pp. 303–322.
9. H. I. McHenry and T. A. Whipple, in: "Material Studies for Magnetic Fusion Energy Applications at Low Temperatures – III" (NBSIR 80-1629), Boulder, Colorado, 1980, pp. 155–166.
10. D. T. Read, H. I. McHenry, P. A. Steinmeyer, and R. D. Thomas Jr., in: "Materials Studies for Magnetic Fusion Energy Applications at Low Temperatures – II" (NBSIR 79-1609), National Bureau of Standards, Boulder, Colorado, 1979, pp. 315–352.
11. C. N. McCowan, T. A. Siewert, and R. L. Tobler, J. Eng. Mater. Technol. 108:340–343 (1986).
12. N. J. Simon and R. P. Reed, in "Materials Studies for Magnetic Fusion Energy Applications at Low Temperatures – XI" (NBSIR 88-3082), National Bureau of Standards, Boulder, Colorado, 1988, pp. 71–87.
13. R. P. Reed, N. J. Simon, P. T. Purtscher, and R. L. Tobler, in: "Materials Studies for Magnetic Fusion Energy Applications at Low Temperatures – IX" (NBSIR 86-3050), 1986, pp. 15–26.
14. K. Easterling, in: "Introduction to the Physical Metallurgy of Welding," Butterworths, Boston (1983), p. 85.
15. M. F. Ashby and R. Ebeling, Trans. AIME 236:1396 (1966).
16. P. T. Purtscher, R. P. Walsh, and R. P. Reed, in: "Materials Studies for Magnetic Fusion Energy Applications at Low Temperatures – XI" (NBSIR 88-3082), National Bureau of Standards, Boulder, Colorado, 1988, pp. 113–129.

NONMETALLICS

NONMETALLICS PROGRAM

CONTRIBUTOR: H. Ledbetter

OBJECTIVES

- Determination of composite-material physical properties that are useful in engineering design, properties such as Young's modulus, torsion modulus, and internal friction.
- Development of analytical and theoretical models to describe and predict these properties.
- Study of physical property interrelationships.

RESEARCH HIGHLIGHTS

- For glass-fiber epoxy-matrix composites, the ambient-temperature torsional modulus, G, and the associated internal friction, Q^{-1}, were measured. To understand how G depends on fiber volume fraction, existing models were modified to allow for nonhomogeneous fiber distribution. All simple models fail to explain the dependence of the torsion-mode Q^{-1} on fiber volume fraction.
- For glass-fiber epoxy-matrix composites, the torsion modulus and the mechanical-loss spectrum, $Q^{-1}(T)$, were measured between 295 and 4 K. Mechanical loss arose entirely from the matrix material, which responded like a typical polymer. Fiber-matrix interfaces showed zero internal friction. Thus, the glass-epoxy composites showed lower damping than the epoxy.

INTERNAL-FRICTION SPECTRUM OF A GLASS–EPOXY COMPOSITE*

M. Weller
Max-Planck-Institut für Metallforschung
Institut für Werkstoffwissenschaften
Stuttgart, Federal Republic of Germany

H. Ledbetter
Fracture and Deformation Division
Institute for Materials Science and Engineering
National Bureau of Standards
Boulder, Colorado

Using a computer-controlled inverted torsion pendulum at frequencies near 1 Hz, we determined the internal-friction spectrum of a uniaxially fiber-reinforced composite. The composite comprised glass fibers in an epoxy-resin matrix. We studied three fiber contents: 0, 41, and 49 volume percent. Three internal-friction peaks appeared: above 300 K, near 200 K, and near 130 K. We label these α, β, and γ, respectively. They correspond closely to α, β, and γ peaks found previously in many polymers. We failed to see an internal-friction peak for either the glass or the glass–resin interface. Between 300 and 4 K, the torsion modulus increased in the resin by a factor of 3.39 and in the 0.49 glass-epoxy by a factor of 1.68.

INTRODUCTION

In composites, internal friction arises from three sources: the occluded phase, the matrix phase, and the interface. In structural composites, the reinforcing phase usually possesses high elastic stiffness and low internal friction. Thus, composites with good (low-internal-friction) interfaces possess a lower internal friction than the matrix phase. How low depends on the reinforcement-phase volume fraction.

---

*Intended for *Journal of Applied Physics*.

Whether usual composite-material interfaces contribute measurably to internal friction remains uncertain. Some studies report an interface contribution.[1] Others found none.[2-4]

This question assumes importance for several reasons. First, internal friction is a fundamental physical property whose understanding pays many dividends.[5] Second, internal friction (or damping) enters many composite-material engineering applications.[6] Third, we need to know whether internal friction provides a useful tool for studying interfaces. A recent review on composite-material plastic deformation concluded that "interfaces play the most important role in the behavior of a composite."[7] Fourth, current theoretical studies[8,9] on interface damping would profit enormously from experimental studies.

This study used a torsion pendulum to determine the low-frequency internal-friction spectrum of glass-fiber-reinforced epoxy-matrix composites. Previously, for these composites, Ledbetter et al.[4] used kilohertz standing-wave methods to measure the Young's modulus and internal friction.

Fig. 1. Photomicrograph of a composite transverse to uniaxial glass-fiber bundles in an epoxy-resin matrix. Fiber volume, c, is 0.41; fiber diameter equals 7 μm. Nonhomogeneous fiber distribution results from fiber bundles used in manufacture.

EXPERIMENT

Materials

Composites were made at NBS by using vacuum-impregnation methods described by Kasen.[10] The manufacturing method yielded 3-mm-diameter cylinders up to 30 cm long. Except for cutting to length, we measured these as received. The matrix material consisted of a commercial epoxide resin formulated for use in a low-temperature radiation environment. The reinforcing phase consisted of tows of commercial glass fibers 7 μm in diameter with a reported mass density of 2.60 g/cm^3 and a Young's modulus of 72.4 GPa. Figure 1 shows a photomicrograph of the 41% glass composite. Table 1 contains the mass densities of all three materials studied. Fiber volume fraction was determined from three parameters: glass mass, glass mass density, and mold volume.

Table 1. Measured properties of glass–epoxy composites

c	ρ (g/cm^3)	G(kHz) (GPa)	G(Hz)	G_0	s	t (K)	t^* (K)
0.0	1.115	1.49	1.0	6.65	35.21	652	397
0.41	1.654	5.41	3.6	4.50	52.40	957	463
0.49	1.852	5.25	3.8	5.35	66.22	956	621

c = fiber volume, ρ = mass density, G = axial torsion modulus, G_0 = torsion modulus at 0 K, s = an adjustable parameter related to zero-point vibrations; T = temperature; t and t^* are parameters relating to the effective Einstein temperature. G(Hz) are relative values. G_0 and s represent values normalized by dividing by G(295).

Measurements

The cylindrical specimens served as the suspension of an inverted Kê-type torsion pendulum. The pendulum was excited to an initial surface strain of approximately $1.5 \cdot 10^{-5}$. The near-1-Hz free-decay torsion amplitude was recorded with a light-beam system and a semiconductor detector. Temperature was measured with a calibrated thermocouple with an inaccuracy of 0.05 K. The overall systematic temperature error is estimated to be 0.5 K. Inside the pendulum a static pressure of 0.1 kPa was maintained; by a cryopump, the partial pressure of other residual gases, such as oxygen and nitrogen, was reduced to approximately 0.1 Pa. For temperature measurements, which were controlled by a desk computer, the mean heating rate was 1.5 K/min. By using a digital measuring system, three quantities—frequency, f; temperature, T; and internal friction, Q^{-1}—were calculated immediately, punched on tape, and plotted.

A Dewar enabled the specimen to be cooled to near liquid-helium temperature. With an internal electrical heater, the specimen could be heated to approximately 500 K. Because of high damping, the heating was stopped at approximately 330 K.

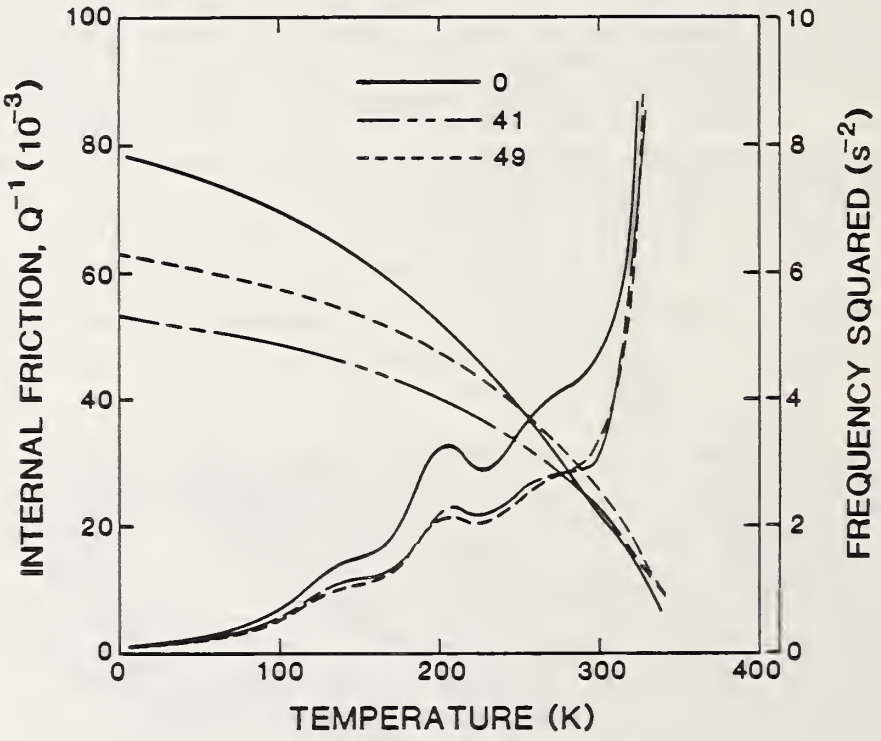

Fig. 2. Variation of f^2 and Q^{-1} for three volume fractions versus temperature.

RESULTS

Figure 2 shows the principal results: internal friction and squared frequency versus temperature.

The squared frequency is proportional to the axial torsion modulus, G:[11]

$$G = 4\rho f^2 \ell^2 \qquad (1)$$

where ρ denotes mass density and ℓ, specimen length. The f^2-versus-T behavior is regular. One can fit such regular behavior to many empirical

equations. One such equation, based on an Einstein-oscillator model, originated with Varshni:[12]

$$G = G_0 - s/[\exp(t/T) - 1] \qquad (2)$$

where G_0 denotes the zero-temperature torsion modulus; s, an adjustable parameter related physically to zero-point vibrations; and t, an adjustable parameter related to the effective Einstein temperature. Table 1 shows the fitting results. Fitting Eq. (2) over the 4- to 340-K region gave poor results. Parameters in Table 1 represent the 140- to 340-K region, except t_2, which represents the 4- to 340-K region.

All three materials show qualitatively similar $Q^{-1}(T)$ behavior: a background that decreases with decreasing temperature and three internal-friction peaks—γ near 130 K, β near 200 K, and α above 300 K.

DISCUSSION

The present $Q^{-1}(T)$ results resemble closely those reported previously for polymers. For example, for nylon, Wert and Weller[13] reported internal-friction peaks at 130, 200, 290, and 340 K. With small temperature shifts, these α, β, and γ peaks occur in various polymeric solids that include oil shale, asphalt, wood, cork, amber, and coal.[14]

Wert and Weller[14] proposed mechanisms for these three relaxation peaks. Gamma arises from twisting under the mechanical stress of linear cross-link methylene units: $-CH_2-CH_2-CH_2-$. Beta arises from reorientation under stress of a small unit such as OH, CH_2OH, or COOH. Alpha arises either from a large reorientation of main chains or from a glass transition.

That all three observed peaks arise from the polymeric matrix means that, in the temperature region studied, neither the reinforcement phase nor the interface contributes measurably to internal friction. Absence of an interface Q^{-1} agrees with the kilohertz measurements of Ledbetter et al.[4]

A theoretical analysis of interface internal friction by Datta et al.[8,9] shows that interface damping increases with increasing vibrational frequency, increasing reinforcement-phase volume fraction, increasing occlusion size, increasing occlusion elastic stiffness, decreasing matrix-phase elastic stiffness, and increasingly spherical occlusion shape. Increasing interface thickness may increase or decrease internal friction. S waves attenuate more than P waves. Thus, we need further studies on a wider range of composites before settling the question of internal friction in composite interfaces.

Finally, we comment on the failure of the f^2 measurements to fit Eq. (2) over the entire temperature range. The good fit obtained between

140 and 340 K suggests a low-temperature change of state. We can imagine this either as an elastic stiffening occurring during cooling below 140 K or an elastic softening occurring above 140 K during cooling.

CONCLUSIONS

From this study of a glass-fiber-reinforced, epoxy-resin composite between 4 and 340 K, there emerged five conclusions:

1. Three internal-friction peaks were discovered by torsion-pendulum measurements.
2. All three peaks correspond to those that occur in macromolecular solids, such as nylon.
3. Neither the glass phase nor the glass–resin interface showed an internal-friction peak.
4. Determination of the significance of internal friction in composite-material interfaces requires more measurements.
5. The shape of the f^2-versus-T curve suggests a different state below approximately 140 K.

ACKNOWLEDGMENTS

Dr. M. B. Kasen of NBS produced the composite materials. Owens–Corning (Granville, Ohio) furnished the glass fibers. S. A. Kim of NBS assisted with numerical analysis. This study was sponsored, in part, by the Office of Fusion Energy, U.S. Department of Energy.

REFERENCES

1. K. Shimizu, in Composite Materials, Proceedings of Japan–United States Conference (Japanese Society of Composite Materials, Tokyo, 1981), p. 111.
2. N. Igata and A. Kohyama, Trans. Jap. Soc. Compos. Mater. 2, 30 (1976).
3. H. M. Ledbetter, J. Phys.(Paris) 46, C10-573 (1985).
4. H. M. Ledbetter, Ming Lei, and M. W. Austin, J. Appl. Phys. 59, 1972 (1986).
5. N. G. McCrum, B. E. Read, and G. Williams, Anelastic and Dielectric Effects in Polymeric Solids (Wiley, London, 1967).
6. "Vibration Damping, 1984 Workshop Proceedings," Air Force Wright Aeronautical Laboratories Report AFWAL-TR-84-3064 (November 1984).
7. Y. Flom and R. J. Arsenault, J. Met. 38, no. 7, 31 (1986).
8. S. K. Datta and H. M. Ledbetter, in Mechanics of Material Interfaces (Elsevier, Amsterdam, 1986), pp. 131–142.
9. S. K. Datta. H. M. Ledbetter, Y. Shindo, and A. H. Shah, in Review of Progress in Quantitative Nondestructive Evaluation, vol. 6 (Plenum, New York, 1987), pp. 1075–1084.

10. M. B. Kasen, in Materials Studies for Magnetic Fusion Energy Applications at Low Temperatures – VIII, NBSIR 85-3075, National Bureau of Standards, Boulder, Colorado (1985), p. 87.
11. H. F. Pollard, Sound Waves in Solids (Pion, London, 1977), p. 89.
12. Y. P. Varshni, Phys. Rev. B 2, 3952 (1970).
13. C. A. Wert and M. Weller, J. Appl. Phys. 53, 6505 (1982).
14. C. A. Wert and M. Weller, J. Phys. (Paris) 46, C10-561 (1985).

TORSION MODULUS AND INTERNAL FRICTION OF A FIBER-REINFORCED COMPOSITE*

H. Ledbetter and Ming Lei
Fracture and Deformation Division
Institute for Materials Science and Engineering
National Bureau of Standards
Boulder, Colorado

By a kilohertz-frequency resonance method, we determined the torsion modulus and internal friction of a uniaxially fiber-reinforced composite. The composite comprised glass fibers in an epoxy-resin matrix. We studied three fiber contents: 0, 41, and 49 vol.%. The internal friction failed to fit a classical free-damped-oscillator model where one assumes a linear rule-of-mixture for three quantities: oscillator mass, force constant, and mechanical-resistance constant. The torsion modulus fit approximately a plane-wave-scattering ensemble-average model. The microstructure showed strong nonhomogeneity of fiber distribution. Considering this nonhomogeneity yielded better agreement between model and observation. Thus, torsion-modulus measurements provide a method to detect and quantify the nonhomogeneity of fiber distribution.

Previously, the authors[1] reported measurements and modeling of the Young's modulus and associated internal friction of a uniaxial-fiber-reinforced epoxy-matrix composite. Here we report new measurements and modeling of torsion modulus and internal friction.

The materials used for the present study are the same as those used for the previous Young's-modulus study.[1] Again, we studied three fiber contents: 0, 41, and 49 vol%. The experimental methods were described previously.[1] To get the torsion modulus, T, we used the relationship

$$T = \rho v^2 = 4\rho f_s^2 \ell_s^2. \qquad (1)$$

---

*Intended for *Journal of Applied Physics*.

Here, ρ and v denote mass density and torsion-wave sound velocity; ℓ_s denotes specimen length; f_s denotes specimen resonance frequency. For torsion-mode oscillation, we obtained f_s from the following relationship:

$$f_s^2 = f_o^2 + (f_o^2 - f_q^2) \frac{m_q}{m_s} \left[\frac{d_q}{d_s}\right]^2 . \tag{2}$$

Here, subscripts o, q, and s denote complete oscillator, quartz-crystal, and specimen, respectively; f denotes resonance frequency, m denotes mass, and d denotes diameter. The specimen's internal friction, Q_s^{-1}, is determined by the following relationship:

$$Q_s^{-1} = Q_o^{-1} + (Q_o^{-1} - Q_q^{-1}) \frac{m_q}{m_s} . \tag{3}$$

Table I contains the properties of constituent materials. Table II shows the principal measurement results. Figures 1 and 2 show graphs of T and Q^{-1} versus fiber volume fraction, c.

Table I. Properties of Constituent Materials

	ρ (g/cm^3)	E (GPa)	μ (GPa)	B (GPa)	k (GPa)	λ (GPa)	ν
Glass	2.577	75.7	30.3	50.5	60.6	30.3	0.250
Resin	1.155	3.11	1.17	3.11	3.50	2.34	0.333

Table II. Measured Properties of Glass-Epoxy Composites

c	T_3 (GPa)	Q^{-1} (10^{-3})	ρ (g/cm^2)	f_s (kHz)	ℓ_s (cm)
0.0	1.75	77.62	1.155	41.20	1.495
0.41	5.41	40.5	1.654	40.48	2.235
0.49	5.25	27.02	1.852	40.756	2.067

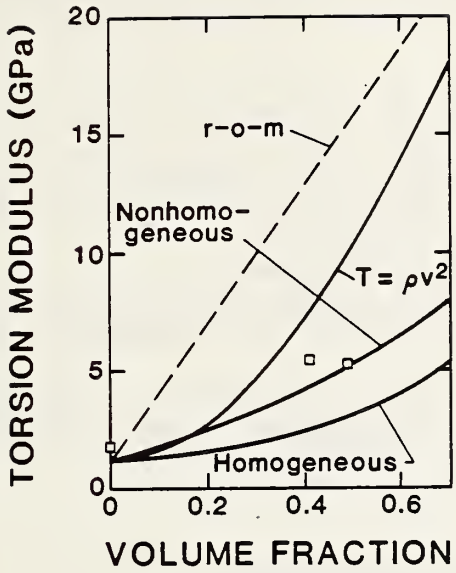

Fig. 1. Torsion modulus versus fiber volume fraction. Points represent measurements. Lower curve represents homogeneous-fiber-distribution case. Upper curve represents an extremely nonhomogeneous case: a single fiber. Middle curve represents a model calculation that allows for fiber bundles. Dashed line represents a linear rule-of-mixture.

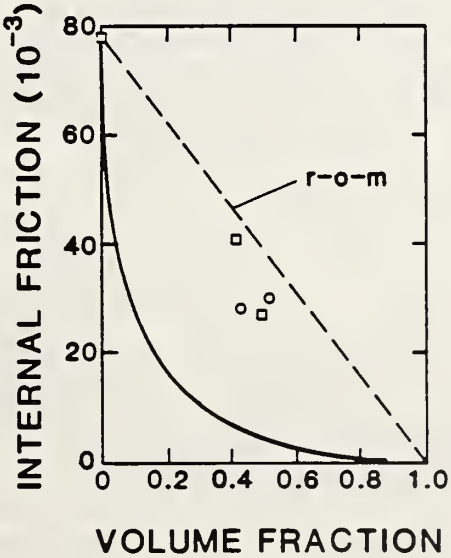

Fig. 2. Internal friction versus fiber volume fraction. Points represent measurements: squares, kHz; circles, near 1 Hz. Curve represents a classical free-damped oscillator model, which fails to explain $Q^{-1}(c)$.

First, we consider a model for the axial torsion modulus, T_3. From standard sources,[2] we know that the torsion modulus along principal axes, i, can be expressed in terms of the elastic-compliance tensor, S_{ijkl}:

$$T_i = \frac{2}{S_{ijij} + S_{ikik}} , \tag{4}$$

where $i \neq j \neq k$. Thus, along the x_1 axis

$$T_1 = \frac{2}{S_{1212} + S_{1313}} = \frac{2}{S_{66} + S_{55}} . \tag{5}$$

We applied the usual Voigt contraction scheme to the second expression in Eq. (5). Similarly,

$$T_2 = \frac{2}{S_{2121} + S_{2323}} = \frac{2}{S_{66} + S_{44}} , \tag{6}$$

and

$$T_3 = \frac{2}{S_{3131} + S_{3232}} = \frac{2}{S_{55} + S_{44}} . \tag{7}$$

We consider the continuous-fiber-reinforced composite as a transversely isotropic material. In this case, we have $S_{44} = S_{55}$. Therefore, Eq. (7) becomes

$$T_3 = \frac{1}{S_{44}} = \mu_{LT} . \tag{8}$$

Here, μ denotes a Lamé constant (shear modulus). Subscript LT denotes shear deformation in any plane containing the x_3 axis, that is, the fiber axis. Using energy methods, Hashin and Rosen[3] derived relationships for the effective moduli of a continuous-fiber-reinforced composite in which the fibers are distributed randomly and homogeneously. They obtained the following relationship for the shear modulus:

$$\mu_{LT} = \mu_m + \frac{2c(\mu_f - \mu_m)\mu_m}{\mu_f + \mu_m - c(\mu_f - \mu_m)} . \tag{9}$$

Here, c denotes fiber volume fraction; subscipts m and f denote matrix and fiber. Using the elastic constants given in Table I, we calculated μ_{LT} and show the results in Fig. 1. The model calculation gives results well below measurements. We believe this disagreement arises from nonhomogeneous fiber distribution, which is visible in Fig. 3. To deal with the nonhomogeneity, we modified the above model to contain two steps. In the first step, we apply the effective-moduli relationships to uniaxial glass-fiber bundles. By assuming fiber volume fraction, c_{fb}, equal to 0.87 in the bundles, we obtain the bundle properties. In the second step, by using the bundle properties as new "fiber" properties and taking bundle volume fraction c_b, instead of c, in Eq. (9), we obtain the nonhomogeneous composite property. The volume fraction c_b relates simply to c:

$$c_b = \frac{c}{c_{fb}} . \tag{10}$$

Figure 1 shows that the effective shear modulus for nonhomogeneous fiber distribution agrees well with measurements, but we found that this approach fails for high volume fraction, above approximately 0.60 for the present system. Figure 1 also shows the torsion modulus of a clad composite cylinder calculated by the relationship[4]

$$T = \rho v^2 = \frac{[c\rho_f + (1 - c)\rho_m][\mu_m - (\mu_m - \mu_f)c^2]}{\rho_m - (\rho_m - \rho_f)c^2} . \tag{11}$$

This represents an extremely nonhomogeneous case: a single glass fiber surrounded by a cylindrical tube of epoxy-resin matrix.

Fig. 3. Photomicrograph of studied composite transverse to uniaxial glass-fiber bundles in an epoxy matrix. Fiber diameter equals 7 μm. Nonhomogenous fiber distribution results from fiber bundles used in manufacture.

Second, we consider internal friction Q^{-1}. In the previous study,[1] starting with an equation for free vibrations and a linear rule-of-mixture for three quantities—mass, m; force constant, k; and mechanical-resistance constant, b—we gave a relationship for Q^{-1}:

$$Q^{-1} = \frac{Q_m^{-1}\left[1 + \frac{c}{1-c}\cdot\frac{b_f}{b_m}\right]}{\left[1 + \frac{c}{1-c}\cdot\frac{k_f}{k_m} + \left(\frac{c}{1-c}\right)^2\frac{\rho_f}{\rho_m} + \left(\frac{c}{1-c}\right)^3\cdot\frac{\rho_f}{\rho_m}\frac{k_f}{k_m}\right]^{1/2}} . \qquad (12)$$

Here,

$$Q_m^{-1} = \frac{b_m}{(m_m k_m)^{1/2}} . \qquad (13)$$

For torsion-mode vibration, we use the following relationship for the force constant:

$$k = Ta . \qquad (14)$$

Here, a denotes a characteristic interatomic spacing. This led to k_f = 9.78 N/m and k_m = 0.117 N/m. We treated a_m as the single adjustable fitting parameter in Eq. (12), using a_m = 1 Å. Figure 2 shows the model calculation and kilohertz measurements for internal friction, Q^{-1}. Figure 2 also shows Q^{-1} determined by the torsion pendulum at a frequency near 1 Hz.[5] Unlike the internal friction measured in longitudinal-mode vibration, the model calculation predicts results much lower than the measurements. Therefore, this model for internal friction fails to apply to the present case. The reason for the failure requires further study.

ACKNOWLEDGMENT

This study was sponsored, in part, by the Office of Fusion Energy, U.S. Department of Energy.

REFERENCES

1. H. M. Ledbetter, Ming Lei, and M. W. Austin, J. Appl. Phys. 59, 1972 (1986).
2. R. F. S. Hearmon, Applied Anisotropic Elasticity (Oxford University Press, London, 1961), p. 51.
3. Z. Hashin and B. W. Rosen, J. Appl. Mech. 31, 223 (1964).
4. A. E. Armenakas, J. Acoust. Soc. Am. 30, 439 (1965).
5. H. Ledbetter and M. Weller, Materials Studies for Magnetic Fusion Energy Applications – XI, NBSIR 88-3082 (National Bureau of Standards, Boulder, Colorado), p. 261.

TECHNOLOGY TRANSFER

TECHNOLOGY TRANSFER PROGRAM

LEADER: N. J. Simon
CONTRIBUTORS: L. Delgado, C. J. King, R. P. Reed

OBJECTIVES

- Organization of workshops to promote interaction between designers and material specialists, to discuss issues related to low-temperature material needs of the fusion energy program, and to present new low-temperature data for structural alloys, composites, and weldments
- Preparation of an annual report, as well as monthly highlight reports to the Office of Fusion Energy, U.S. Department of Energy
- Evaluation of low-temperature mechanical and physical properties of insulator, conductor, and structural materials for cryogenic copper and superconducting magnets; preparation of handbook pages and supporting documentation; distribution of handbook pages to participants in the fusion energy program and to the *Materials Handbook for Fusion Energy Systems*

RESEARCH HIGHLIGHTS

- The Tenth Annual Cryogenic Structural Materials Workshop was organized; it was held October 8–9, 1987 in Pleasanton, California.

- *Materials Studies for Magnetic Fusion Energy Applications – X*, (NBSIR 86-3067, 444 pages, 1987, editor R. P. Reed) was prepared, published, and distributed.

- Additional data were collected for handbook pages on C10100–C10700 copper and C17000–C17510 beryllium copper. Over one thousand documents (reports and journal articles) were acquired, coded for property information, and entered into a data-base management system. Evaluation of documents pertaining to C10100–C10700 copper tensile, elastic, electromagnetic, creep, fatigue, and thermal properties has been completed; data have been extracted and analyzed. Evaluation of documents for similar properties of C17000–C17510 beryllium copper has also been completed; a large amount of data on tensile properties has been extracted and analyzed.

- Handbook pages and supporting documentation covering tensile, electromagnetic, elastic, fatigue, and thermal properties of C10100–C10700 copper have been distributed. Recent NBS data on creep in C10400 copper are being analyzed to elucidate creep mechanisms at cryogenic temperatures. Handbook pages on C17000–C17510 beryllium copper tensile and electromagnetic properties are in preparation.

TENTH ANNUAL

CRYOGENIC STRUCTURAL MATERIALS WORKSHOP

Sheraton Pleasanton
Pleasanton, California
October 8–9, 1987

This workshop provided an opportunity for discussion of problems, advances, and goals in the development of low-temperature materials for cryogenic and superconducting magnets for fusion energy systems. The 1987 workshop emphasized:

- Cryogenic properties of copper alloys and laminates pertaining to design requirements for the compact ignition tokamak (CIT)
- Identification of materials needs for future magnet systems
- New low-temperature materials developments in the United States and international research cooperation

10TH ANNUAL
CRYOGENIC STRUCTURAL MATERIALS WORKSHOP

PROGRAM

THURSDAY, OCTOBER 8

8:30 a.m.	Introduction	V. Der, OFE
	COMPACT IGNITION TOKAMAKS	
8:45 a.m.	Current Status of the CIT	G. Brown, PPPL
9:30 a.m.	Structural Problems of the Alcator C-MOD	H. Becker, MIT
10:00 a.m.	Compression Tests of Copper-Inconel Laminates for CIT Magnets	R. Fields, NBS
10:30 a.m.	Mechanical Properties of Electron Beam Welds in Thick Copper	T. Siewert, NBS
11:00 a.m.	Effects of Grain Size and Cold Rolling on Cryogenic Properties of Copper	R. Reed, NBS
11:30 a.m.	Reinforced Copper Composites for the Alcator C-MOD	H. Becker, MIT
	STRUCTURAL ALLOYS FOR LARGE-SCALE FUSION-ENERGY DEVICES — I. AUSTENITIC STEELS	
1:30 p.m.	Cryogenic Magnet Case and Distributed Structural Materials for High-Field Superconducting Magnets	L. Summers, LLNL
2:00 p.m.	Low Temperature Properties of High-Manganese Stainless Steels	R. Reed, NBS
2:30 p.m.	The Influence of High Magnetic Fields on the Mechanical Properties of Austenitic Steels	J. Morris, Jr., U. California
3:00 p.m.	Effect of Void Nucleation on Fracture Toughness	P. Purtscher, NBS
3:30 p.m.	Fatigue Crack Growth in Metastable Austenitic Steels	Z. Mei, U. California

THURSDAY, OCTOBER 8, *continued*

4:00 p.m.	Inclusions and Fracture Toughness in Stainless Steel Welds at 4 K	C. McCowan, NBS
5:30 – 7:30 p.m.	Reception	

FRIDAY, OCTOBER 9

STRUCTURAL ALLOYS FOR LARGE-SCALE FUSION ENERGY DEVICES – II

8:30 a.m.	Status of U.S.–Japan Development of Test Standards	R. Tobler, NBS
9:00 a.m.	Welding of High-Manganese Cryogenic Steels	J. Chan, U. California
9:30 a.m.	The Cryogenic Mechanical Properties of Structural Aluminum Alloys	J. Morris, Jr. U. California
10:00 a.m.	Structural Properties of Nb_3Sn Superconducting Wires	M. Strum, LLNL

STRUCTURAL COMPOSITE INSULATORS

10:30 a.m.	Composite Insulation Materials: Requirements for a Small Superconducting Ignited Tokamak	L. Summers, LLNL
11:00 a.m.	The Low-Temperature Neutron Irradiation Facility	H. Kerchner, ORNL
11:30 a.m.	Review of Gamma and Neutron Irradiation Effects on Organic Composite Degradation Cryogenic Temperatures	M. Kasen, CTD
12:00 p.m.	SSC Dipole Magnet Suspension System Design	T. Nicol, Fermilab

STRUCTURAL COMPOSITE INSULATORS: LLNL REQUIREMENTS

1:30 p.m.	Open Discussion: Radiation-Tolerant Insulating Materials for Next Generation Fusion Machines	Discussion Leader: V. Der, OFE

TENTH ANNUAL CRYOGENIC STRUCTURAL MATERIALS WORKSHOP —

SUMMARY OF TECHNICAL PRESENTATIONS

COMPACT IGNITION TOKAMAKS

. The Compact Ignition Tokamak (CIT) prototype, a near-term fusion ignition reactor, will operate at 77 K and use copper or copper alloy coils. Toroidal field coils will produce a field of about 16 T, setting up stresses in the nose region of 400 to 550 MPa, considerably above the yield strength of the cold-worked C10700 copper conductor.

Reviewing this and other materials problems of the CIT, G. Brown (PPPL) detailed the use of explosively bonded Inconel 718 to strengthen the conductor structure. The nose region is one of the most critical areas in the design, but the effects of high radiation levels and high compression loads on the insulation are also of concern.

H. Becker (MIT) described the structural problems of the Alcator C-MOD, a 9-T tokamak with reinforced copper rectangular field coils. Fatigue survival controls most of the structural design, since the tokamak is expected to undergo 50,000 operational cycles from 77 K to near ambient temperature.

R. J. Fields (NBS) reported results of recent static and cyclic compression tests of specimens of a copper–Inconel laminate for the CIT. The 0.2%-offset yield strength of the laminate was about 550 MPa; cyclic tests revealed some creep at higher loads.

The design of the CIT requires joining segments of 25-mm-thick C10700 copper. T. Siewert (NBS) reported mechanical properties at 77 and 295 K of electron beam weldments of this material. Weld yield strength was only about 30% of the base metal strength in reduced-section specimens.

R. P. Reed (NBS) presented results of his studies on strengthening C10400 copper by cold working and reduction of grain size. The best ratio of strength to resistivity at cryogenic temperatures was obtained with material that was cold-rolled about 10%.

H. Becker (MIT) described results of compression tests on stacks of loose copper and steel plates (to simulate explosively bonded C10700 copper–Inconel 718 composites). Preliminary results indicated that copper annealed to a yield strength of 48 MPa could survive a 407-MPa load.

STRUCTURAL ALLOYS FOR LARGE-SCALE FUSION ENERGY DEVICES — I. AUSTENITIC STEELS

The prototype fusion reactor that will follow the CIT is expected to use superconducting magnets that operate near 4 K. L. T. Summers (LLNL) discussed the structural requirements of cable-in-conduit conductors for the prototype TIBER-II (Tokamak Ignition/Burn Experimental Reactor) and ITER (International Thermonuclear Experimental Reactor). He reported a proposal to eliminate fatigue problems for the conduit-conductor system by keeping all stresses compressive in the center toroidal field coil set.

R. P. Reed (NBS) characterized recently developed high-manganese austenitic steels with regard to strength and toughness mechanisms. He discussed the physical properties, such as thermal expansion, that are affected by the antiferromagnetic transitions in these steels.

J. W. Morris, Jr. (University of California–Berkeley) described recent measurements of the effects of high magnetic fields on fracture toughness of a metastable austenitic steel. Earlier studies at the University of California – Berkeley had found that fatigue crack growth rate was unchanged in an 8-T field, so the fracture toughness results were unexpected.

P. Purtscher (NBS) presented evidence that void nucleation (rather than void growth) is the controlling mechanism in cryogenic fracture toughness of 304-type alloys.

Z. Mei (University of California-Berkeley) reported effects of the austenite to martensite transformation on fatigue crack growth behavior of 304L and 304LN austenitic steels.

Type 316LN stainless steel is also a candidate structural alloy for superconducting magnet casings. Because the weld toughness of 316LN and other alloys at 4 K generally is lower than that of the base alloy, stainless steel welds of varying inclusion and oxygen content were fabricated with several different welding processes in work carried out by C. N. McCowan (NBS). Like base-metal toughness, the weld-metal toughness at 4 K increased with reduced inclusions and oxygen content. Since welds have more inclusions than base metals, the differences in the inclusion spacing may explain differences in weld- and base-metal toughness.

STRUCTURAL ALLOYS FOR LARGE-SCALE FUSION ENERGY DEVICES — II

R. T. Tobler (NBS) described recent round-robin tests on 4-K tensile and fracture properties carried out in the United States and Japan. New standards for 4-K tensile and fracture-toughness testing are the outcome of this program.

J. W. Chan (LBL) discussed 4-K fracture toughness of a high-manganese austenitic steel, 18Mn–16Cr–5Ni–0.2N. Fracture toughness was related to δ-ferrite microstructure in the weld.

In contrast to the fracture toughness of austenitic steels, that of the aluminum–lithium alloy 2090 increases at cryogenic temperatures. J. Glazer (LBL) reviewed mechanical properties of this alloy and discussed a strain-hardening model that accounts for the observations.

In a new test facility that allows testing in fields up to 15 T, M. J. Strum (LLNL) recently studied the mechanical properties of Nb_3Sn superconducting wires. He reported that the conductor–stabilizer composite is subject to failure at low strains in or near the operating range.

STRUCTURAL COMPOSITE INSULATORS

L. T. Summers (LLNL) descussed the insulation requirements for new prototypes. The inner turns of the toroidal field coils of the TIBER-II compact tokamak are expected to experience a high neutron fluence of 10^{19} n/cm^2, because the reduced size is achieved with less nuclear shielding. The turn-to-turn insulation is expected to consist of ceramic or glass fibers impregnated with an organic resin that will be introduced after the heat treatment of the conductor. The lack of an adequate data base for these insulators at radiation levels of 10^{10} Gy is a serious problem.

H. R. Kerchner described the testing facilities at the Low-Temperature Neutron Irradiation Facility (LTNIF), which are designed to irradiate and test materials at 4 K. When fully operational, this facility will provide needed measurements of radiation effects on cryogenic materials for fusion reactors. The fast neutron flux (energy > 0.15 Mev) will be 1.4×10^{17} n/m^{2}s.

M. B. Kasen (CTD) reviewed gamma and neutron irradiation effects on organic composites. The most comprehensive recent studies were carried out by S. Egusa at ANL on composites fabricated from several types of epoxy and one polymide with type E glass or graphite reinforcements.

T. H. Nicol (FNAL) described the composite suspension system for the proposed SSC dipole magnets. Both graphite and fiberglass-reinforced composite tubes will be utilized.

STRUCTURAL COMPOSITE INSULATORS: LLNL REQUIREMENTS

V. Der (OFE) led the discussion of insulator requirements for the next generation of fusion reactors. The discussion objective was to identify development and testing needs for insulators and to recommend a base-program action plan to address design issues relating to insulators

for both ITER and CIT. Requirements were set forth for an ideal database on composite-insulator tests in a neutron fluence and spectrum equivalent to that of TIBER-II. The CIT requirements for compression strength of insulators were reiterated. New methods of surface preparation to improve interfacial chemical bonding between matrix and reinforcement were discussed (failure in composite insulators often occurs at the interface). Several particpants expressed the need for data on 4-K irradiation of insulators followed by testing without warm-up.

UNITED STATES-JAPAN

DEVELOPMENT OF TEST STANDARDS

UNITED STATES-JAPAN DEVELOPMENT OF TEST STANDARDS PROGRAM

PRINCIPAL INVESTIGATOR: R. L. Tobler

CONTRIBUTING ORGANIZATIONS: National Bureau of Standards,
Tohoku University,
Japan Atomic Energy Research Institute,
Kobe Steel,
National Research Institute for Metals

OBJECTIVES

- Establishment of a standard test method for tensile testing of structural alloys at 4 K
- Establishment of standard test methods for fracture testing at 4 K
- Administration of a round-robin test program to support the standards development
- Administration of experimental research to evaluate critical aspects of test standardization at 4 K
- Liaison with the American Society for Testing and Materials (ASTM) and its task group activities for the purpose of establishing the standards by voluntary consensus

PROGRAM HIGHLIGHTS

- Cryogenic materials scientists were interviewed at government, industrial, and academic institutions in Japan. Their experience and advice were helpful in preparing the drafts of the test procedure standards.

- Five drafts of a proposed standard 4-K tensile test procedure were written and submitted for review at Japanese domestic and United States–Japan workshops. The fifth revision has been formally submitted to ASTM.

- Five drafts of a proposed standard for 4-K fracture toughness testing were written and reviewed at Japanese domestic workshops. The fifth revision was submitted to ASTM to begin due process for standardization.

- Round-robin tensile and fracture tests were conducted on a Fe–24Cr–15Ni alloy. A summary of results is scheduled for presentation at the 1988 United States–Japan International Workshop.

- An experimental research program was completed by participants at NBS and four Japanese laboratories. From 70 J_{Ic} fracture toughness tests, the effects of specimen size, side grooves, test speed, and fatigue cracking on the test procedure were determined. Seven papers describing the results have been published.

- Five workshops were an integral part of the program:

  Standardization of Fracture Toughness Testing of Low-Temperature Structural Materials at Tohoku University, Sendai, Japan in March 1986

  Low-Temperature Structural Materials and Standards at Japan Atomic Energy Research Institute in Tokai-mura, Japan in August 1986

  DOE–JAERI Low Temperature Structural Materials and Standards Workshop in Reno, Nevada in October 1986

  United States–Japan Cooperative Research Program Review at Tohoku University in January 1987

  United States–Japan Cooperative Research Program Review at the Japan Atomic Energy Research Institute, Tokai-mura in May 1988

- At ASTM technical meetings, the draft standards were presented to the task groups that will process these standards. The meeting on fracture testing was held in Reno, Nevada on April 16–17, 1988; the meeting on tensile testing, in Baltimore, Maryland on May 16–17, 1988.

May 11, 1988

MEMORANDUM FOR: Dr. S. Shimamoto
Japan Atomic Energy Research Institute

and

Dr. H. I. McHenry
Fracture and Deformation Division
National Bureau of Standards

FROM: Ralph Tobler
Fracture and Deformation Division
National Bureau of Standards

SUBJECT: Trip Report – ASTM Technical Committee Meetings
- Reno/Sparks, Nevada, April 26–27, 1988
- Baltimore, Maryland, May 16–17, 1988

INTRODUCTION

With ASTM, we are establishing standards for tensile and fracture testing at 4 K. Special standards are necessary because of unusual material behavior at this temperature. The standards we wrote as part of the Japanese cooperative program are now being reviewed in ASTM subcommittees. I participated in selected meetings to answer questions, obtain guidance, and assimulate new advances in room temperature test methodologies.

FRACTURE MEETINGS IN RENO

1. Crack Tip Opening Displacement (CTOD) Concepts (E24.05).

A new CTOD test will soon be officially established by ASTM. At this meeting John Underwood persuaded the attendees that the value of the rotational factor, r_p, should be modified, but all other negative returns from a recent ballot were resolved. This standard should pass on the next ballot. It provides an alternative method of toughness evaluation for metals of intermediate toughness when K_{Ic} and J_{Ic} tests are not valid. This standard could be used for cryogenic testing, and its development is influencing work in other subcommittees, as noted below.

2. Ductile-to-Brittle Transitions (E24.08).

The meeting on ductile-to-brittle transitions included presentations on analysis routines (Ted Anderson), measurement techniques (George Irwin) and design philosophy (Mike Dawes). The basic question is: how do you run tests in the transition region? To resolve the major problem, which is high scatter in measurements, the Metals Properties Council (MPC) plans to run a data-analysis round robin in their Japanese Cooperative Program; they are currently searching for a large quantity of well-characterized material. CTOD tests are applicable to this program.

3. Initiation Concepts (E24.04).

The Initiation Concepts group just revised the J_{Ic} standard E813-87 and published it in the 1987 Annual Book of Standards. The most significant change is the updated definition of J_{Ic}. The meeting consisted of an introduction, a preview of new directions for future work, and two technical presentations: Summary of Suggested Changes for Testing in the Transition Region (J. Joyce) and Update on Standardization of Fracture Testing at 4 K (R. Tobler). Twenty experts were present: Drs. Joyce and Hackett (the chairmen), Wessel, Merkle, Ernst, Landes, Druce, and others. The new directions for work are

1. J-testing in the transition region
2. Dynamic loading effects
3. New specimen geometries, especially the arc tension specimen
4. Small-specimen testing
5. Cryogenic testing

The predominant theme now is transition-region characterization. The thinking in this group seems to reflect developments in the CTOD group. As a result, a new parameter, J_c, may evolve to characterize those nonlinear materials that fail before developing a full J_R-curve. For example, J_c may be defined for abrupt fractures occurring after stable crack extensions of not more than 0.15 mm. (We already specify such a parameter for use in our proposed 4-K standard).

An interesting difference in material behavior is this: slow, stable ductile cracking occurs at room temperature, whereas fast unstable ductile cracking occurs at 4 K, but the latter is overlooked in the existing ASTM standard (see ASTM E 813-87, section 4.3).

Although cryogenic behavior is not a "hot topic" for many of these specialists, several helpful suggestions were made in the discussion following my presentation. In particular, Hugo Ernst (Georgia Tech) wants to cooperate with us on the subject of tearing instability theory as it relates to the material behavior at 4 K. John Merkle recommended that a task group be formally established for this work, including other people with cryogenic experience. The task group assignment is now being pursued by the subcommittee chairmen.

MEETINGS IN BALTIMORE

4. Temperature Effects (E28.10)

This meeting with eleven attendees was chaired by R. McDemus. The agenda included sign-up and introduction of new members, approval of previous minutes, task group reports, and new business.

Task Groups: Task Group E28.10.02 is home for our 4-K tensile standard. At the present time, this standard is in ballot at the subcommittee level. The outcome is forthcoming June 3. At this meeting, four ballots were returned with highly favorable comments. At least eight more ballots are required. If no negatives are sustained, this standard will then advance to general committee ballot and finally to society ballot.

Four other task groups dealing with high-temperature methods were reviewed: standard practices for creep (E139), time to rupture (E292), compression (E209), and tension (E21). Documentation for multiple-specimen test apparatus is needed. In this regard, I can contribute to these task groups by visiting the National Research Institute for Metals in Tokyo to obtain information on such apparatus that are used in Japan.

New Business: The possibility of a general low-temperature tensile test standard was discussed. Since E28 started in 1984, there has never been one. Consequently, Thomas Wilmink agreed to head a new task group designated E28.10.06 — Low-Temperature Tensile Testing. The plan is as follows: First, our 4-K tensile standard will be processed. After that, E28.10.06 will extend the scope of that standard to include all low temperatures. NBS was offered an active role in this.

5. Committee E28 Orientation

This informative introductory meeting gave me a general overview of the scope of the main committee and the standardization procedures of ASTM.

The structure of the main committee, E28, was described, the chairman of the various subcommittees were introduced, and the procedures for creating a standard were reviewed.

Today there are nineteen active subcommittees in E28. The majority of standards within their jurisdiction are undergoing revisions necessitated by three powerful forces: computer automation, international unification of standard practice, and national accreditation of laboratories.

CONCLUSIONS

New developments in toughness testing are evolving. Appropriate methodologies are at hand for all types of material behavior: linear elastic (K_{Ic}), elastic–plastic (CTOD, or J_c), and fully plastic (J_{Ic}). In the future, these methods in refined states may be integrated into a single comprehensive standard.

Our 4-K tensile standard is now well along, undergoing due process. The fracture standard is not quite as far along; the following course seems recommendable: review it with the Japanese in forthcoming meetings (May 26–31) create the sixth draft with all desired changes, form a new task group in E24.04, and initiate the balloting procedure.

LOADING-RATE EFFECTS ON DISCONTINUOUS DEFORMATION IN LOAD-CONTROL TENSILE TESTS*

T. Ogata and K. Ishikawa
Superconducting and Cryogenic Materials Research Group
National Research Institute for Metals
Ibaraki, Japan

R. P. Reed and R. P. Walsh
Fracture and Deformation Division
National Bureau of Standards
Boulder, Colorado

In load-control tensile tests at liquid helium temperature, an abrupt and large discontinuous deformation occurs, which differs from the discontinuous deformation obtained from displacement-control tests. We investigated the effects of loading rate, varied from 0.5 to 5000 N/s, on the tensile properties of AISI 304L, 310, and 316LN steels at 4 K. A large deformation, near 40% strain, occurred in AISI 310. At the high loading rates, the ultimate strength of these materials was 65% of the strength obtained in displacement-control tests; the initiation strength of discontinuous deformation was also less.

INTRODUCTION

The discontinuous deformation that occurs during tensile tests at temperatures near 4 K is caused mainly by the extremely low specific heat and thermal conductivity of the material at this temperature. In load-control tensile tests, the discontinuous deformation is large and abrupt.[1,2] This deformation differs from that reported in displacement-control tests,[3-7] because the amount of displacement in load-control tests is not limited by the testing machine, and no load drop occurs during the deformation. Discontinuous deformation in load-control tests results in a lower ultimate strength than that measured with displacement-control tests. So, it is important to clarify these deformation behaviors and to be able to predict the mechanical properties when a nonrestricted deformation force is applied to structural materials at low temperatures. In this study, we investigated the effects of loading rate on discontinuous deformation behavior and tensile properties.

---

*In *Advances in Cryogenic Engineering – Materials*, vol. 34, Plenum, New York, 1988, pp. 233–240.

EXPERIMENTAL PROCEDURES

Materials tested in this study were commercial AISI 304L, 310, and 316LN, typical austenitic stainless steels for low-temperature applications. Table 1 shows the chemical compositions of these alloys. The materials were in the as-received, annealed condition. The AISI 316LN was solution-heat-treated at 1423 K for 2 h. The grain sizes of AISI 304L, 310, and 316LN were 70, 140, and 100 μm, respectively.

Table 1. Chemical Composition of the Steels Tested in This Study (wt.%)

	C	Mn	P	S	Si	Cr	Ni	Cu	Mo	N	Fe
AISI 304L	0.02	1.4	0.02	0.01	0.6	18.4	9.7	–	–	–	bal.
AISI 310	0.08	1.7	0.02	0.02	0.7	24.8	20.8	0.1	–	–	bal.
AISI 316LN	0.02	1.8	0.02	0.01	0.3	16.8	13.9	–	2.2	0.099	bal.

The round specimens had gauge lengths of 38 mm and reduced-section diameters of 6.35 mm. Specimen strain was measured with two pairs of clip-on strain gage extensometers; each pair included one normal and one high-range extensometer. The normal extensometer, with a 2.5-mm span and a gauge length of 25.4 mm, was used to measure yield strength and initial discontinuous deformation strain of the specimen. The high-range extensometer, with a span of 17.5 mm and a gauge length of 38 mm, was used to measure specimen strain throughout the tensile test. Figure 1 shows a specimen with normal and high-range extensometers.

We used a programmable servohydraulic testing machine (having a maximum load of 250 kN) with a cryostat for the liquid helium tests. With a high-resolution function generator, we varied loading rates from 0.5 to 5000 N/s. The machine was programmed for a ramp function in a load-control mode; that is, the machine uniformly increased the load on the specimen until failure. The strain rate in the linear-elastic region of the stress–strain curves was calculated to be 9×10^{-8} s^{-1} to 9×10^{-4} s^{-1}, corresponding to the loading rates of 0.5 N/s to 5000 N/s. To shorten the testing time in 5-N/s and 0.5-N/s tests, we adopted a loading rate of 50 N/s up to 80% of yield strength and stopped the test after one discontinuous deformation. We determined the dither ratio to be less than 0.1% of the load signal, and from the oil pressure and oil flow, we estimated the actuator velocity of the testing machine to be 50 mm/s.

We also performed displacement-control tensile tests with the same testing machine in a stroke-control mode and with the same extensometers to compare the data obtained from load control and displacement control. The strain rate of this tensile test was 2.2×10^{-4} s^{-1}. All these tensile tests were carried out with specimens submerged in liquid helium.

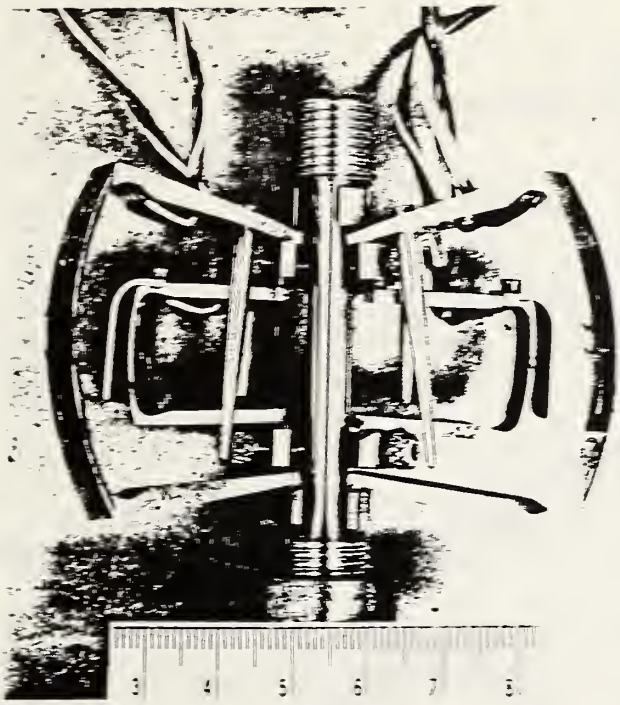

Figure 1. Specimen with normal and high-range extensometers.

Load and strain were recorded on an X–Y recorder and a high-speed digital memory recorder (sampling rate of 500 μs). During load-control testing, we measured strain rate just before discontinuous deformation. Using a bar-magnet, torsion-balance commercial magnetometer, we calculated the amount of α'-martensite in the deformed specimens.

RESULTS

Load–displacement curves for AISI 310 obtained from both load- and displacement-control tensile tests are shown in Figure 2. In the figure, 0.5 mm/min represents displacement-control test; the broken line indicates that the curve was calculated from a stroke signal because specimen extension exceeded the range of the high-range extensometers. No serrations* were observed in load-control tests. At the lowest loading rate, 0.5 N/s, the specimen failed at the first discontinuous deformation. At the loading rate of 5 N/s, the specimen deformed about 15 mm, 40% in strain, within one deformation, and then failed. At 50 N/s, the

*In the displacement-control tests, discontinuous deformation consists of load drops, which we call serrations to distinguish them from the discontinuous deformation the load-control tests.

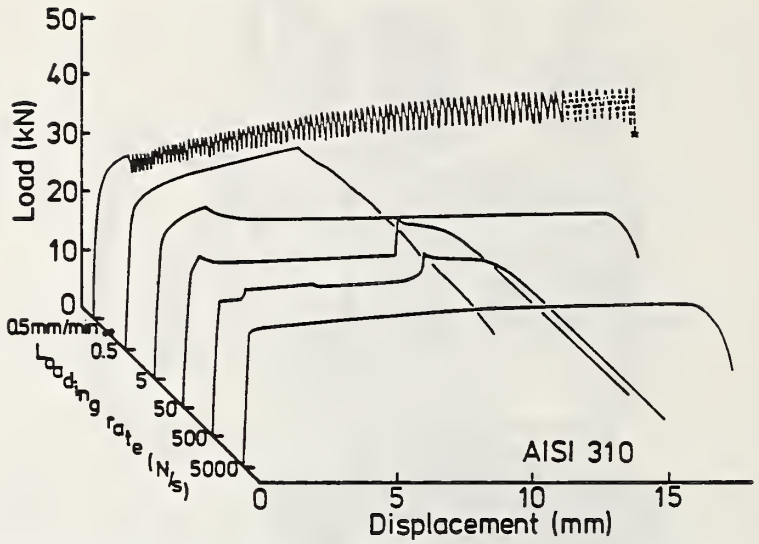

Figure 2. Load–displacement curves obtained at various loading rates for AISI 310.

deformation stopped, and the load increased again. With the increase of loading rate, the stress to initiate discontinuous deformation (initiation strength) decreased. At 500 N/s, the deformation occurred just above the yield strength. The number of deformations in the curve increased. At the highest loading rate, 5000 N/s, no apparent discontinuous deformation was observed owing to specimen heating.

Figure 3 shows the load–displacement curves for AISI 316LN and 304L steel. The curves for AISI 316LN are similar to the curves for AISI 310. The curves for 304L are different from those of AISI 310: the deformation stopped frequently, even at lower loading rates.

During load-control tests, the strain rate increased as the load increased. Table 2 presents the strain rate just before the first discontinuous deformation.

Since the load was kept almost constant during the discontinuous deformation in load-control tests, we could measure the exact velocity of the deformation. In Figure 4, the monitoring screen shows the load-vs.-strain change obtained from AISI 310 at 5 N/s. Curve 1 is the load and curve 2 is the strain change at the first (and the last) deformation. The amount of this deformation was a 15-mm change in length, and it lasted 0.575 s. The average velocity was 26 mm/s (6×10^{-1} s^{-1} in strain rate); the maximum velocity was 32.5 mm/s (7.5×10^{-1} s^{-1} in strain rate), a value close to the maximum actuator velocity. So, at the higher deformation velocity, the load decreased during the deformation.

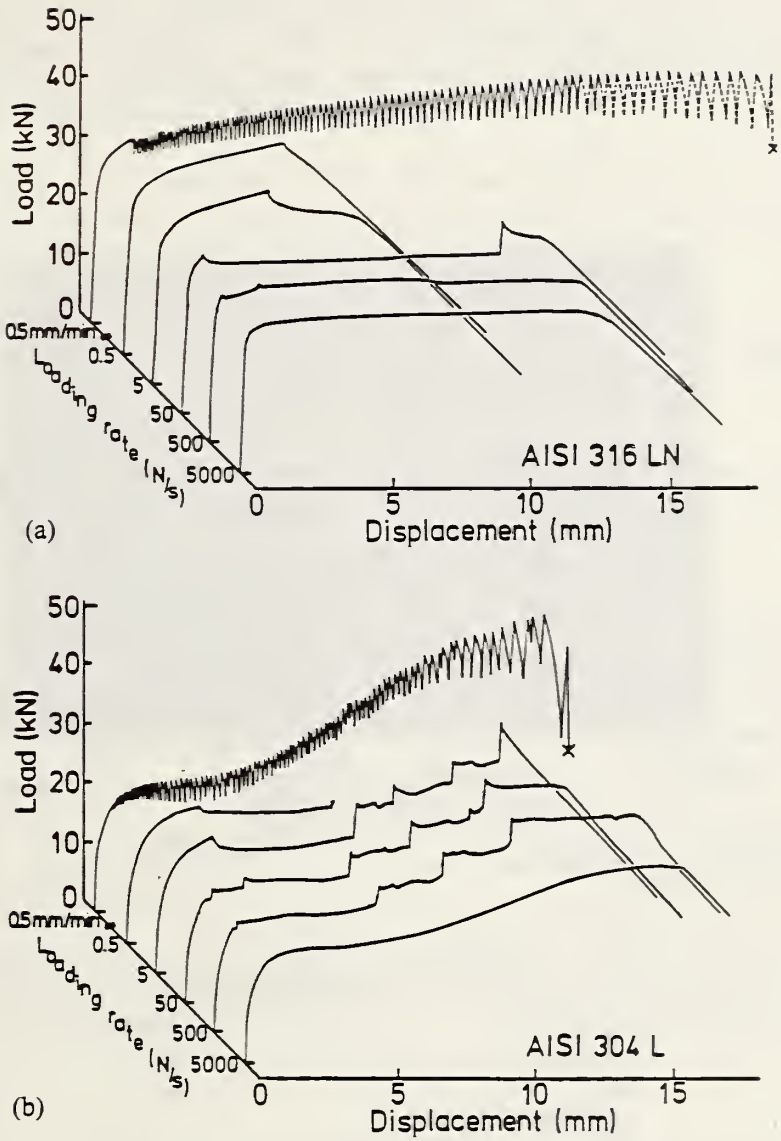

Figure 3. Load–displacement curves obtained at various loading rates for (a) AISI 316LN and (b) for AISI 304L.

Table 2. The Strain Rate Just before the First Discontinuous Deformation

Loading Rate (N/s)	Strain Rate (10^{-4} s^{-1})		
	AISI 310	AISI 316LN	AISI 304L
0.5	0.13	0.14	0.1
5	1.6	1.0	0.7
50	2.2	3.5	1
500	5.7	13	6

The mechanical properties of AISI 310, 316LN, and 304L are shown in Figures 5, 6, and 7 as a function of loading rate. In the figure, S_u, S_i, S_y, El, and RA represent ultimate tensile strength, initiation strength, yield strength, elongation, and reduction of area, respectively. Ultimate tensile strength and initiation strength decreased with

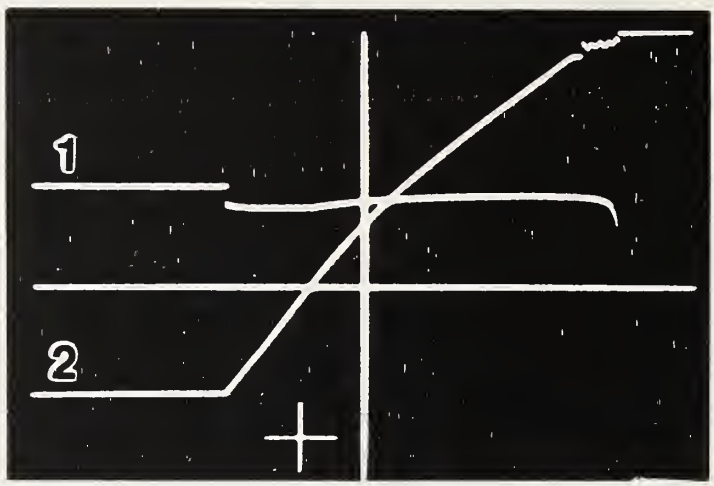

Figure 4. Load and strain during the deformation of AISI 310 at 5 N/s.

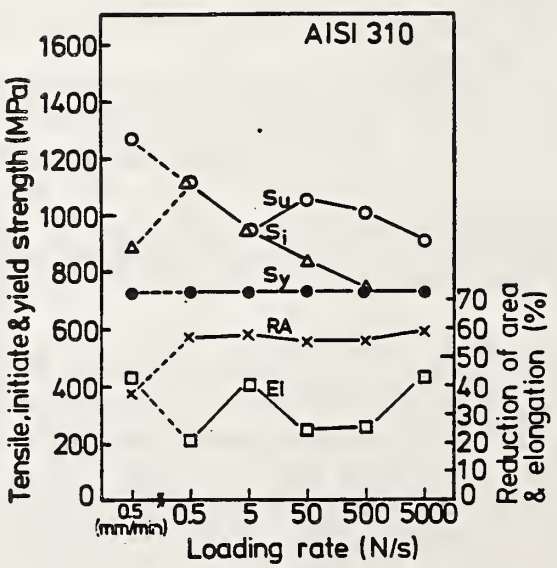

Figure 5. Tensile properties as a function of loading rate for AISI 310.

an increase in loading rate. At the loading rate 5000 N/s, the ultimate strengths of AISI 310, 316LN, and 304L were 71, 66, and 65%, respectively, of those obtained from displacement-control tests. Yield strength was not affected by the loading rate. In load-control tests, elongation decreased for AISI 316LN and most AISI 310 specimens, but it was not significantly different for AISI 304L.

The amounts of α'-martensite in deformed specimens are listed in Table 3. No α'-martensite was detected in the threaded section of any specimen and or in any part of the AISI 310 specimens.

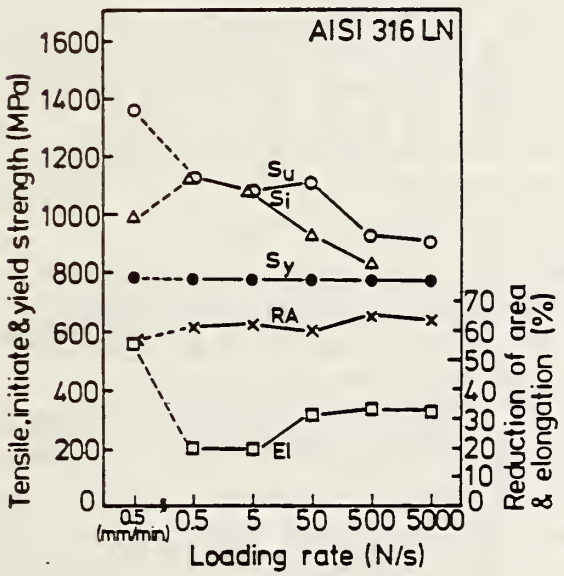

Figure 6. Tensile properties as a function of loading rate for AISI 316LN.

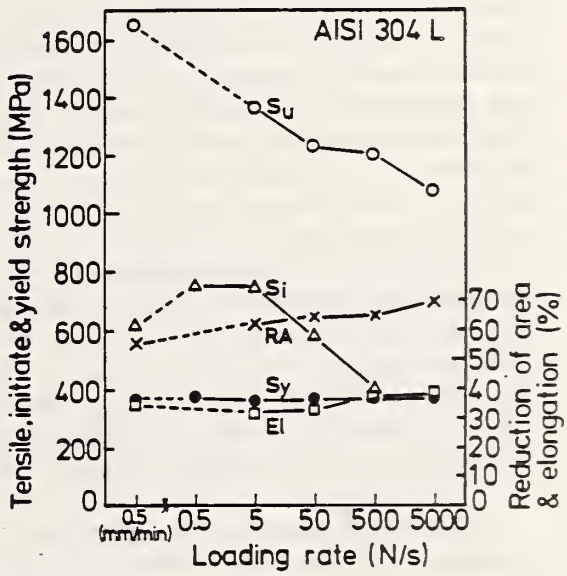

Figure 7. Tensile properties as a function of loading rate for AISI 304L.

Table 3. Amounts (vol.%) of α'-martensite in Deformed Specimens

Location*	AISI 304L			AISI 316LN		
	0.5mm/min	5 N/s	50 N/s	0.5mm/min	5 N/s	50 N/s
Section A	100	73	88	47	21	5
Section B	90	78	79	48	3	5
Section C	99	73	56	40	3	2

* A: close to the fracture surface
B: 15 mm apart from the fracture surface
C: close to the radius of the specimen reduced section

DISCUSSION

Deformation Behavior

We observed discontinuous deformation except at the highest loading rate. At 500 N/s for AISI 310, the deformation occurred just 3% above the yield strength, and the amount of the deformation reached about 0.7 mm, about 2% in strain. The strain rate just before the deformation was 5.7×10^{-4} s^{-1}, which is usual in displacement-control tensile tests. The serrations that occurred near yield strength seemed to be negligible. A large amount of discontinuous deformation is characteristic of load-control tests, as Ogata et al. reported in previous papers.[1,2] The initiation strength increased owing to less specimen heating at the lower strain rate. The change in length during the first deformation for AISI 310 at loading rates of 500, 50, and 5 N/s was about 2, 7, and 15 mm. The deformation locally heats the specimen and stops when a balance occurs between the local strength and the work-hardening at the high temperature. Subsequent discontinuous deformations occur in other areas of the specimen where less local strain hardening has occurred.

During the large deformation (about 15 mm) of AISI 310 at 5 N/s, the entire specimen length continued to deform accompanied by continuous heating during the deformation. During this deformation, the work done was about 30 kN × 15 mm = 450 J, and the power was 450 J/0.575 s = 783 J/s. The normal cooling capacity of this kind of specimen is about 3 J/s, less than the heat generated. The maximum temperature rise was estimated and measured as more than 100 K.[2]

In displacement-control tests, the deformation is suppressed by the testing machine, and when the deforming stress decreases, this suppression results in the serrations of smaller strain increments.

In AISI 304L, the deformation stopped frequently. This was due to its lower initiation strength and also to its high work-hardening accompanied by martensitic transformation. During the deformation, unstable deformation continued because of the transformation.

The temperature rise in the specimen also determines the amount of α'-martensite formed, which was less in the load-control tests than in the displacement-control tests. The effect was significant in the load-control test of AISI 316LN at 50 N/s, though its total elongation was 60% of that in the displacement-control test. We also observed that the specimen deformed less uniformly in the load-control test owing to the temperature gradient at large strains, where the temperature is the highest.

Tensile Properties

Yield strength did not change with the loading rate because the strain rate in the elastic range was lower than 10^{-3} s^{-1}, and specimen heating occurred after the plastic deformation began.

In load-control tests, ultimate tensile strength decreased 65 to 71% at 5000 N/s and 68 to 80% of that in the usual displacement-control tests. This was due to the discontinuous deformation that leads to specimen failure at higher temperature before the specimen is fully work hardened at 4 K. This decrease was larger than that obtained in higher strain-rate displacement-control tests.[3] This phenomenon indicates that if a material at low temperatures is in the freely deforming condition, it will fail at a much lower stress than the stress obtained in the usual displacement-control tensile tests.

The strength to initiate discontinuous deformation decreases with increases in the loading rate; this is closely related to the effect of strain rate on the serrations in displacement-controlled tests.[8] The initiation strength in displacement-control tests corresponds to the range 50 to 500 N/s in load-control tests. The initiation strength in load-control tests for AISI 310 and 316LN equals the ultimate tensile strength at 0.5 and 5 N/s.

In AISI 304L, no effect of either the loading rate or control mode on elongation was observed. This was due to lower initiation strength and higher work-hardening rate supported by the α'-martensite transformation of the alloy.

For both 304L and 316LN alloys, the elongation to fracture was essentially the same for the 5 and 50 N/s load rates (Figures 6 and 7). Therefore, with increasing load rate, the amount of α'-martensite per unit strain increased in 304L and decreased in 316LN. This is similar to the trend observed by Reed and Walsh[9] in these same alloys in displacement-control tests at 4 K. They attributed the trend to specimen heating. Heating produced more α'-martensite in 304L because more martensite forms in this alloy at higher temperatures; conversely, in alloy 316LN there is no C-curve behavior and less α'-martensite forms at higher temperatures. The explanation for the increased α'-martensite in the 316LN during displacement-control tests is the much larger elongation.

CONCLUSIONS

1. Yield strength remained constant with loading rate and reduction of area decreased slightly.

2. Ultimate tensile strength decreased with increased loading rate, reflecting specimen heating at a higher rate, to 65% of the strength obtained in displacement-control tests.

3. The stress at which the first discontinuous deformation occurred with increasing load rate was equivalent to the yield stress at higher rates. The amount of deformation that occurred just above yield strength reached 2%.

4. Large deformation (15 mm) occurred in AISI 310 at 5 N/s. During this deformation, the entire specimen length continued very rapid deformation with specimen heating within one load drop.

5. Average deformation velocities of 26 mm/s (7.5×10^{-1} s^{-1}) were measured.

6. Measurement of α-martensite in the specimens after fracture indicated temperature increases during deformation.

ACKNOWLEDGMENTS

This study was partly sponsored by Office of Fusion Energy, U.S. Department of Energy.

REFERENCES

1. T. Ogata and K. Ishikawa, Cryogenics 26:365–369 (1986).
2. T. Ogata, K. Ishikawa, O. Umezawa, and T. Yuri, Discontinuous deformation during tensile tests in liquid helium, submitted to Cryogenics.
3. T. Ogata, K. Ishikawa, and K. Nagai, Tetsu-to-Hagane 71:1390–1397 (1985), in Japanese.
4. D. T. Read and R. P. Reed, Adv. Cryog. Eng. 26:91 (1980).
5. A. Seeger, Dislocation and Mechanical Properties of Crystals, John Wiley, New York (1957), p. 206
6. Z. S. Basinski, Proc. R. Soc. A240:229 (1957).
7. G. Y. Chin, W. F. Hosford, Jr., and W. A. Backofen, Trans. AIME 230:1043 (1964).
8. R. P. Reed and R. P. Walsh, National Bureau of Standards, Boulder, Colorado, unpublished data.
9. R. P. Reed and R. P. Walsh, Tensile strain rate effects in liquid helium Adv. Cryog. Eng. 34:199 (1988).

ROUND-ROBIN TENSILE AND FRACTURE TEST RESULTS FOR AN Fe–22Mn–13Cr–5Ni AUSTENITIC STAINLESS STEEL AT 4 K*

H. Nakajima, K. Yoshida, and S. Shimamoto
Japan Atomic Energy Research Institute
Tokai-mura, Ibaraki-ken, Japan

R. L. Tobler, P. T. Purtscher, and R. P. Reed
National Bureau of Standards
Boulder, Colorado

Round-robin tests are a part of the U.S.–Japan cooperative program to develop standard tensile and fracture test procedures for austenitic stainless steels at 4 K. The first round of tests for an Fe–22Mn–13Cr–5Ni steel are described in this paper. The interlaboratory scatter in 4-K measurements is reported and relevant aspects of test procedure are discussed.

INTRODUCTION

Cryogenic standards are needed to support magnetic fusion-energy developments. At the United States–Japan meeting on Low Temperature Structural Materials and Standards in December 1984, the development of property measurement standards was cited as a first step towards the ultimate goal of establishing design standards for fusion-energy structures. A program was therefore initiated to evaluate and standardize the existing laboratory procedures. This paper describes the first round of interlaboratory tests that are now under way in the United States and Japan.

APPROACH

Seven laboratories participated, five from Japan and two from the United States. The participants are volunteers from government, academic, and industrial organizations with recognized materials testing experience. Table 1 identifies the laboratories, their abbreviations, and associated personnel.

---

*In *Advances in Cryogenic Engineering – Materials*, vol. 34, Plenum, New York, pp. 241–249.

Table 1. Participating laboratories and personnel

Institute	Supervisor	Researcher	Staff
Hitachi Research Laboratory (HRL)	T. Matsumoto	Y. Wadayama	H. Sato
Japan Atomic Energy Research Institute (JAERI)	S. Shimamoto	H. Nakajima K. Yoshida	M. Oshikiri
Kobe Steel, Ltd. (KSL)	T. Horiuchi	M. Shimada S. Tone	——
Lawrence Livermore National Laboratory (LLNL) and Lawrence Berkeley Laboratory (LBL)	J. Miller and J.W. Morris, Jr.	L.T. Summers	J.W. Chan M. Strum
National Bureau of Standards (NBS)	R.P. Reed	R.L. Tobler P.T. Purtscher	R.P. Walsh
National Research Institute for Metals (NRIM)	K. Ishikawa	T. Ogata K. Nagai	T. Yuri
Tohoku University, Reasearch Institute for Strength and Fracture of Materials (RISFM)	H. Takahashi	T. Shoji	K. Nakano

At the time of our study, standard 4-K tensile and fracture test procedures did not exist. Each laboratory used its own procedures. In general, they followed the established room-temperature standards,[1-8] except where modifications were necessary for tests at 4 K.

The test material was a newly developed Fe–22Mn–13Cr–5Ni austenitic stainless steel; its composition, in wt.%, is Fe–21.79Mn–12.82Cr–4.94Ni–0.05C–0.36Si–0.013P–0.005S–0.212N. It was supplied as 70-mm-thick plate from a 15-metric-ton industrial heat, in the annealed condition. Samples were cut from locations at the midthickness of the original plate. One laboratory (JAERI) machined all the test specimens to minimize variations in preparation. The number of specimens distributed can be inferred from the results in the text. A questionnaire was distributed with the specimens to identify the individual laboratory apparatus and procedures.

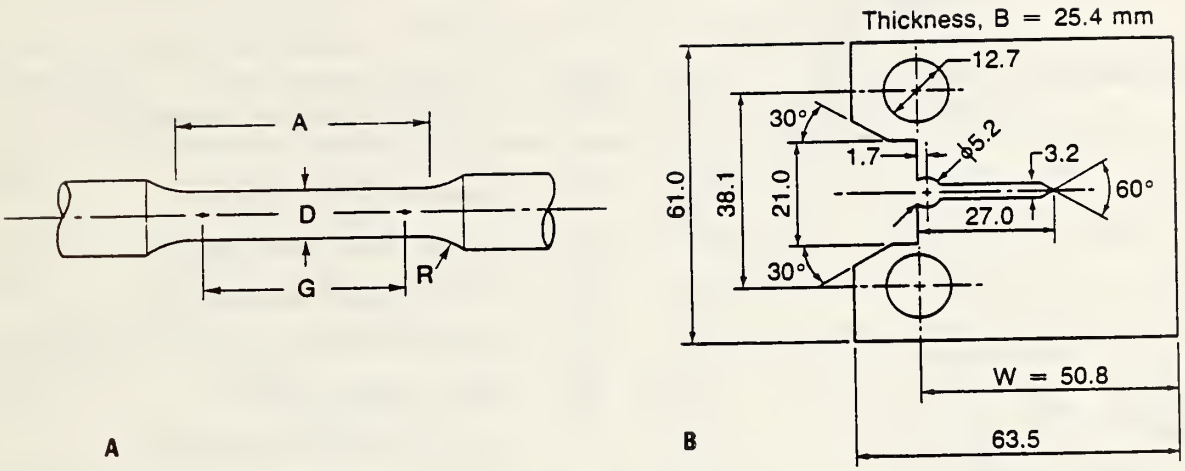

Figure 1. Specimen configurations used in this study: A) tensile specimen, and B) compact specimen. (All dimensions are in mm.)

SPECIMEN CONFIGURATIONS AND PREPARATIONS

Tensile Tests

Cylindrical tensile specimens machined with the load axis parallel to the long-transverse plate direction were used by everyone, but the specimen dimensions were varied to suit individual laboratory preferences. Figure 1 defines the relevant specimen parameters, and Table 2 gives the specimen dimensions for each laboratory. The conventional gage-length-to-diameter (G/D) ratios are 4 or 5 for cylindrical specimens.[2-5] In this study, three laboratories used G/D = 4 and marked the gage length on the reduced specimen length by means of punch or scribe marks. Other laboratories did not mark a gage length but calculated elongation from changes in overall specimen length or distance between fillets before and after testing (see Table 2).

Fracture-Toughness Tests

A compact specimen was used in this study, as shown in Fig. 1. All specimens were identical in thickness (B = 25.4 mm), width (W = 50.8 mm), and notch length (a_n = 27 mm). The notch orientation was TL, and displacement was measured at the loadline.

The specimens tested in Japan were fatigue-cracked by one laboratory (KSL) in air, at 295 K, and at a cycle frequency of 40 Hz. The desired initial crack length, a_0, was 32 mm. The crack was first extended 1.7 mm from the notch by using maximum and minimum fatigue loads of 17.6 and 0.78 kN; further crack extension from 1.7 to 3.5 mm was then accomplished by using loads of 9.8 and 0.78 kN. The specimens tested in the United

Table 2. Tensile specimen dimensions (see Fig. 1 for definition of symbols)

Institute	D (mm)	G (mm)	A (mm)	G/D –	Interval Used for Elongation Measurements
HRL	7.00	28.0	40.0	4	gage marks, punched
JAERI	7.00	–	42.4	–	total specimen length
KSL	7.00	–	42.4	–	total specimen length
LLNL/LBL	6.35	25.4	33.5	4	extensometer screw indentations
NBS	6.25	25.4	38.1	4	gage marks, inked
NRIM	6.25	–	32.0	–	total specimen length
RISFM	6.35	–	31.75	–	distance between ends of fillets

States were fatigue-cracked in liquid nitrogen at 76 or 77 K; the load ratio was 0.1; the maximum stress-intensity factors were less than 30 MPa·m½. After precracking, NBS side-grooved their specimens to a net thickness reduction of 20%. The side grooves were 3.8 mm deep with an included angle of 60° and a notch-tip radius of 0.4 mm. The different precracking temperatures used in the two countries had no measurable effect on the J_{Ic} measurements.

TEST PROCEDURES

Tensile Properties

The tensile properties of interest are the yield strength (YS), the ultimate strength (UTS), the reduction of area (RA), the elongation (EL), and Young's modulus (E). Procedures for testing at 295 K are specified in JIS and ASTM standards.[1-6] Load–extension or load–time curves or both are recorded. Yield strength is measured at 0.2% plastic strain by an offset method applied to load-strain-gage, load-extensometer, or time-chart recordings. Ultimate strength is obtained by dividing the maximum load by the original area. Elongation is computed by dividing the change in length by the original length. Reduction of area is obtained by dividing the change in cross-section area by the original area. The slope of the stress–strain curve in the elastic region gives Young's modulus. Most of the tests were conducted using screw-driven test machines with crosshead displacement control at various speeds. Table 3 lists the nominal strain rates calculated by dividing the free-running crosshead speed by the initial length of the reduced section.

Table 3. Summary of tensile test techniques

Institute	Crosshead Speed (mm/min)	Strain Rate (10^{-4} s^{-1})	Measurement Method for 0.2%-Offset YS
HRL	0.5, 1.0[a]	2.1, 4.2[a]	strain gage
JAERI	0.6, 3.0[a]	2.4, 11.8[a]	strain gage
KSL	1 2[b]	3.9 7.8[b]	strain gage
LLNL/LBL	0.35	1.7	extensometer
NBS	0.2, 0.5[a]	0.9, 2.2[a]	strain gage, time, extensometer
NRIM	0.5	2.6	extensometer
RISFM	1	5.2	strain gage, time

Notes: a. Rate change was used: the first number is the rate during YS measurement; the second, the rate during UTS measurement.
b. Different speeds were used in the second test.

Fracture Properties

The fracture properties of interest are J_{Ic} and $K_{Ic}(J)$, estimated from the expression $K_{Ic}(J) = (J_{Ic} \cdot E)^{1/2}$. The test procedure of interest is the computer-aided single-specimen unloading compliance technique.[8] During the test, the specimen is unloaded periodically, and its stiffness is measured from the slopes of the unloading lines. From changes in stiffness, the crack extensions, Δa, are inferred and plotted versus J, and J_{Ic} is obtained using Method E 813-81 guidelines.[7] That standard imposes no controls on hardware or software. In this study, most tests were conducted using servohydraulic machines in stroke control, but two laboratories used servohydraulic machines in clip-gage-displacement control. Also, one laboratory used specimen rotation and crack growth correction factors to their J–Δa calculations, but other laboratories didn't. The computed initial and end-of-test crack lengths, a_0 and a_p, were compared with direct optical measurements after testing.

RESULTS

Tensile Properties

Figure 2 shows a typical 4-K tensile-test record. Serrations occurred in the plastic-strain range, which is usual for ductile alloys at 4 K. In this steel, the serrations begin at plastic strains near 6% and do not interfere with YS determinations at 0.2% strain.

The YS and UTS values, plotted versus nominal strain rate in Fig. 3, indicate no measurable effect for the range of strain rates covered in this study, 0.9 to 7.9 × $10^{-4}s^{-1}$ for YS and 2.1 to 11.8 × $10^{-4}s^{-1}$ for UTS. Likewise, no size effect is evident. Therefore, the measurements for all fourteen tests were pooled; a summary is given in Table 4. The means and ranges are

YS = 1242 MPa; + 5.0%, − 5.3%
UTS = 1667 MPa; + 2.7%, − 4.2%
EL = 36.0; + 6.0%, − 5.0%
RA = 49.0; + 5.0%, − 5.0%
E = 200 GPa; + 7.5%, − 6.0%.

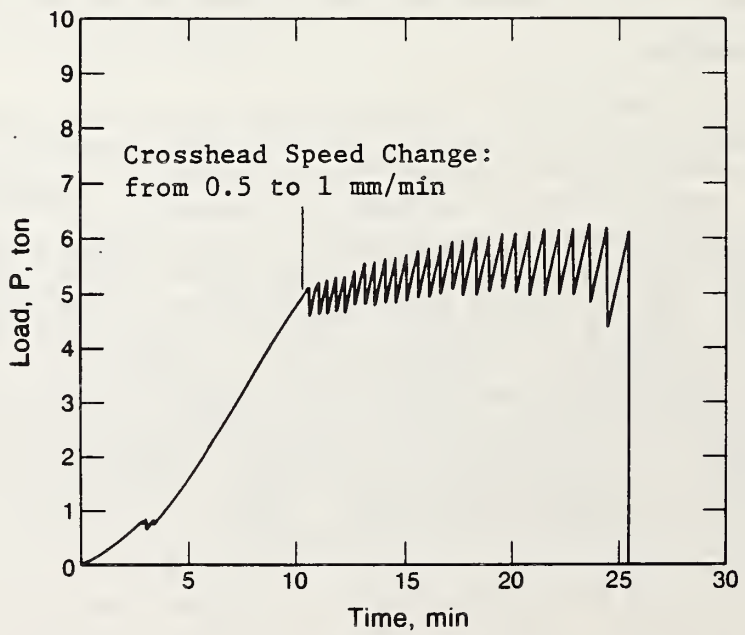

Figure 2. Time-chart record for the Fe–22Mn–13Cr–5Ni steel at 4 K.

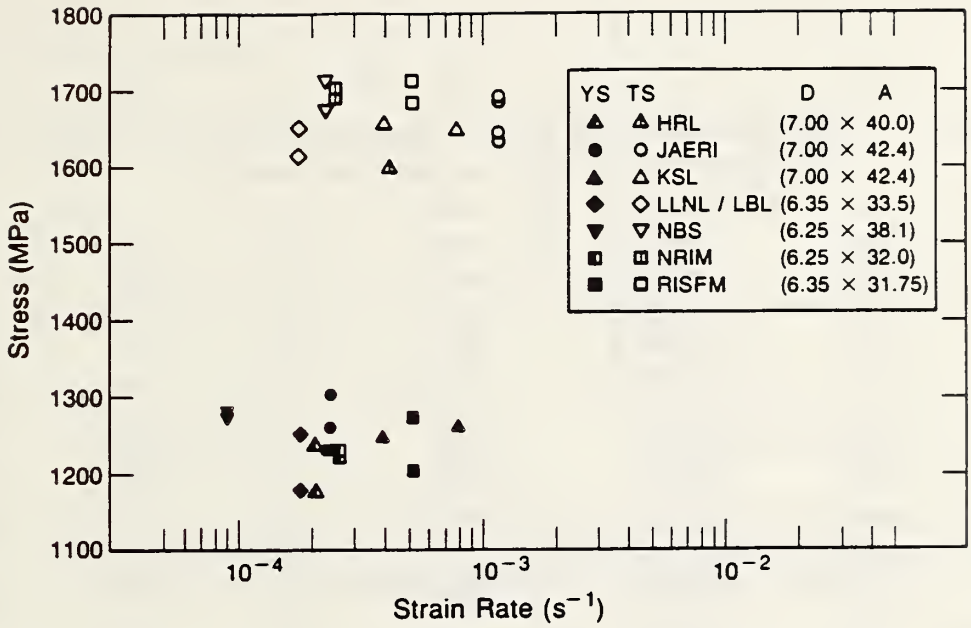

Figure 3. Yield and ultimate strength measurements at 4 K.

The YS values in Table 4 represent strain-gage or (in two cases) extensometer techniques. Time-chart data were also reported by some laboratories. When the 0.2%-offset procedure was applied to the time charts, the YS values were nearly equivalent or slightly higher than values from strain or extensometer plots, with differences ranging from −2 to 6%.

Fracture Toughness

Fourteen J_{Ic} tests were attempted. One specimen (A17) failed owing to computer malfunction and another (A19) was evaluated using a nonstandard method,[9] which will be considered in a separate paper. A typical load–displacement record and resistance curve for a stroke-control compliance test is shown in Fig. 4, and the J_{Ic} data are listed in Table 5. A total of twelve tests were performed by seven laboratories using the compliance technique. The measurements for specimens precracked at 76 K and side-grooved are indistinguishable from the bulk of results for specimens precracked at 295 or 77 K and not side-grooved. Two specimens (A3 and A4), however, gave low toughness values, which could be due to material variability. A summary, including these values, is given in Table 5. The mean values and ranges are

$$J_{Ic} = 135 \text{ kJ/m}^2;\ +23\%,\ -35\%$$

and

$$K_{Ic}(J) = 166 \text{ MPa}\cdot\text{m}^{1/2};\ +8\%,\ -19\%.$$

Table 4. Tensile test results for Fe–22Mn–13Cr–5Ni steel at 4 K (YS from strain gage, except as noted)

Institute	Spec.	YS (MPa)	UTS (MPa)	EL (%)	RA (%)	E (GPa)
HRL	D1	1238	NA	NA	NA	192
	D2	1176	1597	36	48	193
JAERI	B1	1304	1686	31	50	208
	B2	1260	1688	33	51	204
	B5	1227	1633	37	50	205
	B6	1227	1643	37	49	205
KSL	B3	1248	1656	35	46	215
	B4	1261	1648	36	53	204
LLNL/LBL	A2	1181[a]	1613	36[b]	29[b]	194
	A12	1254[a]	1651	32[b]	26[b]	195
NBS	A18	1281	1713	37	50	201
	A19	1275	1676	30[b]	48[b]	205
NRIM	C1	1230[a]	1700	35	47	188
	C2	1230[a]	1690	42	44	192
RISFM	E1	1202	1697	49[d]	51	196
	E2	1276[c]	1710	39	54	NA
SUMMARY:						
Number of tests		16	15	11	12	15
Maximum value		1304	1713	42	54	215
Minimum value		1176	1597	31	44	188
Arithmetic mean		1242	1667	36	49	200
Standard deviation		35.5	35.5	2.9	2.8	7.3

Notes: a. extensometer value
b. broke on gage mark, not used in average
c. time-chart value
d. not used in average

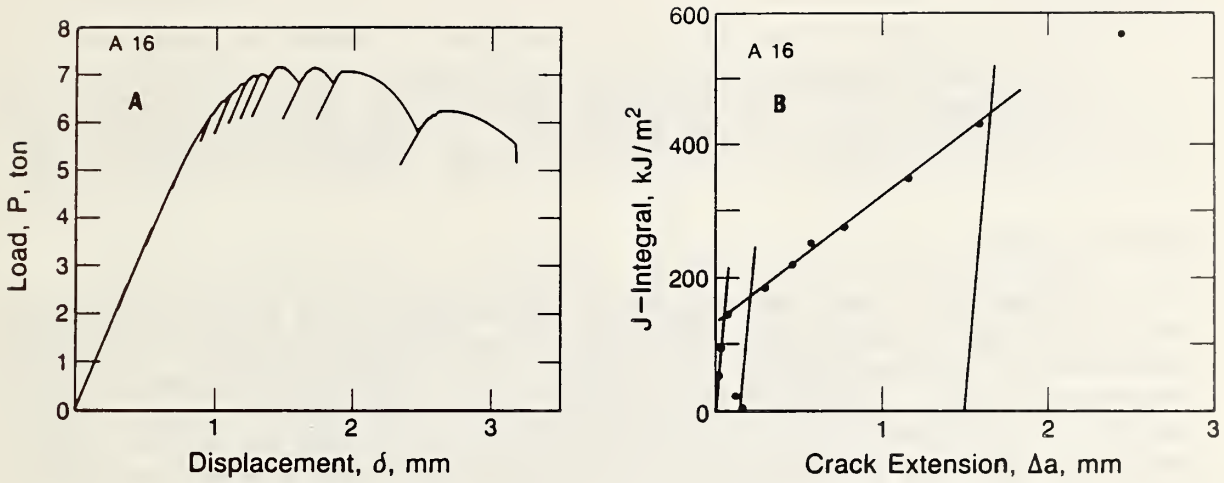

Figure 4. A load-vs-displacement test record and the resulting resistance curve for a J_{Ic} test at 4 K, showing results obtained using servohydraulic machines operated in stroke control.

Table 5. Fracture test results for Fe-22Mn-13Cr-5Ni steel at 4 K

Institute	Spec.	J_{Ic} (kJ/m²)	$K_{Ic}(J)$ (MPa·m$^{1/2}$)	a_o Agreement (%)	a_p Agreement (%)	E (GPa)
HRL	A21	166	179	−0.9	−8.7	193
JAERI	A13	138	169	−1.5	−30.1	208
	A14	147	174	−1.8	−17.8	208
KSL	A15	146	178	0.3	NA	215
	A16	143	175	−4.3	NA	215
LLNL/LBL	A4	103[a]	148[a]	−2.2	−14.3	194
	A5	140	172	−1.8	−16.7	194
	A6	153	180	−2.8	−10.3	194
NBS	A1	127	162	1.5	−16.7	201
	A2	140	170	1.0	−8.3	201
	A3	88[a]	135[a]	−0.7	−4.8	201
NRIM	A17	(computer malfunction)				
	A18	125	154	−3.0	−10.0	190
RISFM	A19	144[b]	168[b]	NA	NA	196
SUMMARY:						
Number of tests		12	12			
Maximum value		166	180			
Minimum value		88	135			
Arithmetic mean		135	166			
Standard dev.		21.5	14			

Notes: a. Low value, possibly due to material variability (see text)
b. Key curve data, not included in the average (see text)

DISCUSSION

This interlaboratory testing of structural alloys is the first ever conducted at 4 K. The measurements show fair agreement despite the lack of formally written 4-K test procedures. Further refinements are possible.

Tensile Tests

Scatter in tensile measurements was highest for E (± 7%) and lowest for UTS (± 4%). In general, the scatter was slightly higher than that reported for a room-temperature study.[10] The scatter in EL may have been increased by the variety of gage-length marking techniques used. Gage-marking techniques should be improved, since three out of six specimens failed at gage marks when gage marks were made on the reduced section.

Concerning YS measurements, this study indicates that perhaps a small bias may be introduced (possibly dependent on the test apparatus) when the 0.2%-offset procedure is applied to time-chart plots, rather than extensometer or strain-gage plots. Time charts usually show some nonlinearity at the start of testing, as well as other irregularities (Fig. 2). For convenience, however, the time-chart method is quite useful in alloy screening or commercial production control, where high precision is not demanded.

Fracture Tests

The fracture-toughness measurements showed fair agreement. The scatter of J_{Ic} for 12 compliance tests (up to 35%) was greater than the ± 17% scatter in a room-temperature study.[11] If our two lowest values are eliminated, with the assumption that they reflect material variability, then the mean values are increased and the ranges are reduced considerably to

$$J_{Ic} = 142.5 \text{ kJ/m}^2; \ +16.5\%, \ -12\%$$

and

$$K_{Ic}(J) = 171 \text{ MPa}\cdot\text{m}^{1/2}; \ +5\%, \ -10\%.$$

The compliance procedure therefore appears to be a reliable method for J_{Ic} determinations at 4 K. Some problems that surfaced in this study should be addressed before standardization. These include the negative crack-growth effect, the disagreement between measured and computed end-of-test crack lengths, and the choice of E modulus.

As shown in Fig. 4A, the resistance curve at the onset of testing shows negative Δa (i.e., an anomalous decrease of crack length). At this stage of development, we treat this by shifting the blunting line to the left on the Δa axis until it coincides with the upper portion of the J–Δa trend, but this procedure is arbitrary and not recognized in Method E 813-81.

As shown in Table 5, most tests for specimens without side grooves did not give good a_p predictions; the measured and calculated values must agree to within 15% according to Method E 813-81, section 9.3.4, for room-temperature testing. The NBS measurements for side-grooved specimens meet this requirement, as suggested in Methods E 813-81, section A1.4.

Young's modulus must be measured or estimated before J_{Ic} tests. Any uncertainty affects the resistance curve, because Δa is inferred from the normalized compliance, $EB\delta/P$. The conversion from J_{Ic} to $K_{Ic}(J)$ is also affected. This was assessed at JAERI in a post-test analysis by substituting various values of E and recalculating $J-\Delta a$, J_{Ic}, and $K_{Ic}(J)$. We found that $K_{Ic}(J)$ increases 10 $MPa \cdot m^{\frac{1}{2}}$ for a 10 GPa increase of E. In Table 4, the reported moduli range from 188 to 215 GPa. Thus, the spread of $K_{Ic}(J)$ data would have been reduced by about ± 7% if everyone had used the same value of E. Since Young's modulus measurements at 4 K are covered by Method E 111, we recommend that future interlaboratory tests incorporate that method and specify one Young's modulus for J-integral tests.

CONCLUSIONS

Seven laboratories performed smooth-bar tensile and J_{Ic} tests of an austenitic stainless steel at 4 K. The tensile results show good agreement, independent of minor variations in specimen size and strain rates below a value of $10^{-4}s^{-1}$. The tensile property measurement ranges were ± 7% or less and not much greater than would be expected for tests at 295 K. Also, the unloading-compliance test appears to be a reliable method for J_{Ic} measurement at 4 K. The range of J_{Ic} measurements was within 35%, or 16.5% if the two lowest values are discounted.

ACKNOWLEDGMENTS

The organizers of this activity wish to express sincere appreciation to all the participants for their contributions. Without such collaboration, the development of consensus standards is impossible.

The study was supported, in part, by the Office of Fusion Energy, U.S. Department of Energy.

REFERENCES

1. Test Pieces for Tensile Test for Metallic Materials, Japanese Industrial Standard, Designation JIS Z 2209-1980. English translation, Japanese Standards Association, Tokyo (1980).

2. Method of Tensile Test for Metallic Materials, Japanese Industrial Standard, Designation JIS Z 2241. English translation, Japanese Standards Association, Tokyo (1980).

3. Standard Methods and Definitions for Mechanical Testing of Steel Products, Designation ANSI/ASTM A 370-77, 1986 Annual Book of ASTM Standards, vol. 03.01, American Society for Testing and Materials, Philadelphia (1986).

4. Standard Methods of Tension Testing of Metallic Materials, Designation E 8-85b, 1986 Annual Book of ASTM Standards, vol. 03.01, American Society for Testing and Materials, Philadelphia (1986).

5. Standard Methods of Tension Testing of Metallic Materials (Metric), Designation E 8M-85, 1986 Annual Book of ASTM Standards, vol. 03.01, American Society for Testing and Materials, Philadelphia, (1986).

6. Standard Test Method for Young's Modulus, Tangent Modulus, and Chord Modulus, Designation E 111-82, 1986 Annual Book of ASTM Standards, vol. 03.01, American Society for Testing and Materials,, Philadelphia (1986).

7. Standard Test Method for J_{Ic} A Measure of Fracture Toughness, Designation E 813-81, 1986 Annual Book of ASTM Standards, vol. 03.01, American Society for Testing and Materials,, Philadelphia (1986).

8. G. A. Clarke, Single-Specimen Tests For J_{Ic} Determination – Revisited, in: Fracture Mechanics: Thirteenth Conference, ASTM STP 743, R. Roberts, Ed., American Society for Testing and Materials, Philadelphia (1981).

9. M. Takeuchi, T. Shoji, H. Takahashi, and T. Anayama, Reports of the Research Institute for Strength and Fracture of Materials, Tohoku University, Sendai, Japan, 17, 1–12 (1984).

10. R. H. Heyer, ASTM Bulletin, Technical Publication TP 83, American Society for Testing and Materials,, Philadelphia, 57–62 (1949).

11. G. A. Clarke, J. D. Landes, and J. A. Begley, Journal of Testing and Evaluation, 8, 221–232 (1980).

SIZE, SIDE-GROOVING, AND FATIGUE-PRECRACKING EFFECTS ON J-INTEGRAL TEST RESULTS FOR SUS 304 STAINLESS STEEL AT 4 K*

M. Shimada
Kobe Steel
Kobe, Japan

R. L. Tobler
National Bureau of Standards
Boulder, Colorado

T. Shoji and H. Takahashi
Research Institute for Strength
and Fracture of Materials
Tohoku University
Sendai, Japan

Tests were conducted to investigate specimen preparation effects on the J-integral fracture-test procedure at 4 K. Proportional compact specimens of a fully plastic steel were tested using the compliance technique. The J_{Ic} measurements were not affected by side grooving, but decreased slightly as specimen thickness increased from 12.5 to 25.4 mm. The resistance curve slope decreased significantly with both thickness and side grooving. Fatigue-precracking and sustained-loading effects are discussed.

INTRODUCTION

The 4-K fracture toughness of austenitic alloys is usually determined by J-integral tests using compact specimens and the unloading-compliance technique. The compliance test procedure was developed for ferritic steels at room temperature,[1-3] and we applied it later[4-7] to austenitic stainless steels at 4 K. Because of dissimilar material behavior (i.e., phase transformations, serrations, and adiabatic heating), several aspects of the 4-K procedure warrant verification. This

---

*In *Advances in Cryogenic Engineering – Materials*, vol. 34, Plenum, New York, 1988, pp. 251–258.

paper investigates the influence of sustained loading, specimen size, side-grooving, and precracking temperature on results for a high-toughness SUS 304 steel. This work was part of the United States–Japan Cooperative Program for 1986 and was conducted to contribute to the development of a standard 4-K test procedure.

MATERIAL AND TEST PROCEDURES

The material selected for these tests was a research heat of type SUS 304 austenitic stainless steel with 4-K yield strength and fracture toughness values of 615 MPa and 300 MPa·$m^{\frac{1}{2}}$. This steel exhibits martensitic phase transformations when deformed at 77 or 4 K, but not at 295 K, and it lies at the high-toughness extreme of the trend for the annealed AISI 304 alloys.[4] A 30-mm-thick plate of this steel was obtained and tested in the annealed (1080°C) and water-quenched condition. The composition and tensile properties are given in Tables 1 and 2.

Three specimen configurations were studied: standard 25-mm-thick compact specimens (1TCT), with and without side grooves, and proportionally reduced 12.5-mm-thick compact specimens (½TCT) without side grooves. Basic dimensions are shown in Fig. 1. The width-to-thickness ratios (W/B) were 2.0, the notch orientations were TL, and razor blades for clip-gage attachment were located on the loadline.[1]

Table 1. Chemical composition for SUS 304 steel (wt.%).

Fe	C	Cr	Ni	Si	Mn	P	S
bal.	0.06	18.23	12.95	0.58	1.21	0.027	0.006

Table 2. Mechanical properties for SUS 304 steel.

Test Temperature (K)	Yield Strength (MPa)	Ultimate Strength (MPa)	Elongation (%)	Red. of Area (%)	Young's Modulus (GPa)	Brinell Hardness
295	215	529	58	—	—	131
4	615	1475	57	52	217	—

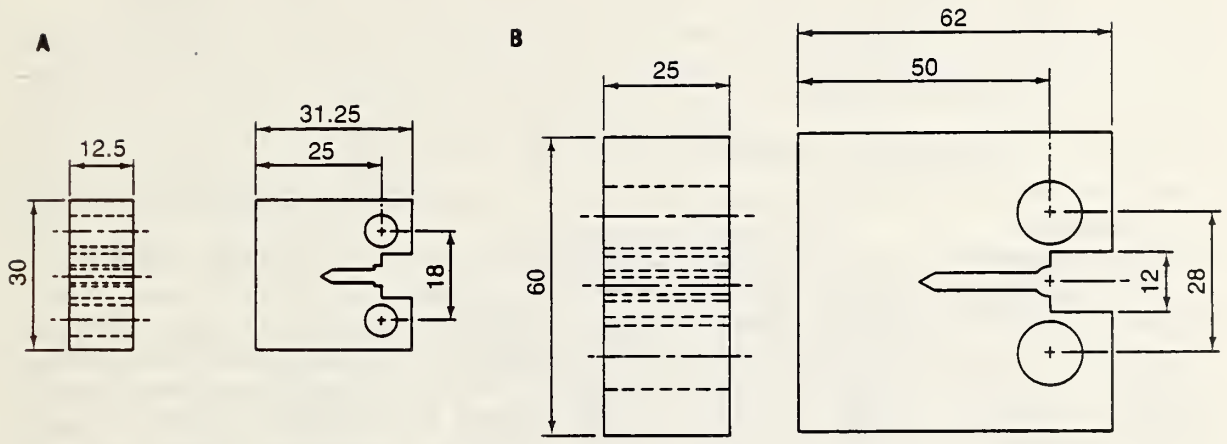

Fig. 1. Compact specimens used in this study. Dimensions are in mm.

The specimens were fatigue-precracked at 295 or 77 K to crack length ratios (a/W) near 0.6, using a load ratio of 0.1 and a cycle frequency of 20 Hz. The maximum fatigue loads (P_{max}) are listed in Table 3. After precracking, two of the 1TCT specimens were side-grooved 2 mm deep on each face. The groove root radius was 0.5 mm and the net thickness reduction was 16%. For the side-grooved specimens, compliance was calculated using the effective thickness (B_{eff}) and J was calculated using the net thickness (B_{net}), per ASTM Methods E 813-81 sections 8.7.1 and 9.1.1.

The specimens were tested at 4 K using a turret-disc computer-aided unloading-compliance apparatus.[6] The load-vs.-displacement ($P-\delta$) curves and resistance ($J-\Delta a$) curves were autographically recorded. Crack-initiation resistance, J_{Ic}, is defined as the point of intersection of the blunting and regression lines; crack-growth resistance, $\Delta J/\Delta a$, is the resistance-curve slope. Since the apparent slope computed for a specimen without side grooves may be inaccurate,[5] a corrected slope was obtained from a line plotted between J_{Ic} and the physically measured end-of-test crack-extension increment, Δa_p. During tests, some specimens were held for 10 min at fixed stroke positions near the limit load while the load cell and clip-gage outputs were monitored for relaxation. After the unloadings were completed, the specimens were heat-tinted and broken apart; the Δa_p values were measured, and the fracture surfaces were examined by scanning electron microscopy (SEM).

Table 3. Precracking conditions (295 and 77 K) and 4-K toughness results

Specimen Description		Fatigue Precracking Conditions				Fracture Toughness		
Type and Number		Temp. (K)	P_{max} (kN)	P_{max}/P_L	K_{max} (MPa·m$^{1/2}$)	a/W	J_{Ic} (kJ/m^2)	$K_{Ic}(J)$ (MPa·m$^{1/2}$)
½TCT, plain	A1[a]	295	4.9	0.70[d]	34.2	0.603	343[e]	272[e]
	A2	295	5.4	0.77[d]	37.7	0.605	453	314
	A3	77	4.9	0.33	35.1	0.610	434	307
	A4	77	5.9	0.41	42.8	0.613	415	300
						average =	434	307
1TCT, plain	B4	295	13.7	0.48d	32.8	0.598	392	292
	B5	295	10.8	0.37	25.7	0.595	373	285
	B6	295	16.7	0.57[d]	39.4	0.594	392	292
	B7[b]	77	13.7	0.22	34.1	0.606	—	—
	B8	77	11.8	0.18	27.5	0.591	412	299
						average =	392	290
1TCT, side grooved	B1	295	11.8	0.42	29.3	0.605	386	289
	B2[c]	295	NA	NA	NA	NA	NA	NA
	B3	77	13.7	0.19	29.5	0.571	397	294
						average =	392	291

Notes:

a – skewed crack front development
b – incomplete resistance curve
c – failure due to machine malfunction
d – final fatigue load cycle shows some hysteresis
e – not used in average

RESULTS AND DISCUSSION

Tables 3 and 4 display the principal results of this study. As we expected, the fracture behavior at 4 K was fully plastic. Representative test records, resistance curves, and fractured specimens are shown in Figs. 2, 3, and 4. Ductile fracture in this steel consisted of stretch zone and dimple formation, as shown in Fig. 5.

Sustained-Loading Behavior

Drift in the load or displacement signals owing to creep can affect compliance results by causing nonlinear unloading slopes.[1] This problem is common for austenitic stainless steels at 295 and 77 K, where load relaxations occur readily during the first few minutes of static holding in J tests. In this study at 4 K, however, load relaxations did not occur. The SUS 304 steel of this study had a rather low yield strength at 4 K, and because time-dependent plasticity effects are even less likely with higher strength at this temperature, time-dependent effects are not expected for most austenitic stainless steels at 4 K.

Table 4. Summary of resistance curve features for SUS 304 steel at 4 K

Specimen Type		Regression Line Slope Computed (Corrected) ($kJ/m^2/mm$)	Points in Exclusion Interval[a]	Accuracy of Δa_p Prediction[b] (%)
½TCT, plain	A1	470 (NA)	7	NA
	A2	360 (170)	9	90
	A3	500 (367)	9	57
	A4	260 (196)	11	33
	average	398 (243)		
1TCT, plain	B4	140 (NA)	NA	NA
	B5	275 (254)	3	43
	B6	230 (203)	5	10
	B8	330 (297)	4	20
	average	279 (251)		
1TCT, side-grooved	B1	115 (120)	3	−5
	B2	NA NA	NA	NA
	B3	195 (199)	2	−2
	average	155 (159)		

Notes: a – at least four points are required by E 813-81, section 9.3
b – agreement within 15% is required by E 813-81, section A1.4

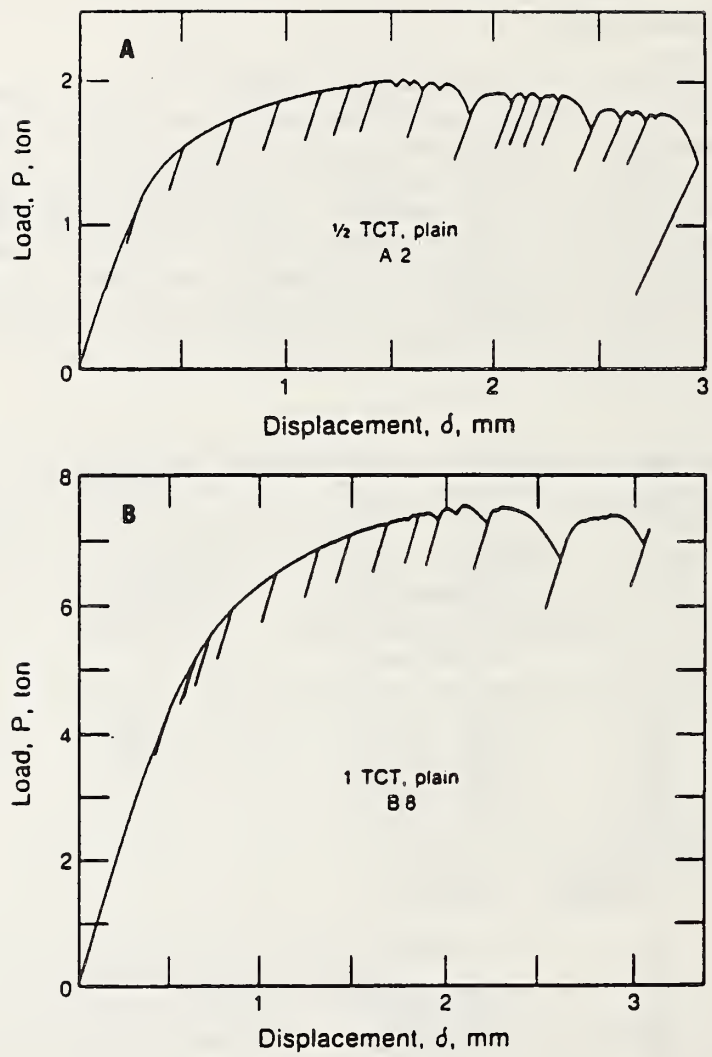

Fig. 2. Load–displacement records for specimens without side grooves: A) ½TCT and B) 1TCT. Load is in metric tons.

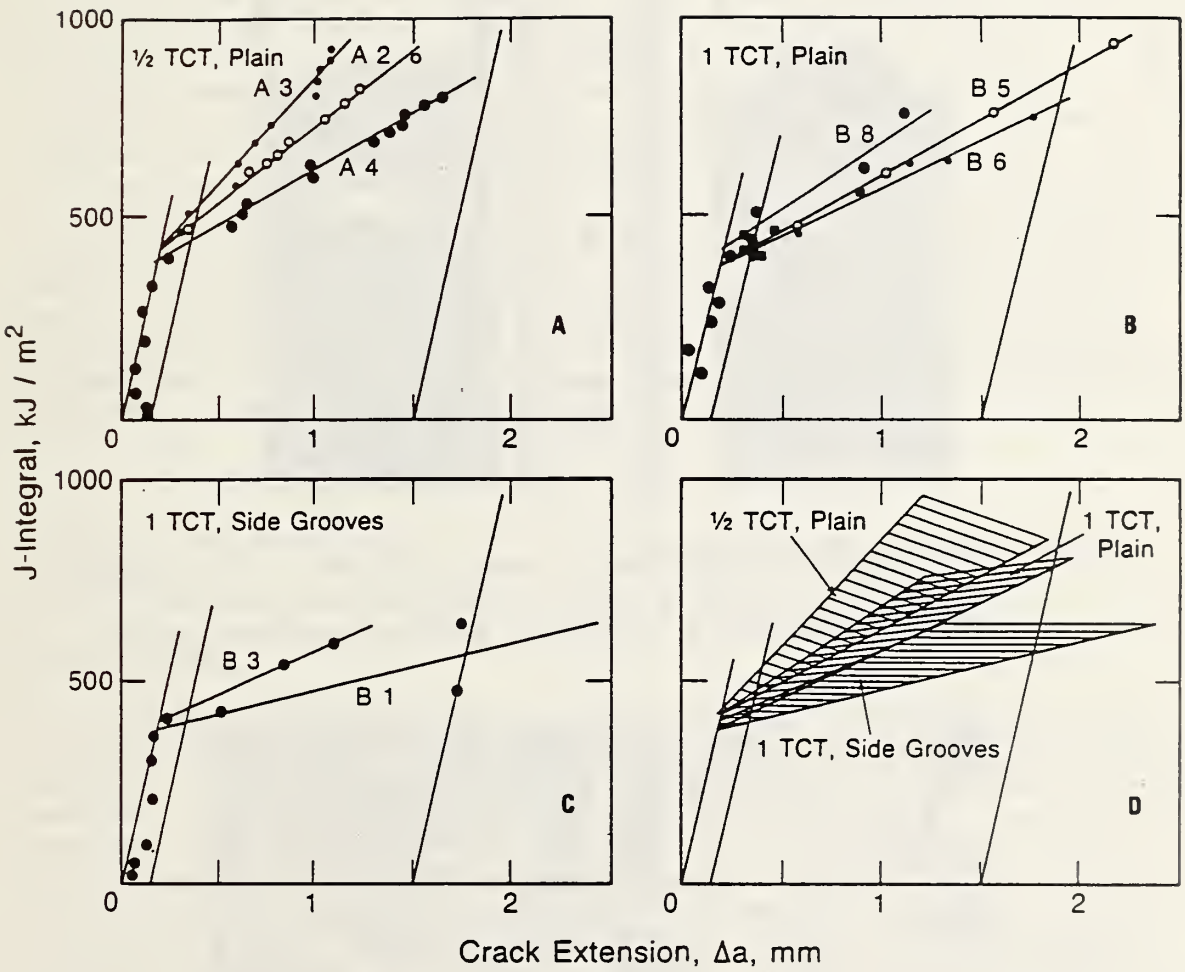

Fig. 3. J–Δa curves for SUS 304 steel at 4 K: A) ½TCT, plain, B) 1TCT plain, C) 1TCT side grooved, and D) comparison.

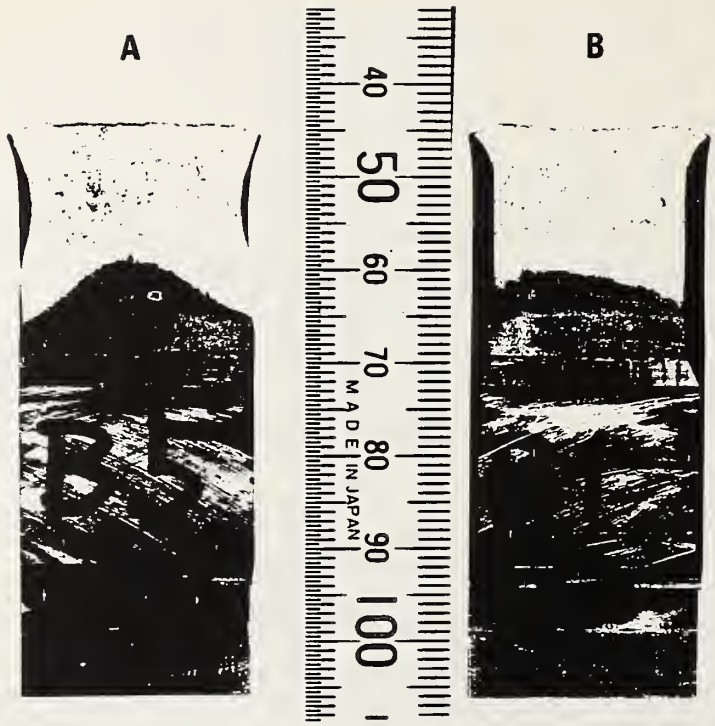

Fig. 4. Fractured 1TCT specimens, showing the heat-tinted crack extension increments: A) without the side grooves, crack tunneling; B) with side grooves, uniform growth.

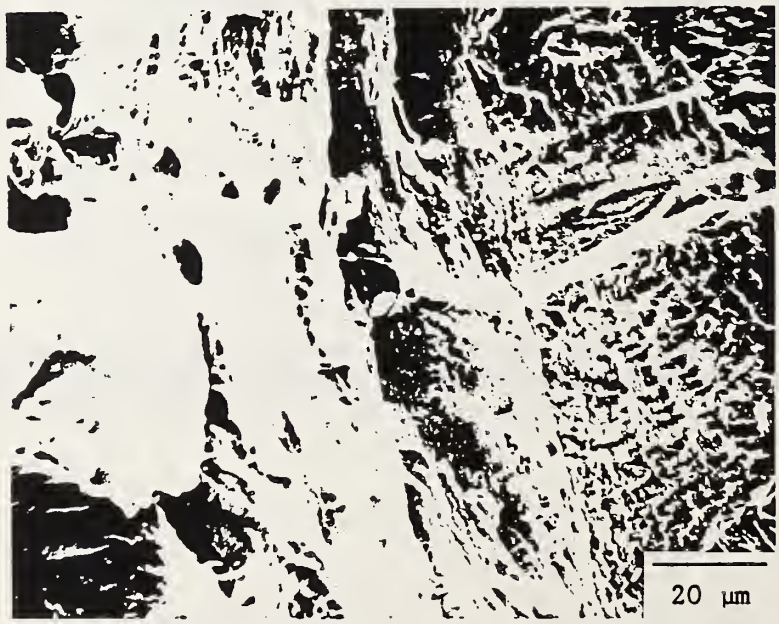

Fig. 5. Fractograph (SEM); specimen B1 at 4 K.

Specimen Size

Specimens smaller than the routine 1TCT size are of practical interest for use in multiple-specimen cryostats or for characterizing stock that has limited dimensions. For specimens precracked at 77 K, the measured J_{Ic} values for ½TCT specimens were slightly higher than those for the 1TCT size, as shown in Table 3. This difference was less than 10% and, therefore, of minor significance. In contrast, the resistance curve slope was more strongly affected, as shown in Table 4 and Fig. 3. The ½TCT specimens curves had the highest slopes, the most data points in the exclusion interval, and the poorest agreement between the measured and computed Δa_p values. Likewise, the resistance-curve slopes for plain 1TCT specimens were higher than those for side-grooved specimens; this is partly due to crack tunneling, as discussed below. Another possible explanation for size effects is a departure from J-controlled crack growth. According to Method E 813-81, the specimen thickness and ligament (b) dimensions must satisfy certain minimum values to ensure J-controlled crack growth. The ligament sizes for our ½TCT tests are borderline at about 9.9 mm, whereas 10 mm is the calculated requirement (Method E 813-81, section 9.3.5.3):

$$B,b \geq 25J_{Ic}/\sigma_Y, \tag{1}$$

where σ_Y, the flow stress, is the average of the yield and ultimate strengths.

Side Grooves

The use of side grooves is a controversial option. Side grooves increase machining costs but may be desirable to alleviate crack-front tunneling in tough materials[1] or to achieve plane-strain conditions more perfectly. In this study, side grooves on 1TCT specimens lowered the apparent resistance-curve slopes to realistic values without affecting J_{Ic}. There were several beneficial effects: the crack tunneling was reduced (Fig. 4), the Δa_p was accurately predicted, and the regression line slope was accurately computed. These results are not unexpected (see Method E 813-81, section A1.4). What is new, however, is the observation that side grooves tended to enhance discontinuous deformation at 4 K. Thus, load drops were more pronounced with side grooves than without them, and side-grooves reduced the number of points within the 0.15- to 1.5-mm exclusion interval. For this reason, our tests of the side-grooved 1TCT specimens did not meet the requirement of obtaining at least four valid J–Δa points within the interval (Method E 813-81, section 9.3). Since the serrations were less pronounced in smaller specimens, in retrospect it appears that tests using side-grooved specimens of an intermediate thickness between the ½T and 1TCT sizes would have satisfied all the requirements of E 813-81.

Fatigue Precracking

Many investigators precrack their specimens at 295 K, assuming that J_{Ic} measurements at 4 K will be unaffected. No proof is available, however, and Method E 813-81 states no guidelines for precracking and fracturing at dissimilar temperatures. The rules (section 7.6 of Method E 813-81) state that P_{max} should be less than 40% of the limit load, P_L:

$$P_{max} \leq 0.4 \times P_L = 0.4 \times Bb^2\sigma_Y/(2W + a), \tag{2}$$

or be such that

$$\Delta K \leq E \times 0.005, \tag{3}$$

whichever is less. The above equation requires $\Delta K \leq 34$ MPa·m$^{\frac{1}{2}}$ for the SUS 304 steel at 295, 77, and 4 K.

Differences in crack-tip plastic-zone size and microstructure do exist for fatigue cracks formed at room or cryogenic temperatures. For SUS 304 steel, the plastic zones at 295 K were fully austenitic, whereas those at 77 or 4 K were partially martensitic. Also, the zones at 295 K were larger. Assuming $K_{max} = 30$ MPa·m$^{\frac{1}{2}}$ and using Irwin's approximation,

$$R = (K_{max}/\sigma_y)^2(1/6\pi), \tag{4}$$

we estimated the plastic zone radii (R) as 1.0, 0.20, and 0.12 mm at 295, 77, and 4 K, respectively. This shows that the differences in plastic zones were clearly much greater between 295 and 77 K than between 77 and 4 K. In previous tests of AISI 310S, precracking at 76 or 4 K had no effect on resistance curves at 4 K.[5] Therefore, in this study we compared precracking at 295 or 77 K.

The following interpretation is offered for the results in Table 3. For the ½TCT specimens: the J_{Ic} values for two specimens precracked at 295 K at high P_{max}/P_L were scattered; hence, the comparison with specimens precracked at 77 K is inconclusive. For the 1TCT specimens: the J_{Ic} values for two specimens precracked at 77 K at low P_{max}/P_L ratios (0.18 and 0.19) were slightly higher than results for four specimens precracked at 295 K at high P_{max}/P_L ratios (0.37 to 0.57). This suggests that precracking at 295 K may give lower J_{Ic} values, but the effect (less than 5%) falls within measurement uncertainty. In these tests, we used high precracking loads to accentuate any possible effects. For routine testing, lower load ratios ($P_{max}/P_L < 0.4$) and ΔK values (~25 MPa·m$^{\frac{1}{2}}$) are normally used, in which case any effects of precracking at 295 K on J_{Ic} measurements at 4 K should be negligible.

SUMMARY

Tests of an SUS 304 austenitic stainless steel were performed at 4 K to evaluate the unloading-compliance J_{Ic} test technique. The validity criteria of the ASTM room-temperature standard were used to interpret the data at 4 K. The following points are significant:

1. There is no evidence of load relaxation during static holding for this material. This indicates that time-dependent plasticity effects on the compliance test procedure are negligible at 4 K.

2. J_{Ic} decreased 10% or less for a specimen-thickness increase from 12.5 to 25.4 mm, whereas the resistance-curve slope decreased rather substantially with thickness, and with side grooving.

3. The J_{Ic} measurements for 1TCT specimens were not affected by side grooves. Side-grooving improved the accuracy of crack-growth predictions by the compliance method but reduced the number of valid data points within the exclusion interval.

4. Limited data indicate that at fatigue precracking at 295 K does not affect J_{Ic} measurements at 4 K if the maximum fatigue loads are kept within reasonable limits, as discussed in the text.

ACKNOWLEDGMENTS

This work was performed as part of the United States–Japan Cooperation Program in magnetic fusion energy for 1986. The research heat of SUS 304 was supplied by Nippon Stainless Steel, and the fatigue precracking was performed at JAERI; the authors greatly appreciate this assistance. This study was supported, in part, by the Office of Fusion Energy, U.S. Department of Energy.

REFERENCES

1. Standard Test Method for J_{Ic}, A Measure of Fracture Toughness, ASTM Designation E 813-81, in: 1986 Annual Book of ASTM Standards, Section 3, vol. 03.01, American Society for Testing and Materials, Philadelphia (1986).

2. G. A. Clarke, W. R. Andrews, P. C. Paris, and D. W. Schmidt, Single-Specimen Tests for J_{Ic} Determination, in: Mechanics of Crack Growth, ASTM STP 590, American Society for Testing and Materials, Philadelphia (1976).

3. G. A. Clarke, Single-Specimen Tests for J_{Ic} Determination–Revisited, in: Fracture Mechanics: Thirteenth Conference, ASTM STP 743, R. Roberts, ed., American Society for Testing and Materials, Philadelphia (1983).

4. R. L. Tobler, D. T. Read, and R. P. Reed, Strength–Toughness Relationship for Interstitially Strengthened AISI 304 Stainless Steels at 4 K Temperature, in: Fracture Mechanics: Thirteenth Conference, R. Roberts, ed., ASTM STP 743, American Society for Testing and Materials, Philadelphia (1981).

5. R. L. Tobler, Ductile Fracture with Serrations in AISI 310S Stainless Steel at Liquid Helium Temperature, in: Elastic–Plastic Fracture: Second Symposium, vol. II – Fracture Resistance Curves and Engineering Applications, ASTM STP 803, C. F. Shih and J. P. Gudas, eds., American Society for Testing and Materials, Philadelphia (1983).

6. M. Shimada, R. Ogawa, T. Moriyama, and T. Horiuchi, Development of a Cryogenic Fracture Toughness Test System, in: Cryogenic Engineering, 21:269–274 (1986).

7. H. Nakajima, K. Yoshida, K. Okuno, M. Oshikiri, E. Tada, S. Shimamoto, R. Miura, M. Shimada, S. Tone, K. Suemune, T. Sakamoto, and K. Nohara, Fracture Toughness of Newly Developed Structural Materials for Superconducting Coils of Fusion Experimental Reactor, in: Advances in Cryogenic Engineering 32:347–354 (1986).

EFFECTS OF SPECIMEN SIZE, SIDE GROOVING, AND PRECRACKING TEMPERATURE ON J-INTEGRAL TEST RESULTS FOR AISI 316LN AT 4 K*

T. Ogata, K. Ishikawa, and T. Yuri
Superconducting and Cryogenic Materials Research Group
National Research Institute for Metals
Ibaraki, Japan

R. L. Tobler, P. T. Purtscher, and R. P. Reed
Fracture and Deformation Division
National Bureau of Standards
Boulder, Colorado

T. Shoji, K. Nakano, and H. Takahashi
Research Institute for Strength and Fracture of Materials
Tohoku University
Sendai, Japan

The effects of specimen size, side grooving, and fatigue-precracking temperature on J-integral fracture toughness test results were investigated to support the development of a standard 4-K test procedure. The test material was an AISI 316LN alloy. The tests used compact specimens and a computer-controlled unloading compliance technique. Fatigue precracking at various temperatures (293, 77, or 4 K) had no apparent effect on fracture-toughness measurements at 4 K. For plain specimens, the fracture toughness decreased with increasing specimen thickness in the range 25 to 38 mm; for side-grooved specimens, the toughness decreased more.

INTRODUCTION

The single-specimen unloading compliance testing technique[1-3] is a useful method to evaluate fracture toughness of materials, especially at liquid-helium temperature. However, there are several problems, such as the effects of specimen size, side grooves, and regression line, that should be understood before a 4-K test standard can be established. At this cryogenic temperature, additional problems occur: serration phenomena, specimen heating, and differences in plastic-zone size. We performed a series of experiments to study the effects of specimen size, side grooves, and fatigue-precracking temperature on fracture-toughness test results at 4 K.

---

*In *Advances in Cryogenic Engineering – Materials*, vol. 34, Plenum, New York, 1988, pp. 259–266.

MATERIAL AND SPECIMEN DESIGN

The test material was a commercial heat of AISI 316LN stainless steel in the form of a 54-mm-thick plate in the mill-annealed condition (solution-treated at a minimum temperature of 1313 K). Table 1 shows the chemical composition. The tensile properties as a function of temperature are summarized in Table 2.

Table 1. Chemical Composition for AISI 316LN Steel (wt.%)

C	Mn	P	S	Si	Cr	Ni	Cu	Mo	Co	N	Fe
0.016	1.10	0.020	0.015	0.54	17.97	10.51	0.17	2.12	0.25	0.139	bal.

Table 2. Tensile Properties for AISI 316LN Steel

Temperature (K)	Yield Strength (MPa)	Ultimate Strength (MPa)	Young's Modulus (GPa)	Elongation (%)	Reduction of Area (%)
293	275	580	205	60	68
76	760	1428	205	53	65
4	894	1640	205	44	48

Three sizes of compact (CT) specimens were machined from the plate in the TL orientation according to ASTM Method E 399-83. Their designations and dimensions are given in Figure 1. The extensometer was attached along the load line, as required in ASTM E 813-81. Modified CT specimens with the planar dimensions of a 1TCT specimen, but only 12.5 mm thick, were also used in some preliminary experiments to study the effect of crack length.

PROCEDURE

Fatigue Cracking

A servohydraulic testing machine was used for fatigue cracking and J_{Ic} tests. Fatigue cracking was done with a minimum-maximum load ratio of 0.1 and a frequency of 10 Hz. The last 2.6 mm of the fatigue cracks were introduced in each size specimen at 293, 77, and 4 K. The maximum stress intensity was kept low, about 24 $MPa \cdot m^{\frac{1}{2}}$, to reduce the plastic-zone size. For the 0.5TCT and 1TCT specimens, the relative crack-length ratio (a/W) was 0.6. For the 1.5TCT specimens, a ratio of 0.7 was adopted to enable testing in a 10-metric-ton-capacity machine.

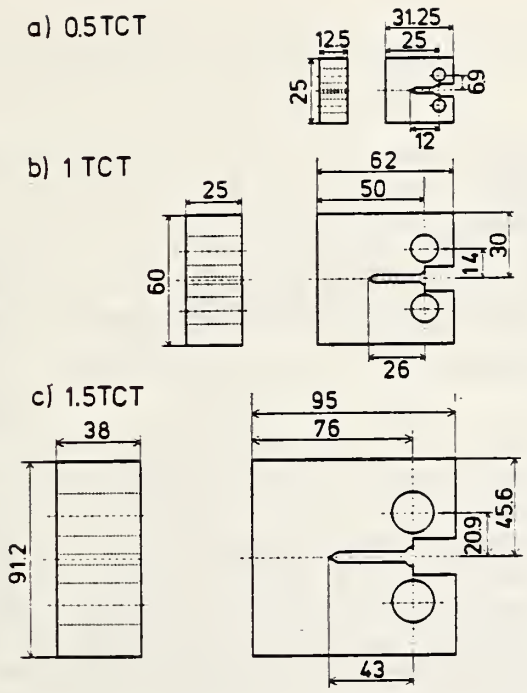

Figure 1. Specimens used in this study (all dimensions are in mm). The notations 0.5TCT, 1TCT, and 1.5TCT refer to specimens 12.5 mm, 25 mm, and 38 mm thick, respectively.

After precracking, for two specimens of each size, side grooves were machined to a net thickness reduction of 25%. The notch-root radii of the 0.5TCT, 1TCT, and 1.5TCT specimens were 0.25, 0.5, and 0.75 mm, respectively. When testing side-grooved specimens, compliance was calculated using the effective thickness, B_{eff}, and J_{Ic} values were calculated using the net thickness, as indicated in ASTM E 813-81, sections 8.7.1 and 9.1.1.[3] B_{eff} is given by

$$B_{eff} = B - (B - B_n)^2/B, \quad (1)$$

where B is specimen thickness and B_n is net thickness.

Fracture-Toughness Testing

The standard CT specimens were tested in liquid helium according to the ASTM Method E 813-81 procedure with a computer-controlled servo-hydraulic testing machine. Figure 2 illustrates the flow chart of this test. Table 3 shows the initial basic testing conditions. The loading rate during strain control was 0.4 mm/min. The compliance during unloading was calculated to within 1%; it includes a rotation correction.[4] The modified CT specimens were tested according to a key-curve method

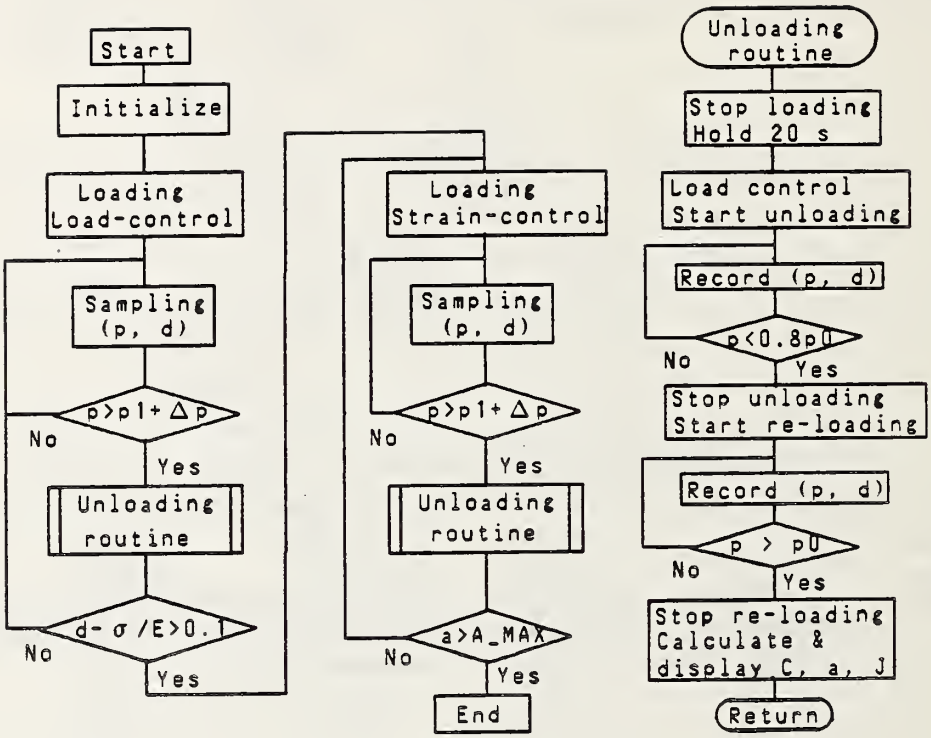

Figure 2. Flow chart of the computer-controlled J_{Ic} test. The symbols p, d, a, C, and E represent load, displacement, crack length, compliance, and Young's modulus, respectively.

Table 3. Initial J_{Ic} Test Conditions

	0.5TCT	1TCT	1.5TCT
First unloading (kN)	5[5]	40[25]	50[30]
Unloading ratio	0.2	0.2	0.2
Loading step (kN)	100	200	200
Strain step (mm)	0.05	0.05	0.05

NOTE: Values in brackets are for specimens with side grooves.

(described in detail in a separate report[5]); in these tests, a fracture-toughness parameter designated J_i was determined and used to evaluate the effect of the a/W ratio on the fracture toughness.

After testing, each specimen was heat-tinted (ASTM E 813-81, section 8.3.1) at 593 K for 1 h to mark the final crack length prior to pulling the specimen apart. The fracture surfaces were examined by scanning electron microscopy (SEM) for any microscopic effect of the fatigue-precracking temperature on the fracture appearance, particularly at the location of the original crack tip prior to fracture-toughness testing.

RESULTS AND DISCUSSION

Test results are summarized in Table 4, and typical load–displacement curves for plain (i.e., non-side-grooved) CT specimens are shown in Figure 3. Large "pop-in" fractures, such as those seen in Figure 3b, occurred sporadically throughout the testing. Several tests were terminated prematurely (i.e., before a four-point resistance curve could be obtained), owing to such pop-ins, as noted in Table 4. Figure 4 shows two examples of the resistance curves. The intersection of the blunting and tearing lines determines the critical value of J, according to ASTM E 813.[3] The serrated yield behavior is commonplace at 4 K but not recognized by the existing test standard, which is written for a test temperature of 295 K. Large pop-ins due to fast fracture are, in fact, excluded by the existing standard (see note 2 of ASTM E 813-81). Therefore, the J_{Ic} values in Table 4 are designated J_Q rather than J_{Ic}. The estimates of $K_{Ic}(J)$ in Table 4 were obtained from the value of J_Q, according to ASTM E 813-81, section 9.4.

The effects of the test variables (specimen size, fatigue-precracking temperature, and side grooving) on $K_{Ic}(J)$ are illustrated by Figure 5. (Invalid data due to skewed crack fronts were also plotted to estimate effects.) The toughness of specimens decreased with increasing specimen thickness (at least in the 25- to 38-mm interval), and the toughness of the side-grooved specimens was lower than that of the plain specimens. The measured values for the two types of CT specimens, however, were nearly equal for the largest specimens, 1.5CT. The effects of specimen thickness and side grooving were attributed to the constraint exerted at the crack tip.

There are no clear effects of fatigue-precracking temperature on the measured toughness in the plain specimens. Fractographs (SEM) from the 1TCT specimens are shown in Figure 6. The crack front of the specimen fatigued at 4 K is clearer than that at 293 K and similar to that at 77 K. None of these specimens exhibited stretch zones between the fatigue precrack and the J_{Ic}-test fracture surface. The J_{Ic}-test fracture surface of each specimen was composed of a uniform distribution of small dimples (1 to 3 μm) with occasional delaminations.

Table 4. Fatigue Testing Matrix and J_{Ic} Results for AISI 316LN Steel

Specimen Type	Specimen Number	Side Grooves	a/W	Fatigue Temperature (K)	K_{max} (MPa·m$^{1/2}$)	J_{Ic} (kJ/m^2)	K_{Ic} (MPa·m$^{1/2}$)
0.5TCT	N1-1	yes	0.66	77	22	107	148*†
	N1-2	yes	0.68	77	23	125	160*
	N1-4	no	NA	77	23	NA	NA‡
	N1-5	no	0.58	77	23	160	182†
1.0TCT	N2-1	yes	0.61	77	24	117	NA‖†
	N2-2	yes	NA	77	24	134	166†
	N2-3	no	0.61	77	24	178	191†
	N2-4	no	0.62	77	24	180	192†
	N2-5	no	0.61	293	24	235	219*†
	N2-6	no	0.61	293	24	176	190†
	N2-7	no	0.61	4	24	189	197*†
	N2-8	no	0.60	4	24	217	NA‖†
1.5TCT	N3-1	yes	0.72	77	23	119	156†
	N3-2	yes	0.72	77	23	112	152†
	N3-3	no	0.71	77	25	123	159
	N3-4	no	0.71	77	23	129	163*

* invalid due to skewed crack front
† "pop-in" fast fracture; test terminated (see Fig. 3b)
‡ failure due to machine malfunction
‖ incomplete resistance curve; J_Q is an estimate from less than four J–Δa points

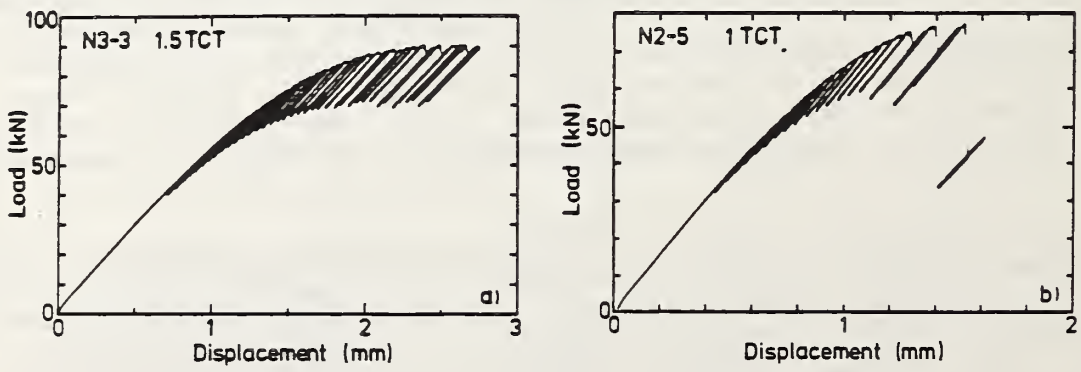

(a) (b)

Figure 3. Load–displacement curves for (a) 1.5TCT and (b) 1TCT specimens; fast fracture terminated the test of the 1TCT specimen.

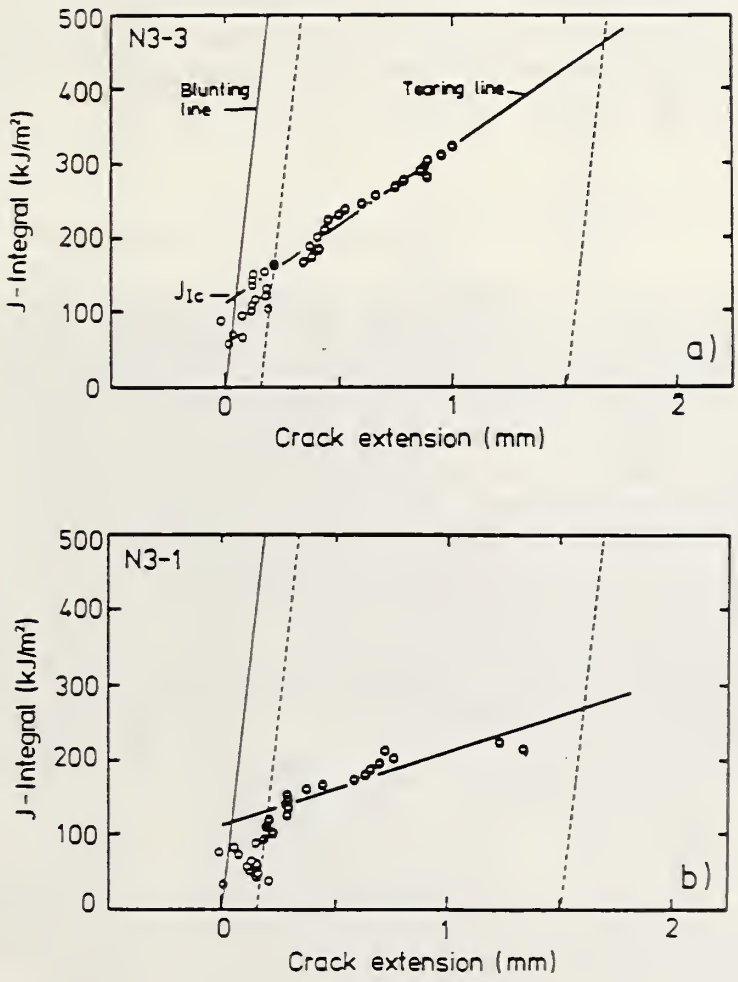

Figure 4. J–Δa curves for 1.5TCT specimens; (a) plain, (b) with side grooves. (The blunting, tearing, and exclusive lines were drawn according to ASTM E 813.[3])

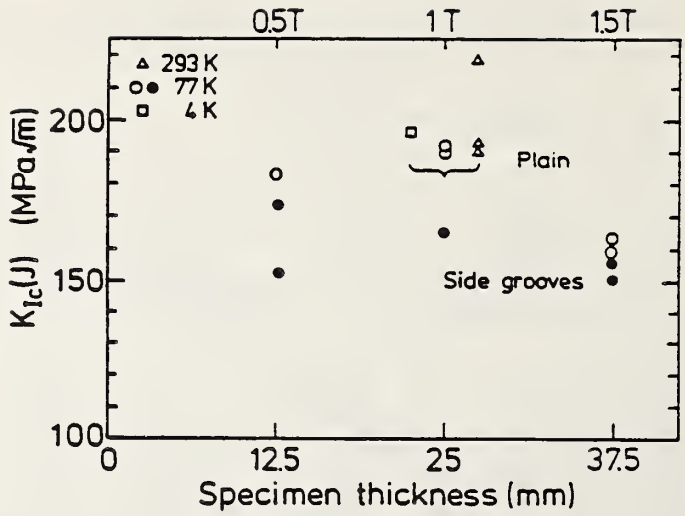

Figure 5. $K_{Ic}(J)$ estimates at 4 K as a function of thickness for proportionally sized specimens (W/B = 2), showing the effects of side grooves. Symbols indicate fatigue-precracking temperatures. Open symbols indicate plain specimens; closed symbols, specimens with side grooves.

The fatigue-precracking temperature had a large effect on the size of the plastic zone (R) in the specimen at the end of the precracking. The size of R can be estimated from the loading conditions and the yield strength (σ_y) by

$$R = (K/\sigma_y)^2/6\pi \qquad (2)$$

where K is the stress-intensity factor at the end of the precracking. Using K = 24 MPa·$m^{\frac{1}{2}}$, we estimated R to be 0.4 mm at 293 K and 0.04 mm at 4 K. Despite the factor of 10 difference in these values, there was no distinguishable effect of precracking temperature on the measured toughness or the fracture appearance.

Prior to the main series of unloading compliance tests, we briefly considered the possibility of an a/W effect at 4 K. Performing one test at a/W ratios of 0.4, 0.5, 0.6, 0.7, and 0.8, we obtained J_i = 179 kJ/m^2, ±6%. This scatter is less than that observed for J_{Ic} tests of six 1TCT specimens by the compliance technique (Table 4). It is clear that J_i values are not equal to J_{Ic} because of the different test methodology used.[3,5] Regarding the a/W effect, however, the J_i values were internally consistent and therefore indicated a/W independence.

Our results for this heat of AISI 316LN indicate that some of the restrictions in the ASTM E 813-81 might be unnecessary for the fracture-toughness test standard at liquid-helium temperature. The fatigue crack

length and precracking conditions apparently do not affect the measured toughness significantly. Also, even though all the specimens tested at 4 K met the ASTM E 813-81 thickness requirement (section 9.3.5.1, $B > 25\ J_{Ic}/\sigma_y$), the results were affected by specimen thickness and side grooving. Other results for austenitic stainless steels of higher toughness than our 316LN material showed that the J_{Ic} values for plain and side-grooved 1TCT specimens were equal.[6,7] This contrasts with our results for the AISI 316LN material and suggests that the effect of side grooving may be material dependent, perhaps because the materials differ in sensitivity to the constraint to plastic deformation imposed by the side grooves.

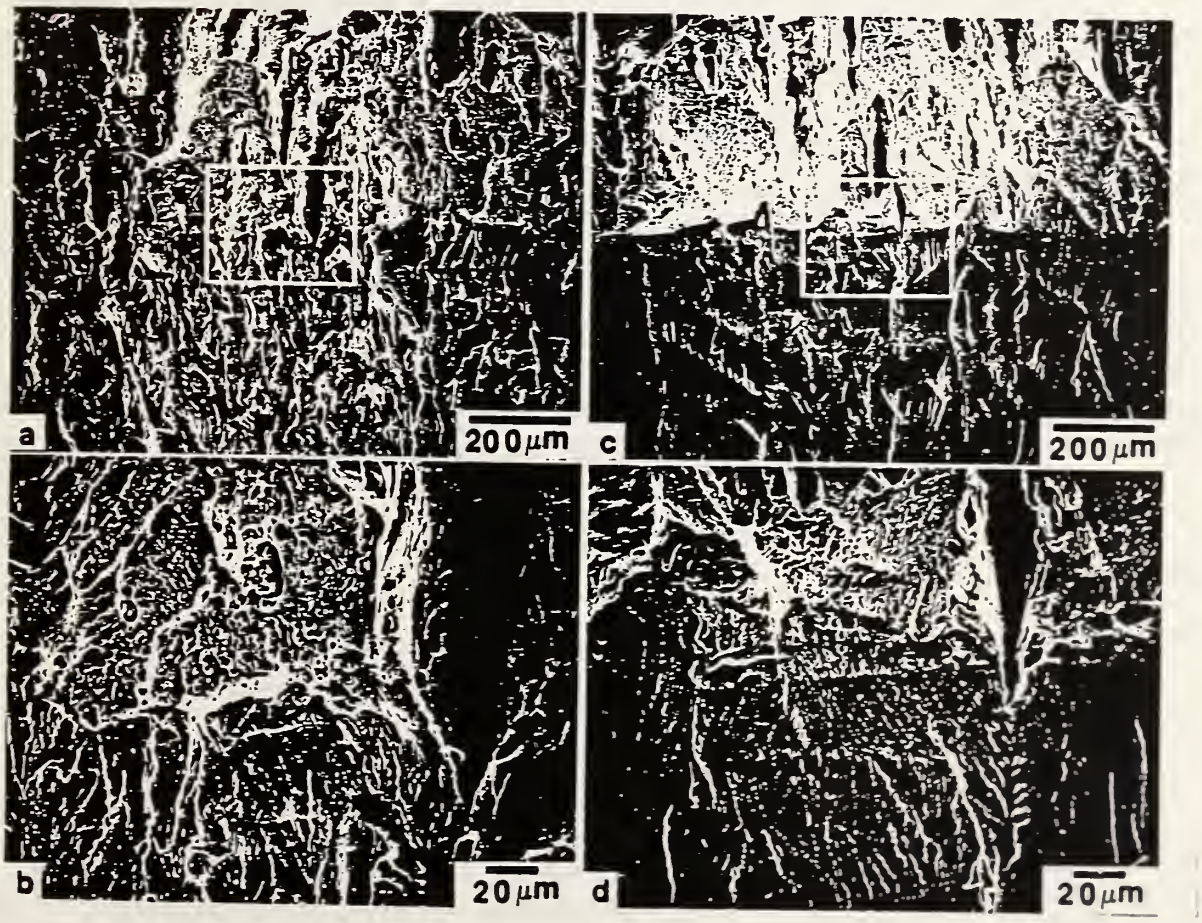

Figure 6. Fractographs (SEM) of a plain 1TCT specimen. (a) and (b) – fatigue at 293 K; (c) and (d) – fatigue at 4 K. Regions within the rectangles in (a) and (c) are shown magnified in (b) and (d).

CONCLUSIONS

We determined the fracture toughness of specimens of different sizes at 4 K using the unloading compliance technique. The specimens fractured in the elastic–plastic region. Trends obtained from this study were

1. The fracture toughness of plain specimens decreased with increasing specimen size in the range 1TCT to 1.5TCT (thickness range 25 to 38 mm).

2. The fracture toughness of this steel at 4 K is reduced by side grooves; however, the effect is small, less than 10%, in the largest specimen size (1.5TCT, or 38 mm thick).

3. Fatigue precracking at 293, 77, or 4 K at a stress-intensity factor of about 24 $MPa \cdot m^{\frac{1}{2}}$ has no measurable effect on the fracture toughness measured at 4 K.

ACKNOWLEDGMENTS

This work was performed as part of the U.S.–Japan Cooperation Program in Magnetic Fusion Energy. In Japan, this program is sponsored by the Ministry of Education of Japan. In the United States, it is sponsored by the U.S. Department of Energy. We thank K. Nagai at the National Research Institute for Metals for his contribution to the J_{Ic} test programming. We are also grateful to L. T. Summers of Lawrence Livermore National Laboratory supplied the test material.

REFERENCES

1. A. Saxena and S. J. Hudak, Jr., Review and extension of compliance information for common crack growth specimens, Int. J. Fract. 14:453–468 (1978).
2. G. A. Clarke, W. R. Andrews, P. C. Paris, and D. W. Schmidt, Single-specimen tests for J_{Ic} determination, in: "Mechanics of Crack Growth," ASTM STP 590, American Society for Testing and Materials, Philadelphia (1976), pp. 27–42.
3. Standard test method for J_{Ic}, a measure of fracture toughness, ASTM Designation E 813-81, in: 1986 Annual Book of ASTM Standards, section 3, Vol. 03.01, American Society for Testing and Materials, Philadelphia (1986) pp. 768–786.
4. H. Takahashi, M. A. Khan, and M. Suzuki, J. Test. and Eval. 8:63–67 (1986).
5. R. L. Tobler, H. Takahashi, and T. Shoji, Key curve method of fracture toughness determination for austenitic stainless steels at 4 K, in preparation.

6. F. J. Loss, B. H. Menke, and R. A. Gray, Jr., Development of J–R curve procedures, in: "NRL–EPRI Research Program (RP 886.2), Evaluation and Prediction of Neutron Embrittlement in Reactor Pressure Vessel Materials," Annual Progress Report for CY 1978, J.R. Hawthorne, ed., NRL Report 8327, Naval Research Laboratory, Washington, D.C. (August 1979).
7. M. Shimada, R. L. Tobler, T. Shoji, and H. Takahashi, Size, side-grooving, and fatigue precracking effects on J-integral test results for SUS 304 stainless steel at 4 K, in: "Materials Studies for Magnetic Fusion Energy Applications at Low Temperatures – XI," NBSIR 88-3082, National Bureau of Standards, Boulder, Colorado (1988) pp. 317–328.

MECHANICAL TESTS OF LARGE SPECIMENS AT 4 K: FACILITIES AND RESULTS*

K. Yoshida, H. Nakajima, M. Oshikiri,
R. L. Tobler,† and S. Shimamoto
Japan Atomic Energy Research Institute
Ibaraki, Japan

R. Miura and J. Ishizaka
Japan Steel Works
Tokyo, Japan

Mechanical tests of large specimens at 4 K were performed using a hundred-metric-ton cryogenic hydraulic test machine at the Japan Atomic Energy Research Institute's Naka Fusion Research Establishment. Specimens were machined from a 140-mm forged steel plate and from a 100-mm hot-rolled steel plate. In 4-K tensile tests, data for a 25-mm-diameter round specimen were obtained and compared with data for a standard 7-mm-diameter specimen. In 4-K fracture tests, data for 75- and 100-mm-thick compact specimens were compared with data for 25-mm- and 12.5-mm-thick specimens of similar geometries. The large cryogenic hydraulic tensile machine, a ten-metric-ton cryogenic multispecimen tensile machine, and a ten-metric-ton cryogenic hydraulic machine are described.

INTRODUCTION

The development of new Japanese cryogenic steels (JCS), a cooperative effort of the Japan Atomic Energy Research Institute (JAERI) and several Japanese steel companies that began in 1981, is nearly completed. Four kinds of steel alloy base metals have satisfied JAERI's requirements: yield strength > 1200 MPa and fracture toughness > 200 $MPa \cdot m^{\frac{1}{2}}$ at 4 K.[1] The gas-tungsten arc weldments of these steels also have good mechanical properties. During the JCS developmental work, the Demonstration Poloidal Coil (DPC) project[3] required and used JCS in superconducting coils and other cryogenic applications. Details of these DPC

*Published in *Advances in Cryogenic Engineering – Materials*, vol. 34, Plenum, New York, 1988, pp. 225–232.

†Visiting scientist, from the National Bureau of Standards, Boulder Colorado, U.S.A.

applications (mainly of thin plate) were reported previously.[2] Plates 100 mm or more thick are now required for the toroidal coil cases and supporting structures of the Fusion Experimental Reactor. For heavy section applications, it is necessary to show that the mechanical properties of the materials are not significantly affected by size effects arising from the scale-up of designs. Therefore, a new hundred-metric-ton cryogenic tensile machine was installed at JAERI-NAKA in 1986 to enable very large specimens to be tested. With this machine, the effects of specimen size on the tensile and fracture toughness behavior of the structural steels were studied.

TESTING MACHINES

Machines for testing at cryogenic temperatures are indispensable tools for the development of high-performance superconducting coils. Innovative technological devices, such as superconducting coils, use materials to the limits of their capabilities. Three mechanical testing machines have been installed at JAERI, as described in Table 1. These testing machines are intended not only for steel developmental work but also for superconductor material and nonmetallic material evaluations.

The ten-ton cryogenic tensile machine (TS10)[4] has both a turret-disk grip (10 samples per cool-down) and a conventional grip. In this study, we used the turret-disk grip, in which can be installed ten round specimens up to 7 mm in diameter or ten plate specimens up to 4 mm thick. A strain gage was epoxied to each specimen to measure the yield strengths.

The ten-ton cryogenic cyclic machine (PL10) was designed for fracture toughness (J_{Ic}), fatigue crack growth rate, and conventional fatigue data measurements. It was used in this study to determine the fracture toughness of the relatively small or standard compact specimens, as shown in Table 1.

Table 1. Machines at JAERI for Testing Structural Materials at 4 K

Machine	TS10	PL10	TS100
Capacity (metric ton)	10	10	100
Feature	turret disk	fatigue test	large size
Specimen			
Tensile – Round (mm in diam.)	7	7	25
– Plate (mm thick)	≤4	NA	NA
Compact tension coding	1T	0.5T, 1T	3T, 4T
Number of specimens tested per day	10	1	0.3
Consumption of liquid helium per specimen (ℓ)	8	80	800

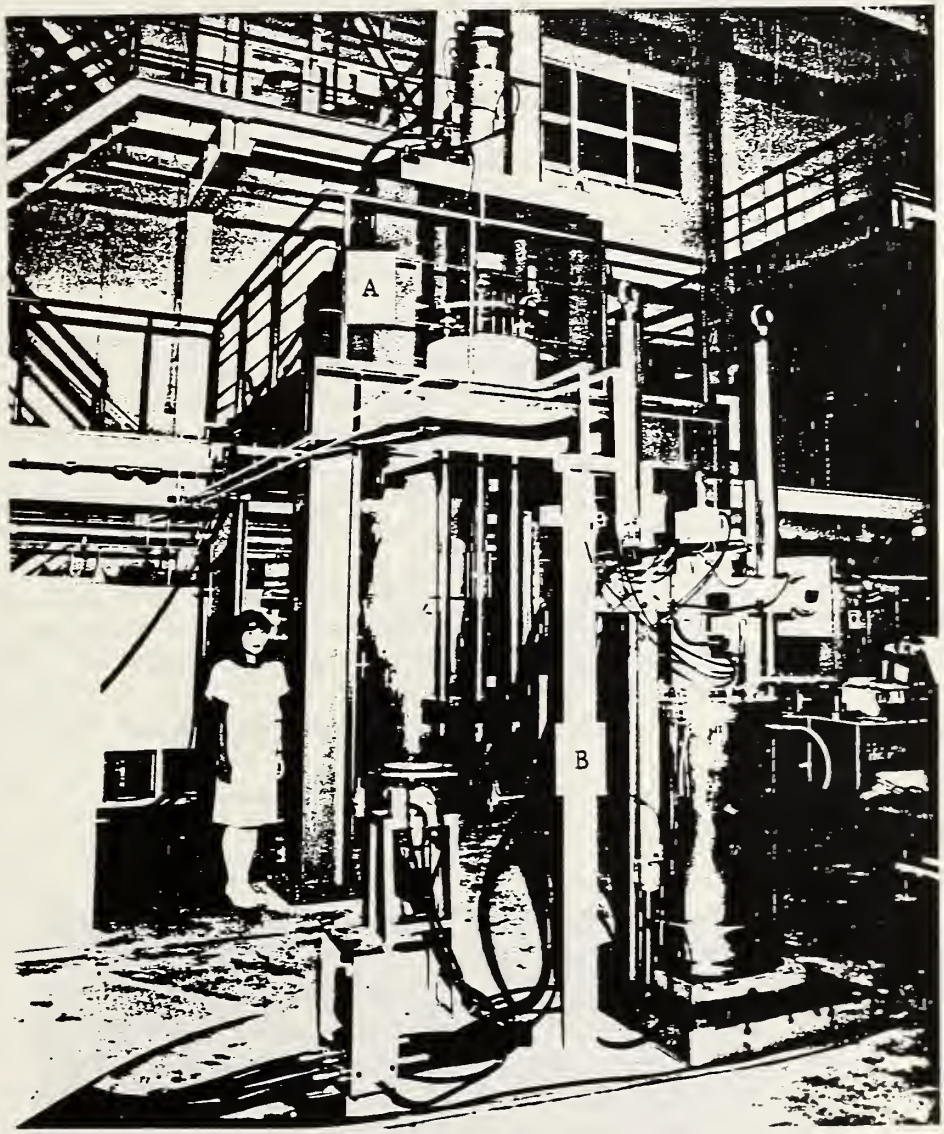

Fig. 1. The TS100 (A) and PL10 (B) cryogenic hydraulic test machines.

The large cryogenic tensile machine (TS100) shown in Fig. 1 was designed to determine the tensile properties and the fracture toughness of steel or superconductor specimens under monotonic loads of up to 100 tons. The total height of the TS100 is about 5 m, and the height of the section to be immersed in cryogenic liquids is 3 m. Figure 2 shows the installation features and grips for a fracture toughness specimen. The shear pins were machined from the same JCS base material because high yield strength is required to resist bending. The space for testing in the TS100 is 1.8 m long and 0.8 m in diameter. This large testing space will be useful in performing several verification tests in the future.

The cryogenic apparatus and the hydraulic cylinder are assembled as one piece; before testing, this assembly is lifted by crane to its position on the test stand. The cryostat is then jacked up and its flange is fastened with bolts. The time required for one measurement cycle (cool-down, testing, and warm-up) is three days. The helium consumed during one cycle of operation is about 800 ℓ, but the heat load to the liquid helium is less than 2 W.

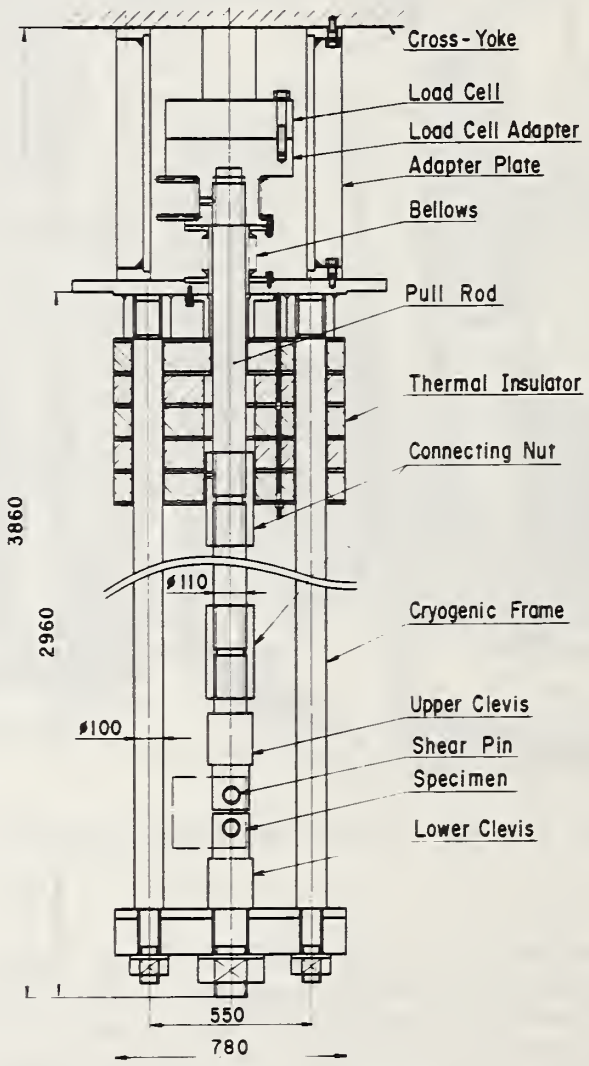

Fig. 2. The TS100 cryogenic apparatus with a compact specimen installed. (All dimensions are in mm).

SPECIMENS

Two JCS materials were selected for this study:

1. CSUS-JJ1:[5] 1Cr-12Ni-10Mn-5Mo-0.2N, 140-mm forged plate (from a 6-metric-ton heat, electroslag remelted)
2. CSUS-JN1:[6] 25Cr-15Ni-4Mn-0.35N, 100-mm hot-rolled plate (from a 50-metric-ton heat)

For tensile tests, 7- and 25-mm-diameter round specimens (as shown in Fig. 3) were machined from the CSUS-JJ1 plate in accordance with Japanese Industrial Standard JIS Z 2201.[7] The specimens were taken from the plate at midthickness and were axially oriented in the long transverse direction. The reduced section lengths of the 7- and 25-mm-diameter specimens were 42.4 and 175 mm, respectively. The specimen ends were threaded for gripping, as shown in Fig. 3.

For fracture toughness tests, CT specimens were machined from the two materials, in accordance with ASTM Method E 813-81.[8] The CT specimens, as shown in Fig. 4, were proportionally sized with thicknesses of 12.5, 25, 75, or 100 mm; the coding used in this study is indicated in the figure caption.

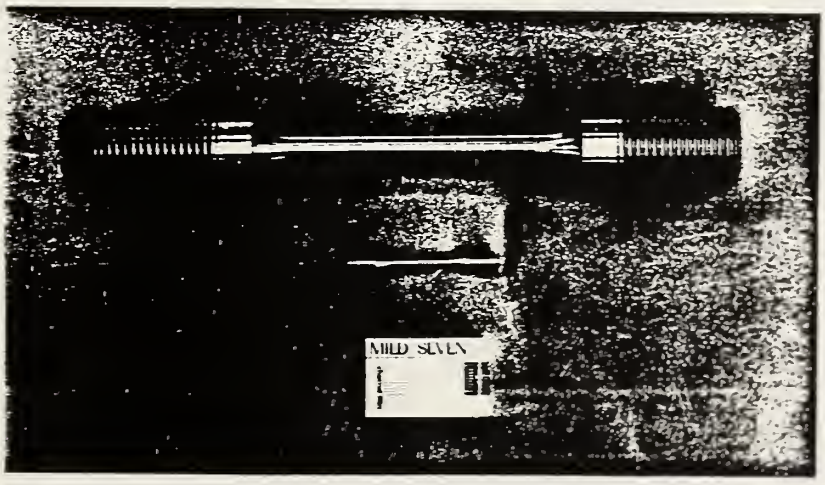

Fig. 3. Tensile specimens machined from the CSUS plate. The large one is 25 mm in diameter; the small one is 7 mm in diameter.

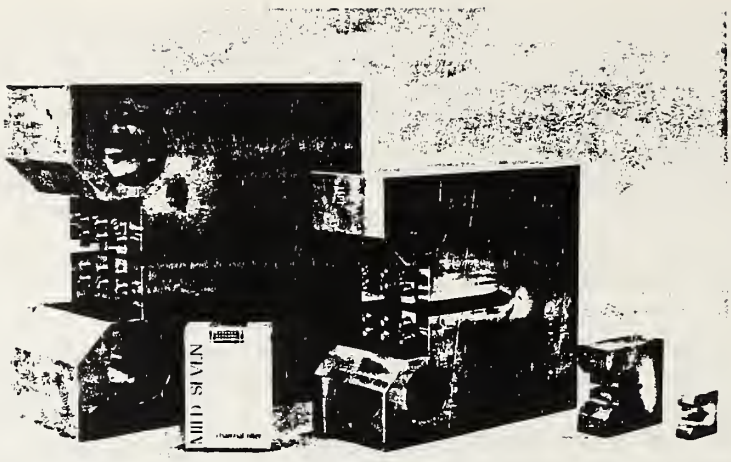

Fig. 4. Compact specimens: 100-mm thick (4-T CT), 75-mm thick (3-T CT), 25-mm thick (1-T CT), and 12.5-mm thick (0.5-T CT).

TEST RESULTS

Tensile Tests

The results of tensile tests at 4 K are shown in Table 2 and Fig. 5. The testing speeds were 0.6 mm/min up to the yield strength and 3 mm/min up to fracture. The nominal strain rate for the 25-mm specimen was about one-fifth that of the 7-mm specimen because the large specimen had a longer reduced section length. The effects of size on the tensile properties were

1. The yield strengths (σ_y) and elongations (El.) were nearly the same for both specimen sizes.
2. The ultimate strength (σ_u) and reduction of area (R.A.) were 4 to 8% less for the 25-mm-diameter specimen than for the 7-mm-diameter specimen.
3. The post-test magnetizations for both specimen sizes were negligibly small.

From a design viewpoint, the differences in the ultimate strength and reduction of area are negligibly small: the size of the 7- and 25-mm-diameter specimens did not affect the tensile properties significantly. Our results indicate that data from small (7-mm) specimens are sufficient to characterize these cryogenic structural steels.

Table 2. Results of JJ1 Tensile Tests at 4 K

Specimen Diameter (mm)	0.2% σ_y (MPa)	σ_u (MPa)	El. (%)	R.A. (%)	Relative Magnetic Permeability
25	1142	1491	43.2	46.1	1.018
7	1132	1574	44.7	54.3	1.006
	1127	1570	43.6	50.0	1.009

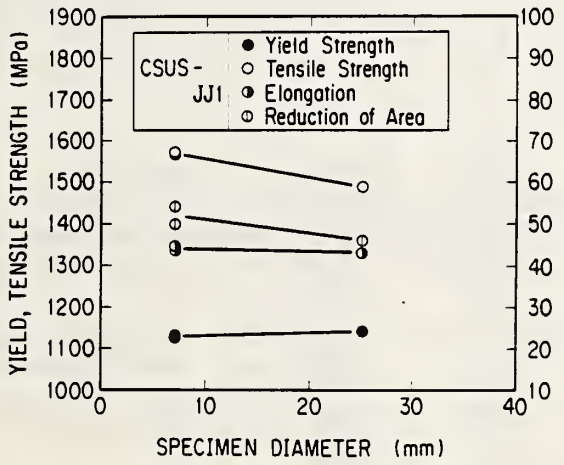

Fig. 5. Specimen size effects on tensile properties at 4 K.

Fracture Toughness Tests

The fracture toughness test results are summarized in Table 3 and Fig. 6. The K_{Ic} values were calculated from the J_{Ic} values according to a formula given in section 9.4 of ASTM E 813-81.[8] The effects of specimen size on fracture toughness were

1. For the CSUS-JN1 steel, there was no size effect on fracture toughness for the range of specimen sizes studied.
2. For the CSUS-JJ1 steel, the 0.5-T CT specimen had a $K_{Ic}(J)$ fracture toughness that was 10% larger than those of the 1-T CT and 4-T CT specimens.
3. No unstable linear-elastic failures were observed in any of the tests, including the tests of the large 3-T CT and 4-T CT specimens.

There was no significant difference in fracture toughness measurements for different specimens of the CSUS-JN1 steel, but the fracture toughness values for the 0.5-T CT specimens of CSUS-JJ1 were larger than those for the larger specimens of that steel. From a design viewpoint, the difference in values for the 1-T and 4-T CT CSUS-JJ1 specimens is negligibly small. Therefore, from the data presently available, we conclude that conventional laboratory tests performed using the usual 1-T CT specimen size are sufficient to characterize the fracture toughness of these steels at 4 K. We intend to examine the fracture surfaces microscopically and to confirm the trend of these results by future tests of other materials.

Table 3. Results of Fracture Toughness Tests at 4 K

Material	JN1			JJ1	
Specimen	J_{Ic} (kJ/m²)	$K_{Ic}(J)$ (MPa·m$^{\frac{1}{2}}$)	Specimen	J_{Ic} (kJ/m²)	$K_{Ic}(J)$ (MPa·m$^{\frac{1}{2}}$)
3-T CT	205	203	4-T CT	343	257
	218	210			
1-T CT	222	216	1-T CT	375	269
	213	208		369	266
0.5-T CT	203	203	0.5-T CT	425	286
	225	213		475	302
				449	294

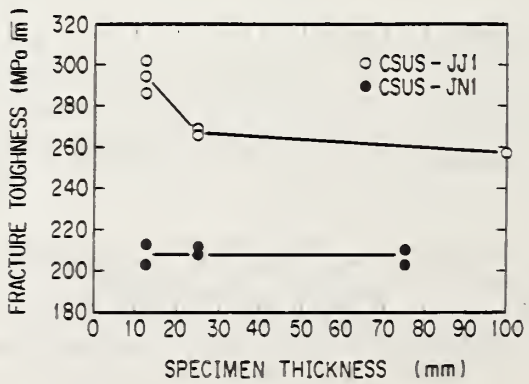

Fig. 6. Specimen size effects on fracture toughness, $K_{Ic}(J)$, at 4 K.

DISCUSSION

As shown in Table 3, the yield strengths of the thick plates tested in this study are lower than the 1200 MPa value specified by JAERI for thinner plates during the JCS development. Therefore, further consideration will be given to this requirement with respect to thick plates.

The fracture toughness requirement specified by JAERI[1] was determined from the design concept that a leak will occur before failure in structural applications. When, under 500-MPa-amplitude stress cycles, an initial crack grows through the thickness of the plate, the stress intensity factor (K) is 200 $MPa \cdot m^{\frac{1}{2}}$. The CT-specimen tests simulated this condition, and yet the thick 3-T CT and 4-T CT specimens of CSUS-JN1 and CSUS-JJ1 did not completely fracture. Evidently the CSUS-JN1 and CSUS JJ1 steels have larger mechanical safety factors than we anticipated; they are now considered ready to be used in coil cases and support structures (more than 100 mm thick) of superconducting coils for fusion reactors. Other JCS steels will be tested in the TS100 in the near future.

CONCLUSIONS

Large specimens were tested using JAERI's hundred-metric-ton cryogenic hydraulic tensile machine. The principal results of the effect of size on tensile properties and fracture toughness were

1. Specimen size had little or no effect on the tensile test results of 7- and 25-mm-diameter round specimens.
2. The fracture toughness varied little from the 1-T CT to the 4-T CT specimens.
3. The fracture toughness values of the 0.5-T CT specimens of CSUS-JJ1 were slightly higher (about 10%) than that of the 4-T CT specimen.
4. No linear-elastic fractures were observed in the 3-T CT and 4-T CT specimens of CSUS–JN1 and CSUS–JJ1 steels, respectively.

ACKNOWLEDGMENTS

The authors thank Drs. S. Mori, K. Tomabechi, and M. Tanaka for their continuous encouragement during this study. The contribution of the Nippon Steel Company is also hereby acknowledged. The study was partially supported by the U.S. Department of Energy, Office of Fusion Energy.

REFERENCES

1. K. Yoshida, H. Nakajima, K. Koizumi, M. Shimada, Y. Sanada, Y. Takahashi, E. Tada, H. Tsuji, and S. Shimamoto, Development of cryogenic structural materials for tokamak reactor, in: "Austenitic Steels at Low Temperatures," R. P. Reed and T. Horiuchi, eds., Plenum Press, New York (1983), pp. 29–39.
2. H. Nakajima, K. Yoshida, M. Oshikiri, T. Takahashi, K. Koizumi, S. Shimamoto, M. Shimada, S. Tone, S. Sakamoto, K. Suemune, and K. Nohara, Tensile properties of new cryogenic steels as conduit materials of forced flow superconductors at 4 K, in: "Advances in Cryogenic Engineering—Materials," vol. 34, Plenum Press, New York (1988), pp. 173–181.
3. H. Tsuji, Design selection for the fabrication on the demonstration poloidal coil, in: "Proceedings, 7th ANS Topical Meeting on the Technology of Fusion Energy," June 15–19, Reno, Nevada (1986).
4. K. Yoshida, Y. Takahashi, E. Tada, M. Shimada, and S. Shimamoto, Mechanical properties of the Japanese LCT coil conductor, in: "Advances in Cryogenic Engineering—Materials," vol. 28, Plenum Press, New York (1982), pp. 781–790.
5. H. Nakajima, K. Yoshida, K. Okuno, M. Oshikiri, E. Tada, S. Shimamoto, R. Miura, M. Shimada, S. Tone, K. Suemune, T. Sakamoto, and K. Nohara, Fracture toughness of newly developed structural materials for superconducting coils of the fusion experimental reactor, in: "Advances in Cryogenic Engineering—Materials," vol. 32, Plenum Press, New York (1986), pp. 347–354.
6. K. Suemune, T. Sakamoto, T. Ogawa, T. Okazaki, and S. Maehara, The manufacture and properties of nitrogen-containing Cr–Mn and Cr–Ni austenitic stainless steels for cryogenic use, in: "Advances in Cryogenic Engineering—Materials," vol. 34, Plenum Press, New York (1988), pp. 123–129.
7. Japanese Industrial Standard JIS Z 2201 in: "JIS Handbook, Steel–1981," p. 23.
8. Standard Test Method for J_{Ic}, A Measure of Fracture Toughness, ASTM E 813-81, in: "1986 Annual Book of ASTM Standards," American Society for Testing and Materials, Philadelphia (1986), pp. 768-786.

ACOUSTIC EMISSION AND ITS APPLICATIONS TO FRACTURE STUDIES OF AUSTENITIC STAINLESS STEELS AT 4 K*

H. Takahashi and T. Shoji
Research Institute for Strength and Fracture of Materials
Tohoku University, Sendai, Japan

R. L. Tobler
National Bureau of Standards
Boulder, Colorado

In contrast to their silent cracking behavior at room temperature, the austenitic stainless steels are highly active acoustically during deformation and fracture at 4 K. Acoustic emission is promoted by low-temperature strengthening and by discontinuous plastic flow in ductile alloys near absolute zero. Consequently, the prospects are quite good for acoustic-emission monitoring as a tool for the study of austenitic steels at 4 K. This paper illustrates some potential applications.

INTRODUCTION

Acoustic emission (AE) may be defined as energy in the form of elastic waves generated by solids undergoing abrupt changes in stress. For three decades, acoustic emission at room temperature has been employed to study materials, to evaluate structures, and to monitor processing operations.[1,2] Cryogenic applications are also growing. Acoustic emission has been used to monitor the operation of superconducting coils and magnet assemblies[3,4] and to study the microdeformation and fracture of epoxies,[4,5] composites,[6] and pure copper.[7]

At Tohoku University's Research Institute for Strength and Fracture of Materials (RISFM), AE techniques are often used to characterize structural steels at room temperature. During conventional fracture mechanics tests, acoustic emission monitoring can provide detailed information about alloy microfailure mechanisms and fracture processes while the usual macroscopic fracture parameters are being determined.

---

*In *Advances in Cryogenic Engineering – Materials*, vol. 34, Plenum, New York, 1988, pp. 387–395.

Recently, the same techniques were applied to austenitic stainless steels at 4 K.[8-10] Selected results for three alloys are reviewed here to illustrate possible applications.

MATERIALS

The materials tested were two wrought and annealed base metals (Fe–18Cr–3Ni–13Mn and AISI 310S BM) and a shielded metal arc weld (AISI 310SWM).[9-10] Table 1 summarizes the relevant material properties and fracture characteristics. Comparison in Fig. 1 of the strength–toughness data with established trends shows that the three studied materials are indeed representative commercial alloys: Fe–18Cr–3Ni–13Mn and AISI 310S BM fall near the low- and high-toughness extremes for base metals;[11] AISI 310S WM, with moderate fracture toughness, lies at the center of the trend for 316- and 308-type welds.[12] Representative scanning-electron microscope (SEM) fractographs from compact specimens tested at 4 K are shown in Fig. 2.

Table 1. Fracture characteristics of test materials at 4 K

Material	Curve Type	σ_y/σ_u (–)	J_{Ic} (kJ/m^2)	K_{Ic} (MPa·m$^{\frac{1}{2}}$)	Fracture Mechanism	Dimple Size (μm)
Fe–18Cr–3Ni–13Mn	LE	0.85	24[a]	71	slip-band cracking	0
AISI 310S WM	EP	0.78	118	159[b]	void coalescence	4
AISI 310S BM	FP	0.60	333	293[b]	void coalescence	25

Notes: [a] estimated from K_{Ic} measurement; [b] estimated from J_{Ic} measurements.

METHODS

Tests were conducted with compact specimens (22 or 25 mm thick, TL orientation[9,10]) submerged in liquid helium at 4 K. A conventional system for detecting, conditioning, and analyzing AE signals is shown in Fig. 3. Such a system[13] was modified for tests at 4 K by employing a waveguide and reducing the gain. The waveguide was a 4-mm-diameter stainless steel rod, welded to the back face of the specimen. The guide transmitted AE signals from the specimen at 4 K to a wideband piezoelectric transducer at 295 K via a coupling outside the cryostat. A significant problem at 4 K is signal saturation owing to the strong emissions from these steels. Therefore, a 20-dB gain was preferred to the usual 60-dB gain at 295 K. The signals were fed into a distribution analyzer, which counted pulses according to their peak amplitudes and determined the individual event energies, E_{AE}. The event energy is the square of

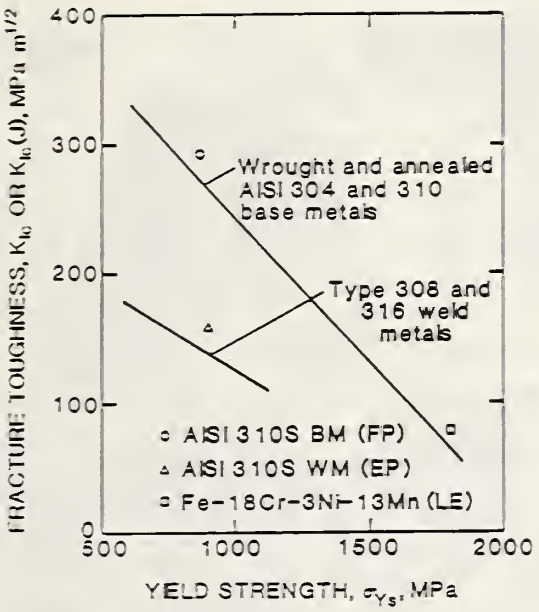

Fig. 1. Strength–toughness data for steels used in the acoustic emission studies.

the output, V, in volts, integrated over the period of its duration. Sometimes the peak voltage, V_p, or its square is taken as a relative measure of signal energy. The square of the peak voltage is proportional to, and correlates well with, the conventional measure of energy.

ACOUSTIC ACTIVITY

Not all materials emit useful AE signals. According to the acoustic rating of steels at room temperature by Ingham et al., annealed austenitic stainless steels rank last.[14] The low yield strengths, high ductilities, high strain-hardening capabilities, and stable cracking mechanisms that typify austenitic steels at 295 K are just not conducive to abrupt physical processes that produce acoustic emission. At 4 K, the circumstances are changed: all the austenitic steels are significantly stronger, their ratios of yield strength (σ_y) to ultimate tensile strength (σ_u) are larger, and the discontinuous deformation process becomes prominent in the ductile alloys. Under these circumstances, significant emissions are likely.

Our survey of austenitic stainless steels includes one representative for each of the three categories: linear elastic (LE), elastic–plastic (EP), and fully plastic (FP). Load–displacement (P–δ) records and acoustic-emission outputs for each case are shown in Fig. 4.

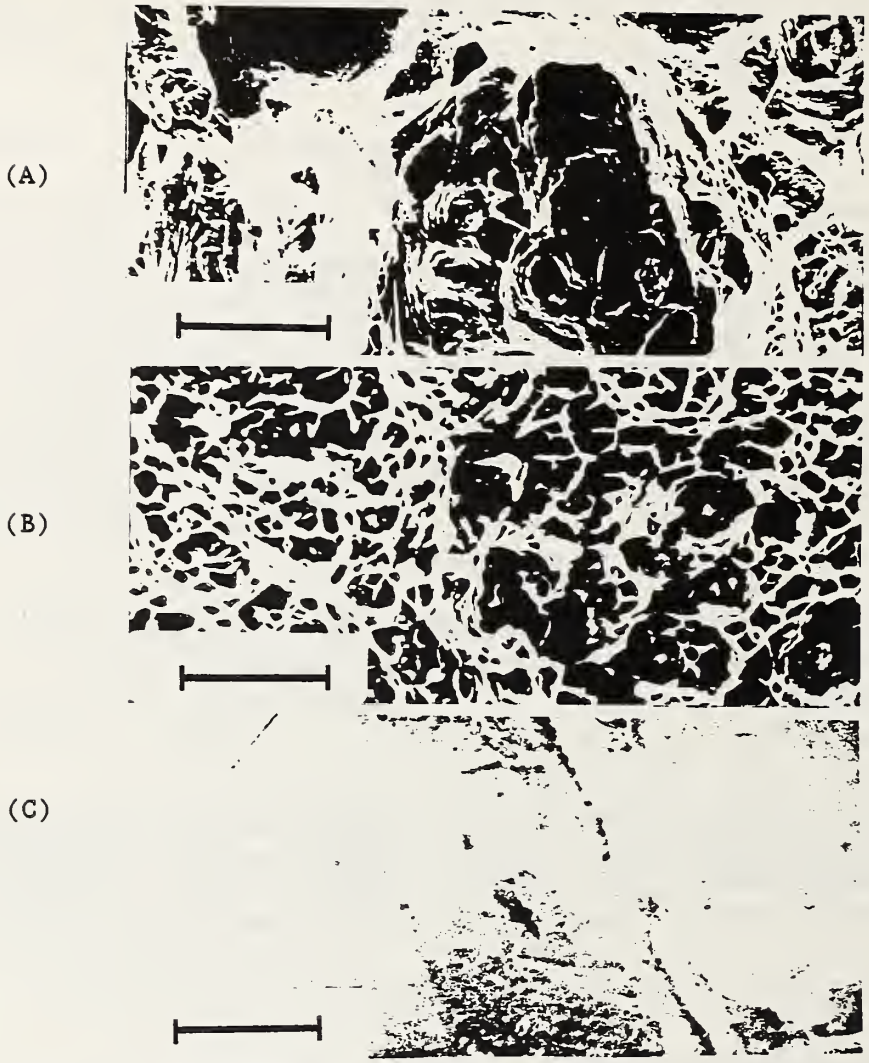

Fig. 2. Fractographs: A) large dimples, AISI 310S BM;
B) small dimples, AISI 310S WM;
C) facets, Fe–18Cr–3Ni–13Mn steel.
Markers are 70, 20, and 2.5 μm, respectively.

The P–δ curve for the high-strength Fe–18Cr–3Ni–13Mn steel is nearly linear except for small deviations from minor pop-ins near the maximum load. The AE begins at low loads and continues until fast fracture finishes the test with a bang.

The AISI 310S weld- and base-metal steels are both ductile at 4 K, and both display nonlinear P–δ curves with serrations. The base metal has much higher toughness and smaller, more numerous serrations; its fully plastic behavior is distinguished from the weld's elastic–plastic behavior by its approach to a limit load. For these materials, acoustic

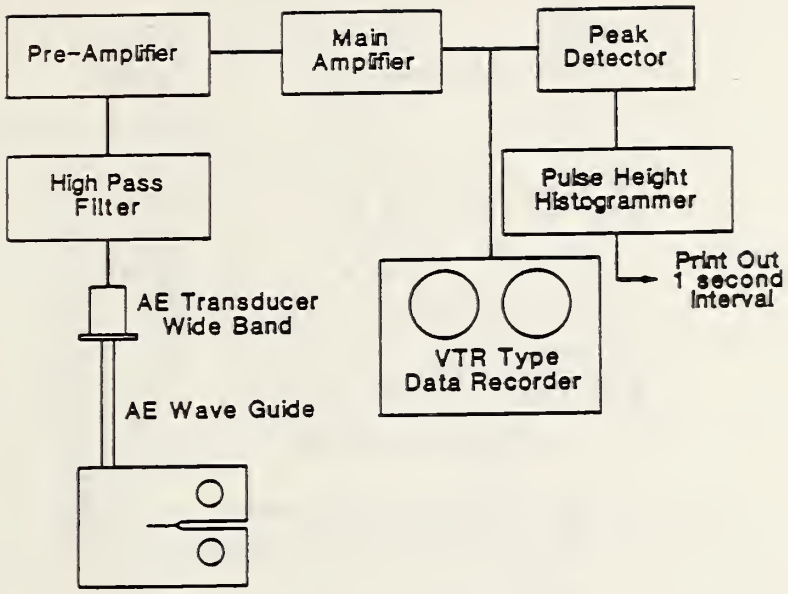

Fig. 3. Acoustic-emission monitoring apparatus.

activity increases as nonlinear loading develops. The event energies increase in magnitude at higher displacements. Later, serrations begin and load drops occur with increasing magnitude accompanied by high-level AE bursts.

In summary, the austenitic stainless steels at 4 K are acoustically active. Pop-ins and serrations are associated with audible AE, as is well-known, but acoustic emissions also occur in early stages of loading. Thus, significant AE precedes macroscopic fracture as measured by the J_{Ic} or K_{Ic} parameters. The precursory emissions are associated with various deformation and cracking processes and may be useful for purposes such as those described below.

APPLICATIONS

Histograms of Acoustic-Emission Events

A representative histogram of AE events for AISI 310S base metal at 4 K is shown in Fig. 5. Usually, histograms for steels at 295 K show a trend of continuously decreasing event numbers (N) at increasing voltages according to the relationship $N \propto V_p^b$, where $b < 0$. This trend is basic evidence of a single-emission mechanism. Instead, the AISI 310S base metal at 4 K shows a bimodal distribution: two active ranges (V_p - 0.30 - 0.65 and 1.0 - 4.0 V) separated by a quiet range (V_p - 0.65 - 1.0 V). This indicates two major sources of acoustic emissions. Thus, austenitic stainless steels are not only highly active at 4 K, but their event histograms differ markedly from typical room-temperature results.

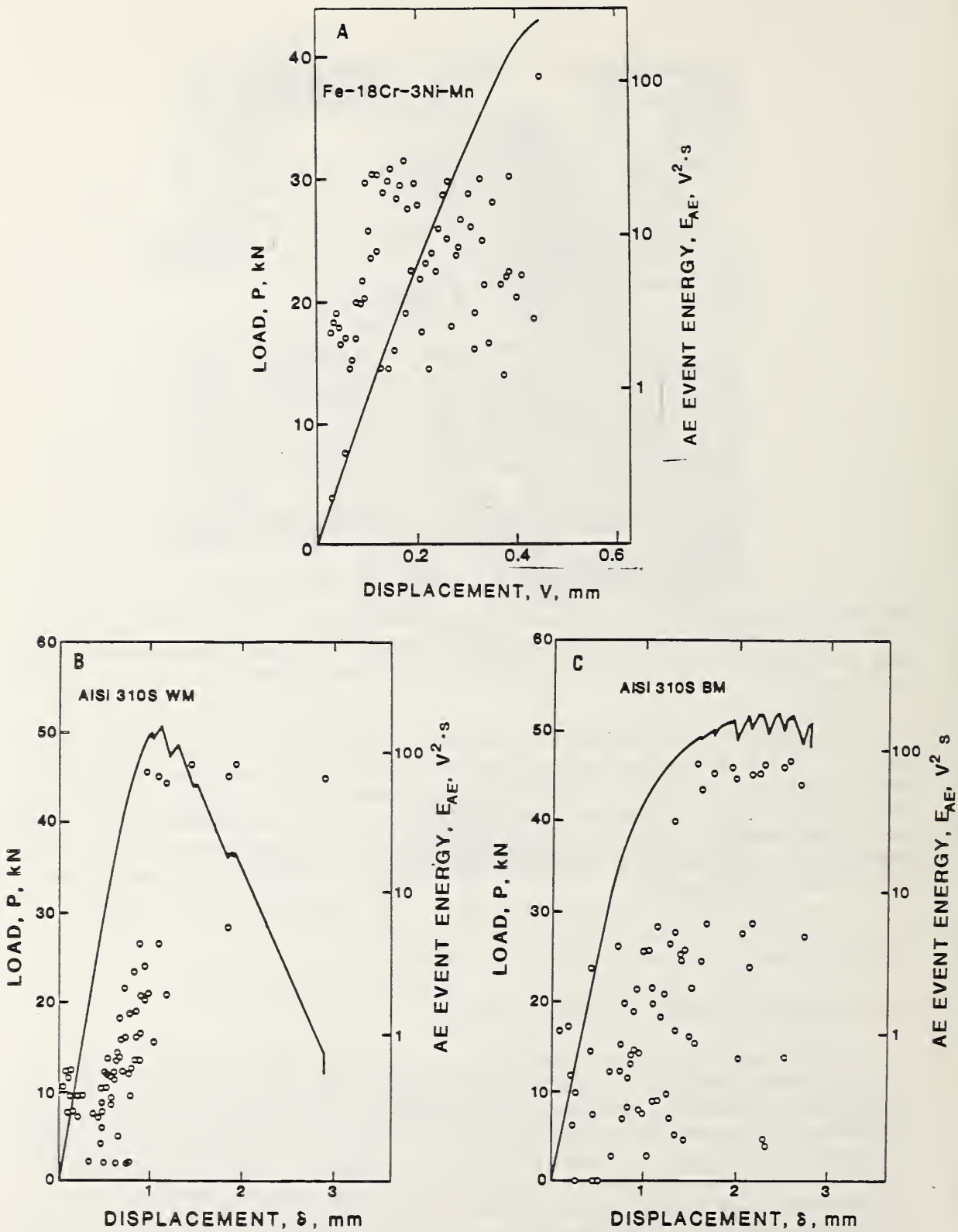

Fig. 4. Load–displacement records and AE outputs for steels at 4 K: A) linear-elastic, B) elastic–plastic, C) fully plastic behavior.

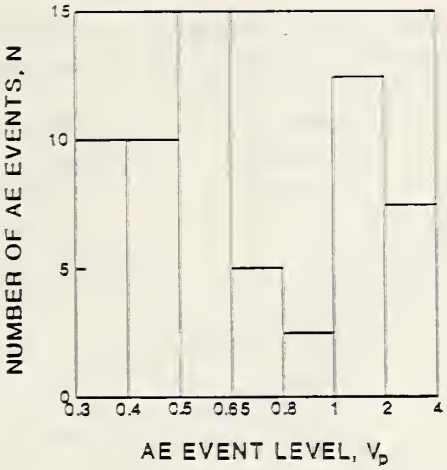

Fig. 5. Events histogram for AISI 310S base metal at 4 K.

Fractography and Identification of Acoustic-Emission Sources

Since fracture in commercial steels occurs as a series of events, many acoustic sources are possible: inclusion–matrix separation, void growth and linking, fast shear, and various types of brittle cracking, to name a few. Following previous studies,[15-18] one can attempt to identify the principal AE sources by correlating event energies with fractographic data from microexaminations. For example, SEM examinations indicated that secondary cracking in the fracture zone near the fatigue crack tip was a possible AE source in the AISI 310S base metal. In Table 2, the number and the lengths of the secondary cracks are compared with the corresponding AE histogram of Fig. 5. As indicated in the table, the number of AE events in the range V_p = 1.0 – 4.0 V nearly equals the number of long secondary cracks observed. Therefore, secondary cracking might constitute an AE source for the higher emission levels, but this conclusion is tentative since only one specimen was examined. The events in the range V_p = 0.30 – 0.65 V do not correlate with secondary cracking but may be due to other processes, such as abrupt plastic deformation.

Fractography revealed no secondary cracks in the AISI 310S weld metal. Instead, high-level emissions were associated with pop-in crack extensions at local areas along the crack front. Pop-ins are increments of subcritical crack extension, and the term normally implies brittle cracking. The distinction between brittle and ductile behavior is somewhat blurred in the case of this intermediate-toughness weld. Cracking occurs in rapid spurts, but post-test inspection shows no faceted fracture, only fine dimples 4 μm in diameter. Thus, both the AISI 310S base metal and the weld show dimpled fracture surfaces; they also have nearly equivalent yield strengths, but the weld's toughness is compromised, probably by its high inclusion content.

Table 2. Evaluation of secondary cracking as an AE source in AISI 310S base metal at 4 K

Secondary Crack Length (mm)	Number of Secondary Cracks	AE Event Level (volts)	Number of AE Events
0 to 0.05	4	0.30 to 0.65	33
0.05 to 0.10	16	0.65 to 1.0	7
0.10 to 0.15	8		
0.15 to 0.20	0 $\sum = 10$	1.0 to 2.0	11
0.20 to 0.25	2		
0.25 to 0.30	4		
0.30 to 0.35	2 $\sum = 6$	2.0 to 4.0	7

The Fe–18Cr–3Ni–13Mn material fails by slip-band cracking, a form of cleavage on {111} planes, as verified by x-ray diffraction and slip-line trace analysis. This brittleness is produced by the high nitrogen content (0.37%). A probable emission source is localized cracking of individual grains or groups of grains. If so, the microfailure process for this high strength steel may well parallel that discussed for other steels of similar strengths that fail by cleavage at room temperature.[18]

The microfailure mechanisms surmised for each steel could be verified or refuted by amassing more evidence from a series of specimens where the tests are interrupted for analysis at progressive stages of fracture. The procedure is fairly laborious, however, and beyond our present scope, which is to illustrate the principles of emission source identification.

Microfracture Toughness

The cumulative sum of AE event energies is plotted versus the applied stress-intensity factor, K, on logarithmic coordinates in Fig. 6. Plots of this type for steels at 295 K demonstrated bilinear trends, with the slope transition points designated K_{IAE}.[15-18] The parameter K_{IAE} marks the point of a rapid increase of emissions and is defined as the microfracture toughness of the alloy.

The steels at 4 K do not always show simple bilinear trends, but K_{IAE} values can still be identified. As shown in Fig. 6, the data for two AISI 310S base metals indicate fair agreement. The results for welds (not shown) were more scattered, reflecting the greater material variability of welds.

Microfracture toughness values and macrofracture toughness measurements are compared in Fig. 7. The K_{IAE} parameter is a more sensitive, conservative measure of toughness than K_{Ic}. The ratio K_{IAE}/K_{Ic} decreases as the level of plastic constraint increases from the FP to the LE case.

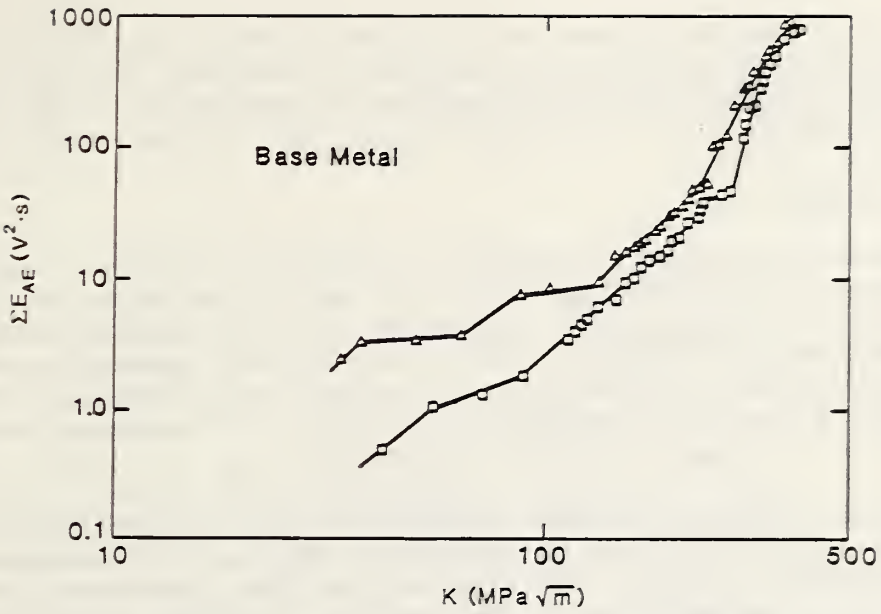

Fig. 6. Cumulative sums of AE energy output versus applied stress-intensity factor for AISI 310S base metals.

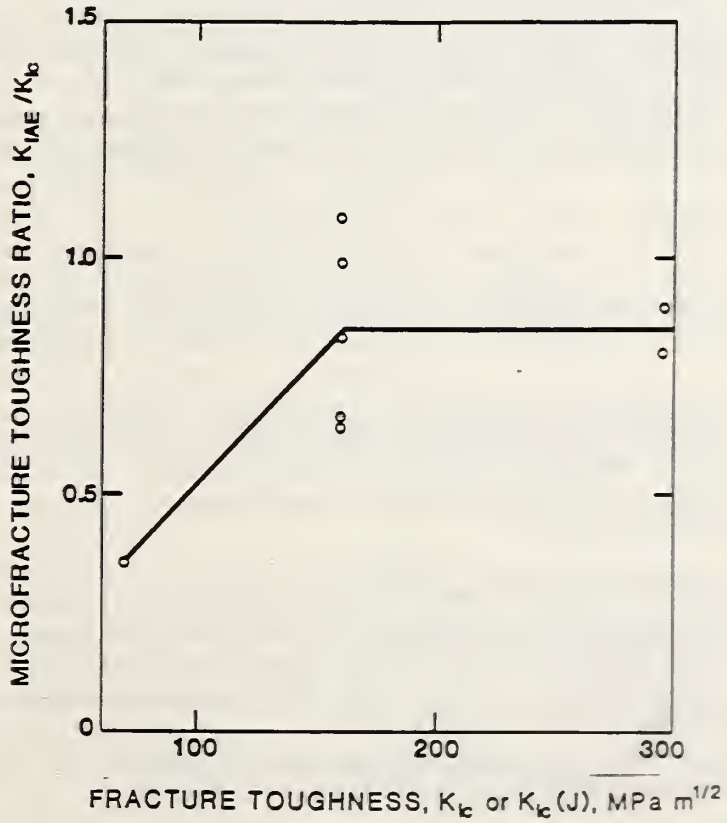

Fig. 7. Microfracture–macrofracture parameter comparisons for alloys at three levels of toughness.

Only one test for the LE case was completed, and a very low K_{IAE} value was obtained. The observed low value has a precedent in high-strength steels at 295 K where the microtoughness values as low as 50% of K_{Ic} have been reported.[18]

Specimen Heating

Adiabatic heating is prominent in cryogenic studies. The specimen temperature rise, ΔT, during deformation at 4 K can be measured using thermocouples; it may also be calculated with assumptions about plastic work. We previously explored a third possibility, seeking correlations between AE outputs and temperature rises in compact specimens where ΔT at the advancing crack tip was measured by means of thermocouples embedded in the ligament along the fracture plane.[10]

During continuous loading in AISI 310S base- and weld-metal specimens, before the occurrence of serrations, we found a relationship between the rate of acoustic emission and specimen temperature that was dependent on crosshead speed. The change of total AE energy per unit time versus $T/\Delta t$ at crosshead speeds of 0.1 and 1.0 mm/min was monitored. A threshold was found in the AE rate at about 8.5×10^{-2} $V^2 \cdot s/s$, below which ΔT during continuous loading was zero for these steels. In the discontinuous yielding regime, the AE energy correlated with temperature rises for individual serrations. The existence of correlations between AE and adiabatic heating suggests that these two quantities describe the same physical processes. Thus, future AE measurements could lead to a better understanding of discontinuous plastic deformation at 4 K.

SUMMARY

1. A conventional apparatus employing a waveguide and reduced gain can be used to monitor acoustic emission during fracture mechanics tests at 4 K.

2. Austenitic stainless steels of all three toughness levels are acoustically active during deformation and fracture at 4 K. This fact is attributed to increased tensile flow strengths and to discontinuous plastic flow at 4 K.

3. The acoustic emissions precede macroscopic fracture and may be used to study microfailure mechanisms or monitor the overall fracture process. Our initial results for three commercial steels indicate that it is possible to: (1) relate the acoustic emission to specific micromechanisms for brittle and ductile fracture, (2) define microfracture toughness values at 4 K, and (3) establish correlations between acoustic emission and adiabatic heating.

ACKNOWLEDGMENTS

This work was sponsored in Japan by the Ministry of Education of Japan and in the United States by the Department of Energy, Office of Magnetic Fusion Energy. The authors thank Dr. T. Hashida for helpful discussions.

REFERENCES

1. H. N. G. Wadley, C. B. Scruby, and J. H. Speake, Int. Met. Rev. 25:41–64 (1980).
2. H. N. G. Wadley and R. Mehrabian, Mater. Sci. Eng. 65:243–263 (1984).
3. R. W. Fast, ed., Adv. Cryo. Eng. 31:259–331 (1986).
4. H. Fujita and Y. Iwasa, Exp. Mech. 26:128–135 (1986).
5. Y. Yasaka and Y. Iwasa, Cryogenics 24:423–428 (1984).
6. T. Nishiura, K. Katagiri, S. Owaki, and T. Okada, Cryogenics 24:329–333 (1984).
7. H. Fujita, E. Bobrov, and Y. Iwasa, in: Progress in Acoustic Emission–III, Japanese Society for Nondestructive Inspection, Tokyo, 222–229 (1986).
8. K. Ohnishi, Master's Thesis, Research Institute for Strength and Fracture of Materials, Tohoku University, Sendai, Japan (1986).
9. K. Ohnishi, T. Shoji, and H. Takahashi, Trans. ISME (A) 52:170–173 (1986).
10. R. L. Tobler, T. Shoji, H. Takahashi, and K. Ohnishi, in: Progress in Acoustic Emission–III, Japanese Society for Nondestructive Inspection, Tokyo, 453–461, (1986).
11. R. L. Tobler, D. T. Read, and R. P. Reed, in: Fracture Mechanics: Thirteenth Conference, ASTM STP 743, American Society for Testing and Materials, Philadelphia, 250–268 (1981).
12. R. L. Tobler, T. A. Siewert, and H. I. McHenry, Cryogenics 26:392–395 (1986).
13. H. Niitsuma, M. Kikuchi, H. Takahashi, M. Suzuki, and R. Sato, Proceedings, Fifth International Acoustical Emission Symposium, Japanese Society for Nondestructive Inspection, Tokyo, 411–420 (1980).
14. T. Ingham, A. L. Stott, and A. Cowan, Int. J. Press. Ves. Piping 3:247–293 (1975).
15. H. Takahashi, M. A. Khan, M. Kikuchi, and M. Suzuki, Exp. Mech. 21:89–99 (1981).
16. M. A. Khan, T. Shoji, and H. Takahashi, Res. Mech. Lett. 1:133–138 (1981).
17. M. A. Khan, T. Shoji, and H. Takahashi, J. Test. Eval. 10:3–11 (1982).
18. M. A. Khan, T. Shoji, and H. Takahashi, Met. Sci. 16:118–126 (1982).

U.S.—JAPAN COOPERATIVE PROGRAM COMMITTEE ON TEST METHODOLOGY
FIFTH DRAFT
SEPTEMBER 1987

NOTE: This is a working document of a standard being developed by the above committee. Some technical aspects are still being resolved and are subject to revision. The document in its present state is intended for committee review purposes, but not for general distribution at this time.

Proposed Standard Methods for FRACTURE TOUGHNESS TESTING OF AUSTENITIC STAINLESS STEELS AT LIQUID HELIUM TEMPERATURE

1. Scope

1.1 This standard describes the equipment, procedures, and data analysis used for measuring the fracture toughness of structural alloys in liquid helium [4 or 4.2 K (−452°F)]. Procedures described in ASTM Methods E 399-83 and E 813-81 are adopted and modified to address the specific needs and concerns of cryogenic testing.

NOTE 1—The boiling point of normal liquid helium (He I) at sea level is 4.2 K. This value decreases slightly with geographic elevation, and it is 4.0 K at NBS in Boulder, Colorado, 1677 m (5500 ft) above sea level. In this standard the test temperature is nominally designated 4 K.

1.2 To measure toughness according to this standard, a fatigue-cracked specimen is cooled in a cryostat to 4 K and then loaded at a moderate speed while fully submerged in normal liquid helium (He I). The standard specimen is a pin-loaded compact specimen, nominally 25 mm thick and 50 mm wide.

1.3 This standard specifies the measurement of K_{Ic}, J_c, or J_{Ic}, whichever is appropriate for the material behavior at 4 K. For fully plastic fracture, J_{Ic} is determined by using a resistance curve technique. Measurements of the resistance-curve slope, $\Delta J/\Delta a$, or the material's tearing modulus are not included in this standard.

1.4 Values stated in SI units are treated as primary; values stated in U.S. customary units, secondary.

1.5 This standard does not address safety issues. Safety guidelines for handling liquid helium and other cryogens are available elsewhere (1). It is the user's responsibility to implement appropriate safety practices.

2. Applicable Documents

2.1 *ASTM Standards*:

E 4 Practices for Load Verification of Testing Machines (*Annual Book of ASTM Standards*, Vols. 03.01, 04.02, 07.01, and 08.03)

E 8 Methods of Tension Testing of Metallic Materials (*Annual Book of ASTM Standards*, Vols. 01.02, 02.01, 02.02, 02.03, and 03.01)

E 8M Methods of Tension Testing of Metallic Materials, Metric (*Annual Book of ASTM Standards*, Vol. 03.01)

E 399 Standard Test Method for Plane-Strain Fracture Toughness of Metallic Materials (*Annual Book of ASTM Standards*, Vol. 03.01)

E 616 Terminology Relating to Fracture Testing (*Annual Book of ASTM Standards*, Vol. 03.01)

E 813 Standard Test Method for J_{Ic}, A Measure of Fracture Toughness (*Annual Book of ASTM Standards*, Vol. 03.01)

3. Definitions

3.1 The terms relating to tensile testing as defined in Definitions E 616 shall apply in this standard.

3.2 *stress intensity factor*, *plane-strain fracture toughness*, and *crack plane orientation*—the definitions in Methods E 399 apply in this standard.

3.3 *J-integral*, *physical crack size*, *original crack size*, *crack extension*, *effective yield strength*, *blunting line*, *initiation of stable crack growth*, *regression line slope*, and *normalized crack size*—the definitions in Methods E 813 shall apply in this standard.

3.4 *fracture cryostat*—an apparatus consisting of a loading frame and Dewar for testing specimens in cryogenic environments. A schematic is shown in Fig. 1.

3.5 *Dewar*—a vacuum-insulated container for cryogenic fluids.

3.6 *adiabatic heating*—the internal heating of a specimen caused by fracture testing under conditions such that the heat generated by plastic work cannot be quickly dissipated to the cryogen.

3.7 J_c—a critical value of J at the onset of fast fracture causing large, uncontrolled crack propagation.

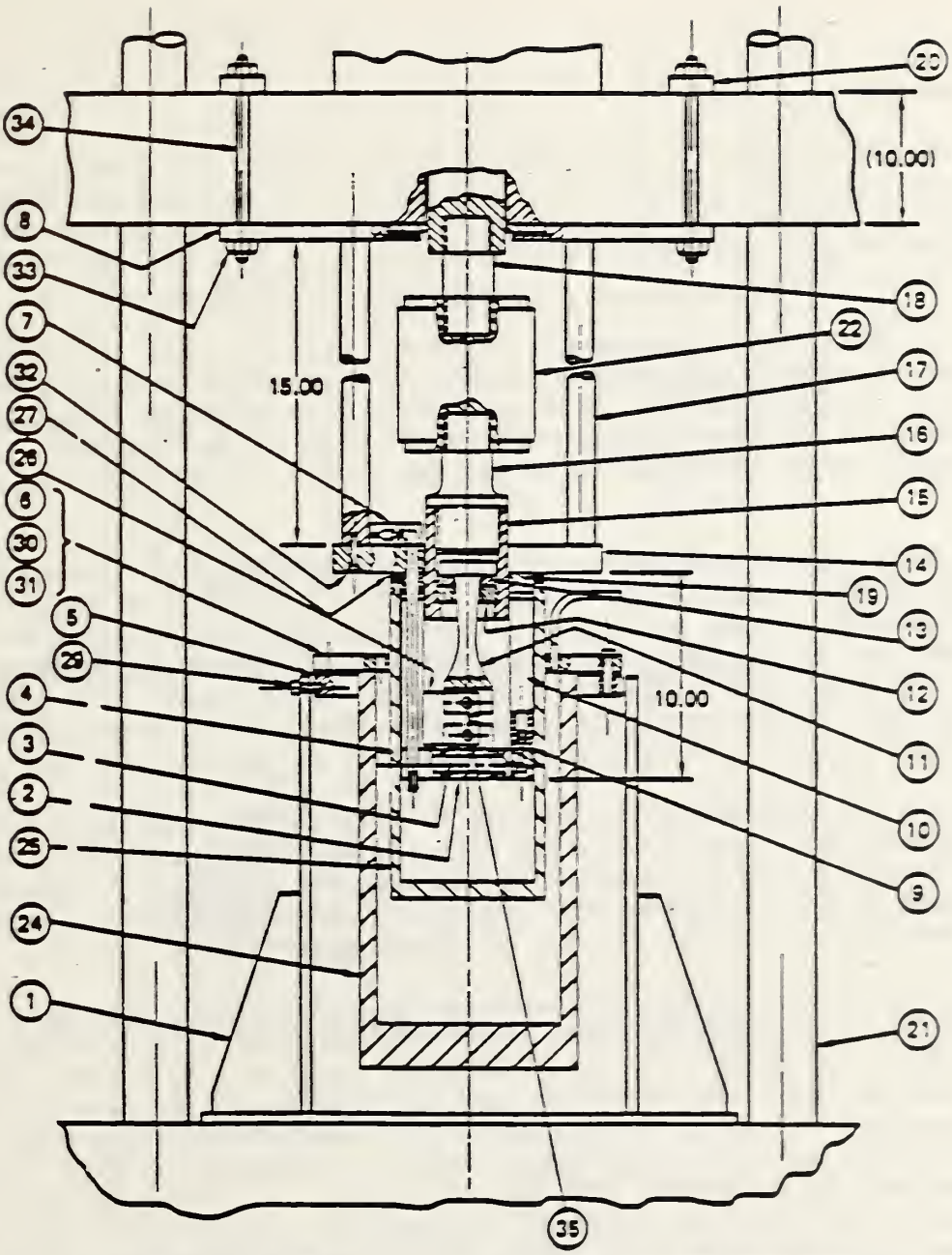

1 - Dewar pivot frame
2 - Specimen clevis
3 - Shear pin
4 - Pivot plate
5 - Outer Dewar top
6 - Inner Dewar clamp
7 - Transfer hose adapter
8 - Adapter plate
9 - Column adapter
10 - Compression column
11 - Clevis pull rod
12 - Pull rod keeper
13 - Pull rod split ring isolator
14 - Load plate
15 - Pull rod coupling
16 - Load cell adapter
17 - Load column
18 - Load cell adapter
19 - Isolator compression ring
20 - Adapter bar
21 - Test machine frame
22 - Load cell
23 - Clip gage
24 - Stainless steel Dewar
25 - Stainless steel Dewar
26 - J-integral compact tension fracture specimen
27 - Seal ring
28 - Liquid helium level meter
29 - Socket head cap screw
30 - Socket head cap screw
31 - Socket head cap screw
32 - Socket head cap screw
33 - Nut
34 - Threaded rod
35 - Shear pin

Figure 1. Cryogenic fracture-toughness test facility.

4. Summary of Methods

4.1 The object of this standard is to measure the fracture toughness of austenitic stainless steels at 4 K using a K- or J-based fracture criterion. The procedures described in Methods E 399-83 and E 813-81 are adopted and modified in this standard for applications at 4 K. Familiarity with those Methods is assumed.

4.2 The compact specimen is emphasized here because it offers a larger fracture-toughness measurement capacity for its size than any other configuration. A relatively low load applied to this specimen produces a large stress-intensity factor; this enables the mass of the cryostat, grips, and load train to be minimized, lowering the cryogen consumption and cost per test.

4.3 To measure the fracture toughness according to this standard, a fatigue-cracked specimen is cooled to 4 K in a suitable cryostat containing liquid helium. Using crosshead, stroke, or clip-gage displacement control, the specimen is slowly loaded while the load-vs-displacement curve is autographically recorded. The type of load-vs-displacement curve observed for the material in the thickness tested will then determine the appropriate method of analysis and fracture criterion to be applied (see Fig. 2).

4.3.1 The parameter K_{Ic} is used to characterize materials with a Type I record where the loading is linear-elastic and the crack-tip plastic zone is small compared with the crack size and specimen dimensions. Except for the provision of the cryogenic test apparatus, the method of K_{Ic} measurement in this standard is similar to that set forth in Methods E 399-83.

4.3.2 The parameter J_c is used in this standard to characterize Type II records where the loading is nonlinear and the plastic zone at the crack-tip is sizable. Although it is not a material constant, J_c can be used to characterize the toughness of alloys that lack sufficient section thickness or toughness for valid K_{Ic} or J_{Ic} tests. For tests terminating with a single fast fracture or a series of large pop-ins (increments of fast fracture), a J_c value may be calculated from the area under the load-vs-displacement curve up to the critical point of instability. The J_c value will vary with specimen type and size; also, there will be sizable scatter, even for a constant geometry, owing to statistical variation of various factors influencing unstable fracture.

4.3.3 The parameter J_{Ic} is used to characterize materials displaying a Type III record where the loading is nonlinear (elastic-plastic, or fully plastic), where the crack-tip plastic zone is large compared with the crack size and specimen dimensions, and where a satisfactory resistance curve can be obtained for the material. The recommended method for J_{Ic} measurement at 4 K is the single-specimen unloading-compliance procedure. That procedure was first developed (2–4) for room temperature tests and was later applied to austenitic stainless steels at 4 K (5–7).

I. **Linear-Elastic Behavior:** K_{Ic} is measured

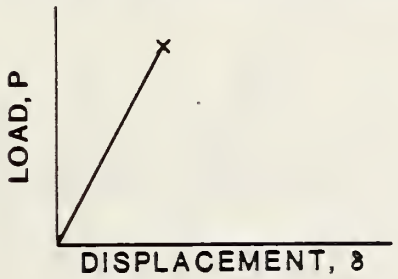

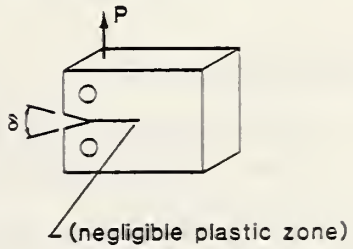

II. **Elastic-Plastic Behavior:** J is measured

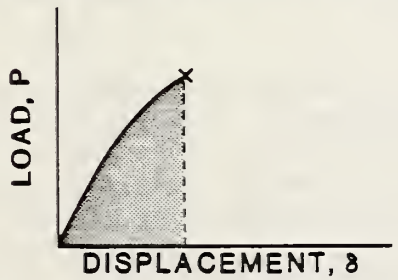

III. **Fully Plastic Behavior:** J_{Ic} is measured

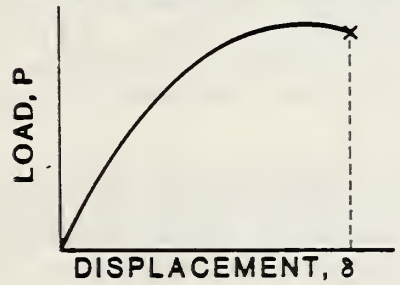

(sizable plastic zone)

Figure 2. Test records and fracture parameters used at 4 K.

4.3.4 A "key-curve" method for characterizing fracture in terms of a parameter J_i has been applied to austenitic steels at 4 K, with some success (8,9). This method is an estimation procedure rather than a measurement procedure, since it involves an assumption about the relationship between crack initiation and crack growth resistances. Since the underlying assumption does not universally hold true for all steels, the parameter J_i determined by the key-curve approach is not recognized by this standard at this time.

5. Significance and Use

5.1 The significance and use of K_{Ic} as a material toughness parameter at 4 K is the same as that discussed in Methods E 399-83, section 4.

5.2 The parameter J_c defined in this standard is not a true material constant since it depends on test specimen geometry. The significance of J_c values with respect to structural design is not addressed in this standard. The J_c measurement is used here only as a relative measure of toughness for materials not amenable to K_{Ic} or J_{Ic} characterizations in practical section thicknesses.

5.3 The significance of J_{Ic} as a toughness parameter at room temperature is discussed in Methods E 813-81, section 4. As originally formulated, the J-integral approach applies strictly to metals that fracture by slow-stable tearing. At 4 K, ductile fractures typically involve discontinuous plastic deformation, and the corresponding test records are marked by serrations (abrupt load drops and momentary temperature rises), as shown in Fig. 3 (10). Instabilities may also arise from pop-in behavior in brittle materials. Consequently, resistance curve slope and tearing modulus calculations at 4 K lack the significance they have at ambient temperatures where crack growth occurs by a slow-stable, isothermal tearing process. To date, however, the experimental evidence (11–13) indicates that the occurrence of serrations does not undermine the use of J_{Ic} as a size-independent material property for austenitic stainless steels at 4 K.

5.4 The J_{Ic} values obtained for high-toughness alloys may be used to estimate K_{Ic} values. Conversions from J_{Ic} to K_{Ic} are performed following Methods E 813-81, section 9.4:

$$K_{Ic}(J) = (J_{Ic} \times E)^{1/2}$$

Such conversions are useful for comparing different materials quantitatively on the basis of a single parameter. The estimated values are identified by the symbol $K_{Ic}(J)$, to distinguish them from K_{Ic} measurements. Thus, $K_{Ic}(J)$ values are obtained using small test specimens that do not display linear-elastic behavior in practical section sizes, but the conversion from J_{Ic} to $K_{Ic}(J)$ is only valid for Type III records.

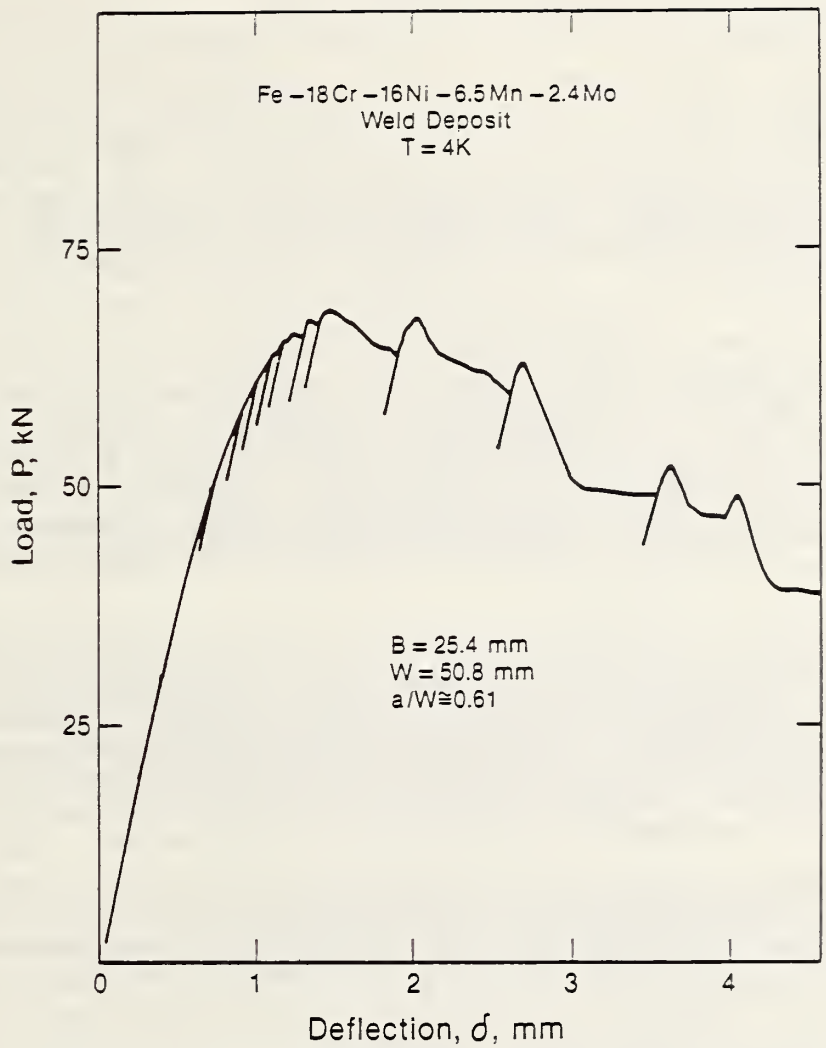

Figure 3. Typical loading behavior at 4 K, showing serrations.

5.5 Owing to adiabatic heating, the fracture resistance of materials at 4 K may be affected by rapid loading. For this reason, 4-K tests are performed at low loading rates (see section 9.4). The possible effects of heating must be considered when applying standard measurements to the design of practical structures subject to high loading rates.

5.6 The parameters K_{Ic}, J_c, and J_{Ic} are suitable for characterizing a wide range of materials at 4 K. Nevertheless, some materials cannot be tested satisfactorily by the methods of this standard. Some materials are too brittle to be properly fatigue-cracked, or too thin ($B < 1.6$ mm) for K_{Ic} testing (see Methods E 399-83, section 1.1). Others are too tough for valid J_{Ic} tests (see Methods E 813-81, section 4.3). Retesting with a change in specimen dimensions may provide valid data in some cases, but there is no assurance that valid results for a given material will be obtained by the procedures of this standard.

6. Apparatus

6.1 *Test Machines*—The tests shall be performed using screw-driven or servohydraulic tensile test machines that meet the requirements of Practices E 4 regarding the verification of load accuracy. The equipment must include a means for autographic recording of the applied loads and specimen crack opening displacements. The compliance of the test machine and its cryostat should be known; it can be measured at 4 K by replacing the specimen with a rigid block.

6.2 *Cryogenic System Design*—For conventional test machines having a maximum load capacity of 10 tons, it is recommended that the cryogenic apparatus be designed to accommodate a standard, 25-mm-thick compact specimen (see section 8.1.3). A servohydraulic test machine with an inverted stage (actuator mounted above the specimen) and a cryogenic loading frame that is free at the lower end is also recommended. Such a system is nearly optimum in regard to operating convenience and cost effectiveness for testing a wide range of materials at 4 K.

6.3 *Cryogenic Construction Materials*—Many common structural materials, including most steels, are brittle at 4 K. Therefore cryostat components must be well designed and fabricated using cryogenic materials of suitable strength and toughness. Austenitic stainless steels are generally recommended. Maraging steels, nickel plated to prevent rusting, are useful for specimen clevises. Alpha–titanium alloys are appropriate for applications requiring high strength-to-thermal conductivity ratios, such as pull rods.

6.4 *Dimension-Measuring Devices*—Micrometers and other devices used for measuring the dimensions of specimens shall be accurate and precise to at least one-half the smallest unit to which the individual dimension is required to be measured.

6.5 *Cryostats and Support Apparatus*:

6.5.1. *Cryostats*—A cryostat capable of retaining liquid helium for the duration of testing is required. Usually, cryostats are custom-built, but they may be designed for use with commercially available Dewars. Efficient designs involve thermal and mechanical trade-offs (14). Several designs are described in the literature, including turret-disc devices for testing many specimens successively with one cooling (7,12,14–16).

6.5.2 *Dewars*—Stainless steel Dewars are recommended for low maintenance, durability, and safety. Glass Dewars are fragile and hazardous, and fiberglass Dewars are relatively expensive. A single Dewar is generally sufficient for tests of short duration, but double-Dewar arrangements using an outer Dewar of liquid nitrogen to surround the inner Dewar containing liquid helium are also possible (14–16).

6.5.3 *Ancillary Equipment*—The Dewars and transfer lines for handling liquid helium must be vacuum insulated. Pressurized gases, vacuum pumps, and liquid nitrogen apparatus are therefore required. After testing, the

helium may be released as a vapor to the atmosphere, recycled, or reliquefied. Recycling or reliquefaction requires substantial investment in purification and cryogenic systems.

6.6 *Clevis Grips and Pins*:

6.6.1 *Design*—Conventional clevis grips conforming to the design given in Fig. 3 of Methods E 813-81 may be used. The loading pin holes have flats flats to allow specimen rotation during testing. To minimize friction, the flats must remain free of plastic indentations. Alloys with adequate 4-K mechanical properties are required for construction.

6.6.2 *Construction*—Materials having adequate 4-K strength, toughness, and fatigue resistance are required for grips and pins. The maraging steels (i.e., 250 and 300 grades) can be used for grips of the conventional design (7,14–16). If lower strength materials such as AISI 304LN are used, the thickness of the clevis arms should be enlarged. Pins must be manufactured from high-strength materials to resist bending.

6.7 *Extensometer*:

6.7.1 *Requirements*—An extensometer device is required to measure edge and load-line displacements for K_{Ic} or J tests, respectively. In addition to rendering accurate displacement measurements at 4 K, the device must be able to sustain cycles of thermal shock, moisture condensation, and mechanical fatigue.

6.7.2 *Types*—Conventional clip gages, such as those described in Methods E 399 and E 813, may be purchased or built using cryogenic materials and fabrication techniques. Ring-shaped clip gages of various sizes are recommended for cryogenic testing (17). The gage design recommended in Methods E 399 may also be used if the total displacement is expected to be 2.5 mm or less. For a larger linear working range, enlarged gages are necessary (see Fig. 4 of Methods E 813).

6.7.3 *Construction*—A satisfactory combination of active strain gage elements, backing materials, and bonding agents must be used for cryogenic extensometers. One common choice is a Ni–Cr-alloy gage with a temperature-compensated active element. Typically, 120- or 350-Ω gages are wired in a Wheatstone bridge arrangement. Electrical wires insulated with polytetrafluoroethylene and soft solders with low tin contents are recommended to reduce mechanical failures and electrical shorts at 4 K.

6.7.4 *Calibration*—The clip gage or other extensometer device must be calibrated at room temperature and at 4 K. This may be done with a barrel-micrometer device fitted with vertical extension tubes with the gage mounted at the lower end and immersed in liquid helium for calibration at 4 K (17). Once the calibration is known and proven linear, accurate, and reproducible, room-temperature checks may be performed to verify the 4-K calibration indirectly. Periodically, the 4-K calibration must be directly verified, especially when damage is suspected or repair has been performed.

6.8 *Temperature Maintenance and Liquid-Level Indicators*—The intended cryogenic environment is maintained by the fixed boiling point of the liquid helium bath. A thermocouple on the specimen is not necessary, but a suitable meter or indicator is required to ensure the proper liquid level. An on–off carbon-resistor meter, a continuous-level meter with superconducting wires, or a cryogenic thermocouple (Chromel-vs-gold + 0.07% iron is most suitable below 20 K) shall be positioned in the cryostat above the specimen to ensure that it remains fully submerged for the duration of the test.

7. Sampling

7.1 *Material Condition*—Samples for specimen preparation shall be taken from the material in its final metallurgical condition. All heat treatments shall be performed prior to sampling and specimen machining.

7.2 *Sample Location*—The sample location shall be chosen to be representative of the stock material. Allowance must be made for areas affected by the cutting process.

7.3 *Specimen Orientation*—The orientation of the specimen notch plane and the direction of load application relative to the principal stock working directions must be stated using the two-letter code of Methods E 399-83, section 5.1.3. The TL orientation is favored for general material evaluations and alloy development at 4 K.

8. Specimens

8.1 *Specimen Configuration:*

8.1.1 *Specimen Types*—Any specimen configuration cited in Methods E 399-83 or 813-81 may be used at 4 K. Current practice, however, favors compact and bend specimens. In comparison, bend specimens require greater mass for an equivalent ligament size. In addition, the long span of the bend specimen transverse to the load axis requires fixtures that are inconvenient for some cryostats. Compact specimens, therefore, are usually preferred at 4 K.

8.1.2 *Standard 4-K Test Specimen*—The standard compact specimen for material evaluations at 4 K has a thickness, B, of 25.4 mm and a width, W, of 50.8 mm. The W/B ratio is 2.0, and the planar dimensions are proportional to W. This specimen is large enough to provide valid data for most austenitic stainless steels tested at 4 K. The specimen may be modified for edge or load-line displacement measurements, as shown in Fig. 4.

8.1.3 *Alternative Specimens*—If the standard specimen of section 8.1.2 is not practical for any reason, an alternative geometry or size may be selected, following Methods E 399 and E 813. Compact specimens with W/B = 2 and planar dimensions proportional to W are generally recommended, but the choice of specimen type and size should be based on the technical purpose, the load limit of the test machine, the stock dimensions, and the need to obtain representative samples of the material being tested.

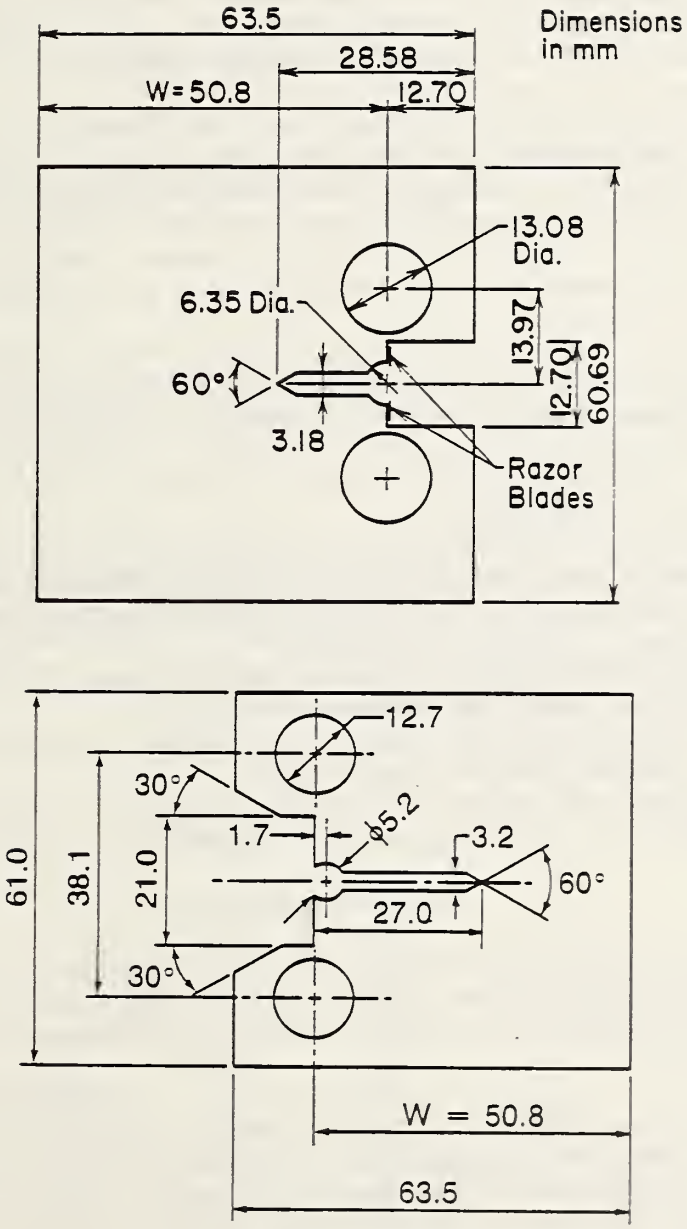

Figure 4. Alternative compact specimens of standard size; see also Methods E 399-83 and E 813-81 for acceptable specimen geometries.

8.2 *Specimen Preparation:*

8.2.1 *Starter Notch*—The notch should be machined according to the guidelines of Methods E 813-81. The notch should be centered along the midplane of the specimen to within 1 mm. The angle between the notch plane and the midplane of the specimen should not exceed 1 degree.

8.2.2 *Load-line Notch Modification*—For J tests, a load-line notch modification (see Methods E 813-81) for clip-gage attachment between razor blades is recommended. Integrally machined knife edges are also possible, but they may tend to increase friction effects. If the displacement is not directly measured at the load-line in J_{Ic} tests, then the method of determining the displacement at the load-line from measurements at the edge location must be described.

NOTE 2—If a load-line modification is used and a Type I load-displacement curve is obtained, then K_{Ic} may be calculated as usual.

8.3 *Fatigue Precracking*:

8.3.1 *General Requirements*—All specimens must be carefully fatigue-cracked. During fatigue, the following requirements always apply:

(1) The maximum stress-intensity factor, K_{max}, during fatigue crack extension shall not exceed 33 MPa·m$^{\frac{1}{2}}$.
(2) The load range (ΔP) during fatigue shall not be less than 90% of the maximum fatigue load, P_{max}.
(3) P_{max} must not exceed $0.4P_L$, where P_L is the limit load for the material at the fatigue test temperature. For compact specimens:

$$P_L = Bb2\sigma_y/(2W + a)$$

8.3.1.1 *High-toughness steels.* If the 4-K fracture toughness exceeds K_{Ic} = 100 MPa·m$^{\frac{1}{2}}$, the fatigue cracking may be conducted at room (295 K) or cryogenic temperatures (77 or 4 K), and the conditions of section 8.3.1 must be satisfied.

8.3.1.2 *Low-toughness steels.* If the 4-K fracture toughness is K_{Ic} = 100 MPa·m$^{\frac{1}{2}}$ or less, the recommended temperature for fatigue cracking is 4 K, and the conditions of section 8.3.1 apply. Also, the maximum stress-intensity factor in fatigue at 4 K, K_{max}, must not exceed 60% of the material's K_{Ic} value at 4 K. If the fatigue cracking is performed at a temperature higher than 4 K (i.e., 295 K), then it must be demonstrated that the procedure has no effect on subsequent toughness measurements at 4 K.

NOTE 3—Sizable reductions of the maximum load during the fatigue precracking should be avoided since they may retard the crack growth rate or increase the degree of crack-front curvature.

8.3.3 *Fatigue Crack Length*—The ratio of the initial fatigue crack length to specimen width, a/W, shall be in the range from 0.45 to 0.70. The optimum value is a function of the material behavior. If a Type I test record is expected and K_{Ic} can be measured directly, then a/W should be 0.45 to 0.55, compatible with Methods E 399-83. If nonlinear behavior is expected and a resistance curve can be determined, the crack-length ratio should be 0.6. For exceptionally strong and tough steels, a ratio near 0.7 may be necessary to meet the test-machine load limitations. For the initial test of an alloy of unknown toughness, a ratio of 0.6 is recommended; this can be adjusted in retests, if necessary.

8.4 *Side Grooves*:

8.4.1 *Acceptable Uses*—Side grooves shall not be used for materials that display Type I or Type II test records. For Type III test records, side grooves may be used to alleviate fatigue crack-front curvature and crack-front tunneling, or to improve the agreement between the optically measured and compliance-calculated end-of-test Δa values.

8.4.2 *Machining*—Side grooves, if used, shall be machined after pre-cracking, following Methods E 813-81, section 7.5.1. For standard compact specimens, which have a thickness of 25 mm, the recommended side-groove geometry is shown in Fig. 5. For standard specimens, the maximum depth of each groove shall be 2.5 mm (a total depth of 20% of the gross specimen thickness).

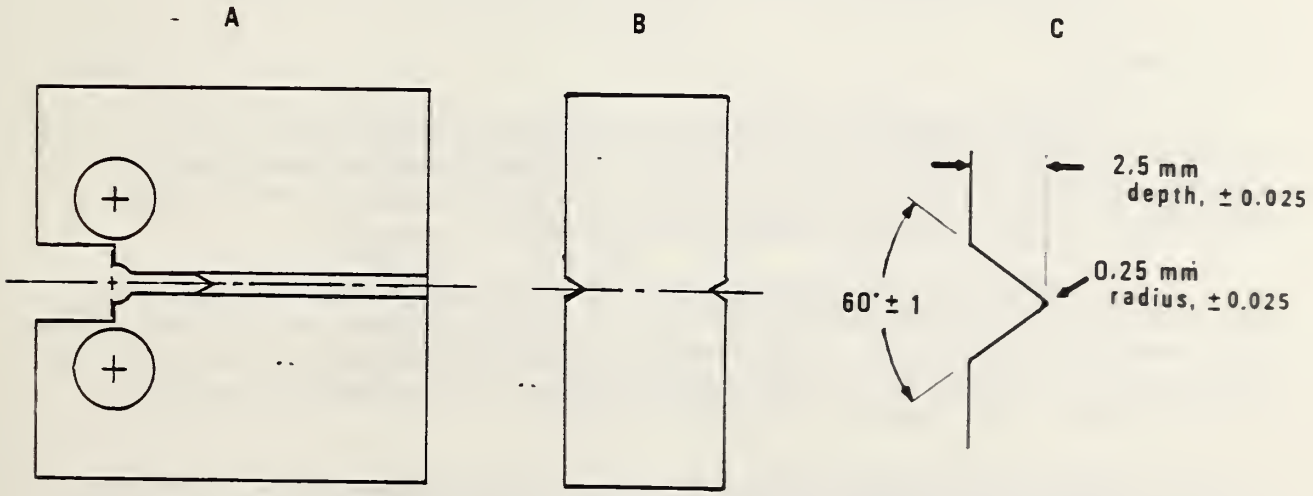

Figure 5. Recommended side-groove geometry: A) plane view, B) side view, and C) details for a standard 25-mm-thick compact specimen.

9. General Procedures

9.1 *Specimen Measurement*—Measure the specimen dimensions according to Methods E 399-83 (section 8.3) and E 813-81 (section 8.8).

9.2 *Installation*—Install the specimen in the apparatus, leaving slack for the instrumentation wires so that they will be neither stretched nor crimped during positioning of the Dewar and testing. Before cooling, check the seating of the specimen and grips at room temperature. The specimen may be preloaded slightly for this purpose.

9.3 *Cooling*—First, dry the apparatus thoroughly with pressurized air or a heating gun. Also, purge any moisture from the cryogenic transfer lines. Ice can block the transfer lines or cause erratic loading behavior if it forms on the loading pins, clevises, specimens, clip gage, or load-train members. Next, position the Dewar and precool the apparatus to 77 K by transferring liquid nitrogen into the cryostat. After reaching equilibrium at 77 K, remove all the liquid nitrogen and transfer liquid helium into the cryostat. Add sufficient liquid helium to compensate for evaporation during the time required to complete the test. Before testing, hold each specimen of standard size in the liquid helium bath for a minimum of 15 min.

> NOTE 4—The heat-transfer characteristics of gaseous helium are inferior to those of liquid helium; therefore full submersion in the liquid is required to minimize specimen heating.

9.4 *Loading*:

9.4.1 *Control Mode*—For tests with a screw-driven machine, the rate of crosshead movement shall be controlled. For tests with a servohydraulic machine, either stroke control or clip-gage displacement control may be used; load control, however, should not be used.

9.4.2 *Load Rate*—Load the specimen at a rate such that the time, t_p, to reach the load at first deviation from the linear portion of the test record is between 0.5 and 10 min. For standard 25-mm-thick compact specimens, the crosshead rate should be 0.5 $mm \cdot min^{-1}$ or less. For additional details of test procedure, see Methods E 813-81, section 8.

9.5 *Test Record*—Record the load-cell and clip-gage outputs autographically, following the guidelines of Methods E 399-83, section 8.4 for K_{Ic} tests, or as appropriate for J_{Ic} tests. For J_{Ic} tests, a recording of the computer-calculated J–Δa curve in real time is also recommended.

10. Interpretation and Calculation of Results

10.1 *General*—Classify the test record as one of the three basic types shown in Fig. 2. Depending on the load-vs-displacement behavior, decide which fracture criterion is to be used. More than one fracture parameter may be applied in some cases.

10.2 K_{Ic} *measurement*—For a Type I test record, calculate the fracture (K_Q or K_{Ic}) according to Methods E 399. Construct the secant offset line, calculate the conditional toughness value, K_Q, and determine if it qualifies as a valid K_{Ic} according to Methods E 399-83, section 9. If the K_Q result fails to qualify as a valid K_{Ic} measurement, calculate J_c according to section 10.3 of this standard.

NOTE 5—Notch modifications for load-line displacement measurements may invalidate K_{Ic} calculations at 4 K. It may be necessary retest some specimens without load-line modifications to prove the validity of K_{Ic} measurements.

10.3 J_c *measurement*—For Type II tests producing nonlinear load-vs-displacement curves, determine J_c as follows: Calculate the value of the J-integral corresponding to the total area under the load-vs-displacement curve up to the critical pop-in or fast fracture event. The area of interest is cross-hatched in Fig. 2. The measurement shall be accurate to 2% and it may be performed using a polar planimeter or numerical integration of the load-vs-displacement signals by computer techniques. For compact specimens, use the following expression to calculate the value of J_c:

$$J_c = f(a_0/W) \cdot A/Bb$$

where

a_0 = original crack length, including precrack length,
W = specimen width,
$f(a_0/W)$ = a dimensionless coefficient that corrects for the tensile component of loading, as given in section 9.1.1 and Table 1 of Methods E 813-81,
A = area under the load-vs-load-line-displacement record in energy units,
B = specimen thickness, and
b = initial uncracked ligament, $W - a_0$.

10.4 J_{Ic} *measurement*—For Type III tests, measure J_{Ic} with a resistance curve technique, where J is plotted versus physical crack growth, Δa_p. The single-specimen unloading compliance method is recommended as the more efficient than the multiple-specimen technique at 4 K because it reduces the required number of test specimens and the cryogenic fluid costs. Guidelines for the compliance test method are given in the appendix of Method E 813-81 and in references (2–7).

10.4.1 Using the expression $J = f(a/W) \cdot A/Bb$, calculate J at points along the load-vs-load-line-displacement curve as a function of the crack length inferred from compliance. For side-grooved specimens use net thickness, B_n, instead of B for J calculations and use the effective thickness, B_{eff}, instead of B for crack growth predictions from unloading compliance data (see Methods E 813-81 sections 8.7.1 and 9.1.1).

10.4.2 Prepare a plot of J-vs-Δa_p spanning the 0.15–1.5-mm exclusion interval, as given by Methods E 813-81. Calculate the area under the load-vs-displacement curve, including the area under serrations. For tests in clip-gage displacement control, the area under a serration is zero. Thus, tests in stroke control are expected to give higher values of J for a given crack extension, owing to the area increase associated with serrations. The intent is not necessarily to measure a physically meaningful J–Δa curve, but rather to obtain a regular data set, enabling linear extrapolation to the initiation of crack extension at J_{Ic}.

10.4.3 Construct the blunting line (assuming $J = 2\sigma_y \Delta a$), plot the four point linear regression line, and qualify the J–Δa calculations following Methods E 813-81, section 9.2 in every respect.

> NOTE 6—Compliance data usually show an anomalous negative crack growth effect in early stages of loading Correct for this effect by shifting the blunting line along the Δa axis until it coincides with the upper portion of J–Δa data, which indicate a normal blunting-line trend. The negative crack growth data are thus ignored (see Fig. 6).

10.4.4 Determine J_Q as the value of J at the blunting- and regression-line intersection. Qualify the data and determine whether the J_Q is a valid J_{Ic} determination according to Methods E 813-81, sections 9.3 and A1.

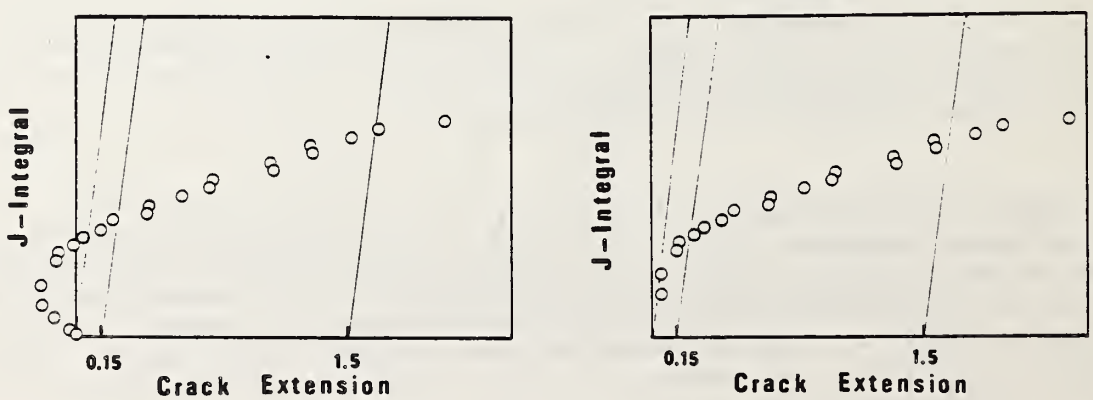

Figure 6. Method of correction for negative crack growth.

11. Report

11.1 *Material Characterization:*

11.1.1 *Material Description*—Describe the material tested. Include the product form (e.g., plate, forging, casting), processing, heat treat-ment, and any other relevant metallurgical information.

11.1.2 *Tensile Properties*—Report the yield strength, tensile strength, and elastic modulus for the tested material at room temperature and at 4 K.

11.2 *Specimen Characterization:*

11.2.1 Report the crack-plane orientation using the identification code of Methods E 399-83.

11.2.2 Report the specimen dimensions, including thickness, width, initial ligament size, and initial crack length.

11.2.3 For side-grooved specimens, report the side-groove geometry, including the included angle, notch-tip radius, and net section thickness.

11.3 *Fatigue-Cracking Characterization:*

11.3.1 Report the maximum fatigue load, the maximum stress-intensity factor, the stress-intensity-factor range, and the temperature used for the fatigue precracking.

11.3.2 Report the final fatigue crack length obtained using the three-point average for K_{Ic} tests or the nine-point average for J_{Ic} tests, as described in Methods E 399-83 or E 813-81, respectively. Also measure the surface crack lengths, and report the maximum deviation of any single measurement from the average.

11.4 *Test Record*—Describe the observed load-vs-displacement behavior, classifying it by type according to the examples shown in Fig. 2.

11.5 *Loading Rate*—Report the loading rate in terms of t_p or the rate of increase of the stress-intensity factor during the region of linear loading. Specify whether crosshead, stroke, or clip-gage displacement control was used.

11.6 *Fracture Toughness Measurements:*

11.6.1 Report the compliance of the test machine and cryostat used.

11.6.2 For a Type I test record, report the toughness in terms of K_Q or K_{Ic} and include an assessment of the validity according to Methods E 399-83.

11.6.3 For Type II test records, report the value of J_c as defined in section 3 of this standard. If a compliance technique was used for $J-\Delta a$

measurements, estimate and report the amount of subcritical crack extension (if any) that occurred prior to the point of instability.

11.6.4 For Type III test records where a full resistance curve can be developed, report the value of J_{Ic} and calculate $K_{Ic}(J)$. Assess the validity of J_{Ic} according to the criteria of Methods E 813-81.

11.7 *Fracture Surface Appearance*—Describe the fracture-surface appearance. For computerized J_{Ic} tests, report the end-of-test crack extension increment. Also report the averaged values of the compliance-predicted and the optically measured final crack lengths.

11.8 *Replicate Tests*—State the number of replicate tests performed, the average fracture toughness values, and a measure of scatter.

11.9 *Anomalies*—Report any anomalies observed in the material behavior, test records, or failure mechanisms.

12. *Accuracy and Precision*

12.1 *Accuracy*—There is no accepted standard fracture toughness value for any material. In the absence of such a true value, any statements about accuracy are meaningless.

12.2 *Precision*—Information on the precision of 4-K fracture tests is being obtained from interlaboratory test programs currently in progress.

REFERENCES

(1) *Cryogenics Safety Manual—A Guide to Good Practice*, 2nd Ed., Mechanical Engineering Publications, London, 1982.

(2) Clarke, G. A., Andrews, W. R., Paris, P. C., and Schmidt, D. W., "Single Specimen Tests for J_{Ic} Determination," in: *Mechanics of Crack Growth*, ASTM STP 590, American Society for Testing and Materials, Philadelphia, 1976, pp. 27–42.

(3) Joyce, J. A. and Gudas, J. P., "Computer Interactive J_{Ic} Testing of Navy Alloys," in: *Elastic-Plastic Fracture*, ASTM STP 668, J. D. Landes, J. A. Begley, and G. A. Clarke, eds., American Society for Testing and Materials, Philadelphia, 1976, pp. 451–468.

(4) Clarke, G. A., "Single Specimen Tests for J_{Ic} Determination—Revisited," in: *Fracture Mechanics: Thirteenth Conference*, ASTM STP 743, R. Roberts, ed., American Society for Testing and Materials, Philadelphia, 1983, pp. 553–575.

(5) Tobler, R. L., "Ductile Fracture with Serrations in AISI 310S Stainless Steel at Liquid Helium Temperature," in: *Elastic-Plastic Fracture: Second Symposium*, Vol. II—Fracture Resistance Curves and Engineering Applications, ASTM STP 803, C. F. Shih and J. P. Gudas, eds., American Society for Testing and Materials, Philadelphia, 1983, pp. 763–776.

(6) Shimamoto, S., Nakajima, H., Yoshida, K., and Tada, E., "Requirements for Cryogenic Structural Alloys for Superconducting Magnet Cases," in: *Advances in Cryogenic Engineering—Materials*, Vol. 32, Plenum Press, New York, 1986, pp. 23–32.

(7) Shimada, M., Ogawa, R., Moriyama, T., and Horiuchi, T., "Development of a Cryogenic Fracture Toughness Test System," *Cryogenic Technology*, Vol. 21, No. 5, 1986, pp. 269–274.

(8) Takeuchi, M., Shoji, T., Takahashi, H., and Anayama, T., "Evaluation of fracture Toughness of Cryogenic Materials," *Reports of the Research Institute for Strength and Fracture of Materials*, Vol. 17, 1984, pp. 1–12.

(9) Nakajima, H., Yoshida, K., Shimamoto, S., Tobler, R. L., Purtscher, P. T., and Reed, R. P., "Round Robin Tensile and Fracture Test Results for an Fe–22Mn–13Cr–5Ni Austenitic Stainless Steel at 4 K," in: *Advances in Cryogenic Engineering—Materials*, Vol. 34, Plenum Press, New York, 1989, pp. 241–249.

(10) Ohnishi, K., Shoji, T., and Takahashi, H., "Effects of Loading Rate and Machine Compliance on Heat Generation During Cryogenic Fracture Toughness Testing," in: *Workshop on Standardization of Fracture Toughness Testing of Low Temperature Structural Materials*, Tohoku University, Sendai, Japan, 1986, pp. 27–35.

(11) Shimada, M., Tobler, R. L., Shoji, T., and Takahashi, H., "Size, Side-Grooving, and Precracking Effects on J_{Ic} Data for an SUS 304 Stainless Steel at 4 K," in: *Advances in Cryogenic Engineering—Materials*, Vol. 34, Plenum Press, New York, 1988, pp. 251–258.

(12) Ogata, T., Ishikawa, K., Yuri, T., Tobler, R. L., Purtscher, P. T., Reed, R. P., Shoji, T., Nakano, K., and Takahashi, H., "Effects of Specimen Size, Side-Grooving, and Precracking Temperature on J-Integral Test Results for AISI 316LN at 4 K," in: *Advances in Cryogenic Engineering—Materials*, Vol. 34, Plenum Press, New York, 1988, pp. 259–266.

(13) Yoshida, K., Nakajima, H., Oshikiri, M., Tobler, R. L., Shimamoto, S., Miura, R., and Ishizaka, J., "Mechanical Tests of Large Specimens at 4 K: Facilities and Results," in: *Advances in Cryogenic Engineering—Materials*, Vol. 34, Plenum Press, New York, 1988, pp. 225–232.

(14) Fowlkes, C. F. and Tobler, R. L., "Fracture Testing and Results for a Ti–6Al–4V Alloy at Liquid Helium Temperature," *Engineering Fracture Mechanics*, Vol. 8, 1976, pp. 487–500.

(15) Read, D. T. and Tobler, R. L., "Mechanical Property Measurements at Low Temperatures," in: *Advances in Cryogenic Engineering—Materials*, Vol. 28, Plenum Press, New York, 1982, pp. 17–28.

(16) Juhas, M. C., Duncan, D. B., and Streit, R. D., "Development of a Facility for Fatigue and Fracture Testing of Stainless Steels at Liquid Helium Temperature," *Cryogenics*, Vol. 23, 1983, pp. 603-607.

(17) Tobler, R. L. and Shepic, J. A., "Design and Performance of a Ring-shaped Clip Gage for Fracture Mechanics Testing," *Journal of Testing and Evaluation*, Vol. 13, 1985, pp. 299–302.

JAPAN—U.S. COOPERATIVE PROGRAM COMMITTEE ON TEST METHODOLOGY

FIFTH DRAFT
SEPTEMBER 1987

NOTE: This is a working document of a standard being developed by the above committee for eventual submission to ASTM; it is intended for committee review purposes, but not for general distribution at this time.

Proposed Standard Method for TENSILE TESTING OF STRUCTURAL ALLOYS AT LIQUID HELIUM TEMPERATURE

1. Scope

1.1 This standard describes the procedures to be used for the tensile testing of metals in liquid helium [4 or 4.2 K (−452°F)]. The format is similar to that of other ASTM tensile test standards, but the contents include modifications for cryogenic testing, which requires special apparatus, smaller specimen size, and concern for serrated yielding, adiabatic heating, and strain-rate effects.

1.2 To conduct a tensile test by this standard, the specimen in a cryostat is fully submerged in normal liquid helium (He I) and tested using crosshead displacement control at a moderate strain rate. Tests that use load control or high strain rates are not considered in this standard.

1.3 This standard details methods for the measurement of yield strength, tensile strength, elongation, and reduction of area. The determination of the elastic modulus is treated in Method E 111.

1.4 Values stated in SI units are treated as primary; values stated in U.S. customary units are treated as secondary.

1.5 This standard does not address the issue of safety associated with cryogenic testing. It is the user's responsibility to learn and observe appropriate safety practices. Safety guidelines for handling liquid helium and other cryogens are available elsewhere (1).

NOTE 1—The boiling point of normal liquid helium (He I) at sea level is 4.2 K. This value decreases slightly with geographic elevation; it is 4.0 K at NBS in Boulder, Colorado, 1677 m (5500 ft) above sea level. In this standard, the test temperature is nominally designated 4 K.

2. Applicable Documents

2.1 *ASTM Standards:*

A 370 Methods and Definitions for Mechanical Testing of Steel Products (*Annual Book of ASTM Standards*, Vol. 01.04)

E 4 Practices for Load Verification of Testing Machines (*Annual Book of ASTM Standards*, Vols. 03.01, 04.02, 07.01, and 08.03)

E 6 Definition of Terms Relating to Methods of Mechanical Testing (*Annual Book of ASTM Standards*, Vols. 03.01 and 08.03)

E 8 Methods for Tension Testing of Metallic Materials (*Annual Book of ASTM Standards*, Vols. 01.02, 02.01, 02.02, 02.03, and 03.01)

E 8M Methods for Tension Testing of Metallic Materials, Metric (*Annual Book of ASTM Standards*, Vol. 03.01)

E 29 Recommended Practice for Indicating Which Places of Figures Are to Be Considered Significant in Specified Limiting Values (*Annual Book of ASTM Standards*, Vols. 02.03, 03.01, 03.03, 03.05, and 14.02)

E 83 Practice for Verification and Classification of Extensometers (*Annual Book of ASTM Standards*, Vol. 03.01)

E 111 Method for Young's Modulus, Tangent Modulus, and Chord Modulus (*Annual Book of ASTM Standards*, Vol. 03.01)

2.2 *Japanese Industrial Standards (JIS):*

B 7721 Tensile Testing Machines

B 7728 Load Calibration Devices for Verifying Material Testing Machines

G 0567 Method of High Temperature Tensile Test for Steels and Heat-Resisting Alloys

Z 2201 Test Pieces for Tensile Test for Metallic Materials

Z 2241 Method of Tensile Test for Metallic Materials

Z 8103 Glossary of Terms Used in Instrumentation

Z 8401 Rules for Rounding Off of Numerical Values

NOTE 2—Japanese and English versions of these standards are published by the Japanese Standards Association, 1-24, Akasaka 4, Minato-ku, Tokyo, 107 Japan.

3. Definitions

3.1 The definitions of terms relating to tension testing that appear in ASTM Standard E 6 shall apply here. The following definitions also apply:

3.1.1 *tensile cryostat*—a test apparatus for applying loads to test specimens in cryogenic environments. A schematic illustration is shown in Fig. 1.

3.1.2 *Dewar*—a vacuum-insulated container for cryogenic fluids.

3.1.3 *adiabatic heating*—the internal heating of a specimen resulting from tensile testing under conditions such that the heat generated by plastic work cannot be quickly dissipated to the surrounding cryogen.

3.1.4 *reduced section*—section in the central portion of the specimen, which has a cross section smaller than the gripped ends.

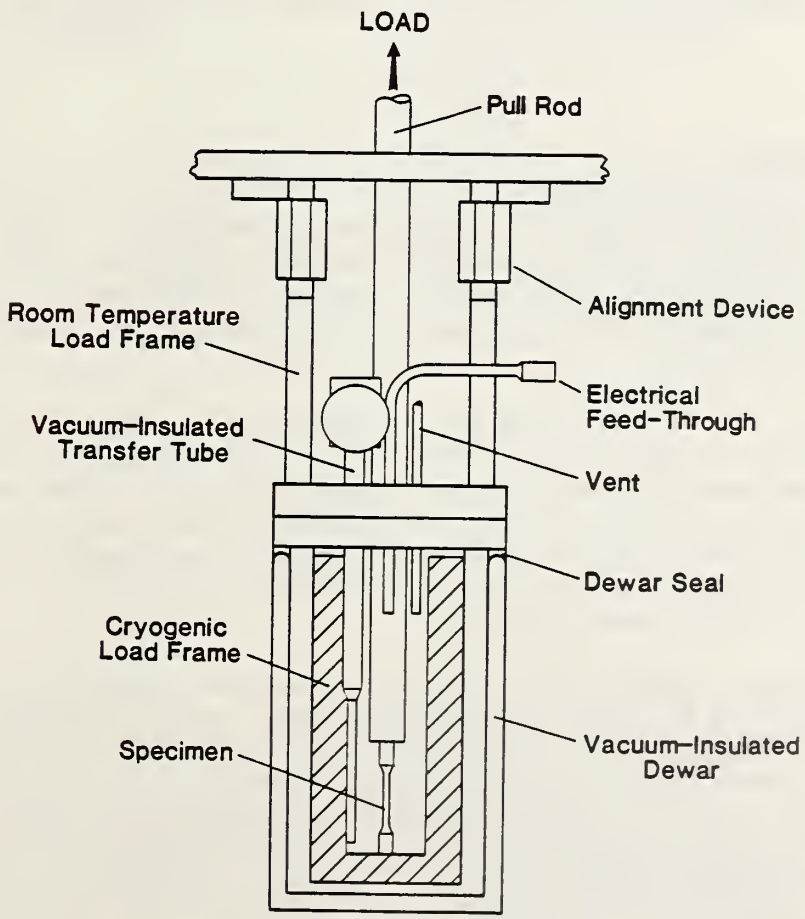

FIG 1 Example of a Cryostat with Double-Dewar Arrangement for Tensile Testing at 4 K

3.1.5 *length of the reduced section*—the distance between the tangent points of the fillets that bound the reduced section.

3.1.6 *adjusted length of the reduced section*—the length of the reduced section plus an amount calculated to compensate for strain in the fillet region.

3.1.7 *gage length*—the original distance between gage marks made on the specimen for determining elongation after fracture.

3.1.8 *axial strain*—the average of the strain measured on opposite sides of the specimen at equal distances from the specimen axis.

3.1.9 *bending strain*—the difference between the strain at the surface of the specimen and the axial strain. The bending strain varies from point to point around and along the reduced section of the specimen.

3.1.10 *maximum bending strain*—the largest value of bending strain in the reduced section of the specimen. It is calculated from strains measured at three circumferential positions, at each of two different longitudinal positions.

4. Significance and Use

4.1 In general, tensile tests provide information on the strength and ductility of materials under uniaxial tensile stresses. This information may be useful for alloy development, comparison and selection of materials, and quality control. Under certain circumstances, the information may also be useful for design.

4.2 At 4 K, the load–time and load–deflection record for metals tested in displacement control are serrated (2). Serrations are formed by repeated bursts of unstable plastic flow, followed by arrests. The unstable plastic flow (or discontinuous yielding) is a free-running process that occurs locally with sizable heat evolution at higher than nominal rates of strain. Typical stress–strain curves for an austenitic stainless steel with serrated yielding at 4 K are shown in Fig. 2.

4.3 Constant specimen temperature cannot be maintained at all times during tests in a liquid helium environment. Owing to adiabatic heat, the specimen temperature temporarily rises above that of the cryogen at 4 K during the discontinuous yielding events (see Fig. 2). This behavior varies with specimen size and testing speed, but altering the mechanical test variables cannot eliminate the periods of internal heating (3). Therefore, tensile property measurements of alloys in liquid helium (especially ultimate strength, elongation, and reduction of area) lack the full significance of property measurements at higher temperatures where discontinuous yielding does not occur.

4.4 At 4 K, the stress–strain behavior of a material during unstable plastic deformation depends on whether load control or displacement control is used (4). Crosshead displacement control is specified because the goal of this standard is material characterization by conventional methods. This limitation must be taken into account when data are used for structural design in applications when actual circumstances may approach load-controlled conditions.

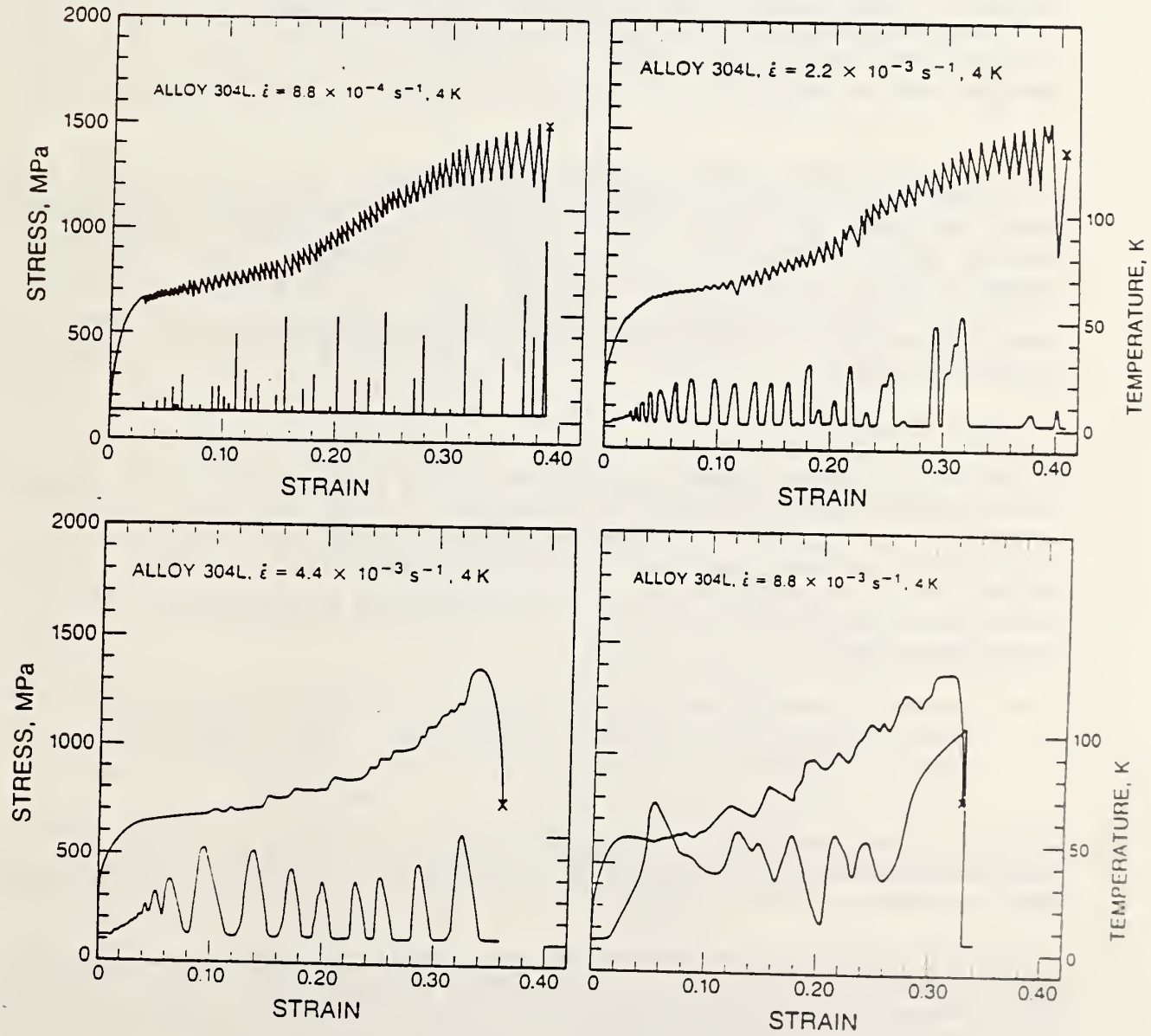

FIG 2 Engineering Stress–Strain Curves for an AISI 304L Austenitic Stainless Steel at 4 K

5. Apparatus

5.1 *Test Machines*—Machines used for tensile testing shall meet the requirements of Practices E 4 regarding verification of load accuracy. The machine compliance (displacement per unit load of the apparatus itself) shall be measured. This can be done by removing the specimen from the load train, or by replacing the specimen with a rigid block.

5.2 *System Design*—Alloy strengths often double or triple between room temperature and 4 K. For the same specimen geometry, higher loads must be applied to the cryostat, test specimen, load train members, and grips at cryogenic temperatures. For most conventional test machines, which have a maximum load capacity of 10 tons, it is recommended that the apparatus be designed to accommodate one of the small specimens cited in section 7.2.2 of this standard.

5.3 *Construction Materials*—Many construction materials, including the vast majority of ferritic steels, are brittle at 4 K. To resist embrittlement, the grips and other load-train members must be fabricated using strong, tough, cryogenic alloys. Austenitic stainless steels (AISI 304LN), maraging steels (200, 250, or 300 grades, with nickel plating to prevent rust), and extra-low-interstitial (ELI) grade titanium alloys (Ti–6Al–4V and Ti–5Al–2.5Sn) have been used, with proper design, grips, pull rods, and cryostat frames.

5.4 *Alignment*:

5.4.1 *Single-Specimen Apparatus*—To avoid bending strains in the specimen, proper system alignment is essential. For a conventional single-specimen test apparatus, the machine and grips shall be capable of loading a precisely machined specimen so that the maximum bending strain does not exceed 10% of the axial strain. This calculation is based on the strain readings taken at zero load and at the highest load for which the machine is being qualified.

NOTE 3—This requirement will minimize contributions from the test apparatus to the bending strain. Tests performed with a qualified apparatus may still vary in percent bending strain owing to small variations in the specimens.

5.4.2 *Multiple-Specimen Apparatus*—For this type of cryostat, the alignment depends on the type of fixtures used. The maximum bending strain shall be measured and reported.

5.4.3 The testing apparatus may be qualified by axiality measurements at room temperature and at 4 K. To perform axiality tests of the apparatus, the specimen form should be the same as that used during cryogenic tests, the specimen concentricity should be as nearly perfect as possible, and no plastic strains should occur in the reduced section. In some cases, this may necessitate the use of a relatively stiff, high-strength calibration specimen.

5.4.3.1 For round bar specimens, the maximum bending strain, as defined in 3.1.10, is calculated from the strains measured at three circumferential positions, at each of two different longitudinal positions. The strains are measured with three electrical-resistance strain gages equally spaced around the reduced section of the specimen. The two longitudinal positions should be as far apart as possible, but not closer than one diameter to a fillet.

5.4.3.2 For specimens of rectangular cross section, strain may be measured at the center of each of the four sides, or in the case of thin strips, near the outer edges of each of the two broad sides.

5.4.3.3 To eliminate the effect of specimen bias, repeat the axiality measurements with the specimen rotated 180 degrees, but with the grips and pull rods retained in their original positions. The maximum bending strain and strain at the specimen axis are then calculated as the average of the two readings at the same position relative to the machine.

5.4.4 *Strain Averaging Technique*—Nonaxiality of loading is usually sufficient to introduce errors in tensile tests at small strains when strain is measured on only one side of the specimen. To rectify this, two extensometers or strain gages may be attached to opposite sides of the specimen. The reported strain should be the average of the strains on both sides.

5.5 *Gripping Mechanisms*—The choice of gripping mechanism to be used at 4 K is influenced by specimen type. Any suitable mechanism described in Methods E 8 and E 8M may be used.

5.6 *Dimension-Measuring Devices*—Micrometers and devices used for measuring the dimensions of specimens shall be accurate and precise to at least one-half the smallest unit to which a given dimension must be measured.

5.7 *Cryostats and Support Apparatus*

5.7.1 *Cryostats*—A cryostat capable of retaining liquid helium is prerequisite. In general, cryostat load frames for existing test machines must be custom-built, but they may accommodate commercially available Dewars. The cryostat may employ adjustable load columns to facilitate alignment. Several practical designs, including turret-disc designs for multiple-specimen testing with a single cooling, are discussed in the literature (5–9).

5.7.2 *Dewars*—Stainless steel Dewars are recommended because they are safer than glass Dewars and less expensive than fiberglass Dewars. A single helium Dewar (see Fig. 1) is usually sufficient for short-term tests, but a double-Dewar arrangement, in which an outer Dewar of liquid nitrogen jackets the inner Dewar of liquid helium, is also possible.

5.7.3 *Ancillary Equipment*—Dewars and transfer lines for liquid helium must be vacuum insulated. Vacuum pumps, pressurized gas, and liquid nitrogen facilities are therefore required. After testing, the helium may be released to the atmosphere, recycled as a gas, or reliquefied. Recycling or reliquefaction requires large investments in purification and support systems.

5.8 *Temperature Maintenance and Liquid-Level Indicators:*

5.8.1 *Thermocouples*—The intended temperature of 4 K is ensured by maintaining a liquid helium environment. A thermocouple to measure the specimen temperature is not required for routine tests.

5.8.2 *Indicators*—Although a thermocouple attached to the specimen is not necessary, an indicator or meter is required to ensure that the specimen remains fully submerged for the duration of testing. On–off indicators of the carbon-resistor type may be used to verify that the liquid level always exceeds some reference point above the specimen, or the liquid level may be continuously monitored with superconducting wire sensors of appropriate lengths positioned vertically inside the cryostat.

5.9 *Strain Gages:*

5.9.1 *Selection*—Strain-gage films bonded directly to the specimen surface may be used to measure strain at 4 K (10). A satisfactory combination of gage active element, backing material, and bonding agent should be selected on the basis of experience and manufacturer's recommendations. One common choice is a Ni–Cr-alloy gage with a temperature-compensated active element (7,11).

5.9.2 *Characteristics*—Strain gages are typically wired to a dummy bridge using a three-wire temperature-compensating hookup, like that shown in Fig. 3. The gage resistance is typically 120 or 350 Ω. A low excitation voltage of about 1 to 2 V is recommended at 4 K to reduce Joule heating. Typical full-scale operating ranges are 1% at room temperature and 2% at 4 K.

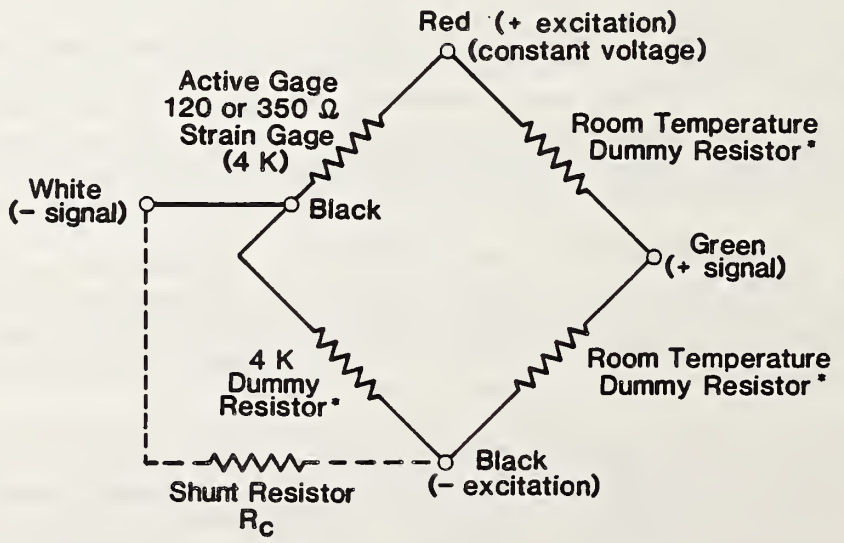

FIG 3 Method of Strain-Gage Wiring for Cryogenic Tests

5.9.3 *Calibration*—Strain-gage calibration at room temperature requires calibration of the electronics to changes in resistance. Calibration at 4 K requires consideration of the temperature dependence of the resistance in the electronic calibration. Gage factors as a function of temperature are provided by the manufacturers and in published research.

5.10 *Clip-Gage Extensometers:*

5.10.1 *Types*—Detachable clip-gage extensometers for use at 4 K may be built or purchased. An example is the beam gage, which uses four strain-gage films bonded in a Wheatstone bridge arrangement (11). Extension within the specimen gage length is sensed by the extensometer, which is clipped to retaining pins that are fixed to the specimen reduced section.

5.10.2 *Characteristics*—To measure the 0.2% offset yield strength, a Class B-2 extensometer, as identified in Method E 83, may be used. The extensometer shall meet the sensitivity and accuracy requirements of Method E 83 and shall be tested to ensure accuracy at 4 K. Whenever possible, the extensometer should be mounted directly to the specimen reduced section.

5.10.3 *Calibration*—Extensometers should be calibrated at room temperature and at 4 K with a suitable device. For calibrations at 4 K, a micrometer with vertical extension tubes can be used with the extensometer(s) mounted at the lower end and immersed in liquid helium. Once the calibration is known and proven to be accurate, linear, and reproducible, room-temperature checks may be performed prior to each test series for indirect verification of the calibration at 4 K. Direct calibration at 4 K, however, must be performed periodically, when damage is suspected or repairs have been made.

5.11 *Capacitance Extensometers*—Extensometers that use capacitance measurement to monitor strain may be used (10). The type with overlapping concentric cylinders has an extended strain range, an output that is linear with displacement, and an adjustable sensitivity. The type with parallel plates has high sensitivity, but the output must be compensated for the hyperbolic dependence of the capacitance on displacement.

6. Sampling

6.1 Samples for tensile testing should be taken from the material in its final condition to ensure that the properties measured are representative of the end product. Allowance should be made for any superficial effects introduced by cutting operations.

6.2 Specimens should be cut from locations thought to be most representative of the stock material, realizing that test results for specimens taken from selected locations of a part or material may not be representative of the whole. The conventional locations should normally be used:

6.2.1 For products 40 mm or less in thickness, diameter, or distance between flats, the location should be at the center.

6.2.2 For products over 40 mm in thickness, diameter, or distance between flats, the location should be midway from the surface to the center.

6.3 The choice of specimen size and shape should be based on the requirements necessary to obtain representative samples of the material, and on test-machine load capability (section 5.2).

6.4 The orientation of the specimen axis relative to the principal working directions of the stock shall be specified using the notation in section 4 of Method A 370.

7. Test Specimens

7.1 *General*:

7.1.1 *Types and Specifications*—Any specimen configuration cited in Methods E 8 or E 8M may be used. The specifications for dimensions, tolerances, and surface finish are stated in sections 6.1 through 6.17 of those standards.

7.1.2 *Size*—Specimens from sheet or wire products having relatively small cross-sectional areas can be tested within the load limits of conventional apparatus. Specimens from thick plate or bar products, however, may need to be machined to a reduced cross-sectional area so the load capacity of the machine is not exceeded.

7.2 *Round Bar Specimens*:

7.2.1 *Standard Room-Temperature Specimens*—A 12.5-mm (0.5-in) diameter round bar specimen is the standard configuration for room-temperature tests according to Methods E 8 and E 8M. Specimens of such strong alloys, however, require excessive loads at 4 K. For example, 210 kN is required to test typical AISI 304LN steel at 4 K, whereas 100 kN or 10 tons is the limit for most machines.

7.2.2 *Standard 4-K Specimens*—To meet the load limitations of conventional test machines, the round bar specimens in sections 7.2.2.1 and 7.2.2.2 are recommended as standard for 4-K tests. The required dimensions and tolerances for these specimens are given in Table 1. Threaded or shouldered ends are common for gripping these specimens, and the requirement of section 5.4.1 can be met by precise machining.

7.2.2.1 *Standard, small metric specimens*. These specimens have a 7-mm diameter and a gage-length-to-diameter ratio of 5:1.

7.2.2.2 *Standard, small U.S. customary specimens*. These specimens have a 6.25-mm (0.25-in) diameter and a gage-length-to-diameter ratio of 4:1.

7.2.3 *Alternatives*—If the 4-K standard specimens recommended above are not appropriate, other sizes may be selected following the guidelines of Methods E 8 and E 8M. The proportions of such specimens should be similar to those of the standard specimens (see Fig. 4 of this standard and Fig. 8 of Methods E 8 and E 8M).

TABLE 1 Standard Specimens for Room-Temperature Tests and Recommended Proportionally Reduced, Standard Small Specimens for 4-K Tests[1]

(a)

Metric Versions G/D ratio = 5 (dimensions, mm)	Standard Specimen (room temperature)	Standard Small Specimen (4 K)
Nominal Diameter	12.5	7
G, gage length	62.5 ± 0.1	35 ± 0.1
D, diameter	12.5 ± 0.1	7 ± 0.1
R, fillet radius	10	7
A, reduced section	75	42

(b)

U.S. Customary Versions G/D ratio = 4 (dimensions, in)	Standard Specimen (room temperature)	Standard Small Specimen (4 K)
Nominal Diameter	0.5	0.25
G, gage length	2.000 ± 0.005	1.000 ± 0.005
D, diameter	0.500 ± 0.010	0.250 ± 0.005
R, fillet radius	0.375	0.1875
A, reduced section	2.25	1.25

[1]See also the notes to Fig. 8 in Methods E 8 and E 8M.

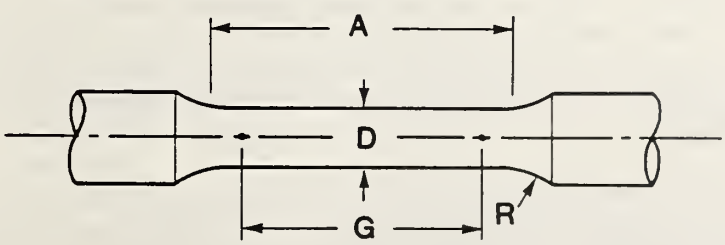

FIG 4 Round Bar Specimen Configuration (see Table 1)

7.2.4 *Subsize specimens*—Special care in fabrication and testing is required for specimens with diameters less than 6 mm. As the specimen size is reduced, factors such as machining, surface finish, alignment, and the number of grains per cross section are of increasing importance.

8. Procedures

8.1 *Marking and Measuring the Test Specimen:*

8.1.1 *Gage Length*—Gage length marks should be lightly punched, scribed, or inked at appropriate locations on the reduced section of the specimen, which is the conventional method. The gage length should normally be five times the diameter for metric specimens or four times the diameter for U.S. customary specimens. If another gage length is used, it must be described in the report. Measure the gage length to the nearest 0.05 mm.

> NOTE 4—For metals of low ductility, gage marks punched or scribed on the reduced section may induce failure at those locations due to stress concentrations. To avoid this, it may be possible to coat the reduced section with layout ink, and then mark the gage length by rotating the specimen in a jig with knife edges scraping off the ink at the appropriate intervals. Alternatively, gage marks may be placed on the specimen shoulders, or the overall length of the specimen may be measured.

8.1.2 *Reduced Section*—Measure the length of the reduced section and the adjusted length of the reduced section, if applicable, to the nearest 0.05 mm.

8.1.3 *Cross Section*—Measure the cross-sectional area of the reduced section as specified in section 7.1.1 of Methods E 8 and E 8M.

8.2 *Specimen Installation*—Install the specimen in the cryostat, leaving sufficient slack for instrumentation wires so they will not be stretched or crimped during positioning of the Dewar and subsequent testing.

8.3 *Seating and Alignment*—If the gripping fixture involves loose-fitting components, such as spherically seated bearings, prevent friction or mismatch of the bearing surfaces at 4 K by first checking the seating and alignment at room temperature. During this process of alignment, the applied loads should be kept below one-third of the proportional limit of the test material.

8.4 *Cooling Procedure*—Remove any moisture from the apparatus prior to cooling by drying it thoroughly with a pressurized air jet or heat gun. Ice can block cryogenic transfer lines or cause erratic loading behavior if it forms between various parts of the specimen, clip gage, and load train.

Next, position the Dewar and precool the apparatus to 77 K by transferring liquid nitrogen into the cryostat. After attaining equilibrium at 77 K, remove all the liquid nitrogen from the cryostat, and transfer liquid helium into the cryostat until the specimen and grips are fully submerged. Testing may begin after the system has reached thermal equilibrium at 4 K. The specimen must remain fully submerged at all times during the test.

NOTE 5—The heat-transfer characteristics of gaseous helium are inferior to those of liquid helium; therefore, a liquid helium environment is required to minimize specimen heating effects during discontinuous yielding.

8.5 *Testing Speed:*

8.5.1 *Rate Control*—Owing to adiabatic heating, tensile property measurements at 4 K can be significantly affected by the testing speed. Therefore, the test procedure must include a means of measuring and controlling the rate of crosshead motion. A nominal strain rate must be specified, since the actual rate cannot be precisely controlled or maintained when discontinuous yielding occurs. The nominal strain rate is calculated by dividing the crosshead rate by the length of the reduced section. Alternatively, a pacing or indicating device may be used to monitor the strain rate or an average strain rate may be determined by observing the time required to effect a known increment of strain.

8.5.2 *Rate Limit*—The nominal strain rate at any time during the test shall not exceed 1×10^{-3} s^{-1}. Higher rates may cause excessive specimen temperature rises and therefore are not satisfactory for determining the acceptability of materials.

8.5.3 *Rate Change*—The strain at which discontinuous yielding begins usually increases with decreasing strain rate. If the first serration for a given material occurs near 0.2% plastic strain, it may be desirable to reduce the speed to prevent interference in the measurement of the yield strength (see Fig. 5). Then, a relatively low strain rate may be used to determine the yield strength, followed by a higher strain rate to complete the test. Any convenient crosshead speed may be used up to a stress of one-half the yield strength; after that, the crosshead speed must be such that the nominal strain rate does not exceed the 1×10^{-3} s^{-1} limit.

8.6 *Measurement of Mechanical Properties:*

8.6.1 *Load-Extension-Curve Method*—To measure the yield strength, a record of load versus extension must be obtained, up to at least 0.2% plastic strain. The use of a strain measurement device for autographic recording is recommended.

Measure the yield strength via the 0.2% offset method, following Methods E 8 or E 8M, section 7.3.1. If the 0.2% offset line intersects the curve at a load drop owing to discontinuous yielding, then report the highest stress prior to that load drop as the yield strength.

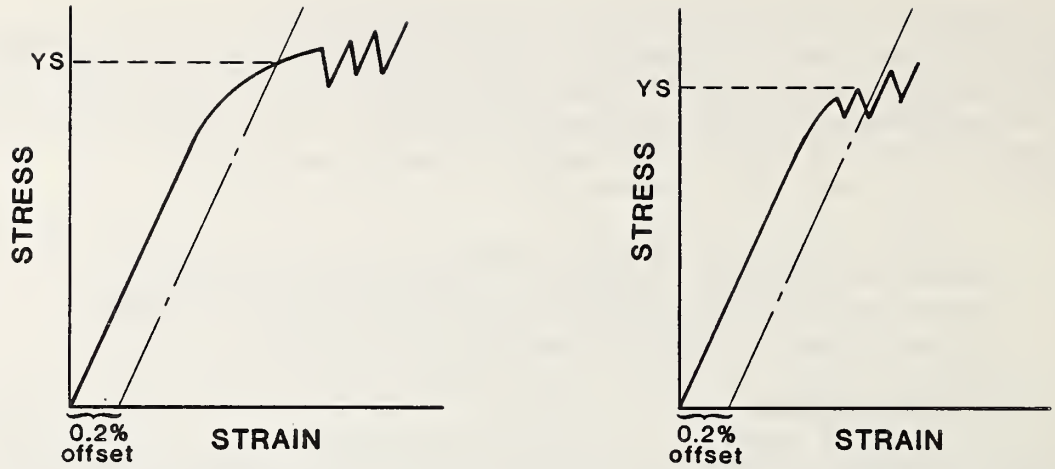

A – Serrations after 0.2% strain B – Serrations before 0.2% strain

FIG 5 Stress–Strain Diagram for Determination of Yield Strength by the Offset Method.

8.6.2 *Load–Time-Curve Method*—Yield strength measurements based on a 0.2% offset procedure applied to load-versus-time curves at 4 K are generally not recommended, but may be used for commercial test purposes with the agreement of all parties involved. If this method is used, it should be stated clearly in the report.

NOTE 6—Load–time curves for tests at 4 K are typically nonlinear at the start and less regular than load–extension curves. Also, the effective modulus of a thermally efficient load train may be low and dependent on the liquid helium level and the degree of temperature stabilization achieved throughout the system in the temperature range 295 to 4 K. As a result, yield strength data from load–time curves may be less accurate than those of the recommended method.

8.6.3 *Tensile Strength*—Calculate the tensile strength by dividing the maximum load carried by the specimen during the tensile test by the original cross-sectional area of the specimen.

8.6.4 *Elongation*—Calculate the percentage increase of elongation according to Methods E 8 or E 8M, section 7.6.

8.6.5 *Reduction of Area*—Calculate the percentage of reduction of area according to Methods E 8 or E 8M, section 7.7.

8.6.6 *Rounding Reported Test Data*—Round-off the calculated numerical test results according to Methods E 8 or E 8M, section 7.8.

8.6.7 *Replacement Specimens*—If necessary, discard any invalid data and test replacement specimens as per Methods E 8 or E 8M, section 7.9.

9. Report

9.1 *General:*

9.1.1 *Material Characterization*—Describe the test material, including manufacturing, processing, and metallurgical information.

9.1.2 *Specimen Characterization*—Describe the specimen location and its orientation relative to the principal working directions of the stock. Also report the specimen dimensions, including the cross-section dimensions, the fillet radius, the reduced section length, and the adjusted length of the reduced section (if used).

9.1.3 *Strain Rate*—Report the crosshead speed and the nominal strain rate during yielding and after yielding, if a rate change is used.

9.1.4 *Mechanical Property Measurements*—Report the yield strength, the ultimate strength, and the method of offset yield strength determination. Include the method of extension measurement and the location of extensometer attachment, if used. Also report the tensile elongation and its method of calculation, the gage-length-to-diameter ratio for round specimens, and the reduction of area.

9.2 *Optional Data*—Report any optional data, such as measurements of Young's modulus at 4 K, the mechanical properties at room temperature, and the average grain size of the test material. Report the compliance of the test machine with its cryostat.

9.3 *Replicate Tests*—If replicate specimens are tested, report the number of tests, the average values of all mechanical property measurements, and a measure of scatter.

9.4 *Subsize Specimens*—If subsize specimens are tested, state any precautions taken with respect to specimen machining, surface condition, or alignment, and report the grain size of the test material.

9.5 *Anomalies*—Report any anomalies in material behavior, test records, or failure type and location.

10. Precision and Bias

10.1 *Precision*—The precision of these methods is being established by a series of interlaboratory tests.

10.2 *Bias*—The bias of these methods includes quantitative estimates of uncertainties of the dimension-measuring devices, the calibration of test equipment, and the skill of the operators. At present, bias statements should be limited to the documented performance of individual laboratories.

REFERENCES

(1) *Cryogenics Safety Manual*—A Guide to Good Practice, 2nd Ed., Mechanical Engineering Publications, London, 1982.

(2) Basinski, Z. S., "The Instability of Plastic Flow of Metals at Very Low Temperatures," *Proceedings of the Royal Society*, Vol. A240, 1957, pp. 229–242.

(3) Ogata, T., Ishikawa, K., and Nagai, K., "Effects of Strain Rate on the Tensile Behavior of Stainless Steels, Copper, and an Aluminum Alloy at Cryogenic Temperatures," *Tetsu-to-Hagane*, Vol. 71, No. 10, 1985, pp. 1390-1397.

(4) Ogata, T. and Ishikawa, K. "Time-dependent Deformation of Austenitic Stainless Steels at Cryogenic Temperatures," *Cryogenics*, Vol. 26, 1986, pp. 365–369.

(5) Schwartzberg, F. R., "Mechanical Property Testing Techniques for the Cryogenic Temperature Range," in: *Advances in Cryogenic Engineering*, Vol. 8, Plenum Press, New York, 1963, pp. 608–623.

(6) Evans, D., Simmonds, G. E., and Stapleton, G. B., "Improved Facility for Determining Mechanical Properties of Materials in Liquid Helium," in: *Proceedings, Fourth International Cryogenic Engineering Conference*, IPC Science and Technology Press, Guildford, Surrey, England, 1972, pp. 331–337.

(7) Hartwig, G. and Wuchner, F., "Low Temperature Mechanical Testing Machine," *Review of Scientific Instruments*, Vol. 46, 1975, pp. 481–485.

(8) Novikov, N. V. "Mechanical Property Measurement Techniques of Structural Materials at Cryogenic Temperatures," in: *Advances in Cryogenic Engineering*, Vol. 22, Plenum Press, New York, 1977, pp. 113–118.

(9) Horiuchi, T., Shimada, M., Fukutsuka, T., and Tokuda, S., "Design and Construction of an Apparatus for Testing Materials at Cryogenic Temperatures," in: *Proceedings, Fifth International Cryogenic Engineering Conference*, IPC Science and Technology Press, Guildford, Surrey, England, 1977, pp. 465–468.

(10) Sparks, L. L., "Temperature, Strain, and Magnetic Field Measurements," in: *Materials at Low Temperatures*, R. P. Reed and A. F. Clark, eds., American Society for Metals, Metals Park, Ohio, 1983.

(11) Read, D. T. and Tobler, R. L., "Mechanical Property Measurements at Low Temperatures," in: *Advances in Cryogenic Engineering—Materials*, Vol. 28, Plenum Press, New York, 1982, pp. 17–28.

NBS-114A (REV. 2-8C)

U.S. DEPT. OF COMM. BIBLIOGRAPHIC DATA SHEET (See instructions)	1. PUBLICATION OR REPORT NO. NBSIR 88-3082	2. Performing Organ. Report No.	3. Publication Date May 1988

4. TITLE AND SUBTITLE

Materials Studies for Magnetic Fusion Energy Applications at Low Temperatures — XI

5. AUTHOR(S)

R. P. Reed, Editor

6. PERFORMING ORGANIZATION (If joint or other than NBS, see instructions)

NATIONAL BUREAU OF STANDARDS
DEPARTMENT OF COMMERCE
WASHINGTON, D.C. 20234

7. Contract/Grant No.

8. Type of Report & Period Covered

9. SPONSORING ORGANIZATION NAME AND COMPLETE ADDRESS (Street, City, State, ZIP)

Department of Energy
Office of Fusion Energy
Washington, DC 20545

10. SUPPLEMENTARY NOTES

Previous reports in this series: NBSIR 87-3067, NBSIR 86-3050, NBSIR 85-3025, NBSIR 84-3000, NBSIR 83-1690, NBSIR 82-1667, NBSIR 81-1645, NBSIR 80-1627, NBSIR 79-1609, NBSIR 78-884

☐ Document describes a computer program; SF-185, FIPS Software Summary, is attached.

11. ABSTRACT (A 200-word or less factual summary of most significant information. If document includes a significant bibliography or literature survey, mention it here)

This report contains the results of a research program to determine the properties of materials that may be used in cryogenic structures for the superconducting magnets of magnetic fusion energy power plants and prototypes. Its purpose is to facilitate their design and development. The program was developed jointly by the staffs of the National Bureau of Standards and the Office of Fusion Energy of the Department of Energy; it is managed by NBS and sponsored by DOE. Research is conducted at NBS and at other laboratories through subcontracts with NBS.

Research results for 1987 are presented in technical papers under five headings that reflect the main program areas: Structural Alloys, Welding, Nonmetallics, Technology Transfer, and United States-Japan Development of Test Standards. Objectives and research highlights are summarized in the introduction to each program area.

12. KEY WORDS (Six to twelve entries; alphabetical order; capitalize only proper names; and separate key words by semicolons)

austenitic steels; composites; cryogenic properties; elastic properties; low temperatures; mechanical properties; nonmetallics; stainless steels; structural alloys; welds

13. AVAILABILITY

☒ Unlimited

☐ For Official Distribution. Do Not Release to NTIS

☐ Order From Superintendent of Documents, U.S. Government Printing Office, Washington, D.C. 20402.

☒ Order From National Technical Information Service (NTIS), Springfield, VA. 22161

14. NO. OF PRINTED PAGES 388

15. Price $30.95